



Universiteit
Leiden
The Netherlands

Alkynes in covalent enzyme inhibitors: down the kinetic rabbit hole

Mons, E.

Citation

Mons, E. (2024, April 11). *Alkynes in covalent enzyme inhibitors: down the kinetic rabbit hole*. Retrieved from <https://hdl.handle.net/1887/3734191>

Version: Publisher's Version

[Licence agreement concerning inclusion of doctoral thesis in the Institutional Repository of the University of Leiden](#)

License: <https://hdl.handle.net/1887/3734191>

Note: To cite this publication please use the final published version (if applicable).

Alkynes in Covalent Enzyme Inhibitors

— Down the Kinetic Rabbit Hole —



Alkynes in Covalent Enzyme Inhibitors: Down the Kinetic Rabbit Hole

Elma Mons

The research described in this dissertation was performed at the Leiden University Medical Center (Department of Cell & Chemical Biology, Leiden, the Netherlands) and at the Netherlands Cancer Institute (Department of Cell Biology II, Amsterdam, the Netherlands). The work was financially supported by NWO VIDI (724.013.002) and NWO Oncodrugs (731.014.205).

ISBN: 978-94-6496-048-8

Design cover and inside layout: Elma Mons
Font '*Magical Science EM*': Elma Mons

Financial support for printing this thesis: The Netherlands Cancer Institute and Leiden University
Printed by: Gildeprint

Copyright © 2024 by Elma Mons. All rights reserved. No part of this publication may be reproduced or transmitted in any form or by any means without prior written permission of the author, or where appropriate, of the publisher of the articles.

Alkynes in Covalent Enzyme Inhibitors: Down the Kinetic Rabbit Hole

Proefschrift

ter verkrijging van
de graad van doctor aan de Universiteit Leiden,
op gezag van rector magnificus prof.dr.ir. H. Bijl,
volgens besluit van het college voor promoties
te verdedigen op donderdag 11 april 2024

klokke 15:00 uur

door

Maria Wilhelmina Elisabeth Mons
geboren te Almere
in 1989

Promotoren

prof. dr. H. Ovaa

prof. dr. J.J.C. Neefjes

Co-promotoren

dr. M.P.C. Mulder

dr. R.Q. Kim

Promotiecommissie

prof. dr. A.C.O. Vertegaal

prof. dr. L.H. Heitman – LEI, Leiden

prof. dr. S.I. van Kasteren – LEI, Leiden

prof. dr. M. van der Stelt – LEI, Leiden

prof. dr. J.H. van Maarseveen – UvA, Amsterdam

Wandering another path
often leads us where we need to go



Once Upon a Time [TV Series] – Season 7, Episode 15



Table of Contents

Prologue	Abbreviations, Acronyms, and Symbols	8
Chapter 1	<i>Once Upon a Time: Serendipitous Discovery of Alkynes as Electrophiles</i>	11
Chapter 2	Technologies for Direct Detection of Covalent Protein–Drug Adducts	33
Chapter 3	Kinetic Evaluation of Covalent Inhibition in Enzymatic Assays	83
Chapter 4	Nonactivated Alkynes in Irreversible Covalent Cathepsin K Inhibitors	167
Chapter 5	Covalent EGFR Inhibitors With a Nonactivated Alkyne Warhead	207
Chapter 6	The Versatility of Substituted Propargyl Warheads in Ub-ABPs	243
Chapter 7	<i>Happily Ever After: A Summary and Discussion</i>	291
Epilogue	Nederlandse Samenvatting	312
	Curriculum Vitae	314
	List of Publications	315
	Acknowledgements	316

Abbreviations, Acronyms, and Symbols

Ab	Antibody	EDTA	Ethylenediaminetetraacetic acid
ABP	Activity-Based Probe	EGF	Epidermal Growth Factor
ABPP	Activity-Based Protein Profiling	EGFR	Epidermal Growth Factor Receptor
Ac-	Acetyl	eq	Equivalents
ADME	Absorption, Distribution, Metabolism, and Excretion	ESI	Electrospray Ionization
AMC	7-amino-4-methylcoumarin	Et-	Ethyl
APT	Attached Proton Test (NMR)	EWG	Electron-Withdrawing Group
aq	Aqueous	FA	Formic acid
ATP	Adenosine Triphosphate	FCC	Flash Column Chromatography
AU/A.U.	Arbitrary Units	FCS	Fetal Calf Serum
BME	β -mercaptoethanol	FDA	Food and Drug Administration USA
Boc-	<i>tert</i> -butyloxycarbonyl	FI	Fluorescence Intensity
BODIPY	Fluorinated Boron-Dipyrromethene	FL	Full-Length
BSA	Bovine Serum Albumin	Fmoc-	9-fluorenylmethyloxycarbonyl
calc.	Calculated	FP	Fluorescence Polarization
CatK	Cathepsin K	FRET	Fluorescence Resonance Energy Transfer
CD	Catalytic Domain	GSH	Glutathione
ChEF	Chelation-Enhanced Fluorescence	GST-	Glutathione S-Transferase (<i>protein tag</i>)
conc.	Concentration	HA-	Human Influenza Hemagglutinin (<i>protein tag</i>)
cryo-EM	Cryogenic Electron Microscopy	HATU	Hexafluorophosphate azabenzotriazole tetramethyl uronium
CSox	Cysteine Modified with a Sox fluorophore	HCV	Hepatitis C Virus
CuAAC	Copper-Catalyzed Alkyne–Azide Cycloaddition	HEPES	4-(2-hydroxyethyl)-1-piperazineethanesulfonic acid (<i>buffer</i>)
Cy5	Cyanine-5 (<i>fluorophore</i>)	HFIP	1,1,1,3,3,3-hexafluoroisopropylalcohol
CYP	Cytochrome P450	His-	Polyhistidine (<i>protein tag</i>)
CysDUB	Cysteine Deubiquitinating Enzyme	HRP	Horseradish Peroxidase
Da	Dalton (<i>mass unit</i>)	HRMS	High-Resolution Mass Spectrometry
DCE	1,2-dichloroethane (<i>solvent</i>)	HTS	High-Throughput Screening
DCM	Dichloromethane (<i>solvent</i>)	IAC	Iodoacetamide
DIAD	Diisopropyl azodicarboxylate	IEDDA	Inverse Electron-Demand Diels-Alder Reaction
DIC	<i>N,N</i> '-diisopropylcarbodiimide	iPr-	<i>iso</i> -propyl
DIPEA	<i>N,N</i> -diisopropylethylamine	IRREV	Irreversible
diUb	Diubiquitin	kPCA	Kinetic Probe Competition Assay
DMAc	<i>N,N</i> -dimethylacetamide (<i>solvent</i>)	LC	Liquid Chromatography
DME	1,2-dimethoxyethane (<i>solvent</i>)	M	mol/L (<i>concentration unit</i>)
DMF	Dimethylformamide (<i>solvent</i>)	M-CSF	Macrophage Colony Stimulating Factor
DMSO	Dimethyl sulfoxide (<i>solvent</i>)	Me-	Methyl
DODt	3,6-dioxa-1,8-octanedithiol	MES	2-(<i>N</i> -morpholino)ethanesulfonic acid (<i>buffer</i>)
DRC	Dose-Response Curve	MMTS	<i>S</i> -methyl methanethiosulfonate
DTT	1,4-dithiothreitol	MOPS	3-(<i>N</i> -morpholino)propanesulfonic acid (<i>buffer</i>)
DUB	Deubiquitinating Enzyme	M ^{pro}	Viral Main Protease
E1	Ubiquitin Activating Enzyme	MS	Mass Spectrometry
E2	Ubiquitin Conjugating Enzyme	Ms-	Mesyl/methanesulfonyl
E3	Ubiquitin Ligase	NBS	Non-Binding Surface
ECD	Extracellular Domain	NBS	<i>N</i> -bromosuccinimide
EDC	<i>N</i> -ethyl- <i>N'</i> -(3-dimethylamino-propyl) carbodiimide	NEM	<i>N</i> -ethylmaleimide
EDG	Electron-Donating Group		

NMM	<i>N</i> -methylmorpholine	SAR	Structure-Activity Relationship
NMP	<i>N</i> -methyl-2-pyrrolidone (<i>solvent</i>)	SARS-CoV-2	Severe Acute Respiratory Syndrome Coronavirus 2
NMR	Nuclear Magnetic Resonance	SD	Standard Deviation
NSCLC	Non-Small Cell Lung Carcinoma	SDS-PAGE	Sodium Dodecyl Sulfate Poly-Acrylamide Gel Electrophoresis
OC	Osteoclast	SILAC	Stable-Isotope Labeling by Amino Acids in Cell Culture
ODN	Odanacatib	Sox	Sulfonamido-oxine (<i>fluorophore</i>)
PBMC	Peripheral Blood Mononuclear Cell	SUMO	Small Ubiquitin-like Modifier
PBS	Phosphate-Buffered Saline (<i>buffer</i>)	tBu-	<i>tert</i> -butyl
PD	Pharmacodynamics	TCEP	Tris(2-carboxyethyl)phosphine
PDB	Protein Data Bank	TCI	Targeted Covalent Inhibitor
pEGFR	Phosphorylated EGFR	TFA	Trifluoroacetic acid
Phth-	Phthalimide	THF	Tetrahydrofuran (<i>solvent</i>)
PK	Pharmacokinetics	TIC	Total Ion Count
ppm	Parts Per Million (<i>NMR unit</i>)	TKD	Tyrosine Kinase Domain
prepHPLC	Preparative HPLC	TKI	Targeted Kinase Inhibitor
Prg	Propargyl (<i>warhead</i>)	TLC	Thin Layer Chromatography
PROTAC	Proteolysis-Targeting Chimera	TMEDA	Tetramethylethylenediamine
Prp	Propyl (<i>warhead</i>)	TAMRA/TMR	Tetramethylrhodamine
PTM	Post-Translational Modification	TMS-	Trimethylsilyl
pY	Phosphorylated Tyrosine	TRAcP	Tartrate-Resistant Acid Phosphatase
PyBOP	Benzotriazol-1-yloxytritypyrrolidino-phosphonium hexafluorophosphate	TR-FRET	Time-Resolved Fluorescence Resonance Energy Transfer
qABP	Quenched Fluorescent ABP	Tris	Tris(hydroxymethyl)-aminomethane (<i>buffer</i>)
quant	Quantitative yield	Tween20	Polyoxyethylene (20) Sorbitan Monolaurate
RANKL	Receptor Activator of Nuclear Factor κ B Ligand	Ub	Ubiquitin
REV	Reversible	Ubl	Ubiquitin-Like Modifier
Rf	Retention Factor (<i>TLC</i>)	UPLC	Ultra Performance Liquid Chromatography
RFU	Relative Fluorescence Unit	UV	Ultraviolet
Rho-	5-carboxy-Rhodamine110 (<i>fluorophore</i>)	VME	Vinyl Methyl Ester (<i>warhead</i>)
RP-HPLC	Reversed-Phase High-Performance Liquid Chromatography	VS	Vinyl Sulfone (<i>warhead</i>)
Rt	Retention Time (<i>HPLC, LC-MS</i>)	WB	Western Blotting
rt	Room Temperature	WHO	World Health Organization
RTK	Receptor Tyrosine Kinase	WT/ ^{WT}	Wild-Type

Amino Acids

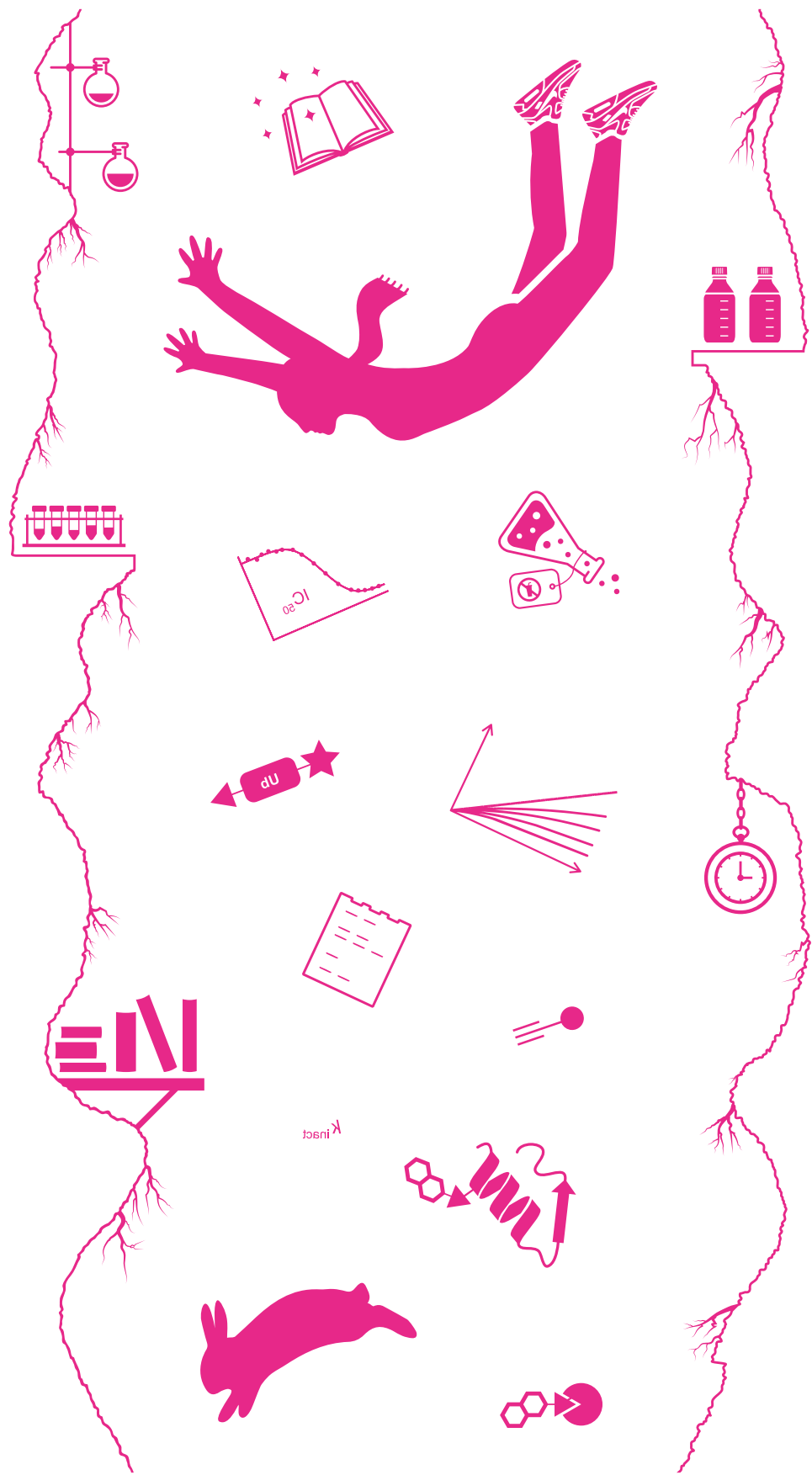
Ala	A	Alanine
Arg	R	Arginine
Cys	C	Cysteine
Gly	G	Glycine
Lys	K	Lysine
Met	M	Methionine
Nle	—	Norleucine
Phe	F	Phenylalanine
Ser	S	Serine
Tyr	Y	Tyrosine

one- and three-letter abbreviations of amino acids according to IUPAC recommendations.

Symbols

IC_{50}	[Inhibitor] resulting in 50% inhibition
K_D	Equilibrium Dissociation Constant
K_i	Noncovalent Inhibition Constant
K_i	Covalent Inactivation Constant (<i>2-step IRREV</i>)
K_i^*	Steady-State Inhibition Constant
K_M	Michaelis Constant (<i>enzyme</i>)
k_{cat}	Substrate Turnover Number (<i>enzyme</i>)
k_{inact}	Maximum Rate of Inactivation (<i>2-step IRREV</i>)
k_{obs}	Observed Reaction Rate
$\lambda_{ex}/\lambda_{em}$	Emission/Excitation wavelength
$t^{1/2}$	Half-life

Full list of symbols can be found in **Chapter 3**



Chapter 1



Once Upon a Time:
Serendipitous Discovery of
Alkynes as Electrophiles

1. Resurgence of Covalent Drugs

Enzymes are involved in all biochemical processes, ranging from (proteolytic) degradation of macromolecules to the installation and removal of post-translational modifications (PTMs). PTMs can affect protein affinity and/or function, but can also function as 'messenger tags' that facilitate communication among cellular components. Receptor kinases phosphorylate downstream effector proteins to relay extracellular growth signals, initiating a signaling cascade that affects gene expression by relocation of transcription factors to the nucleus, effectively enabling the cell to respond to changes in the extracellular environment.¹ This process is tightly regulated by phosphatases that reverse phosphorylation.² Histone methyltransferases (HMTs) and histone acetyltransferases (HATs) respectively methylate or acetylate histones thus affecting gene transcription. These epigenetic alterations are reversed by histone demethylases (HDMs) and histone deacetylases (HDACs).³⁻⁴ Ligases install ubiquitin (Ub) chains onto (misfolded) proteins to mark them for proteasomal degradation, which is counteracted by proteases that cleave Ub from the protein.⁵ Interference with enzymatic activity has proven to be a viable drug development strategy as the pathophysiology of many diseases is associated with enzyme deficiency or overexpression, aberrant activity, and/or incorrect enzyme function.⁶⁻⁷ Enzyme inhibitors have been approved for treatment of various pathological conditions including metabolic and degenerative diseases, viral/bacterial infections, cancer, and inflammation. Small molecules that interfere with enzyme activity have always been popular, but the past decade marked the rise of highly effective targeted covalent inhibitors (TCIs) – designed to interact with their target through the formation of a covalent adduct.⁸

Conventional small molecule inhibitors (<500 Da) interfere with protein function as long as they are bound to their protein target.^{6, 9-10} The noncovalent interactions with the protein target are reversible, and protein function will be regained when unbound protein is released upon inhibitor dissociation. The drug target engagement can be prolonged by covalent modifiers that harbor a – strategically placed – electrophilic moiety (commonly referred to as the 'warhead') to form a covalent bond with a nucleophilic amino acid residue in the protein (e.g. cysteine, serine, threonine).^{8, 11-12} The resulting protein-drug adduct is linked through a(n) (ir)reversible covalent bond that is much stronger than typical noncovalent interactions. Irreversible inhibition – typically defined as a drug residence time exceeding the normal lifespan of the target protein^{7, 13} – has clear therapeutic advantages: systemic drug exposure is minimized as protein function can only be restored by *de novo* protein synthesis. Consequently, therapeutic effect is maintained long after the compound has been cleared from circulation (PK-PD decoupling).^{10-11, 14-15}

Irreversible covalent modifiers were actively avoided in pharmaceutical drug development programs: the ability to covalently modify the target protein raised concerns about promiscuous reactivity with off-target proteins.^{8, 16-19} Reactive electrophilic moieties have been implied as a risk factor for idiosyncratic adverse drug reactions (IADRs) and hepatotoxicity,²⁰⁻²⁵ though it must be mentioned that the majority of this research was based on the unintentional formation of highly reactive, highly electrophilic metabolites.²⁶ The complex underlying mechanism of IADRs – the possibly life-threatening toxicity affecting a small subset of susceptible patients – is largely unclear but may be immune-mediated, making them difficult to predict.^{23, 27-29}

Furthermore, even if the covalent inhibitor is perfectly target-selective, covalent modification may lead to hapten formation – immune activation by a covalently modified protein (fragment) that, in case of an irreversible binding mode, persists after protein degradation.²⁹⁻³⁰ Reversible covalent drugs were perceived as a safer alternative,³¹⁻³³ as they will eventually dissociate from their protein target and have a lower propensity to form a proteolysis-stable hapten.

From avoided liabilities and accidental discoveries...

Approved drugs that act through irreversible covalent modification of their (protein) target are more prevalent than would be expected based on the efforts of pharmaceutical companies to eliminate compounds with potentially reactive functionalities.^{8, 12} Ironically, there are many examples of effective covalent drugs with satisfying toxicity profiles among the most-prescribed drugs worldwide,¹¹ and many can be found on the WHO (World Health Organization) Essential Medicines Lists.³⁴ Their covalent mechanism of action was often discovered after their clinical utility had been well established, typically years after their first synthesis and sometimes long after they hit the market (Figure 1).³⁵ The most well-known unintended covalent inhibitor is **acetylsalicylic acid** (aspirin), the pharmaceutically active component in ancient medicinal consumption of willow bark.³⁶ Marketed in 1899 as a pain reliever and anti-inflammatory agent, aspirin is without doubt the most used drug worldwide: approximately 40,000 tons are produced annually – good for >111 billion tablets of 325 mg. Its mechanism of action remained elusive until the 1970s,³⁷⁻³⁸ when aspirin and other non-steroidal anti-inflammatory drugs (NSAIDs) were found to block biosynthetic production of prostaglandins causing inflammation, a discovery awarded with the 1982 Nobel Prize in Physiology or Medicine. The exact molecular mechanism was elucidated decades after its first clinical use: aspirin acetylates Ser530 of the cyclooxygenase (COX) enzymes (isoforms COX-1 and COX-2), thereby irreversibly inhibiting the biosynthetic transformation of arachidonic acid to prostaglandins.^{36, 39-41}

Pharmaceutical companies remained reluctant to include irreversible covalent modifiers in their drug development efforts, despite numerous examples of efficient and safe breakthrough therapies that were later found to have a covalent mode of action such as β -lactam **penicillin** antibiotics,⁴² proton pump inhibitor **(es)omeprazole** (Prilosec, Nexium) for treatment of esophageal reflux and heartburn,⁴³⁻⁴⁴ and antiplatelet agent **clopidogrel** (Plavix) to prevent thrombosis events.⁴⁵⁻⁴⁶ These covalent (pro)drugs are successfully used as long-term therapies and have shown to be safe in millions of patients.¹¹ Their bad reputation is not helped by the irreversible covalent binding mode of chemical warfare agents such as nerve gas sarin (a fluorophosphonate that phosphorylates the catalytic Ser203 of acetylcholinesterase AChE)⁴⁷ and blister agent **mustard gas** (a class of sulfur mustards – bearing a 2-chloroethyl sulfide warhead – that alkylate the N7 guanine in DNA).⁴⁸ Controversially, mustard gas sparked the development of cancer chemotherapy: victim autopsy revealed leucopenia and affected bone marrow function,⁴⁹ which resulted in the development of the less volatile nitrogen mustard DNA alkylating agents (e.g. **mechlorethamine** (Mustargen), **chlorambucil** (Leukeran)) that became the first cytotoxic therapeutics for treatment of lymphoma.⁵⁰⁻⁵³ This is not the only class of covalent chemotherapy drugs developed in the previous century: DNA cross-linking agent **cisplatin** (Platinol, cis-diamminedichloroplatinum(II)), proteasome inhibitor **carfilzomib** (Kyprolis, PX-171-007), antimetabolites **fluorouracil** (Adrucil, 5-FU)

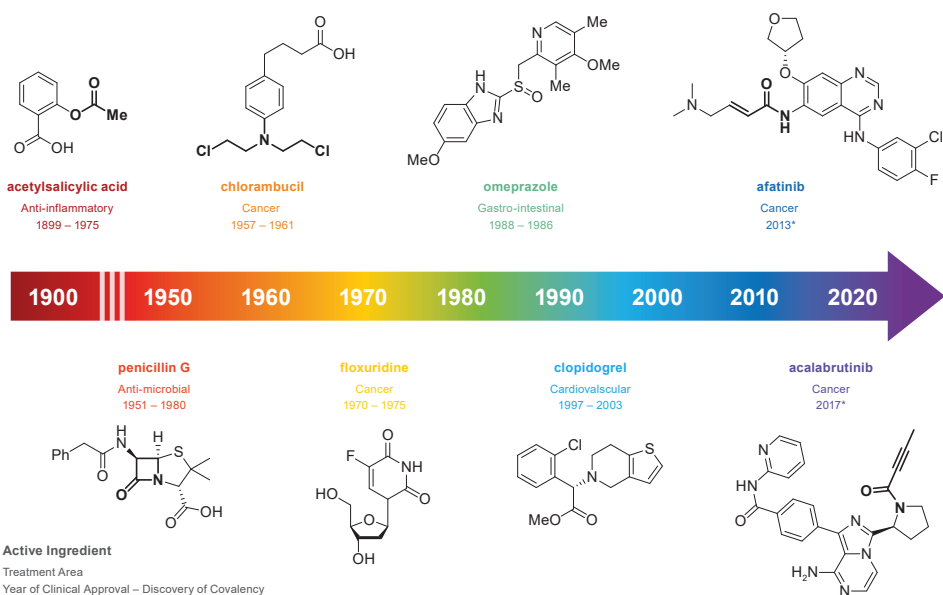


Figure 1 | Development timeline of (ir)reversible covalent drugs. Shown are the chemical structure, name of the active ingredient, the year of first clinical approval, and the year that the irreversible covalent binding mechanism was reported. The covalent warhead is shown in bold. Asterix marks targeted covalent inhibitors (TCIs) that were designed to have a covalent binding mode.

and **floxuridine** (Fudr),⁵⁴⁻⁵⁵ and many more chemotherapeutic agents have an (unintentional) irreversible covalent binding mode.¹²

... To desired modalities

A shift in paradigm was initiated in the 1990s, when the pharmaceutical industry was presented with pharmacological kinase targets that required complete and sustained inhibition.^{10, 56-58} Noncovalent screening hits could only suppress EGFR signaling of the acquired EGFR^{T790M} mutant for a short period, and prolonged inhibition was required to improve *in vivo* antitumor activity. Computational analysis revealed a nonconserved cysteine residue near the inhibitor binding site,⁵⁹ which could be covalently targeted by incorporation of a strategically placed electrophilic acrylamide warhead. This led to the development of multiple irreversible covalent clinical drug candidates⁶⁰⁻⁶¹ that showed no remarkable toxicity and were able to overcome (acquired) T790M-mediated resistance to noncovalent EGFR inhibitors **gefitinib** (Iressa, ZD1839) and **erlotinib** (Tarceva, CP-358774) with ‘pretty spectacular’ antitumor activity in patients suffering from non-small cell lung carcinoma (NSCLC).⁵⁶⁻⁵⁷ In 2013, the first two irreversible targeted covalent inhibitors (TCIs) – inhibitors designed to have a covalent binding mode – were approved for clinical use:^{8, 35} **afatinib** (Gilotrif, BIBW 2992) for treatment of gefitinib-resistant NSCLC and **ibrutinib** (Imbruvica, PCI-32765) for treatment of B-cell malignancies. Coincidentally, both teams chose to incorporate an acrylamide warhead – a cysteine-reactive Michael acceptor that covalently modifies the target protein and shows

moderate intrinsic reactivity with nontargeted thiols.⁶² Lack of promiscuous reactivity with nontargeted thiols is a desirable feature: cross-reactivity with nontargeted nucleophiles not only increases the risk of aforementioned idiosyncratic adverse effects, but adduct formation with biologically relevant thiols – such as glutathione (GSH) present in serum and cytochrome P450 (CYP) enzymes in human liver microsomes (HLM) – also renders the inhibitor susceptible to rapid depletion and (extrahepatic) metabolic inactivation.^{21, 63-65} Nowadays, pharmaceutical drug discovery programs still favor the acrylamide warhead because it balances on-target reactivity with acceptable selectivity: in 2022, nine out of ten clinically approved TCIs feature an acrylamide warhead.^{12, 66-67} There is a clear need for novel cysteine-targeting electrophiles extending beyond these Michael acceptors to further improve the reactivity and safety profiles of irreversible TCIs.^{8, 62, 68}

2. Acetylenes in Drug Development and Chemical Tools

The acetylene group is a privileged structural element that has been featured in clinical compounds targeting various therapeutic areas.⁶⁹ In these noncovalent drugs, the alkyne is used as an isostere for many functional groups to improve potency or modulate the drug metabolism pharmacokinetic (DMPK) profile. Covalent reactions of nonactivated alkynes with cellular nucleophiles are either metal-catalyzed or radical-mediated (e.g. thiol-yne coupling (TYC)⁷⁰⁻⁷³), or are enabled by (metabolic) conversion to form a reactive intermediate. Inactivation of enzymes in the CYP family has been reported for nonactivated acetylenes: metabolic oxidation of alkynes generates ketene or alkynone intermediates, and these electrophilic intermediates can form a covalent adduct with nucleophilic residues in CYP enzymes (**Figure 2A**).⁷⁴⁻⁷⁶ An exception are clinically approved Parkinson inhibitors **selegiline** (Eldepryl, E-250) and **rasagiline** (Azilect, VP-1012) that form a covalent adduct with monoamine oxidase B (MAO-B) through a nonactivated propargylamine moiety (**Figure 2B**).⁷⁷ However, a more electrophilic ynimine/allenamine intermediate is likely responsible for the observed covalent adduct with the flavin adenine dinucleotide (FAD) co-factor N5 nitrogen.

The most prominent application of terminal alkynes is in chemical biology, where they are frequently used as bioorthogonal Click handles.⁶⁹ These reagents are unreactive toward biological functionalities (bioorthogonal) while participating in simple and high yielding reactions that are compatible with mild (aqueous) conditions and – aside from the desired product – only generate unoffensive byproducts (Click reaction).⁷⁸⁻⁷⁹ Terminal alkynes have a low propensity of spontaneous engagement in covalent adducts with cellular components but can selectively form a triazole adduct in the Copper-catalyzed azide–alkyne cycloaddition (CuAAC) (**Figure 2C**).⁸⁰⁻⁸¹ The CuAAC is extensively used in various protein labeling strategies such as the popular activity-based protein profiling (ABPP):^{67, 82} proteome incubation with a residue-selective reagent bearing an alkyne handle is followed by treatment with a tagged azide and a Cu(I) catalyst, after which the labeled proteins can be enriched and/or visualized, depending on the detection tag on the azide reagent (**Figure 2C**). The toxic copper catalyst in the CuAAC is not compatible with living cells and organisms, which was overcome by the development of a strain-promoted azide–alkyne cycloaddition (SPAAC) that employs a cyclooctyne derivatives of the alkynyl motif (**Figure 2D**).⁸¹ The drawback of the SPAAC is

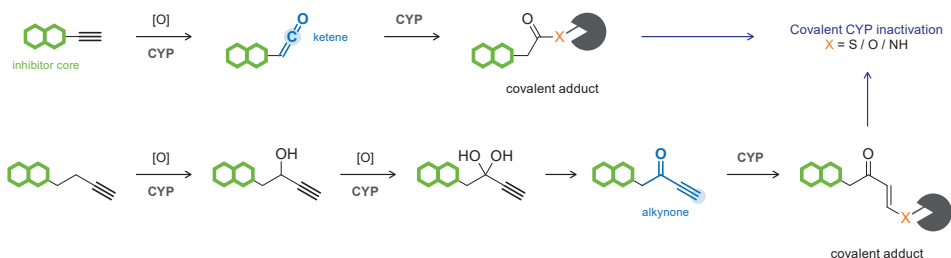
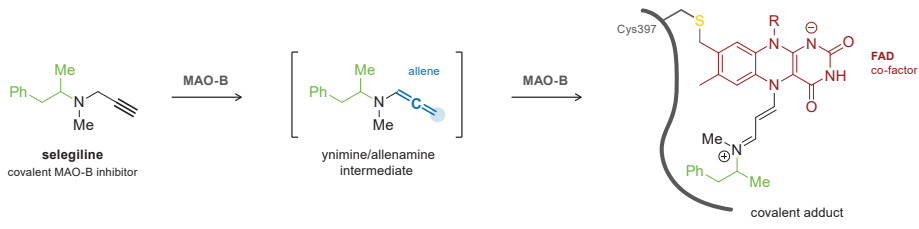
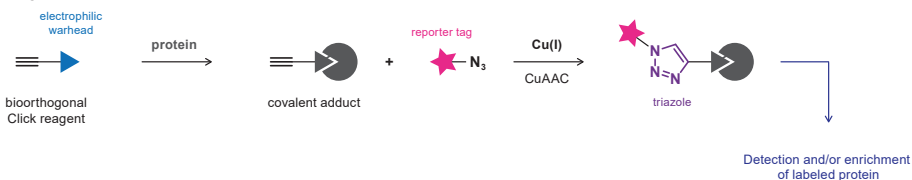
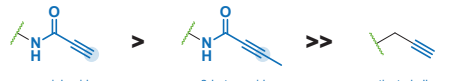
A Metabolic Alkyne Activation**B** Reactive Intermediates**C** CuAAC**D** SPAAC**E** Activated Alkyne Warheads**F** Thiol Reactivity

Figure 2 | The acetylene group in covalent drug development and chemical biology tools. Electrophilic warheads are shown in blue, with the reactive carbon marked with a blue circle. **(A)** Metabolic activation of acetylenes to form reactive ketene or alkynone intermediates can result in undesired inactivation of cytochrome P450 (CYP) isoforms. **(B)** Covalent MAO-B inhibitors **selegiline** (Eldepryl, E-250) and **rasagiline** (Azilect, VP-1012) form a covalent adduct with the FAD (flavin adenine dinucleotide) co-factor through a propargylamine group. An allenic intermediate is responsible for the observed reactivity. **(C)** Terminal nonactivated alkynes as bioorthogonal Click handles in chemical biology reagents. The proteome is incubated with alkyne-tagged protein-reactive reagent followed by Cu(I)-catalyzed coupling of the azide-labeled reporter tag in a copper-catalyzed azide–alkyne cycloaddition (CuAAC) to visualize protein labeling. **(D)** Cyclooctynes as bioorthogonal Click handles. The strain-promoted azide–alkyne cycloaddition (SPAAC) does not require toxic Cu(I)-catalyst. **(E)** Activated alkynes form adducts with (biological) thiols such as glutathione (GSH). Introduction of an electron-withdrawing group on the C1 carbon generates a thiol-reactive electron-deficient alkyne warhead. **(F)** Electron-deficient ynamide warheads used in chemical tools and TCI have a higher (indiscriminate) thiol reactivity with GSH than nonactivated alkynes.

azide-independent labeling of biological functionalities, as the ring-strain and/or increased hydrophobicity of a strained alkyne also enhances undesired reactivity with cysteine thiols.⁸³ The importance of bioorthogonal and Click chemistry was recognized by the 2022 Nobel Prize in Chemistry.⁸⁴

An electron-rich acetylene motif is unlikely to spontaneously engage in covalent adduct formation with biological thiols, but so-called electron-deficient alkynes are an upcoming class of cysteine-targeting warheads. Electron-deficient alkynes are generated by introduction of an electron-withdrawing group (EWG) onto the alkyne C1 or C3 carbon that increases the electrophilicity, while introduction of an electron-donating group (EDG) has the opposite effect (**Figure 2E**).⁸⁵ The intrinsic thiol reactivity of activated (electron-deficient) alkynes has been employed in chemical tools for chemoselective cysteine modification – specifically alkynoic amides/esters and alkynones,⁸⁶ ethynyl-triazolyl-phosphinates (ETPs),⁸⁷ and arylpropiolonitriles (APNs).^{68, 88} Moreover, electron-deficient ynamide warheads have been prominently featured in various drug candidates, including clinical covalent BTK inhibitors **acalabrutinib** (Calquence, ACP-196)⁸⁹ and **tirabrutinib** (Velexbru, ONO/GS-4059).⁹⁰ The increased electrophilicity of the 2-butyranamide and propynamide/propiolamide warheads compared to nonactivated alkynes comes at the cost of promiscuous adduct formation with nontargeted cellular thiols (**Figure 2F**),^{85, 91} though the 2-butyranamide in **acalabrutinib** was still less reactive towards GSH than the corresponding acrylamide.⁸⁹ Increased promiscuous thiol reactivity is also observed for the class of alkynyl-substituted heteroarenes⁶⁸ – (electron-deficient) heteroaryl moieties modified with an alkynyl group – including but not limited to the 2-alkynylthiazoles,⁹² alkynyl benzoxazines,⁹³ alkynylpyrimidines,⁹⁴ ethynylthienopyrimidines,⁹⁵ and ethynylpurines.⁹⁶

Nonactivated acetylenes were considered 'inert' towards proteins under physiological conditions until 2013, when two research groups – both active in the field of chemical biology to study the ubiquitin-proteasome system – independently discovered that nonactivated terminal alkynes can covalently modify catalytic cysteines.⁹⁷⁻⁹⁸

3. On Terminal Alkynes that React with Catalytic Cysteines

Ubiquitination is a post-translational modification (PTM) that involves installation of ubiquitin (Ub) – a 76-amino acid protein – onto a lysine residue of the target protein by the E1-E2-E3 ligase cascade enzymes.⁹⁹⁻¹⁰⁰ The target protein can be monoubiquitinated on multiple residues but commonly Ub chains are formed by conjugating one of the ubiquitin lysine amines or the N-terminal amine to the C-terminus of another Ub (**Figure 3**). Which linkage is formed is driven by the E2-E3 ligase combination, and chain topology impacts the destiny of the ubiquitinated protein: K48 chains enhance proteasomal degradation of the ubiquitinated protein, while K63 chains have a role in inflammatory signaling.¹⁰⁰⁻¹⁰² The process of ubiquitination is reversed by deubiquitinating enzymes (DUBs) – proteases that cleave the native isopeptide bond between the C-terminus of the distal Ub and the Lys residue in the target protein or a Lys residue or the N-terminus of M1 in the proximal Ub (**Figure 3A**).¹⁰³⁻¹⁰⁴ Human DUBs are divided into classes: there is one class of zinc-dependent metalloDUBs (JAMM) and six known classes

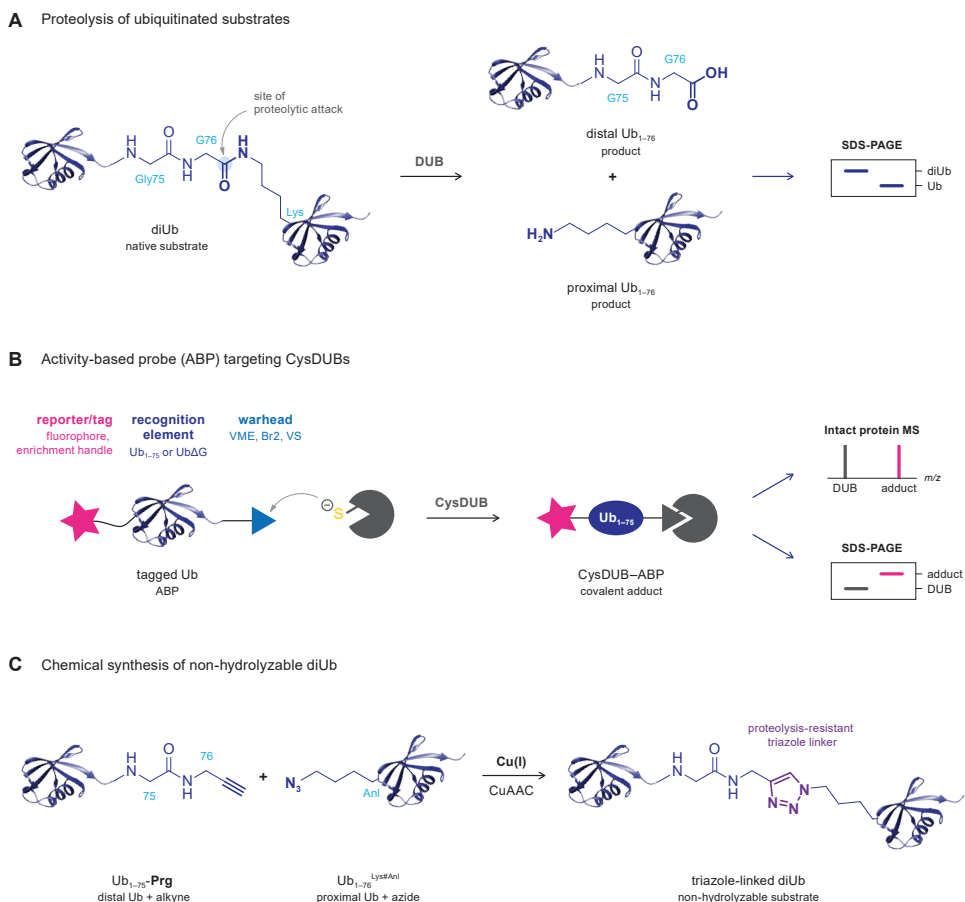


Figure 3 | Chemical tools to study deubiquitinase (DUB) activity. **(A)** DUB-mediated proteolysis of native diUb chains. **(B)** General design of CysDUB activity-based probes (ABPs). The reactive carbon in the electrophilic warhead is aligned with the carbonyl in native ubiquitinated substrates. Covalent adduct is typically visualized by an increase in deconvoluted mass (intact protein MS) or a band shift after gel electrophoresis with detection by protein staining, in-gel fluorescence, or immunoblotting. **(C)** Chemical synthesis of triazole-linked non-hydrolyzable diUb substrates.

of human cysteine DUBs (CysDUBs) based on the catalytic domain (USP, OTU, UCH, MJD, MINDY, and ZUFSP).⁹⁹ Some DUBs indiscriminately cleave all linkage types (e.g. USP21)¹⁰³ while others exhibit a specificity or preference for proteolytic cleavage of a certain diUb linkage (e.g., OTULIN for M1, OTUB1 for K48).¹⁰⁴ The full ‘ubiquitin code’ is much more complex, with mixed linkages, branched chains, phosphorylated or acetylated Ub, and incorporation of ubiquitin-like (Ubl) modifiers SUMO, Nedd8, ISG15, or UFM.¹⁰⁰⁻¹⁰¹

Chemical tools to study *in vitro* DUB and Ubl protease activity have a key role in our current understanding of the Ub(I) system.¹⁰⁴⁻¹⁰⁶ Proteolytic DUB activity can be evaluated using a ubiquitinated model substrate (e.g. diUb), with resolution of the substrate (diUb) and the

smaller product (monoUb) by gel electrophoresis, but this is restricted to recombinant purified proteases. Early on, activity-based probes (ABPs) with a monoUb recognition element enabled identification of novel CysDUBs and concurrent assessment of DUB activity profiles in cell lysates (**Figure 3B**).^{5, 105} On the C-terminus of the recognition element (Ub₁₋₇₅ or UbΔG), an electrophilic warhead (e.g. VME, VS, Br2) is installed with careful positioning of the reactive center in alignment with a native isopeptide bond, and a detection element (e.g. a fluorophore such as Rho, TMR, or Cy5, or an epitope/reporter tag such as biotin or HA) is usually placed at the N-terminus.¹⁰⁵⁻¹⁰⁶ Nucleophilic attack of the catalytic Cys residue (CysDUB) to the warhead (ABP) generates a covalent adduct that can be detected by protein resolution using SDS-PAGE followed by immunoblotting (reporter tag) or direct in-gel fluorescence scanning (fluorophore).

Nowadays, the molecular toolbox to monitor proteolytic activity of DUBs and Ubl proteases contains a variety of assay reagents based on (chemically) modified Ub(l).^{5, 106-107} Advances in the chemical Ub(l) synthesis have been instrumental in the efficient synthesis of Ub(l)-based assay reagents.¹⁰⁸⁻¹¹⁰ Linear chemical synthesis of Ub(l) by solid phase peptide synthesis (SPPS)¹¹¹ conveniently enables introduction of (fluorescent) detection tags,^{104, 112} synthesis of Ub(l) variants,¹¹³⁻¹¹⁵ and selective modification of a single amino acid residue – essential features in the preparation of assay tools to interrogate DUB activity/specificity towards specific linkage types.¹⁰⁹ The cellular role and binding affinity of various Ub(l) chains can be studied with non-hydrolyzable Ub(l) conjugates¹¹⁶ – synthetic conjugates linked by an enzymatically stable amide isostere that mimics the native isopeptide bond but is resistant to DUB cleavage (e.g. triazole¹¹⁶⁻¹¹⁷ or oxime¹¹⁸) (**Figure 3C**). The distal building block Ub-**Prg** is obtained by coupling propargylamine to chemically synthesized Ub₁₋₇₅, thus replacing the C-terminal Gly76 to mimic the alignment of native diUb. In the proximal building block, an azidonorleucine (Anl) residue replaces the lysine residue that will be ubiquitinated. Finally, the proteolytically stable triazole-linked diUb is obtained by Click chemistry.

Serendipitous discovery of the *in Situ* thiol–alkyne addition

To study the inhibitory potency of various diUb linkages spanning the active site of UCHL3, Ekkebus and co-workers from the Ovaa group prepared nonhydrolyzable diUBs to prevent premature proteolytic degradation of the inhibitory diUb (**Figure 3C**).⁹⁷ Surprisingly, building block Ub-**Prg** inhibited the UCHL3 proteolytic activity by itself with unprecedented potency ($IC_{50} < 40$ pM) (**Figure 4A**). Intact protein analysis of recombinant purified UCHL3 incubated with Ub-**Prg** revealed an increased deconvoluted mass, corresponding to covalent addition of a single Ub-**Prg** (**Figure 4B**). SDS-PAGE analysis indicated quantitative formation of a stable covalent adduct within one minute, which was resistant to reducing agents (BME, DTT) and denaturing conditions (heating to 94 °C) (**Figure 4C**). Preincubation of UCHL3 with thiol alkylating agents (NEM, IAc) abolished adduct formation, indicative of cysteine modification. Adduct formation in MelJuSo cells expressing wild-type or catalytic CS mutant CysDUBs upon incubation with TMR-Ub-**Prg** – a Ub-**Prg** analogue modified with the fluorophore 5-carboxytetramethylrhodamine (TMR) on the N-terminus – was in line with specific modification of the catalytic cysteine residue. Covalent adduct with (TMR-)Ub-**Prg** was detected for members of all four CysDUB families known at that time (UCH, USP, OTU, and MJD), including notoriously unreactive members of the OTU DUB family that could not be

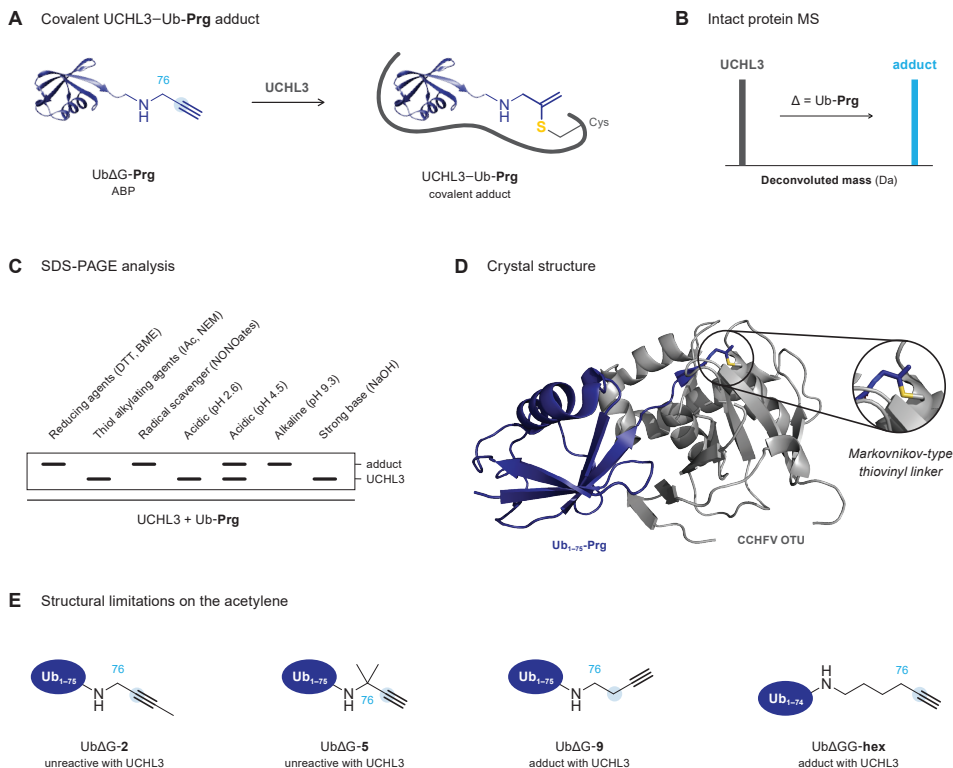


Figure 4 | Serendipitous discovery of terminal alkynes that react with cysteine deubiquitinases (CysDUBs) by Ekkebus et al.⁹⁷ **(A)** Building block Ub-Prg (synthetic Ub₁₋₇₅ or UbΔG modified with a propargyl warhead on the C-terminus) inhibits proteolytic UCHL3 activity through covalent modification of the catalytic cysteine residue. The reactive carbon is aligned with the carbonyl in native ubiquitinated substrates. **(B)** Intact protein MS of covalent UCHL3-Ub-Prg adduct reveals an increase in deconvoluted mass corresponding with addition of a single Ub-Prg. **(C)** SDS-PAGE gel analysis of recombinant UCHL3 incubated with Ub-Prg under different reaction conditions. Visualization by Coomassie protein staining. **(D)** Protein crystallography of Ub-Prg bound to CCHFV (Crimean Congo Hemorrhagic Fever Virus) OTU domain reveals a covalent Markovnikov-type thiovinyl adduct (PDB: 3ZNH). **(E)** Covalent adduct formation of propargylamide analogues with recombinant UCHL3, as detected by SDS-PAGE analysis. Alignment with site of cysteine attack in native substrate (see **Figure 3A**) is marked with blue.

probed with other Ub-ABPs. This reactivity was combined with an excellent target selectivity: Ub-Prg adduct was not observed with the nontargeted cysteines in cysteine proteases of other classes (e.g. SENP6, UBE1) nor with cysteine-rich BSA.

The covalent UCHL3-Ub-Prg adduct was stable to mild acid but was labile to strong acid, as is to be expected for a thiovinyl linker. However, preincubation of UCHL3 with NONOates (producing the water-soluble radical scavenger NO) or galvinoxyl free radical did not impair adduct formation (**Figure 4C**), contradicting a radical-mediated thiol-yne mechanism. Finally, the crystal structure of Ub-Prg bound to the vOTU (viral ovarian tumor DUB) of CCHFV (Crimean Congo hemorrhagic fever virus) unambiguously revealed a covalent adduct

with a Markovnikov-type vinyl thioether between the catalytic cysteine thiol and the internal alkyne carbon (**Figure 4D**). UCHL3-ABP adduct formation with Ub(Δ G)-Prg analogues provided insight on the structural limitations of the terminal alkyne warhead (**Figure 4E**). Terminal methylation of the alkyne disrupted adduct formation with Ub(Δ G)-2, suggesting the terminal CH proton has an important role. The backbone amide was found to be unimportant as covalent adduct was still observed with but-3-ynyl analogue Ub(Δ G)-9 as well as with Ub(Δ G)-Prg isostere Ub(Δ GG)-Hex. Geminal dimethylation of the internal carbon impaired adduct formation with Ub(Δ G)-5, so it was not possible to exclude formation of an allenic intermediate at the enzyme active site.

Another serendipitous discovery of covalent adduct formation with Ub(I)-Prg

Around the same time, Sommer and co-workers⁹⁸ independently discovered that SUMO2-Prg can form a covalent adduct with SENP1, a human SUMO-specific cysteine protease (**Figure 5A**). In agreement with the findings of Ekkebus *et al.*,⁹⁷ SDS-PAGE analysis revealed an mass increase corresponding with a covalent SENP1-SUMO2-Prg adduct that was stable to denaturing and reducing conditions, and its formation was unaffected by strict exclusion of light, presence of radical scavenger sodium ascorbate or mildly acidic conditions.⁹⁸ Mutagenesis studies of key catalytic residues provided valuable insight into the reaction mechanism (**Figure 5B**). SENP1 has a catalytic triad that consists of Cys603, His533 and Asp550, in which Cys603 acts as the nucleophile after His533 deprotonates the thiol to form the active thiolate (**Figure 5C**).¹¹⁹ The

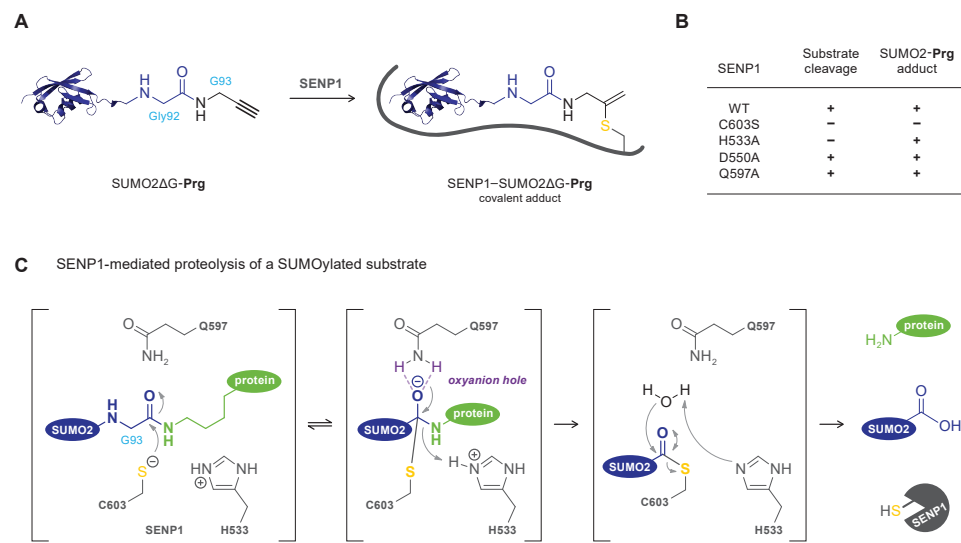


Figure 5 | Serendipitous discovery of covalent adduct formation of SUMO2-Prg with SENP1 by Sommer *et al.*⁹⁸ Structural SUMO2 representation based on noncovalent SENP1-SUMO2 complex (PDB: 2CKH). **(A)** Formation of a covalent SENP1-SUMO2-Prg adduct. **(B)** Mutagenesis studies with (mutant) recombinant SENP1. Proteolytic activity against a SUMOylated model substrate and covalent adduct formation with SUMO2-Prg were detected by gel analysis. **(C)** Simplified reaction mechanism for SENP1-mediated proteolysis of SUMOylated protein substrates, adapted from the general mechanism for CysDUBs.¹²⁰ The stepwise reaction involves stabilization of the anionic tetrahedral intermediate in the oxyanion hole, *via* stabilizing interactions with the Gln597 residue.

SEN $P1^{C603S}$ and SEN $P1^{H533A}$ mutants were proteolytically inactive and were no longer able to process the SUMOylated model protein (**Figure 5B**). Covalent adduct with ABPs SUMO2-**Prg** and SUMO2-**VS** was not observed for the C603S mutant but the H533A mutation did not affect adduct formation with either ABP, indicating the thiol–alkyne reaction may not require formation of an active thiolate. SEN $P1$ -catalyzed proteolysis of native SUMOylated substrates involves stabilization of an anionic tetrahedral intermediate in the oxyanion hole, through interaction with the polar Gln597 residue (**Figure 5C**).¹¹⁹ Based on the maintained covalent adduct formation with the SEN $P1^{Q597A}$ mutant, the authors proposed an *in situ* proximity-driven reaction mechanism that does not involve stabilization in the oxyanion hole, though the role of stabilizing interactions with backbone amides cannot be excluded.

Mechanism of covalent thiol–alkyne addition

The serendipitous discoveries that Ub(l)-alkyne ABPs can form a Markovnikov-type thiovinyll adduct with the catalytic cysteine thiol of cysteine proteases prompted investigations into the reaction mechanism of this novel and unexpected reaction (**Scheme 1**). The proposed mechanisms can be divided into four general classes: radical-mediated addition to the alkyne (**Scheme 1A**), nucleophilic concerted thiolate addition to the alkyne (**Scheme 1B**), nucleophilic/radical addition to a more reactive allenic intermediate (**Scheme 1C**), and nucleophilic stepwise thiolate addition to the alkyne (**Scheme 1D**).

One of the best-known thiol–alkyne reactions forming a thiovinyll product is the radical-mediated thiol–yne coupling (TYC) (*mechanism A1* in **Scheme 1A**).¹²¹ Here, the sulfonyl radical attacks at the terminal C1 carbon forming an anti-Markovnikov-type thiovinyll product.¹²² This mechanism was quickly excluded after the crystal structure of the vOTU–Ub-**Prg** adduct revealed a Markovnikov-type vinyl thioether adduct (**Figure 4D**). Ekkebus and co-workers⁹⁷ comment that existence of an alkyne radical in solution seems unlikely in presence of radical scavengers, but they argue that the potential existence of radical species at the enzyme active site cannot be eliminated. They proposed another radical-mediated mechanism that does generate the correct Markovnikov-type adduct (*mechanism A2* in **Scheme 1A**) but this thiol radical addition to the more substituted C2 carbon contradicts the established reactivity in radical alkyne reactions: acetylenes undergo radical addition on the least substituted carbon – the terminal C1 carbon of propargylamine.¹²³

Ekkebus⁹⁷ and Sommer⁹⁸ both proposed a concerted proximity-driven *in situ* thiol(ate)–alkyne addition mechanism (*mechanism B* in **Scheme 1B**). Here, the Markovnikov-type thiovinyll adduct is formed *via* direct nucleophilic attack of the catalytic cysteine thiol(ate) to the quaternary C2 carbon of the alkyne, with concurrent protonation of the terminal C1 carbon.

An alternative explanation to the observed thiol–alkyne addition provided in the work of Ekkebus *et al.*⁹⁷ is that the unreactive alkyne is in equilibrium with a more reactive allenic intermediate at the enzyme active site (**Scheme 1C**).¹²⁴ Ynamine and ynamide groups are known to undergo base-mediated isomerization to form the more electrophilic allenamines/allenamides^{125–126} that exhibit reactivity towards cysteine residues.¹²⁷ Moreover, allenamides are bioisosteres of the popular acrylamide warhead.^{68, 128} It is unlikely that the thiol–alkyne addition proceeds *via* base-mediated formation of an allenic Ub-**Prg** intermediate in solution,

prior to enzyme binding, since covalent adduct proceeded to form in acidic buffers (**Figure 4C**). However, formation of an allenic intermediate at the enzyme active site cannot be ruled out based on the current data. Nucleophilic attack of a thiolate to the internal C2 carbon of the allenimide warhead generates a Markovnikov-type thioviny product (*mechanism C1* in **Scheme 1C**).¹²⁷ Alternatively, radical intermediates are known to be involved in thiol addition of cysteine proteases to allenyl esters/amides (*mechanism C2* in **Scheme 1C**).¹²⁹ Thiy radical addition to terminal allenes is possible at the terminal C1 and the quaternary C2 carbon and, contrary to radical attack on propargylamine (**Scheme 1A**), is expected to form the observed Markovnikov-type thioviny product.^{123, 130}

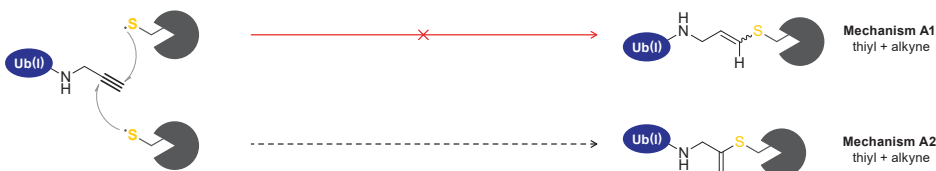
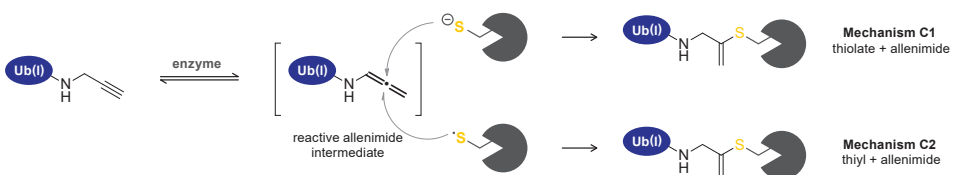
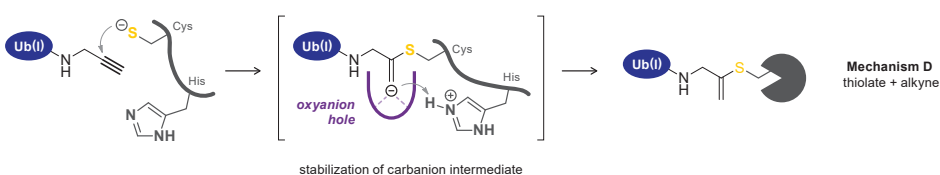
Finally, an alternative nucleophilic mechanism is suggested by Arkona and Rademann.¹³¹ They propose an enzyme-templated stepwise reaction, with stabilization of a secondary carbanion intermediate in the protease oxyanion hole (*mechanism D* in **Scheme 1D**). This stepwise mechanism resembles the mechanism of cysteine/serine protease-mediated proteolysis of native amide bonds (**Figure 5C**): proteolysis involves stabilization of an anionic intermediate in the oxyanion hole, *via* interactions with polar residues such as glutamine.^{120, 132} Covalent adduct formation of SUMO2-**Prg** with the SENP1^{Q597A} mutant does not support this mechanism (**Figure 5B**), though the role of stabilizing interactions with backbone amides cannot be excluded.

4. Scope of this Dissertation

In this dissertation, the scope and versatility of the thiol–alkyne addition to covalently modify targeted cysteine residues with nonactivated alkynes is further evaluated. The nonactivated terminal alkynes have the potential to be the perfect electrophile for irreversible covalent drug development: alkynes exhibit an unprecedented target reactivity with excellent thiol selectivity, thereby outperforming cysteine-reactive electrophilic moieties currently used in targeted covalent inhibitors (TCIs).

An essential step in covalent drug development is experimental detection of the covalent adduct to validate the covalent binding mode. In the first part of this thesis, we elaborate on the theoretical framework for evaluation of (ir)reversible covalent inhibitors. The wide array of technologies that have been employed in (recent) drug discovery are reviewed in **Chapter 2**. These technologies strictly discriminate between a noncovalent protein–drug complexes and protein and drug engaged in a covalent protein–drug adduct. Next, as a covalent binding mode affects the relevant kinetic parameters to assess the structure–activity relationship (SAR) of an inhibitor, the theoretical background on kinetic evaluation of (ir)reversible covalent inhibitors is provided in **Chapter 3**. Here we illustrate how reaction conditions affect the read-out and what assumptions are embedded in the algebraic equations to fit kinetic data. The theory is accompanied by kinetic simulations, step-wise protocols for experimental enzymatic activity assays and subsequent data analysis tailored to various covalent binding modes.

In the second part, the potential of the nonactivated alkyne as latent electrophile in small molecule covalent inhibitors is explored. Ekkebus⁹⁷ and Sommer⁹⁸ both used relatively large recognition elements (>8 kDa). Preliminary evaluations with small molecule CatS/Casp1

A Radical Addition to Alkyne**B** Concerted Nucleophilic Addition to Alkyne**C** Nucleophilic or Radical Addition to Allenic Intermediate**D** Stepwise Nucleophilic Addition to Alkyne

Scheme 1 | Proposed reaction mechanisms for Markovnikov-type thiovinylic adduct formation between a catalytic cysteine thiol(ate) and an Ub(I)-Prg ABP. **(A)** Direct addition of thiyl radical to the terminal alkyne. **(B)** Proximity-driven *in situ* thiol-alkyne addition with concerted nucleophilic attack and protonation. **(C)** Tautomerization of the terminal alkyne moiety to a thiol-reactive allenic intermediate at the enzyme active site prior to nucleophilic (*top*) or radical (*bottom*) addition. **(D)** Stepwise enzyme-templated thiol(ate)-alkyne addition *via* stabilization of a secondary carbanion intermediate in the enzyme oxyanion hole.

inhibitors (<1.8 kDa) – replacing the aldehyde warhead with an alkyne – were unsuccessful. In *Chapter 4*, we first evaluate whether replacing an isoelectric nitrile warhead with an alkyne is a successful approach, as this is more likely to correctly place the internal alkyne

carbon in juxtaposition to the catalytic cysteine residue. As a proof-of-principle, we designed several alkyne derivatives of odanacatib (ODN), a reversible covalent inhibitor of cysteine protease cathepsin K (CatK) with a nitrile warhead. Potency, reversibility and covalent adduct formation of the alkyne analogues are evaluated on recombinant CatK as well as cultures of human osteoclast cells. Finally, protein crystallography is employed to validate formation of a Markovnikov-type covalent thioviny linker. In **Chapter 5**, the scope is extended to noncatalytic cysteines – less nucleophilic (nonconserved) cysteine residues that are targeted by covalent kinase inhibitors. Aside from compatibility with kinases – the most popular protein class for irreversible drug development – adduct formation with a noncatalytic cysteine residue could also provide mechanistic insight as kinases do not have an oxyanion hole to stabilize anionic intermediates (**Scheme 1D**). The irreversible covalent acrylamide warhead in dual EGFR/HER2 inhibitor neratinib is replaced by an alkyne warhead, and preliminary results on covalent adduct formation with the tyrosine kinase domain of EGFR are reported.

The third part focuses on the versatility and mechanism of the *in situ* thiol–alkyne reaction. In **Chapter 6**, the impact of substituents on the alkyne warhead is explored. Covalent adduct formation with a panel of ubiquitin-based ABPs bearing substituents on the internal and terminal position of the propargylamide warhead is evaluated in cellular lysates and on recombinant DUBs. Moreover, MS evaluation of a covalent adduct with a deuterated propargylamide analogue provides evidence on the existence of an allenic intermediate (**Scheme 1C**).

Finally, the most important findings are summarized in **Chapter 7**. The potential impact of the *in situ* thiol–alkyne reaction is placed in the context of covalent drug discovery and an outlook will be provided on the future prospects of this work.

5. References

1. Lemmon, M.A.; Schlessinger, J. Cell Signaling by Receptor Tyrosine Kinases. *Cell* **2010**, *141*, 1117–1134. doi: 10.1016/j.cell.2010.06.011.
2. Turdo, A.; D’Accardo, C.; Glaviano, A.; Porcelli, G.; Colarossi, C.; Colarossi, L.; Mare, M.; Faldetta, N.; Modica, C.; Pistone, G.; Bongiorno, M.R.; Todaro, M.; Stassi, G. Targeting Phosphatases and Kinases: How to Checkmate Cancer. *Front. Cell Dev. Biol.* **2021**, *9*, 690306. doi: 10.3389/fcell.2021.690306.
3. Hyun, K.; Jeon, J.; Park, K.; Kim, J. Writing, Erasing and Reading Histone Lysine Methylation. *Exp. Mol. Med.* **2017**, *49*, e324. doi: 10.1038/emm.2017.11.
4. Fallah, M.S.; Szarics, D.; Robson, C.M.; Eubanks, J.H. Impaired Regulation of Histone Methylation and Acetylation Underlies Specific Neurodevelopmental Disorders. *Front. Genet.* **2021**, *11*, 613098. doi: 10.3389/fgene.2020.613098.
5. Hameed, D.S.; Sapmaz, A.; Ovaa, H. How Chemical Synthesis of Ubiquitin Conjugates Helps To Understand Ubiquitin Signal Transduction. *Bioconjugate Chem.* **2017**, *28*, 805–815. doi: 10.1021/acs.bioconjchem.6b00140.
6. Copeland, R.A. *Evaluation of Enzyme Inhibitors in Drug Discovery: A Guide for Medicinal Chemists and Pharmacologists*. Second ed.; John Wiley & Sons, Inc.: Hoboken, New Jersey, 2013. doi: 10.1002/9781118540398.
7. Holdgate, G.A.; Meek, T.D.; Grimley, R.L. Mechanistic Enzymology in Drug Discovery: A Fresh Perspective. *Nat. Rev. Drug Discov.* **2017**, *17*, 115. doi: 10.1038/nrd.2017.219.
8. Singh, J. The Ascension of Targeted Covalent Inhibitors. *J. Med. Chem.* **2022**, *65*, 5886–5901. doi: 10.1021/acs.jmedchem.1c02134.
9. Copeland, R.A. The Drug–Target Residence Time Model: A 10-Year Retrospective. *Nat. Rev. Drug Discov.* **2016**, *15*, 87–95. doi: 10.1038/nrd.2015.18.
10. Barf, T.; Kaptein, A. Irreversible Protein Kinase Inhibitors: Balancing the Benefits and Risks. *J. Med. Chem.* **2012**, *55*, 6243–6262. doi: 10.1021/jm3003203.
11. Singh, J.; Petter, R.C.; Baillie, T.A.; Whitty, A. The Resurgence of Covalent Drugs. *Nat. Rev. Drug Discov.* **2011**, *10*, 307–317. doi: 10.1038/nrd3410.
12. De Vita, E. 10 Years into the Resurgence of Covalent Drugs. *Future Med. Chem.* **2021**, *13*, 193–210. doi: 10.4155/fmc-2020-0236.
13. Mons, E.; Roet, S.; Kim, R.Q.; Mulder, M.P.C. A Comprehensive Guide for Assessing Covalent Inhibition in Enzymatic Assays Illustrated with Kinetic Simulations. *Curr. Protoc.* **2022**, *2*, e419. doi: 10.1002/cp2.419.
14. Abdeldayem, A.; Raouf, Y.S.; Constantinescu, S.N.; Moriggl, R.; Gunning, P.T. Advances in Covalent Kinase Inhibitors. *Chem. Soc. Rev.* **2020**, *49*, 2617–2687. doi: 10.1039/C9CS00720B.
15. Kim, H.; Hwang, Y.S.; Kim, M.; Park, S.B. Recent Advances in the Development of Covalent Inhibitors. *RSC Med. Chem.* **2021**, *12*, 1037–1045. doi: 10.1039/D1MD00068C.

16. Baillie, T.A. Drug–Protein Adducts: Past, Present, and Future. *Med. Chem. Res.* **2020**, *29*, 1093–1104. doi: 10.1007/s00044-020-02567-8.
17. Park, B.K.; Boobis, A.; Clarke, S.; Goldring, C.E.P.; Jones, D.; Kenna, J.G.; Lambert, C.; Laverty, H.G.; Naissib, D.J.; Nelson, S.; Nicoll-Griffith, D.A.; Obach, R.S.; Routledge, P.; Smith, D.A.; Tweedie, D.J.; Vermeulen, N.; Williams, D.P.; Wilson, I.D.; Baillie, T.A. Managing the Challenge of Chemically Reactive Metabolites in Drug Development. *Nat. Rev. Drug Discov.* **2011**, *10*, 292–306. doi: 10.1038/nrd3408.
18. Baillie, T.A. Future of Toxicology—Metabolic Activation and Drug Design: Challenges and Opportunities in Chemical Toxicology. *Chem. Res. Toxicol.* **2006**, *19*, 889–893. doi: 10.1021/tx060062z.
19. Potashman, M.H.; Duggan, M.E. Covalent Modifiers: An Orthogonal Approach to Drug Design. *J. Med. Chem.* **2009**, *52*, 1231–1246. doi: 10.1021/jm8008597.
20. Schwöbel, J.A.H.; Koleva, Y.K.; Enoch, S.J.; Bajot, F.; Hewitt, M.; Madden, J.C.; Roberts, D.W.; Schultz, T.W.; Cronin, M.T.D. Measurement and Estimation of Electrophilic Reactivity for Predictive Toxicology. *Chem. Rev.* **2011**, *111*, 2562–2596. doi: 10.1021/cr100098n.21. Dahal, U.P.; Obach, R.S.; Gilbert, A.M. Benchmarking *In Vitro* Covalent Binding Burden As a Tool To Assess Potential Toxicity Caused by Nonspecific Covalent Binding of Covalent Drugs. *Chem. Res. Toxicol.* **2013**, *26*, 1739–1745. doi: 10.1021/tx0400301q.
22. Nakayama, S.; Atsumi, R.; Takakusa, H.; Kobayashi, Y.; Kurihara, A.; Nagai, Y.; Nakai, D.; Okazaki, O. A Zone Classification System for Risk Assessment of Idiosyncratic Drug Toxicity Using Daily Dose and Covalent Binding. *Drug Metab. Dispos.* **2009**, *37*, 1970. doi: 10.1124/dmd.109.027797.
23. Mosedale, M.; Watkins, P.B. Understanding Idiosyncratic Toxicity: Lessons Learned from Drug-Induced Liver Injury. *J. Med. Chem.* **2020**, *63*, 6436–6461. doi: 10.1021/acs.jmedchem.9b01297.
24. Gan, J.; Ruan, Q.; He, B.; Zhu, M.; Shyu, W.C.; Humphreys, W.G. In Vitro Screening of 50 Highly Prescribed Drugs for Thiol Adduct Formation—Comparison of Potential for Drug-Induced Toxicity and Extent of Adduct Formation. *Chem. Res. Toxicol.* **2009**, *22*, 690–698. doi: 10.1021/tx080368n.
25. Gan, J.; Zhang, H.; Humphreys, W.G. Drug–Protein Adducts: Chemistry, Mechanisms of Toxicity, and Methods of Characterization. *Chem. Res. Toxicol.* **2016**, *29*, 2040–2057. doi: 10.1021/acs.chemrestox.6b00274.
26. Miller, J.A. The Metabolism of Xenobiotics to Reactive Electrophiles in Chemical Carcinogenesis and Mutagenesis: A Collaboration with Elizabeth Caveritt Miller and our Associates. *Drug Metab. Rev.* **1998**, *30*, 645–674. doi: 10.3109/03602539808996326.
27. Liebler, D.C.; Guengerich, F.P. Elucidating Mechanisms of Drug-Induced Toxicity. *Nat. Rev. Drug Discov.* **2005**, *4*, 410–420. doi: 10.1038/nrd1720.
28. Ulrich, R.G. Idiosyncratic Toxicity: A Convergence of Risk Factors. *Annu. Rev. Med.* **2007**, *58*, 17–34. doi: 10.1146/annurev.med.58.072905.160823.
29. Utrecht, J. Immune-Mediated Adverse Drug Reactions. *Chem. Res. Toxicol.* **2009**, *22*, 24–34. doi: 10.1021/tx080389u.
30. Kalgutkar, A.S.; Dalvie, D.K. Drug Discovery for a New Generation of Covalent Drugs. *Expert Opin. Drug Discov.* **2012**, *7*, 561–581. doi: 10.1517/17460441.2012.688744.
31. Lee, C.-U.; Grossmann, T.N. Reversible Covalent Inhibition of a Protein Target. *Angew. Chem. Int. Ed.* **2012**, *51*, 8699–8700. doi: 10.1002/anie.201203341.
32. Serafimova, I.M.; Pufall, M.A.; Krishnan, S.; Duda, K.; Cohen, M.S.; Magliathlin, R.L.; McFarland, J.M.; Miller, R.M.; Frödin, M.; Taunton, J. Reversible Targeting of Noncatalytic Cysteines with Chemically Tuned Electrophiles. *Nat. Chem. Biol.* **2012**, *8*, 471–476. doi: 10.1038/nchembio.925.
33. Faridoom, Ng, R.; Zhang, G.; Li, J.J. An Update on the Discovery and Development of Reversible Covalent Inhibitors. *Med. Chem. Res.* **2023**, *32*, 1039–1062. doi: 10.1007/s00044-023-03065-3.
34. World Health Organization. *Model Lists of Essential Medicines*. <https://www.who.int/groups/expert-committee-on-selection-and-use-of-essential-medicines/essential-medicines-lists> (accessed 2023-05-21).
35. Ghosh, A.K.; Samanta, I.; Mondal, A.; Liu, W.R. Covalent Inhibition in Drug Discovery. *ChemMedChem* **2019**, *14*, 889–906. doi: 10.1002/cmde.201900107.
36. Fuster, V.; Sweeny, J.M. Aspirin: A Historical and Contemporary Therapeutic Overview. *Circulation* **2011**, *123*, 768–778. doi: 10.1161/CIRCULATIONAHA.110.963843.
37. Vane, J.R. Inhibition of Prostaglandin Synthesis as a Mechanism of Action for Aspirin-like Drugs. *Nature New Biol.* **1971**, *231*, 232–235. doi: 10.1038/newbio231232a0.
38. Roth, G.J.; Majerus, P.W. The Mechanism of the Effect of Aspirin on Human Platelets. I. Acetylation of a Particulate Fraction Protein. *J. Clin. Invest.* **1975**, *56*, 624–632. doi: 10.1172/JCI108132.
39. Vane, J.R.; Botting, R.M. The Mechanism of Action of Aspirin. *Thromb. Res.* **2003**, *110*, 255–258. doi: 10.1016/S0049-3848(03)00379-7.
40. Roth, G.J.; Stanford, N.; Majerus, P.W. Acetylation of Prostaglandin Synthase by Aspirin. *Proc. Natl. Acad. Sci.* **1975**, *72*, 3073–3076. doi: 10.1073/pnas.72.8.3073.
41. Blobaum, A.L.; Marnett, L.J. Structural and Functional Basis of Cyclooxygenase Inhibition. *J. Med. Chem.* **2007**, *50*, 1425–1441. doi: 10.1021/jm0613166.
42. Yocom, R.R.; Rasmussen, J.R.; Strominger, J.L. The Mechanism of Action of Penicillin. Penicillin Acylates the Active Site of *Bacillus Stearothermophilus* D-Alanine Carboxypeptidase. *J. Biol. Chem.* **1980**, *255*, 3977–3986. doi: 10.1016/S0021-9258(19)85621-1.
43. Olbe, L.; Carlsson, E.; Lindberg, P. A Proton-Pump Inhibitor Expedition: the Case Histories of Omeprazole and Esomeprazole. *Nat. Rev. Drug Discov.* **2003**, *2*, 132–139. doi: 10.1038/nrd1010.
44. Lindberg, P.; Nordberg, P.; Alminger, T.; Braendstroem, A.; Wallmark, B. The Mechanism of Action of the Antisecretory Agent Omeprazole. *J. Med. Chem.* **1986**, *29*, 1327–1329. doi: 10.1021/jm00158a001.
45. Ding, Z.; Kim, S.; Dorsam, R.T.; Jin, J.; Kunapuli, S.P. Inactivation of the Human P2Y12 Receptor by Thiol Reagents Requires Interaction with Both Extracellular Cysteine Residues, Cys17 and Cys270. *Blood* **2003**, *101*, 3908–3914. doi: 10.1182/blood-2002-10-3027.
46. Maffrand, J.-P. The Story of Clopidogrel and Its Predecessor, Ticlopidine: Could These Major Antiplatelet and Antithrombotic Drugs be Discovered and Developed Today? *C. R. Chim.* **2012**, *15*, 737–743. doi: 10.1016/j.crci.2012.05.006.
47. Allgardsson, A.; Berg, L.; Aksur, C.; Hörrnberg, A.; Worek, F.; Linusson, A.; Ekström, F.J. Structure of a Prereaction Complex Between the Nerve Agent Sarin, Its Biological Target Acetylcholinesterase, and the Antidote HI-6. *Proc. Natl. Acad. Sci.* **2016**, *113*, 5514–5519. doi: 10.1073/pnas.1523362113.
48. Shakarjian, M.P.; Heck, D.E.; Gray, J.P.; Sisko, P.J.; Gordon, M.K.; Casillas, R.P.; Heindel, N.D.; Gerecke, D.R.; Laskin, D.L.; Laskin, J.D. Mechanisms Mediating the Vesicant Actions of Sulfur Mustard after Cutaneous Exposure. *Toxicol. Sci.* **2010**, *114*, 5–19. doi: 10.1093/toxsci/kfp253.
49. Krumbhaar, E.B.; Krumbhaar, H.D. The Blood and Bone Marrow in Yellow Cross Gas (Mustard Gas) Poisoning: Changes Produced in the Bone Marrow of Fatal Cases. *J. Med. Res.* **1919**, *40*, 497–508.3.
50. DeVita, V.T., Jr.; Chu, E.A History of Cancer Chemotherapy. *Cancer Res.* **2008**, *68*, 8643–8653. doi: 10.1158/0008-5472.CAN-07-6611.

51. Singh, R.K.; Kumar, S.; Prasad, D.N.; Bhardwaj, T.R. Therapeutic Journey of Nitrogen Mustard as Alkylating Anticancer Agents: Historic to Future Perspectives. *Eur. J. Med. Chem.* **2018**, *151*, 401-433. doi: 10.1016/j.ejmchem.2018.04.001.
52. Brookes, P.; Lawley, P. The Reaction of Mono- and Di-Functional Alkylating Agents with Nucleic Acids. *Biochem. J.* **1961**, *80*, 496-503. doi: 10.1042/bj0800496.
53. Millard, J.T.; Raucher, S.; Hopkins, P.B. Mechlorethamine Cross-Links Deoxyguanosine Residues at 5'-GNC Sequences in Duplex DNA Fragments. *J. Am. Chem. Soc.* **1990**, *112*, 2459-2460. doi: 10.1021/ja00162a079.
54. Moore, M.A.; Ahmed, F.; Dunlap, R.B. Evidence for the Existence of Covalent Nucleotide-Thymidylate Synthase Complexes, Identification of Site of Attachment, and Enhancement by Folates. *J. Biol. Chem.* **1986**, *261*, 12745-12749. doi: 10.1016/S0021-9258(18)67155-8.
55. Myers, C.E.; Young, R.C.; Chabner, B.A. Biochemical Determinants of 5-Fluorouracil Response In Vivo. The Role of Deoxyuridylate Pool Expansion. *J. Clin. Invest.* **1975**, *56*, 1231-1238. doi: 10.1172/JCI108199.
56. Guterman, L. Covalent Drugs Form Long-lived Ties. *Chem. Eng. News Archive* **2011**, *89*, 19-26. doi: 10.1021/cen-v089n036.p019.
57. Bauer, R.A. Covalent Inhibitors in Drug Discovery: From Accidental Discoveries To Avoided Liabilities and Designed Therapies. *Drug Discov. Today* **2015**, *20*, 1061-1073. doi: 10.1016/j.drudis.2015.05.005.
58. Roskoski, R. Orally Effective FDA-Approved Protein Kinase Targeted Covalent Inhibitors (TCIs). *Pharmacol. Res.* **2021**, *165*, 105422. doi: 10.1016/j.phrs.2021.105422.
59. Singh, J.; Dobrusin, E.M.; Fry, D.W.; Haske, T.; Whitty, A.; McNamara, D.J. Structure-Based Design of a Potent, Selective, and Irreversible Inhibitor of the Catalytic Domain of the erbB Receptor Subfamily of Protein Tyrosine Kinases. *J. Med. Chem.* **1997**, *40*, 1130-1135. doi: 10.1021/jm960380s.
60. Li, D.; Ambrogio, L.; Shimamura, T.; Kubo, S.; Takahashi, M.; Chirieac, L.R.; Padera, R.F.; Shapiro, G.I.; Baum, A.; Himmelsbach, F.; Rettig, W.J.; Meyerson, M.; Solca, F.; Greulich, H.; Wong, K.K. BIBW2992, an Irreversible EGFR/HER2 Inhibitor Highly Effective in Preclinical Lung Cancer Models. *Oncogene* **2008**, *27*, 4702-4711. doi: 10.1038/onc.2008.109.
61. Engelman, J.A.; Zejnullah, K.; Gale, C.-M.; Lifshits, E.; Gonzales, A.J.; Shimamura, T.; Zhao, F.; Vincent, P.W.; Naumov, G.N.; Bradner, J.E.; Althaus, I.W.; Gandhi, L.; Shapiro, G.I.; Nelson, J.M.; Heymach, J.V.; Meyerson, M.; Wong, K.-K.; Jänne, P.A. PF00299804, an Irreversible Pan-ERBB Inhibitor, Is Effective in Lung Cancer Models with EGFR and ERBB2 Mutations that Are Resistant to Gefitinib. *Cancer Res.* **2007**, *67*, 11924-11932. doi: 10.1158/0008-5472.Can-07-1885.
62. McAulay, K.; Bilsland, A.; Bon, M. Reactivity of Covalent Fragments and Their Role in Fragment Based Drug Discovery. *Pharmaceuticals* **2022**, *15*, 1366. doi: 10.3390/ph15111366.
63. Baillie, T.A. Targeted Covalent Inhibitors for Drug Design. *Angew. Chem. Int. Ed.* **2016**, *55*, 13408-13421. doi: 10.1002/anie.201601091.
64. Jianyao, W.; Xiao Xian, L.-C.; Jim, A.; Lin, D.; Robert, E.; Lanning, Y.; Peter, H.; Steven, R.; Susan, L.; Syed, A.; Appavu, C.; Aram, O.; JoAnn, S.; Abdul, M.; Rasmy, T. Characterization of HKI-272 Covalent Binding to Human Serum Albumin. *Drug Metab. Dispos.* **2010**, *38*, 1083. doi: 10.1124/dmd.110.032292.
65. Shibata, Y.; Chiba, M. The Role of Extrahepatic Metabolism in the Pharmacokinetics of the Targeted Covalent Inhibitors Afatinib, Ibrutinib, and Neratinib. *Drug Metab. Dispos.* **2015**, *43*, 375.
66. Yver, A. Osimertinib (AZD9291)—A Science-Driven, Collaborative Approach to Rapid Drug Design and Development. *Ann. Oncol.* **2016**, *27*, 1165-1170. doi: 10.1093/annonc/mdw129.
67. Mons, E.; Kim, R.Q.; Mulder, M.P.C. Technologies for Direct Detection of Covalent Protein–Drug Adducts. *Pharmaceuticals* **2023**, *16*, 547. doi: 10.3390/ph16040547.
68. Gehring, M.; Laufer, S.A. Emerging and Re-Emerging Warheads for Targeted Covalent Inhibitors: Applications in Medicinal Chemistry and Chemical Biology. *J. Med. Chem.* **2019**, *62*, 5673-5724. doi: 10.1021/acs.jmedchem.8b01153.
69. Talele, T.T. Acetylene Group, Friend or Foe in Medicinal Chemistry. *J. Med. Chem.* **2020**, *63*, 5625-5663. doi: 10.1021/acs.jmedchem.9b01617.
70. Lowe, A.B. Thiol-Yne 'Click'/Coupling Chemistry and Recent Applications in Polymer and Materials Synthesis and Modification. *Polymer* **2014**, *55*, 5517-5549. doi: 10.1016/j.polymer.2014.08.015.
71. Orlov, N.V. Metal Catalysis in Thiolation and Selenation Reactions of Alkynes Leading to Chalcogen-Substituted Alkenes and Dienes. *ChemistryOpen* **2015**, *4*, 682-697. doi: 10.1002/open.201500137.
72. Castarlenas, R.; Di Giuseppe, A.; Pérez-Torrente, J.J.; Oro, L.A. The Emergence of Transition-Metal-Mediated Hydrothiolation of Unsaturated Carbon–Carbon Bonds: A Mechanistic Outlook. *Angew. Chem. Int. Ed.* **2012**, *52*, 211-222. doi: 10.1002/anie.201205468.
73. Müller, T.E.; Hultsch, K.C.; Yus, M.; Foubelo, F.; Tada, M. Hydroamination: Direct Addition of Amines to Alkenes and Alkynes. *Chem. Rev.* **2008**, *108*, 3795-3892. doi: 10.1021/cr0306788.
74. Hollenberg, P.F.; Kent, U.M.; Bumpus, N.N. Mechanism-Based Inactivation of Human Cytochromes P450s: Experimental Characterization, Reactive Intermediates, and Clinical Implications. *Chem. Res. Toxicol.* **2008**, *21*, 189-205. doi: 10.1021/tx7002504.
75. Ortiz de Montellano, P.R. Acetylenes: Cytochrome P450 Oxidation and Mechanism-Based Enzyme Inactivation. *Drug Metab. Rev.* **2019**, *51*, 162-177. doi: 10.1080/03602532.2019.1632891.
76. Wright, A.T.; Song, J.D.; Cravatt, B.F. A Suite of Activity-Based Probes for Human Cytochrome P450 Enzymes. *J. Am. Chem. Soc.* **2009**, *131*, 10692-10700. doi: 10.1021/ja9037609.
77. Tandarić, T.; Vianello, R. Computational Insight into the Mechanism of the Irreversible Inhibition of Monoamine Oxidase Enzymes by the Anti-Parkinsonian Propargylamine Inhibitors Rasagiline and Selegiline. *ACS Chem. Neurosci.* **2019**, *10*, 3532-3542. doi: 10.1021/acscchemneuro.9b00147.
78. Parker, C.G.; Pratt, M.R. Click Chemistry in Proteomic Investigations. *Cell* **2020**, *180*, 605-632. doi: 10.1016/j.cell.2020.01.025.
79. Kolb, H.C.; Finn, M.G.; Sharpless, K.B. Click Chemistry: Diverse Chemical Function from a Few Good Reactions. *Angew. Chem. Int. Ed.* **2001**, *40*, 2004-2021. doi: 10.1002/1521-3773(20010601)40:11<2004::AID-ANIE2004>3.0.CO;2-5.
80. Bird, R.E.; Lemmel, S.A.; Yu, X.; Zhou, Q.A. Bioorthogonal Chemistry and Its Applications. *Bioconjugate Chem.* **2021**, *32*, 2457-2479. doi: 10.1021/acs.bioconjchem.1c00461.
81. Agard, N.J.; Baskin, J.M.; Prescher, J.A.; Lo, A.; Bertozzi, C.R. A Comparative Study of Bioorthogonal Reactions with Azides. *ACS Chem. Biol.* **2006**, *1*, 644-648. doi: 10.1021/cb6003228.
82. Cravatt, B.F.; Hsu, K.-L.; Weerapana, E. Activity-Based Protein Profiling. *Curr. Top. Microbiol. Immunol.* **2019**, *420*, 1-417. doi: 10.1007/978-3-030-11143-4.
83. van Geel, R.; Plijm, G.J.M.; van Delft, F.L.; Boelens, W.C. Preventing Thiol-Yne Addition Improves the Specificity of Strain-Promoted Azide–Alkyne Cycloaddition. *Bioconjugate Chem.* **2012**, *23*, 392-398. doi: 10.1021/bc200365k.
84. Ramström, O. *Click Chemistry and Bioorthogonal Chemistry*; The Royal Swedish Academy of Sciences: NobelPrize.org, 5 October, 2022; pp 1-18. <https://www.nobelprize.org/uploads/2022/10/advanced-chemistryprize2022-2.pdf>.

85. Hermann, M.R.; Tautermann, C.S.; Sieger, P.; Grundl, M.A.; Weber, A. Breactive: Expanding the Scope of Reactivity Predictions to Propynamides. *Pharmaceuticals* **2023**, *16*, 116. doi: 10.3390/ph16010116.

86. Shiu, H.-Y.; Chan, T.-C.; Ho, C.-M.; Liu, Y.; Wong, M.-K.; Che, C.-M. Electron-Deficient Alkynes as Cleavable Reagents for the Modification of Cysteine-Containing Peptides in Aqueous Medium. *Chem. Eur. J.* **2009**, *15*, 3839-3850. doi: 10.1002/chem.200800669.

87. Stieger, C.E.; Park, Y.; de Geus, M.A.R.; Kim, D.; Huhn, C.; Slenzcka, J.S.; Ochtrop, P.; Müchler, J.M.; Süßmuth, R.D.; Broichhagen, J.; Baik, M.-H.; Hackenberger, C.P.R. DFT-Guided Discovery of Ethynyl-Triazolyl-Phosphinates as Modular Electrophiles for Chemoselective Cysteine Bi conjugation and Profiling. *Angew. Chem. Int. Ed.* **2022**, *61*, e202205348. doi: 10.1002/anie.202205348.

88. Koniev, O.; Leriche, G.; Nothisen, M.; Remy, J.-S.; Strub, J.-M.; Schaeffer-Reiss, C.; Van Dorselaer, A.; Baati, R.; Wagner, A. Selective Irreversible Chemical Tagging of Cysteine with 3-Arylpropionitriles. *Bioconjugate Chem.* **2014**, *25*, 202-206. doi: 10.1021/bc400469d.

89. Barf, T.; Covey, T.; Izumi, R.; van de Kar, B.; Gulrajani, M.; van Lith, B.; van Hoei, M.; de Zwart, E.; Mittag, D.; Demont, D.; Verkaik, S.; Krantz, F.; Pearson, P.G.; Ulrich, R.; Kaptein, A. Acalabrutinib (ACP-196): A Covalent Bruton Tyrosine Kinase Inhibitor with a Differentiated Selectivity and In Vivo Potency Profile. *J. Pharmacol. Exp. Ther.* **2017**, *363*, 240. doi: 10.1124/jpet.117.242909.

90. Licilican, A.; Serafini, L.; Xing, W.; Czerwieniec, G.; Steiner, B.; Wang, T.; Brenda, K.M.; Lutz, J.D.; Keegan, K.S.; Ray, A.S.; Schultz, B.E.; Sakowicz, R.; Feng, J. Biochemical Characterization of Tirabrutinib and Other Irreversible Inhibitors of Bruton's Tyrosine Kinase Reveals Differences in On- and Off-Target Inhibition. *Biochim. Biophys. Acta, Gen. Subj.* **2020**, *1864*, 129531. doi: 10.1016/j.bbagen.2020.129531.

91. Cordon, M.B.; Jacobsen, K.M.; Nielsen, C.S.; Hjerrild, P.; Poulsen, T.B. Forward Chemical Genetic Screen for Oxygen-Dependent Cytotoxins Uncovers New Covalent Fragments that Target GPX4. *ChemBioChem* **2022**, *23*, e202100253. doi: 10.1002/cbic.202100253.

92. Karaj, E.; Sindi, S.H.; Kuganesan, N.; Perera, L.; Taylor, W.; Tillekeratne, L.M.V. Tunable Cysteine-Targeting Electrophilic Heteroaromatic Warheads Induce Ferroptosis. *J. Med. Chem.* **2022**, *65*, 11788-11817. doi: 10.1021/acs.jmedchem.2c00909.

93. McAulay, K.; Hoyt, E.A.; Thomas, M.; Schimpl, M.; Bodnarchuk, M.S.; Lewis, H.J.; Barratt, D.; Bhavsar, D.; Robinson, D.M.; Deery, M.J.; Ogg, D.J.; Bernardes, G.J.L.; Ward, R.A.; Waring, M.J.; Kettle, J.G. Alkynyl Benzoxazines and Dihydroquinazolines as Cysteine Targeting Covalent Warheads and Their Application in Identification of Selective Irreversible Kinase Inhibitors. *J. Am. Chem. Soc.* **2020**, *142*, 10358-10372. doi: 10.1021/jacs.9b13391.

94. Al-Khalawdeh, I.; Al Yasiri, M.J.; Aldred, G.G.; Basmadjian, C.; Bordoni, C.; Harnor, S.J.; Heptinstall, A.B.; Hobson, S.J.; Jennings, C.E.; Khalifa, S., et al. An Alkynylpyrimidine-Based Covalent Inhibitor That Targets a Unique Cysteine in NF-κB-Inducing Kinase. *J. Med. Chem.* **2021**, *64*, 10001-10018. doi: 10.1021/acs.jmedchem.0c01249.

95. Wood, E.R.; Shewchuk, L.M.; Ellis, B.; Brignola, P.; Brashier, R.L.; Cafiero, T.R.; Dickerson, S.H.; Dickson, H.D.; Donaldson, K.H.; Gaul, M., et al. 6-Ethynylthieno[3,2-d]- and 6-Ethynylthieno[2,3-d]pyrimidin-4-anilines as Tunable Covalent Modifiers of ErbB Kinases. *Proc. Natl. Acad. Sci.* **2008**, *105*, 2773. doi: 10.1073/pnas.0708281105.

96. Matheson, C.J.; Coxon, C.R.; Bayliss, R.; Boxall, K.; Carbain, B.; Fry, A.M.; Hardcastle, I.R.; Harnor, S.J.; Mas-Droux, C.; Newell, D.R.; Richards, M.W.; Sivaprakasam, M.; Turner, D.; Griffin, R.J.; Golding, B.T.; Cano, C. 2-Arylamino-6-ethynylpurines are Cysteine-Targeting Irreversible Inhibitors of Nek2 Kinase. *RSC Med. Chem.* **2020**, *11*, 707-731. doi: 10.1039/DOMD00074D.

97. Ekkebus, R.; van Kasteren, S.I.; Kulathu, Y.; Scholten, A.; Berlin, I.; Geurink, P.P.; de Jong, A.; Goerdhayal, S.; Neefjes, J.; Heck, A.J.R.; Komander, D.; Ovaai, H. On Terminal Alkynes That Can React with Active-Site Cysteine Nucleophiles in Proteases. *J. Am. Chem. Soc.* **2013**, *135*, 2867-2870. doi: 10.1021/ja309802n.

98. Sommer, S.; Weikart, N.D.; Linne, U.; Mootz, H.D. Covalent Inhibition of SUMO and Ubiquitin-Specific Cysteine Proteases by an In Situ Thiol-Alkyne Addition. *Bioorg. Med. Chem.* **2013**, *21*, 2511-2517. doi: 10.1016/j.bmc.2013.02.039.

99. Kemp, M. Chapter Three - Recent Advances in the Discovery of Deubiquitinating Enzyme Inhibitors. *Prog. Med. Chem.* **2016**, *55*, 149-192. doi: 10.1016/bs.pmc.2015.10.002.

100. Swatek, K.N.; Komander, D. Ubiquitin Modifications. *Cell Res.* **2016**, *26*, 399-422. doi: 10.1038/cr.2016.39.

101. Komander, D.; Rape, M. The Ubiquitin Code. *Annu. Rev. Biochem.* **2012**, *81*, 203-229. doi: 10.1146/annurev-biochem-060310-170328.

102. Xu, P.; Duong, D.M.; Seyfried, N.T.; Cheng, D.; Xie, Y.; Robert, J.; Rush, J.; Hochstrasser, M.; Finley, D.; Peng, J. Quantitative Proteomics Reveals the Function of Unconventional Ubiquitin Chains in Proteasomal Degradation. *Cell* **2009**, *137*, 133-145. doi: 10.1016/j.cell.2009.01.041.

103. van Tol, B.D.M.; van Doodewaerd, B.R.; Lageveen-Kammeijer, G.S.M.; Jansen, B.C.; Talavera Ormeño, C.M.P.; Hekking, P.J.M.; Sapmaz, A.; Kim, R.Q.; Moutsiopoulou, A.; Komander, D.; Wührer, M.; van der Heden van Noort, G.J.; Ovaai, H.; Geurink, P.P. Neutron-Encoded Diubiquitins to Profile Linkage Selectivity of Deubiquitinating Enzymes. *Nat. Commun.* **2023**, *14*, 1661. doi: 10.1038/s41467-023-37363-6.

104. Pruneda, J.N.; Komander, D. Evaluating Enzyme Activities and Structures of DUBs. *Meth. Enzymol.* **2019**, *618*, 321-341. doi: 10.1016/bs.mie.2019.01.001.

105. Gorka, M.; Magnusson, H.M.; Kulathu, Y. Chemical Biology Tools to Study Deubiquitinases and Ubl Proteases. *Semin. Cell Dev. Biol.* **2022**, *132*, 86-96. doi: 10.1016/j.semcdb.2022.02.006.

106. Geurink, P.P.; van der Heden van Noort, G.J.; Mulder, M.P.C.; Knaap, R.C.M.; Kikkert, M.; Ovaai, H. Chapter Sixteen - Profiling DUBs and Ubl-Specific Proteases with Activity-Based Probes. *Meth. Enzymol.* **2019**, *618*, 357-387. doi: 10.1016/bs.mie.2018.12.037.

107. Ernst, A.; Avvakumov, G.; Tong, J.; Fan, Y.; Zhao, Y.; Alberts, P.; Persaud, A.; Walker, J.R.; Neculai, A.-M.; Neculai, D., et al. A Strategy for Modulation of Enzymes in the Ubiquitin System. *Science* **2013**, *339*, 590-595. doi: 10.1126/science.1230161.

108. Ekkebus, R.; Flierman, D.; Geurink, P.P.; Ovaai, H. Catching a DUB in the Act: Novel Ubiquitin-Based Active Site Directed Probes. *Curr. Opin. Chem. Biol.* **2014**, *23*, 63-70. doi: 10.1016/j.cbpa.2014.10.005.

109. de Jong, A.; Merkx, R.; Berlin, I.; Rodenko, B.; Wijdeven, R.H.M.; El Atmioui, D.; Yaçin, Z.; Robson, C.N.; Neefjes, J.J.; Ovaai, H. Ubiquitin-Based Probes Prepared by Total Synthesis To Profile the Activity of Deubiquitinating Enzymes. *ChemBioChem* **2012**, *13*, 2251-2258. doi: 10.1002/cbic.201200497.

110. Huppelschoten, Y.; van der Heden van Noort, G.J. State of the Art in (Semi-)Synthesis of Ubiquitin- and Ubiquitin-like Tools. *Semin. Cell Dev. Biol.* **2022**, *132*, 74-85. doi: 10.1016/j.semcdb.2021.11.025.

111. El Oualid, F.; Merkx, R.; Ekkebus, R.; Hameed, D.S.; Smit, J.J.; de Jong, A.; Hilkmann, H.; Sixma, T.K.; Ovaai, H. Chemical Synthesis of Ubiquitin, Ubiquitin-Based Probes, and Diubiquitin. *Angew. Chem. Int. Ed.* **2010**, *49*, 10149-10153. doi: 10.1002/anie.201005995.

112. Hewings, D.S.; Flygare, J.A.; Bogyo, M.; Wertz, I.E. Activity-Based Probes for the Ubiquitin Conjugation–Deconjugation Machinery: New Chemistries, New Tools, and New Insights. *FEBS J.* **2017**, *284*, 1555-1576. doi: 10.1111/febs.14039.

113. Gjonaj, L.; Sapmaz, A.; Flierman, D.; Janssen, G.M.C.; van Veelen, P.A.; Ovaai, H. Development of a DUB-Selective Fluorogenic Substrate. *Chem. Sci.* **2019**, *10*, 10290-10296. doi: 10.1039/C9SC02226K.

114. Gjonaj, L.; Sapmaz, A.; González-Prieto, R.; Vertegaal, A.C.O.; Flierman, D.; Ovaai, H. USP7: Combining Tools towards Selectivity. *Chem. Commun.* **2019**, *55*, 5075-5078. doi: 10.1039/C9CC00969H.

115. Caba, C.; Mohammadzadeh, A.; Tong, Y. On the Study of Deubiquitinases: Using the Right Tools for the Job. *Biomolecules* **2022**, *12*, 703. doi: 10.3390/biom12050703.

116. Weikart, N.D.; Mootz, H.D. Generation of Site-Specific and Enzymatically Stable Conjugates of Recombinant Proteins with Ubiquitin-Like Modifiers by the Cu(I)-Catalyzed Azide–Alkyne Cycloaddition. *ChemBioChem* **2010**, *11*, 774–777. doi: 10.1002/cbic.200900738.

117. Rećnik, L.-M.; Kandioller, W.; Mindt, T.L. 1,4-Disubstituted 1,2,3-Triazoles as Amide Bond Surrogates for the Stabilisation of Linear Peptides with Biological Activity. *Molecules* **2020**, *25*, 3576. doi: 10.3390/molecules25163576.

118. Shanmugham, A.; Fish, A.; Luna-Vargas, M.P.A.; Faesen, A.C.; el Ouaid, F.; Sikma, T.K.; Ovaa, H. Nonhydrolyzable Ubiquitin-Isopeptide Isosteres as Deubiquitinating Enzyme Probes. *J. Am. Chem. Soc.* **2010**, *132*, 8834–8835. doi: 10.1021/ja101803s.

119. Xu, Z.; Au, S.W.N. Mapping Residues of SUMO Precursors Essential in Differential Maturation by SUMO-Specific Protease, SENP1. *Biochem. J.* **2005**, *386*, 325–330. doi: 10.1042/bj20041210.

120. Hanpude, P.; Bhattacharya, S.; Dey, A.K.; Maiti, T.K. Deubiquitinating Enzymes in Cellular Signaling and Disease Regulation. *IUBMB Life* **2015**, *67*, 544–555. doi: 10.1002/iub.1402.

121. Fairbanks, B.D.; Sims, E.A.; Anseth, K.S.; Bowman, C.N. Reaction Rates and Mechanisms for Radical, Photoinitiated Addition of Thiols to Alkynes, and Implications for Thiol-Yne Photopolymerizations and Click Reactions. *Macromolecules* **2010**, *43*, 4113–4119. doi: 10.1021/ma1002968.

122. Jayasree, E.G.; Reshma, S. A Computational Study on the Reaction Mechanism and Energetics of Markovnikov and Anti-Markovnikov Addition in Alkyne Hydrothiolation Reactions. *Comput. Theor. Chem.* **2016**, *1098*, 13–21. doi: 10.1016/j.comptc.2016.10.012.

123. Dénès, F.; Pichowicz, M.; Povie, G.; Renaud, P. Thiy Radical in Organic Synthesis. *Chem. Rev.* **2014**, *114*, 2587–2693. doi: 10.1021/cr400441m.

124. Hashmi, A.S.K. Synthesis of Allenes by Isomerization Reactions. *Mod. Allene Chem.* **2004**, *2*, 50. doi: 10.1002/9783527619573.ch1.

125. Lu, T.; Lu, Z.; Ma, Z.-X.; Zhang, Y.; Hsung, R.P. Allenamides: A Powerful and Versatile Building Block in Organic Synthesis. *Chem. Rev.* **2013**, *113*, 4862–4904. doi: 10.1021/cr400015d.

126. Cameron, A.J.; Harris, P.W.R.; Brimble, M.A. On-Resin Preparation of Allenamidyl Peptides: A Versatile Chemoselective Conjugation and Intramolecular Cyclisation Tool. *Angew. Chem. Int. Ed.* **2020**, *59*, 18054–18061. doi: 10.1002/anie.202004656.

127. Abbas, A.; Xing, B.; Loh, T.-P. Allenamides as Orthogonal Handles for Selective Modification of Cysteine in Peptides and Proteins. *Angew. Chem. Int. Ed.* **2014**, *53*, 7491–7494. doi: 10.1002/anie.201403121.

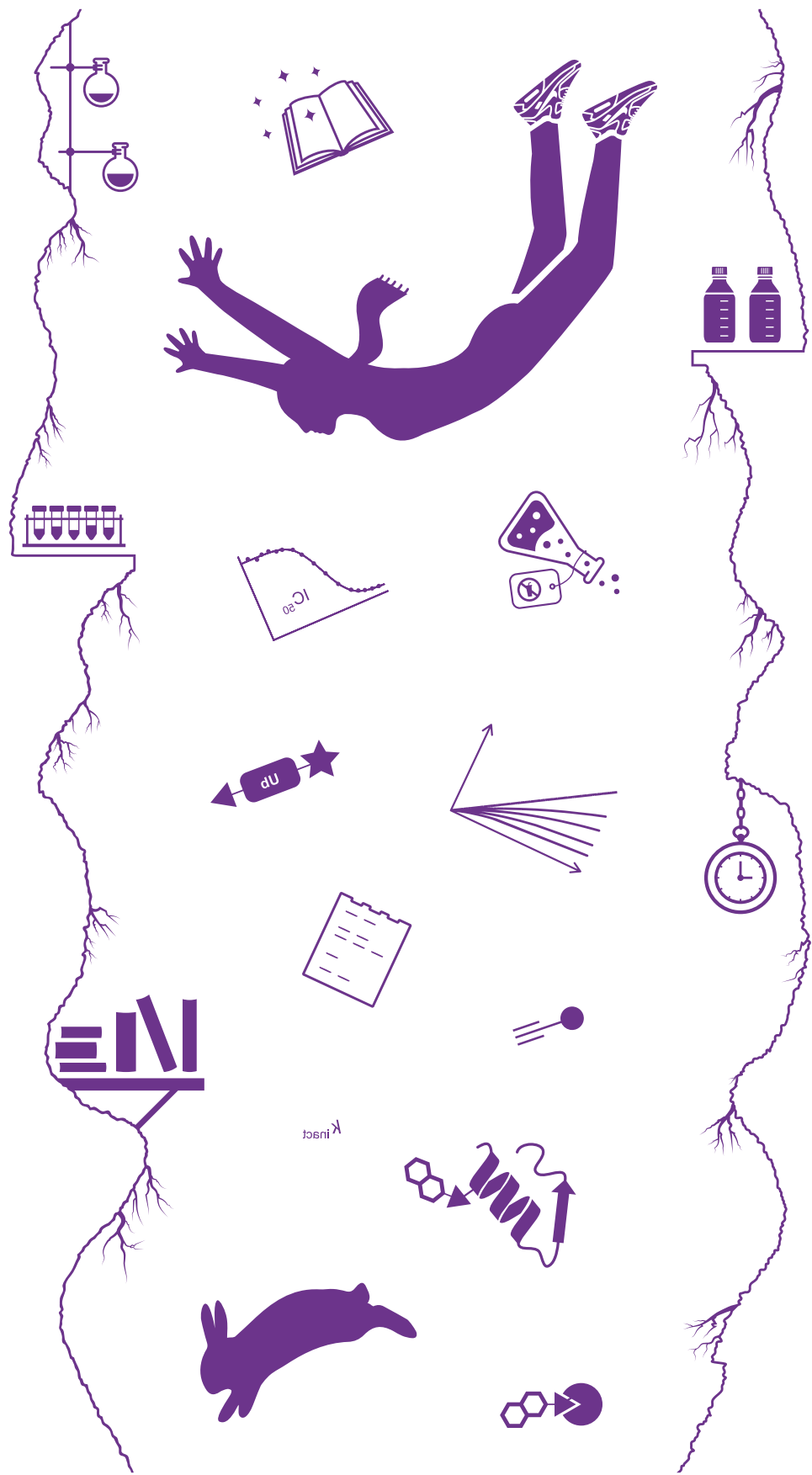
128. Chen, D.; Guo, D.; Yan, Z.; Zhao, Y. Allenamide As a Biosostere of Acrylamide in the Design and Synthesis of Targeted Covalent Inhibitors. *MedChemComm* **2018**, *9*, 244–253. doi: 10.1039/C7MD00571G.

129. Takeuchi, Y.; Fujiwara, T.; Shimone, Y.; Miyataka, H.; Satoh, T.; Kirk, K.L.; Hori, H. Possible Involvement of Radical Intermediates in the Inhibition of Cysteine Proteases by Allenyl Esters and Amides. *Bioorg. Med. Chem. Lett.* **2008**, *18*, 6202–6205. doi: 10.1016/j.bmcl.2008.10.007.

130. Liu, L.; Ward, R.M.; Schomaker, J.M. Mechanistic Aspects and Synthetic Applications of Radical Additions to Allenes. *Chem. Rev.* **2019**, *119*, 12422–12490. doi: 10.1021/acs.chemrev.9b00312.

131. Arkona, C.; Rademann, J. Propargyl Amides as Irreversible Inhibitors of Cysteine Proteases—A Lesson on the Biological Reactivity of Alkenes. *Angew. Chem. Int. Ed.* **2013**, *52*, 8210–8212. doi: 10.1002/anie.201303544.

132. Ménard, R.; Storer, A.C. Oxyanion Hole Interactions in Serine and Cysteine Proteases. *Biol. Chem.* **1992**, *373*, 393–400. doi: 10.1515/bchm3.1992.373.2.393.



Chapter 2

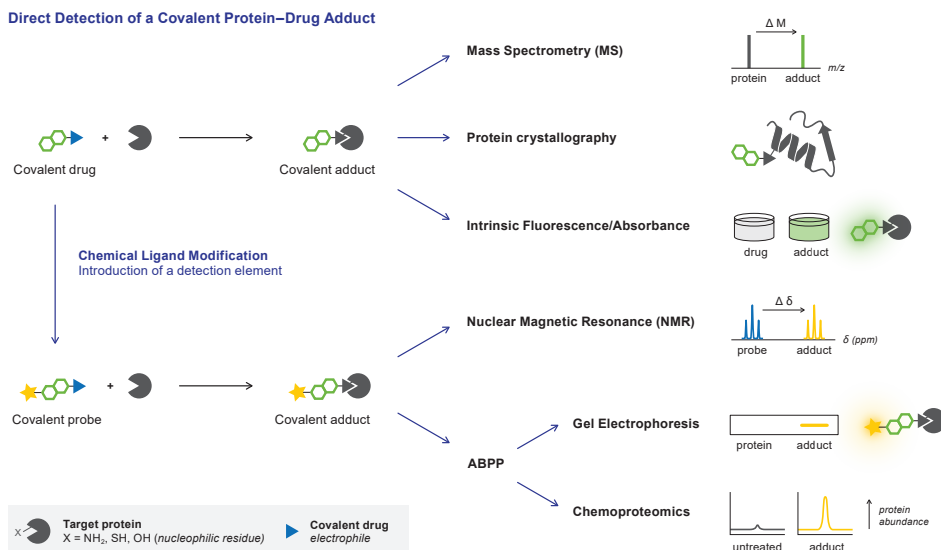


Technologies for Direct Detection of Covalent Protein–Drug Adducts

Adapted from:

Mons, E.; Kim, R.Q.; Mulder, M.P.C. Technologies for Direct Detection of Covalent Protein–Drug Adducts. *Pharmaceuticals* **2023**, *16*, 547. doi: 10.3390/ph16040547.

Abstract. In the past two decades, drug candidates with a covalent binding mode have gained interest of medicinal chemists, as several covalent anticancer drugs have successfully reached the clinic. As a covalent binding mode changes the relevant parameters to rank inhibitor potency and investigate structure-activity relationship (SAR), it is important to gather experimental evidence on the existence of a covalent protein–drug adduct. Here, we review established methods and technologies for direct detection of a covalent protein–drug adduct, illustrated with examples from (recent) drug development endeavors. These technologies include subjecting covalent drug candidates to mass spectrometric (MS) analysis, protein crystallography, or monitoring intrinsic spectroscopic properties of the ligand upon covalent adduct formation. Alternatively, chemical modification of the covalent ligand is required to detect covalent adducts by NMR analysis or activity-based protein profiling (ABPP). Some techniques are more informative than others and can also elucidate the modified amino acid residue or bond lay-out. Here, we will discuss the compatibility of these techniques with reversible covalent binding modes, and possibilities to evaluate reversibility or obtain kinetic parameters. Finally, we expand upon current challenges and future applications. Overall, these analytical techniques present an integral part of covalent drug development in this exciting new era of drug discovery.



1. Introduction

Among the most prescribed drugs in the US are successful drugs that were later found to have a covalent binding mode (**Figure 1A**),¹⁻² including established pain killer/anti-inflammatory agent **aspirin**,³ β -lactam antibiotic **penicillin**,⁴ anticoagulant **clopidogrel** (Plavix),⁵ and proton-pump inhibitor (**es**)**omeprazole** (Nexium) for gastroesophageal reflux.⁶ In the past two decades, the paradigm shift from covalent inhibition as an avoided liability toward the development of targeted covalent inhibitors (TCIs) has led to the approval of various drugs with a covalent binding mode (**Figure 1B**).^{1,7-8} Covalent targeting of noncatalytic cysteine residues at the ATP-binding site of kinases has since proven to be a successful approach to overcome competition by the native substrate,⁹⁻¹⁰ as illustrated by clinically approved covalent Bruton's Tyrosine Kinase (BTK) inhibitors,¹¹⁻¹³ and covalent (mutant) EGFR inhibitors.¹⁴⁻¹⁷ Furthermore, a covalent binding mode enabled inhibition of challenging targets for which noncovalent inhibitors could not successfully be developed, as illustrated by two recently approved first-in-class drugs: **sotorasib** (AMG 510) modifies Cys12 in the oncogenic KRAS^{G12C} mutant¹⁸ and **mobocertinib** (TAK788) modifies noncatalytic Cys797 of the EGFR^{ex20ins} mutant.¹⁹ An extensive overview of all FDA-approved drugs (1900-2019) with a known covalent mechanism of action has been compiled by De Vita,²⁰ listing their therapeutic application along with the electrophilic warhead. An update (2020-2022) can be found in **Table S1**.

Typically, a covalent adduct is formed when an electrophilic moiety (or warhead) in the inhibitor is positioned in juxtaposition of a nucleophilic residue in the protein target.²¹⁻²² Commonly targeted amino acid residues are catalytic cysteine and serine residues as the activated Cys thiolate and Ser hydroxylate are more nucleophilic (low pKa) than their noncatalytic (protonated) counterparts (Cys: pKa = 8-9, Ser: pKa > 13).²³ Popular noncatalytic nucleophilic residues include cysteines, lysines and (N-terminal) threonines.²³⁻²⁴ The selection of warhead depends on the identity of the amino acid residue, the nucleophilicity of the targeted amino acid residue, and the desired binding mode (reversible or irreversible).^{10, 24-25} A warhead should have the right balance between intrinsic chemical reactivity and selectivity, quickly forming a covalent adduct with the desired target but not (or much slower) with undesired cellular components.²⁶⁻²⁷ For cysteine-targeting inhibitors, this is typically assessed in indiscriminate thiol reactivity assays with biological thiols such as glutathione (GSH)²⁸ or cysteine.²⁹ The acrylamides and related Michael acceptors – employed in several approved kinase inhibitors – are among the most popular warheads for irreversible covalent targeting of noncatalytic cysteine thiols as the balance of their intrinsic chemical reactivity and selectivity results in a favorable safety profile.^{10, 20} Available warheads, popular as well as upcoming, and their application have been reviewed elsewhere.^{23-24, 30-31} Generally, development of novel TCIs entails introduction of a warhead onto a potent noncovalent scaffold,^{1, 21, 32-34} or high-throughput screening (HTS) of small molecule covalent ligands³⁵⁻³⁷ or covalent fragment libraries,^{31, 37-43} with structure-based lead optimization supported by *in silico* approaches (e.g. covalent docking, virtual screening).^{32, 44-46}

Reversible covalent inhibition is becoming increasingly popular⁴⁷⁻⁵³ as it combines the high affinity and long residence time of a covalent binding mode with a reduced risk of undesired idiosyncratic toxicity associated with the intrinsic ability to irreversibly modify off-target

proteins.⁴⁹ This approach is especially useful for targets with a relatively short cellular half-life as (proteasomal/proteolytic) degradation of the protein target will induce release of the reversibly bound covalent inhibitor that can engage in inhibition of another target protein. Introduction of an electron-withdrawing cyano group on the α -position of an irreversible covalent acrylamide warhead generates the cyanoacrylamide warhead, which was found to convert the inhibitors into reversible covalent inhibitors with a tunable residence time.⁵⁴⁻⁵⁵ The cyanoacrylamide moiety has gained popularity,⁵⁶⁻⁵⁸ most notably illustrated by reversible covalent BTK inhibitor **rilzabrutinib** (PRN-1008) currently in phase III clinical trials (Figure 1C).⁴⁹ Another recent example of the success of reversible covalent inhibition is **nirmatrelvir** (PF-07321332), the principle/novel component of Pfizer's oral antiviral agent Paxlovid that received emergency use authorization in 2021 for treatment of mild-to-moderate coronavirus disease (COVID-19).^{47, 59} **Nirmatrelvir** inhibits SARS-CoV-2 main protease M^{Pro} by formation of a reversible covalent thioimide bond between an electrophilic nitrile warhead and the catalytic cysteine thiolate.⁴⁷

As a covalent binding mode changes the relevant parameters to rank drug potency and investigate structure-activity relationship (SAR),^{1, 60-63} it is important to gather experimental evidence on the existence of a covalent protein-drug adduct. Compounds sharing a warhead do not necessarily have the same covalent reactivity, and an electrophile is no guarantee for a covalent protein-drug adduct. Most claims pertaining a covalent binding mode are based on data obtained with the drug itself but there still are examples of clinically approved drugs for which the covalent binding mode is not explicitly demonstrated but assumed based on related compounds or covalent docking (e.g. **remdesivir**).⁶⁴ In this work we review the available methods in the toolbox to validate covalent adduct formation, rather than identification of novel covalent ligands/inhibitors (Table 1). Please note that the term inhibitor implies that target binding impairs protein function or blocks a protein-protein interaction, thus not reflecting covalent (partial) agonists⁶⁵⁻⁶⁷ and covalent PROTACs.⁶⁸⁻⁶⁹ We will use the more appropriate neutral term covalent ligand as it describes any covalent modifier without specifying how target engagement affects protein function/binding. We focus on technologies enabling direct detection of the covalent protein-ligand adduct under conditions that distinguish covalent adducts from noncovalent complexes (e.g. an increase in the total mass under denaturing conditions), while indirect covalent adduct detection protocols (e.g. competitive activity-based probe labeling) are occasionally mentioned to exemplify their use as orthogonal validation tools.

Most direct methods only discriminate between noncovalent and covalent protein modification, while others are more informative and provide direct evidence on which amino acid residue is modified. Although it is generally safe to assume that the most nucleophilic (catalytic) amino acid residue will be targeted for covalent modification, TCIs that were unexpectedly found to covalently modify allosteric (less nucleophilic) residues⁷⁰ or even a completely different amino acid⁷¹ illustrate why it is important to identify the modified amino acid residue. Importantly, covalent adduct formation is not completed instantly upon treating the target protein with an excess covalent ligand.⁶¹ Unless otherwise noted, all procedures involve incubation of protein target and covalent ligand for a sufficient time (ranging from minutes to hours) to allow covalent adduct formation prior to analysis, as it is not possible to detect a covalent adduct

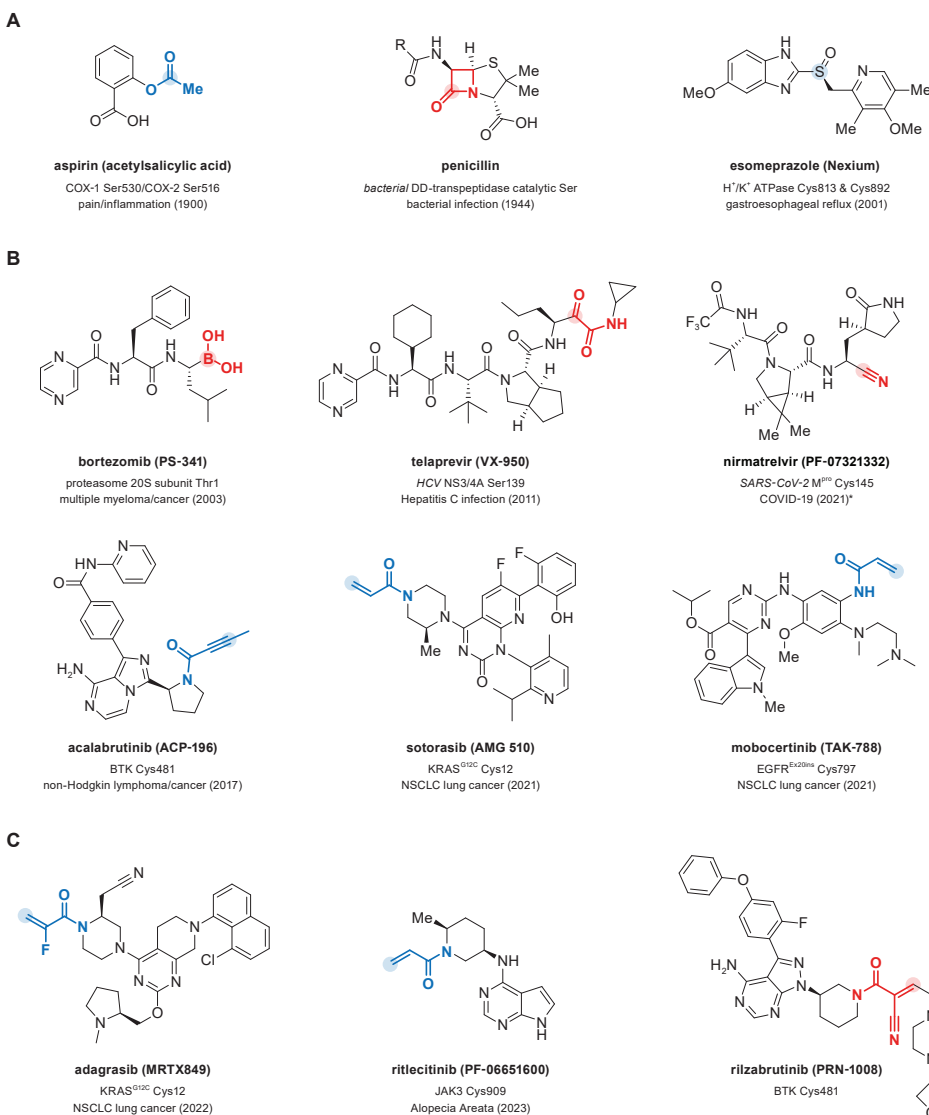


Figure 1 | Drugs with a known covalent binding mode. Structure with reversible warheads in red, irreversible warhead in blue, and the covalently modified atom marked. Compound name, protein target and covalently modified amino acid, therapeutic application and year of first approval. **(A)** Approved covalent inhibitors that were later found to have a covalent binding mode. Warhead not indicated for esomeprazole: metabolic activation of the prodrug precedes formation of a disulfide bond with its target.⁶ **(B)** Approved targeted covalent inhibitors (TCIs) designed to covalently modify their protein target. **(C)** Covalent inhibitors with a novel protein target and/or warhead.

that has not (yet) been formed. Conversion to covalent adduct does not have to be complete but high amounts of unbound protein can complicate detection, especially if unbound protein cannot easily be removed. The focus of this review is on the qualitative detection of covalent

protein–ligand adducts but some of the methods enable quantification of time-dependent covalent occupancy, which might be employed to calculate kinetic rate constants reflecting irreversible covalent inhibitor potency.^{1, 60–61} Details on the kinetic background of covalent adduct formation and potency are beyond the scope of this work,^{61–62} but compatibility with quantification of covalent occupancy will be highlighted. Moreover, special attention will be paid to compatibility with reversible covalent ligands and reversibility assays to assess the (ir)reversible ligand binding mode. Detection of reversible covalent adducts has its unique challenges compared to irreversible covalent adduct detection: detection (and purification) of the reversible covalent protein–ligand adduct is more complicated as the unbound enzyme and covalent adduct are at an equilibrium,⁵⁴ and the covalent occupancy is thus driven by the concentration of (excess) inhibitor.^{48, 61} Furthermore, standard sample preparation conditions (e.g. denaturation, proteolytic digestion, dilution), designed to induce noncovalent inhibitor dissociation, can also induce dissociation of reversible covalent ligands.^{54, 72} Traditional reversibility assays are based on regained enzymatic activity after rapid dilution⁷³ or washout,³⁴ or on detection of released unbound inhibitor upon protein denaturation/digestion⁵⁵ or chasing with a competitive irreversible ABP.⁷⁴ These assays serve to evaluate the reversibility of the adduct formation but irreversible protein modification provides by no means direct evidence of covalency: a covalent drug can have a reversible binding mode, and noncovalent binders can be irreversible.⁶¹

In this work, we will discuss methods for direct detection of covalent protein–ligand adducts (an overview of the methods can be found in **Table 1**). In general, whether the covalent adduct will be detected using a certain technique depends on intrinsic properties of the protein target (e.g. mass, ionizability, crystalline) as well as the inhibitor/ligand (e.g. binding mode, solubility, fluorescence). Each method will be illustrated with examples of advantages and limitations, with specific attention to compatibility with reversible covalent inhibition, identification of the modified amino acid residue and application in (kinetic) evaluation of inhibitor binding mode and/or potency. We start with techniques to detect the covalent protein–drug adduct without chemical modification of the ligand, using the same compound stocks prepared for biochemical *in vitro/in vivo* assays. Predominantly used techniques mass spectrometry (*section 2*) and protein crystallography (*section 3*) will be discussed first, followed by less ubiquitous detection based on the changes in intrinsic spectroscopic properties of the ligand upon covalent adduct formation (*section 4*). Alternatively, ¹³C NMR analysis (*section 5*) and activity-based protein profiling (*section 6*) require chemical modification of the covalent ligand to enable detection of the covalent protein–drug adduct (e.g. introduction of a bioorthogonal handle, reporter tag or isotope labeling). Finally, we expand on current challenges and future applications (*section 7*).

2. Mass Spectrometry (MS)

Initial confirmation of a covalent binding mode is predominantly achieved through mass spectrometric (MS) analysis of the covalent protein–ligand adduct.³⁶ Here, validation of the covalent binding mode is based on the mass increase upon modification of an unbound protein with a covalent ligand, compared to the mass of the unbound protein (**Figure 2**). MS analysis provides confirmation of the biophysical binding event between the protein and ligand but

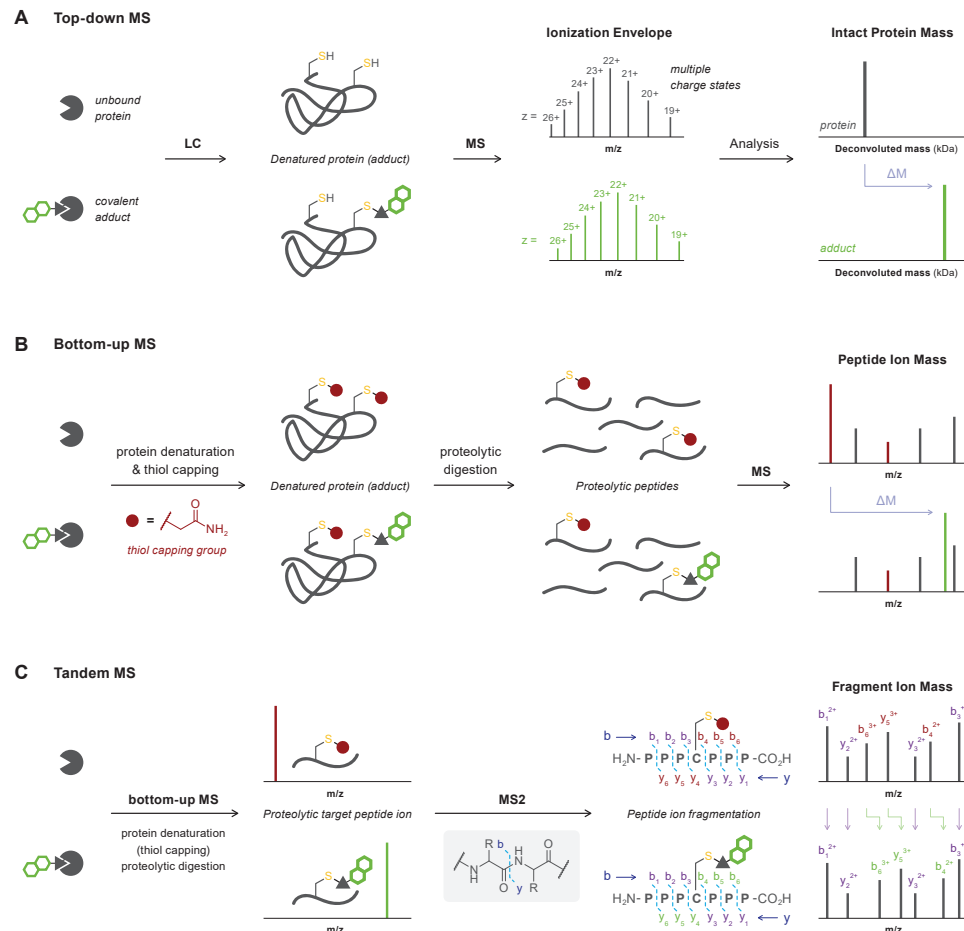
Table 1 | Technologies for direct detection of covalent protein–drug adducts included in this review.

Detection Method	Prerequisites		Compatibility		Structural		Characterization		Notes
	Ligand Resynthesis	Protein Optimization	Reversible Covalent	Whole proteome ^a	Modified Amino Acid ^b	Bond Isoform	Covalent Occupancy	Reversibility	
2. Mass Spectrometry									
2.1. Top-down MS	–	+	+	~ ^c	–	–	+	+	Relatively fast and easy. Bottom-up MS(/MS) is compatible with large proteins (in mixtures)
2.2. Bottom-up MS	–	–	~	+	~ ^d	–	~	–	
2.3. MS/MS	–	–	~	+	+	–	+	–	
3. Protein Crystallography	–	+	++	–	+	+	–	–	Most informative but laborious
4. Intrinsic Fluorescence/Absorbance	– ^e	–	+	–	–	–	~	+	Limited ligand compatibility
5. Nuclear Magnetic Resonance	+	~	++	+	~	++	+	+	Compatible with labile adduct detection in solution
6. Activity-Based Protein Profiling									
6.1. Gel Electrophoresis	+	–	~	++	–	–	+	+	Detection of modified (off-)target proteins in whole proteomes
6.2. Chemoproteomic Platforms	+	–	~	++	+	–	~ ^f	+	
6.3. Homogeneous/plate-based	+	–	+	++	–	–	+	–	

^a Adduct formation in complex mixtures (e.g. lysates, live cells or *in vivo*). ^b Direct detection, not including indirect identification through site-directed mutagenesis of the modified amino acid. ^c Requires enrichment for (modified) protein target. ^d Identification of the peptide containing the modified amino acid residue. ^e Prerequisite for drug ligand class: covalent adduct formation must induce a change in intrinsic spectroscopic properties (e.g. fluorescence, absorbance). ^f Typically assessed in (indirect) competition assays.

does not elucidate the bond lay-out. MS analysis is generally favored because it consumes a relatively low amount of material and it is compatible with most protein targets. This versatile technique is not only used to validate a covalent binding mode, but also in the discovery of new covalent ligands.^{41–42} Detailed guidelines for mass spectrometric characterization (and quantification) of covalent protein–drug (metabolite) adducts are available elsewhere.^{36, 75–76} Generally, the covalent adduct is formed by incubation of protein with excess inhibitor in an MS-compatible buffer, followed by a purification step such as liquid chromatography (LC) or gel electrophoresis.^{76–77} MS analysis must be performed for the covalent adduct as well as unbound protein, to confirm that the detected mass increase corresponds with covalent ligand modification. For top-down MS analysis (section 2.1), the adduct is separated from the unbound protein/inhibitor under denaturing conditions to ensure all noncovalent interactions are disrupted prior to MS analysis of the intact protein–inhibitor adduct (Figure 2A). Alternatively, the adduct is submitted to proteolytic digestion with bottom-up MS analysis (section 2.2) of the protein-derived proteolytic peptides to identify the peptide sequence modified by an

irreversible covalent ligand (**Figure 2B**). Subsequent peptide ion fragmentation for MS/MS analysis (*section 2.3*) can enable identification of the modified amino acid residue (**Figure 2C**).



2.1. Top-Down MS

It should not be surprising that intact protein analysis by top-down MS is the most popular technique to validate covalent adduct formation with a wide variety of targets:⁶³ most (academic) drug discovery labs are equipped with an LC-MS system (**Figure 2A**), and sample preparation is relatively straightforward when the protein–ligand adduct is formed using recombinant purified protein. Benchmark protocols are composed by Donnelly and co-workers for intact protein analysis by top-down MS.⁷⁷ Generally, the unbound protein and protein (adduct) are ionized after denaturation and removal of unbound ligand on the LC, generating (positively or negatively) charged ions ($z > 1$) detectable by MS. The total mass of the parent protein or adduct is calculated by deconvolution of the charge states in the ionization envelope. It is important to note that sample preparation is conducted under denaturing conditions that ensure noncovalent interactions are disrupted, but detection of noncovalently bound protein–ligand complexes is theoretically possible with native MS, with dedicated conditions to ensure noncovalent interactions are maintained.⁷⁸⁻⁷⁹ The main practical limitations to intact protein analysis by top-down MS are the incompatibility with larger proteins (>50 kDa), proteins that ionize poorly,⁸⁰⁻⁸¹ proteins that require MS-incompatible detergents or surfactants, and complex (cellular) mixtures that have not been enriched for the protein target: bottom-up MS analysis (*section 2.2*) might be more suitable as ionization of peptides is often better.

Intact protein analysis by top-down MS is one of the less informative methods as it does not reveal the bond layout or identifies which amino acid residue is covalently modified. Mitigation of covalent adduct formation by site-directed mutagenesis provides (indirect) evidence on the modified amino acid residue, and is part of most covalent drug development workflows.⁶³ Intact protein analysis has recently been employed to validate covalent adduct formation with proteases,⁸²⁻⁸⁵ recombinant kinase domains,^{74, 86-88} and other (potential) clinical targets.⁸⁹⁻⁹¹ Biophysical confirmation of covalent binding is also an important step in the ongoing industrial efforts to develop covalent kinase inhibitors with an improved selectivity/potency profile, as illustrated by intact protein analysis of covalent adducts between the BTK kinase domain and clinical candidates **evobrutinib** (Merck),⁸⁶ **remibrutinib** (Novartis),⁸⁷ and **tirabrutinib** (Ono Pharmaceutical/Gilead Sciences).⁸⁸

Covalent Fragment-Based Drug Development (FBDD). Intact protein analysis has a prominent role in target-directed covalent fragment-based ligand discovery (FBLD). MS analysis is utilized to identify (cysteine-reactive) covalent ligands, that serve as a starting point for medicinal chemistry optimization after validation of inhibitory properties associated with biophysical binding.^{36, 38-39} Kathman and co-workers developed an MS-based assay to screen mixtures of fragments containing a vinyl methyl ester (VME) warhead for covalent adduct formation with cysteine protease papain.^{42, 85} This assay has since successfully been employed to screening cysteine-reactive covalent fragment libraries with mixed electrophile chemotypes,^{41, 92} covalent ligand identification for E3 ligases,⁹⁰⁻⁹¹ and several other recombinant protein targets.^{38, 93}

Reversible binding mode. The reversible covalent adduct of **odanacatib** (ODN, MK-0822) bound to recombinant cysteine protease CatK can be detected by top-down MS analysis (**Figure 3A**),⁸³ provided that inhibitor concentration exceeds its steady-state

equilibrium constant K_i^{*app} to ensure sufficient covalent occupancy.⁶¹ The reversible covalent cTnC-levosimendan adduct was detected in endogenous thin and thick filament proteins extracted from porcine cardiomyofibrils.⁹⁴ However, sample preparation and denaturing conditions can induce inhibitor dissociation, and detection of the reversible covalent protein–inhibitor adduct is not possible if the covalent dissociation rate is relatively fast. Incubation of RSK2 with cyanoacrylamide **CN-NHiPr** failed to produce a detectable adduct,^{54, 72} but this is highly context-dependent as covalent adducts with other cyanoacrylamides have since successfully been detected by top-down MS.^{57, 74}

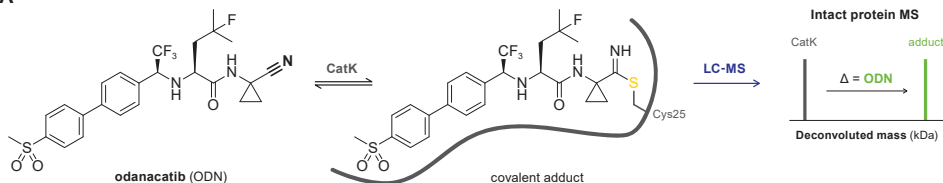
Reversibility assays. The Rauh group developed a top-down MS-based reversibility assay,⁷⁴ illustrated for reversible covalent EGFR inhibitors bearing a cyanoacrylamide warhead (**Figure 3B**). EGFR kinase domain and reversible covalent inhibitor (CRI) are incubated to form the covalent EGFR–CRI adduct, followed by incubation with excess chaser COV2 – an irreversible covalent ligand selectively targeting the same amino acid residue (e.g. **osimertinib**, **ibrutinib**) – that displaces the reversible covalent inhibitor, forming a covalent EGFR–COV2 adduct. Displacement is indicative of a reversible binding mode, as it is not possible to displace an irreversibly bound covalent inhibitor. Prerequisites to this reversibility assay are the availability of a selective irreversible chaser targeting the same amino acid residue, that forms a covalent protein–chaser adduct with a mass difference to the protein–inhibitor adduct. This method has since been employed in the preclinical development of irreversible covalent BTK inhibitor **tirabrutinib** (ONO-4059),^{88, 95} which was resistant to chasing with **ibrutinib**. Indirect methods with MS detection of released free ligand upon induction of ligand dissociation (e.g. dilution, dialysis, washout, denaturation, competition) will not be further discussed here.⁵⁴

Quantification covalent occupancy. The research groups of House (Crick–GSK Biomedical LinkLabs) and Rittinger (Francis Crick Institute) recently reported a quantitative covalent occupancy assay for kinetic analysis of irreversible ligand binding to the RBR domain of HOIP, an RBR E3 ubiquitin ligase for which quantitative HTS activity assays are not available (**Figure 3C**).⁹⁰ Time-dependent covalent occupancy was calculated from the total ion count (TIC) of the deconvoluted mass of covalent HOIP–fragment adduct relative to the unbound HOIP. LC-MS approaches were also employed to assess the potency of covalent KRAS^{G12C} inhibitors.^{36, 96–97} Differences in ionization efficiency of the unbound protein and adduct are only a minor concern as the protein size is significantly larger than the covalent ligand. Alternatively, indirect methods based on quantification of remaining unbound inhibitor (excess protein)⁹⁶ or unbound protein (excess inhibitor)^{89, 98} are employed to assess the biochemical rate of covalent target modification.

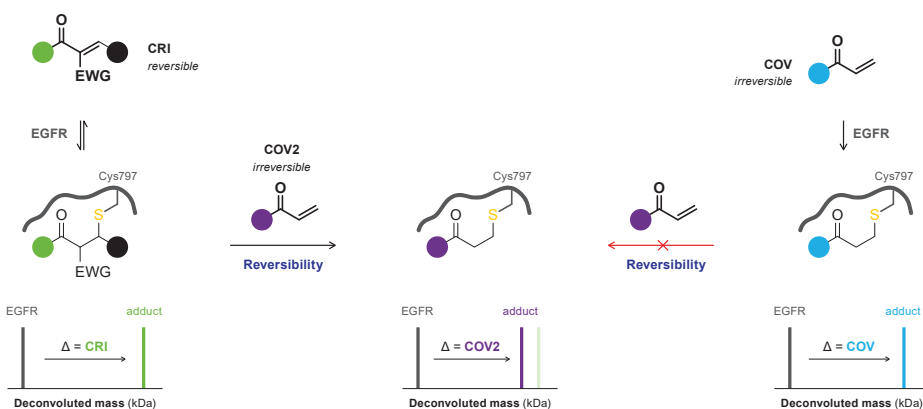
2.2. Bottom-Up MS

Bottom-up MS analysis (**Figure 2B**) is the preferred method to verify covalent adduct formation with large proteins (>50 kDa), proteins that are poorly ionized, and for detection of covalent adducts in complex mixtures (e.g. cell lysates and samples from living organisms). A comprehensive overview of bottom-up MS methodologies is available elsewhere.⁷⁶ Generally, the protein–ligand adduct and the unbound protein are subjected to a thiol-alkylating reagent

A



B



C

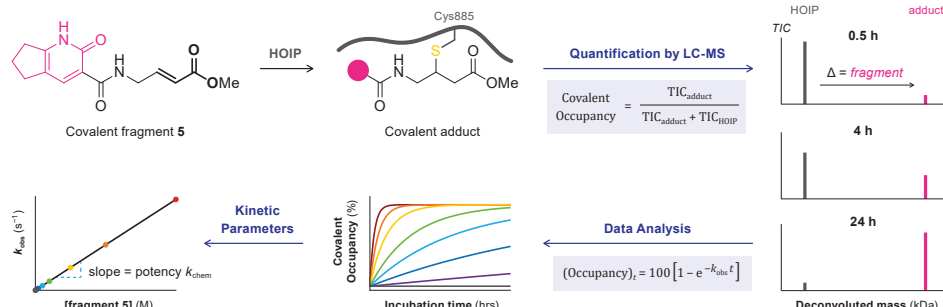


Figure 3 | Biophysical covalent adduct detection with intact protein analysis by top-down MS. **(A)** Covalent CatK–ODN adduct formation between recombinant purified cathepsin K (CatK) and reversible covalent CatK inhibitor odanacatib (ODN) is confirmed by intact protein analysis:⁸³ the higher deconvoluted mass for the adduct compared to unbound CatK is in agreement with covalent ODN binding. **(B)** MS-based reversibility assay illustrated with recombinant purified EGFR^{T790M/L858R} mutant and reversible covalent cyanoacrylamide-based inhibitor CRI.⁷⁴ Detection of covalent EGFR–COV2 adduct rather than reversible covalent EGFR–CRI adduct upon competition with irreversible covalent chaser COV2 is indicative of a reversible binding mode. **(C)** Quantitative biochemical covalent occupancy assay illustrated for incubation of recombinant purified HOIP(RBR)^{WT} protein with excess covalent fragment 5.⁹⁰ Adduct formation is detected by top-down MS and covalent occupancy is quantified from the total ion count (TIC) of covalent adduct and unbound HOIP(RBR). Biochemical rate of covalent target engagement k_{obs} is calculated for each fragment concentration from the time-dependent covalent occupancy, which can be used to calculate the kinetic rate constant reflecting binding efficiency of an irreversible covalent fragment (more details in reference^{60–61}).

such as **iodoacetamide** (IAc) to cap free cysteine thiols (and sometimes lysine amines) with a carbamidomethyl group (+57.021 u), followed by trypsin- or pepsin-mediated proteolytic digestion (other proteases are also possible).⁷⁶ The proteolytic peptides are separated by LC, ionized and the peptide ions are detected by MS (Figure 4). Each parent peptide will be charged once or multiple times ($z \geq 1$) to generate ionized peptides, and a database is used to correlate found m/z values with the predicted mass of various amino acid stretches. In the protein-ligand adduct, a peptide with a covalently modified amino acid residue appears along with a decrease or even disappearance of the (capped) unmodified peptide with the same sequence. Consequently, not only the covalent adduct is validated, but the peptide sequence containing the modified amino acid is also identified.⁷⁶ Optionally, sample preparation may involve purification by gel electrophoresis prior to capping and proteolytic digestion, to remove unbound ligand and MS-incompatible buffer components (e.g. surfactants, detergents), and enrich the sample for the desired protein (adduct). Proteolytic digestion ensures that only stable covalent adducts are detected but these harsh conditions also have a drawback: incompatibility with sensitive/labile functional groups. LC-MS detection of unbound inhibitor after digestion-induced inhibitor dissociation is commonly used to assess binding reversibility,^{49, 55} but does not involve direct detection of the covalent adduct.

Bottom-up MS analysis is compatible with complex mixtures and native systems. For example, covalent adduct formation of clinically approved covalent KRAS^{G12C} inhibitor **sotorasib** (AMG 510) in (*in vitro* or *in vivo*) treated tumor cells was detected (Figure 4A).^{18, 99} RAS proteins were isolated from lysates by immunocapture on anti-RAS beads, eluted proteins were denatured (8M urea), free thiols were alkylated with IAc, and proteins were digested with trypsin prior to mass spectrometric analysis. Bottom-up MS analysis has been employed to validate covalent adduct formation with oncogenic KRAS^{G12C},^{18, 99-100} proteases,⁸³⁻⁸⁴ and various other (potential) clinical targets.^{70, 90}

The detected mass of the modified proteolytic peptide ions can correspond to the simple adduct (peptide + full ligand) but can be smaller if the ligand contains bonds sensitive to proteolysis (e.g. amide bonds), as is frequently seen for binding of ubiquitin(-like modifiers).⁸² Furthermore, covalent modification can block the proteolytic cleavage site, resulting in a missed cleavage and larger peptide sequences in the ligand-treated sample compared to the untreated (free protein) sample. This is exemplified by bottom-up MS analysis of the covalent adduct of SUMO-activating enzyme (SUMO E1 or SAE) with inhibitor **COH000** (Figure 4B):⁷⁰ pepsin-mediated proteolytic peptide A14-L32 was found in the untreated sample, but covalent modification of Cys30 in the COH000-treated sample blocked access to the pepsin cleavage site after Leu32, resulting in the simple COH000 adduct of peptide A14-N35 (missed cleavage). More importantly, bottom-up MS analysis was instrumental in the initial identification of the unexpected allosteric Cys30 modification: COH000 was expected to modify the catalytic (nucleophilic) Cys173 residue but only the unmodified A131-C185 peptide was found. The importance of careful interpretation of MS data is further illustrated by the work of Pettinger and co-workers.⁷¹ Their covalent acrylamide ligand was designed to covalently target Cys17 in stress-inducible ATPase molecular chaperone heat shock 70 kDa protein 1 (HSP72) but no evidence of Cys17 labeling was found after proteolytic digestion and subsequent MS analysis

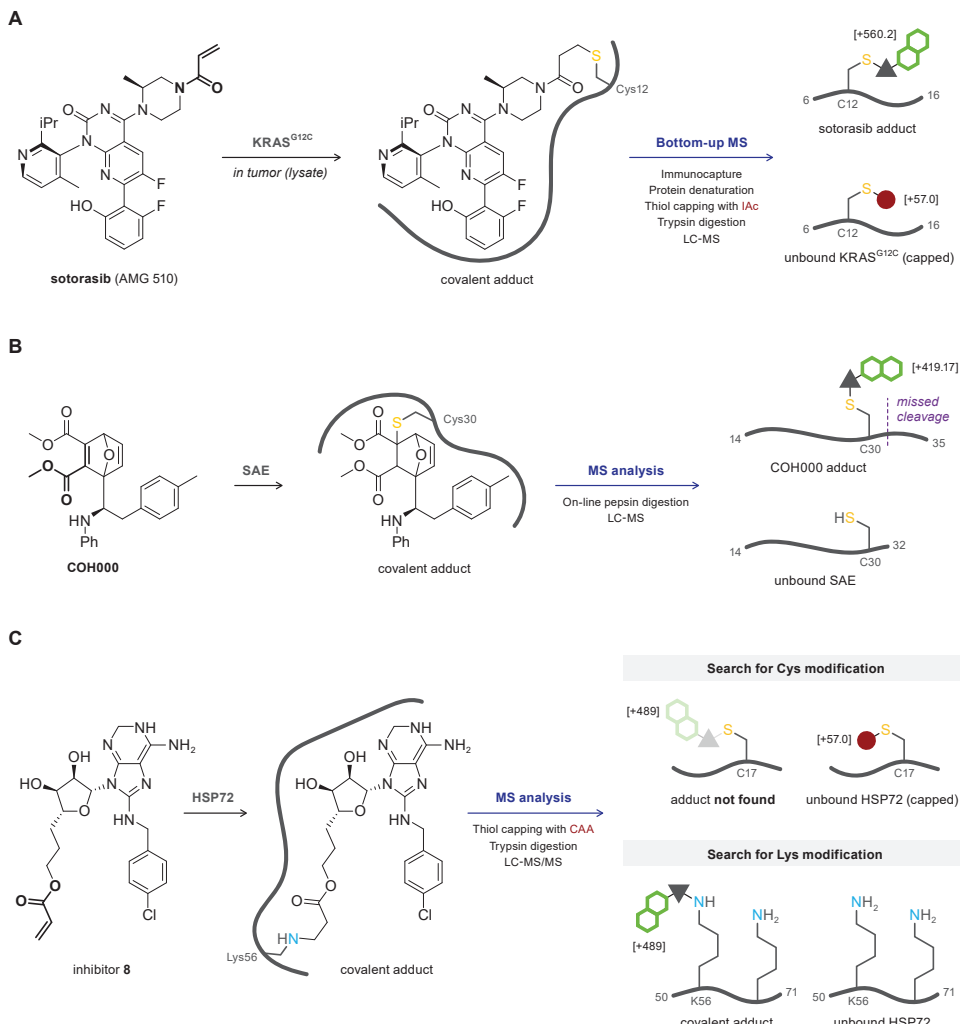


Figure 4 | Bottom-up MS analysis of covalent protein–drug adducts. **(A)** Detection of covalent adduct formation for clinically approved covalent inhibitor sotorasib (AMG 510) with KRAS^{G12C} isolated from lysates originating from (*in vitro* or *in vivo*) treated tumor cells.^{18,99} **(B)** Identification of covalent adduct formation between recombinant SUMO E1 (SAE) and covalent inhibitor COH000 reveals unexpected modification of allosteric Cys30 rather than catalytic Cys173.⁷⁰ Covalent modification of Cys30 interferes with pepsin-mediated digestion, generating longer adduct peptides than in the untreated control (missed cleavage). **(C)** Bottom-up MS analysis of recombinant HSP72 incubated with covalent acrylamide ligand **8** revealed covalent modification of Lys56 rather than catalytic Cys17.⁷¹ Data analysis focused on lysine modification resulted in detection of the simple adduct of L50–K71 peptide.

(Figure 4C). Instead, they found evidence suggesting allosteric Cys267 was modified, but site-directed mutagenesis revealed that this modification only contributed to a minor covalent adduct and is not responsible for inhibition of protein function. Finally, expanding the search to modification of other nucleophiles (lysine) revealed the modified L50–K71 peptide. A reliable

MS2 spectrum confirming Lys56 as the modified amino acid could not be obtained (details on MS/MS analysis in *section 2.3*) but the unanticipated covalent modification of Lys56 driving the inhibitory activity was confirmed with the HSP72^{K56A} mutant.

Reversible binding mode. Direct detection of the proteolytic peptide modified with a reversible covalent inhibitor (CRI) or ligand can be challenging because denaturation and proteolytic digestion are known to promote CRI dissociation,^{49, 54-55} and treatment with alkylating reagent to cap free thiols can block CRI rebinding. As such, modified peptides are more likely to be detected when thiol capping precedes denaturation and proteolytic digestion. It is possible to detect the modified tryptic peptides with bottom-up MS-based methods if the dissociation rate of the reversible covalent modifier is slow enough, as exemplified by detection of proteolytic UCHL1 peptides modified with reversible covalent cyanimide IMP-1710.⁸⁴

Quantification of covalent occupancy. Covalent target engagement is often quantified indirectly from depletion of the unmodified proteolytic peptide in the treated sample relative to the untreated sample^{96-97, 101} as unbiased quantification of the (modified) proteolytic peptide can be challenging: ionization efficiency differences can occur following modification with a covalent ligand. The (LC-)MS/MS methods to overcome this bias will be discussed in the next section.¹⁰⁰

2.3. MS/MS or Tandem MS

Bottom-up MS analysis is frequently coupled to a subsequent MS analysis (tandem MS or MS/MS) to enable identification of the covalently modified amino acid (**Figure 2C**). Specific precursor peptides are isolated after MS1 and subjected to collision/fragmentation conditions to generate charged fragment ions. The amino acid sequence of the precursor ion can be deduced from the mass of the fragment ions in MS2. For covalent adducts, fragment ions containing the covalently modified amino acid residue have a higher mass than fragment ions derived from the unmodified peptide, thus enabling identification of the modified amino acid. Tandem MS procedures have frequently been used to identify the modified amino acid residue covalent inhibitors targeting different protein classes.^{18, 22, 70-71, 83-84, 90} For the unambiguous assignment of the modified noncatalytic cysteine in the kinase domains affected by clinical irreversible covalent EGFR inhibitor **afatinib** (BIBW 2992) (**Figure 5A**),¹⁴ LC-MS/MS analysis following pepsin-digestion proved very valuable. The modified Q791-L798 peptide ion was found in the MS1 spectrum, and MS2 data identified Cys797 as the modified amino acid. Moreover, detection of a sulfurized afatinib fragment ion resultant from fragmentation of the C-S bond between the thiol and the cysteine β -carbon further confirmed covalent thiol addition to **afatinib**.

Covalent modification can (negatively) affect the ionization of peptide fragments, and it is not uncommon to only detect unmodified fragment ions (**Figure 5B**):^{83-84, 88} LC-MS/MS analysis of the trypsin- and GluC-digested covalent adduct confirmed covalent binding of **tirabrutinib** (ONO-4059)⁸⁸ to the BTK Y476-R487 precursor peptide (MS1) but only unmodified fragment ions and fragmentation of the parent inhibitor were found in MS2. However, the unmodified fragment ions indicate ligand modification occurred at one of the A478-C481 residues, of which Cys481 is the most nucleophilic residue. Interpretation of MS/MS data is usually tailored

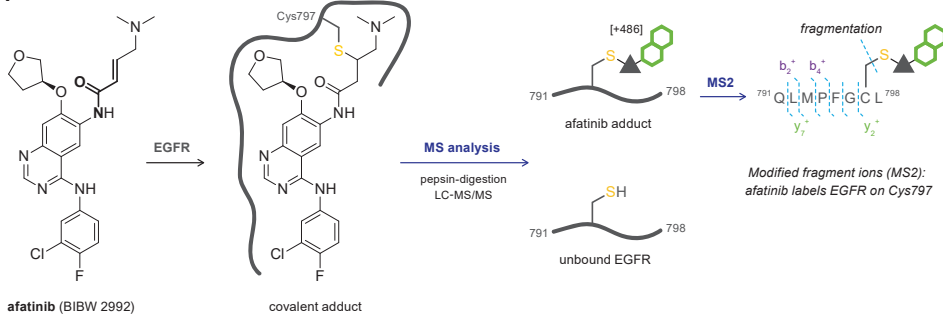
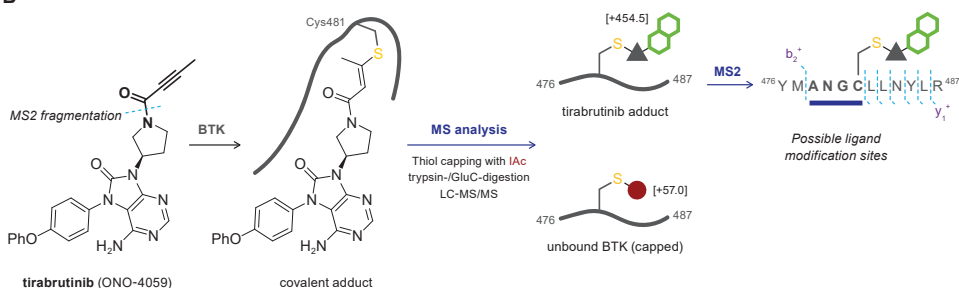
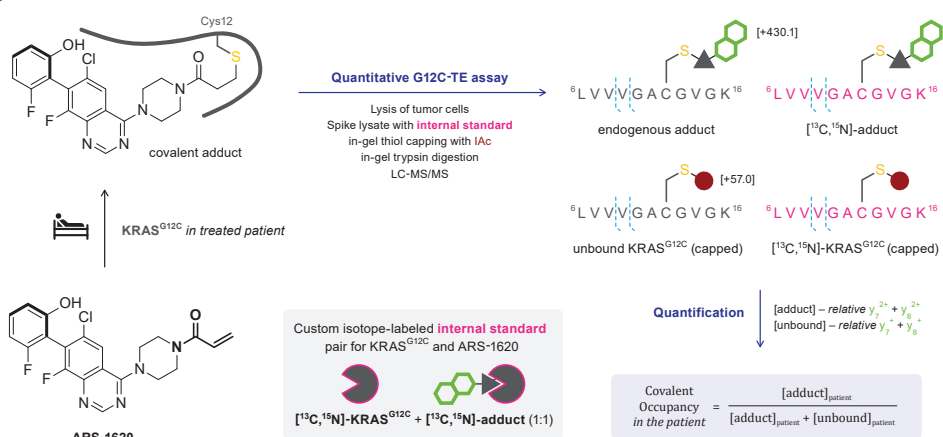
A**2****B****C**

Figure 5 | LC-MS/MS analysis of covalent protein–drug adducts. **(A)** Identification of the covalently targeted amino acid by afatinib (BIBW 2992) in purified EGFR^{T790M/L858R} kinase domain.¹⁴ **(B)** Identification of covalently modified amino acids in recombinant BTK kinase domain by BTK inhibitor tirabrutinib (ONO-4059).⁸⁵ MS2 detection only showed unmodified fragment ions, and ligand fragmentation of unbound tirabrutinib. **(C)** Internally-controlled quantitative KRAS^{G12C} Target Engagement (G12C-TE) assay illustrated with KRAS^{G12C} inhibitor ARS-1620.¹⁰⁰ Lysates originating from clinical tumor biopsies are spiked with an internal standard: recombinant stable isotope-labeled KRAS^{G12C}(1-169) internal standard – consisting of a 1:1 mixture of free $[^{13}\text{C}, ^{15}\text{N}]\text{-KRAS}^{\text{G12C}}$ and covalent $[^{13}\text{C}, ^{15}\text{N}]\text{-KRAS}^{\text{G12C}}\text{-ARS-1620}$ adduct – to calculate the *in vivo* covalent target occupancy from the relative abundance of fragment ions corresponding to endogenous or stable isotope-labeled adducts as well as unbound KRAS^{G12C}.

towards modification of a specific amino acid class or even a single specific residue, searching only for modification of cysteine residues and performing MS2 for peptide ions containing the catalytic cysteine. Although it is generally safe to assume that covalent inhibitors bearing a thiol-reactive electrophile will target the nucleophilic catalytic cysteine residue, covalent modification of less reactive cysteines^{70, 91} or even unexpected amino acids has been reported in exceptional cases.⁷¹

Reversible binding mode. Limitations and challenges for reversible covalent ligands are similar to bottom-up MS analysis. Detection of the simple adduct and fragment ions containing the covalent ligand has been reported for reversible covalent ligands with a slow dissociation rate.⁸⁴

Quantification of covalent occupancy. Covalent *in vivo* target engagement of clinically approved KRAS^{G12C} inhibitor **sotorasib** (AMG 510) has been quantified from the percentage of modified KRAS^{G12C} peptide normalized to the total KRAS^{G12C} peptides in tumor cells recovered from treated mice.¹⁸ However, caution is advised as this method does not take the possible effect of covalent modification onto the ionization of the fragment ions into account. Quantitative covalent KRAS^{G12C} Target Engagement (G12C-TE) assays are typically indirect, using [¹³C, ¹⁵N]-KRAS^{G12C} (peptide) as an internal control to determine the absolute level of unoccupied KRAS^{G12C}.^{89, 98, 101-103} Cellular/biochemical occupancy is calculated from comparison of unbound KRAS^{G12C} levels in the treated sample to the untreated control. However, these indirect methods are not compatible with clinical development of solid tumor treatment because pretreatment or patient-matched reference biopsies are typically not available.¹⁰⁴ Scientists at Wellspring Biosciences developed a direct internally controlled quantitative MS/MS-method for the accurate determination of target occupancy in FFPE (formalin fixed paraffin embedded) samples prepared from clinical tumor biopsies without the requirement of pretreatment or untreated controls, illustrated for KRAS^{G12C} inhibitor **ARS-1620** as a proof-of-concept study (**Figure 5C**).¹⁰⁰ Here, tumor-derived lysates are spiked with an internal standard consisting of a 1:1 mixture of unbound [¹³C, ¹⁵N]-KRAS^{G12C} and covalent [¹³C, ¹⁵N]-KRAS^{G12C}-inhibitor adduct, thereby enabling absolute quantification of endogenous unbound as well as modified KRAS^{G12C} peptide ions. The samples were then exposed to reducing conditions, with in-gel thiol capping with IAc and trypsin digestion of RAS proteins, before being submitted to LC-MS/MS analysis. Using the respective internal standard peptides, the ratio between endogenous unbound and ARS-1620-bound KRAS^{G12C} could be determined, allowing calculation of *in vivo* covalent occupancy. This method is generally applicable for proteins with endogenous expression levels well above the limit of quantification by MS, but its application will be practically limited by the production of recombinant stable isotope-labeled protein and the required generation of an isotope-labeled internal standard for each individual inhibitor.

3. Protein Crystallography

X-ray crystallography is a technique used to elucidate the 3D structure of crystalline compounds, from small molecules to (large) proteins.¹⁰⁵ Protein crystallography is the most informative technique discussed in this work: providing biophysical evidence on the covalent adduct

along with detailed structural information on the modified amino acid residue and the bond layout of the protein-bound ligand. Covalent bonds between individual atoms are not directly observed: the distance between the individual atoms is detected, along with a continuous electron density, from which the likeliness that these atoms are involved in a covalent bond is determined, with performance of orthogonal experiments (e.g. MS, mutagenesis) to validate covalency (Figure 6). One of the major practical drawbacks is the consumption of large amounts of highly pure soluble protein, and not all soluble proteins (or protein complexes) form suitably, diffracting crystals (if any at all).¹⁰⁵ In comparison: smaller protein amounts (of lower purity) are sufficient for less informative methods (e.g. MS). For protein crystals with appropriate diffraction, resolved macromolecular (ligand-bound) structures are deposited to the publicly accessible Protein Data Bank (PDB),¹⁰⁶⁻¹⁰⁷ enabling other researchers to access this wealth of structural information. High resolution structures of covalent adducts are available for various clinically approved TCIs including BTK inhibitors **ibrutinib** (PCI-32765, PDB: 5P9J)¹⁰⁸ and **zanubrutinib** (BGB-3111, PDB: 6J6M),¹² EGFR inhibitor **afatinib** (BIBW 2992, PDB: 4G5J),¹⁴ and proteasome inhibitor **bortezomib** (PS-341, PDB: 2F16).⁵¹ The structural binding information can be used to gain insight on ligand binding driving target selectivity and/or reactivity,¹⁰⁹⁻¹¹² and can be combined with (covalent) docking studies^{44, 113-115} to aid structure-based design of covalent ligands with improved potency and/or selectivity.^{22, 45, 116-119} Structure-guided drug design approaches are employed to optimize the proximity of the electrophilic warhead to the nucleophilic amino acid.²² The potency of clinical candidate **ARS-1620** (PDB: 5V9U) was improved by surface groove occupation, resulting in enhanced interactions with the KRAS^{G12C} protein eventually leading to the development of clinically approved KRAS^{G12C} inhibitor **sotorasib** (AMG 510, PDB: 6OIM).⁹⁹

A typical workflow starts with expression and purification of recombinant protein (domain), treatment with ligand, and screening hundreds of crystallization conditions to produce sufficiently large, singular crystals.^{105, 120} Suitable crystals of, hopefully, the covalent protein–ligand adduct are then fished, flash frozen and exposed to an X-ray beam at a synchrotron. The atoms in a crystalline structure (at low temperature) ideally are stationary and the diffraction pattern will be collected over different angles. The resulting intensities are then indexed to determine the space group and integrated into a dataset from which a 3D model can be determined.¹²¹ As the dataset is a reciprocal space representation of the structure, the intensities need phases to actually solve the structure. Using one of the various phasing methods,¹²² an initial structure model and electron density can be determined. After various iterative rounds of model building and structure refinement, hopefully electron density for the (covalent) ligand can be seen. The most reliable structural data is obtained when the model is first refined for the protein (based on the apo structure of the protein) and the remaining electron density is used to fit the ligand as this minimizes the bias for the inhibitor binding site.¹²³ For some proteins, apo structures of active, uninhibited enzymes may not be available for autoproteolytic/cannibalistic reasons (e.g. cysteine cathepsins) due to self-proteolysis or autodigestion.¹²⁴⁻¹²⁵ Occasionally, one can obtain mixed crystals, consisting of free protein, noncovalent protein–ligand complex and covalent protein–ligand adduct. This can decrease the quality and may impair detection altogether, thus requiring purification of the covalent adduct prior to crystallization. Alternatively, crystals of the free (apo) protein are allowed to form,

before soaking in the (covalent) ligand, though this can result in mixed crystals or cracking of the crystal.¹⁴ Soaking is popular in structure-based ligand screens as it conveniently sidesteps the optimization of crystallization conditions for each individual ligand.¹²⁶ However, soaking is not recommended for covalent drugs as the rigid crystalline protein can hinder formation of a covalent adduct, especially if the crystalline apo protein is in the incorrect conformation for ligand binding; if noncovalent ligand binding induces a conformational change before covalent adduct formation,¹²⁷ or if the crystalline protein has lost its catalytic activity essential for covalent adduct formation with mechanism-based inhibitors.⁴⁸

Non-crystallographers are advised to consult the works of Wlodawer and co-workers on interpretation and critical evaluation of structural data.^{120, 128} The value for resolution is expressed as the smallest resolved distance (in Å = 10⁻¹⁰ m) in the structure model. Although the resolution applies to the whole map, parts of the structure may suffer from disorder and have high temperature factors as a result.¹²⁸⁻¹²⁹ It is important to realize that covalent adduct formation in these areas may not be reliably detected. Hydrogen atoms are not shown in most structures obtained by X-ray diffraction (XRD) as hydrogen atoms only weakly scatter X-ray beams: they only have one electron, which is always involved in a bond with another atom, and are therefore not precisely localized at the usual resolution.¹³⁰ A low numeric value correlates with a high resolution: individual atoms (including some hydrogens) can be observed at <1.2 Å, most backbones and sidechains are clear at 2.5 Å, while only the general backbone can be solved at a resolution of 5 Å.¹²¹ The average distance between a thiol atom and carbon atom in a covalent single C-S bond is 1.82 Å and cannot reliably be observed when the resolution at the ligand binding site is too low.

Protein crystallography has revealed unexpected modification of noncatalytic (allosteric) cysteine residues rather than the catalytic cysteine residue. Solving the crystal structure provided molecular insight on why a covalent E3 ubiquitin ligase Nedd4-1 inhibitor (PDB: 5C91) inhibits elongation of polyubiquitin chains but does not completely inhibit all catalytic activity:⁹¹ the inhibitor targets allosteric Cys627 positioned at the substrate binding site rather than the more nucleophilic catalytic cysteine residue Cys867 (**Figure 6A**). Covalent modification of allosteric Cys30 in SUMO-activating enzyme (SUMO E1 or SAE) by **COH000** rather than catalytic Cys173 (see **Figure 4B**) was validated by solving the X-ray crystal structure (PDB: 6CWY).¹³¹ Of note, protein crystallography reveals the protein-ligand complex or adduct that forms the best crystals but this does not have to be the most prevalent binding mode in solution: modification of a specific (unexpected) amino acid should be validated with orthogonal techniques to ensure the modification is representative for ligand binding in solution. As such, protein crystallography is not a suitable technique for quantification of covalent adduct formation.

Natural product **salinosporamide A** (SalA, NPI-0052, marizomib) is a clinically approved covalent 20S proteasome inhibitor with an irreversible binding mode, whereas closely related natural product **salinosporamide B** (SalB, NPI-0047) has a reversible binding mode (**Figure 6B**).¹³² Crystal structure analysis reveals that threonine Thr1 addition to the chloroalkyl β-lactone in SalA resulting in β-lactone ring opening is followed by intramolecular nucleophilic substitution to irreversibly form a stable cyclic tetrahydrofuran (THF) ring (PDB: 2FAK)¹¹⁰

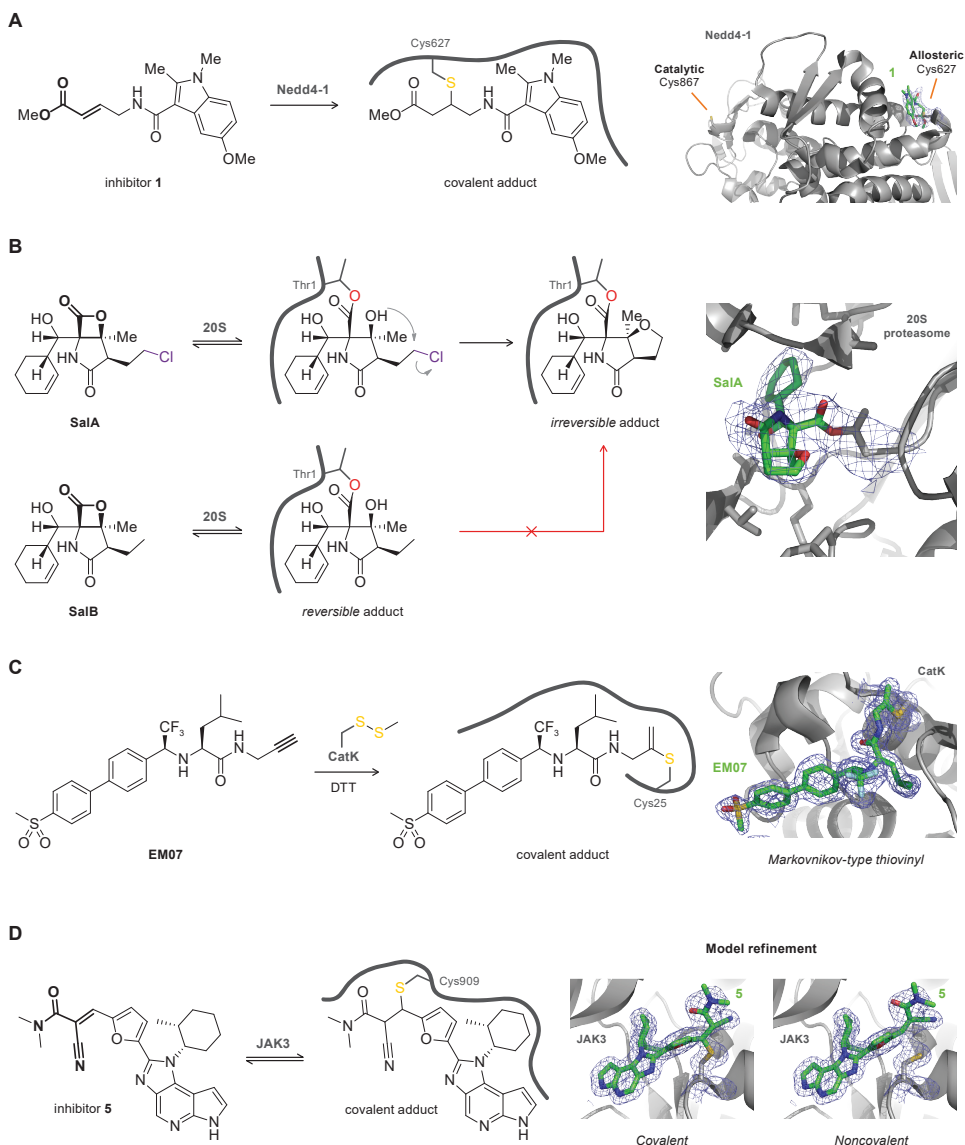


Figure 6 | Structural binding information on covalent protein–drug adducts obtained by protein crystallography. **(A)** Identification of unexpected modified amino acid residue. Inhibitor **1** modifies ubiquitin E3 ligase Nedd4-1 on allosteric cysteine residue Cys627 rather than the more nucleophilic catalytic cysteine residue Cys867 (PDB: 5C91).⁹¹ **(B)** Protein crystallography of closely related 20S proteasome inhibitors salinosporamide A (SalA, NPI-0052, marizomib) and salinosporamide B (SalB) aids mechanistic understanding on their different binding modes:¹³² SalA (PDB: 2FAK)¹¹⁰ forms an irreversible adduct by ring closure with a chloride leaving group following initial formation of the reversible covalent acyl ester with Thr1-OH. **(C)** Structural analysis confirms thiol–alkyne addition of catalytic Cys25 in human cathepsin K (hCatK) to the internal alkyne carbon on odanacatib derivative EM07 (PDB: 6QBS),⁸³ forming a covalent adduct with a Markovnikov thiovinyl bond lay-out similar to the thioimidate adduct of hCatK with the odanacatib nitrile (PDB: 5TD1).¹³⁴ **(D)** Refined electron density maps assuming covalent ligand binding (*left*) or noncovalent ligand binding (*right*) indicate a mixture of both states upon co-crystallization of reversible covalent cyanoacrylamide **5** with Janus kinase JAK3 (PDB: 5LWN).¹³⁵

that cannot be formed with the β -lactone of SalB, thus aiding molecular understanding of the irreversible binding mode of SalA. Similarly, protein crystallography provided mechanistic insight on the superior selectivity of clinical multiple myeloma drug **carfilzomib** (PR-171, PDB: 4R67)¹³³ for the 20S proteasome over non-proteasomal proteases, and why such selectivity is not observed for **bortezomib** (PS-341, PDB: 2F16).⁵¹ **Carfilzomib** forms a dual covalent adduct with the 20S proteasome, and the additional engagement of the Thr1 primary amine is specific for proteasomal proteins.

Protein crystallography provides valuable structural information on the bond layout of the covalently bound ligand. In our group, solving the crystal structure of ABP (activity-based probe) Ub-**Prg** with cysteine protease vOTU revealed an unexpected Markovnikov-type thiovinylic bond between the active site cysteine thiol in the protease and internal carbon of the alkyne in Ub-**Prg** (PDB: 3ZNH).¹³⁶ This thiovinylic bond layout has since been observed for propargyl-containing ABPs targeting various cysteine proteases (listed in Table S1 of citation⁸²), and for small molecule CatK inhibitor **EM07** (PDB: 6QBS)⁸³ (**Figure 6C**). Active, mature CatK had to be treated with S-methyl methanethiosulfonate (MMTS) to prevent autodigestion in absence of competing substrate, which is more prone to occur at the high concentrations (>10 mg/mL) used for crystallography.^{124-125, 137} The thiomethyl protecting group is removed with reducing agent (e.g. BME, TCEP or DTT), to allow covalent adduct formation with the simultaneously added inhibitor.¹³⁸

Reversible binding mode. Crystallography does not involve stringent washing or (harsh) denaturing conditions that would promote ligand dissociation, thus being particularly suitable for the evaluation of reversible covalent ligands. Co-crystallization of clinical Hepatitis C virus (HCV) drug **telaprevir** (VX-950) with serine protease NS3/4A confirms the bond layout of catalytic Ser139 bound to the C- α carbon of the ketoamide warhead (PDB: 3SV6).⁵³ Ligand interactions with frequently mutated protein sites provides a molecular basis for clinically occurring drug resistance. Importantly, covalent and noncovalently bound ligand may coexist in the crystal structure, as was demonstrated for reversible covalent cyanoacrylamide inhibitors targeting nonconserved cysteine Cys909 in an induced fit binding pocket of Janus kinase JAK3 (PDB: 5LWN)¹³⁵ (**Figure 6D**). Other notable examples of reversible inhibitors are crystal structures of the first clinically approved proteasome inhibitor **bortezomib** (PS-341)¹³⁹ covalently bound to Thr1 of yeast 20S proteasome through the boronic acid moiety (PDB: 2F16),⁵¹ COVID-19 drug **nirmatrelvir** (PF-07321332) forming a reversible covalent thioimidate adduct with catalytic cysteine Cys145 of SARS-CoV-2 M^{pro} protease in crystals formed by co-crystallization (PDB: 7RFW) or by soaking the apo crystal (PDB: 7RFS),⁴⁷ and the structure-based design of reversible covalent BTK inhibitors with tunable residence times.⁵⁵

4. Intrinsic Fluorescence/Absorbance

Covalent thiol addition can change the intrinsic spectroscopic properties of certain ligands and can be used to monitor covalent adduct formation in plate-based fluorescence/absorbance assays. Generating a chemical tool or an activity-based probe (ABP) by introducing a fluorophore or fluorescent leaving group to the ligand core will be discussed in more detail in

section 6. Here, we will focus on ligands that do not require late-stage structural modifications because they contain a structural motif that has intrinsic spectroscopic properties,¹⁴⁰ with a detectable change upon covalent adduct formation. This method is not generally applicable as there are strict structural limitations to the ligand core and nature of the electrophilic warhead. The main advantage of intrinsic spectroscopic methods is the compatibility with plate-based HTS assays, and catalytic activity is not required. The latter is directly a major drawback as it is impossible to discriminate between desired adduct formation with the intended cysteine thiol and undesired adduct formation with untargeted thiols present in the reaction buffer. This method always needs orthogonal validation as noncovalent binding events can also induce detectable changes in intrinsic fluorescence/absorbance.¹⁴¹

The Rauh group reported a plate-based assay for direct detection of covalent bond formation of quinazoline- and quinoline-based kinase inhibitors with an attached conjugated electron-deficient group such as an acrylamide warhead (Figure 7A).¹⁴² The unbound inhibitor exhibits

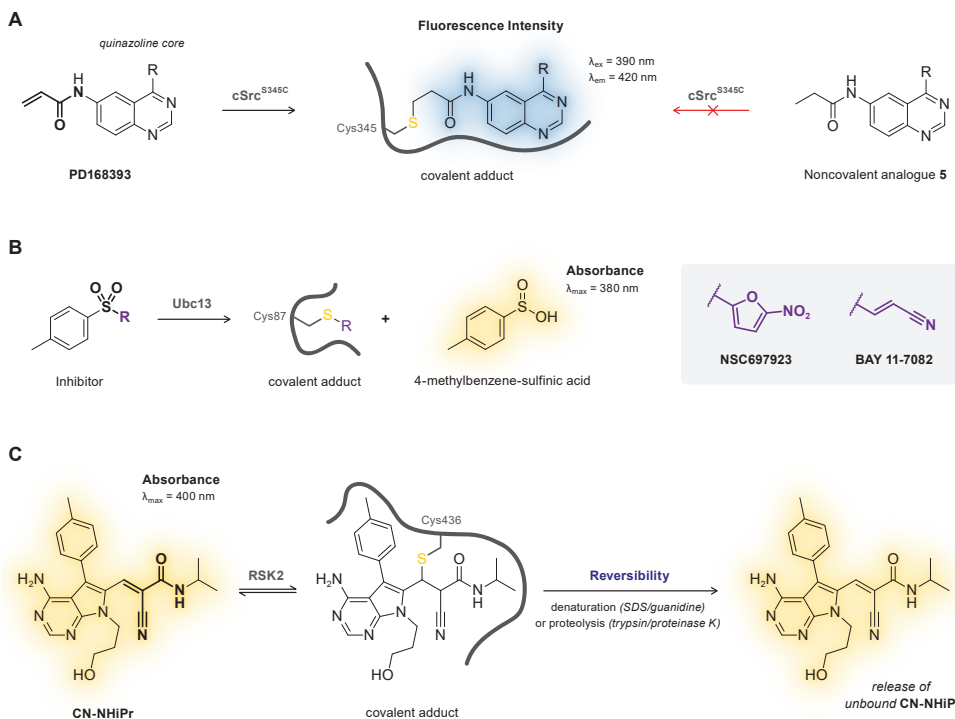


Figure 7 | Direct detection of changes in intrinsic spectroscopic properties upon covalent thiol addition. **(A)** Thiol addition increases intrinsic fluorescence intensity of quinazoline and quinoline cores with an attached conjugated Michael acceptor.¹⁴² Detection of increased fluorescence intensity upon adduct formation for irreversible covalent inhibitor PD168393 with cSrccS345C but not for the noncovalent analogue. **(B)** Release of 4-methylbenzenesulfinic acid results in a detectable absorption increase upon covalent adduct formation of inhibitors NSC697923 and BAY 11-7082 with Ubc13^{WT}.¹⁴³ **(C)** Intrinsic absorption in the UV-visible spectrum of *N*-isopropyl cyanoacrylamide CN-NHPr decreases upon nucleophilic thiol addition.⁵⁴ Reappearance of signal upon protein denaturation or proteolysis-induced inhibitor dissociation is indicative of a reversible covalent binding mode.

weak fluorescence emission upon excitation due to photo-induced electron transfer (PET) from the quinazoline/quinoline core to the attached conjugated Michael acceptor. Covalent thiol adduct formation enhances the quantum yield and can thus be detected as an increase in the fluorescence emission as was illustrated for recombinant cSrc^{S345C} mutant (Cys345 mutation on an isostructural position to Cys797 in EGFR) with irreversible covalent quinazoline **PD168393**, but not with a noncovalent analogue.¹⁴²

Analogous to fluorogenic substrates that release a fluorescent group upon proteolytic cleavage,¹⁴⁴ certain irreversible covalent inhibitors release a (detectable) leaving group upon covalent thiol addition (**Figure 7B**). This concept has been utilized to monitor covalent adduct formation of covalent inhibitors **NSC697923** and **BAY 11-7082** with E2 ubiquitin conjugating enzyme Ubc13:¹⁴³ elimination of 4-methylbenzene-sulfinic acid upon covalent thiol addition can be monitored by an increase in absorbance in the UV-visible spectrum directly related to covalent adduct formation.

Reversible covalent binding and reversibility assays. Detection of intrinsic fluorescence is compatible with reversible covalent inhibition, as demonstrated by the Taunton group for thiol addition to reversible covalent kinase inhibitors bearing a cyanoacrylamide warhead.⁵⁴ They report that unbound *N*-isopropyl cyanoacrylamide **CN-NHiPr** has a strong intrinsic absorption in the UV-visible spectrum which disappears upon treatment with excess recombinant RSK2 kinase domain, consistent with nucleophilic thiol addition of Cys436 to the cyanoacrylamide warhead (**Figure 7C**). Reversibility could then be assessed by exposing covalent RSK2–CN-NHiPr adduct to denaturing conditions or proteolytic digestion to induce target dissociation: reappearance of the absorption peak (and LC-MS detection of recovered unbound cyanoacrylamide) is in agreement with a reversible covalent binding mode.

5. Nuclear Magnetic Resonance (NMR)

Ligand-observed NMR analysis was the predominant method to detect covalent bond formation between enzyme and covalent inhibitor prior to rise in popularity of MS analysis or protein crystallography.³⁹ A change in the chemical environment resultant from (non) covalent interactions causes a detectable change in the resonance frequency (typically reported as ‘chemical shift’) and the coupling of nuclei with a nonzero nuclear spin (e.g. ¹H, ¹³C, ¹⁵N) in the magnetic field of the NMR spectrometer. An overview of NMR spectroscopy principles for protein-ligand interactions can be found elsewhere.^{145–147} Nowadays, NMR studies are employed in structure-based drug discovery and NMR screening for covalent (fragment) ligands,^{148–149} and have been used for ligand binding site mapping and structural elucidation of various covalent ligands. In macromolecular structure determination, NMR and protein crystallography can be complementary techniques,^{150–151} and NMR-resolved macromolecular (ligand-bound) structures are also deposited to the publicly accessible Protein Data Bank (PDB). Solution structures of covalent adducts have been deposited for compounds bound to protein targets,^{152–154} but also to minor groove duplex DNA: for example the covalent adduct of chemotherapy drug **mitomycin C** (UGN-101) a DNA 9-mer (PDB: 199D),¹⁵⁵ and alkylating agent **duocarmycin A** covalently bound to a DNA 7-mer (PDB: 107D).¹⁵⁶ Contrary to protein

crystallography, NMR techniques are compatible with characterization of binding mode reversibility by performing dialysis experiments,¹⁵⁴ and ligand binding can be quantified to determine kinetic parameters (e.g. dissociation constant K_D).^{146–147, 157–158}

Macromolecular structure determination typically involves multiple different NMR experiments to interrogate the different facets of the covalent adduct but 2D NMR techniques that detect the scalar (through multiple bonds) correlation of protein atoms to ligand atoms (e.g. pulse programs based on (HSQC)-TOCSY, HMBC, or 2D-INADEQUATE) ultimately provide the most conclusive NMR-based evidence of a covalent protein–drug adduct because these correlations are exclusive to covalent adducts. Unfortunately, protein signals often overlap with ligand signals, making it practically impossible to confidently discern the correlation between a ligand atom and a protein atom in a covalent adduct because correlations of atoms residing in the same ligand/protein (that do not require a covalent adduct) overlap.¹⁵³ Here we will feature the two main detection principles: protein-observed NMR (*section 5.1*) and ligand-observed NMR (*section 5.2*).

5.1. Protein-Observed NMR

Protein-observed NMR experiments compare the signals originating from the protein in unbound state to the protein–ligand complex; ligand binding changes the chemical environment of amino acids in proximity of the ligand, inducing chemical shift perturbations that can be used to map the ligand binding site onto the protein structure.^{147, 159} Given the vast number of atoms in a protein and the low natural abundance of the most suitable isotopes (e.g. ^{13}C , ^{15}N), protein-observed NMR spectroscopy typically involves production and purification of a uniform isotope-labeled protein along with recording a reference spectrum of the unbound protein to enable assignment of peaks to specific protein atoms.^{160–162} Protein-observed NMR experiments can be used to gain structural insight to ligand binding in solution, which is particularly useful for targets that are not compatible with crystallization or conformations that do not crystallize: for example, solution protein-observed NMR spectra revealed that noncovalent kinase inhibitor **imatinib** binds to c-Abl in an previously unidentified open state.¹⁶³ Furthermore, NMR experiments were employed to identify the binding site of covalent inhibitors of the *S. aureus* Sortase A enzyme (*Sa-SrtA*), and used to solve the structure of the covalent adduct (PDB: 2MLM, 6R1V).^{153–154} However, protein-observed NMR techniques are typically restricted to relatively small proteins (<50 kDa), and most techniques used in macromolecular structure elucidation (e.g. [^{15}N , ^1H]-HSQC) cannot directly discriminate between a covalent or a noncovalent ligand. It is advisable to employ additional ligand-observed experiments or orthogonal techniques (e.g. MS analysis) for covalent adduct validation: protein-observed NMR experiments technically only provide indirect evidence on covalency.^{160, 164}

5.2. Ligand-Observed NMR

In ligand-observed NMR experiments, a change in chemical shift of the ligand signals in the protein–ligand complex is compared relative to the ligand signals in the unbound ligand. The most popular ligand-observed NMR techniques for fragment screening (e.g. saturation transfer difference spectroscopy and its variants) are based on the NOE principle (proximity in

space) and thus cannot discriminate between binding of covalent or noncovalent ligands.^{160, 165} ¹H NMR chemical shift perturbations can be employed to distinguish unbound ligand from a covalent protein–ligand adduct, and support identification of the adduct isoform.¹⁶⁶ In addition to validation of covalent adduct formation, 1D ¹H NMR approaches enable indirect quantification of covalent occupancy by integration of the disappearing unbound ligand signals.^{39, 167} However, ¹H NMR experiments are typically only performed for adduct formation with small molecule thiol reagents (e.g. GSH) as overlapping background signals originating from protein hydrogens limit the practical application.

Direct detection of the covalent protein–ligand adduct by ligand-observed ¹³C NMR experiments is a more feasible approach but requires chemical synthesis of ligand with a ¹³C-labeled warhead to improve the signal over the background, otherwise the naturally occurring ¹³C signals in the ligand will be lost among those originating from the protein. The ¹³C chemical shift perturbations of adjacent carbons in the electrophilic warhead can be significant upon covalent thiol modification, especially compared to the less pronounced shifts induced by noncovalent binding interactions.¹⁶⁸ Detection of chemical shift perturbations of (isotope-labeled) epoxy succinyl peptides upon cysteine protease papain binding was successfully utilized to detect the covalent adduct along with identification of the covalent modification site.¹⁶⁹ Moreover, ¹³C NMR APT (attached proton test) experiments can be indicative of covalent adduct formation with unsaturated electrophiles (e.g. acrylamide): the phasing of the vinyl carbon adjacent to the reactive carbon in the unbound acrylamide is negative (CH) but is positive (CH₂) in the covalent adduct. Future application of ligand-observed NMR may be extended beyond the common ¹³C NMR and ¹H NMR without chemical introduction of an isotope-labeled atom for warheads bearing naturally abundant reactive atoms compatible with NMR (e.g. ³¹P or ¹⁹F in fluorophosphonates). ¹¹B NMR has been employed to detect the tetrahedral adduct of boronic acid covalently bound to Ser195 in serine protease trypsin.¹⁷⁰ This label-free approach has only been employed to study model reagents,¹⁷¹ but there still are seemingly unexplored opportunities for covalent adduct detection of boronic acid-bearing inhibitors (e.g. proteasome inhibitor **bortezomib**) with their pharmaceutical target.

Reversible inhibition and reversibility assays. An important advantage of NMR-based detection of covalent adducts is the compatibility with reversible covalent inhibitors. Especially when the covalent adduct is too short-lived to be isolated or detected due to rapid inhibitor dissociation under MS/sample preparation conditions as NMR enables detection in (aqueous) solution.⁵⁴ Ligand-observed ¹³C NMR analyses were already performed in 1986 to obtain evidence for the formation of a thioimide ester adduct between a nitrile ligand and the active site sulphhydryl of cysteine protease papain (**Figure 8A**).¹⁷² Incubation of active papain with the [¹³C]-labeled nitrile inhibitor resulted in appearance of a resonance signal at 182 ppm in ¹³C NMR in accordance with a covalent thioimide ester adduct. Rapid disappearance of the thioimide signal and increase of unbound inhibitor signal (~117 ppm) was detected upon treatment of the covalent adduct with glacial acid (AcOH) and thiol-trapping reagent 2,2'-dipyridyldisulfide (DPS), indicative of a reversible covalent binding mode. Similar ligand-observed NMR studies have been performed to provide evidence for reversible covalent adduct formation of cathepsin K with a [¹³C, ¹⁵N₄]-diacylhydrazine,¹⁷⁴ and papain with a [¹³C]-cyanimide.¹⁷⁵ A more

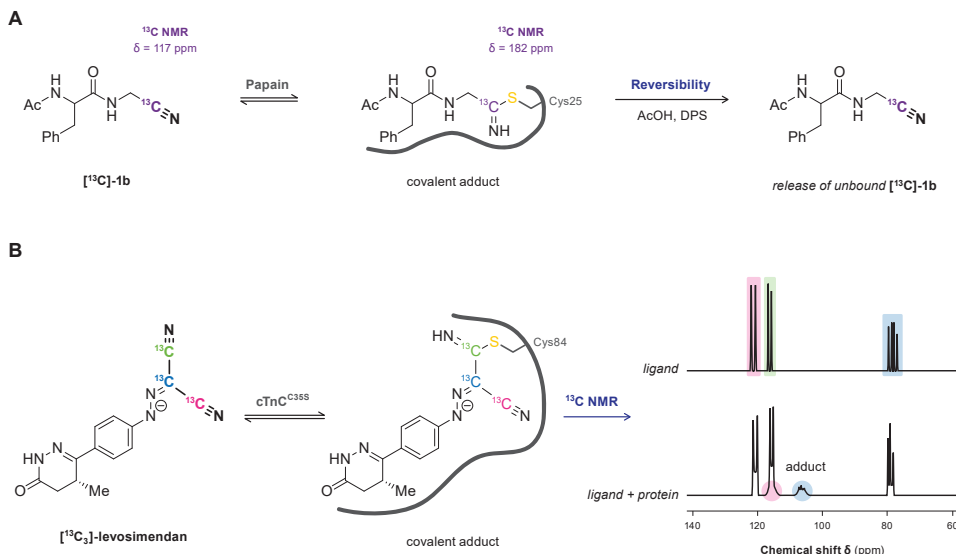


Figure 8 | Ligand-observed ¹³C NMR detection of covalent protein–drug adducts. **(A)** Chemical shift perturbation of the electrophilic ¹³C-labeled carbon in unbound nitrile [¹³C]-1b relative to the thioimidate ester adduct provides evidence of a covalent papain–nitrile adduct.¹⁷² Detection of unbound nitrile upon treatment with glacial acid (AcOH) and thiol-trapping reagent 2,2'-dipyridyldisulfide (DPS) is indicative of a reversible covalent binding mode. **(B)** Ligand-observed NMR studies with ¹³C-labeled levosimendan provide evidence for reversible covalent binding to a cysteine thiol in cardiac troponin C (cTnC).¹⁷³

recent example of ligand-observed NMR analysis aided elucidation of the binding mode of Ca²⁺ sensitizer **levosimendan** (Figure 8B), a clinical drug for heart failure treatment whose exact mechanism of action remained elusive for over 20 years after its discovery. Formation of a thioimidate bond between the electrophilic malonitrile moiety and cardiac troponin C (cTnC) was always assumed to have an important role,¹⁷⁶ but evidence for this reversible covalent binding mode was finally provided in 2016 by employing [¹³C₃]-levosimendan in ligand-observed ¹³C NMR studies.¹⁷³ Disappearance of unbound [¹³C₃]-levosimendan signals (~120 ppm) along with appearance of new signals (~160 ppm) is in agreement with predicted chemical shifts for a thioimidate adduct between the electrophilic malonitrile moiety on **levosimendan** and a cysteine thiol in cTnC. Lack of adduct in presence of cTnC^{C84S} but not cTnC^{C35S} validates Cys84 as the covalently modified amino acid residue.²⁹

6. Activity-Based Protein Profiling (ABPP)

Activity-based protein profiling (ABPP) is a chemical biology technique that employs covalent activity-based probes (ABPs) to characterize covalent enzyme modification in relevant biological systems (e.g. live cells, *in vivo*).^{104, 177–180} Pioneered in the labs of Cravatt¹⁸¹ and Bogyo,¹⁸² ABPs entailed a reactive group with a detection tag (e.g. fluorophore, radiolabeled isotope) or enrichment handle (e.g. biotin), that covalently modified catalytic serine/cysteine residues in active and uninhibited enzyme.^{178, 183} This general structure design is mostly maintained in

modern ABPs which typically comprise of an electrophilic moiety that forms a covalent bond with a nucleophilic amino acid residue, a reporter group (e.g. fluorophore, enrichment handle, bioorthogonal handle) to detect the covalent adduct, and, optionally, a recognition element for target/class-selectivity (**Figure 9A**). Nowadays, ABP development is not limited to catalytic amino acid residues: a wide range of ABPs is available from general residue-specific agents (e.g. **iodoacetamide** (IAc)-based thiol-alkylating reagents for cysteines)¹⁸⁴ and class-specific ABPs (e.g. fluorophosphonate-based probes for serine hydrolyses,¹⁷⁷ ubiquitin-based probes for DUBs,¹⁸⁵ ATP-based probes for kinases¹⁸⁶) to target-selective ABPs³⁷ (e.g. **ibrutinib**-based ABPs for BTK).¹¹ The field has since expanded beyond truly activity-based probes: ABPs targeting noncatalytic residues also label catalytic inactive mutants thus not requiring catalytic activity.¹¹ ABPP has a prominent role in covalent drug discovery:^{178, 187-188} not only for identification of new covalent hits in covalent (fragment) screening,¹⁸⁹ but also to identify cellular/*in vivo* covalently modified (off-target) proteins thereby derisking covalent inhibitor development.^{2, 190} The latter is emphasized by the recent work of van Esbroeck *et al.*:¹⁹¹ multiple off-target lipases targeted by fatty acid amide hydrolase (FAAH) inhibitor **BIA 10-2474** were identified by competitive ABPP, providing a possible explanation to the clinical neurotoxicity with lethal outcome for one of the human subjects in the phase I clinical trial (2016). This tragic example highlights why identification of potential covalent off-target modifications by (competitive) ABPP is recommended to be an integral part of early-stage covalent drug development.¹⁹⁰

Drug-derived ABPs are designed in two flavors: one-step ABPs (**Figure 9B**) and two-step ABPs (**Figure 9C**). One-step ABPs are generated by introduction of a (fluorescent) detection tag or an enrichment handle onto the parent drug by chemical synthesis. The tag or handle is introduced in a position that does not interfere with target binding, as indicated by structural data (e.g. crystal structure, docking simulations) or SAR analysis. Introduction of a large tag/handle can modify ligand reactivity, target selectivity, as well as cell permeability.¹⁹² Similar to one-step ABPs, two-step ABPs are generated from the parent drug but now a small and nonperturbing bioorthogonal handle is introduced, to which the actual detection group (fluorophore, enrichment handle) is clicked in the second step (**Figure 9C**). This bioorthogonal handle is less likely to have a pronounced effect on ligand selectivity, which is why evaluation of a two-step ABP is recommended in an early stage of covalent drug development to identify potential off-target effects.^{32, 190} Here, the proteome is treated with the two-step ABP bearing a small bioorthogonal handle (*step 1*), followed by coupling of a relatively large detection tag or enrichment handle (*step 2*). Traditionally, the coupling reaction employs the Huisgen Copper-catalyzed Alkyne–Azide Cycloaddition (CuAAC) reaction between alkynes and azides ('Click' chemistry)¹⁹³⁻¹⁹⁴ but alternative bioorthogonal reactions are available^{192, 195} – such as the Strain-Promoted Alkyne–Azide Cycloaddition (SPAAC) between strained alkynes and azides,¹⁹⁶ or the Inverse Electron Demand Diels Alder (IEDDA) reaction between (fluorogenic) tetrazines and strained dienophiles.¹⁹⁷ Two-step ABPs enable incubation in the native environment and are more likely to retain the membrane penetrating properties of the parent inhibitor, and are thus compatible with *in situ* and *in vivo* applications.^{104, 198} The success of this approach has recently been illustrated for inhibitors with various targets³² among which are BTK inhibitor **ibrutinib**,^{11, 190} JAK3 inhibitor **ritlecitinib** (PF-06651600),¹⁹⁹ KRAS^{G12C} inhibitor **adagrasib** (MRTX849),¹⁰³ and anti-obesity drug **orlistat**.²⁰⁰ Two-step clickable ABPs facilitate

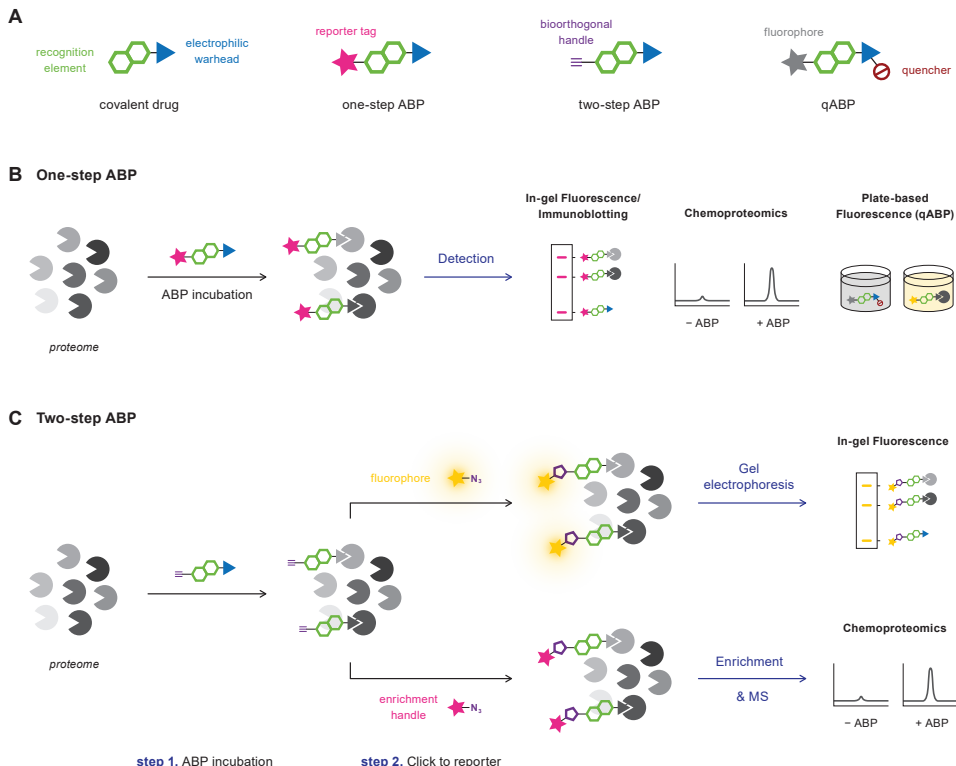


Figure 9 | Strategies for covalent adduct detection with drug-derived activity-based probes (ABPs). **(A)** General design principle for covalent drug-derived ABPs. A fluorophore, detection tag or enrichment handle is introduced onto the parent covalent drug bearing a recognition element and a covalent warhead. **(B)** Detection of covalently modified proteins with one-step ABPs. Proteome is treated with one-step ABP, proteins are resolved by gel electrophoresis or affinity purification, and modified targets are detected by in-gel fluorescence or immunoblotting, or by chemoproteomic evaluation. **(C)** Detection of covalent adducts with two-step ABPs. Proteome is incubated with a two-step ABP bearing a small bioorthogonal handle (*step 1*), followed by bioorthogonal coupling of a fluorophore, detection tag or enrichment handle (*step 2*), with subsequent analysis as shown for the one-step ABPs.

the coupling of a dual biotin/TAMRA-azide, allowing both in-gel fluorescence scanning for the TAMRA fluorophore and immunoblotting for the biotin tag in gel-based evaluation, and the biotin tag can also be utilized as an enrichment handle in chemoproteomic evaluation. The success of this dual approach is illustrated by clickable two-step ABPs equipped with a bioorthogonal alkyne handle: ABP PF-06789402 based on the scaffold of JAK3/TEC family kinase inhibitor **ritlecitinib** (PF-06651600),¹⁹⁹ and ABP selinexor-yne derived from clinically approved covalent XPO1 inhibitor **selinexor** (KPT-330).²⁰¹

Altogether, ABPP is a powerful tool to identify (un)desired covalent modification in a relevant biological setting. Here, we will discuss the detection of the covalent adduct in whole proteome with gel electrophoresis platforms (*section 6.1*), chemoproteomic platforms (*section 6.2*), and homogeneous (plate-based) platforms (*section 6.3*).

6.1. Gel Electrophoresis Platforms (In-gel Fluorescence, Immunoblotting)

Gel electrophoresis platforms were among the earliest ABPP methods to interrogate enzyme activity in complex mixtures, and are still a common method for rapid evaluation of inhibitor specificity.¹⁷⁸ A typical workflow (**Figure 9B**) involves incubation of recombinant protein or a whole proteome (e.g. cell lysate) with a one-step ABP followed by sample preparation under denaturing conditions (e.g. heating in presence of a reducing agent such as BME or TCEP) to simultaneously remove unreacted ABP and promote dissociation of noncovalent complexes. Then, the treated proteome is submitted to gel electrophoresis, and covalent adducts are visualized by in-gel fluorescence scanning for the fluorophore (e.g. TAMRA, Cy5, BODIPY)^{11, 199, 201} or immunoblotting for a reporter tag or enrichment handle (e.g. biotin, GST, His),²⁰² with a band appearing at the adduct mass (kDa). Gel-based ABP analysis is fast but is less informative than chemoproteomic approaches (discussed in *section 6.2*). Identifying the exact protein target in a proteome can be challenging as proteins of similar mass may overlap on gel, which may be addressed by comparative ABPP with knock-out cell lines.²⁰³⁻²⁰⁴ Competitive ABPP experiments are typically conducted to validate that the ABP has the same specificity as the inhibitor:^{11, 199, 205-206} treatment with parent BTK inhibitor **ibrutinib** (PCI-32765) precludes labeling with cell permeable fluorescent ABP PCI-33380 (**Figure 10A**).¹¹ The modified amino acid can be identified indirectly by treatment of (recombinant) protein with a single point-mutation,^{11, 82, 206} or by competitive labeling of the parent inhibitor with a validated residue-selective ABP (that is not derived from the parent inhibitor of interest).^{178, 207}

Reversible inhibition. ABPs bearing a reversible covalent warhead are compatible with gel-based analysis, as illustrated with cyanimide-based ABPs **IMP-1710**⁸⁴ and **8RK59**²⁰⁷ targeting deubiquitinating enzyme UCHL1 (**Figure 10B**). Importantly, reaction conditions required careful optimization as the fluorescent covalent adduct could not be detected after sample preparation under denaturing conditions: heating BODIPY-labeled UCHL1-8RK59 adduct to 94 °C in presence of reducing agent β-mercaptoethanol (BME) promoted covalent target disengagement.²⁰⁷ Subsequent chemoproteomic evaluation with **8RK64**, an alkyne-bearing derivative of **8RK59**, revealed enrichment of not only UCHL1 but also protein deglycase PARK7/DJ1, an attractive target in Parkinson's disease with a similar molecular mass that overlaps with UCHL1 by gel analysis. The discovery of this off-target modification has since aided the development of selective chemical tools to study PARK7 activity.²⁰⁸

Quantification of covalent occupancy. Direct gel-based strategies are typically used for qualitative (visual) identification of binding partners in cellular proteomes as low throughput gel electrophoresis strategies are associated with large error margins originating from deviations in gel loading volumes and protein distribution on gel. Our group reported a direct quantitative approach to calculate relevant kinetic parameters from time-dependent covalent occupancy of purified recombinant cysteine protease USP16 with irreversible covalent Rho-Ub-ABPs.⁸² Cellular JAK3 occupancy after pretreatment with **ritlecitinib** (PF-06651600) was assessed with two-step ABP **PF-06789402**.¹⁹⁹ Lysate was treated with biotin/TAMRA-azide, enriched for ABP-modified uninhibited proteins by pulldown with streptavidin beads and resolved by SDS-PAGE gel electrophoresis to quantify the remaining uninhibited JAK3 by immunoblotting. A popular though indirect approach in preclinical development of BTK inhibitors is to derive

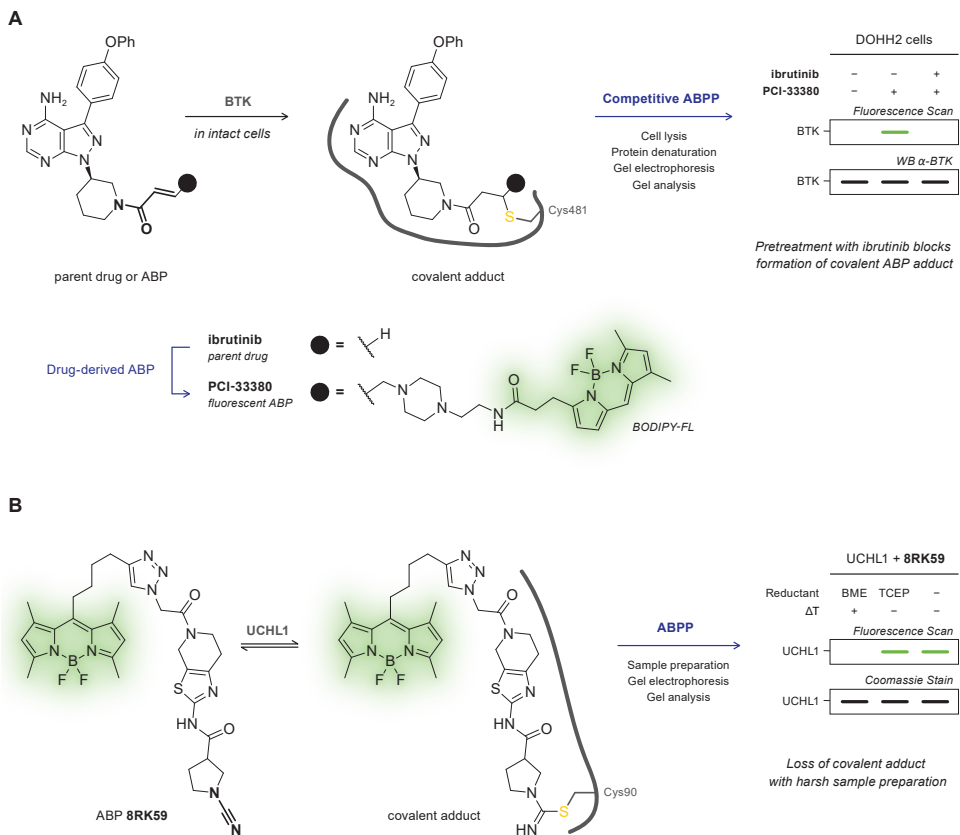


Figure 10 | Gel electrophoresis platforms for covalent adduct detection with drug-derived ABPs. **(A)** Competitive ABPP. Fluorescence scan for the BODIPY-FL fluorophore reveals that BTK labeling in DOHH2 cells by cell permeable one-step fluorescent ABP PCI-33380 is precluded by pretreatment with irreversible covalent parent inhibitor ibrutinib.¹¹ **(B)** Fluorescent signal originating from reversible covalent UCHL1–8RK59 adduct is not observed using harsh sample treatment prior to gel electrophoresis (boiling in presence of reducing agent BME) but can be observed using milder conditions (sample preparation in presence of reducing agent TCEP).²⁰⁷ Covalent adduct formation is validated using intact protein analysis by top-down MS.

inhibitor target engagement from the fluorescent ABP labeling of the remaining unbound protein: inhibitor-treated proteome is incubated with a target-selective fluorescent ABP (not necessarily derived from the parent inhibitor) that only binds to unbound BTK, and ABP-bound BTK is quantified by in-gel fluorescence. This approach has been successfully applied with irreversible BODIPY-labeled BTK-selective ABP PRN-933 to assess occupancy of reversible covalent BTK inhibitor **rilzabrutinib** (PRN-1008) in human PBMCs,⁴⁹ and in the development of reversible covalent BTK inhibitors with irreversible ABP PP-BODIPY.⁵⁵ Competition with general thiol-reactive ABPs (e.g. IAc-alkyne, TMR-maleimide) is of little use in gel-based ABP analysis as blocking a single cysteine residue will not perturb the ABP from binding to other available cysteine residues in the same protein, thus still resulting in a detectable signal on gel. Importantly, blocking adduct formation with a selective irreversible ABP provides indirect

evidence on the ligand binding site⁷⁴ but is not suitable to identify the modified amino acid by itself as this also could be a(n) (allo)steric effect.

DNA electrophoretic mobility shift. Most covalent drugs are too small to cause a detectable shift in electrophoresis upon covalent adduct formation, thus requiring modification with a detection group. Nevertheless, a DNA electrophoretic mobility shift assay has been employed to validate the covalent binding mode of **lurbinectedin** (PM01183) to naked DNA, despite its relatively small mass (785 Da).²⁰⁹

Scintillation autoradiography (fluorography). Drug-derived ABPs bearing a radioisotope tag (e.g. ¹²⁵I) used to be the primary mode for detection of catalytically active cysteine proteases.²¹⁰⁻²¹¹ Nowadays, radiolabeled inhibitors prepared for *in vivo* ADME (Absorption, Distribution, Metabolism, and Excretion) studies and PK (pharmacokinetic) profiling are occasionally employed as radioactive ABPs where the radioactive atom (typically ¹⁴C or ³H) serves as a small, non-perturbing tag.²¹² Radioactivity originating from the radiolabeled covalent adduct is detected after removal of unbound and noncovalently bound radiolabeled inhibitor by gel electrophoresis on polyacrylamide/SDS-PAGE gels (fluorography),²¹³ or filtration with stringent washing (liquid scintillation counting).²¹³⁻²¹⁴ This technique has recently been employed to validate covalent adduct formation of **neratinib** (HKI-272) with HER2, using neratinib-derived ABP [¹⁴C]HKI-272 ([¹⁴C]-25o) on recombinant HER2 cytoplasmic domain or in intact BT474 cells.^{16, 215} Similarly, *in vivo* covalent alkylation of hemoglobin by **RRx-001** (ABDNAZ) in red blood cells from various species was detected using radiolabeled ABP [¹⁴C]RRx-001.²¹⁶ Finally, scientists at Takeda Pharmaceutical developed a direct competitive ligand binding assay to quantify covalent occupancy and determine the inhibitory potency (k_{inact}/K_i) of irreversible EGFR inhibitor **canertinib** (CI-1033): time-dependent radioactivity originating from the covalent adduct with radiolabeled ABP [³H]CI-1033 (after filtration to remove unbound ABP) was quantified by liquid scintillation counting.²¹⁴

6.2. Chemoproteomic Platforms

Chemoproteomic protein profiling is a sensitive MS-based ABPP technology predominantly employed to evaluate the proteome-wide selectivity of covalent inhibitors, and identify (undesired) cellular targets for covalent modification in complex mixtures (e.g. cell lysate, live cells, tissue).^{38, 104, 190-191, 217-219} A general chemoproteomic procedure involves incubation of the proteome with ABP, coupling to an enrichment handle (e.g. biotin-azide, **Figure 9C**) and pull-down to enrich for ABP-modified proteins on beads. Stringent washing is performed to remove noncovalently bound proteins and eliminate nonspecific binders, followed by bottom-up MS/MS analysis of modified proteins. Quantification of relative protein abundance can be achieved with label-free quantitative methods comparing relative changes in two (or more) individual biological samples.^{198, 219-221} The majority of chemoproteomic formats are indirect, detecting proteins modified by a general thiol-alkylating or cysteine ABP (e.g. IAc-alkyne)^{189, 222-223} in presence and absence of the covalent inhibitor of interest, from which inhibitor-binding is deduced.^{178, 187, 222} For this purpose, classic broad-spectrum reactivity ABPs targeting various amino acid residues and protein classes are (commercially) available.^{37-38, 186, 222} In particular, the isoTOP-ABPP (isotopic Tandem Orthogonal Activity-Based Protein Profiling) platform is

an established indirect competitive method to simultaneously identify (off-)target modified proteins in whole proteomes together with the exact site of protein modification.^{2, 190, 223–224} The role of predominantly indirect competition methods in (fragment-based) covalent drug development has been reviewed before.^{37–38, 225} Here, we will focus on the (less prevalent) direct approaches in which the ABP is derived from the parent inhibitor. Direct (competitive) chemoproteomic approaches with drug-derived ABPs have the potential to identify lower abundance protein targets and can overcome the bias in global cysteine reactivity experiments with general thiol-reactive ABPs: inhibitor binding is only detected if the amino acid residue is targeted by the competing ABP, even though the inhibitor might be interacting with other amino acid residues.^{103, 198} Such targetable, or ‘druggable’, cysteines in human proteins were recently collated in publicly available curated repository CysDB.²²⁶ The success of a direct approach is illustrated by FDA-approved anti-obesity drug **tetrahydrolipstatin** (THL, orlistat) (**Figure 11A**): MS analysis following pull-down of modified proteins in cancer cell lines treated with two-step ABP **THL-R** did not only confirm binding to fatty acid synthase (FAS) but also identified other (off-)target proteins that aid its early development as an anticancer agent.²⁰⁰

High-throughput proteomic methods may involve metabolic or chemical labeling with stable heavy isotopes prior to MS analysis to enable absolute protein quantification and multiplexed measurements (mix of multiple samples/reaction conditions) minimizing run-to-run deviations.^{221, 227} The popular SILAC-ABPP platform (**Figure 11B**) is a metabolic isotope-labeling methodology, thus being restricted to stable cell lines as generating isotope-labeled controls is challenging for tissue or primary cell line samples.²²⁸ SILAC-ABPP combines ABPP with SILAC (stable-isotope labeling by amino acids in cell culture)^{229–230} to assess identity of covalent modified proteins. Cells are cultured in normal (*light*) or isotope-labeled (*heavy*) medium, treated with DMSO or ABP, and mixed after lysis. Modified proteins are detected by bottom-up LC/LC-MS/MS analysis after enrichment for covalent protein–ABP adducts. The isotope-labeling of the proteome is crucial to calculate the SILAC ratio compared to the untreated sample – proteins with SILAC ratios ≥ 3 –5 are designated as targeted. SILAC-ABPP analysis with an ibrutinib-derived ABP identified established off-target kinases as well as specific non-kinase targets from structurally and functionally diverse protein families in Ramos cells, including the uncharacterized protein FAM213A.¹⁹⁰ Typically, complementary competitive SILAC-ABPP experiments are performed to ensure that the drug-derived ABP has the same selectivity as the parent inhibitor: over 400 proteins were identified in a SILAC experiment with an adagrasib-derived ABP (**Figure 11B**) but only KRAS^{G12C} significantly decreased upon pretreatment with clinically approved KRAS^{G12C} inhibitor **adagrasib** (MRTX849).¹⁰³

Chemical isotope-labeling methods are compatible with samples that are not amendable for SILAC, such as endogenous (human) tissue samples,¹⁰⁴ as chemical isotope-labeling can be performed during sample preparation.^{221, 232} These methods are typically indirect, employing classic broad-spectrum reactivity ABPs. Among the most popular methodologies are isoTOP-ABPP^{223–224, 233} using isotope-labeled TEV protease-cleavable Click reagents (TEV tags), isoDTB-ABPP employing isotopically-labeled desthiobiotin (isoDTB) tags,²³⁴ rdTOP-ABPP²³⁵ employing stable-isotope diMe labeling of primary amines (peptide N-terminus and lysine ε-amino group),^{227, 236–239} and TMT-ABPP²⁴⁰ employing tandem mass tags (TMT) such as

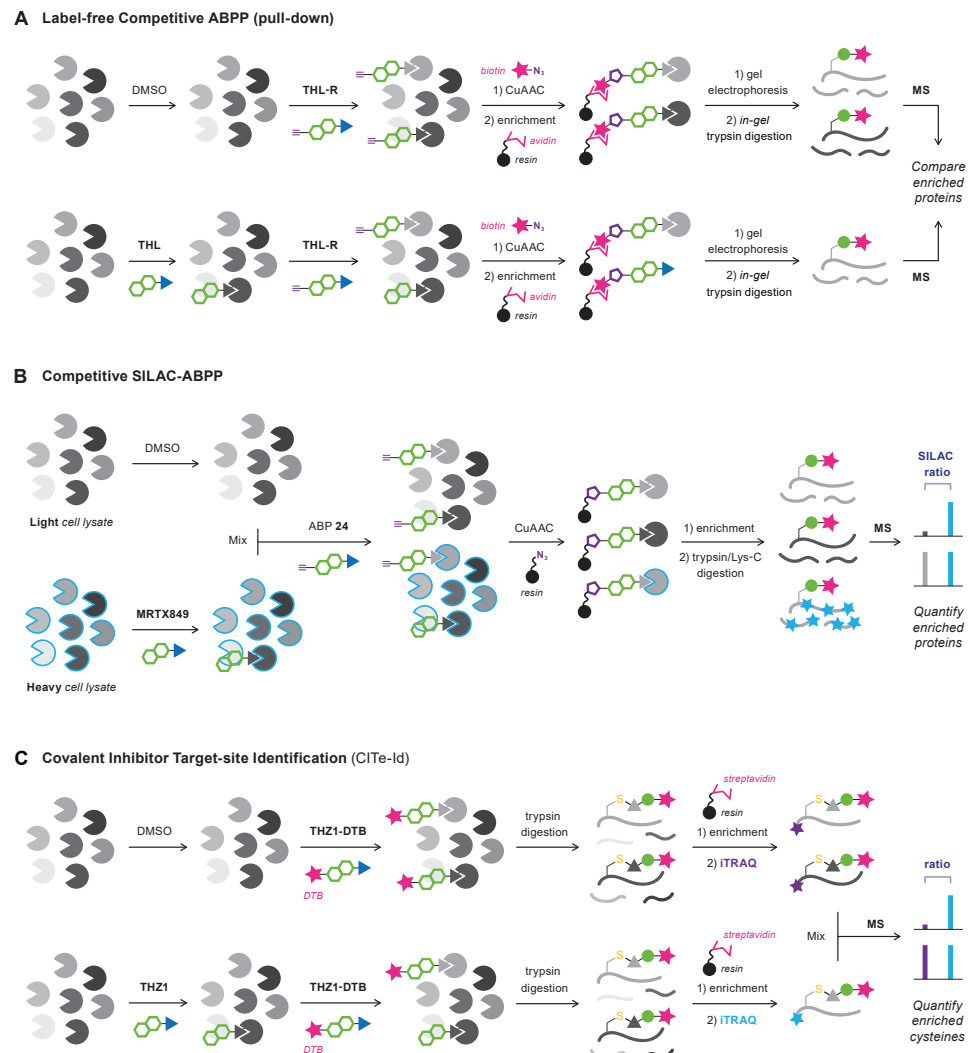


Figure 11 | Chemoproteomic approaches to identify covalently modified (off-)target proteins in whole proteomes. Pretreatment with inhibitor blocks drug-derived ABP binding and protein enrichment, resulting in a lower abundance of target protein compared to the DMSO-treated (control) sample. **(A)** Label-free protein target detection in pull-down experiment with drug-derived ABP THL-R to identify *in situ* protein targets of orlistat (THL) in HepG2 cells.²⁰⁰ ABP-bound proteins are enriched on avidin-agarose beads and submitted to bottom-up MS/MS evaluation. **(B)** Multiplexed detection of cellular protein targets of KRAS^{G12C} inhibitor adagrasib (MRTX849) in a competitive SILAC-ABPP experiment.¹⁰³ NCI-H358 cells cultured in normal (*light*) or isotope-labeled (*heavy*) medium (metabolic stable isotope-labeling) are incubated with DMSO or adagrasib, and the mixture of heavy and light lysate is then treated with drug-derived two-step ABP **24**. ABP-bound proteins are enriched on azide-labeled agarose beads and submitted to bottom-up MS/MS for identification and relative quantitation of enriched protein abundance (SILAC ratio). **(C)** Identification and quantitation of novel protein targets for inhibitor THZ1 in a CITe-ID experiment.²³¹ Cell lysates preincubated with DMSO (*control*) or THZ1 (*inhibitor*) are treated with drug-derived desthiobiotinylated ABP THZ1-DTB and enriched for DTB-modified proteolytic peptides. Primary amines are labeled with a unique isobaric iTRAQ reagent in each sample, and samples are combined for multiplexed RP-SAX-MS/MS analysis.

isobaric amine-reactive iTRAQ or TMT™ multiplex tags.^{221, 241} Recently, the CITE-Id (Covalent Inhibitor Target-site Identification) platform was reported,²³¹ enabling unbiased identification and detection of modified proteins and inhibitor target site in the whole proteome by competing drug-derived desthiobiotinylated ABP with its parent inhibitor (**Figure 11C**). The success of this approach was illustrated with one-step ABP THZ1-DTB, a desthiobiotinylated analog of cyclin-dependent kinase (CDK7) inhibitor **THZ1**, focusing on the eight cysteine residues competitively modified by THZ1 in a dose-dependent manner.²³¹ Among the newly identified THZ1 targets was Cys840 of PKN3, and CITE-Id streamlined the development of first-in-class PKN3 inhibitor **JZ128**. Proteomic platforms to assess the global electrophile selectivity are under development,²⁴² as are improved competitive platforms to assess covalent inhibitor reactivity.²²⁵

Reversible inhibition and reversibility assays. Direct chemoproteomic assessment of cellular protein targets can be challenging for reversible covalent inhibitors, as proteolytic digestion can induce dissociation of a reversible covalent ABP. Successful identification of cellular targets for (slow) reversible covalent cyanimides targeting UCHL1 has been reported with biotinylated one-step ABP **11RK73**, and clickable two-step ABP **8RK64**.²⁰⁷ The proteome-wide reactivity of reversible inhibitors is typically assessed in competitive proteomic experiments, which is not necessarily restricted to covalent binding modes.^{239, 243} The Cravatt group demonstrated that it is not only possible to evaluate the proteome-wide reactivity of reversible covalent cysteine-directing compounds with competitive isoTOP-ABPP,²⁴⁴ but that adaptation of this method by introduction of a gel filtration (GF) step before treatment with the thiol-alkylating ABP can be employed to evaluate reversibility of the covalent adduct.

Quantification of covalent occupancy. Application of broad-spectrum ABPs to monitor ligand target engagement in native systems has been performed in model organisms (*in vivo* or *ex vivo*) and human tissue (*ex vivo*), with quantitation of relative protein abundance in presence of inhibitor compared to an untreated sample.^{104, 198} Occasionally, competitive ABPP experiments with drug-derived ABPs are performed. Time-dependent JAK3 occupancy in mouse spleen upon oral administration of **ritlecitinib** (PF-06651600) was monitored with drug-derived ABP PF-06789402: homogenized spleens were treated (*ex vivo*) with drug-derived ABP PF-06789402, enriched for ABP-modified proteins, and each sample was treated with a unique isobaric TMT-10plex tag to label (reactive) amines for multiplexed MS/MS analysis.¹⁹⁹

6.3. Homogeneous (Plate-based) Platforms

Gel electrophoresis (*section 6.1*) and chemoproteomic platforms (*section 6.2*) require removal of the unbound ABP or enrichment for modified proteins prior to detection of a covalent protein–ABP adduct. In this section we will discuss a few approaches that enable covalent adduct detection directly in a complex mixture (compatible with *in situ*/live cell imaging).

Traditional fluorescent ABPs suffer from a high fluorescence background as they are also fluorescent in their unbound state, and are thus less suitable for homogeneous applications that do not involve removal of the unbound ABP (e.g. live cell imaging, *in vitro* microplate-based activity assays). Turn-on fluorogenic and quenched ABPs are a subtype of fluorescent ABPs that only become fluorescent after covalent adduct formation. Quenched ABPs (qABPs) were

originally developed in the Bogyo lab to enable dynamic imaging of cysteine protease activity in living cells.²⁴⁵ Here, the fluorophore is ‘dark’ until the quencher is released or removed upon covalent thiol addition, generating a fluorescent covalent enzyme–inhibitor adduct. Adduct formation can be monitored by traditional in-gel fluorescence, but the low intrinsic fluorescent background also enables monitoring fluorescence intensity in homogeneous plate-based read-outs and even non-invasive real time optical imaging of cysteine protease activity in intact (live) cells, and even *in vivo*.^{246–248} Most qABPs targeting serines^{249–250} and cysteines^{182, 246–248, 251} were developed as chemical tools to study enzyme activity. Target-selective qABP typically have a peptidic recognition element with exception of a BTK kinase qABP derived from the noncovalent core of **ibrutinib** (Figure 12A).²⁵² The major drawback to turning a covalent ligand into a qABP is the mandatory replacement of the warhead with a suitable electrophile (e.g. acyloxymethyl ketone (AOMK),²⁴⁵ phenoxymethyl ketone (PMK),²⁴⁶ urea triazole^{249, 253}) to enable nucleophilic substitution of the quencher/fluorophore upon covalent adduct formation: the thiol-reactive electrophiles consisting of a carbonyl with a leaving group on the α -carbon may have a different intrinsic chemical reactivity than the original warhead,^{26–27, 254} and the qABP (thiol) reactivity may no longer be representative of the parent ligand.

A more generally applicable approach for thiol-reactive covalent small molecule inhibitors was recently reported by the London group:²⁵⁵ CoLDR (Covalent Ligand Directed Release) turn-on ABPs were generated by late-stage functionalization of covalent inhibitors containing the popular acrylamide warhead (Figure 12B). Modification of the acrylamide warhead on the α -carbon generates substituted α -methacrylamide warheads that release a (detectable) leaving group upon thiol addition turning the covalent inhibitor into a turn-on fluorogenic, chemiluminescent or otherwise functionalized ABP while maintaining the acrylamide geometry. This elegant approach was illustrated with a turn-on fluorogenic ABP based on covalent BTK inhibitor **ibrutinib**, that releases a fluorescent 7-hydroxycoumarin group upon thiol addition allowing homogeneous plate-based kinetic detection of irreversible covalent adduct formation.²⁵⁵ The versatility of this approach was illustrated with turn-on fluorogenic ABPs based on covalent EGFR inhibitor **afatinib**, covalent KRAS^{G12C} inhibitor **AMG-510** functionalized with coumarin, and a chemiluminescent **ibrutinib**-based ABP.²⁵⁵ Note: turn-on fluorescence probes do not have to be covalent as there are examples of increased fluorescence induced by a noncovalent binding event,²⁵⁶ and covalent adduct formation with the desired target should be validated with orthogonal techniques such as intact protein analysis. Alternatively, two-step ABPs can be employed as bioorthogonal fluorogenic probes, reacting the protein–ABP adduct with photophysically quenched fluorogenic dyes (e.g. azido-BODIPY, dibenzocyclooctyne) that are activated by Click chemistry.^{197, 257–258}

To date, qABPs and turn-on ABPs have limited clinical applications as the optical signal of most fluorophores is plagued by insufficient tissue penetration, thus obstructing their application as non-invasive diagnostic tools in living patients.²⁵⁹ Research endeavors in the qABP field have since progressed to advanced theranostic probes that combine detection and simultaneous inhibition of cathepsins with induction of sensitivity to Photodynamic Therapy (PDT) at the sites with high (aberrant) protease activity,^{260–261} which may one day find application in non-invasive (clinical) diagnosis and treatment.

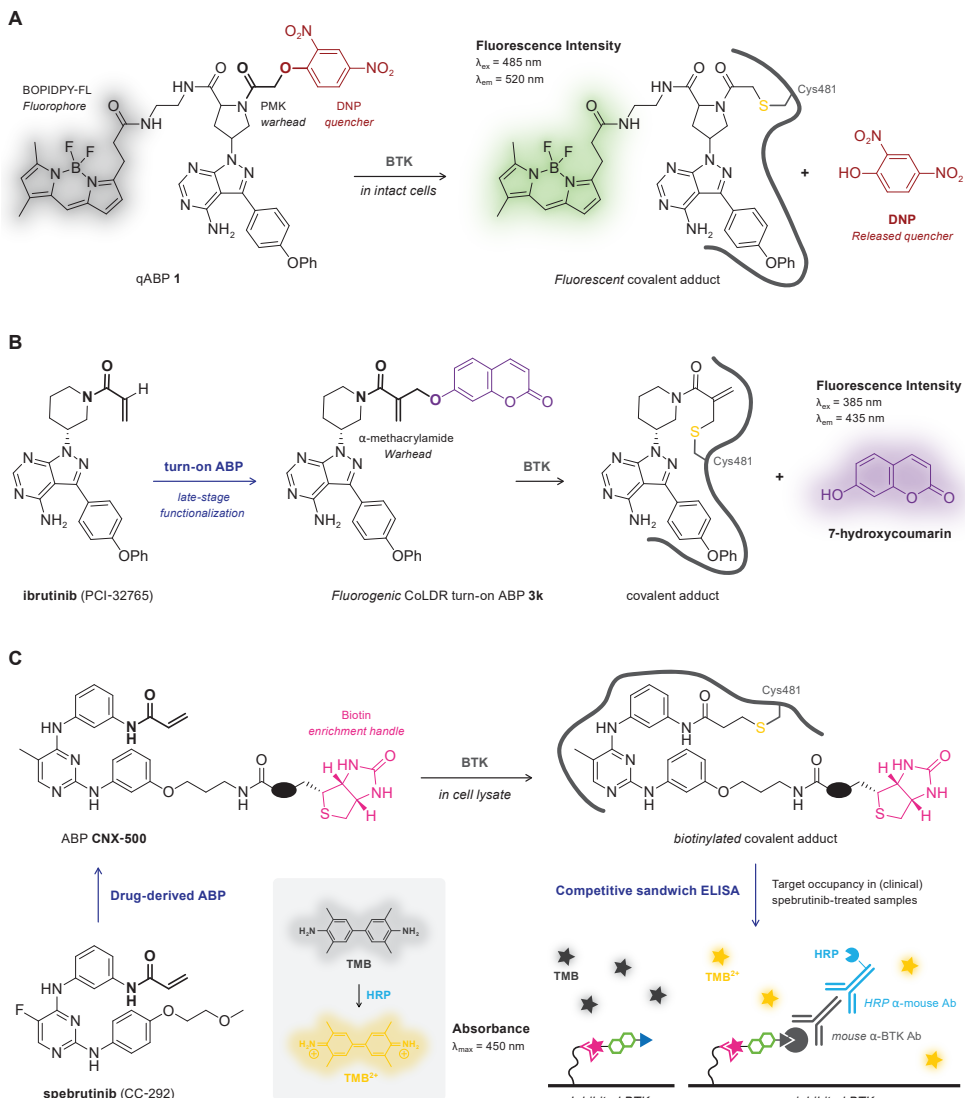


Figure 12 | Homogeneous (plate-based) approaches to detect covalent adduct formation with drug-derived ABPs. **(A)** Quenched fluorescent ABP (qABP) with a recognition element based on the ibrutinib scaffold to selectively target BTK.²⁵² The DNP (2,4-dinitrophenyl) quencher is expelled upon covalent adduct formation, enabling fluorescence detection of the BODIPY-FL fluorophore in the covalent adduct but not in unbound or noncovalently-bound qABP. **(B)** Covalent ligand directed release (CoLDR) chemistry to generate turn-on fluorogenic ABPs.²⁵⁵ Adduct formation of ibrutinib-derived turn-on fluorogenic ABP **3k** with BTK is monitored by fluorescence intensity as thiol addition to the substituted α -methacrylamide warhead results in release of fluorescent 7-hydroxycoumarin. **(C)** Quantification of cellular BTK occupancy in a competitive ELISA (enzyme-linked immunosorbent assay) experiment.²⁶² Spebrutinib-treated lysates originating from tissue (culture) or clinical samples are incubated with biotinylated ABP CNX-500 to detect free, uninhibited BTK. Biotinylated BTK–ABP adducts are captured on streptavidin-coated ELISA plate, treated with primary mouse α -BTK Ab and secondary HRP anti-mouse Ab, and developed by addition of HRP substrate tetramethyl benzidine (TMB). Uninhibited BTK is quantified from the concentration of the yellow HRP product TMB^{2+} , with calculation of inhibitor occupancy from the OD_{450} in the treated samples relative to the untreated sample.

Quantification of covalent occupancy. Relative fluorescence intensity can be employed to quantify covalent adduct formation with quenched or turn-on fluorogenic ABPs.²⁵⁵ Recently, competitive approaches employing biotin-labeled ABPs to assess the cellular occupancy of covalent BTK inhibitors have been reported, where detection of the covalent BTK-ABP adduct is facilitated by an enzyme-linked immunosorbent assay (ELISA)^{12-13, 262} or an Amplified Luminescent Proximity Homogeneous Assay (ALPHA).⁵⁵ BTK occupancy is calculated from normalization of the signal in inhibitor-treated samples to the untreated control as covalent BTK-ABP adduct is formed with uninhibited BTK but not with BTK-inhibitor adducts. Cellular BTK occupancy of irreversible covalent BTK inhibitor **spebrutinib** (CC-292) in human B cell lysate was assessed using spebrutinib-derived biotinylated ABP **CNX-500** (Figure 12C),²⁶² with capture of the biotinylated BTK-ABP adducts on streptavidin-coated ELISA plates. Uninhibited BTK was quantified from the optical density (OD₄₅₀) originating from BTK-ABP adduct after subsequent addition of a primary BTK antibody, a secondary antibody modified with horseradish peroxidase (HRP), and development with the HRP substrate. The stepwise ELISA technology has been employed to assess BTK occupancy in the development of various covalent BTK inhibitors: **zanubrutinib** (BGB-3111) with zanubrutinib-derived biotinylated ABP **P-1** on neutravidin-coated ELISA plates,¹² and **acalabrutinib** (ACP-196) with acalabrutinib-derived biotinylated ABP ACP-4016 on BTK antibody-coated ELISA plates with HRP-linked streptavidin.¹³ The general BTK-selective biotinylated ABP S49 was employed rather than a drug-derived ABP to quantify cellular BTK occupancy of **remibrutinib** (LOU064).⁸⁷ Finally, the Taunton lab reports a high-throughput method using AlphaScreen technology based on competition with ibrutinib-derived ABP PP-biotin,⁵⁵ that does not only enable quantification of cellular BTK occupancy in Ramos cells but also elucidates inhibitor reversibility in washout experiments. An indirect competitive AlphaScreen methodology has since been used in the preclinical development of reversible BTK inhibitor **rilzabrutinib** (PRN-1008): BTK target occupancy in Ramos B cells was assessed using a BTK-selective biotinylated ABP.⁴⁹ Importantly, these methods do not provide direct evidence on inhibitor or ABP covalency: a stringent washing step promoting dissociation of noncovalent complexes has to be introduced to discriminate between noncovalent or covalent ligands. Nevertheless, these methodologies are attractive as they are complementary proteomic approaches by using the same biotin-labeled ABPs.

7. Conclusions, Current Challenges, and Future Directions

Biophysical detection of covalent adduct is an important step in covalent drug development as a(n) (ir)reversible covalent binding mode affects the SAR analysis and kinetic behavior.⁶¹ In this work, we reviewed the available methods for direct detection of the covalent protein-drug adduct, as opposed to deduction from the decrease of unbound drug. To ensure the detected signal originates from a covalent protein-drug adduct, covalent adduct formation is validated with at least two orthogonal methods. With a wide variety of techniques to choose from (Table 1), method selection is dictated by compatibility with (fluorescent) read-out, the available amount and purity of protein, the complexity of the reaction mixture (from purified recombinant protein to *in vivo*), and the desired level of information. Beyond the

simple detection of a covalent adduct, some techniques can aid identification of the targeted amino acid residue, but often protein mutagenesis is key to validate the modified amino acid residue.^{70–71}

This work includes most commonly used methods but is by no means complete. Although protein crystallography thus far remains the most informative method for structural evaluation of covalent adducts, there is a shift towards cryo-EM for the structural elucidation of large protein complexes.²⁶³ The phenomenal progress in the past years has resulted in highly detailed structures, wherein features of <2 Å can be resolved, but structure determination of small (<50 kDa) proteins is often hindered by intrinsically noisy micrographs and low image contrast.^{264–265} Currently, single-particle cryo-EM can successfully map small molecule ligands onto (large) proteins,^{266–270} making it a promising technique to also resolve covalent adducts or as an alternative for protein–drug complexes that are difficult to crystallize. Depending on the system studied, scientists may employ a plethora of different biophysical techniques. Importantly, covalent adduct formation may require identification of the reactive metabolite to assess covalent adduct formation with prodrugs (e.g. **omeprazole**).²⁷¹ Other challenging systems involve (membrane-bound) protein targets that are inactive in isolation, in absence of the other components of a protein complex. The majority of the described techniques are compatible with detection of reversible covalent adducts. The main challenge is to maintain intact protein–drug adduct during sample preparation as the sample preparation can induce target dissociation for reversible covalent ligands. The intrinsic property of a reversible covalent ligand to dissociate from its protein target upon protein denaturation^{54,72} or chasing with an irreversible competitive tracer⁷⁴ has been exploited to assess binding reversibility of various clinically approved TCIs.^{88,95}

The unavailability of (quantitative) high-throughput screening techniques can hamper widespread discovery of covalent ligands. Although intact protein MS can overcome this hurdle,⁹⁰ potential hits should always be validated in a functional assay,³⁹ as covalent modification does not necessarily mean altered protein function.⁷¹ Another factor is monitoring and quantifying covalent target occupancy in living patients, since drug levels in serum are not representative for irreversible binders. MS-based assays to quantify target engagement have been developed,¹⁰⁰ though practical application in clinical drug development is still limited by the optimization for each individual protein–drug pair.

Beyond validation of covalent adduct formation with the desired target, ABPP has the advantage that it can be used to evaluate target selectivity in a cellular, biological setting. Although detection of low-abundance proteins remains a challenge, the approach is in general very versatile, as evidenced by the various subtypes of ABPP. The prevalent indirect competitive ABPP with a general reactive ABP has successfully been employed to identify off-target protein targets in patient-derived samples,¹⁹¹ but this indirect approach is biased for the amino acid residues labeled by the general ABP and will miss labeling of other residues. Here, opportunities arise for the lower throughput use of drug-derived ABPs that have the same selectivity as the parent drug. Drug-derived ABPs have since been used to evaluate target selectivity of approved

covalent inhibitors,^{103, 200} quantify target occupancy in inhibitor-treated patients,^{199, 262} and identify novel targetable proteins.²⁰⁷ Further developments in ABP techniques are always limited by the deviation from the parent drug when a tag/handle is introduced. At the same time, general indirect (non-drug derived) methods to evaluate proteome-wide electrophile reactivity towards other nucleophilic residues (e.g. histidine, arginine, lysine)^{23, 242, 272-276} are becoming more prevalent as these nucleophilic residues are attractive targets (e.g. Arg12 in oncogenic mutant KRAS^{G12R},²⁷⁷ catalytic Lys271 in BCR-ABL²⁷⁸). All taken together, such chemoproteomic approaches will likely become an integral part of standard covalent drug development to identify covalently modified off-target proteins at an early stage,²⁷⁹ thereby further derisking covalent drug development.²

To conclude, there is a broad toolbox available for the evaluation and detection of covalent protein–drug adducts, ranging from recombinant protein to live patients. The techniques are instrumental in the evaluation of covalent drug reactivity and selectivity, and have guided covalent drug development programs and SAR optimization studies. Beyond the methods covered in this review, novel techniques will continue to be developed and improved to cater to the exciting and fast-paced field of covalent drug development.

Acknowledgments

In memory of prof. dr. Huib Ova, his passion for science will always be an inspiration to us. E.M. would like to thank Bianca van Tol for sharing her insights and knowledge on mass spectrometry techniques. This work was supported by funds from the EU/EFPIA/OICR/McGill/KTH/Diamond Innovative Medicines Initiative 2 Joint Undertaking (EUbOPEN grant no. 875510) and NWO (VIDI Grant VI. 213.110 to M.P.C.M.).

Author Contributions

E.M.: Conceptualization, Investigation, Visualization, Writing – Original Draft, Writing – Review & Editing. R.Q.K.: Writing – Review & Editing. M.P.C.M.: Supervision, Writing – Review & Editing.

8. References

1. Singh, J.; Petter, R.C.; Baillie, T.A.; Whitty, A. The Resurgence of Covalent Drugs. *Nat. Rev. Drug Discov.* **2011**, *10*, 307-317. doi: 10.1038/nrd3410.
2. Johnson, D.S.; Weerapana, E.; Cravatt, B.F. Strategies for Discovering and Derisking Covalent, Irreversible Enzyme Inhibitors. *Future Med. Chem.* **2010**, *2*, 949-964. doi: 10.4155/fmc.10.21.
3. Vane, J.R.; Botting, R.M. The Mechanism of Action of Aspirin. *Thromb. Res.* **2003**, *110*, 255-258. doi: 10.1016/S0049-3848(03)00379-7.
4. Yocom, R.R.; Rasmussen, J.R.; Strominger, J.L. The Mechanism of Action of Penicillin. Penicillin Acylates the Active Site of *Bacillus Stearothermophilus* D-Alanine Carboxypeptidase. *J. Biol. Chem.* **1980**, *255*, 3977-3986. doi: 10.1016/S0021-9258(19)85621-1.
5. Ding, Z.; Kim, S.; Dorsam, R.T.; Jin, J.; Kunapuli, S.P. Inactivation of the Human P2Y12 Receptor by Thiol Reagents Requires Interaction with Both Extracellular Cysteine Residues, Cys17 and Cys270. *Blood* **2003**, *101*, 3908-3914. doi: 10.1182/blood-2002-10-3027.
6. Shin, J.M.; Cho, Y.M.; Sachs, G. Chemistry of Covalent Inhibition of the Gastric (H⁺, K⁺)-ATPase by Proton Pump Inhibitors. *J. Am. Chem. Soc.* **2004**, *126*, 7800-7811. doi: 10.1021/ja049607w.
7. Bauer, R.A. Covalent Inhibitors in Drug Discovery: From Accidental Discoveries To Avoided Liabilities and Designed Therapies. *Drug Discov. Today* **2015**, *20*, 1061-1073. doi: 10.1016/j.drudis.2015.05.005.
8. Gehring, M. Covalent Inhibitors: Back On Track? *Future Med. Chem.* **2020**, *12*, 1363-1368. doi: 10.4155/fmc-2020-0118.
9. Barf, T.; Kaptein, A. Irreversible Protein Kinase Inhibitors: Balancing the Benefits and Risks. *J. Med. Chem.* **2012**, *55*, 6243-6262. doi: 10.1021/jm3003203.
10. Chaikud, A.; Koch, P.; Laufer, S.A.; Knapp, S. The Cysteinome of Protein Kinases as a Target in Drug Development. *Angew. Chem. Int. Ed.* **2018**, *57*, 4372-4385. doi: 10.1002/anie.201707875.

11. Honigberg, L.A.; Smith, A.M.; Sirisawad, M.; Verner, E.; Loury, D.; Chang, B.; Li, S.; Pan, Z.; Thamm, D.H.; Miller, R.A.; Buggy, J.J. The Bruton Tyrosine Kinase Inhibitor PCI-32765 Blocks B-cell Activation and is Efficacious in Models of Autoimmune Disease and B-cell Malignancy. *Proc. Natl. Acad. Sci.* **2010**, *107*, 13075–13080. doi: 10.1073/pnas.1004594107.
12. Guo, Y.; Liu, Y.; Hu, N.; Yu, D.; Zhou, C.; Shi, G.; Zhang, B.; Wei, M.; Liu, J.; Luo, L.; et al. Discovery of Zanubrutinib (BGB-3111), a Novel, Potent, and Selective Covalent Inhibitor of Bruton's Tyrosine Kinase. *J. Med. Chem.* **2019**, *62*, 7923–7940. doi: 10.1021/acs.jmedchem.9b00687.
13. Barf, T.; Covey, T.; Izumi, R.; van de Kar, B.; Gulrajani, M.; van Lith, B.; van Hoek, M.; de Zwart, E.; Mittag, D.; Demont, D.; Verkaik, S.; Krantz, F.; Pearson, P.G.; Ulrich, R.; Kaptein, A. Acalabrutinib (ACP-196): A Covalent Bruton Tyrosine Kinase Inhibitor with a Differentiated Selectivity and In Vivo Potency Profile. *J. Pharmacol. Exp. Ther.* **2017**, *363*, 240. doi: 10.1124/jpet.117.242909.
14. Solca, F.; Dahl, G.; Zoepfl, A.; Bader, G.; Sanderson, M.; Klein, C.; Kraemer, O.; Himmelsbach, F.; Haaksma, E.; Adolf, G.R. Target Binding Properties and Cellular Activity of Afatinib (BIBW 2992), an Irreversible ErBB Family Blocker. *J. Pharmacol. Exp. Ther.* **2012**, *343*, 342–350. doi: 10.1124/jpet.112.197756.
15. Cross, D.A.E.; Ashton, S.E.; Ghiorghiu, S.; Eberlein, C.; Nebhan, C.A.; Spitzler, P.J.; Orme, J.P.; Finlay, M.R.V.; Ward, R.A.; Mellor, M.J.; et al. AZD9291, an Irreversible EGFR TKI, Overcomes T790M-Mediated Resistance to EGFR Inhibitors in Lung Cancer. *Cancer Discov.* **2014**, *4*, 1046–1061. doi: 10.1158/2159-8290.Cd-14-0337.
16. Rabindran, S.K.; Discsafani, C.M.; Rosfjord, E.C.; Baxter, M.; Floyd, M.B.; Golas, J.; Hallett, W.A.; Johnson, B.D.; Nilakantan, R.; Overbeek, E.; Reich, M.F.; Shen, R.; Shi, X.; Tsou, H.-R.; Wang, Y.-F.; Wissner, A. Antitumor Activity of HKI-272, an Orally Active, Irreversible Inhibitor of the HER-2 Tyrosine Kinase. *Cancer Res.* **2004**, *64*, 3958–3965. doi: 10.1158/0008-5472.CAN-03-2868.
17. Gonzales, A.J.; Hook, K.E.; Althaus, I.W.; Ellis, P.A.; Trachet, E.; Delaney, A.M.; Harvey, P.J.; Ellis, T.A.; Amato, D.M.; Nelson, J.M.; et al. Antitumor Activity and Pharmacokinetic Properties of PF-00299804, a Second-Generation Irreversible Pan-erbB Receptor Tyrosine Kinase Inhibitor. *MoL. Cancer Ther.* **2008**, *7*, 1880–1889. doi: 10.1158/1535-7163.Mct-07-2232.
18. Lanman, B.A.; Allen, J.R.; Allen, J.G.; Amegadzie, A.K.; Ashton, K.S.; Booker, S.K.; Chen, J.J.; Chen, N.; Frohn, M.J.; Goodman, G.; et al. Discovery of a Covalent Inhibitor of KRAS^{G12C} (AMG 510) for the Treatment of Solid Tumors. *J. Med. Chem.* **2020**, *63*, 52–65. doi: 10.1021/acs.jmedchem.9b01180.
19. Gonzalvez, F.; Vincent, S.; Baker, T.E.; Gould, A.E.; Li, S.; Wardwell, S.D.; Nadworny, S.; Ning, Y.; Zhang, S.; Huang, W.-S.; et al. Mobocertinib (TAK-788): A Targeted Inhibitor of EGFR Exon 20 Insertion Mutants in Non-Small Cell Lung Cancer. *Cancer Discov.* **2021**, *11*, 1672–1687. doi: 10.1158/2159-8290.Cd-20-1683.
20. De Vita, E. 10 Years into the Resurgence of Covalent Drugs. *Future Med. Chem.* **2021**, *13*, 193–210. doi: 10.4155/fmc-2020-0236.
21. Ward, R.A.; Grinster, N.P. The Design of Covalent-Based Inhibitors. *Annu. Rep. Med. Chem.* **2021**, *56*, 2–284. <https://www.sciencedirect.com/bookseries/annual-reports-in-medicinal-chemistry/vol/56/suppl/C>
22. Borsari, C.; Keles, E.; McPhail, J.A.; Schaefer, A.; Sriramaratnam, R.; Goch, W.; Schaefer, T.; De Pascale, M.; Bal, W.; Gstaiger, M.; Burke, J.E.; Wyman, M.P. Covalent Proximity Scanning of a Distal Cysteine to Target PI3Ka. *J. Am. Chem. Soc.* **2022**, *144*, 6326–6342. doi: 10.1021/jacs.1c13568.
23. Gehringer, M.; Laufer, S.A. Emerging and Re-Emerging Warheads for Targeted Covalent Inhibitors: Applications in Medicinal Chemistry and Chemical Biology. *J. Med. Chem.* **2019**, *62*, 5673–5724. doi: 10.1021/acs.jmedchem.8b01153.
24. Shindo, N.; Ojida, A. Recent Progress in Covalent Warheads for In Vivo Targeting of Endogenous Proteins. *Bioorg. Med. Chem.* **2021**, *47*, 116386. doi: 10.1016/j.bmc.2021.116386.
25. Ray, S.; Murkin, A.S. New Electrophiles and Strategies for Mechanism-Based and Targeted Covalent Inhibitor Design. *Biochemistry* **2019**, *58*, 5234–5244. doi: 10.1021/acs.biochem.9b00293.
26. Martin, J.S.; MacKenzie, C.J.; Fletcher, D.; Gilbert, I.H. Characterising Covalent Warhead Reactivity. *Bioorg. Med. Chem.* **2019**, *27*, 2066–2074. doi: 10.1016/j.bmc.2019.04.002.
27. Lonsdale, R.; Burgess, J.; Colclough, N.; Davies, N.L.; Lenz, E.M.; Orton, A.L.; Ward, R.A. Expanding the Armory: Predicting and Tuning Covalent Warhead Reactivity. *J. Chem. Inf. Model.* **2017**, *57*, 3124–3137. doi: 10.1021/acs.jcim.7b00553.
28. Guan, I.; Williams, K.; Pan, J.; Liu, X. New Cysteine Covalent Modification Strategies Enable Advancement of Proteome-wide Selectivity of Kinase Modulators. *Asian J. Org. Chem.* **2021**, *10*, 949–963. doi: 10.1002/ajoc.202100036.
29. Oballa, R.M.; Truchon, J.-F.; Bayly, C.I.; Chauvet, N.; Day, S.; Crane, S.; Berthelette, C. A Generally Applicable Method for Assessing the Electrophilicity and Reactivity of Diverse Nitrile-Containing Compounds. *Bioorg. Med. Chem. Lett.* **2007**, *17*, 998–1002. doi: 10.1016/j.bmcl.2006.11.044.
30. Pęczka, N.; Orgován, Z.; Ábrányi-Balogh, P.; Keserű, G.M. Electrophilic Warheads in Covalent Drug Discovery: An Overview. *Expert Opin. Drug Discov.* **2022**, *17*, 413–422. doi: 10.1080/17460441.2022.2034783.
31. McAulay, K.; Bilsland, A.; Bon, M. Reactivity of Covalent Fragments and Their Role in Fragment Based Drug Discovery. *Pharmaceutics* **2022**, *15*, 1366. doi: 10.3390/ph15111366.
32. De Cesco, S.; Kurian, J.; Dufresne, C.; Mittermaier, A.K.; Moitessier, N. Covalent Inhibitors Design and Discovery. *Eur. J. Med. Chem.* **2017**, *138*, 96–114. doi: 10.1016/j.ejmech.2017.06.019.
33. Engel, J.; Richters, A.; Getlik, M.; Tomassi, S.; Keul, M.; Termathé, M.; Lategahn, J.; Becker, C.; Mayer-Wrangowski, S.; Grütter, C.; et al. Targeting Drug Resistance in EGFR with Covalent Inhibitors: A Structure-Based Design Approach. *J. Med. Chem.* **2015**, *58*, 6844–6863. doi: 10.1021/acs.jmedchem.5b01082.
34. Zhang, T.; Hatcher, J.M.; Teng, M.; Gray, N.S.; Kostic, M. Recent Advances in Selective and Irreversible Covalent Ligand Development and Covalent Inhibitors. *Chem. Biol.* **2019**, *26*, 1486–1500. doi: 10.1016/j.chembio.2019.09.012.
35. Chen, S.; Lovell, S.; Lee, S.; Fellner, M.; Mace, P.D.; Bogyo, M. Identification of Highly Selective Covalent Inhibitors by Phage Display. *Nat. Biotechnol.* **2021**, *39*, 490–498. doi: 10.1038/s41587-020-0733-7.
36. Campuzano, I.D.G.; San Miguel, T.; Rowe, T.; Onea, D.; Cee, V.J.; Arvedson, T.; McCarter, J.D. High-Throughput Mass Spectrometric Analysis of Covalent Protein-Inhibitor Adducts for the Discovery of Irreversible Inhibitors: A Complete Workflow. *J. Biomol. Screen.* **2015**, *21*, 136–144. doi: 10.1177/1087057115621288.
37. Dalton, S.E.; Campos, S. Covalent Small Molecules as Enabling Platforms for Drug Discovery. *ChemBioChem* **2020**, *21*, 1080–1100. doi: 10.1002/cbic.201900674.
38. Lu, W.; Kostic, M.; Zhang, T.; Che, J.; Patricelli, M.P.; Jones, L.H.; Chouchani, E.T.; Gray, N.S. Fragment-Based Covalent Ligand Discovery. *RSC Chem. Biol.* **2021**, *2*, 354–367. doi: 10.1039/DOCB00222D.
39. Keeley, A.; Petri, L.; Ábrányi-Balogh, P.; Keserű, G.M. Covalent Fragment Libraries in Drug Discovery. *Drug Discov. Today* **2020**, *25*, 983–996. doi: 10.1016/j.drudis.2020.03.016.
40. Miller, R.M.; Paavilainen, V.O.; Krishnan, S.; Serafimova, I.M.; Taunton, J. Electrophilic Fragment-Based Design of Reversible Covalent Kinase Inhibitors. *J. Am. Chem. Soc.* **2013**, *135*, 5298–5301. doi: 10.1021/ja01221b.

41. Resnick, E.; Bradley, A.; Gan, J.; Douangamath, A.; Krojer, T.; Sethi, R.; Geurink, P.P.; Aimon, A.; Amitai, G.; Bellini, D., et al. Rapid Covalent-Probe Discovery by Electrophile-Fragment Screening. *J. Am. Chem. Soc.* **2019**, *141*, 8951-8968. doi: 10.1021/jacs.9b02822.
42. Kathman, S.G.; Statsyuk, A.V. Methodology for Identification of Cysteine-Reactive Covalent Inhibitors. *Methods Mol. Biol.* **2019**, *1967*, 245-262. doi: 10.1007/978-1-4939-9187-7_15.
43. Kathman, S.G.; Statsyuk, A.V. Covalent Tethering of Fragments for Covalent Probe Discovery. *MedChemComm* **2016**, *7*, 576-585. doi: 10.1039/C5MD00518C.
44. Kumalo, H.M.; Bhakat, S.; Soliman, M.E.S. Theory and Applications of Covalent Docking in Drug Discovery: Merits and Pitfalls. *Molecules* **2015**, *20*, 1984-2000. doi: 10.3390/molecules2021984.
45. Lonsdale, R.; Ward, R.A. Structure-Based Design of Targeted Covalent Inhibitors. *Chem. Soc. Rev.* **2018**, *47*, 3816-3830. doi: 10.1039/C7CS00220C.
46. Zaidman, D.; Gehrtz, P.; Filep, M.; Fearon, D.; Gabizon, R.; Douangamath, A.; Prilusky, J.; Duberstein, S.; Cohen, G.; Owen, C.D.; Resnick, E.; Strain-Damerell, C.; Lukacik, P.; Barr, H.; Walsh, M.A.; von Delft, F.; London, N. An Automatic Pipeline for the Design of Irreversible Derivatives Identifies a Potent SARS-CoV-2 M^{pro} Inhibitor. *Cell Chem. Biol.* **2021**, *28*, 1795-1806.e5. doi: 10.1016/j.chembiol.2021.05.018.
47. Owen, D.R.; Allerton, C.M.N.; Anderson, A.S.; Aschenbrenner, L.; Avery, M.; Berritt, S.; Boras, B.; Cardin, R.D.; Carlo, A.; Coffman, K.J., et al. An Oral SARS-CoV-2 M^{pro} Inhibitor Clinical Candidate for the Treatment of COVID-19. *Science* **2021**, *374*, 1586-1593. doi: 10.1126/science.abl4784.
48. Tuley, A.; Fast, W. The Taxonomy of Covalent Inhibitors. *Biochemistry* **2018**, *57*, 3326-3337. doi: 10.1021/acs.biochem.8b00315.
49. Langrish, C.L.; Bradshaw, J.M.; Francesco, M.R.; Owens, T.D.; Xing, Y.; Shu, J.; LaStant, J.; Bisconte, A.; Outerbridge, C.; White, S.D.; Hill, R.J.; Brameld, K.A.; Goldstein, D.M.; Nunn, P.A. Preclinical Efficacy and Anti-Inflammatory Mechanisms of Action of the Bruton Tyrosine Kinase Inhibitor Rilzabrutinib for Immune-Mediated Disease. *J. Immunol.* **2021**, *206*, 1454-1468. doi: 10.4049/jimmunol.2001130.
50. Gauthier, J.Y.; Chauret, N.; Cromlish, W.; Desmarais, S.; Duong, L.T.; Falgueyret, J.-P.; Kimmel, D.B.; Lamontagne, S.; Léger, S.; LeRiche, T.; Li, C.S., et al. The Discovery of Odanacatib (MK-0822), a Selective Inhibitor of Cathepsin K. *Bioorg. Med. Chem. Lett.* **2008**, *18*, 923-928. doi: 10.1016/j.bmcl.2007.12.047.
51. Groll, M.; Berkers, C.R.; Ploegh, H.L.; Ovaa, H. Crystal Structure of the Boronic Acid-Based Proteasome Inhibitor Bortezomib in Complex with the Yeast 20S Proteasome. *Structure* **2006**, *14*, 451-456. doi: 10.1016/j.str.2005.11.019.
52. Perni, R.B.; Almquist, S.J.; Byrn, R.A.; Chandorkar, G.; Chaturvedi, P.R.; Courtney, L.F.; Decker, C.J.; Dinehart, K.; Gates, C.A.; Harbeson, S.L., et al. Preclinical Profile of VX-950, a Potent, Selective, and Orally Bioavailable Inhibitor of Hepatitis C Virus NS3-4A Serine Protease. *Antimicrob. Agents Chemother.* **2006**, *50*, 899-909. doi: 10.1128/AAC.50.3.899-909.2006.
53. Romano, K.P.; Ali, A.; Aydin, C.; Soumana, D.; Özén, A.; Deveau, L.M.; Silver, C.; Cao, H.; Newton, A.; Petropoulos, C.J.; Huang, W.; Schiffer, C.A. The Molecular Basis of Drug Resistance against Hepatitis C Virus NS3/4A Protease Inhibitors. *PLoS Pathog.* **2012**, *8*, e1002832. doi: 10.1371/journal.ppat.1002832.
54. Serafimova, I.M.; Pufall, M.A.; Krishnan, S.; Duda, K.; Cohen, M.S.; Maglathlin, R.L.; McFarland, J.M.; Miller, R.M.; Frödin, M.; Taunton, J. Reversible Targeting of Noncatalytic Cysteines with Chemically Tuned Electrophiles. *Nat. Chem. Biol.* **2012**, *8*, 471-476. doi: 10.1038/nchembio.925.
55. Bradshaw, J.M.; McFarland, J.M.; Paavilainen, V.O.; Bisconte, A.; Tam, D.; Phan, V.T.; Romanov, S.; Finkle, D.; Shu, J.; Patel, V., et al. Prolonged and Tunable Residence Time using Reversible Covalent Kinase Inhibitors. *Nat. Chem. Biol.* **2015**, *11*, 525-531. doi: 10.1038/nchembio.1817.
56. Krenske, E.H.; Petter, R.C.; Houk, K.N. Kinetics and Thermodynamics of Reversible Thiol Additions to Mono- and Diaminated Michael Acceptors: Implications for the Design of Drugs That Bind Covalently to Cysteines. *J. Org. Chem.* **2016**, *81*, 11726-11733. doi: 10.1021/acs.joc.6b02188.
57. Basu, D.; Richters, A.; Rauh, D. Structure-Based Design and Synthesis of Covalent-Reversible Inhibitors to Overcome Drug Resistance in EGFR. *Bioorg. Med. Chem.* **2015**, *23*, 2767-2780. doi: 10.1016/j.bmcl.2015.04.038.
58. Forster, M.; Gehringer, M.; Laufer, S.A. Recent Advances in JAK3 Inhibition: Isoform Selectivity by Covalent Cysteine Targeting. *Bioorg. Med. Chem. Lett.* **2017**, *27*, 4229-4237. doi: 10.1016/j.bmcl.2017.07.079.
59. U.S. Food & Drug Administration. Coronavirus (COVID-19) Update: FDA Authorizes First Oral Antiviral for Treatment of COVID-19. *FDA News Release* [Online], 22 December 2021. <https://www.fda.gov/news-events/press-announcements/coronavirus-covid-19-update-fda-authorizes-first-oral-antiviral-treatment-covid-19>.
60. Strelow, J.M. A Perspective on the Kinetics of Covalent and Irreversible Inhibition. *SLAS Discov.: Adv. Life Sci. R&D* **2017**, *22*, 3-20. doi: 10.1177/1087057116671509.
61. Mons, E.; Roet, S.; Kim, R.Q.; Mulder, M.P.C. A Comprehensive Guide for Assessing Covalent Inhibition in Enzymatic Assays Illustrated with Kinetic Simulations. *Curr. Protoc.* **2022**, *2*, e419. doi: 10.1002/cp21.419.
62. McWhirter, C. Chapter One - Kinetic Mechanisms of Covalent Inhibition. *Annu. Rep. Med. Chem.* **2021**, *56*, 1-31. doi: 10.1016/bs.armc.2020.11.001.
63. Harris, C.M.; Foley, S.E.; Goedken, E.R.; Michalak, M.; Murdock, S.; Wilson, N.S. Merits and Pitfalls in the Characterization of Covalent Inhibitors of Bruton's Tyrosine Kinase. *SLAS Discov.: Adv. Sci. Drug Discov.* **2018**, *23*, 1040-1050. doi: 10.1177/2472555218787445.
64. Al-Khafaji, K.; Al-Duhaidahawi, D.; Taskin Tok, T. Using Integrated Computational Approaches to Identify Safe and Rapid Treatment for SARS-CoV-2. *J. Biomol. Struct. Dyn.* **2021**, *39*, 3387-3395. doi: 10.1080/07391102.2020.1764392.
65. Yang, X.; Dilweg, M.A.; Osemwengie, D.; Burggraaff, L.; van der Es, D.; Heitman, L.H.; Ijzerman, A.P. Design and Pharmacological Profile of a Novel Covalent Partial Agonist for the Adenosine A1 Receptor. *Biochem. Pharmacol.* **2020**, *180*, 114144. doi: 10.1016/j.bcp.2020.114144.
66. Yang, X.; van Veldhoven, J.P.D.; Offringa, J.; Kuiper, B.J.; Lenselink, E.B.; Heitman, L.H.; van der Es, D.; Ijzerman, A.P. Development of Covalent Ligands for G Protein-Coupled Receptors: A Case for the Human Adenosine A3 Receptor. *J. Med. Chem.* **2019**, *62*, 3539-3552. doi: 10.1021/acs.jmedchem.8b02026.
67. Weichert, D.; Kruse, A.C.; Manglik, A.; Hiller, C.; Zhang, C.; Hübner, H.; Kobilka, B.K.; Gmeiner, P. Covalent Agonists for Studying G Protein-Coupled Receptor Activation. *Proc. Natl. Acad. Sci.* **2014**, *111*, 10744-10748. doi: 10.1073/pnas.1410415111.
68. Grimster, N.P. Covalent PROTACs: The Best of Both Worlds? *RSC Med. Chem.* **2021**, *12*, 1452-1458. doi: 10.1039/D1MD00191D.
69. Gabizon, R.; Shraga, A.; Gehrtz, P.; Livnah, E.; Shorer, Y.; Gurwitz, N.; Avram, L.; Unger, T.; Aharoni, H.; Albeck, S.; Brandis, A.; Shulman, Z.; Katz, B.-Z.; Herishanu, Y.; London, N. Efficient Targeted Degradation via Reversible and Irreversible Covalent PROTACs. *J. Am. Chem. Soc.* **2020**, *142*, 11734-11742. doi: 10.1021/jacs.9b13907.
70. Li, Y.-J.; Du, L.; Wang, J.; Vega, R.; Lee, T.D.; Miao, Y.; Aldana-Masangkay, G.; Samuels, E.R.; Li, B.; Ouyang, S.X.; Colayco, S.A.; Bobkova, E.V.; Divljanaka, D.B.; Sergienko, E.; Chung, T.D.Y.; Fakih, M.; Chen, Y. Allosteric Inhibition of Ubiquitin-like Modifications by a Class of Inhibitor of SUMO-Activating Enzyme. *Cell. Chem. Biol.* **2019**, *26*, 278-288.e6. doi: 10.1016/j.chembiol.2018.10.026.
71. Pettinger, J.; Le Bihan, Y.-V.; Widya, M.; van Montfort, R.L.M.; Jones, K.; Cheeseman, M.D. An Irreversible Inhibitor of HSP72 that Unexpectedly Targets Lysine-56. *Angew. Chem. Int. Ed.* **2017**, *56*, 3536-3540. doi: 10.1002/anie.201611907.
72. Abdeldayem, A.; Raouf, Y.S.; Constantinescu, S.N.; Moriggl, R.; Gunning, P.T. Advances in Covalent Kinase Inhibitors. *Chem. Soc. Rev.* **2020**, *49*, 2617-2687. doi: 10.1039/C9CS00720B.

73. Copeland, R.A.; Basavapathruni, A.; Moyer, M.; Scott, M.P. Impact of Enzyme Concentration and Residence Time on Apparent Activity Recovery in Jump Dilution Analysis. *Anal. Biochem.* **2011**, *416*, 206–210. doi: 10.1016/j.ab.2011.05.029.

74. Smith, S.; Keul, M.; Engel, J.; Basu, D.; Eppmann, S.; Rauh, D. Characterization of Covalent-Reversible EGFR Inhibitors. *ACS Omega* **2017**, *2*, 1563–1575. doi: 10.1021/acsomega.7b00157.

75. Tailor, A.; Waddington, J.C.; Meng, X.; Park, B.K. Mass Spectrometric and Functional Aspects of Drug–Protein Conjugation. *Chem. Res. Toxicol.* **2016**, *29*, 1912–1935. doi: 10.1021/acs.chemrestox.6b00147.

76. Zhang, Y.; Fonslow, B.R.; Shan, B.; Baek, M.-C.; Yates, J.R. Protein Analysis by Shotgun/Bottom-Up Proteomics. *Chem. Rev.* **2013**, *113*, 2343–2394. doi: 10.1021/cr300353s.

77. Donnelly, D.P.; Rawlins, C.M.; DeHart, C.J.; Fornelli, L.; Schachner, L.F.; Lin, Z.; Lippens, J.L.; Aluri, K.C.; Sarin, R.; Chen, B., et al. Best Practices and Benchmarks for Intact Protein Analysis for Top-Down Mass Spectrometry. *Nat. Meth.* **2019**, *16*, 587–594. doi: 10.1038/s41592-019-0457-0.

78. Tokmina-Lukaszewska, M.; Patterson, A.; Berry, L.; Scott, L.; Balasubramanian, N.; Bothner, B. The Role of Mass Spectrometry in Structural Studies of Flavin-Based Electron Bifurcating Enzymes. *Front. Microbiol.* **2018**, *9*, 1397. doi: 10.3389/fmicb.2018.01397.

79. Hilton, G.R.; Benes, J.L.P. Two Decades of Studying Non-covalent Biomolecular Assemblies by Means of Electrospray Ionization Mass Spectrometry. *J. R. Soc. Interface* **2012**, *9*, 801–816. doi: 10.1098/rsif.2011.0823.

80. Han, X.; Jin, M.; Breuker, K.; McLafferty, F.W. Extending Top-Down Mass Spectrometry to Proteins with Masses Greater Than 200 Kilodaltons. *Science* **2006**, *314*, 109–112. doi: 10.1126/science.1128868.

81. Melby, J.A.; Roberts, D.S.; Larson, E.J.; Brown, K.A.; Bayne, E.F.; Jin, S.; Ge, Y. Novel Strategies to Address the Challenges in Top-Down Proteomics. *J. Am. Soc. Mass Spectrom.* **2021**, *32*, 1278–1294. doi: 10.1021/jasms.1c00099.

82. Mons, E.; Kim, R.Q.; van Doodewaerd, B.R.; van Veelen, P.A.; Mulder, M.P.C.; Ovaa, H. Exploring the Versatility of the Covalent Thiol–Alkyne Reaction with Substituted Propargyl Warheads: A Deciding Role for the Cysteine Protease. *J. Am. Chem. Soc.* **2021**, *143*, 6423–6433. doi: 10.1021/jacs.0c10513.

83. Mons, E.; Jansen, I.D.C.; Loboda, J.; van Doodewaerd, B.R.; Hermans, J.; Verdoes, M.; van Boeckel, C.A.A.; van Veelen, P.A.; Turk, B.; Turk, D.; Ovaa, H. The Alkyne Moiety as a Latent Electrophile in Irreversible Covalent Small Molecule Inhibitors of Cathepsin K. *J. Am. Chem. Soc.* **2019**, *141*, 3507–3514. doi: 10.1021/jacs.8b11027.

84. Panyain, N.; Godinat, A.; Lanyon-Hogg, T.; Lachiondo-Ortega, S.; Will, E.J.; Soudy, C.; Mondal, M.; Mason, K.; Elkhaliha, S.; Smith, L.M.; Harrigan, J.A.; Tate, E.W. Discovery of a Potent and Selective Covalent Inhibitor and Activity-Based Probe for the Deubiquitylating Enzyme UCHL1, with Antifibrotic Activity. *J. Am. Chem. Soc.* **2020**, *142*, 12020–12026. doi: 10.1021/jacs.0c04527.

85. Kathman, S.G.; Xu, Z.; Statsyuk, A.V. A Fragment-Based Method to Discover Irreversible Covalent Inhibitors of Cysteine Proteases. *J. Med. Chem.* **2014**, *57*, 4969–4974. doi: 10.1021/jm500345q.

86. Caldwell, R.D.; Qiu, H.; Askew, B.C.; Bender, A.T.; Brugger, N.; Camps, M.; Dhanabal, M.; Dutt, V.; Eichhorn, T.; Gardberg, A.S., et al. Discovery of Eovabrutinib: An Oral, Potent, and Highly Selective, Covalent Bruton’s Tyrosine Kinase (BTK) Inhibitor for the Treatment of Immunological Diseases. *J. Med. Chem.* **2019**, *62*, 7643–7655. doi: 10.1021/acs.jmedchem.9b00794.

87. Angst, D.; Gessier, F.; Janser, P.; Vulpetti, A.; Wälchli, R.; Beerli, C.; Littlewood-Evans, A.; Dawson, J.; Nuesslein-Hildesheim, B.; Wieczorek, G.; Gutmann, S.; Scheufer, C.; Hinniger, A.; Zimmerlin, A.; Funhoff, E.G.; Pulz, R.; Cenni, B. Discovery of LOU064 (Remibrutinib), a Potent and Highly Selective Covalent Inhibitor of Bruton’s Tyrosine Kinase. *J. Med. Chem.* **2020**, *63*, 5102–5118. doi: 10.1021/acs.jmedchem.9b01916.

88. Liclican, A.; Serafini, L.; Xing, W.; Czerwieniec, G.; Steiner, B.; Wang, T.; Brenda, K.M.; Lutz, J.D.; Keegan, K.S.; Ray, A.S.; Schultz, B.E.; Sakowicz, R.; Feng, J.Y. Biochemical Characterization of Tirabrutinib and Other Irreversible Inhibitors of Bruton’s Tyrosine Kinase Reveals Differences in On- and Off-Target Inhibition. *Biochim. Biophys. Acta, Gen. Subj.* **2020**, *1864*, 129531. doi: 10.1016/j.bbagen.2020.129531.

89. Patricelli, M.P.; Janes, M.R.; Li, L.-S.; Hansen, R.; Peters, U.; Kessler, L.V.; Chen, Y.; Kucharski, J.M.; Feng, J.; Ely, T.; Chen, J.H.; Firdaus, S.J.; Babbar, A.; Ren, P.; Liu, Y. Selective Inhibition of Oncogenic KRAS Output with Small Molecules Targeting the Inactive State. *Cancer Discov.* **2016**, *6*, 316–329. doi: 10.1158/2159-8290.CD-15-1105.

90. Johansson, H.; Tsai, Y.-C.I.; Fantom, K.; Chung, C.-W.; Kümpfer, S.; Martino, L.; Thomas, D.A.; Eberl, H.C.; Muelbaier, M.; House, D.; Rittinger, K. Fragment-Based Covalent Ligand Screening Enables Rapid Discovery of Inhibitors for the RBR E3 Ubiquitin Ligase HOIP. *J. Am. Chem. Soc.* **2019**, *141*, 2703–2712. doi: 10.1021/jacs.8b13193.

91. Kathman, S.G.; Span, I.; Smith, A.T.; Xu, Z.; Zhan, J.; Rosenzweig, A.C.; Statsyuk, A.V. A Small Molecule That Switches a Ubiquitin Ligase From a Processive to a Distributive Enzymatic Mechanism. *J. Am. Chem. Soc.* **2015**, *137*, 12442–12445. doi: 10.1021/jacs.5b06839.

92. Dubiella, C.; Pinch, B.J.; Koikawa, K.; Zaidman, D.; Poon, E.; Manz, T.D.; Nabet, B.; He, S.; Resnick, E.; Rogel, A., et al. Sulfopin is a Covalent Inhibitor of Pin1 that Blocks Myc-Driven Tumors In Vivo. *Nat. Chem. Biol.* **2021**, *17*, 954–963. doi: 10.1038/s41589-021-00786-7.

93. Douangamath, A.; Fearon, D.; Gehrzt, P.; Krojer, T.; Lukacik, P.; Owen, C.D.; Resnick, E.; Strain-Damerell, C.; Aimon, A.; Ábrányi-Balogh, P., et al. Crystallographic and Electrophilic Fragment Screening of the SARS-CoV-2 Main Protease. *Nat. Commun.* **2020**, *11*, 5047. doi: 10.1038/s41467-020-18709-w.

94. Klein, B.A.; Reiz, B.; Robertson, I.M.; Irving, M.; Li, L.; Sun, Y.-B.; Sykes, B.D. Reversible Covalent Reaction of Levosimendan with Cardiac Troponin C in Vitro and In Situ. *Biochemistry* **2018**, *57*, 2256–2265. doi: 10.1021/acs.biochem.8b00109.

95. Dhillon, S. Tirabrutinib: First Approval. *Drugs* **2020**, *80*, 835–840. doi: 10.1007/s40265-020-01318-8.

96. Hansen, R.; Peters, U.; Babbar, A.; Chen, Y.; Feng, J.; Janes, M.R.; Li, L.-S.; Ren, P.; Liu, Y.; Zarrinkar, P.P. The Reactivity-Driven Biochemical Mechanism of Covalent KRAS^{G12C} Inhibitors. *Nat. Struct. Mol. Biol.* **2018**, *25*, 454–462. doi: 10.1038/s41594-018-0061-5.

97. Li, K.S.; Quinn, J.G.; Saabye, M.J.; Guerrero, J.F.S.; Nonomiya, J.; Lian, Q.; Phung, W.; Izrayelit, Y.; Walters, B.T.; Gustafson, A.; Endres, N.F.; Beresini, M.H.; Mulvihill, M.M. High-Throughput Kinetic Characterization of Irreversible Covalent Inhibitors of KRAS^{G12C} by Intact Protein MS and Targeted MRM. *Anal. Chem.* **2022**, *94*, 1230–1239. doi: 10.1021/acs.analchem.1c04463.

98. Janes, M.R.; Zhang, J.; Li, L.-S.; Hansen, R.; Peters, U.; Guo, X.; Chen, Y.; Babbar, A.; Firdaus, S.J.; Darjania, L., et al. Targeting KRAS Mutant Cancers with a Covalent G12C-Specific Inhibitor. *Cell* **2018**, *172*, 578–589.e17. doi: 10.1016/j.cell.2018.01.006.

99. Canon, J.; Rex, K.; Saiki, A.Y.; Mohr, C.; Cooke, K.; Bagal, D.; Gaida, K.; Holt, T.; Knutson, C.G.; Koppada, N., et al. The Clinical KRAS(G12C) Inhibitor AMG 510 Drives Anti-Tumour Immunity. *Nature* **2019**, *575*, 217–223. doi: 10.1038/s41586-019-1694-1.

100. Hansen, R.; Firdaus, S.J.; Li, S.; Janes, M.R.; Zhang, J.; Liu, Y.; Zarrinkar, P.P. An Internally Controlled Quantitative Target Occupancy Assay for Covalent Inhibitors. *Sci. Rep.* **2018**, *8*, 14312. doi: 10.1038/s41598-018-32683-w.

101. Kantaev, B.; Polanski, R.; Lewis, H.J.; Haider, A.; Barratt, D.; Srinivasan, B. Accelerating the Validation of Endogenous On-Target Engagement and In Cellulo Kinetic Assessment for Covalent Inhibitors of KRAS^{G12C} in Early Drug Discovery. *ACS Chem. Biol.* **2022**, *17*, 2366–2376. doi: 10.1021/acschembio.2c00483.

102. Lito, P.; Solomon, M.; Li, L.-S.; Hansen, R.; Rosen, N. Allele-Specific Inhibitors Inactivate Mutant KRAS G12C By a Trapping Mechanism. *Science* **2016**, *351*, 604–608. doi: 10.1126/science.aad6204.

103. Fell, J.B.; Fischer, J.P.; Baer, B.R.; Blake, J.F.; Bouhana, K.; Briere, D.M.; Brown, K.D.; Burgess, L.E.; Burns, A.C.; Burkard, M.R., et al. Identification of the Clinical Development Candidate MRTX849, a Covalent KRASG12C Inhibitor for the Treatment of Cancer. *J. Med. Chem.* **2020**, *63*, 6679-6693. doi: 10.1021/acs.jmedchem.9b02052.
104. Simon, G.M.; Niphakis, M.J.; Cravatt, B.F. Determining Target Engagement in Living Systems. *Nat. Chem. Biol.* **2013**, *9*, 200-205. doi: 10.1038/nchembio.1211.
105. McPherson, A.; Gavira, J.A. Introduction to Protein Crystallization. *Acta Crystallogr., Sect. F* **2014**, *70*, 2-20. doi: 10.1107/S2053230X13033141.
106. Berman, H.; Henrick, K.; Nakamura, H. Announcing the Worldwide Protein Data Bank. *Nat. Struct. Mol. Biol.* **2003**, *10*, 980-980. doi: 10.1038/nsb1203-980.
107. Berman, H.M.; Westbrook, J.; Feng, Z.; Gilliland, G.; Bhat, T.N.; Weissig, H.; Shindyalov, I.N.; Bourne, P.E. The Protein Data Bank. *Nucleic Acids Res.* **2000**, *28*, 235-242. doi: 10.1093/nar/28.1.235.
108. Bender, A.T.; Gardberg, A.; Pereira, A.; Johnson, T.; Wu, Y.; Grenningloh, R.; Head, J.; Morandi, F.; Haselmayer, P.; Liu-Bujalski, L. Ability of Bruton's Tyrosine Kinase Inhibitors to Sequester Y551 and Prevent Phosphorylation Determines Potency for Inhibition of Fc Receptor but not B-Cell Receptor Signaling. *Mol. Pharmacol.* **2017**, *91*, 208-219. doi: 10.1124/mol.116.107037.
109. Engel, J.; Smith, S.; Lategahn, J.; Tumbrink, H.L.; Goebel, L.; Becker, C.; Hennes, E.; Keul, M.; Unger, A.; Müller, H.; Baumann, M.; Schultz-Fademrecht, C.; Günther, G.; Hengstler, J.G.; Rauh, D. Structure-Guided Development of Covalent and Mutant-Selective Pyrazolopyrimidines to Target T790M Drug Resistance in Epidermal Growth Factor Receptor. *J. Med. Chem.* **2017**, *60*, 7725-7744. doi: 10.1021/acs.jmedchem.7b00515.
110. Groll, M.; Huber, R.; Potts, B.C.M. Crystal Structures of Salinosporamide A (NPI-0052) and B (NPI-0047) in Complex with the 20S Proteasome Reveal Important Consequences of β -Lactone Ring Opening and a Mechanism for Irreversible Binding. *J. Am. Chem. Soc.* **2006**, *128*, 5136-5141. doi: 10.1021/ja058320b.
111. Uhlenbrock, N.; Smith, S.; Weisner, J.; Landel, I.; Lindemann, M.; Le, T. A.; Hardick, J.; Gontla, R.; Scheinpflug, R.; Czodrowski, P.; Janning, P.; Depta, L.; Quambusch, L.; Müller, M.P.; Engels, B.; Rauh, D. Structural and Chemical Insights into the Covalent-Allosteric Inhibition of the Protein Kinase Akt. *Chem. Sci.* **2019**, *10*, 3573-3585. doi: 10.1039/C8SC05212C.
112. Lockbaum, G.J.; Henes, M.; Lee, J.M.; Timm, J.; Nalivaika, E.A.; Thompson, P.R.; Kurt Yilmaz, N.; Schiffer, C.A. Pan-3C Protease Inhibitor Rupintrivir Binds SARS-CoV-2 Main Protease in a Unique Binding Mode. *Biochemistry* **2021**, *60*, 2925-2931. doi: 10.1021/acs.biochem.1c00414.
113. London, N.; Miller, R.M.; Krishnan, S.; Uchida, K.; Irwin, J.J.; Eidam, O.; Gibold, L.; Cimermančič, P.; Bonnet, R.; Shiochet, B.K.; Taunton, J. Covalent Docking of Large Libraries for the Discovery of Chemical Probes. *Nat. Chem. Biol.* **2014**, *10*, 1066-1072. doi: 10.1038/nchembio.1666.
114. Scarpino, A.; Ferenczy, G.G.; Keserű, G.M. Comparative Evaluation of Covalent Docking Tools. *J. Chem. Inf. Model.* **2018**, *58*, 1441-1458. doi: 10.1021/acs.jcim.8b00228.
115. Gao, M.; Moumbock, A.F.A.; Qaseem, A.; Xu, Q.; Günther, S. CovPDB: A High-Resolution Coverage of the Covalent Protein–Ligand Interactome. *Nucleic Acids Res.* **2022**, *50*, D445-D450. doi: 10.1093/nar/gkab868.
116. Shraga, A.; Olshvng, E.; Davidzohn, N.; Khoshkenar, P.; Germain, N.; Shurush, K.; Carvalho, S.; Avram, L.; Albeck, S.; Unger, T.; Lefker, B.; Subramanyam, C.; Hudkins, R.L.; Mitchell, A.; Shulman, Z.; Kinoshita, T.; London, N. Covalent Docking Identifies a Potent and Selective MKK7 Inhibitor. *Cell. Chem. Biol.* **2019**, *26*, 98-108.e5. doi: 10.1016/j.chembiol.2018.10.011.
117. Wan, X.; Yang, T.; Cuesta, A.; Pang, X.; Balias, T.E.; Irwin, J.J.; Shiochet, B.K.; Taunton, J. Discovery of Lysine-Targeted eIF4E Inhibitors through Covalent Docking. *J. Am. Chem. Soc.* **2020**, *142*, 4960-4964. doi: 10.1021/jacs.9b10377.
118. Becker, D.; Kaczmarski, Z.; Arkona, C.; Schulz, R.; Tauber, C.; Wolber, G.; Hilgenfeld, R.; Coll, M.; Rademann, J. Irreversible Inhibitors of the 3C Protease of Coxsackievirus Through Templated Assembly of Protein-Binding Fragments. *Nat. Commun.* **2016**, *7*, 12761. doi: 10.1038/ncomms12761.
119. Serafin, R.A.M.; da Silva Santiago, A.; Schwalm, M.P.; Hu, Z.; dos Reis, C.V.; Takarada, J.E.; Mezzomo, P.; Massirer, K.B.; Kudolo, M.; Gerstenecker, S.; Chaikud, A.; Zender, L.; Knapp, S.; Laufer, S.; Couñago, R.M.; Gehring, M. Development of the First Covalent Monopolar Spindle Kinase 1 (MPS1/TTK) Inhibitor. *J. Med. Chem.* **2022**, *65*, 3173-3192. doi: 10.1021/acs.jmedchem.1c01165.
120. Włodawer, A.; Minor, W.; Dauter, Z.; Jaskolski, M. Protein Crystallography for Aspiring Crystallographers or How to Avoid Pitfalls and Traps in Macromolecular Structure Determination. *FEBS J.* **2013**, *280*, 5705-5736. doi: 10.1111/febs.12495.
121. Rupp, B. *Biomolecular Crystallography: Principles, Practice, and Application to Structural Biology*. Garland Science: New York, 2009. doi: 10.1201/9780429258756.
122. Taylor, G. Introduction to Phasing. *Acta Crystallogr., Sect. D* **2010**, *66*, 325-338. doi: 10.1107/S0907444910006694.
123. Hodel, A.; Kim, S.-H.; Brunger, A.T. Model Bias in Macromolecular Crystal Structures. *Acta Crystallogr., Sect. A* **1992**, *48*, 851-858. doi: 10.1107/S0108767392006044.
124. Ferrall-Fairbanks, M.C.; Kieslich, C.A.; Platt, M.O. Reassessing Enzyme Kinetics: Considering Protease-As-Substrate Interactions in Proteolytic Networks. *Proc. Natl. Acad. Sci.* **2020**, *117*, 3307. doi: 10.1073/pnas.1912207117.
125. Lee, G.M.; Balouch, E.; Goetz, D.H.; Lazic, A.; McKerrow, J.H.; Craik, C.S. Mapping Inhibitor Binding Modes on an Active Cysteine Protease via Nuclear Magnetic Resonance Spectroscopy. *Biochemistry* **2012**, *51*, 10087-10098. doi: 10.1021/bi301305k.
126. Hassell, A.M.; An, G.; Bledsoe, R.K.; Bynum, J.M.; Carter, H.L.; II; Deng, S.-J.J.; Gampe, R.T.; Grisard, T.E.; Madauss, K.P.; Nolte, R.T.; Rocque, W.J.; Wang, L.; Weaver, K.L.; Williams, S.P.; Wisely, G.B.; Xu, R.; Shewchuk, L.M. Crystallization of Protein-Ligand Complexes. *Acta Crystallogr., Sect. D* **2007**, *63*, 72-79. doi: 10.1107/S090744906047020.
127. Wienen-Schmidt, B.; Oebbeke, M.; Ngo, K.; Heine, A.; Klebe, G. Two Methods, One Goal: Structural Differences between Cocrystallization and Crystal Soaking to Discover Ligand Binding Poses. *ChemMedChem* **2021**, *16*, 292-300. doi: 10.1002/cmdc.202000565.
128. Włodawer, A.; Minor, W.; Dauter, Z.; Jaskolski, M. Protein Crystallography for Non-crystallographers, or How to Get the Best (But Not More) from Published Macromolecular Structures. *FEBS J.* **2008**, *275*, 1-21. doi: 10.1111/j.1742-4658.2007.06178.x.
129. Martz, E.; Sussman, J.L.; Decatur, W.; Hodis, E.; Jiang, Y.; Prilusky, J. Resolution. In *Proteopedia* [Online]; 2022. Updated 2022-05-16. <https://proteopedia.org/wiki/index.php/Resolution> (accessed 2022-08-21).
130. Woińska, M.; Grabowsky, S.; Dominiak, P.M.; Woźniak, K.; Jayatilaka, D. Hydrogen Atoms Can Be Located Accurately and Precisely by X-ray Crystallography. *Sci. Adv.* **2016**, *2*, e1600192. doi: 10.1126/sciadv.1600192.
131. Lv, Z.; Yuan, L.; Atkison, J.H.; Williams, K.M.; Vega, R.; Sessions, E.H.; Divilanska, D.B.; Davies, C.; Chen, Y.; Olsen, S.K. Molecular Mechanism of a Covalent Allosteric Inhibitor of SUMO E1 Activating Enzyme. *Nat. Commun.* **2018**, *9*, 5145. doi: 10.1038/s41467-018-07015-1.
132. Obaidat, A.; Weiss, J.; Wahlgren, B.; Manam, R.R.; Macherla, V.R.; McArthur, K.; Chao, T.-H.; Palladino, M.A.; Lloyd, G.K.; Potts, B.C.; Enna, S.J.; Neuteboom, S.T.C.; Hagenbuch, B. Proteasome Regulator Marizomib (NPI-0052) Exhibits Prolonged Inhibition, Attenuated Efflux, and Greater Cytotoxicity than Its Reversible Analogs. *J. Pharmacol. Exp. Ther.* **2011**, *337*, 479-486. doi: 10.1124/jpet.110.177824.

133. Harshbarger, W.; Miller, C.; Diedrich, C.; Sacchettini, J. Crystal Structure of the Human 20S Proteasome in Complex with Carfilzomib. *Structure* **2015**, *23*, 418-424. doi: 10.1016/j.str.2014.11.017.

134. Law, S.; Andrault, P.-M.; Aguda, A.H.; Nguyen, N.T.; Kruglyak, N.; Brayer, G.D.; Brömmé, D. Identification of Mouse Cathepsin K Structural Elements that Regulate the Potency of Odanacatib. *Biochem. J.* **2017**, *474*, 851-864. doi: 10.1042/BCJ20160985.

135. Forster, M.; Chaikud, A.; Bauer, S.M.; Holstein, J.; Robers, M.B.; Corona, C.R.; Gehringer, M.; Pfaffenrot, E.; Ghoreshi, K.; Knapp, S.; Laufer, S.A. Selective JAK3 Inhibitors with a Covalent Reversible Binding Mode Targeting a New Induced Fit Binding Pocket. *Cell Chem. Biol.* **2016**, *23*, 1335-1340. doi: 10.1016/j.chembiol.2016.10.008.

136. Ekkebus, R.; van Kesteren, S.I.; Kulathu, Y.; Scholten, A.; Berlin, I.; Geurink, P.P.; de Jong, A.; Goerdhayal, S.; Neefjes, J.; Heck, A.J.R.; Komander, D.; Ovaa, H. On Terminal Alkynes That Can React with Active-Site Cysteine Nucleophiles in Proteases. *J. Am. Chem. Soc.* **2013**, *135*, 2867-2870. doi: 10.1021/ja309802n.

137. Barbosa da Silva, E.; Dall, E.; Briza, P.; Brandstetter, H.; Ferreira, R.S. Cruzain Structures: Apocruzain and Cruzain Bound to S-Methyl Thiometanesulfonate and Implications for Drug Design. *Acta Crystallogr., Sect. F* **2019**, *75*, 419-427. doi: 10.1107/S2053230X19006320.

138. Kara, A.R.; Ruddock, L.W. Does S-Methyl Methanethiosulfonate Trap the Thiol–Disulfide State of Proteins? *Antioxid. Redox Signal.* **2007**, *9*, 527-531. doi: 10.1089/ars.2006.1473.

139. Adams, J.; Kauffman, M. Development of the Proteasome Inhibitor Velcade™ (Bortezomib). *Cancer Invest.* **2004**, *22*, 304-311. doi: 10.1081/CNV-120030218.

140. Kabir, M.L.; Wang, F.; Clayton, A.H.A. Intrinsically Fluorescent Anti-Cancer Drugs. *Biology* **2022**, *11*, 1135. doi: 10.3390/biology11081135.

141. Wilson, J.N.; Liu, W.; Brown, A.S.; Landgraf, R. Binding-Induced, Turn-On Fluorescence of the EGFR/ERBB Kinase Inhibitor, Lapatinib. *Org. Biomol. Chem.* **2015**, *13*, 5006-5011. doi: 10.1039/C5OB00239G.

142. Klüter, S.; Simard, J.R.; Rode, H.B.; Grüter, C.; Pawar, V.; Raaijmakers, H.C.A.; Barf, T.A.; Rabiller, M.; van Otterlo, W.A.L.; Rauh, D. Characterization of Irreversible Kinase Inhibitors by Directly Detecting Covalent Bond Formation: A Tool for Dissecting Kinase Drug Resistance. *ChemBioChem* **2010**, *11*, 2557-2566. doi: 10.1002/cbic.201000352.

143. Hodge, C.D.; Edwards, R.A.; Markin, C.J.; McDonald, D.; Pulpino, M.; Huen, M.S.Y.; Zhao, J.; Spyrapopoulos, L.; Hendzel, M.J.; Glover, J.N.M. Covalent Inhibition of Ubc13 Affects Ubiquitin Signaling and Reveals Active Site Elements Important for Targeting. *ACS Chem. Biol.* **2015**, *10*, 1718-1728. doi: 10.1021/acscchembio.5b00222.

144. Niu, L.-Y.; Chen, Y.-Z.; Zheng, H.-R.; Wu, L.-Z.; Tung, C.-H.; Yang, Q.-Z. Design Strategies of Fluorescent Probes for Selective Detection Among Biothiols. *Chem. Soc. Rev.* **2015**, *44*, 6143-6160. doi: 10.1039/C5CS00152H.

145. Kwan, A.H.; Mobli, M.; Gooley, P.R.; King, G.F.; Mackay, J.P. Macromolecular NMR Spectroscopy for the Non-Spectroscopist. *FEBS J.* **2011**, *278*, 687-703. doi: 10.1111/j.1742-4658.2011.08004.x.

146. Maity, S.; Gundampati, R.K.; Suresh Kumar, T.K. NMR Methods to Characterize Protein–Ligand Interactions. *Nat. Prod. Commun.* **2019**, *14*, 1-17. doi: 10.1177/1934578X19849296.

147. Keiffer, S.; Carneiro, M.G.; Hollander, J.; Kobayashi, M.; Pogorelyev, D.; Ab, E.; Theisgen, S.; Müller, G.; Siegal, G. NMR in Target Driven Drug Discovery: Why Not? *J. Biomol. NMR* **2020**, *74*, 521-529. doi: 10.1007/s10858-020-00343-9.

148. Ishima, R. Protein–Inhibitor Interaction Studies Using NMR. *Appl. NMR Spectrosc.* **2015**, *1*, 143-181. doi: 10.2174/9781608059621115010007.

149. Sugiki, T.; Furuita, K.; Fujiwara, T.; Kojima, C. Current NMR Techniques for Structure-Based Drug Discovery. *Molecules* **2018**, *23*, 148. doi: 10.3390/molecules23010148.

150. Krishnan, V.V.; Rupp, B. Macromolecular Structure Determination: Comparison of X-ray Crystallography and NMR Spectroscopy. In *eLS* [Online]; John Wiley & Sons, 2012. Updated 2012-06-15. doi: 10.1002/9780470015902.a0002716.pub2. (accessed 2023-03-26).

151. Schirò, A.; Carlon, A.; Parigi, G.; Mursudov, G.; Calderone, V.; Ravera, E.; Luchinat, C. On the Complementarity of X-ray and NMR Data. *J. Struct. Biol.* **X** **2020**, *4*, 100019. doi: 10.1016/j.jsbx.2020.100019.

152. Bjorndahl, T.C.; Andrew, L.C.; Semchenko, V.; Wishart, D.S. NMR Solution Structures of the Apo and Peptide-Inhibited Human Rhinovirus 3C Protease (Serotype 14): Structural and Dynamic Comparison. *Biochemistry* **2007**, *46*, 12945-12958. doi: 10.1021/bi7010866.

153. Zhulenkova, D.; Rudevica, Z.; Jaudzems, K.; Turks, M.; Leonchik, A. Discovery and Structure–Activity Relationship Studies of Irreversible Benzisothiazolinone-Based Inhibitors Against *Staphylococcus aureus* Sortase A Transpeptidase. *Bioorg. Med. Chem.* **2014**, *22*, 5988-6003. doi: 10.1016/j.bmc.2014.09.011.

154. Jaudzems, K.; Kurbatska, V.; Jēkabsons, A.; Bobrovs, R.; Rudevica, Z.; Leonchik, A. Targeting Bacterial Sortase A with Covalent Inhibitors: 27 New Starting Points for Structure-Based Hit-to-Lead Optimization. *ACS Infect. Dis.* **2020**, *6*, 186-194. doi: 10.1021/acsinfecdis.9b00265.

155. Sastry, M.; Fiala, R.; Lipman, R.; Tomasz, M.; Patel, D.J. Solution Structure of the Monoalkylated Mitomycin C–DNA Complex. *J. Mol. Biol.* **1995**, *247*, 338-359. doi: 10.1006/jmbi.1994.0143.

156. Lin, C.H.; Patel, D.J. Solution Structure of the Covalent Duocarmycin A–DNA Duplex Complex. *J. Mol. Biol.* **1995**, *248*, 162-179. doi: 10.1006/jmbi.1995.0209.

157. Meyer, B.; Peters, T. NMR Spectroscopy Techniques for Screening and Identifying Ligand Binding to Protein Receptors. *Angew. Chem. Int. Ed.* **2003**, *42*, 864-890. doi: 10.1002/anie.200390233.

158. Furukawa, A.; Konuma, T.; Yanaka, S.; Sugase, K. Quantitative Analysis of Protein–Ligand Interactions by NMR. *Prog. Nucl. Magn. Reson. Spectrosc.* **2016**, *96*, 47-57. doi: 10.1016/j.pnms.2016.02.002.

159. Olp, M.D.; Sprague, D.J.; Goetz, C.J.; Kathman, S.G.; Wynia-Smith, S.L.; Shishodia, S.; Summers, S.B.; Xu, Z.; Statsyuk, A.V.; Smith, B.C. Covalent-Fragment Screening of BRD4 Identifies a Ligandable Site Orthogonal to the Acetyl-Lysine Binding Sites. *ACS Chem. Biol.* **2020**, *15*, 1036-1049. doi: 10.1021/acschembio.0c00058.

160. Becker, W.; Bhattacharjee, K.C.; Gubensäk, N.; Zangger, K. Investigating Protein–Ligand Interactions by Solution Nuclear Magnetic Resonance Spectroscopy. *ChemPhysChem* **2018**, *19*, 895-906. doi: 10.1002/cphc.201701253.

161. Felli, I.C.; Pierattelli, R. ^{13}C Direct Detected NMR for Challenging Systems. *Chem. Rev.* **2022**, *122*, 9468-9496. doi: 10.1021/acs.chemrev.1c00871.

162. Cook, E.C.; Usher, G.A.; Showalter, S.A. Chapter Five - The Use of ^{13}C Direct-Detect NMR to Characterize Flexible and Disordered Proteins. *Meth. Enzymol.* **2018**, *611*, 81-100. doi: 10.1016/bs.mie.2018.08.025.

163. Skora, L.; Mestan, J.; Fabbro, D.; Jahnke, W.; Grzesiek, S. NMR Reveals the Allosteric Opening and Closing of Abelson Tyrosine Kinase by ATP-Site and Myristoloyl Pocket Inhibitors. *Proc. Natl. Acad. Sci.* **2013**, *110*, E4437-E4445. doi: 10.1073/pnas.1314712110.

164. Metzler, W.J.; Yunchunas, J.; Weigelt, C.; Kish, K.; Klei, H.E.; Xie, D.; Zhang, Y.; Corbett, M.; Tamura, J.K.; He, B.; Hamann, L.G.; Kirby, M.S.; Marcinkeviciene, J. Involvement of DPP-IV Catalytic Residues in Enzyme–Saxagliptin Complex Formation. *Protein Sci.* **2008**, *17*, 240-250. doi: 10.1101/ps.073253208.

165. Harner, M.J.; Frank, A.O.; Fesik, S.W. Fragment-Based Drug Discovery Using NMR Spectroscopy. *J. Biomol. NMR* **2013**, *56*, 65-75. doi: 10.1007/s10858-013-9740-z.

166. Gowda, G.A.N.; Pascua, V.; Neto, F.C.; Raftery, D. Hydrogen–Deuterium Addition and Exchange in N-Ethylmaleimide Reaction with Glutathione Detected by NMR Spectroscopy. *ACS Omega* **2022**, *7*, 26928-26935. doi: 10.1021/acsomega.2c03482.

167. Krishnan, S.; Miller, R.M.; Tian, B.; Mullins, R.D.; Jacobson, M.P.; Taunton, J. Design of Reversible, Cysteine-Targeted Michael Acceptors Guided by Kinetic and Computational Analysis. *J. Am. Chem. Soc.* **2014**, *136*, 12624-12630. doi: 10.1021/ja50194w.

168. Boudreau, E.A.; Pelczer, I.; Borer, P.N.; Heffron, G.J.; LaPlante, S.R. Changes in Drug ^{13}C NMR Chemical Shifts as a Tool for Monitoring Interactions with DNA. *Biophys. Chem.* **2004**, *109*, 333-344. doi: 10.1016/j.bpc.2003.12.005.

169. Yabe, Y.; Guillaume, D.; Rich, D.H. Irreversible Inhibition of Papain by Epoxysuccinyl Peptides. Carbon-13 NMR Characterization of the Site of Alkylation. *J. Am. Chem. Soc.* **1988**, *110*, 4043-4044. doi: 10.1021/ja00220a056.

170. Transeau, T.R.; Krahm, J.M.; Gabel, S.A.; DeRose, E.F.; London, R.E. X-ray and NMR Characterization of Covalent Complexes of Trypsin, Borate, and Alcohols. *Biochemistry* **2004**, *43*, 2829-2839. doi: 10.1021/bi035782y.

171. Glynn, S.J.; Gaffney, K.J.; Sainz, M.A.; Louie, S.G.; Petasis, N.A. Molecular Characterization of the Boron Adducts of the Proteasome Inhibitor Bortezomib with Epigallocatechin-3-gallate and Related Polyphenols. *Org. Biomol. Chem.* **2015**, *13*, 3887-3899. doi: 10.1039/C4OB02512A.

172. Moon, J.B.; Coleman, R.S.; Hanzlik, R.P. Reversible Covalent Inhibition of Papain by a Peptide Nitrile. ^{13}C NMR Evidence for a Thioimidate Ester Adduct. *J. Am. Chem. Soc.* **1986**, *108*, 1350-1351. doi: 10.1021/ja00266a066.

173. Robertson, I.M.; Pineda-Sanabria, S.E.; Yan, Z.; Kampourakis, T.; Sun, Y.-B.; Sykes, B.D.; Irving, M. Reversible Covalent Binding to Cardiac Troponin C by the Ca^{2+} -Sensitizer Levosimendan. *Biochemistry* **2016**, *55*, 6032-6045. doi: 10.1021/acs.biochem.6b00758.

174. Thompson, S.K.; Halbert, S.M.; Bossard, M.J.; Tomaszek, T.A.; Levy, M.A.; Zhao, B.; Smith, W.W.; Abdel-Meguid, S.S.; Janson, C.A.; D'Alessio, K.J., et al. Design of Potent and Selective Human Cathepsin K Inhibitors That Span the Active Site. *Proc. Natl. Acad. Sci.* **1997**, *94*, 14249. doi: 10.1073/pnas.94.26.14249.

175. Falgueyret, J.-P.; Oballa, R.M.; Okamoto, O.; Wesolowski, G.; Aubin, Y.; Rydzewski, R.M.; Prasit, P.; Riendeau, D.; Rodan, S.B.; Percival, M.D. Novel, Nonpeptidic Cyanamides as Potent and Reversible Inhibitors of Human Cathepsins K and L. *J. Med. Chem.* **2001**, *44*, 94-104. doi: 10.1021/jm0003440.

176. Sorsa, T.; Heikkinen, S.; Abbott, M.B.; Abusamhadneh, E.; Laakso, T.; Tilgmann, C.; Serimaa, R.; Annila, A.; Rosevear, P.R.; Drakenberg, T.; Pollesello, P.; Kilpeläinen, I. Binding of Levosimendan, a Calcium Sensitizer, to Cardiac Troponin C. *J. Biol. Chem.* **2001**, *276*, 9337-9343. doi: 10.1074/jbc.M007484200.

177. Liu, Y.; Patricelli, M.P.; Cravatt, B.F. Activity-Based Protein Profiling: The Serine Hydrolases. *Proc. Natl. Acad. Sci.* **1999**, *96*, 14694-14699. doi: 10.1073/pnas.96.26.14694.

178. Cravatt, B.F.; Wright, A.T.; Kozarich, J.W. Activity-Based Protein Profiling: From Enzyme Chemistry to Proteomic Chemistry. *Annu. Rev. Biochem.* **2008**, *77*, 383-414. doi: 10.1146/annurev.biochem.75.101304.124125.

179. Nomura, D.K.; Dix, M.M.; Cravatt, B.F. Activity-Based Protein Profiling for Biochemical Pathway Discovery in Cancer. *Nat. Rev. Cancer* **2010**, *10*, 630-638. doi: 10.1038/nrc2901.

180. Cravatt, B.F.; Hsu, K.-L.; Weerapana, E. Activity-Based Protein Profiling. *Curr. Top. Microbiol. Immunol.* **2019**, *420*, 1-417. doi: 10.1007/978-3-030-11143-4.

181. Bachovchin, D.A.; Cravatt, B.F. The Pharmacological Landscape and Therapeutic Potential of Serine Hydrolases. *Nat. Rev. Drug Discov.* **2012**, *11*, 52-68. doi: 10.1038/nrd3620.

182. Kato, D.; Boatright, K.M.; Berger, A.B.; Nazif, T.; Blum, G.; Ryan, C.; Chehade, K.A.H.; Salvesen, G.S.; Bogyo, M. Activity-Based Probes that Target Diverse Cysteine Protease Families. *Nat. Chem. Biol.* **2005**, *1*, 33-38. doi: 10.1038/nchembio707.

183. Chakrabarty, S.; Kahler, J.P.; van de Plassche, M.A.T.; Vanhoutte, R.; Verhelst, S.H.L. Recent Advances in Activity-Based Protein Profiling of Proteases. *Curr. Top. Microbiol. Immunol.* **2019**, *420*, 253-281. doi: 10.1007/82_2018_138.

184. Hoch, D.G.; Abegg, D.; Adibekian, A. Cysteine-reactive Probes and their Use in Chemical Proteomics. *Chem. Commun.* **2018**, *54*, 4501-4512. doi: 10.1039/C8CC01485J.

185. Hameed, D.S.; Sapsam, A.; Ovaa, H. How Chemical Synthesis of Ubiquitin Conjugates Helps To Understand Ubiquitin Signal Transduction. *Bioconjug. Chem.* **2017**, *28*, 805-815. doi: 10.1021/acs.bioconjchem.6b00140.

186. Patricelli, M.P.; Szardeningis, A.K.; Liyanage, M.; Nomanbhoy, T.K.; Wu, M.; Weissig, H.; Aban, A.; Chun, D.; Tanner, S.; Kozarich, J.W. Functional Interrogation of the Kinome Using Nucleotide Acyl Phosphates. *Biochemistry* **2007**, *46*, 350-358. doi: 10.1021/bi062142x.

187. Deng, H.; Lei, Q.; Wu, Y.; He, Y.; Li, W. Activity-Based Protein Profiling: Recent Advances in Medicinal Chemistry. *Eur. J. Med. Chem.* **2020**, *191*, 112151. doi: 10.1016/j.ejmech.2020.112151.

188. Fang, H.; Peng, B.; Ong, S.Y.; Wu, Q.; Li, L.; Yao, S.Q. Recent Advances in Activity-Based Probes (ABPs) and Affinity-Based Probes (AfBPs) for Profiling of Enzymes. *Chem. Sci.* **2021**, *12*, 8288-8310. doi: 10.1039/D1SC01359A.

189. Backus, K.M.; Correia, B.E.; Lum, K.M.; Forli, S.; Horning, B.D.; González-Páez, G.E.; Chatterjee, S.; Lanning, B.R.; Teijaro, J.R.; Olson, A.J.; Wolan, D.W.; Cravatt, B.F. Proteome-Wide Covalent Ligand Discovery in Native Biological Systems. *Nature* **2016**, *534*, 570-574. doi: 10.1038/nature18002.

190. Lanning, B.R.; Whitby, L.R.; Dix, M.M.; Douhan, J.; Gilbert, A.M.; Hett, E.C.; Johnson, T.O.; Joslyn, C.; Kath, J.C.; Niessen, S.; Roberts, L.R.; Schnute, M.E.; Wang, C.; Hulce, J.J.; Wei, B.; Whiteley, L.O.; Hayward, M.M.; Cravatt, B.F. A Road Map to Evaluate the Proteome-Wide Selectivity of Covalent Kinase Inhibitors. *Nat. Chem. Biol.* **2014**, *10*, 760-767. doi: 10.1038/nchembio.1582.

191. van Esbroeck, A.C.M.; Janssen, A.P.A.; Cognetta, A.B.; Ogasawara, D.; Shpak, G.; van der Kroeg, M.; Kantae, V.; Baggelaar, M.P.; de Vrij, F.M.S.; Deng, H., et al. Activity-Based Protein Profiling Reveals Off-Target Proteins of the FAAH Inhibitor BIA 10-2474. *Science* **2017**, *356*, 1084-1087. doi: 10.1126/science.aaf7497.

192. Bird, R.E.; Lemmel, S.A.; Yu, X.; Zhou, Q.A. Bioorthogonal Chemistry and Its Applications. *Bioconjug. Chem.* **2021**, *32*, 2457-2479. doi: 10.1021/acs.bioconjchem.1c00461.

193. Rostovtsev, V.V.; Green, L.G.; Fokin, V.V.; Sharpless, K.B. A Stepwise Huisgen Cycloaddition Process: Copper(I)-Catalyzed Regioselective “Ligation” of Azides and Terminal Alkynes. *Angew. Chem. Int. Ed.* **2002**, *41*, 2596-2599. doi: 10.1002/1521-3773(20020715)41:14<2596::AID-ANIE2596>3.0.CO;2-4.

194. Parker, C.G.; Pratt, M.R. Click Chemistry in Proteomic Investigations. *Cell* **2020**, *180*, 605-632. doi: 10.1016/j.cell.2020.01.025.

195. Smeenk, M.L.W.J.; Agramunt, J.; Bonger, K.M. Recent Developments in Bioorthogonal Chemistry and the Orthogonality Within. *Curr. Opin. Chem. Biol.* **2021**, *60*, 79-88. doi: 10.1016/j.cbpa.2020.09.002.

196. Agard, N.J.; Prescher, J.A.; Bertozzi, C.R. A Strain-Promoted [3 + 2] Azide–Alkyne Cycloaddition for Covalent Modification of Biomolecules in Living Systems. *J. Am. Chem. Soc.* **2004**, *126*, 15046–15047. doi: 10.1021/ja044996f.

197. Oliveira, B.L.; Guo, Z.; Bernardes, G.J.L. Inverse Electron Demand Diels–Alder Reactions in Chemical Biology. *Chem. Soc. Rev.* **2017**, *46*, 4895–4950. doi: 10.1039/C7CS00184C.

198. van Rooden, E.J.; Florea, B.I.; Deng, H.; Baggelaar, M.P.; van Esbroeck, A.C.M.; Zhou, J.; Overkleef, H.S.; van der Stelt, M. Mapping *In Vivo* Target Interaction Profiles of Covalent Inhibitors using Chemical Proteomics with Label-Free Quantification. *Nat. Protoc.* **2018**, *13*, 752–767. doi: 10.1038/nprot.2017.159.

199. Xu, H.; Jesson, M.I.; Seneviratne, U.I.; Lin, T. H.; Sharif, M. N.; Xue, L.; Nguyen, C.; Everley, R.A.; Trujillo, J.I.; Johnson, D.S.; Point, G.R.; Thorarensen, A.; Kilti, I.; Telliez, J.-B. PF-06651600, a Dual JAK3/TEC Family Kinase Inhibitor. *ACS Chem. Biol.* **2019**, *14*, 1235–1242. doi: 10.1021/acscchembio.9b00188.

200. Yang, P.-Y.; Liu, K.; Ngai, M.H.; Lear, M.J.; Wenk, M.R.; Yao, S.Q. Activity-Based Proteome Profiling of Potential Cellular Targets of Orlistat – An FDA-Approved Drug with Anti-Tumor Activities. *J. Am. Chem. Soc.* **2010**, *132*, 656–666. doi: 10.1021/ja907716f.

201. Martin, J.G.; Ward, J.A.; Feyertag, F.; Zhang, L.; Couvertier, S.; Guckian, K.; Huber, K.V.M.; Johnson, D.S. Chemoproteomic Profiling of Covalent XPO1 Inhibitors to Assess Target Engagement and Selectivity. *ChemBioChem* **2021**, *22*, 2116–2123. doi: 10.1002/cbic.202100038.

202. Lee, J. H.; Hou, X.; Kummaré, E.; Borazjani, A.; Edelmann, M.J.; Ross, M.K. Endocannabinoid Hydrolases in Avian HD11 Macrophages Identified by Chemoproteomics: Inactivation by Small-Molecule Inhibitors and Pathogen-Induced Downregulation of Their Activity. *Mol. Cell. Biochem.* **2018**, *444*, 125–141. doi: 10.1007/s11010-017-3237-0.

203. Gjonaj, L.; Sapmaz, A.; Flierman, D.; Janssen, G.M.C.; van Veelen, P.A.; Ovaa, H. Development of a DUB-Selective Fluorogenic Substrate. *Chem. Sci.* **2019**, *10*, 10290–10296. doi: 10.1039/CSC02226K.

204. van Rooden, E.J.; van Esbroeck, A.C.M.; Baggelaar, M.P.; Deng, H.; Florea, B.I.; Marques, A.R.A.; Ottenhoff, R.; Boot, R.G.; Overkleef, H.S.; Aerts, J.M.F.G.; van der Stelt, M. Chemical Proteomic Analysis of Serine Hydrolase Activity in Niemann-Pick Type C Mouse Brain. *Front. Neurosci.* **2018**, *12*, 440. doi: 10.3389/fnins.2018.00440.205. Li, W.; Blankman, J.L.; Cravatt, B.F. A Functional Proteomic Strategy to Discover Inhibitors for Uncharacterized Hydrolases. *J. Am. Chem. Soc.* **2007**, *129*, 9594–9595. doi: 10.1021/ja073650c.

205. van der Wel, T.; Hilhorst, R.; den Dulk, H.; van den Hooven, T.; Prins, N.M.; Wijnakker, J.A.P.M.; Florea, B.I.; Lenselink, E.B.; van Westen, G.J.P.; Ruitjenbeek, R.; Overkleef, H.S.; Kaptein, A.; Barf, T.; van der Stelt, M. Chemical Genetics Strategy to Profile Kinase Target Engagement Reveals Role of FES in Neutrophil Phagocytosis. *Nat. Commun.* **2020**, *11*, 3216. doi: 10.1038/s41467-020-17027-5.

206. Kooij, R.; Liu, S.; Sapmaz, A.; Xin, B.-T.; Janssen, G.M.C.; van Veelen, P.A.; Ovaa, H.; ten Dijke, P.; Geurink, P.P. Small-Molecule Activity-Based Probe for Monitoring Ubiquitin C-Terminal Hydrolase L1 (UCHL1) Activity in Live Cells and Zebrafish Embryos. *J. Am. Chem. Soc.* **2020**, *142*, 16825–16841. doi: 10.1021/jacs.0c00772.

207. Jia, Y.; Kim, R.Q.; Kooij, R.; Ovaa, H.; Sapmaz, A.; Geurink, P.P. Chemical Toolkit for PARK7: Potent, Selective, and High-Throughput. *J. Med. Chem.* **2022**, *65*, 13288–13304. doi: 10.1021/acs.jmedchem.2c01113.

208. Leal, J.; Martínez-Díez, M.; García-Hernández, V.; Moneo, V.; Domingo, A.; Bueren-Calabuig, J.; Negri, A.; Gago, F.; Guillén-Navarro, M.; Avilés, P.; Cuevas, C.; García-Fernández, L.; Galmarini, C. PM01183, a New DNA Minor Groove Covalent Binder with Potent *In Vitro* and *In Vivo* Anti-Tumour Activity. *Br. J. Pharmacol.* **2010**, *161*, 1099–1110. doi: 10.1111/j.1476-5381.2010.00945.x.

209. Dana, D.; Pathak, S.K. A Review of Small Molecule Inhibitors and Functional Probes of Human Cathepsin L. *Molecules* **2020**, *25*, 698. doi: 10.3390/molecules25030698.

210. Bogyo, M.; Verhelst, S.; Bellringard-Dubouchaud, V.; Toba, S.; Greenbaum, D. Selective Targeting of Lysosomal Cysteine Proteases with Radiolabeled Electrophilic Substrate Analogs. *Chem. Biol.* **2000**, *7*, 27–38. doi: 10.1016/S1074-5521(00)00061-2.

211. Pellegatti, M. Preclinical *In Vivo* ADME Studies in Drug Development: A Critical Review. *Expert Opin. Drug Metab. Toxicol.* **2012**, *8*, 161–172. doi: 10.1517/17425255.2012.652084.

212. Harding, C.R.; Scott, I.R. Fluorography—Limitations on Its Use for the Quantitative Detection of 3 H- and 14 C-Labeled Proteins in Polyacrylamide Gels. *Anal. Biochem.* **1983**, *129*, 371–376. doi: 10.1016/0003-2697(83)90564-X.

213. Miyahisa, I.; Sameshima, T.; Hixon, M.S. Rapid Determination of the Specificity Constant of Irreversible Inhibitors (k_{inact}/K_1) by Means of an Endpoint Competition Assay. *Angew. Chem. Int. Ed.* **2015**, *54*, 14099–14102. doi: 10.1002/anie.201505800.

214. Tsou, H.-R.; Overbeek-Klumpers, E.G.; Hallett, W.A.; Reich, M.F.; Floyd, M.B.; Johnson, B.D.; Michalak, R.S.; Nilakantan, R.; Discenzo, C.; Golas, J.; Rabindran, S.K.; Shen, R.; Shi, X.; Wang, Y.-F.; Uspelacis, J.; Wissner, A. Optimization of 6,7-Disubstituted-4-(arylamino)quinoline-3-carbonitriles as Orally Active, Irreversible Inhibitors of Human Epidermal Growth Factor Receptor-2 Kinase Activity. *J. Med. Chem.* **2005**, *48*, 1107–1131. doi: 10.1021/jm040159c.

215. Scicinski, J.; Orsony, B.; Taylor, M.; Luo, G.; Musick, T.; Marini, J.; Adams, C.M.; Fitch, W.L. Preclinical Evaluation of the Metabolism and Disposition of RRx-001, a Novel Investigative Anticancer Agent. *Drug Metab. Dispos.* **2012**, *40*, 1810–1816. doi: 10.1124/dmd.112.046755.

216. McClure, R.A.; Williams, J.D. Impact of Mass Spectrometry-Based Technologies and Strategies on Chemoproteomics as a Tool for Drug Discovery. *ACS Med. Chem. Lett.* **2018**, *9*, 785–791. doi: 10.1021/acsmmedchemlett.8b00181.

217. Counihan, J.L.; Ford, B.; Nomura, D.K. Mapping Proteome-Wide Interactions of Reactive Chemicals Using Chemoproteomic Platforms. *Curr. Opin. Chem. Biol.* **2016**, *30*, 68–76. doi: 10.1016/j.cbpa.2015.11.007.

218. Maura, A.J.; Weerapana, E. Reactive-Cysteine Profiling for Drug Discovery. *Curr. Opin. Chem. Biol.* **2019**, *50*, 29–36. doi: 10.1016/j.cbpa.2019.02.010.

219. Neilson, K.A.; Ali, N.A.; Muralidharan, S.; Mirzaei, M.; Mariani, M.; Assadourian, G.; Lee, A.; van Sluyter, S.C.; Haynes, P.A. Less Label, More Free: Approaches in Label-free Quantitative Mass Spectrometry. *Proteomics* **2011**, *11*, 535–553. doi: 10.1002/pmic.201000553.

220. Nikolov, M.; Schmidt, C.; Urlaub, H. Quantitative Mass Spectrometry-Based Proteomics: An Overview. *Methods Mol. Biol.* **2012**, *893*, 85–100. doi: 10.1007/978-1-61779-885-6_7.

221. Benns, H.J.; Wincott, C.J.; Tate, E.W.; Child, M.A. Activity- and Reactivity-Based Proteomics: Recent Technological Advances and Applications in Drug Discovery. *Curr. Opin. Chem. Biol.* **2021**, *60*, 20–29. doi: 10.1016/j.cbpa.2020.06.011.

222. Wang, C.; Weerapana, E.; Blewett, M.M.; Cravatt, B.F. A Chemoproteomic Platform to Quantitatively Map Targets of Lipid-Derived Electrophiles. *Nat. Meth.* **2014**, *11*, 79–85. doi: 10.1038/nmeth.2759.

223. Weerapana, E.; Wang, C.; Simon, G.M.; Richter, F.; Khare, S.; Dillon, M.B.D.; Bachovchin, D.A.; Mowen, K.; Baker, D.; Cravatt, B.F. Quantitative Reactivity Profiling Predicts Functional Cysteines in Proteomes. *Nature* **2010**, *468*, 790–795. doi: 10.1038/nature09472.

224. Kuljanin, M.; Mitchell, D.C.; Schewpke, D.K.; Gikandi, A.S.; Nusinow, D.P.; Bullock, N.J.; Vinogradova, E.V.; Wilson, D.L.; Kool, E.T.; Mancias, J.D.; Cravatt, B.F.; Gygi, S.P. Reimagining High-Throughput Profiling of Reactive Cysteines for Cell-Based Screening of Large Electrophile Libraries. *Nat. Biotechnol.* **2021**, *39*, 630–641. doi: 10.1038/s41587-020-00778-3.

226. Boatner, L.M.; Palafox, M.F.; Schweppe, D.K.; Backus, K.M. CysDB: A Human Cysteine Database based on Experimental Quantitative Chemoproteomics. *Cell Chem. Biol.* **2023**, *30*, 683-698.e3. doi: 10.1016/j.chembiol.2023.04.004.

227. Hsu, J.-L.; Chen, S.-H. Stable Isotope Dimethyl Labelling for Quantitative Proteomics and Beyond. *Philos. Trans. R. Soc., A* **2016**, *374*, 20150364. doi: 10.1098/rsta.2015.0364.

228. Adibekian, A.; Martin, B.R.; Wang, C.; Hsu, K.-L.; Bachovchin, D.A.; Niessen, S.; Hoover, H.; Cravatt, B.F. Click-Generated Triazole Ureas as Ultrapotent *In Vivo*-Active Serine Hydrolase Inhibitors. *Nat. Chem. Biol.* **2011**, *7*, 469-478. doi: 10.1038/nchembio.579.

229. Mann, M. Functional and Quantitative Proteomics Using SILAC. *Nat. Rev. Mol. Cell Biol.* **2006**, *7*, 952-958. doi: 10.1038/nrm2067.

230. Ong, S.-E.; Blagoev, B.; Kratchmarova, I.; Kristensen, D.B.; Steen, H.; Pandey, A.; Mann, M. Stable Isotope Labeling by Amino Acids in Cell Culture, SILAC, as a Simple and Accurate Approach to Expression Proteomics. *Mol. Cell. Proteom.* **2002**, *1*, 376-386. doi: 10.1074/mcp.M200025-MCP200.

231. Browne, C.M.; Jiang, B.; Ficarro, S.B.; Doctor, Z.M.; Johnson, J.L.; Card, J.D.; Sivakumaren, S.C.; Alexander, W.M.; Yaron, T.M.; Murphy, C.J.; Kwiatkowski, N.P.; Zhang, T.; Cantley, L.C.; Gray, N.S.; Marto, J.A. A Chemoproteomic Strategy for Direct and Proteome-Wide Covalent Inhibitor Target-Site Identification. *J. Am. Chem. Soc.* **2019**, *141*, 191-203. doi: 10.1021/jacs.8b07911.

232. Chen, X.; Sun, Y.; Zhang, T.; Shu, L.; Roepstorff, P.; Yang, F. Quantitative Proteomics Using Isobaric Labeling: A Practical Guide. *Genom. Proteom. Bioinf.* **2021**, *19*, 689-706. doi: 10.1016/j.gpb.2021.08.012.

233. Weerapana, E.; Speers, A.E.; Cravatt, B.F. Tandem Orthogonal Proteolysis-Activity-Based Protein Profiling (TOP-ABPP)—a General Method for Mapping Sites of Probe Modification in Proteomes. *Nat. Protoc.* **2007**, *2*, 1414-1425. doi: 10.1038/nprot.2007.194.

234. Zanon, P.R.A.; Lewald, L.; Hacker, S.M. Isotopically Labeled Desthiobiotin Azide (isoDTB) Tags Enable Global Profiling of the Bacterial Cysteome. *Angew. Chem. Int. Ed.* **2020**, *59*, 2829-2836. doi: 10.1002/anie.201912075.

235. Yang, F.; Gao, J.; Che, J.; Jia, G.; Wang, C. A Dimethyl-Labeling-Based Strategy for Site-Specifically Quantitative Chemical Proteomics. *Anal. Chem.* **2018**, *90*, 9576-9582. doi: 10.1021/acs.analchem.8b02426.

236. Hsu, J.-L.; Huang, S.-Y.; Chow, N.-H.; Chen, S.-H. Stable-Isotope Dimethyl Labeling for Quantitative Proteomics. *Anal. Chem.* **2003**, *75*, 6843-6852. doi: 10.1021/ac0348625.

237. Boersema, P.J.; Raijmakers, R.; Lemeer, S.; Mohammed, S.; Heck, A.J.R. Multiplex Peptide Stable Isotope Dimethyl Labeling for Quantitative Proteomics. *Nat. Protoc.* **2009**, *4*, 484-494. doi: 10.1038/nprot.2009.21.

238. Li, N.; Kuo, C.-L.; Paniagua, G.; van den Elst, H.; Verdoes, M.; Willems, L.I.; van der Linden, W.A.; Ruben, M.; van Genderen, E.; Gubbens, J.; van Wezel, G.P.; Overkleet, H.S.; Florea, B.I. Relative Quantification of Proteasome Activity by Activity-Based Protein Profiling and LC-MS/MS. *Nat. Protoc.* **2013**, *8*, 1155-1168. doi: 10.1038/nprot.2013.065.

239. Baggelaar, M.P.; Chameau, P.J.P.; Kantae, V.; Hummel, J.; Hsu, K.-L.; Janssen, F.; van der Wel, T.; Soethoudt, M.; Deng, H.; den Dulk, H.; Allara, M.; Florea, B.I.; Di Marzo, V.; Wadman, W.J.; Kruse, C.G.; Overkleet, H.S.; Hankemeier, T.; Werkman, T.R.; Cravatt, B.F.; van der Stelt, M. Highly Selective, Reversible Inhibitor Identified by Comparative Chemoproteomics Modulates Diacylglycerol Lipase Activity in Neurons. *J. Am. Chem. Soc.* **2015**, *137*, 8851-8857. doi: 10.1021/jacs.5b04883.

240. Vinogradova, E.V.; Zhang, X.; Remillard, D.; Lazar, D.C.; Suci, R.M.; Wang, Y.; Bianco, G.; Yamashita, Y.; Crowley, V.M.; Schafroth, M.A.; et al. An Activity-Guided Map of Electrophile-Cysteine Interactions in Primary Human T Cells. *Cell* **2020**, *182*, 1009-1026.e29. doi: 10.1016/j.cell.2020.07.001.

241. Werner, T.; Becher, I.; Sweetman, G.; Doce, C.; Savitski, M.M.; Bantscheff, M. High-Resolution Enabled TMT 8-plexing. *Anal. Chem.* **2012**, *84*, 7188-7194. doi: 10.1021/ac301553x.

242. Zanon, P.R.A.; Yu, F.; Musacchio, P.; Lewald, L.; Zollo, M.; Krauskopf, K.; Mrdović, D.; Raunft, P.; Maher, T.E.; Cigler, M.; Chang, C.; Lang, K.; Toste, F.D.; Nesvizhskii, A.I.; Hacker, S.M. Profiling the Proteome-Wide Selectivity of Diverse Electrophiles. *ChemRxiv* **2021**. doi: 10.26434/chemrxiv-2021-w7rzs-v2.

243. Adibekian, A.; Martin, B.R.; Chang, J.W.; Hsu, K.-L.; Tsuboi, K.; Bachovchin, D.A.; Speers, A.E.; Brown, S.J.; Spicer, T.; Fernandez-Vega, V.; Ferguson, J.; Hodder, P.S.; Rosen, H.; Cravatt, B.F. Confirming Target Engagement for Reversible Inhibitors *In Vivo* by Kinetically Tuned Activity-Based Probes. *J. Am. Chem. Soc.* **2012**, *134*, 10345-10348. doi: 10.1021/ja303400u.

244. Senkane, K.; Vinogradova, E.V.; Suci, R.M.; Crowley, V.M.; Zaro, B.W.; Bradshaw, J.M.; Brameld, K.A.; Cravatt, B.F. The Proteome-Wide Potential for Reversible Covalency at Cysteine. *Angew. Chem. Int. Ed.* **2019**, *58*, 11385-11389. doi: 10.1002/anie.201905829.

245. Blum, G.; Mullins, S.R.; Keren, K.; Fonović, M.; Jedeszko, C.; Rice, M.J.; Sloane, B.F.; Bogyo, M. Dynamic Imaging of Protease Activity with Fluorescently Quenched Activity-Based Probes. *Nat. Chem. Biol.* **2005**, *1*, 203-209. doi: 10.1038/nchembio.728.

246. Edgington-Mitchell, L.E.; Bogyo, M.; Verdoes, M. Live Cell Imaging and Profiling of Cysteine Cathepsin Activity Using a Quenched Activity-Based Probe. *Methods Mol. Biol.* **2017**, *1491*, 145-159. doi: 10.1007/978-1-4939-6439-0_11.

247. Blum, G.; Weimer, R.M.; Edgington, L.E.; Adams, W.; Bogyo, M. Comparative Assessment of Substrates and Activity Based Probes as Tools for Non-invasive Optical Imaging of Cysteine Protease Activity. *PLoS ONE* **2009**, *4*, e6374. doi: 10.1371/journal.pone.0006374.

248. Blum, G.; von Degenfeld, G.; Merchant, M.J.; Blau, H.M.; Bogyo, M. Noninvasive Optical Imaging of Cysteine Protease Activity using Fluorescently Quenched Activity-Based Probes. *Nat. Chem. Biol.* **2007**, *3*, 668-677. doi: 10.1038/nchembio.2007.26.

249. van Rooden, E.J.; Kohsieck, M.; Kreekel, R.; van Esbroeck, A.C.M.; van den Nieuwendijk, A.M.C.H.; Janssen, A.P.A.; van den Berg, R.J.B.H.N.; Overkleet, H.S.; van der Stelt, M. Design and Synthesis of Quenched Activity-based Probes for Diacylglycerol Lipase and α,β -Hydrolase Domain Containing Protein 6. *Chem. Asian J.* **2018**, *13*, 3491-3500. doi: 10.1002/asia.201800452.

250. Serim, S.; Baer, P.; Verhelst, S.H.L. Mixed Alkyl Aryl Phosphonate Esters as Quenched Fluorescent Activity-Based Probes for Serine Proteases. *Org. Biomol. Chem.* **2015**, *13*, 2293-2299. doi: 10.1039/C4OB02444C.

251. Verdoes, M.; Oresin, Bender, K.; Segal, E.; van der Linden, W.A.; Syed, S.; Withana, N.P.; Sanman, L.E.; Bogyo, M. Improved Quenched Fluorescent Probe for Imaging of Cysteine Cathepsin Activity. *J. Am. Chem. Soc.* **2013**, *135*, 14726-14730. doi: 10.1021/ja4056068.

252. Zhang, Q.; Liu, H.; Pan, Z. A General Approach for the Development of Fluorogenic Probes Suitable for No-Wash Imaging of Kinases in Live Cells. *Chem. Commun.* **2014**, *50*, 15319-15322. doi: 10.1039/C4CC07429G.

253. Janssen, A.P.A.; van Hengst, J.M.A.; Béquignon, O.J.M.; Deng, H.; van Westen, G.J.P.; van der Stelt, M. Structure Kinetics Relationships and Molecular Dynamics Show Crucial Role for Heterocycle Leaving Group in Irreversible Diacylglycerol Lipase Inhibitors. *J. Med. Chem.* **2019**, *62*, 7910-7922. doi: 10.1021/acs.jmedchem.9b00686.

254. Petri, L.; Ábrányi-Balogh, P.; Varga, P.R.; Imre, T.; Keserű, G.M. Comparative Reactivity Analysis of Small-Molecule Thiol Surrogates. *Bioorg. Med. Chem.* **2020**, *28*, 115357. doi: 10.1016/j.bmc.2020.115357.

255. Reddi, R.N.; Resnick, E.; Rogel, A.; Rao, B.V.; Gabizon, R.; Goldenberg, K.; Gurwicz, N.; Zaidman, D.; Plotnikov, A.; Barr, H.; Shulman, Z.; London, N. Tunable Methacrylamides for Covalent Ligand Directed Release Chemistry. *J. Am. Chem. Soc.* **2021**, *143*, 4979-4992. doi: 10.1021/jacs.0c10644.

256. Kawahata, W.; Asami, T.; Fujii, I.; Sawa, M. ‘Turn On/Off’ Fluorescence Probe for the Screening of Unactivated Bruton’s Tyrosine Kinase. *Bioorg. Med. Chem. Lett.* **2015**, *25*, 2141–2145. doi: 10.1016/j.bmcl.2015.03.063.

257. Li, X.; Gao, X.; Shi, W.; Ma, H. Design Strategies for Water-Soluble Small Molecular Chromogenic and Fluorogenic Probes. *Chem. Rev.* **2014**, *114*, 590–659. doi: 10.1021/cr300508p.

258. Shie, J.-J.; Liu, Y.-C.; Lee, Y.-M.; Lin, C.; Fang, J.-M.; Wong, C.-H. An Azido-BODIPY Probe for Glycosylation: Initiation of Strong Fluorescence upon Triazole Formation. *J. Am. Chem. Soc.* **2014**, *136*, 9953–9961. doi: 10.1021/ja5010174.

259. Blau, R.; Epstein, Y.; Pisarevsky, E.; Tiram, G.; Israeli Dangoor, S.; Yeini, E.; Krivitsky, A.; Eldar-Boock, A.; Ben-Shushan, D.; Gibori, H., et al. Image-Guided Surgery using Near-Infrared Turn-ON Fluorescent Nanoprobes for Precise Detection of Tumor Margins. *Theranostics* **2018**, *8*, 3437–3460. doi: 10.7150/thno.23853.

260. Ben-Nun, Y.; Merquiol, E.; Brandis, A.; Turk, B.; Scherz, A.; Blum, G. Photodynamic Quenched Cathepsin Activity Based Probes for Cancer Detection and Macrophage Targeted Therapy. *Theranostics* **2015**, *5*, 847–862. doi: 10.7150/thno.10854.

261. Weiss-Sadan, T.; Ben-Nun, Y.; Maimon, D.; Merquiol, E.; Abd-Erlahman, I.; Gotsman, I.; Blum, G. A Theranostic Cathepsin Activity-Based Probe for Noninvasive Intervention in Cardiovascular Diseases. *Theranostics* **2019**, *9*, 5731–5738. doi: 10.7150/thno.34402.

262. Evans, E.K.; Tester, R.; Aslanian, S.; Karp, R.; Sheets, M.; Labenski, M.T.; Witkowski, S.R.; Lounsbury, H.; Chaturvedi, P.; Mazdiyasi, H.; Zhu, Z.; Nacht, M.; Freed, M.I.; Petter, R.C.; Dubrovskiy, A.; Singh, J.; Westlin, W.F. Inhibition of Btk with CC-292 Provides Early Pharmacodynamic Assessment of Activity in Mice and Humans. *J. Pharmacol. Exp. Ther.* **2013**, *346*, 219. doi: 10.1124/jpet.113.203489.

263. Callaway, E. Revolutionary Cryo-EM is Taking Over Structural Biology. *Nature* **2020**, *578*, 201. doi: 10.1038/d41586-020-00341-9.

264. Chiu, Y.-H.; Ko, K.-T.; Yang, T.-J.; Wu, K.-P.; Ho, M.-R.; Draczkowski, P.; Hsu, S.-T.D. Direct Visualization of a 26 kDa Protein by Cryo-Electron Microscopy Aided by a Small Scaffold Protein. *Biochemistry* **2021**, *60*, 1075–1079. doi: 10.1021/acs.biochem.0c00961.

265. Liu, Y.; Huynh, D.T.; Yeates, T.O. A 3.8 Å Resolution Cryo-EM Structure of a Small Protein Bound To an Imaging Scaffold. *Nat. Commun.* **2019**, *10*, 1864. doi: 10.1038/s41467-019-09836-0.

266. Borgnia, M.J.; Banerjee, S.; Merk, A.; Matthies, D.; Bartesaghi, A.; Rao, P.; Pierson, J.; Earl, L. A.; Falconieri, V.; Subramanian, S.; Milne, J.L.S. Using Cryo-EM to Map Small Ligands on Dynamic Metabolic Enzymes: Studies with Glutamate Dehydrogenase. *Mol. Pharmacol.* **2016**, *89*, 645. doi: 10.1124/mol.116.103382.

267. Toelzer, C.; Gupta, K.; Yadav, S.K.N.; Borucu, U.; Davidson, A.D.; Kavanagh Williamson, M.; Shoemark, D.K.; Garzoni, F.; Stauffer, O.; Milligan, R.; Capin, J.; Mulholland, A.J.; Spatz, J.; Fitzgerald, D.; Berger, I.; Schaffitzel, C. Free Fatty Acid Binding Pocket in the Locked Structure of SARS-CoV-2 Spike Protein. *Science* **2020**, *370*, 725–730. doi: 10.1126/science.abb3255.

268. Greber, B.J.; Perez-Bertoldi, J.M.; Lim, K.; Iavarone, A.T.; Toso, D.B.; Nogales, E. The Cryoelectron Microscopy Structure of the Human CDK-Activating Kinase. *Proc. Natl. Acad. Sci.* **2020**, *117*, 22849–22857. doi: 10.1073/pnas.2009627117.

269. Robertson, M.J.; van Zundert, G.C.P.; Borrelli, K.; Skiniotis, G. GemSpot: A Pipeline for Robust Modeling of Ligands into Cryo-EM Maps. *Structure* **2020**, *28*, 707–716.e3. doi: 10.1016/j.str.2020.04.018.

270. Chengalroyen, M.D.; Mason, M.K.; Borsellini, A.; Tassoni, R.; Abrahams, G.L.; Lynch, S.; Ahn, Y.-M.; Ambler, J.; Young, K.; Crowley, B.M.; Olsen, D.B.; Warner, D.F.; Barry, C.E.III; Boshoff, H.I.M.; Lamers, M.H.; Mizrahi, V. DNA-Dependent Binding of Nargenicin to DnaE1 Inhibits Replication in *Mycobacterium tuberculosis*. *ACS Infect. Dis.* **2022**, *8*, 612–625. doi: 10.1021/acsinfidis.1c00643.

271. Lindberg, P.; Nordberg, P.; Alminger, T.; Braendstroem, A.; Wallmark, B. The Mechanism of Action of the Antisecretory Agent Omeprazole. *J. Med. Chem.* **1986**, *29*, 1327–1329. doi: 10.1021/jm00158a001.

272. Mukherjee, H.; Grimster, N.P. Beyond Cysteine: Recent Developments in the Area of Targeted Covalent Inhibition. *Curr. Opin. Chem. Biol.* **2018**, *44*, 30–38. doi: 10.1016/j.cbpa.2018.05.011.

273. Jones, L.H. Chapter Four – Design of Next-Generation Covalent Inhibitors: Targeting Residues Beyond Cysteine. *Annu. Rep. Med. Chem.* **2021**, *56*, 95–134. doi: 10.1016/bs.armc.2020.10.001.

274. Gambini, L.; Baggio, C.; Udompholkul, P.; Jossart, J.; Salem, A.F.; Perry, J.J.P.; Pellecchia, M. Covalent Inhibitors of Protein–Protein Interactions Targeting Lysine, Tyrosine, or Histidine Residues. *J. Med. Chem.* **2019**, *62*, 5616–5627. doi: 10.1021/acs.jmedchem.9b00561.

275. Pettigner, J.; Jones, K.; Cheeseman, M.D. Lysine-Targeting Covalent Inhibitors. *Angew. Chem. Int. Ed.* **2017**, *56*, 15200–15209. doi: 10.1002/anie.201707630.

276. Zhang, Z.; Guiley, K.Z.; Shokat, K.M. Chemical Acylation of an Acquired Serine Suppresses Oncogenic Signaling of K-Ras(G12S). *Nat. Chem. Biol.* **2022**, *18*, 1177–1183. doi: 10.1038/s41589-022-01065-9.

277. Zhang, Z.; Morstein, J.; Ecker, A.K.; Guiley, K.Z.; Shokat, K.M. Chemosselective Covalent Modification of K-Ras(G12R) with a Small Molecule Electrophile. *J. Am. Chem. Soc.* **2022**, *144*, 15916–15921. doi: 10.1021/jacs.2c05377.

278. Chen, P.; Sun, J.; Zhu, C.; Tang, G.; Wang, W.; Xu, M.; Xiang, M.; Zhang, C.-J.; Zhang, Z.-M.; Gao, L.; Yao, S.Q. Cell-Active, Reversible, and Irreversible Covalent Inhibitors That Selectively Target the Catalytic Lysine of BCR-ABL Kinase. *Angew. Chem. Int. Ed.* **2022**, *61*, e202203878. doi: 10.1002/anie.202203878.

279. Lill, J.R.; Mathews, W.R.; Rose, C.M.; Schirle, M. Proteomics in the Pharmaceutical and Biotechnology Industry: A Look to the Next Decade. *Expert Rev. Proteom.* **2021**, *18*, 503–526. doi: 10.1080/14789450.2021.1962300.

280. Aranda, J.; Orozco, M. RNA-Dependent RNA Polymerase From SARS-CoV-2. Mechanism Of Reaction And Inhibition By Remdesivir. *bioRxiv* **2020**. doi: 10.1101/2020.06.21.163592.

281. Kalyukina, M.; Yosaatmadja, Y.; Middleditch, M.J.; Patterson, A.V.; Smaill, J.B.; Squire, C.J. TAS-120 Cancer Target Binding: Defining Reactivity and Revealing the First Fibroblast Growth Factor Receptor 1 (FGFR1) Irreversible Structure. *ChemMedChem* **2019**, *14*, 494–500. doi: 10.1002/cmdc.201800719.

282. Zhao, Y.; Fang, C.; Zhang, Q.; Zhang, R.; Zhao, X.; Duan, Y.; Wang, H.; Zhu, Y.; Feng, L.; Zhao, J.; Shao, M.; Yang, X.; Zhang, L.; Peng, C.; Yang, K.; Ma, D.; Rao, Z.; Yang, H. Crystal Structure of SARS-CoV-2 Main Protease in Complex with Protease Inhibitor PF-07321332. *Protein Cell* **2022**, *13*, 689–693. doi: 10.1007/s13238-021-00883-2.

283. Shekh-Ahmad, T.; Eckel, R.; Dayalan Naidu, S.; Higgins, M.; Yamamoto, M.; Dinkova-Kostova, A.T.; Kovac, S.; Abramov, A.Y.; Walker, M.C. KEAP1 Inhibition Is Neuroprotective and Suppresses the Development of Epilepsy. *Brain* **2018**, *141*, 1390–1403. doi: 10.1093/brain/awy071.

284. Totir, M.A.; Helfand, M.S.; Carey, M.P.; Sheri, A.; Buynak, J.D.; Bonomo, R.A.; Carey, P.R. Sulbactam Forms Only Minimal Amounts of Irreversible Acrylate-Enzyme with SHV-1 β -Lactamase. *Biochemistry* **2007**, *46*, 8980–8987. doi: 10.1021/bi7006146.

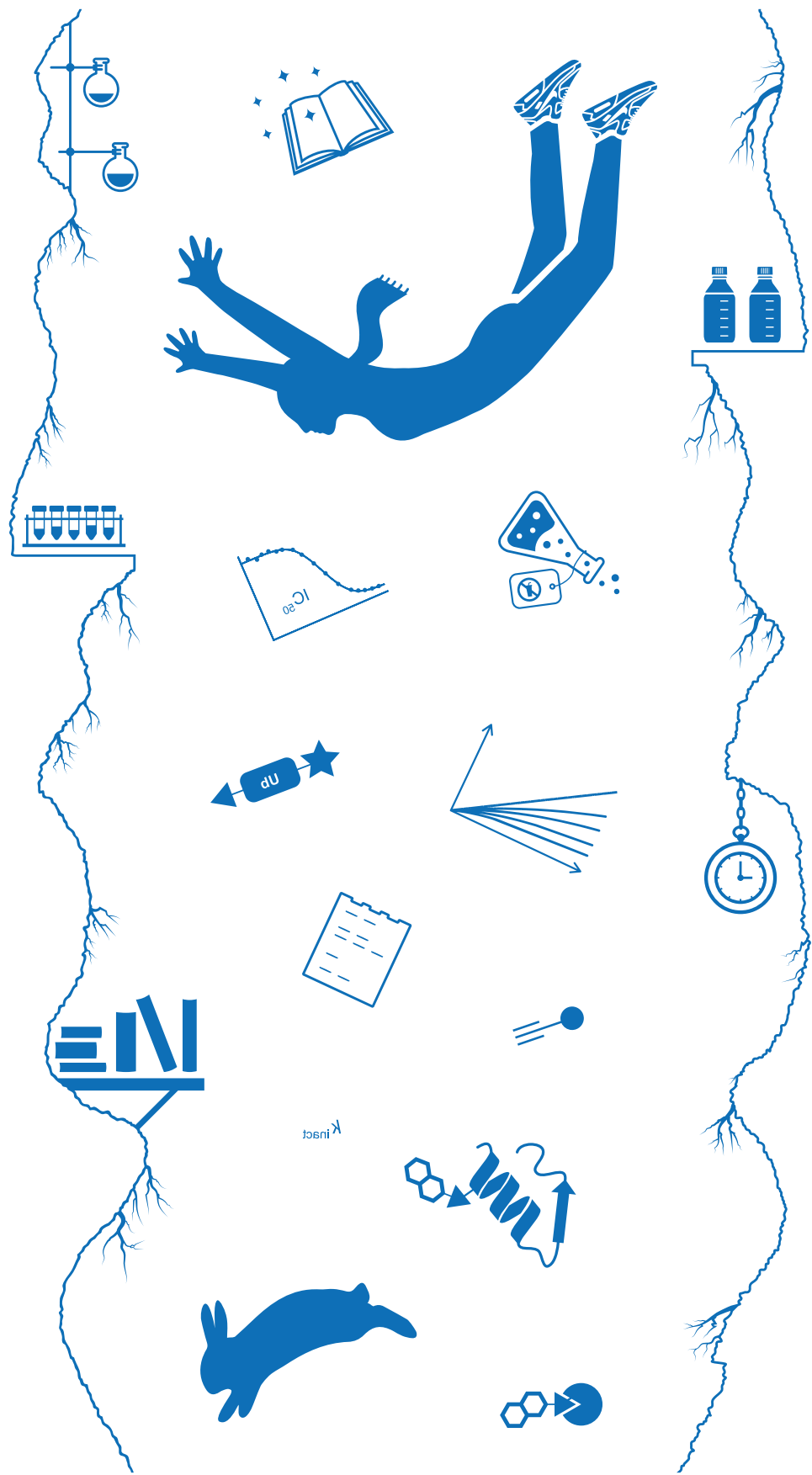
285. Shapiro, A.B.; Moussa, S.H.; McLeod, S.M.; Durand-Réville, T.; Miller, A.A. Durlobactam, a New Diazabicyclooctane β -Lactamase Inhibitor for the Treatment of Acinetobacter Infections in Combination With Sulbactam. *Front. Microbiol.* **2021**, *12*, 709974. doi: 10.3389/fmicb.2021.709974.

9. Supporting Information

Table S1 | FDA approved drugs (2020-2023) with a known covalent mechanism of action.^a

Active Ingredient ^b	Drug Brand Name	Sponsor ^c	Approval Year	Target	Indication	Treatment Area	Warhead	Reversibility	Target Residue	Ref
Lurbinectedin (PM01183)	Zepzelca	PharmaMar	2020	DNA minor groove (alkylation)	Metastatic SCLC	Cancer	Highly reactive carbinalamine (Imine intermediate)	Reversible	Guanine N2	209
Remdesivir (GS-5734) ^d	Veklury	Gilead Sciences	2020	SARS-CoV-2 RdRp SARS-CoV-2 M ^{pro}	COVID-19	Anti-microbial	Nitrile	Reversible	Ser861 (RdRp) Cys145 (M ^{pro})	64, 280
Sotorasib (AMG 510)	Lumakras	Amgen	2021	KRAS _{G12C}	KRAS _{G12C} -mutated NSCLC	Cancer	Acrylamide	Irreversible	Cys12	18
Mobocertinib (TAK788)	Exkivity	Takeda	2021	EGFR _{ex20ins}	Metastatic EGFR _{ex20ins} -mutated NSCLC	Cancer	Acrylamide	Irreversible	Cys797	19
Futibatinib (TAS-120)	Lygobi Oncology	Tahbo	2022	FGFR1-4	FGFR2 fusion-positive ICC	Cancer	Acrylamide	Irreversible	Cys488 (FGFR1) Cys492 (FGFR2-IIIb)	281
Adgrasib (MRTX849)	Krazati Therapeutics	Mirati Therapeutics	2022	KRAS _{G12C}	KRAS _{G12C} -mutated NSCLC	Cancer	Acrylamide	Irreversible	Cys12	103
Nirmatrelvir (PF-07321332)	Paxlovid	Pfizer	2023	SARS-CoV-2 M ^{pro}	COVID-19	Anti-microbial	Nitrile	Reversible	Cys145	47, 282
Omaveloxolone (RTA 408)	Skydarys	Reata Pharmaceuticals	2023	KEAP1	Friedreich's ataxia	Neurodegenerative disease	Cyanoenone	Reversible	Cys151	283
Sulbactam/ Durlabactam	Xacduro	Entasis Therapeutics	2023	PB23 β -lactamase	Bacterial pneumonia	Anti-microbial	β -lactam Diazabicyclooctane	Reversible	Ser130 (SHV-1) Ser81 (OXA-24/40)	284, 285
Rituximab (PF-06651600)	Littulo	Pfizer	2023	JAK3	Alopecia Areata	Autoimmune	Acrylamide	Irreversible	Cys909	199

Last updated: August 2023. FDA approved covalent drugs (1900-2019) are listed in Table S1 of citation²⁰. ^a Data source: FDA database. ^b Only the New Chemical Entity (NCE) approved in the specified year is reported for combination drugs. ^c Refers to the original sponsor for FDA first approval. ^d Covalent binding mode suspected based on covalent docking studies.



Chapter 3



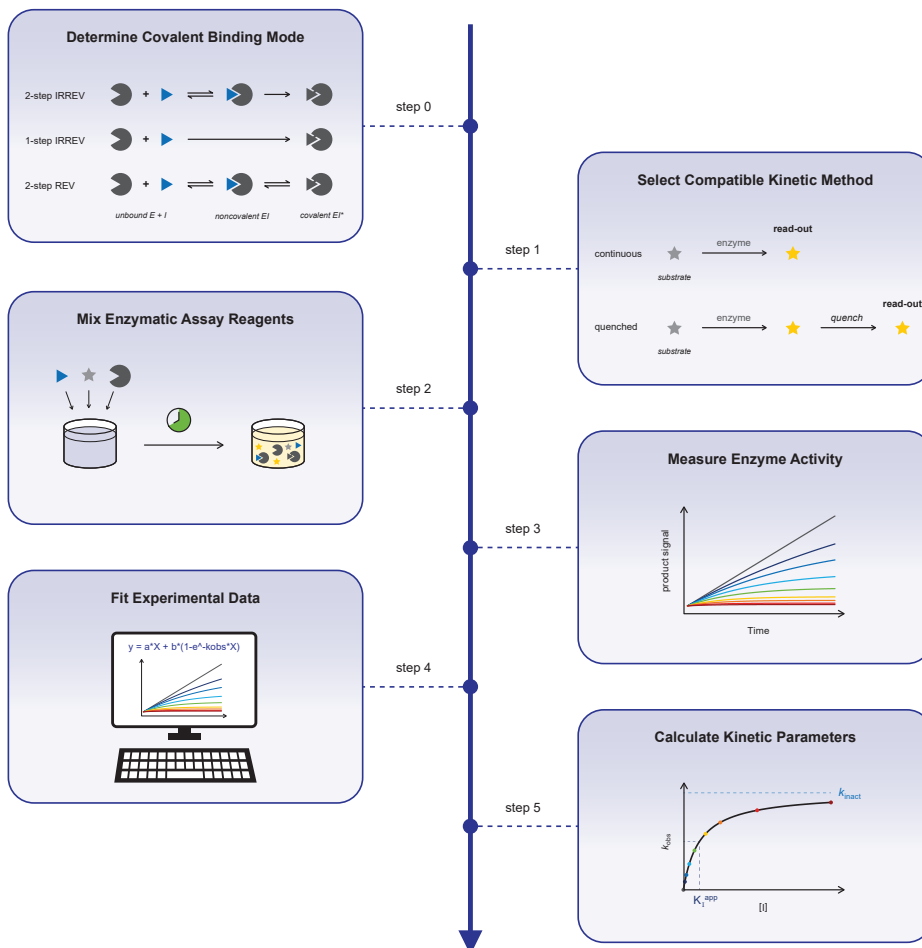
Kinetic Evaluation of Covalent Inhibition in Enzymatic Assays

Adapted from:

Mons, E.; Roet, S.; Kim, R.Q.; Mulder, M.P.C. A Comprehensive Guide for Assessing Covalent Inhibition in Enzymatic Assays Illustrated with Kinetic Simulations. *Curr. Protoc.* **2022**, 2, e419. doi: 10.1002/cpz1.419.

Abstract. Covalent inhibition has become more accepted in the past two decades, as illustrated by the clinical approval of several irreversible inhibitors designed to covalently modify their target. Elucidation of the structure-activity relationship and potency of such inhibitors requires a detailed kinetic evaluation. Here, we elucidate the relationship between the experimental read-out and the underlying inhibitor binding kinetics. Interactive kinetic simulation scripts are employed to highlight the effects of *in vitro* enzyme activity assay conditions and inhibitor binding mode, thereby showcasing which assumptions and corrections are crucial. Four stepwise protocols to assess the biochemical potency of (ir)reversible covalent enzyme inhibitors targeting a nucleophilic active site residue are included, with accompanying data analysis tailored to the covalent binding mode. Together, this will serve as a guide to make an educated decision regarding the most suitable method to assess covalent inhibition potency.

A Comprehensive Guide for Assessing Covalent Inhibition in Enzymatic Assays Illustrated with Kinetic Simulations



1. Introduction

Traditionally, drug design efforts were focused on small molecules that interact with their biological target through noncovalent interactions in a reversible manner. In contrast, covalent inhibitors have the ability to form a much stronger covalent bond with a nucleophilic amino acid residue at the target protein, which is positioned in close proximity to a reactive (electrophilic) moiety in the inhibitor.¹ Risks associated with covalent reactions that can take place not only with the desired target but also with off-target proteins, often undiscovered until late-stage clinical development, resulted in drug discovery programs moving away from candidates bearing intrinsically reactive electrophilic moieties.²⁻³ Nonetheless, the clinical success of covalent drugs that were being used in the clinic long before their mechanism of action was elucidated, which include aspirin and penicillin, along with the more recent clinical approval and success of targeted covalent inhibitors (TCIs) bearing moderately reactive electrophilic warheads, ultimately triggered the current resurgence of covalent drugs.³⁻⁵

The covalent inhibitor development process typically involves identification of noncovalent inhibitors by high-throughput screening (HTS), followed by modification with a moderately reactive electrophilic warhead to improve inhibition potency and selectivity.⁶⁻⁷ Alternatively, an electrophilic fragment that forms a covalent bond with the desired enzyme target is first identified in covalent fragment-based drug discovery,⁸⁻¹⁰ followed by optimization of the noncovalent affinity and positioning of the electrophile. A prerequisite here is that the molecular target must contain a nucleophilic residue (e.g. cysteine, serine, lysine) to form a covalent bond with the electrophilic warhead of the inhibitor.¹¹⁻¹² Whether covalent adduct formation is reversible or irreversible depends on the selected electrophilic warhead.¹³⁻¹⁶ The PK-PD decoupling is one of the major advantages of irreversible inhibition: an infinite target residence time, resulting in a prolonged therapeutic effect after the inhibitor has been cleared from circulation.^{5, 17-19} Here, restoration of enzyme activity can only be achieved by *de novo* protein synthesis. At the same time, if the consequences of continued on-target inhibition are poorly understood, this same property can provide a safety concern. Consequently, inhibitors with a reversible covalent binding mode have become increasingly popular, with (tunable) target residence times ranging from several hours to multiple days.^{13, 20-21}

Although traditional methods to evaluate inhibitor potency, such as determining half-maximal inhibitory concentration (IC_{50} values), are sufficient to identify hits in high-throughput screens, a more detailed kinetic evaluation is required to elucidate the structure-activity relationship (SAR) of irreversible covalent inhibitors.^{4, 22-23} There are many extensive reviews on the history, development, and success of covalent inhibitors,^{4-5, 12, 24} and experimental methods to assess undesired time-dependent inactivation (TDI) of CYP enzymes have been excellently reviewed,²⁵ but a comprehensive overview of experimental methods compatible with the desired covalent binding mode of TCIs targeting nucleophilic active-site residues has been missing. In *section 2*, we will introduce our customized set of interactive kinetic simulation scripts to study the kinetic concepts of different experimental methods, followed by a general background on (covalent) inhibitor binding modes, the assumptions on experimental enzyme activity assay conditions, and an introduction on time-dependent inhibitor kinetics. In *section 3*, we use kinetic simulations to evaluate four kinetic methods and discuss how assay

conditions affect the outcome in the subsequent data analysis. Stepwise experimental protocols with data analysis protocols tailored to the different covalent binding modes are provided in *section 4*, allowing readers to evaluate their covalent (ir)reversible inhibitor, together with the troubleshooting guidelines in *section 5*.

2. Kinetic Background

This guide has been composed to aid readers that have identified a(n) (ir)reversible covalent inhibitor and are contemplating which experimental method to select for the follow-up SAR analysis. Here, the performance of the enzymatic assay is not expected to be troublesome, but the challenge lies in the design of an assay method that complies with (often implied but not explicitly mentioned) assumptions on experimental conditions, and recognition of artifacts/errors in the interpretation of experimental outcome. As such, we assume that a functioning enzymatic assay with a robust read-out is already in place, and we will focus on the connection between (algebraic) data analysis methods and the respective assumptions on experimental conditions. It is important to note that this work is tailored to enzyme activity assays with a (fluorescence) read-out upon substrate processing to form a detectable product, and as such may not be compatible with other assay formats such as ligand binding competition assays or direct detection of the covalent enzyme–inhibitor adduct.

In *section 2.1*, we introduce the interactive kinetic simulation scripts used to illustrate the methods and kinetic concepts in this work. All figures are composed with *in silico* data generated in kinetic simulations and can be recreated with the information in this section. *Section 2.2* provides an overview of the (covalent) inhibition binding modes compatible with the methods in this work. It is paramount to select the appropriate algebraic model for data analysis, as the inhibitor binding mode changes the obtainable parameters as well as the compatibility with experimental methods. Covalent EI* adduct formation should be validated by direct detection with MS, protein crystallography or NMR.^{23, 26-28} Reversibility of covalent adduct formation is commonly assessed in rapid/jump dilution or washout assays with detection of regained enzymatic activity after dilution/washout,²⁹ MS detection of unbound inhibitor upon denaturation or digestion-mediated dissociation,¹³ or competitive binding of a (selective) irreversible (activity-based) probe.^{27, 30} It is important to note that noncovalent binding can also irreversibly inhibit enzyme activity by aggregation or precipitation.³¹ Next, we investigated which assumptions on experimental enzyme activity assay conditions are embedded in the algebraic models used for kinetic analysis. Our findings are outlined in *section 2.3*, highlighting which assumptions are crucial and what the consequences are when these assumptions are violated. Finally, we provide a kinetic background on time-dependent (covalent) inhibition in *section 2.4*. Readers new to the field of enzyme inhibition kinetics are strongly encouraged to familiarize themselves with the work of Copeland³²⁻³³ for a general introduction into enzyme kinetics before studying advanced kinetic concepts associated with (ir)reversible covalent enzyme inhibition and their relation to experimental enzyme activity read-out.

2.1. Kinetic Simulations

Keeping assay requirements in mind, it may seem a daunting task to design, perform, and analyze proper inhibition experiments. In general, practice is the best teacher to get a feeling for these assays and the expected output. Kinetic simulations are essential to understand the importance of reaction conditions and support assay design optimization.³⁴ In such simulations, one can freely change the parameters to visualize the effect on the output and validate that kinetic parameters found after data analysis correlate with the input values. This design precludes assay artifacts and human error, and also outputs the underlying concentrations of the different reaction species (e.g. unbound enzyme, enzyme–substrate complex), illustrating the relevance of the experimental assay conditions. Finally, kinetic simulations can validate if fitted experimental parameters correlate with the experimental read-out and aid the rational design of follow-up experiments by predicting the outcome.³⁵ Here, we use a set of customized kinetic simulation scripts based on numerical integration of the differential equations³⁶ to simulate the time-dependent product concentration as well as the underlying concentrations of various enzyme species (e.g. unbound, bound to inhibitor or substrate). Some concentrations are essentially constant under specific assay conditions, and treating these parameters as constants rather than variables reduces the computing/simulation time. An overview of our kinetic scripts and the assumptions on experimental assay conditions can be found in **Table 1**. Since understanding kinetics can be greatly facilitated by the ability to adjust reaction conditions and changing parameters without using expensive reagents, we have made interactive versions of these simulation scripts available free of charge at <https://tinyurl.com/kineticsimulations>. We encourage our readers to perform simulations with their own kinetic parameters to visualize how the underlying concentrations of enzyme species affect the detected read-out, and to get a feeling for realistic values and assay conditions. We selected one model inhibitor for each binding mode to generate the figures that exemplify the methods described (the kinetic parameters of each model inhibitor can be found in **Table 2**). All figures in this work can be recreated with the information in **Table 1** and **Table 2**.

Our kinetic simulation scripts are tailored to competitive inhibition, where an intrinsically reactive inhibitor bearing an electrophilic warhead covalently targets a nucleophilic amino acid residue at the enzymatic substrate binding site, thus blocking substrate access.^{22,33} Other covalent binding modes – e.g. prodrugs,³⁷ covalent allosteric inhibitors,³⁸ and multi-step mechanism-based inhibitors³⁹⁻⁴⁰ – are outside the scope of this work, although the described experimental protocols can be useful in specific cases. For further instructions and detailed information on restrictions, we refer to the webpage itself. At the start of the simulations, we define the (pre)incubation time. The preincubation time is the elapsed time since the onset of enzyme inhibition by mixing enzyme and inhibitor, but before the onset of product formation by adding substrate. The incubation time is the elapsed time since onset of product formation: after substrate addition. In this work, we will distinguish between incubation and preincubation by using different symbols for preincubation t' (enzyme and inhibitor) and incubation t (enzyme, substrate and inhibitor) in all figures and equations to avoid confusion.

Table 1 | Kinetic simulation scripts used in this work.^a

Reaction dynamics	Script	Simulation constants	Experimental restrictions	
	KinGen	Unbound inhibitor	$[I]_0 = [I]_t = [I]_t$	
		Unbound substrate	$[S]_0 = [S]_t$	
	KinSubDpl	Volume	$V_t = V_t$	
	KinSubDpl	Unbound inhibitor	$[I]_0 = [I]_t = [I]_t$	
		Volume	$V_t = V_t$	
	KinVol	Unbound inhibitor	$[I]_0 = [I]_t = (1 + (V_{sub}/V_t)) \times [I]_t$	
		Unbound substrate	$[S]_0 = [S]_t$	
	KinInhDpl	Volume	$V_t = V_t$	
	KinDeg^b	Unbound inhibitor	$[I]_0 = [I]_t = [I]_t$	
		Unbound substrate	$[S]_0 = [S]_t$	
		Volume	$V_t = V_t$	
	KinVolDeg^b	Unbound inhibitor	$[I]_0 = [I]_t = (1 + (V_{sub}/V_t)) \times [I]_t$	
		Unbound substrate	$[S]_0 = [S]_t$	

^a Available at <https://tinyurl.com/kineticsimulations>. ^b First order spontaneous enzyme degradation/denaturation. $[I]_0$ = unbound inhibitor concentration at onset of inhibition, before (optional) enzyme binding. $[I]_t$ = unbound inhibitor concentration during preincubation, after (optional) enzyme binding. $[I]_t'$ = unbound inhibitor concentration during incubation, after (optional) enzyme binding. $[S]_0$ = unbound substrate concentration at onset of product formation, before enzyme binding. $[S]_t$ = unbound substrate concentration during incubation, after (optional) enzyme binding and product formation. V_t = reaction volume during preincubation. V_{sub} = volume containing substrate. V_t = reaction volume during incubation ($V_t = V_{sub} + V_t'$).

Table 2 | Kinetic parameters for simulated inhibitors used in this work to illustrate methods.

Reagent	Input			Kinetic parameters ^a				
	k_1 ($M^{-1}s^{-1}$)	k_2 (s^{-1})	k_{cat} (s^{-1})	K_D (μM)		K_M (μM)	k_{cat}/K_M ($M^{-1}s^{-1}$)	
Substrate S1	10^8	100	1			1.00	1.01	9.9×10^5
Ligand L1	10^8	100	0			1.00	—	—
Inhibitor^b	k_3 ($M^{-1}s^{-1}$)	k_4 (s^{-1})	k_5 (s^{-1})	k_6 (s^{-1})	K_i (nM)	K_i^* (nM)	K_I (nM)	k_{inact}/K_I or k_{chem} ($M^{-1}s^{-1}$)
A	10,000	0.0001	0	0	10	—	—	—
B	10^8	10	0.001	0.0001	100	9.1	—	—
C	10^8	10	0.001	0	100	—	100	10^4
D	10,000	0	0	0	—	—	—	10^4

Reaction dynamics are illustrated in **Table 1**. ^a Calculated from microscopic rate constants in **Table S1** and **Figure S1D**. ^b Mechanisms in **Figure 1**.

2.2. Inhibitor Binding Modes

Reversible noncovalent inhibitors inhibit enzymatic activity by formation of noncovalent EI complex in a single reaction step (**Figure 1A**). When the initial unbound inhibitor concentration is equal to inhibition constant K_i , the concentration of unbound enzyme E will be equal to the concentration of inhibitor-bound enzyme complex EI after steady-state equilibrium has been reached. For traditional fast-binding reversible inhibitors this equilibrium will be reached almost instantly, as association rate constant k_3 and dissociation rate constant k_4 are fast. In this work, the term 'reaction completion' relates to the endpoint of enzyme–inhibitor binding, which refers to reaching an equilibrium for reversible inhibitors (**Figure 1A** and **Figure 1B**) or reaching full inactivation for irreversible inhibitors (**Figure 1C** and **Figure 1D**). Contrary to classic fast-binding inhibitors, time-dependent or slow-binding inhibition is observed when the steady-state equilibrium or irreversible inactivation is reached relatively slowly on the assay timescale.^{41–42} Typically, this is observed for inhibitors with a covalent binding mode (**Figure 1B–D**), as formation of a covalent adduct is not an instantaneous process.

Reversible covalent adduct formation (**Figure 1B**) is a 2-step process consisting of (rapid) initial association to form noncovalent EI complex (*rapid equilibrium approximation*, discussed in more detail in *section 2.3*) preceding covalent EI* adduct formation. Covalent EI* adduct is at equilibrium with the noncovalent EI complex, as covalent adduct formation is reversible ($k_6 > 0$), with inhibition constant K_i reflecting the initial noncovalent $E + I \leftrightarrow EI$ equilibrium and steady-state inhibition constant K_i^* reflecting the steady-state (overall) $E + I \leftrightarrow EI + EI^*$ equilibrium. Development of reversible covalent inhibitors typically involves optimization of overall affinity (reflected in low K_i^* values), preferably by slowing dissociation rates (**Figure 1B**). A slow off-rate (k_{off}) is favorable, as this is reciprocal with the drug-target residence time τ ($\tau = 1/k_{off}$), and a longer residence time has been linked to superior therapeutic potency.^{43–44} An overview of relevant kinetic parameters can be found in **Table S1**.

Inhibition is considered irreversible when its residence time exceeds the normal lifespan of the target enzyme.²² Dissociation from covalent EI* adduct is negligible, resulting in full enzyme engagement when reaction completion is reached for irreversible covalent inhibitors (**Figure 1C** and **Figure 1D**). The irreversible binding mode changes the obtainable kinetic parameters to rank inhibitor potency, as the biochemical IC_{50} may vary depending on the (pre)incubation time.^{3, 22} The potency of 2-step irreversible inhibitors that engage in an initial noncovalent enzyme–inhibitor complex EI prior to formation of covalent adduct EI* is driven by noncovalent affinity – reflected in inactivation constant K_i – along with the maximum rate of inactivation k_{inact} (**Figure 1C**). Rate constant k_{inact}/K_i is generally accepted as a more suitable measure of 2-step irreversible inhibitor potency,^{3, 22, 37, 45} in an analogous fashion to k_{cat}/K_M reflecting the efficiency of enzymatic substrate conversion (a detailed comparison can be found in **Figure S1**). The binding mode becomes 1-step when noncovalent equilibrium is nonexistent, for example for highly reactive thiol-alkylating reagents,^{37, 46} with the parameter k_{chem} or $k_{obs}/[I]$ reflecting potency/efficiency (**Figure 1D**).

Drug development of irreversible covalent inhibitors is typically geared towards simultaneous improvement of the binding affinity (reflected in a lower K_i value) and faster covalent bond formation (reflected in a higher k_{inact} value) to generate irreversible covalent inhibitors

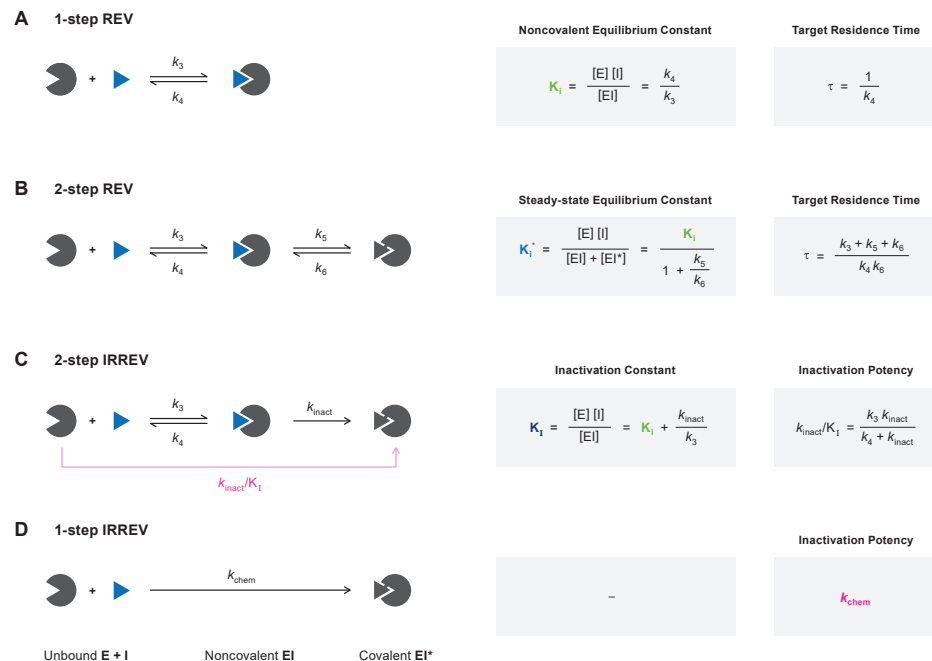


Figure 1 | Schematic overview of inhibitor binding modes.³⁹ E = unbound enzyme. I = unbound inhibitor. EI = noncovalent enzyme–inhibitor complex. EI* = covalent enzyme–inhibitor adduct. An overview of kinetic constants can be found in **Table S1**. **(A)** Classic 1-step reversible inhibition. Inhibitor potency ranking based on inhibition constant K_1 (in M) or target residence time τ (in s). **(B)** Covalent 2-step reversible inhibition. Inhibitor potency ranking based on steady-state inhibition constant K_{1^*} (in M) for total E + I \leftrightarrow EI + EI* equilibrium or based on target residence time τ (in s). **(C)** Covalent 2-step irreversible inhibition (affinity label model). Inhibitor potency ranking based on inactivation efficiency: maximum rate of covalent adduct formation over inactivation constant k_{inact}/K_1 (in $M^{-1}s^{-1}$). **(D)** Covalent 1-step irreversible inhibition (residue-specific reagent model). Inhibitor potency ranking based on inactivation efficiency: k_{chem} (in $M^{-1}s^{-1}$) = $k_{obs}/[I]$ (in $M^{-1}s^{-1}$).

with a high k_{inact}/K_1 value for the desired enzyme target,^{45, 47} while minimizing the intrinsic reactivity with undesired enzymes such as GSH.⁴⁸⁻⁵⁰ Typical reported k_{inact}/K_1 values range from 10^5 – 10^7 $M^{-1}s^{-1}$ for kinase inhibitors,^{45, 51-52} 10^1 – 10^5 $M^{-1}s^{-1}$ for protease inhibitors,^{28, 53-54} 10^2 – 10^4 $M^{-1}s^{-1}$ for other target classes,⁵⁵⁻⁵⁷ to 10^{-2} – 10^2 $M^{-1}s^{-1}$ for covalent fragments.⁵⁸⁻⁵⁹ Ranges of clinically relevant k_{inact}/K_1 values are highly dependent on the nucleophilicity of the targeted amino acid (cysteine typically being more reactive than serine) and concentration of naturally present competitors (e.g. ATP-competitive inhibitors need to overcome competition by ATP at physiological concentrations far exceeding the $K_{M,ATP}$).

2.3. Assumptions on Experimental Assay Conditions

Experimental conditions should meet certain criteria in order to use algebraic fitting methods. In this section, we focus on the assumptions on the experimental conditions that are embedded in algebraic equations to analyze time-dependent (covalent) inhibition (summarized in **Table 3**). Generally, these assumptions involve simplifying the enzyme–inhibitor binding reaction to a

single rate-determining step along with fixing inhibitor/substrate concentrations to a constant value. To use algebraic fitting, the experiment should meet all the required conditions outlined in this section. More complex systems – such as bisubstrate assays or other binding modes like allosteric – violate one or more of these, and require a different method of fitting. For such systems, numerical integration with dedicated software packages – e.g. KinTek,⁶⁰ DynaFit⁶¹ – is recommended. These packages are very powerful, and can fit anything with good error even when the model does not reflect the biological situation.⁶² For these complex systems, it is crucial to ensure that the initial values are reasonable and the amount of (orthogonal) data is sufficient for the amount of parameters that are fitted. The first step, however, whether working with complex systems or reactions with a single rate-determining step, should always be optimization of the experimental conditions.

There are two distinct types of algebraic analysis: linear regression (fitting straight curves, compatible with commonly available software such as EXCEL) and nonlinear regression (fitting exponential curves, requiring sophisticated data fitting software). Linear regression was the predominant method to analyze kinetic data, but has now been surpassed by the more accurate nonlinear regression.⁶³ For our analyses, we use least-squares nonlinear regression with GraphPad Prism (RRID:SCR_002798), but other software packages are available too.⁶⁴ Please consult the detailed (online) guide on how to implement user-defined equations for nonlinear regression in GraphPad Prism.⁶⁵⁻⁶⁶

Michaelis-Menten enzyme kinetics. All experimental methods in this manuscript are based on enzyme activity assays with multiple turnovers per enzyme, with enzyme release after product formation. We assume that the uninhibited enzymatic substrate processing reaction ($E + S \leftrightarrow ES \rightarrow E + P$) complies with Michaelis-Menten enzyme kinetics.^{35, 64} The concentration of unbound substrate has to be constant ($[S]_t = [S]_0$) and not depleted by engagement in a (non)covalent complex ES ($[ES]_t < 0.1[S]_0$) or conversion into product. Therefore, substrate is added in a large excess over the enzyme ($[S]_0 > 10[E]_0$), and the uninhibited velocity of product formation (v^{ctrl}) is calculated over the linear part corresponding to less than 10% substrate conversion ($[P]_t < 0.1[S]_0$).⁶⁷ The signal corresponding to 10% substrate conversion can be

Table 3 | General assumptions on experimental assay conditions.

	Substrate concentration is constant <i>Substrate is not depleted by complexation with enzyme</i>	$[S]_t = [S]_0$ $[S]_0 > 10[E]_0$
Michaelis-Menten enzyme kinetics	Uninhibited product formation is linear <i>Product formation does not deplete substrate</i> <i>Enzyme activity is not affected by product inhibition</i> <i>The enzyme does not degrade significantly</i>	$k_{ctrl} = 0$ $[P]_t < 0.1[S]_0$ $[P]_t << 0.1K_{D,P}$ $k_{deg} = 0$
Pseudo-first order kinetics	The unbound inhibitor concentration is constant <i>Inhibitor is not depleted by complexation with enzyme</i>	$[I]_t = [I]_0$ $[I]_0 > 10[E]_0$
Rapid equilibrium approximation	Noncovalent equilibrium is reached quickly for 2-step inhibitors <i>Covalent adduct formation is rate-determining</i>	$k_{inact} \ll k_4$ $k_5 \ll k_4$

estimated from a product calibration/titration curve to avoid substrate depletion.⁶⁸⁻⁶⁹ The effect of substrate depletion can be investigated with the kinetic simulation script **KinSubDpl**. More complex enzymatic (bisubstrate) assays are outside of the scope of this work.³² However, the methods described herein could still be applicable under pseudo-single substrate (Hit-and-Run) conditions.

Enzyme stability. Unless otherwise noted, time-dependent decrease of enzyme activity is attributed solely to the presence of a (slow-binding) inhibitor. It is thus assumed that the enzyme activity is constant throughout the whole experiment, although this does not necessarily reflect the actual experimental situation. Recombinant enzymes do not have an eternal life; thus, time-dependent loss of enzyme activity will inevitably occur due to spontaneous protein denaturation, degradation, or unfolding.⁷⁰ The Selwyn test is a relatively simple test to see if time-dependence of uninhibited enzyme activity is due to (spontaneous) enzyme inactivation.⁷¹ Spontaneous enzyme degradation/denaturation is similar to radioactive decay in a sense that inactivation is a first order reaction (*degradation rate* = $k_{\text{degE}} \times [\text{E}]$). Enzyme stability might be promoted by optimization of the assay buffer, and is less significant at shorter (pre)incubation times, but degradation cannot completely be avoided. Therefore, we included data analysis methods to account for spontaneous first order enzyme degradation/denaturation. Cannibalistic proteases follow a second order (auto)proteolysis rate (*degradation rate* = $k_{\text{degE}} \times [\text{E}]^2$)⁷² and are as such outside of the scope of these methods. In simulations to illustrate the methods described herein (with kinetic simulation scripts **KinDeg** and **KinVolDeg**), we assumed that first order decay is uniform for all enzyme species ($k_{\text{degE}} = k_{\text{degES}} = k_{\text{degEI}} = k_{\text{degEI}^*}$) and combined the individual degradation rates into the enzyme degradation rate constant k_{deg} .

Constant uninhibited product formation velocity. The uninhibited controls should be linear for the whole measurement when analyzing time-dependent inhibition. There are various factors contributing to a slight time-dependent decrease of product formation velocity in the absence of inhibitor,³² thus violating this assumption. An overview of common troubleshooting options is listed in **Table 6** (located in *section 5*). As discussed above, substrate depletion ($[\text{P}] > 0.1[\text{S}]_0$) negatively influences the linearity over time, as does product inhibition ($[\text{P}] > 0.1K_{\text{D,P}}$). Fortunately, this can be avoided by decreasing the enzyme concentration and/or shortening the incubation time to reduce substrate turnover, thereby lowering the absolute and relative product concentration. Other factors can make the results look nonlinear – such as quenching of the fluorescent product signal by photobleaching.⁷³ This effect can be reduced by increasing the measurement interval and/or reducing the number of excitation cycles. Finally, optimization of assay conditions can minimize the effect of spontaneous loss of enzyme activity ($k_{\text{deg}} > 0$) but cannot be resolved completely. In this work, we will refer to the overall rate of nonlinearity in the uninhibited control (k_{obs} of $[\text{I}] = 0$) with the symbol k_{ctrl} , regardless of the underlying mechanism that causes the time-dependent decrease of product formation velocity.

Rapid equilibrium approximation. Algebraic analysis of (covalent) inhibition is based on the assumption that time-dependent inhibition is driven by a single rate-determining step. For 2-step covalent inhibitors (**Figure 1B** and **Figure 1C**), this means that the noncovalent $\text{E} + \text{I} \leftrightarrow \text{EI}$ equilibrium that precedes covalent EI^* adduct formation should be reached almost instantly after the onset of inhibition. After this rapid equilibrium, a much slower step

of covalent adduct formation follows ($k_{\text{inact}} \ll k_4$). Whether the noncovalent equilibrium indeed is reached rapidly is an intrinsic inhibitor property, and (kinase) inhibitors with a low-nM noncovalent potency are likely to violate this assumption: the association rate constant is diffusion-limited ($k_3 \leq 10^9 \text{ M}^{-1}\text{s}^{-1}$), and thus k_4 must be relatively slow if $K_i \leq 10^{-8} \text{ M}$.⁷⁴ Unfortunately, a slow initial, noncovalent step is not easily recognized from raw kinetic data, resulting in overestimation of the rate of inactivation k_{inact} and underestimation of the inactivation constant K_i with algebraic rather than numerical data analysis. The inactivation constant K_i approximates inhibition constant K_i ($K_i \approx K_i$) when covalent bond formation is driven by the rate-determining conversion of noncovalent complex EI into covalent adduct EI* ($k_{\text{inact}} \ll k_4$) (**Figure 1C**), analogous to the Briggs–Haldane treatment of enzyme–substrate kinetics where $K_M \approx K_S$ if k_{cat} is rate-limiting.⁴⁶ Consequently, K_i and K_i may have the same value, but they are not interchangeable, and it is as such recommended to report k_{inact}/K_i rather than k_{inact}/K_i .

Pseudo-first order reaction kinetics without inhibitor depletion. Algebraic analysis of (covalent) inhibition is typically based on the assumption that the unbound inhibitor concentration is a constant value ($[I]_t = [I]_0$) unaffected by enzyme binding.³⁵ This assumption is only valid when the inhibitor is present in large excess with respect to the enzyme ($[I]_0 > 10[E]_0$) at reaction initiation. The enzyme occupancy after reaching the noncovalent equilibrium is driven solely by the excess inhibitor concentration relative to the (apparent) inhibition constant K_i^{app} : $[EI]_{\text{eq}}/[E]_0 = 1/(1 + (K_i^{\text{app}}/[I]))$. The effect of inhibitor depletion can be investigated with the kinetic simulation script **KinInhDpl**. Violation of this assumption results in an appreciable reduction of the remaining population of unbound inhibitor upon complexation with enzyme. Consequently, the inhibitor occupancy at equilibrium no longer reflects the apparent inhibition constant K_i^{app} because the equilibrium is now driven by both enzyme and inhibitor concentration (**Figure 2A**). Algebraic correction for inhibitor depletion ($[I]_t < [I]_0$) to find the equilibrium constant K_i is often performed for 1-step reversible inhibitors displaying tight-

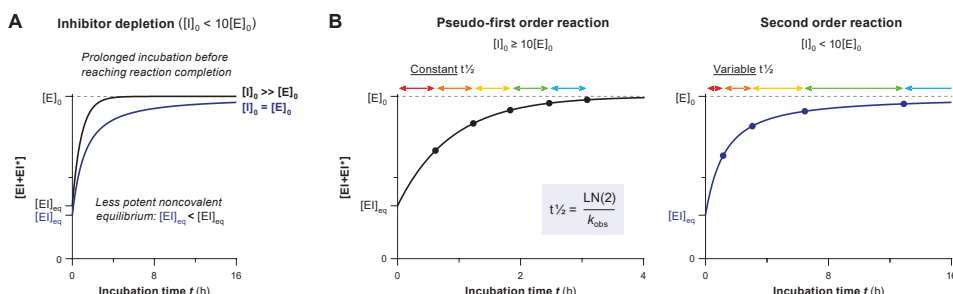


Figure 2 | Consequences of inhibitor depletion. Simulated with **KinInhDpl** for 50 nM inhibitor **C** with 5 nM enzyme ($[I]_0 = 10[E]_0$) or 50 nM enzyme ($[I]_0 = [E]_0$). **(A)** Inhibitor depletion (blue line) results in lower noncovalent equilibrium occupancy $[E]_{\text{eq}}$ and slower reaction rates, resulting in longer incubation time to reach full inactivation than for excess inhibitor (black line). **(B)** First order reaction conditions with constant half-life $t\frac{1}{2}$ when inhibitor is present in excess (left). Second order reaction conditions with variable half-life $t\frac{1}{2}$ and longer overall reaction time when inhibitor is depleted (right).

binding behavior (with low inhibitor concentrations because K_i^{app} approaches $[E]^{\text{total}}$), by fitting the (steady-state) equilibrium product formation velocity to (variants of) Morrison's quadratic equation that treat the inhibitor concentration as a variable rather than a constant value.⁷⁵⁻⁷⁶ However, these equations are only compatible with inhibitors with a reversible binding mode after equilibrium has been reached, and are thus not suitable for irreversible inhibition.

Binding of inhibitor to enzyme is, in principle, a second order reaction: the association rate depends on the concentration of unbound enzyme as well as unbound inhibitor, which both decrease upon formation of association product EI. Towards the end of the reaction, the reaction rate is significantly slower when less of the unbound components are left. Algebraic analysis of second order (ir)reversible association curves is complicated (data not included, simulated with simulation script **KinInhDpl**) – even for inhibitors with a 1-step binding mode – thus, it is strongly advised to analyze second order reactions of 2-step (ir)reversible inhibitors by numeric integration.⁷⁷ However, as mentioned above, unbound inhibitor concentrations remain more or less constant during the reaction if the inhibitor is present in excess at reaction initiation ($[I]_0 > 10[E]_0$). Consequently, the second order binding reaction of enzyme and inhibitor behaves like a first order reaction when the inhibitor is present in excess: pseudo-first order reaction kinetics.⁷⁷ The time-dependent association reaction for a (pseudo-)first order reaction has a constant half-life $t_{1/2}$, and the progress curves can be fitted to standard one-phase exponential association equations (**Figure 2B, left**), as will be discussed in more detail in *section 2.4*. Second order kinetic association reactions require a longer overall time to reach reaction completion of the enzyme–inhibitor binding reaction (inactivation or equilibrium) with a variable half-life $t_{1/2}$ (**Figure 2B, right**), because the association reaction rate slows down when the remaining unbound inhibitor concentration decreases. For 2-step (ir)reversible inhibitors, the time-dependent reduction in covalent reaction rate is a direct consequence of the decreasing noncovalent occupancy upon inhibitor depletion. The rate-determining step of covalent adduct formation is preceded by noncovalent EI complex formation, and is thus limited by noncovalent occupancy, which decreased over time.

2.4. Time-Dependent Inhibitor Potency

Methods to analyze time-dependent inhibitors are based on the fact that it takes time to reach completion, and we use this information to obtain kinetic parameters. Under pseudo-first order conditions based on a single rate-determining step,⁷⁷ inhibitor binding follows an exponential one-phase association reaction³⁵ from the rapid initial binding (*rapid equilibrium approximation*) to (slowly) reaching a plateau at reaction completion: equilibrium for reversible inhibitors (**Figure 3A, left**) or inactivation for irreversible inhibitors (**Figure 3A, right**). The incubation time to reaction completion is infinite, but after five half-lives ($t = 5t_{1/2}$) the reaction progress is at 97%, which is generally sufficient to be considered reaction completion. Reaction half-life $t_{1/2}$ is inversely related to observed reaction rate k_{obs} : $t_{1/2} = \text{LN}(2)/k_{\text{obs}}$.⁷⁷ k_{obs} is the experimental reaction rate for reaction progress from initial binding to reaction completion under the specific assay conditions. Inhibitor concentration as well as competing substrate concentration are major contributors to the observed reaction rate k_{obs} . The experimental k_{obs} value can be obtained by fitting the time-dependent binding/occupancy curve to exponential one-phase association **Equation 1** (shown in **Figure 3B**) from initial to final enzyme occupancy.

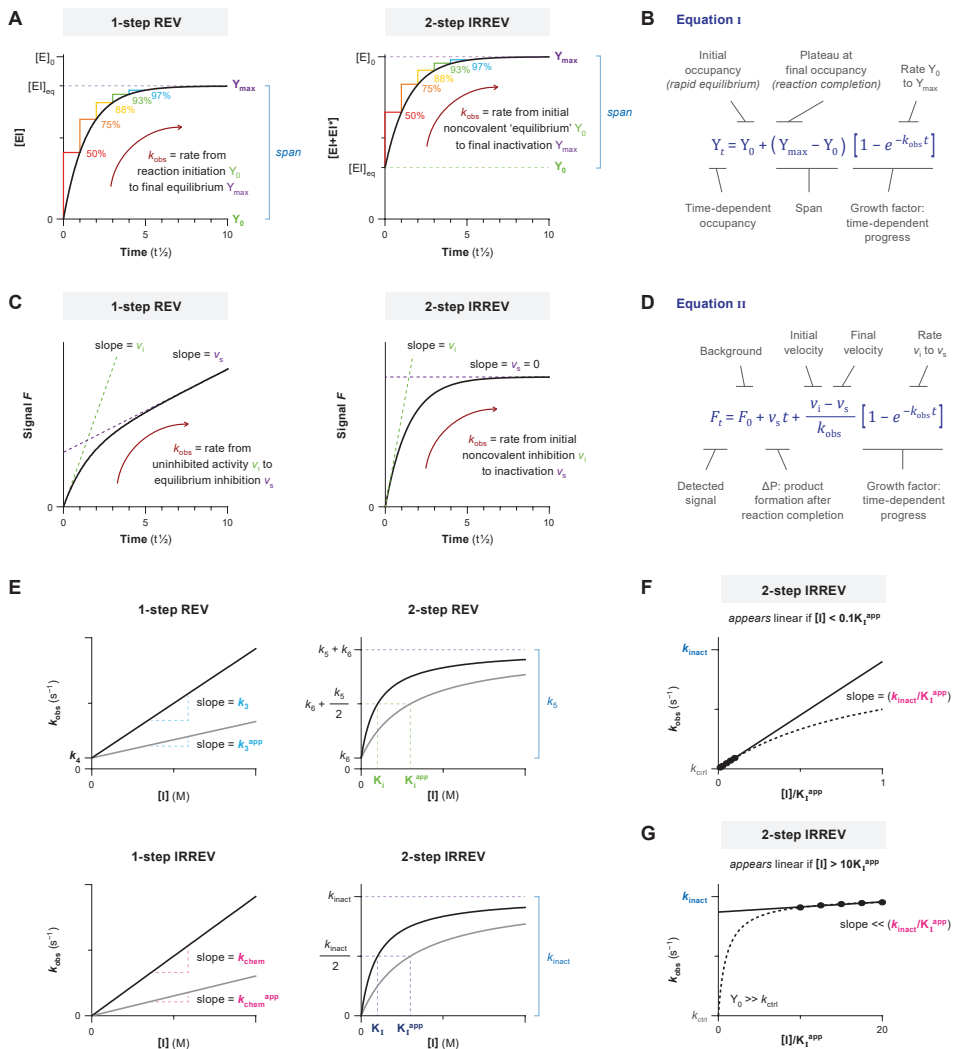


Figure 3 | Time-dependent inhibition and reaction completion. Simulated with **KinGen** for 1 pM enzyme with substrate **S1**. **(A)** Time-dependent enzyme occupancy simulated for 50 nM 1-step reversible inhibitor **A** (left) or 2-step irreversible inhibitor **C** (right) in presence of 100 nM substrate **S1**. Each half-life $t\frac{1}{2}$, the occupancy increases by 50% (of the remaining span). After 5 $t\frac{1}{2}$, occupancy is at 97% of its maximum (equilibrium concentration $[E]_{\text{eq}}$ or total enzyme concentration $[E]_0$) and generally considered as reaction completion. Half-life $t\frac{1}{2}$ is inversely related with observed reaction rate k_{obs} (under pseudo-first order conditions). **(B)** Bounded exponential association **Equation I** from initial occupancy (rapid equilibrium) to final occupancy (reaction completion). **(C)** Progress curve of time-dependent product formation for enzyme inhibition in panel A. Product formation velocity (slope, in AU/s), reflecting the (remaining) enzyme activity decreases until reaction completion is reached (steady-state equilibrium or inactivation). **(D)** Exponential association **Equation II** from initial velocity v_i (rapid equilibrium) to final velocity v_s (reaction completion). **(E)** k_{obs} curves in absence (black, $[S] = 0$) or presence (gray, $[S] = 2K_M$) of competing substrate. Apparent values are not yet corrected for substrate competition. **(F)** 2-step irreversible covalent inhibitors display 1-step behavior at non-saturating inhibitor concentrations ($[I] \leq 0.1K_1$). Fit straight line with Y-intercept = k_{ctrl} to obtain $k_{\text{chem}} = (k_{\text{inact}}/K_1)$ from the linear slope. **(G)** 2-step irreversible covalent inhibitors display 1-step behavior at saturating inhibitor concentrations ($[I] > 10K_1$). Distinguish from non-saturating inhibitor concentrations in panel F: Y-intercept $> k_{\text{ctrl}}$ when fitting a straight line to the k_{obs} curve.

Biochemical inhibitor potency is seldom assessed by direct observation of enzyme complex/adduct. Typically, enzyme inhibition is indirectly assessed in *in vitro* assays with a detectable read-out for product formation as a measure of (remaining) enzyme activity. Consequently, reversible enzyme inhibition may have reached the enzyme–inhibitor binding equilibrium (*reaction completion*), but not all enzyme is occupied (unless $[I] \gg K_i^{\text{app}}$) so the remaining fraction of unbound enzyme continues to convert substrate into product (**Figure 3C, left**). The reaction is no longer accurately reflected by **Equation 1** (shown in **Figure 3B**), as product concentration at reaction initiation does not reflect the initial binding equilibrium, and product concentration does not reach a plateau after reaching the noncovalent equilibrium (*reaction completion*) for reversible inhibitors. Therefore, time-dependent product formation is fitted to exponential one-phase association **Equation 2** (shown in **Figure 3D**) to obtain observed reaction rate k_{obs} from initial to final product formation velocity. For irreversible inhibitors, the initial velocity v_i reflects the (remaining) enzyme activity after rapid noncovalent association, and final velocity $v_s = 0$ as this reflects full enzyme inactivation (**Figure 3C, right**).

Typically, substrate competition assays are run at various inhibitor concentrations, and the concentration-dependent k_{obs} is fitted to obtain kinetic parameters (**Figure 3E**). In this work, equations and simulations are tailored to competitive binding of inhibitor and substrate.^{22, 64} Consequently, the observed reaction rate k_{obs} in the presence of competing substrate is slower, and apparent kinetic constants (marked with ^{app}) need to be corrected for substrate competition to reflect the kinetic inhibitor potency. Unless otherwise noted, nonlinearity in the uninhibited control k_{ctrl} (k_{obs} of $[I] = 0$) is assumed to be 0. The relation between k_{obs} and inhibitor concentration holds important information on the inhibitor binding mechanism. A linear k_{obs} increase with inhibitor concentration is a hallmark of a 1-step binding mode, as reaction rates are only limited by experimental factors such as solubility. Plots of k_{obs} against 2-step inhibitor concentrations are hyperbolic, as the experimental covalent EI^* association rate is limited by EI occupancy, which reaches its maximum (k_{inact} or k_5) at saturating inhibitor concentration, as shown in **Figure 3E**: $[I] > 10K_i$ for 2-step irreversible inhibitors or $[I] > 10K_i$ for 2-step reversible inhibitors. An exception to this general observation is inhibitors with a 2-step binding mode that will display a linear relationship when assessed at all non-saturating inhibitor concentrations (**Figure 3F**) or all saturating inhibitor concentrations (**Figure 3G**).³⁷ These 1-step binding behaviors can be distinguished from the Y-intercept ($Y_0 = k_{\text{ctrl}}$ for $[I] \ll K_i^{\text{app}}$ and $Y_0 > k_{\text{ctrl}}$ for $[I] \gg K_i^{\text{app}}$) along with the noncovalent inhibition of enzyme activity ($v_i = v^{\text{ctrl}}$ for $[I] \ll K_i^{\text{app}}$) and $v_i < v^{\text{ctrl}}$ for $[I] \gg K_i^{\text{app}}$).

3. Theoretical Framework for Experimental Methods and Data Analysis

We will discuss four methods in this work, that all have accompanying data analysis procedures tailored to the inhibitor binding mode (summarized in **Table 4**). In this section, we will first give an overview of the general conceptual background and assay design considerations for each assay method. Subsequent data analysis is tailored to a specific inhibitor binding mode, and we will illustrate the ‘ideal’ situation with kinetic simulations to guide interpretation of results. Furthermore, pointers on identification of deviations such as nonlinearity in the uninhibited control ($k_{\text{ctrl}} > 0$) will be given along with algebraic corrections or troubleshooting options to

resolve issues. The stepwise assay protocols and accompanying data analysis protocols can be found in *section 4*. A practical comment on the nomenclature used: we use the word 'fit' for nonlinear fits of raw data (in e.g. GraphPad Prism, as part of the *Data Analysis Protocols* in *section 4*) and 'calculate' to denote that we calculate parameters from experimental values (in EXCEL, as part of the *Sample Calculations* in *section 4*).

Methods I and *II* are based on incubation time-dependent enzyme inhibition (**Figure 4**). Here, substrate and inhibitor are mixed, and the reaction is initiated by addition of enzyme: i.e. simultaneous onset of product formation and enzyme inhibitor. *Methods III* and *IV* are based on enzyme inhibition after preincubation. Here, enzyme is preincubated with inhibitor before substrate addition. Two major factors contribute to selection of the appropriate experimental method for your enzymatic inhibition assay: the available enzyme activity assay and the inhibitor binding mode (the most important considerations are summarized for each method and inhibitor binding mode in **Table 4**). Recombinant enzyme inhibition is assessed in an *in vitro* enzyme activity assay with detectable product formation.⁷⁸⁻⁷⁹ This can be a continuous read-out for enzymatic processing of fluorogenic substrates (e.g. fluorescence intensity, FRET) or be a stopped/quenched assay that may require a secondary development/quenching or separation step to detect the formed product (or remaining substrate) such as LCMS-based

Table 4 | Concise Summary of Methods.

Assay Method	Data Analysis Protocol	Binding Mode	Read-out and Assay Conditions ^a	Obtainable Kinetic Parameters	Comments/Remarks	Ref
I	1A	2-step IRREV	Continuous	k_{inact} K_i k_{inact}/K_i	Continuous detection of enzyme activity. Optimization of reaction conditions to minimize assay artefacts can be challenging but rewards with the simplest experimental procedure.	
	1B	1-step IRREV	Continuous	k_{chem}	<i>Method I</i> is generally favored: most informative in a single measurement. Favored for very potent inhibitors because competing substrate is always present	41
	1C	2-step REV	Continuous $k_{\text{ctrl}} \ll k_{\text{inact}}$	k_{inact}/K_i	<i>Method I</i> is disfavored over <i>Method III</i> as algebraic correction for spontaneous loss of enzyme activity is NOT possible for 2-step REV inhibitors.	
	1D	2-step IRREV	Continuous $[P]_t > 0.1[S]_0$ $[S] \ll 0.1K_M$	k_{inact} K_i k_{inact}/K_i	Algebraic correction for substrate depletion.	80
II	2	2-step IRREV	Continuous, Quenched $k_{\text{ctrl}} = 0$	k_{inact} K_i k_{inact}/K_i	Incubation time-dependent potency. Compatible with quenched assays but is sensitive to spontaneous loss of enzyme activity.	81

Table 4 continues on the next page

Table 4 | Concise Summary of Methods. (continued)

Assay Method	Data Analysis Protocol	Binding Mode	Read-out and Assay Conditions ^a	Obtainable Kinetic Parameters	Comments/Remarks	Ref
III	3 + 3Ai	2-step IRREV	Continuous, Quenched [S] << K _M V _{sub} << V _{t'}	k _{inact} K _I k _{inact} /K _I	Enzyme activity after preincubation, with detection of inhibition by EI and EI* formed during preincubation. Experimental assays are relatively time-consuming.	
	3 + 3Aii	2-step IRREV	Continuous, Quenched [S] << K _M V _{sub} << V _{t'}	k _{inact} K _I k _{inact} /K _I		
	3 + 3Bi	1-step IRREV	Continuous, Quenched [S] << K _M V _{sub} << V _{t'}	k _{chem}		
	3 + 3Bi	2-step IRREV	Continuous, Quenched [S] << K _M V _{sub} << V _{t'} [I] << K _I	k _{inact} /K _I	Favored for inhibitors with low potency and disfavored for very potent (tight-binding) inhibitors as preincubation is performed in absence of competing substrate.	82
	3 + 3Bii	1-step IRREV	Continuous, Quenched [S] << K _M V _{sub} << V _{t'}	k _{chem} k _{obs} /I	Data Analysis Protocols 3Ai and 3Bi are favored for comparison of multiple inhibitors on a single target. Data Analysis Protocols 3Aii and 3Bii are favored for selectivity evaluation of a single inhibitor on multiple targets.	
	3 + 3Bii	2-step IRREV	Continuous, Quenched [S] << K _M V _{sub} << V _{t'} [I] << K _I	k _{inact} /K _I		
	3 + 3C	2-step REV	Continuous, Quenched [S] << K _M V _{sub} << V _{t'}	K [*]	Favored over Method I for 2-step REV: normalization enables algebraic correction for spontaneous loss of enzyme activity.	
IV	4 + 4Ai	2-step IRREV	Continuous, Quenched [S] >> K _M V _{sub} >> V _{t'}	k _{inact} K _I k _{inact} /K _I	Enzyme activity after preincubation, with detection of inhibition by covalent adduct EI* formed during preincubation (comparable to direct detection): dilution into (excess) substrate promotes noncovalent EI dissociation.	
	4 + 4Aii	2-step IRREV	Continuous, Quenched [S] >> K _M V _{sub} >> V _{t'}	k _{inact} K _I k _{inact} /K _I		
	4 + 4Bi	1-step IRREV	Continuous, Quenched [S] >> K _M V _{sub} >> V _{t'}	k _{chem}		
	4 + 4Bi	2-step IRREV	Continuous, Quenched [S] >> K _M V _{sub} >> V _{t'} [I] << K _I	k _{inact} /K _I	Favored for inhibitors with low (noncovalent) affinity, or to study the contribution of covalent bond formation.	83
	4 + 4Bii	1-step IRREV	Continuous, Quenched [S] >> K _M V _{sub} >> V _{t'}	k _{chem} k _{obs} /I	Data Analysis Protocols 4Ai and 4Bi are favored for comparison of multiple inhibitors on a single target. Data Analysis Protocols 4Aii and 4Bii are favored for selectivity evaluation of a single inhibitor on multiple targets.	
	4 + 4Bii	2-step IRREV	Continuous, Quenched [S] >> K _M V _{sub} >> V _{t'} [I] << K _I	k _{inact} /K _I k _{obs} /I		

^a General assay conditions for all methods unless otherwise specified: [I] > 10[E]. [S] > 10[E]. [P]_t < 0.1[S]₀.

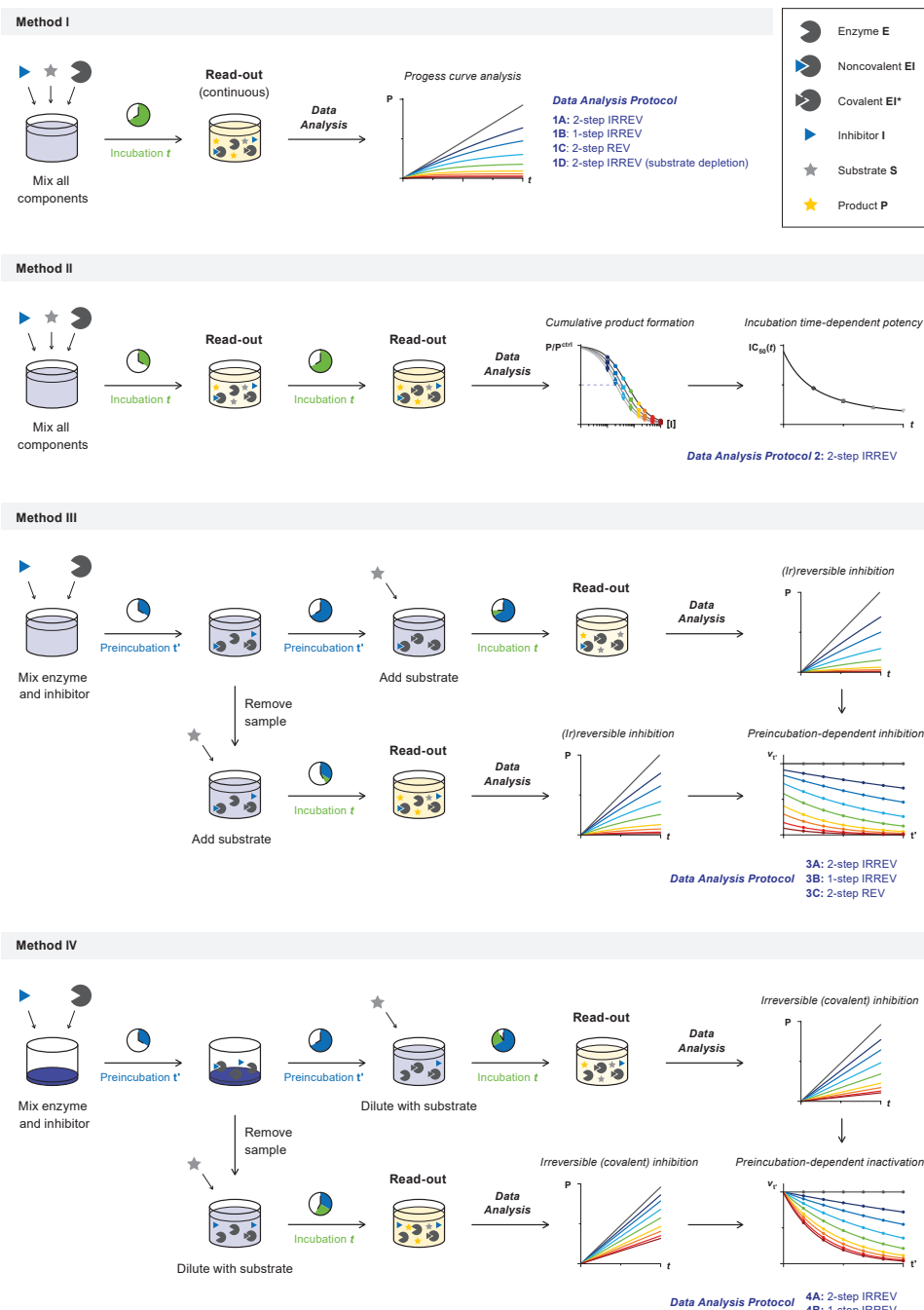


Figure 4 | Schematic overview of experimental protocols to analyze covalent inhibitor potency included in this work. Incubation time-dependent enzyme inhibition in *Method I* and *II*. Preincubation time-dependent enzyme inhibition in *Method III* and *IV*. Data analysis is tailored to 2-step irreversible inhibition (shown in **Figure 1C**), 1-step irreversible inhibition (shown in **Figure 1D**), or 2-step reversible inhibition (shown in **Figure 1B**).

assays, conversion of radiolabeled substrate, and commercial assay technologies including ADP-Glo™ (Promega) ATP consumption/ADP production assays, HTRF® KinEASE™ (Cisbio) and Z'-LYTE (Invitrogen) phosphorylation assays, and Amplex® Red (Invitrogen) hydrogen peroxide/peroxidase assays.⁷⁸⁻⁷⁹ *Method I* is only compatible with homogeneous enzymatic assays that allow continuous read-out, such as cleavage of fluorogenic reporter peptides by proteases. *Methods II-IV* are also compatible with quenched/stopped assays with development step prior to read-out.

METHOD I: Progress Curve Analysis of Substrate Association Competition

Progress curve analysis is an established method for kinetic analysis of slow-binding inhibitors based on continuous detection of product formation after the substrate processing/product formation reaction has been initiated by addition of enzyme to a mixture of inhibitor and substrate (**Figure 5A**). A single measurement at each inhibitor concentration is sufficient, which is convenient when comparing the potency of multiple inhibitors on the same target. However, this method requires the availability of an activity assay format with a continuous read-out, thereby limiting the substrates that can be used. Additionally, assay optimization for progress curve analysis is labor intensive: it is not uncommon to perform multiple pilot experiments to find suitable concentrations of substrate, enzyme, and inhibitor that ensure linear product formation in the uninhibited control (consult **Table 6** in section 5 for troubleshooting).

For ‘slow-binding’ inhibitors, the slope of time-dependent product formation exponentially decreases from initial product formation velocity v_i (rapid noncovalent inhibition) to the final product formation velocity v_s (reaction completion) (**Figure 5B**).⁴¹ The progress curve of time-dependent product formation (as detected signal F_t in AU) is fitted to a general exponential inhibitor association **Equation 11** (shown in **Figure 5C**) to obtain the observed rate of reaction completion k_{obs} (in s^{-1}) from initial velocity v_i (in AU/s) to final velocity v_s (in AU/s). A 1-step or 2-step binding mode can be identified by (visual) inspection of the initial velocity (**Figure 5B**). The value of initial velocity v_i is inhibitor concentration-dependent for 2-step (ir)reversible inhibitors that form a rapid (noncovalent) equilibrium ($v_i < v^{ctrl}$) because the noncovalent enzyme–inhibitor complex already inhibits the enzyme activity (*rapid equilibrium approximation*). Similarly, the value of initial velocity v_i is equal to the uninhibited velocity v^{ctrl} in lieu of a rapid initial binding step, as can be observed for 2-step (ir)reversible inhibitors at non-saturating concentrations ($[I] \ll K_i^{app}$) and 1-step (ir)reversible inhibitors ($v_i < v^{ctrl}$). Irreversible inhibitors are expected to reach 100% inhibition at reaction completion for all inhibitor concentrations, provided inhibitor is present in large excess and the reaction does not exceed the dynamic enzyme lifetime. Therefore, the final velocity v_s is restrained to full inhibition ($v_s = 0$) for 2-step irreversible inhibitors (*Data Analysis 1A*) and 1-step irreversible inhibitors (*Data Analysis 1B*). A 2-step reversible inhibitor will reach a reversible steady-state equilibrium ($v_s \geq 0$) upon reaction completion (*Data Analysis 1C*). Be aware that the product formation progress curve is not only linear for fast-binding inhibitors but will also appear linear for slow-binding inhibitors if reaction completion is much slower than the time course of the

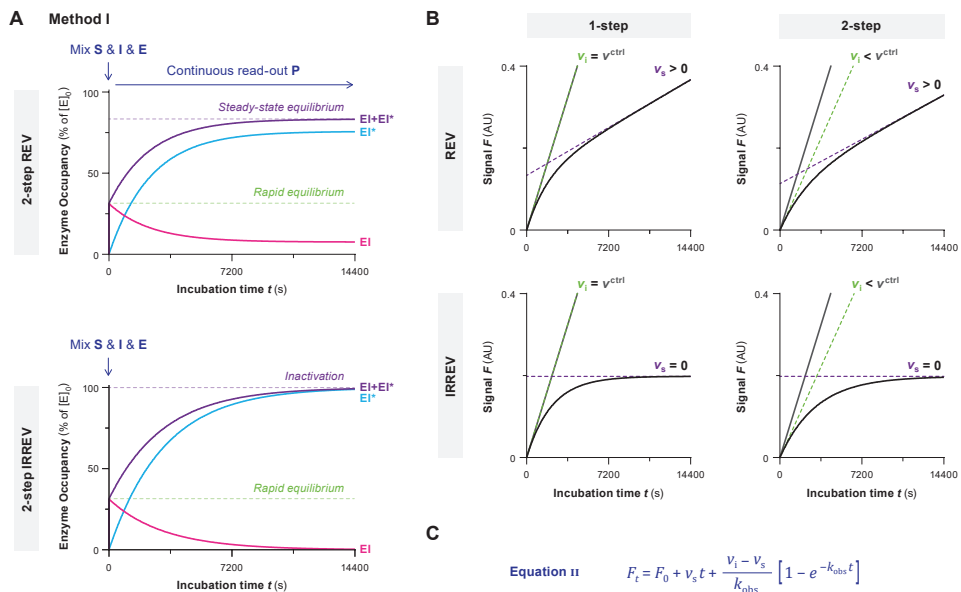


Figure 5 | Method I: Progress curve analysis of substrate association competition. Simulated with **KinGen** for 1 pM enzyme and 100 nM substrate **S1**. **(A)** The reaction between enzyme, inhibitor, and substrate is initiated by addition of enzyme. Product formation is monitored continuously to detect the time-dependent enzyme activity. Simulated for 50 nM inhibitor **B** (*top*) and inhibitor **C** (*bottom*). Enzyme inhibition increases with time-dependent formation of covalent EI^* until reaching reaction completion. Initially, total enzyme occupancy $[EI + EI^*]$ reflects the rapid noncovalent equilibrium $[EI]_{eq}$. At reaction completion ($t > 5t\%$), total enzyme occupancy $EI + EI^*$ reflects the steady-state equilibrium (*reversible*) or inactivation (*irreversible*). **(B)** Typical progress curves for enzyme activity in presence of time-dependent inhibitors. Time-dependent product formation decreases exponentially from initial velocity v_i (*dashed green line*) to the steady-state velocity v_s (*dashed purple line*) at reaction completion ($t > 5t\%$), with $v^ctrl = \text{linear product formation in uninhibited control (gray line)}$. $v_i = v^ctrl$ for 1-step IRREV inhibitors and for 2-step IRREV inhibitors when $[I] \ll K_i^{app}$. Simulated for 50 nM 1-step REV inhibitor **A**, 2-step REV inhibitor **B**, 1-step IRREV inhibitor **D**, and 2-step IRREV inhibitor **C**. **(C)** General exponential association Equation II to fit progress curves of time-dependent inhibition. Parameters are constrained depending on the inhibitor binding mode. $v_s = 0$ for irreversible inhibition: inactivation at reaction completion. $v_i = v^ctrl$ for 1-step inhibition: noncovalent complex is not significant at non-saturating inhibitor concentrations. The uninhibited controls are also fitted to obtain reference values for uninhibited velocity v^ctrl and the rate of nonlinearity in the uninhibited control k_{ctrl} . $F_t = \text{time-dependent signal resulting from product formation}$. $F_0 = \text{Y-intercept} = \text{background signal at reaction initiation}$. $v_i = \text{initial product formation velocity}$. $v_s = \text{final/steady-state product formation velocity}$. $t = \text{incubation time after enzyme addition}$. $k_{obs} = \text{observed rate of time-dependent inhibition from initial } v_i \text{ to final } v_s$.

assay ($t \ll t\%$). Importantly, the noncovalent equilibrium is assumed to be reached instantly for 2-step inhibitors (*rapid equilibrium approximation*). An algebraic solution to analyze irreversible 2-step inhibitors violating the rapid equilibrium approximation is available as a preprint.⁷⁴

It is crucial to have linear product formation in the uninhibited control (F^ctrl), as progress curve fitting for time-dependent (ir)reversible inhibition relies on the assumption that uninhibited product formation is absolutely linear. This ideal situation is often not feasible to achieve

experimentally, as there are many factors contributing to a slight time-dependent decrease of product formation velocity in the uninhibited control, and not all of them are resolvable (common troubleshooting options are listed in **Table 6**, section 5). Algebraic correction for nonlinearity in the uninhibited control k_{ctrl} caused by spontaneous enzyme degradation/denaturation is possible for irreversible inhibitors (*Data Analysis 1A-B*). Furthermore, it is also possible to perform an algebraic correction for substrate depletion for 2-step irreversible inhibitors (*Data Analysis 1D*).⁸⁴ Ultimately, numerical integration is the preferred method in complex systems where multiple events contribute to the observed nonlinearity.

Data Analysis 1A: 2-Step Irreversible Covalent Inhibition.

Data obtained for 2-step irreversible inhibitors with *Method 1* (**Figure 6A**) is processed with *Data Analysis Protocol 1A*. The progress curve of time-dependent product formation of each inhibitor concentration is fitted to exponential **Equation II** (shown in **Figure 5C**) constraining final velocity to 100% inhibition ($v_s = 0$) at reaction completion (**Figure 6B**). The inhibitor concentration-dependent observed rate of inactivation k_{obs} reflects the rate from initial velocity v_i (rapid noncovalent equilibrium) to final velocity v_s (inactivation at reaction completion). The plot of inhibitor concentration-dependent k_{obs} (**Figure 6C**) reaches maximum rate of inactivation k_{inact} in the presence of saturating inhibitor concentration ($[I] \gg K_i^{app}$) with the Y-intercept at 0 when the progress curve in absence of inhibitor is strictly linear. Importantly, the inhibitor concentration that results in half-maximum enzyme inactivation ($k_{obs} = \frac{1}{2}k_{inact}$) has to be corrected for competition by the substrate during incubation but maximum rate of inactivation k_{inact} is unaffected.

A linear plot of inhibitor concentration-dependent k_{obs} (with Y-intercept = k_{ctrl}) and an initial velocity independent of inhibitor concentration ($v_i = v^{ctrl}$) are indicative of a 1-step binding mechanism: the inhibitor concentration is not saturating ($[I] \leq 0.1K_i^{app}$ and $[I] \leq 0.1K_i^{app}$). This can be resolved by increasing the inhibitor concentration, reducing the substrate concentration, or processing the data with *Data Analysis Protocol 1B*. Inhibitors with a high noncovalent potency ($[I] \gg K_i^{app}$) might exhibit tight-binding behavior: complete inactivation is reached at reaction initiation ($v_i = 0$), even at the lowest inhibitor concentration, without violating the pseudo-first order reaction conditions ($[I]_0 \geq 10[E]_0$). This can be resolved by lowering the inhibitor concentration, but only if the assay robustness is sufficient to also lower the enzyme concentration, and/or by increasing the concentration of competing substrate, thus increasing the apparent inhibition constant K_i^{app} . Unfortunately, algebraic correction for progress curve analysis of 1-step inhibitors with inhibitor depletion ($[I]_0 < 10[E]_0$) is not compatible with 2-step inhibition.⁴¹ Numeric fitting is a possibility to fit progress curves with depletion of substrate as well as inhibitor.⁸⁰ Alternatively, tight-binding 2-step irreversible covalent inhibition can be assessed with *Method IV* if covalent adduct formation is relatively slow.

Spontaneous enzyme degradation/denaturation (**Figure 6D**) causes a nonlinearity in the uninhibited control ($k_{ctrl} > 0$) that violates the assumption that time-dependence in the inhibitor-treated samples is a direct effect of the inhibitor (**Figure 6E**). The first order enzymatic degradation rate contributes to k_{obs} independent of inhibitor concentration ($k_{degE} = k_{degES} = k_{degEI}$). Consequently, the Y-intercept of the k_{obs} against inhibitor concentration plot now corresponds to observed rate k_{ctrl} in absence of inhibitor, and k_{max} is higher

Data Analysis 1A: 2-step IRREV

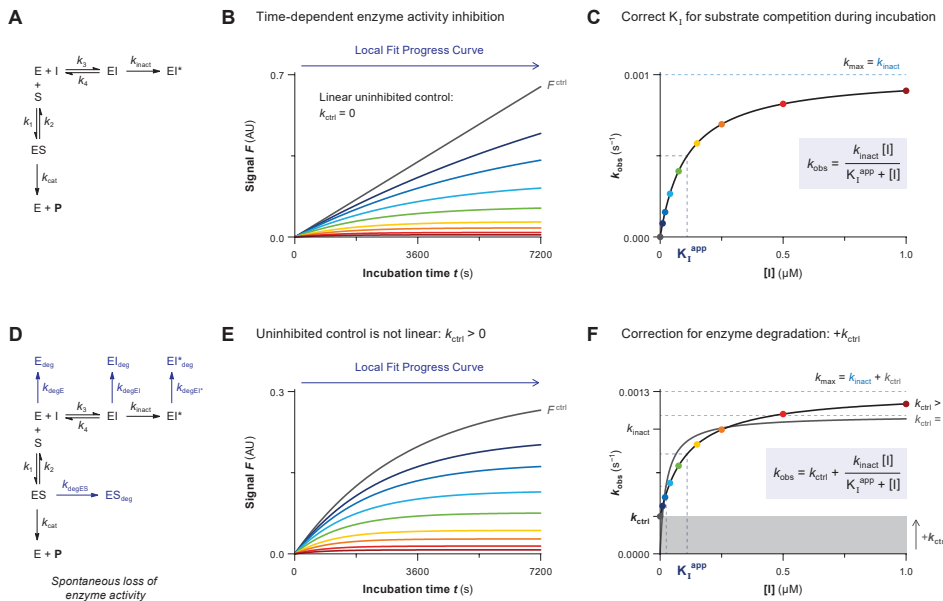


Figure 6 | Data Analysis 1A: Progress curve analysis for 2-step irreversible covalent inhibition. Simulated with **KinGen** (panel A-C) or **KinDeg** (panel D-F) for 2-step IRREV inhibitor **C** with 1 pM enzyme and 100 nM substrate **S1**. **(A)** Schematic enzyme dynamics during incubation. **(B)** Time-dependent product formation in absence of inhibitor F^{ctrl} or in presence of inhibitor. The progress curve for each inhibitor concentration is fitted individually to **Equation II** (shown in **Figure 5C**) (constraining $v_s = 0$) to obtain the observed rate of inactivation k_{obs} . **(C)** Inhibitor concentration-dependent k_{obs} reaches k_{inact} at saturating inhibitor concentration ($k_{max} = k_{inact}$). Half-maximum $k_{obs} = \frac{1}{2}k_{inact}$ is reached when inhibitor concentration equals the apparent inactivation constant K_I^{app} . **(D)** Schematic enzyme dynamics during incubation with spontaneous loss of enzyme activity. Simulated with $k_{degE} = k_{degES} = k_{degEI} = 0.0003 \text{ s}^{-1}$. **(E)** Time-dependent product formation in absence of inhibitor F^{ctrl} is not linear because $k_{ctrl} > 0$. The progress curves for each inhibitor concentration and uninhibited control are fitted individually to **Equation II** (shown in **Figure 5C**) (constraining $v_s = 0$) to obtain the observed rates of inactivation k_{obs} . **(F)** Inhibitor concentration-dependent k_{obs} with spontaneous enzyme degradation increases with k_{ctrl} , but the span from k_{min} ($= k_{ctrl}$) to k_{max} ($= k_{inact} + k_{ctrl}$) still equals k_{inact} . Fit with algebraic correction for nonlinearity (black line, $k_{ctrl} > 0$). Ignoring the nonlinearity (gray line, constrain $k_{ctrl} = 0$) results in underestimation of K_I^{app} (overestimation of potency) and overestimation of k_{inact} .

($k_{max} = k_{inact} + k_{ctrl}$) (**Figure 6F**). Performing a simple algebraic correction for the observed nonlinearity due to spontaneous enzyme degradation results in good estimates for k_{inact} and K_I^{app} (**Figure 6F**). Ignoring the nonlinearity in the uninhibited control by restraining $k_{ctrl} = 0$ implies that all time-dependent loss of enzyme activity should be attributed to inhibitor-mediated inactivation, resulting in an underestimation of inactivation constant K_I^{app} (overestimation of potency) and overestimation of k_{inact} . This effect is less pronounced when spontaneous enzyme degradation is much slower than the maximum rate of covalent adduct formation ($k_{inact} \gg k_{ctrl}$). It is important to note that stabilization of the enzyme species by (noncovalent) inhibitor binding also decreases the contribution of k_{ctrl} to the observed rate k_{obs} at saturating inhibitor concentrations ($k_{max} = k_{inact}$). This impairs the accuracy of the algebraic correction

unless k_{ctrl} is relatively small (k_{max} approaches k_{inact} if $k_{inact} >> k_{ctrl}$). This algebraic correction does not accurately correct for nonlinearity due to substrate depletion ($[P]_t > 0.1[S]_0$): substrate depletion is dependent on the total product formation and does not (significantly) contribute to k_{max} at saturating inhibitor concentration because enzyme inhibition reduces the total amount of product formed ($k_{max} = k_{inact}$). Please consult *Data Analysis 1D* for algebraic correction of nonlinearity due to substrate depletion.

Data Analysis 1B: 1-Step Irreversible Covalent Inhibition.

Data obtained for 1-step irreversible inhibitors with *Method 1* (**Figure 7A**) is processed with *Data Analysis Protocol 1B*. The progress curve of time-dependent product formation of each inhibitor concentration is fitted to exponential **Equation 11** (shown in **Figure 5C**) constraining final velocity to inactivation ($v_s = 0$) at reaction completion (**Figure 7B**). The initial velocity v_i equals the uninhibited product formation velocity ($v_i = v^{ctrl}$), as noncovalent inhibitor binding

Data Analysis 1B: 1-step IRREV

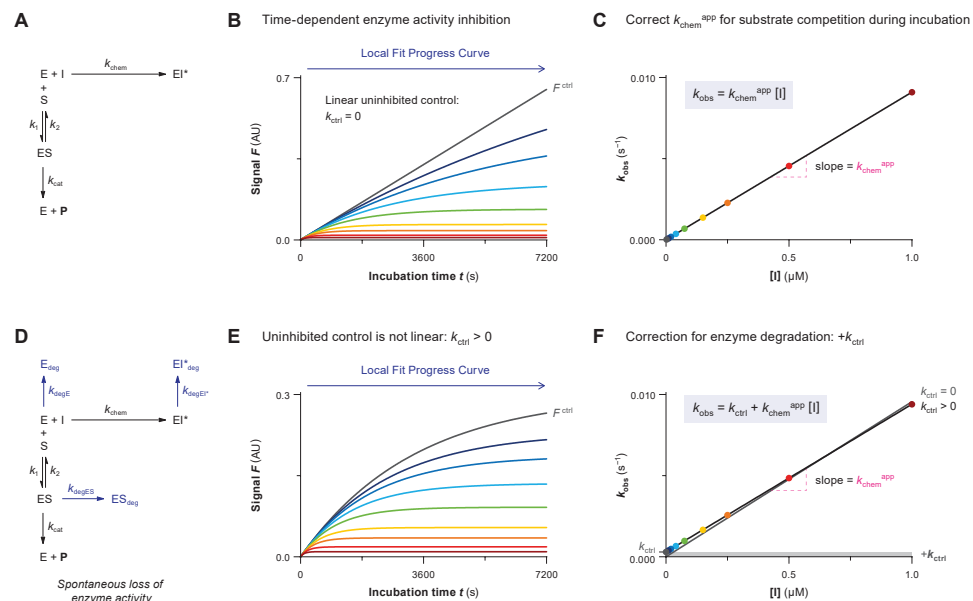


Figure 7 | Data Analysis 1B: Progress curve analysis for 1-step irreversible covalent inhibition. Simulated with *KinGen* (panel A-C) or *KinDeg* (panel D-F) for 1-step IRREV inhibitor **D** with 1 pM enzyme and 100 nM substrate **S1**. **(A)** Schematic enzyme dynamics during incubation. **(B)** Time-dependent product formation in absence of inhibitor F^{ctrl} or in presence of inhibitor. The progress curve for each inhibitor concentration is fitted individually to **Equation 11** (shown in **Figure 5C**) (constraining $v_s = 0$) to obtain the observed rate of inactivation k_{obs} , $v_i = v^{ctrl}$ for 1-step irreversible inhibitors and 2-step irreversible inhibitors at non-saturating concentrations ($[I] \ll k_i^{app}$). **(C)** Inhibitor concentration-dependent k_{obs} increases linearly with inhibitor concentration, with k_{chem}^{app} as the slope. **(D)** Schematic enzyme dynamics during incubation with spontaneous loss of enzyme activity. Simulated with $k_{degE} = k_{degES} = k_{degEI} = 0.0003 \text{ s}^{-1}$. **(E)** Time-dependent product formation in absence of inhibitor F^{ctrl} is not linear because $k_{ctrl} > 0$. The progress curves for each inhibitor concentration and uninhibited control are fitted individually to **Equation 11** (shown in **Figure 5C**) (constraining $v_s = 0$) to obtain the observed rates of inactivation k_{obs} . **(F)** Inhibitor concentration-dependent k_{obs} with spontaneous enzyme degradation/denaturation increases by k_{ctrl} . Fit with algebraic correction for nonlinearity (black line, $k_{ctrl} > 0$) or ignoring nonlinearity (gray line, constrain $k_{ctrl} = 0$). Ignoring the nonlinearity (assuming Y-intercept = 0) results in overestimation of k_{chem}^{app} (steeper slope).

does not contribute to enzyme inhibition by 1-step irreversible inhibitors. A linear plot of inhibitor concentration-dependent k_{obs} is indicative of a 1-step binding mechanism with $k_{\text{chem}}^{\text{app}}$ as the slope (**Figure 7C**). A 2-step irreversible covalent inhibitor also has a linear k_{obs} against inhibitor concentration plot at non-saturating concentrations ($[I] \leq 0.1K_i^{\text{app}}$): $k_{\text{chem}}^{\text{app}} = k_{\text{inact}}/K_i^{\text{app}}$. The slope has to be corrected for substrate competition to obtain the inactivation constant k_{chem} . Substrate will occupy a fraction of the unbound enzyme to reach the noncovalent $E + S \leftrightarrow ES$ equilibrium (how much depends on $[S]/K_M$), thus reducing the unbound enzyme concentration. It may seem counterintuitive to correct for substrate competition, as the pseudo-first order rate of covalent adduct formation ($k_{\text{obs}} = k_{\text{chem}}^{\text{app}} \times [I]$) does not seem to involve unbound enzyme (provided inhibitor is present in large excess), but formation of EI^* is limited by the available unbound enzyme at that moment and it is not possible to form covalent adduct EI^* when competing substrate blocks access to the enzyme active site.

It is important to have linear product formation in the uninhibited control ($k_{\text{ctrl}} = 0$) or to perform an algebraic correction for nonlinearity in the uninhibited control ($k_{\text{ctrl}} > 0$) caused by spontaneous first order enzyme degradation/denaturation (**Figure 7D-F**). Failure to correct for the contribution of enzyme degradation when fitting the observed rate of inactivation k_{obs} against inhibitor results in overestimation of $k_{\text{chem}}^{\text{app}}$ (**Figure 7F**, gray line). The contribution of nonlinearity k_{ctrl} becomes less pronounced at elevated inhibitor concentrations as k_{ctrl} becomes significantly smaller than k_{obs} ($k_{\text{ctrl}} \ll k_{\text{chem}}^{\text{app}} \times [I]$). (De)stabilization of enzyme upon inhibitor binding ($k_{\text{deg}EI^*}$) does not affect k_{obs} , as EI^* formation is already irreversible, thus removing the species from the available pool of catalytic enzyme. To our knowledge, methods to algebraically correct for substrate depletion have not been reported.

Data Analysis 1C: 2-Step Reversible Covalent Inhibition.

Data obtained for 2-step reversible inhibitors with *Method 1* (**Figure 8A**) is processed with *Data Analysis Protocol 1B*. The progress curve of time-dependent product formation of each inhibitor concentration (**Figure 8B**) is fitted to exponential **Equation 11** (shown in **Figure 5C**). The inhibitor concentration-dependent observed rate for reaction completion k_{obs} reflects the rate from initial velocity v_i (rapid noncovalent equilibrium) to final velocity v_s (slow steady-state equilibrium). Contrary to irreversible inhibition, steady-state velocity v_s is not constrained to inactivation ($v_s > 0$) because the reversible steady-state equilibrium is reached at reaction completion. Maximum rate of reaction completion k_{max} is reached in the presence of saturating inhibitor concentration ($[I] \gg K_i^{\text{app}}$), and the covalent association rate constant k_5 is obtained from the span between k_{min} and k_{max} (**Figure 8C**). Interestingly, the Y-intercept k_{min} is equal to covalent dissociation rate constant k_6 ; therefore, the k_{obs} of uninhibited control (k_{ctrl}) is excluded from the fit. Steady-state inhibition constant K_i^{app} can be calculated from the fitted values of K_i^{app} , k_5 , and k_6 , but this is not the preferred approach, as a small error in k_6 has huge implications for the calculation of K_i^* . Other methods such as jump dilution assays generate more reliable estimates of k_6 , which is especially important for very potent 2-step reversible covalent inhibitors: relatively small k_6 -values cannot accurately be estimated from the Y-intercept.^{29, 33} Generally, more reliable estimates of the apparent steady-state inhibition constant K_i^{app} are generated from the dose-response curve of steady-state velocity v_s against inhibitor concentration (**Figure 8D**).

Data Analysis 1C: 2-step REV

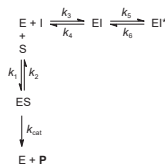
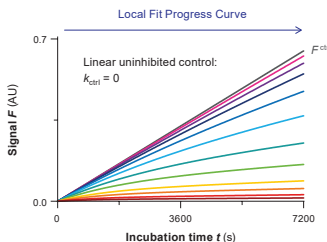
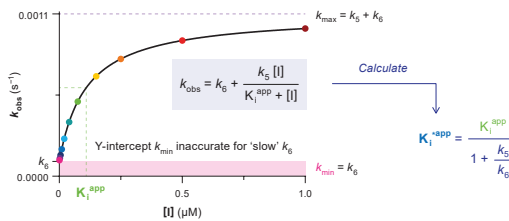
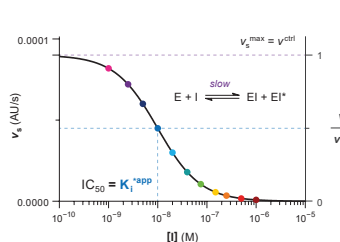
A**B** Time-dependent enzyme activity inhibition**C** K_i^{app} is sensitive to errors in k_{obs} ; Y-intercept = k_6 requires strictly linear control**D** IC_{50} from final velocity v_s reflects steady-state inhibition constant K_i^{app} 

Figure 8 | Data Analysis 1C: Progress curve analysis for 2-step reversible covalent inhibition. Simulated with KinGen for 2-step REV inhibitor **B** with 1 pM enzyme and 100 nM substrate **S1**. **(A)** Schematic enzyme dynamics during incubation. **(B)** Time-dependent product formation in absence of inhibitor F^{ctrl} or in presence of inhibitor. The progress curve for each inhibitor concentration is fitted individually to **Equation II** (shown in **Figure 5C**) to obtain the observed rate of inactivation k_{obs} and steady-state velocity v_s . **(C)** Inhibitor concentration-dependent k_{obs} equals k_{max} at saturating inhibitor concentration ($k_{max} = k_5 + k_6$) and approaches k_6 in absence of inhibitor ($k_{min} = k_6$). Half-maximum $k_{obs} = k_{min} + \frac{1}{2}(k_{max} - k_{min}) = k_6 + \frac{1}{2}k_5$ is reached when inhibitor concentration equals the apparent inhibition constant K_i^{app} . Steady-state inhibition constant K_i^{app} has to be calculated from the fitted values of k_5 , k_6 and K_i^{app} , thus being very sensitive to errors and (non)linearity in the uninhibited background (illustrated in **Figure 9**). **(D)** Steady-state inhibition constant K_i^{app} is equal to the IC_{50} of steady-state velocity v_s .

Contrary to irreversible covalent inhibitors that become more potent with a faster k_{inact} , reversible covalent inhibitors are more potent if they have a longer residence time τ , which is driven by a slow dissociation rate k_6 (**Figure 1B**).⁴³⁻⁴⁴ It is crucial to have strictly linear product formation in the uninhibited control ($k_{ctrl} = 0$) because it is not possible to perform an algebraic correction for spontaneous enzyme degradation/denaturation (**Figure 9A-B**). Unfortunately, potent reversible covalent inhibitors are likely to violate this condition. Violation of this assumption ($k_{ctrl} > 0$) can be identified by fitting the uninhibited product formation F^{ctrl} to **Equation II** (shown in **Figure 5C**): initial velocity v_i^{ctrl} should not be larger than steady-state v_s^{ctrl} . The consequence of nonlinearity in the uninhibited control is ‘contamination’ of reaction rate k_{obs} and final velocity v_s (based on the reversible reaction to reach steady-state equilibrium: $v_s > 0$) with the rate of enzyme degradation k_{ctrl} (based on an inactivation reaction: $v_s = 0$). Y-intercept approaching k_{ctrl} instead of k_6 even though the uninhibited control is not included in the fit is an indication that spontaneous enzyme degradation dominates k_{obs} at low inhibitor concentrations (**Figure 9C**). This ‘red flag’ should not be ignored, as it will result in over/underestimation of kinetic parameters. To our knowledge, models to perform an

Data Analysis 1C: 2-step REV

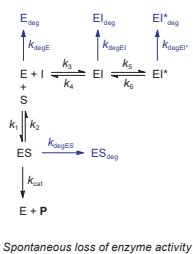
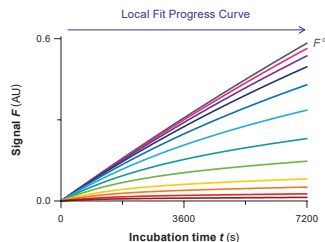
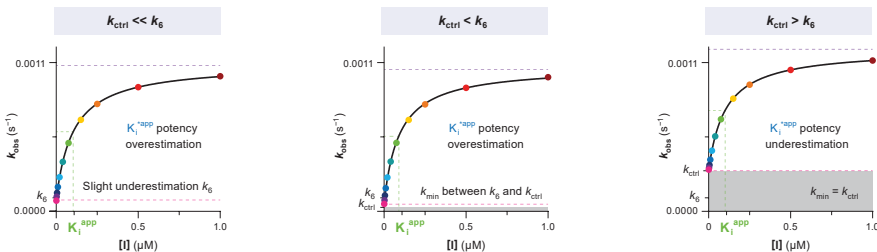
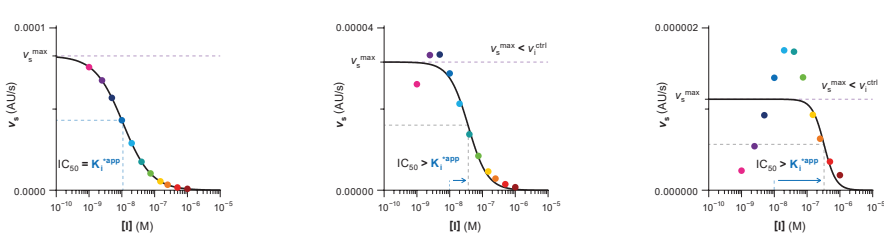
A**B** Uninhibited control is not linear: $k_{ctrl} > 0$ **C****D**

Figure 9 | Data Analysis 1C: Incompatibility with spontaneous loss of enzyme activity (2-step REV). Simulated with **KinDeg** for 2-step REV inhibitor **B** with 1 pM enzyme, 100 nM substrate **S1**, and $k_{ctrl} = k_{degE} = k_{degES} = k_{degEI} = k_{degEI^*}$. **(A)** Schematic enzyme dynamics during incubation with spontaneous loss of enzyme activity due to degradation/denaturation. **(B)** Time-dependent product formation in absence of inhibitor F^{ctrl} is not linear because $k_{ctrl} > 0$. The progress curve for each inhibitor concentration is fitted individually to **Equation II** (shown in **Figure 5C**) to obtain the observed rate of inactivation k_{obs} and steady-state velocity v_s . Simulated for $k_{ctrl} = 0.00003 \text{ s}^{-1}$. **(C)** Inhibitor concentration-dependent k_{obs} is driven by spontaneous enzyme degradation at low inhibitor concentrations, thus lowering the Y-intercept (k_{min} approaches k_{ctrl}). Ignoring the nonlinearity in the uninhibited control k_{ctrl} results in poor fits with underestimation of k_6 , even if k_{ctrl} is slower than k_6 . Simulated for $k_{ctrl} = 0.000003 \text{ s}^{-1}$ (left), $k_{ctrl} = 0.00003 \text{ s}^{-1}$ (middle) and $k_{ctrl} = 0.0003 \text{ s}^{-1}$ (right). **(D)** Final velocity v_s has been ‘contaminated’ by the contribution of irreversible inactivation to the time-dependent inhibition, and approaches $v_s = 0$ at low inhibitor concentrations. Final velocity v_s no longer reflects the steady-state equilibrium: IC_{50} is larger than K_i^{app} (underestimation of steady-state potency) unless k_{ctrl} is much smaller than k_6 .

algebraic correction have not been reported. Calculating steady-state inhibition constant K_i^* from final velocity v_s also results in an underestimation of the steady-state potency because the contribution of spontaneous enzyme degradation to final velocity v_s is dominant at low inhibitor concentrations (**Figure 9D**). Underestimation of the steady-state potency of reversible covalent inhibitors that have a relatively slow k_6 is more severe than for the less potent counterpart with a faster k_6 . We were able to find reasonable estimates of K_i^* when the contribution of nonlinearity was significantly smaller than covalent adduct dissociation ($k_{ctrl} \ll k_6$). Preincubation time-

dependent inhibition (*Method III*) is a more suitable method to analyze 2-step reversible inhibition affected by enzyme instability: it is possible to algebraically correct for enzyme instability in this method (*Data Analysis 3C*).

Data Analysis 1D: Algebraic Correction for Substrate Depletion (2-Step Irreversible Covalent Inhibition).

Scientists from BioKin and Pfizer derived an algebraic model for 2-step irreversible covalent inhibitors to correct for nonlinearity caused by substrate depletion in *Method I* (**Figure 10A**).⁸⁴ Substrate depletion causes a nonlinearity in the uninhibited control because the unbound substrate concentration is no longer constant ($[S]_t < [S]_0$) when a significant fraction of the substrate has been converted into product ($[P]_t > 0.1[S]_0$). The contribution of substrate depletion to the progress curve is directly related to the enzyme activity, as >10% substrate conversion is more likely to be exceeded when enzyme activity is high (**Figure 10B**). Algebraic correction is performed by globally fitting all progress curves in presence of inhibitor (**Figure 10C**) to **Equation III** (shown in **Figure 10D**) with shared values for k_{inact} and K_i^{app} . Substrate depletion should be the only factor contributing to nonlinearity, because the uninhibited control is not included in the global fit. Violation of this (and other) assumption requires data analysis by numerical solving.⁸⁰

The authors demonstrate their algebraic model to correct for substrate depletion with the EGFR inhibitor afatinib in a homogeneous kinase activity assay. A bisubstrate kinase activity

Data Analysis 1D: 2-step IRREV with substrate depletion

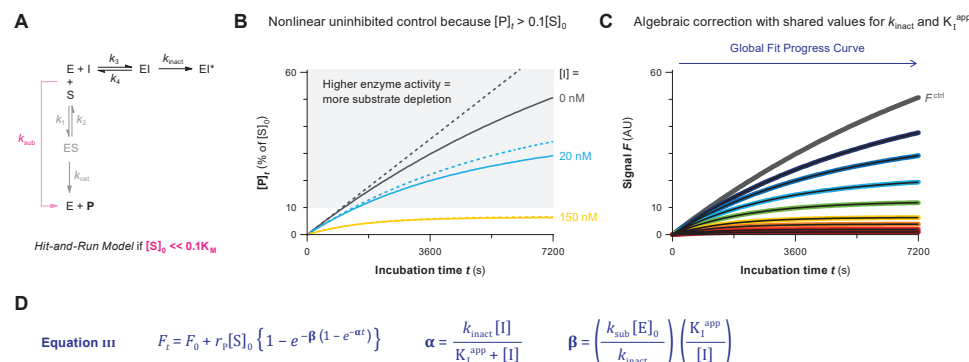


Figure 10 | Data Analysis 1D: Algebraic correction for substrate depletion in progress curve analysis for 2-step irreversible covalent inhibition. Simulated with **KinSubDpl** for 2-step IRREV inhibitor **C** with 100 pM enzyme and 10 nM substrate **S1**. **(A)** Enzyme dynamics. Algebraic correction for substrate depletion is restricted to a Hit-and-Run model ($E + S \rightarrow E + P$) for product formation. **(B)** Substrate depletion ($[P]_t > 0.1[S]_0$) results in a decrease of product formation in the uninhibited control (solid line) compared to product formation, assuming substrate conversion does not affect product formation rates (dashed line, simulated with **KinGen**). The contribution of substrate depletion to nonlinearity increases with higher enzyme activity (less inhibition). **(C)** Time-dependent product formation in the absence of inhibitor F^{ctrl} or in presence of inhibitor with time-dependent loss of enzyme activity due to substrate depletion. Inhibitor-treated progress curves are globally fitted to **Equation III** with shared values for k_{inact} and K_i^{app} . **(D)** **Equation III.** Algebraic model to correct for substrate depletion at low substrate concentrations.⁸⁰ F_0 = Y-intercept = background signal at reaction initiation (in AU). r_p = product coefficient for detected signal F per formed product $[P]$ (in AU/M). k_{sub} = reaction rate constant for Hit-and-Run model of enzymatic product formation $E + S \rightarrow E + P$ (in $M^{-1}s^{-1}$).

assay is different from our simulations with a single substrate, but this algebraic model can be applied in both systems: product formation in single-substrate as well as bisubstrate reactions can be simplified to a Hit-and-Run model ($E + S \rightarrow E + P$) with rate constant $k_{\text{sub}} = k_{\text{cat}}/K_M$ as long as the substrate concentration is far below its K_M ($[S] < 0.1K_M$) (Figure 10A). The accuracy of k_{inact} and K_I was very good with low substrate concentrations ($[S] \leq 0.01K_M$). A slightly higher substrate concentration ($[S] \geq 0.1K_M$) resulted in underestimation of k_{inact} and overestimation of K_I , but a good estimation of overall second order inactivation rate constant k_{inact}/K_I . Importantly, a calibration/titration should be performed prior to data analysis to determine product coefficient r_p (in AU/M) that transforms the detected signal F_t into product concentration $[P]_r$.⁶⁸⁻⁶⁹

METHOD II: Incubation Time-dependent Potency $IC_{50}(t)$

The observed potency of irreversible inhibitors increases with longer (pre)incubation time, as more enzyme is irreversibly bound. In this method, sometimes dubbed 'the Krippendorff method', the time-dependence of potency $IC_{50}(t)$ is utilized to directly find the relevant kinetic parameters for 2-step irreversible covalent inhibition. Contrary to progress curve analysis (*Method I*), this method is compatible with quenched/stopped assays that require a development/separation/quenching step before read-out, as continuous measurement of product formation is not required (but optional).

The incubation time-dependent potency $IC_{50}(t)$ reflects the inhibitor concentration resulting in a 50% decrease of cumulative product formed F_t during incubation compared to cumulative product formed in the uninhibited control F^{ctrl} . Enzymatic product formation is initiated by enzyme addition without preincubation of enzyme and inhibitor (Figure 11A). Fractional cumulative product formation F_t/F^{ctrl} decreases with longer incubation times (Figure 11B). Importantly, this does not reflect the current enzyme activity because read-out F_t reflects that

3

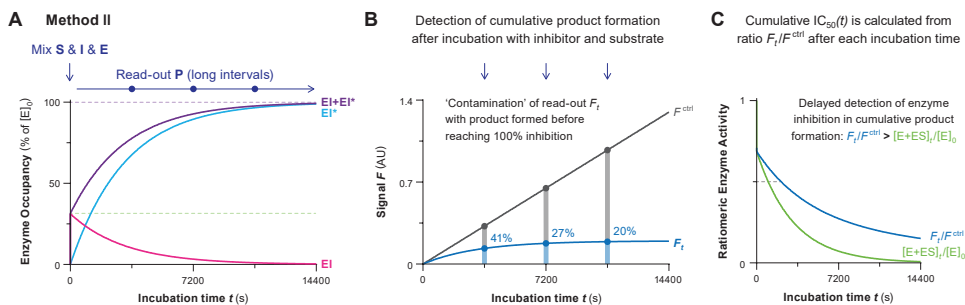


Figure 11 | Method II: Incubation time-dependent potency $IC_{50}(t)$. Simulated with **KingGen** for 50 nM 2-step IRREV inhibitor **C** with 1 pM enzyme and 100 nM substrate **S1**. **(A)** The reaction between enzyme, inhibitor, and substrate is initiated by addition of enzyme. Enzyme inhibition increases with time-dependent formation of covalent EI* until reaching reaction completion. **(B)** Read-out of cumulative product formation (reflected in signal F_t) in presence of 2-step irreversible covalent inhibitor relative to product formed the uninhibited control (F^{ctrl}) decreases upon longer incubation. **(C)** Cumulative product F_t (blue line) is ‘contaminated’ with product formed prior to reaching 100% inhibition even if the current enzyme activity (green line) is fully inhibited.

the cumulative product formed during incubation will be ‘contaminated’ with product that was formed before full inhibition was reached. Consequently, incubation time-dependent potency $IC_{50}(t)$ calculated from the fractional product formation F_t/F^{ctrl} against inhibitor concentration will increase with longer incubation times (for slow-binding inhibitors), but will underestimate the potency compared to the values based on the current enzyme activity $[E+ES]/[E]_0$ (**Figure 11C**). $IC_{50}(t)$ does not approach K_i^{app} (2-step reversible inhibition) or $\frac{1}{2}[E]_0$ (irreversible inhibition) at infinite incubation times. An implicit algebraic model based on multipoint $IC_{50}(t)$ values has been derived for 2-step irreversible covalent inhibitors (*Data Analysis 2*).⁸¹ Additionally, a two-point $IC_{50}(t)$ method for 2-step irreversible covalent inhibitors as well as a one-point $IC_{50}(t)$ method for 1-step irreversible covalent inhibitors have been reported in a preprint.⁸⁵ To our knowledge, algebraic methods to calculate K_i^{app} for 2-step reversible covalent inhibitors from (endpoint) $IC_{50}(t)$ values have not been reported.

Data Analysis 2: 2-Step Irreversible Covalent Inhibition.

Krippendorff and co-workers report an algebraic model to calculate k_{inact} and K_i of irreversible covalent inhibitors from the incubation time-dependent potency $IC_{50}(t)$ after multiple incubation times (**Figure 12A**).⁸¹ Detection of cumulative product formation after several incubation times is compatible with continuous assays, but more importantly also with

Data Analysis 2: 2-step IRREV

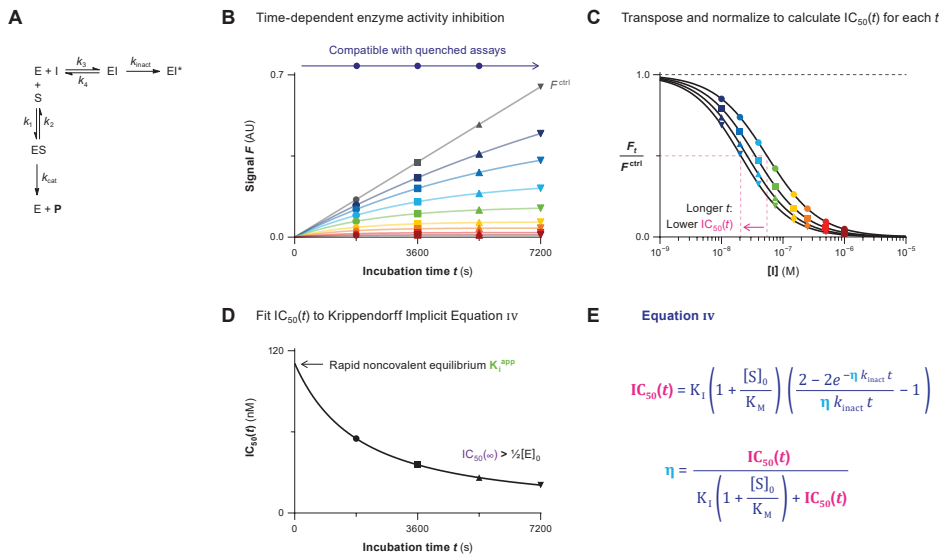


Figure 12 | Data Analysis 2: Incubation time-dependent potency $IC_{50}(t)$ for 2-step irreversible covalent inhibition. Simulated with **KinGen** for 2-step IRREV inhibitor **C** with 1 pM enzyme and 100 nM substrate **S1**. **(A)** Schematic enzyme dynamics during incubation. **(B)** Time-dependent cumulative product formation in absence of inhibitor F^{ctrl} or in presence of inhibitor F_t is detected with longer measurement intervals compatible with quenched assays. **(C)** Incubation time-dependent potency $IC_{50}(t)$ reflects the inhibitor concentration that reduces cumulative product formation during incubation by 50% compared to the uninhibited control. **(D)** Incubation time-dependent potency $IC_{50}(t)$ against incubation time is fitted to **Equation IV**. $IC_{50}(0)$ approaches apparent noncovalent inhibition constant K_i^{app} but $IC_{50}(0)$ is never included in the fit because product formation does not start until initiation of the incubation ($F_0 = F^{ctrl} = 0$). **(E)** Implicit algebraic **Equation IV** derived by Krippendorff *et al.*⁸¹

stopped/quenched assays that require a development step to visualize product formation (**Figure 12B**). Incubation time-dependent potency $IC_{50}(t)$ is calculated for each incubation time from fractional product formation F_t/F^{ctrl} (**Figure 12C**) and plotted against the incubation time (**Figure 12D**). Finally, the authors derived *implicit* algebraic **Equation IV** (shown in **Figure 12E**) to calculate k_{inact} and K_I from the incubation time-dependent potency $IC_{50}(t)$. This method is restricted to substrate-competitive irreversible (multi-step) covalent inhibitors: k_{inact} and K_I do not have a biological meaning for reversible inhibitors or for 1-step covalent inhibitors. This method requires software (e.g. GraphPad Prism) that allows fitting a model defined by an implicit equation (where Y appears on both sides of the equal sign).

Product formation in the uninhibited control should be strictly linear ($k_{ctrl} = 0$): normalization of cumulative product formation (F_t/F^{ctrl}) does not correct for spontaneous loss of enzyme activity or substrate depletion. It is relatively easy to miss violations of this assumption because nonlinearity in the uninhibited control ($k_{ctrl} > 0$) is not evident from visual inspection of the dose-response curves. Violation of this assumption results in a significant underestimation of k_{inact} and K_I values, also when nonlinearity is relatively small ($k_{ctrl} \ll k_{inact}$) (**Figure 13A**). Another

Data Analysis 2: 2-step IRREV

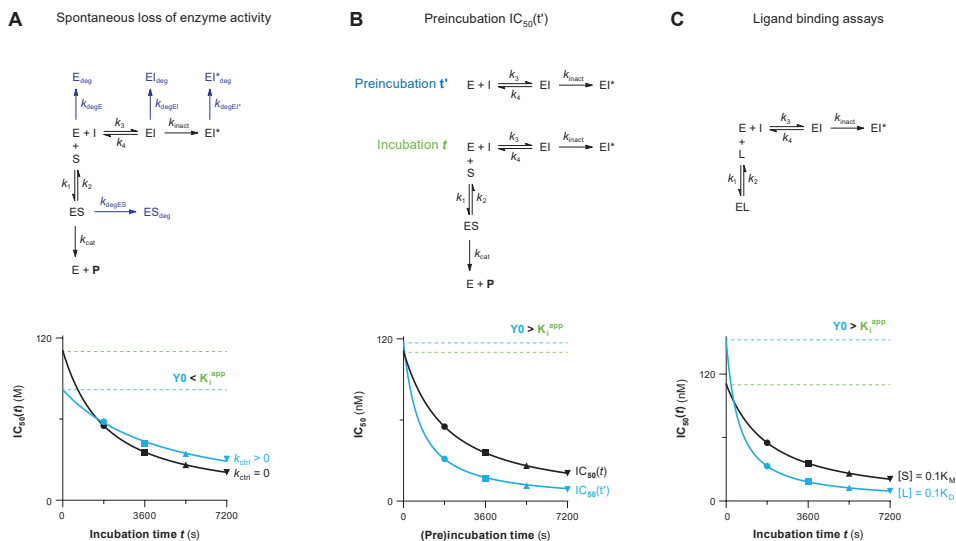


Figure 13 | Data Analysis 2: Experimental/Assay Restrictions. (A) Enzyme degradation/denaturation simulated with **KinDeg** for 2-step IRREV inhibitor **C** with 1 pM enzyme, 100 nM substrate **S1**, and $k_{ctrl} = k_{degE} = k_{degEI} = k_{degEI^*}$ with $k_{ctrl} = 0 \text{ s}^{-1}$ (black) or $k_{ctrl} = 0.0003 \text{ s}^{-1}$ (blue). The rate of inactivation k_{inact} is significantly underestimated and the potency of inactivation constant K_I is overestimated when $k_{ctrl} > 0$. (B) Preincubation time-dependent potency $IC_{50}(t')$ simulated with **KinGen** for 2-step IRREV inhibitor **C** with 1 pM enzyme and 100 nM substrate **S1**. The rate of inactivation k_{inact} is overestimated, resulting in overestimation of the inactivation efficiency k_{inact}/K_I when preincubation-dependent $IC_{50}(t')$ (blue) is fitted instead of incubation-dependent $IC_{50}(t)$ (black). Accurate values for preincubation-dependent potency can be obtained by performing the analysis in *Data Analysis 3A* (details in **Figure 15**). (C) Ligand binding assay simulated with **KinGen** for 2-step IRREV inhibitor **C** with 1 pM enzyme and 100 nM ligand **L1**. The rate of inactivation k_{inact} is overestimated while the potency of inactivation constant K_I is underestimated, resulting in overestimation of the inactivation efficiency k_{inact}/K_I when time-dependent $IC_{50}(t)$ from ligand binding inhibition (blue) is fitted instead of substrate cleavage (black).

important assumption is that the onset of product formation and enzyme inhibition occur simultaneously: inhibition and product formation are both initiated by addition of enzyme, without preincubation of enzyme and inhibitor prior to substrate addition. Unfortunately, numerous publications refer to preincubation of enzyme and inhibitor as ‘incubation’, resulting in the understandable but incorrect fitting of preincubation time-dependent potency $IC_{50}(t')$ to the Krippendorff model (**Figure 13B**).⁸⁵ Preincubation time-dependent potency $IC_{50}(t')$ is calculated from product formation velocity v_t , reflecting the enzyme activity after preincubation rather than cumulative product formation F_t/F^{ctrl} . Enzyme activity v_t is not ‘contaminated’ by product formed prior to read-out because product formation is initiated after preincubation. Furthermore, substrate does not compete with inhibitor for enzyme binding during preincubation. Fitting $IC_{50}(t')$ values to the Krippendorff model resulted in an overestimation of k_{inact} and an overestimation of the overall inactivation potency k_{inact}/K_1 (**Figure 13B**). This method is not compatible with ligand binding competition assays (such as the LanthaScreen kinase binding assay) where inhibitor binding competes with ligand (tracer) binding to form enzyme–ligand complex EL as the detectable product (**Figure 13C**). The enzyme–ligand equilibrium after incubation in presence of inhibitor reflects the current inhibitor competition and is unaffected by binding equilibria prior to read-out (not cumulative). Furthermore, unbound enzyme is not released after formation of product EL, thereby limiting the product formation to a single turnover per enzyme. Fitting $IC_{50}(t)$ values obtained in ligand binding assays to the Krippendorff model result in overestimation of k_{inact} and/or unstable parameters (**Figure 13C**).

METHOD III: Preincubation Time-Dependent Inhibition Without Dilution

Preincubation of enzyme and inhibitor prior to initiation of product formation by addition of substrate is an established method for kinetic analysis of slow-binding (ir)reversible (covalent) inhibitors.^{41, 82} In the benchmark protocol by Ito and co-workers, a low substrate concentration ($[S] \ll K_M$) is added in a relatively small volume ($V_{sub} \ll V_t$) to keep the noncovalent enzyme–inhibitor $E + I \leftrightarrow EI$ equilibrium intact. However, (partial) disruption of the noncovalent equilibrium does not affect the accuracy of preincubation experiments for irreversible inhibition, as is illustrated by *Method IV*. Product formation is inhibited by formation of EI and EI^* during preincubation in absence of competing substrate (**Figure 14A**). Preincubation time-dependent product formation velocity v_t reflects the total inhibition by noncovalent as well as covalent inhibitor binding, and is calculated after a relatively short incubation time ($t \ll t'$) to minimize additional (time-dependent) inhibition of enzyme activity during incubation resultant from enzyme–inhibitor complex/adduct formation during incubation (**Figure 14B**). Enzyme activity after preincubation in the presence of time-dependent inhibitors v_t decreases exponentially from rapid (initial) equilibrium K_i^{app} (Y-intercept: v_i) to reach a plateau at reaction completion ($t' > 5t\%$), corresponding to the steady-state equilibrium ($v_s > 0$) or inactivation ($v_s = 0$) (**Figure 14C**). Observed rate of reaction completion k_{obs} (from enzyme activity without preincubation v_i to final enzyme activity v_s) is obtained by fitting to bounded exponential decay **Equation v** (shown in **Figure 14D**). Importantly, this equation fits enzyme activity v_t rather than directly fitting product signal F .

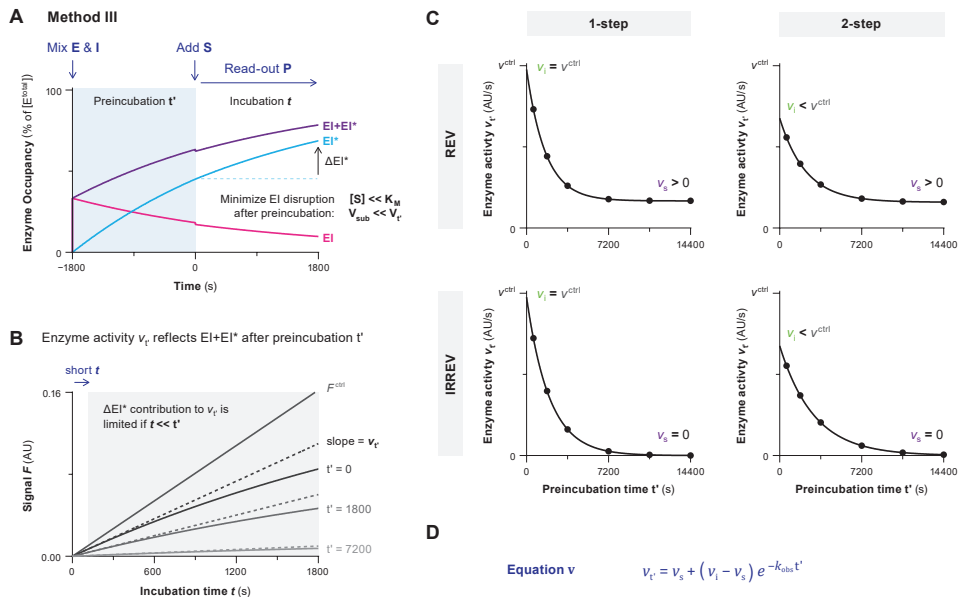


Figure 14 | Method III: Preincubation time-dependent inhibition without dilution. Simulated with **KinGen** for 1 pM enzyme and 100 nM substrate **S1**. **(A)** Enzyme is preincubated with inhibitor to form noncovalent complex EI and covalent adduct EI* in absence of competing substrate, followed by addition of substrate. Addition of a low substrate concentration in a small volume to avoid disruption of the noncovalent $E + I \leftrightarrow EI$ equilibrium. Simulated for 50 nM 2-step IRREV inhibitor **C** with preincubation $t' = 1800$ s. **(B)** Preincubation time-dependent enzyme activity v_t is obtained from the slope of (initial) linear product formation velocity with a short incubation time t relative to preincubation t' to minimize ΔEI^* formation after substrate addition. This measurement is performed separately for each preincubation time, thus requiring more material than incubation time-dependent inhibition protocols with continuous product read-out. Simulated for 50 nM 2-step IRREV inhibitor **C** with preincubation $t' = 0-1800$ s. **(C)** Enzyme activity v_t of time-dependent inhibitors decreases exponentially from rapid (initial) equilibrium K_i^{app} (y -intercept = enzyme activity without preincubation v_i) to reaching reaction completion ($t' > 5t\frac{1}{2}$): inactivation for irreversible inhibitors ($v_s = 0$) and steady-state equilibrium K_i^{*app} for reversible inhibitors ($v_s > 0$). Enzyme activity without preincubation v_i equals the uninhibited enzyme activity v^{ctrl} for 1-step inhibitors and for 2-step inhibitors at non-saturating concentration ($[I] << K_i^{app}$). Simulated for 50 nM 1-step REV inhibitor **A**, 2-step REV inhibitor **B**, 1-step IRREV inhibitor **D**, and 2-step IRREV inhibitor **C**. **(D)** General bounded exponential decay Equation **v** to fit preincubation time-dependent enzyme activity v_t against preincubation time t' . Parameters are constrained depending on the inhibitor binding mode. $v_s = 0$ for irreversible inhibition: inactivation at reaction completion. $v_i = v^{ctrl}$ for 1-step inhibition: noncovalent complex is not significant at non-saturating inhibitor concentrations. v_t = preincubation time-dependent enzyme activity. v_i = enzyme activity based without preincubation. v_s = enzyme activity after preincubation based on reaching reaction completion ($t' > 5t\frac{1}{2}$). t' = preincubation time of enzyme and inhibitor before substrate addition. k_{obs} = observed rate of time-dependent inhibition from initial v_i to final v_s .

Preincubation assays are generally disfavored because their experimental execution requires more material and is more laborious than substrate competition assays with continuous read-out (*Method I* and *II*). Here, substrate has to be added after the indicated preincubation time, thus requiring multiple individual measurements for each inhibitor concentration. However, preincubation experiments are still favored when reaction completion is too slow for detection during the normal time course of a substrate competition assay ($t \ll t\frac{1}{2}$ in *Method I*): substrate competition reduces the (covalent) reaction rate and inhibitor solubility limits the

maximum inhibitor concentration. Instead, preincubation is performed in the absence of competing substrate, thus reaching the maximum reaction rate at a low inhibitor concentration. Therefore, preincubation experiments are frequently conducted for compounds that display 1-step irreversible inhibition behavior because they have a poor noncovalent affinity, such as covalent fragments.⁸ Additionally, preincubation times can exceed the maximum incubation time of progress curve analysis, which is limited by linear product formation ($[P]_t > 0.1[S]_0$), as the onset of product formation does not start until preincubation is completed.

This method is less suitable for enzymatic assays with a relatively slow uninhibited product formation velocity v^{ctrl} , as assay sensitivity might be insufficient to produce enough product signal F_t during a short incubation time. Reaction completion ($t' > 5t^{1/2}$) and/or full inhibition ($v_{t'} = 0$) should not be reached before the first (shortest) preincubation time because it will be impossible to detect time-dependent changes in enzyme activity. This can be resolved by increasing the measurement interval (shorter dt'), reduction of the inhibitor concentration, or selection of a different experimental protocol. This method is compatible with 2-step irreversible inhibition (*Data Analysis 3A*) and 1-step irreversible inhibition (*Data Analysis 3B*), but also with (2-step) reversible inhibition (*Data Analysis 3C*). Algebraic analysis by linear regression to obtain k_{obs} from the (initial) linear slope of LN(enzyme activity) against preincubation time t' is still frequently reported. This is probably because linear regression is part of benchmark protocols for kinetic analysis of preincubation time-dependent enzyme inactivation.⁸²⁻⁸³ It is important to note that these benchmark protocols were published before dedicated data analysis software for nonlinear regression was available.⁶³ Visualization of this 'linear' relationship is possible by plotting the enzyme activity against preincubation time t' on a semilog scale (illustrated in **Figure S2**).

Data Analysis 3A: 2-Step Irreversible Covalent Inhibition.

Data obtained for 2-step irreversible inhibitors (**Figure 15A**) is processed with *Data Analysis Protocol 3*, followed by *Data Analysis Protocol 3Ai* or *3Aii*. Time-dependent product formation is fitted to a straight line for each inhibitor concentration to obtain the enzyme activity after preincubation $v_{t'}$ from the linear (initial) slope (**Figure 15B, left**). It is important that the incubation time be relatively short ($t < 0.1t^{1/2}$) to minimize artifacts caused by significant formation of covalent adduct EI^* after substrate addition (ΔEI^*) because $v_{t'}$ should reflect the enzyme activity at the end of preincubation. As a rule of thumb, incubation time t should be much shorter than the shortest preincubation time t' . A short incubation time may result in insufficient product formation for a robust signal, which can be resolved by increasing the incubation time and obtaining enzyme activity $v_{t'}$ from the initial velocity of the exponential association progress curve, provided that the assay is compatible with progress curve analysis (continuous read-out) (**Figure 15B, right**). Enzyme activity after preincubation $v_{t'}$ is fitted to bounded exponential decay **Equation v** (shown in **Figure 14D**) (constraining $v_s = 0$) for each inhibitor concentration to obtain the observed rate of reaction completion k_{obs} from enzyme activity without preincubation (Y-intercept at v_i) to reaching the final enzyme inactivation (plateau at $v_s = 0$) (**Figure 15C**). Enzyme activity without preincubation in presence of inhibitor v_i is lower than the uninhibited enzyme activity v^{ctrl} for 2-step (ir)reversible inhibitors, because v_i reflects the rapid noncovalent equilibrium (K_i^{app}) after substrate addition.⁴¹ The

plot of inhibitor concentration-dependent k_{obs} reaches maximum rate of inactivation k_{inact} in presence of saturating inhibitor concentration ($[I] \gg K_I$) with the Y-intercept at $k_{\text{ctrl}} = 0$ when uninhibited enzyme activity v^{ctrl} is independent of preincubation time (**Figure 15D**). Inhibitor concentrations should correspond with the inhibitor concentration during preincubation (rather than after substrate addition). Correction of inactivation constant K_I for substrate competition is not necessary because preincubation is performed in absence of substrate. The rapid noncovalent $E + I \leftrightarrow EI$ equilibrium does not significantly contribute to inhibition at non-saturating inhibitor concentrations ($[I] \ll K_I^{\text{app}}$), resulting in 1-step binding behavior (illustrated in **Figure 3F**). This will be apparent from the observation that initial velocity v_i is independent of inhibitor concentration ($v_i = v^{\text{ctrl}}$) along with a linear plot of k_{obs} against $[I]$. This is resolved either by increasing the inhibitor concentration or performing *Data Analysis 3B*. Increasing the substrate concentration can resolve issues with assay sensitivity associated with short incubation times, as this will result in a higher product signal. However, substrate addition in a relatively large volume ($V_{\text{sub}} > 0.1V_t$) and/or addition of a competitive substrate concentration

Data Analysis 3A: 2-step IRREV

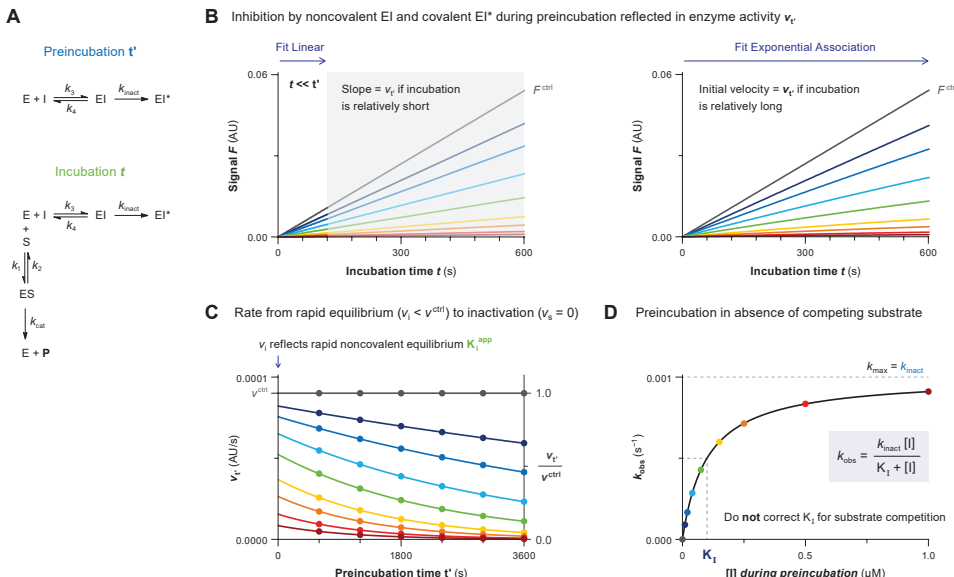


Figure 15 | Data Analysis 3A: Preincubation time-dependent inhibition without dilution for 2-step irreversible covalent inhibition. Simulated with **KinGen** for 2-step IRREV inhibitor **C** with 1 pM enzyme and 100 nM substrate **S1**. **(A)** Schematic enzyme dynamics during preincubation in absence of substrate and during incubation after substrate addition. **(B)** Time-dependent product formation after preincubation in absence of inhibitor F^{ctrl} or in presence of inhibitor ($t' = 1800$ s). *Left:* Enzyme activity after preincubation v_t is obtained from the linear slope if the incubation time is relatively short ($t \ll t'$): gray area is excluded from the fit. *Right:* Enzyme activity after preincubation v_t is obtained from the initial velocity of the exponential association progress curve of each inhibitor concentration. **(C)** Preincubation time-dependent enzyme activity v_t is fitted to **Equation V** (shown in **Figure 14D**) (constraining $v_s = 0$) for each inhibitor concentration to obtain observed rates of inactivation k_{obs} . Alternatively, v_t can be normalized to a fraction of the uninhibited enzyme activity v^{ctrl} . **(D)** Inhibitor concentration-dependent k_{obs} reaches k_{inact} at saturating inhibitor concentration ($k_{\text{max}} = k_{\text{inact}}$). Half-maximum $k_{\text{obs}} = \frac{1}{2}k_{\text{inact}}$ is reached when inhibitor concentration equals the inactivation constant K_I . v_t reflects the enzyme activity after preincubation in absence of competing substrate.

($[S] > 0.1K_M$) causes (partial) disruption of the reversible equilibrium, although this does not affect the accuracy of k_{obs} for irreversible inhibitors. In fact, disruption of the noncovalent complex can be employed to detect covalent adduct formation of 2-step irreversible inhibitors that exhibit tight-binding behavior resulting from very potent noncovalent inhibition,⁷⁵⁻⁷⁶ as will be discussed in *Method IV*.

Uninhibited enzyme activity v^{ctrl} decreases when preincubation is long enough for significant spontaneous enzyme degradation ($t' \gg 0.1t^{1/2}$) (Figure 16A-B). A simple algebraic correction for spontaneous enzyme degradation results in good estimates for k_{inact} and K_I if all enzyme species have the same first order enzymatic degradation rate ($k_{degE} = k_{degES} = k_{degEI}$) (Figure 16C). Alternatively, normalizing the enzyme activity v_t to uninhibited enzyme activity v_t^{ctrl} at each preincubation time corrects for enzyme degradation (Figure 16D), and k_{obs} obtained from normalized enzyme activity v_t/v^{ctrl} results in good estimates of k_{inact} and K_I without further correction (Figure 16E).

Data Analysis 3A: 2-step IRREV

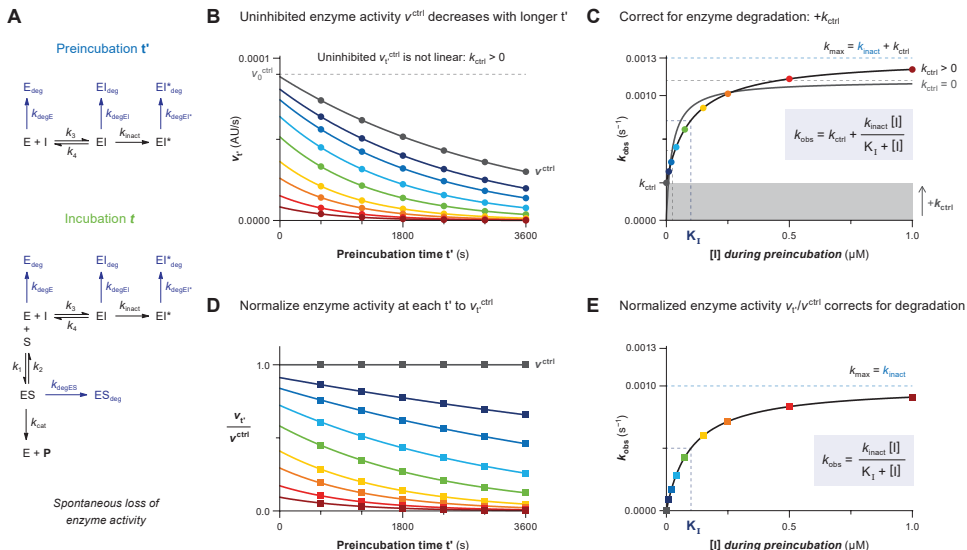


Figure 16 | Data Analysis 3A: Corrections for spontaneous loss of enzyme activity (2-step IRREV). Simulated with KinDeg for 2-step IRREV inhibitor C with 1 pM enzyme, 100 nM substrate S1, and $k_{degE} = k_{degES} = k_{degEI} = 0.0003\text{ s}^{-1}$. (A) Schematic enzyme dynamics during preincubation in absence of substrate and during incubation after substrate addition with spontaneous enzyme degradation/denaturation. (B) Uninhibited enzyme activity after preincubation v_t^{ctrl} is not linear. Preincubation time-dependent enzyme activity v_t is fitted to Equation V (shown in Figure 14D) (constraining $v_s = 0$) for each inhibitor concentration to obtain observed rates of inactivation k_{obs} , as well as fitting uninhibited activity v_t^{ctrl} to obtain the rate of nonlinearity k_{ctrl} . (C) Inhibitor concentration-dependent k_{obs} with spontaneous enzyme degradation increases with k_{ctrl} but the span from k_{min} ($= k_{ctrl}$) to k_{max} ($= k_{inact} + k_{ctrl}$) still equals k_{inact} . Fit with algebraic correction for nonlinearity (black line, $k_{ctrl} > 0$). Ignoring the nonlinearity (gray line, constrain $k_{ctrl} = 0$) results in underestimation of K_I (overestimation of potency) and overestimation of k_{inact} . (D) Normalized enzyme activity v_t/v^{ctrl} is fitted to Equation V (shown in Figure 14D) (constraining $v_s = 0$) for each inhibitor concentration to obtain corrected observed rates of inactivation k_{obs} . (E) Inhibitor concentration-dependent k_{obs} has been corrected for enzyme degradation by fitting normalized enzyme activity v_t/v^{ctrl} and does not require further corrections.

Data Analysis 3B: 1-Step Irreversible Covalent Inhibition.

Data obtained for 1-step irreversible inhibitors (**Figure 17A**) is processed with *Data Analysis Protocol 3*, followed by *Data Analysis Protocol 3Bi* or *3Bii*. Time-dependent product formation is fitted to a straight line for each inhibitor concentration to obtain the enzyme activity after preincubation v_t from the linear slope (**Figure 17B, left**). Incubation must be short enough to minimize formation of covalent adduct EI^* after substrate addition ($t \ll t^{1/2}$); otherwise k_{chem} will be overestimated. Similar to *Data Analysis 3A*, preincubation-dependent enzyme activity v_t can also be obtained from the initial velocity of the exponential association progress curve, provided that the read-out is continuous (**Figure 17B, right**). Enzyme activity after preincubation v_t (**Figure 17C**) is fitted to bounded exponential decay **Equation v** (shown in **Figure 14D**) to obtain observed rate of reaction completion k_{obs} from uninhibited enzyme activity without preincubation (Y -intercept at $v_i = v^{\text{ctrl}}$) to reaching the final enzyme inactivation (constraining $v_s = 0$). Inhibited enzyme activity without preincubation is equal to uninhibited enzyme activity ($v_i = v^{\text{ctrl}}$), as rapid noncovalent inhibitor binding does not contribute to

Data Analysis 3B: 1-step IRREV

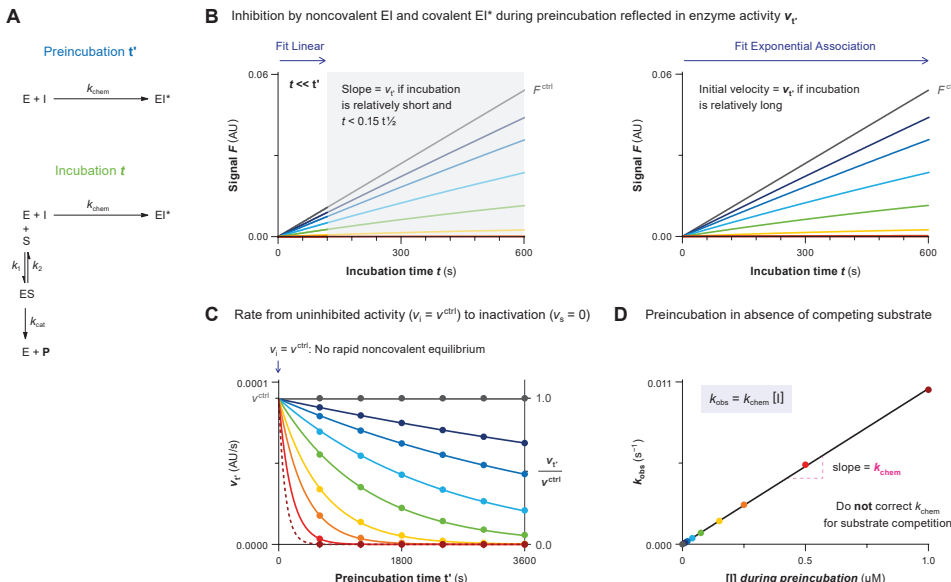


Figure 17 | Data Analysis 3B: Preincubation time-dependent inhibition without dilution for 1-step irreversible covalent inhibition. Simulated with **KinGen** for 1-step IRREV inhibitor **D** with 1 pM enzyme and 100 nM substrate **S1**. **(A)** Schematic enzyme dynamics during preincubation in absence of substrate and during incubation after substrate addition. **(B)** Time-dependent product formation after preincubation in absence of inhibitor F^{ctrl} or in presence of inhibitor ($t' = 1800$ s). *Left*: Enzyme activity after preincubation v_t is obtained from the linear slope if the incubation time is relatively short ($t \ll t'$): gray area is excluded from the fit. *Right*: Enzyme activity after preincubation v_t is obtained from the initial velocity of the exponential association progress curve of each inhibitor concentration. **(C)** Preincubation time-dependent enzyme activity v_t is fitted to **Equation v** (shown in **Figure 14D**) (constraining $v_s = 0$) for each inhibitor concentration to obtain observed rates of inactivation k_{obs} . $v_i = v^{\text{ctrl}}$ for 1-step irreversible inhibitors and 2-step irreversible inhibitors at non-saturating concentrations ($[I] \ll K_{\text{app}}$). Alternatively, v_t can be normalized to a fraction of the uninhibited enzyme activity v^{ctrl} . **(D)** Inhibitor concentration-dependent k_{obs} increases linearly with inhibitor concentration, with k_{chem} as the slope. v_t reflects the enzyme activity after preincubation in absence of competing substrate.

enzyme inhibition by 1-step irreversible inhibitors. The slope of the linear plot of k_{obs} against inhibitor concentration during preincubation is equal to k_{chem} (Figure 17D), which should not be corrected for substrate competition as preincubation is performed in absence of competing substrate. Substrate addition in a relatively large volume ($V_{sub} > 0.1V_t$) and/or addition of a competitive substrate concentration ($[S] > 0.1K_M$) does not significantly affect the accuracy of k_{obs} because 1-step irreversible inhibition does not involve a rapid noncovalent equilibrium that can be disrupted (also see *Method IV*). Increasing the substrate concentration can resolve issues with assay sensitivity: higher substrate concentration results in a higher product concentration after the same incubation time ($v^{ctrl} = V_{max}[S]/([S]+K_M)$), which in turn will result in a better signal to noise ratio.

Uninhibited enzyme activity v^{ctrl} decreases with longer preincubation due to spontaneous enzyme degradation (Figure 18A-B). This especially affects assays where preincubation is long

Data Analysis 3B: 1-step IRREV

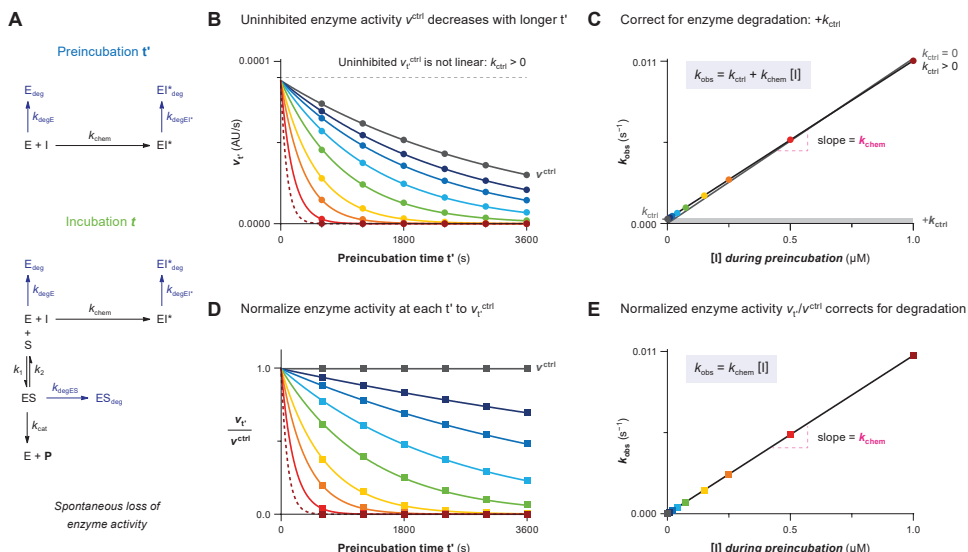


Figure 18 | Data Analysis 3B: Corrections for spontaneous loss of enzyme activity (1-step IRREV). Simulated with KinDegr for 1-step IRREV inhibitor D with 1 pM enzyme, 100 nM substrate S1, and $k_{degE} = k_{degES} = k_{degEI} = 0.0003 s^{-1}$. (A) Schematic enzyme dynamics during preincubation in absence of substrate and during incubation after substrate addition with spontaneous enzyme degradation/denaturation. (B) Uninhibited enzyme activity after preincubation v_t^{ctrl} is not linear: $k_{ctrl} > 0$. Preincubation time-dependent enzyme activity v_t is fitted to Equation V (shown in Figure 14D) (constraining $v_s = 0$ and shared value for v_i = uninhibited enzyme activity without preincubation v_0^{ctrl}) for each inhibitor concentration to obtain observed rates of inactivation k_{obs} , as well as fitting uninhibited activity v_t^{ctrl} to obtain the rate of nonlinearity k_{ctrl} . (C) Inhibitor concentration-dependent k_{obs} with spontaneous enzyme degradation/denaturation increases by k_{ctrl} . Fit with algebraic correction for nonlinearity (black line, $k_{ctrl} > 0$) or ignoring nonlinearity (gray line, constrain $k_{ctrl} = 0$). Ignoring the nonlinearity (assuming Y-intercept = 0) results in overestimation of k_{chem} (steeper slope). (D) Normalized enzyme activity v_t/v_t^{ctrl} is fitted to Equation V (shown in Figure 14D) (constraining $v_s = 0$ and Y-intercept = $v_t/v_0^{ctrl} = 1$) for each inhibitor concentration to obtain corrected observed rates of inactivation k_{obs} . (E) Inhibitor concentration-dependent k_{obs} has been corrected for enzyme degradation/denaturation by fitting normalized enzyme activity v_t/v_t^{ctrl} and does not require further corrections.

enough for significant enzyme degradation ($t' > 0.1t^{1/2}$). Algebraic correction for spontaneous enzyme degradation ($k_{\text{degE}} = k_{\text{degES}}$) in the secondary k_{obs} plot is relatively simple (Figure 18C). Alternatively, correction for enzyme degradation is performed by normalizing enzyme activity v_t to uninhibited enzyme activity v_t^{ctrl} at each preincubation time (Figure 18D-E). Stabilization of enzyme upon inhibitor binding ($k_{\text{degEI}^*} < k_{\text{degE}}$) does not affect k_{obs} , as EI^* formation is already irreversible thus removing the species from the available pool of catalytic enzyme.

Data Analysis 3C: 2-step Reversible Covalent Inhibition.

Data obtained for 2-step reversible inhibitors (Figure 19A) is processed with *Data Analysis Protocol 3*, followed by *Data Analysis Protocol 3C*. Time-dependent product formation is

Data Analysis 3C: 2-step REV

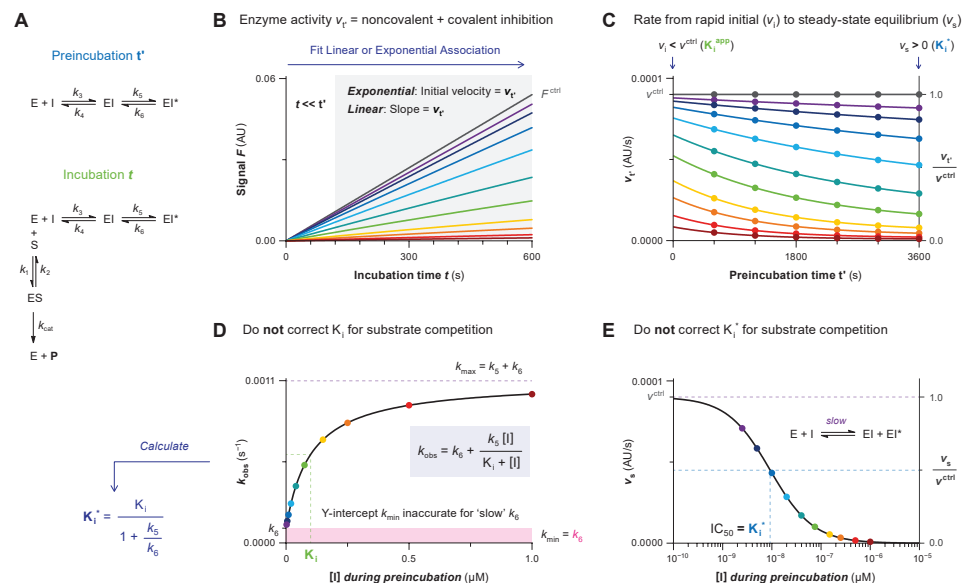


Figure 19 | Data Analysis 3C: Preincubation time-dependent inhibition without dilution for 2-step reversible covalent inhibition. Simulated with *KinGen* for 2-step REV inhibitor B with 1 pM enzyme and 100 nM substrate S1. (A) Schematic enzyme dynamics during preincubation in absence of substrate and during incubation after substrate addition. (B) Time-dependent product formation after preincubation in absence of inhibitor F^{ctrl} or in presence of inhibitor ($t' = 1800$ s). Enzyme activity after preincubation v_t is obtained from the linear slope if the incubation time is relatively short ($t \ll t'$): gray area is excluded from the fit. Alternatively, enzyme activity after preincubation v_t is obtained from the initial velocity of the exponential association progress curve of each inhibitor concentration. (C) Preincubation time-dependent enzyme activity v_t is fitted to Equation V (shown in Figure 14D) for each inhibitor concentration to obtain observed rates of inactivation k_{obs} and steady-state velocity v_s (plateau > 0). Alternatively, v_t can be normalized to a fraction of the uninhibited enzyme activity v_t^{ctrl} . (D) Inhibitor concentration-dependent k_{obs} equals k_{max} at saturating inhibitor concentration ($k_{\text{max}} = k_6 + k_5$) and approaches k_6 in absence of inhibitor ($k_{\text{min}} = k_5$). Half-maximum $k_{\text{obs}} = k_{\text{min}} + \frac{1}{2}(k_{\text{max}} - k_{\text{min}}) = k_6 + \frac{1}{2}k_5$ is reached when inhibitor concentration equals the inhibition constant K_i . Steady-state inhibition constant K_i^* calculated from the fitted values of k_5 , k_6 , and K_i is thus very sensitive to errors and (non)linearity in the uninhibited background (illustrated in Figure 9C). No correction: v_t reflects the enzyme activity after preincubation in absence of competing substrate. (E) Steady-state inhibition constant K_i^* corresponds with the IC_{50} of steady-state velocity v_s obtained by fitting the dose-response curve to the Hill equation.³³ No correction: v_t reflects the enzyme activity after preincubation in absence of competing substrate.

fitted to a straight line for each inhibitor concentration to obtain the enzyme activity after preincubation v_t from the linear slope (**Figure 19B**). Again, it is important that the incubation time be much shorter than the shortest preincubation time t' ($t \ll t'$), but enzyme activity v_t can also be calculated from the initial velocity of the exponential association progress curve, provided that the assay is compatible with progress curve analysis (continuous read-out). Enzyme activity after preincubation v_t is fitted to bounded exponential decay **Equation v** (shown in **Figure 14D**) for each inhibitor concentration to obtain observed rate of reaction completion k_{obs} from rapid noncovalent equilibrium (Y-intercept at $v_i < v^{ctrl}$) to slowly reaching steady-state equilibrium (plateau at $v_s > 0$) (**Figure 19C**). Enzyme activity without preincubation in presence of inhibitor v_i is lower than the uninhibited enzyme activity v^{ctrl} for 2-step (ir)reversible inhibitors because v_i reflects the rapid noncovalent equilibrium (K_i^{app}) after substrate addition.⁴¹ Contrary to irreversible inhibition, the plateau ($v_s > 0$) does not approximate enzyme inactivation but reaches the steady-state equilibrium (K_i^*) instead.

Steady-state inhibition constant K_i^* can be calculated from the fitted values of K_i , k_5 and k_6 (**Figure 19D**), but this is not the preferred approach as a small error in k_6 has huge implications for the calculation of K_i^* (as illustrated in **Figure 9C**). Generally, more reliable estimates of the steady-state inhibition constant K_i^* are generated from dose-response curves of steady-state velocity v_s against inhibitor concentration during preincubation (**Figure 19E**). Steady-state inhibition constant K_i^* reflects the reversible $E + I \leftrightarrow EI + EI^*$ equilibrium that can be disrupted by substrate addition in a relatively large volume ($V_{sub} > 0.1V_t$) and/or addition of a competitive substrate concentration ($[S] > 0.1K_M$). Simulations with high substrate concentration ($[S] = 10K_M$) show that the IC_{50} of the dose-response curve for steady-state velocity v_s was slightly higher than steady-state inhibition constant K_i^* , but still significantly lower than K_i^{app} , as covalent dissociation will not be significant provided the incubation time is significantly shorter than the dissociation half-life ($t \ll t_{1/2,diss}$). Altogether, fitting exponential association rather than increasing the substrate concentration is the desired solution to resolve issues with assay sensitivity associated with short incubation times. Alternatively, reasonable estimates of the steady-state inhibition constant K_i^* were obtained from the endpoint preincubation time-dependent potency $IC_{50}(t')$ with minimal substrate competition ($[S] \ll K_M$) and preincubation times exceeding the required time to reach reaction completion at all inhibitor concentrations ($t' > 5t_{1/2}$).

As mentioned before, spontaneous loss of enzyme activity (**Figure 20A**) due to first order degradation and/or denaturation of enzyme species ($k_{degE} = k_{degES} = k_{degEI}$) results in a preincubation time-dependent decrease of uninhibited enzyme activity v^{ctrl} (**Figure 20B**). The biggest advantage of *Method III (Data Analysis 3C)* over *Method I (Data Analysis 1C)* is that it is possible to perform an algebraic correction for the enzyme instability in kinetic analysis of 2-step reversible covalent inhibitors with *Data Analysis 3C*. Enzyme activity v_t is normalized to uninhibited enzyme activity v_t^{ctrl} at each preincubation time (**Figure 20C**), and the normalized enzyme activity after preincubation v_t/v^{ctrl} is fitted to bounded exponential decay **Equation v** (shown in **Figure 14D**) for each inhibitor concentration to obtain observed rate of reaction completion k_{obs} and steady-state velocity v_s . Kinetic analysis of k_{obs} (**Figure 20D**) and steady-state velocity v_s (**Figure 20E**) against inhibitor concentration during preincubation result in

Data Analysis 3C: 2-step REV

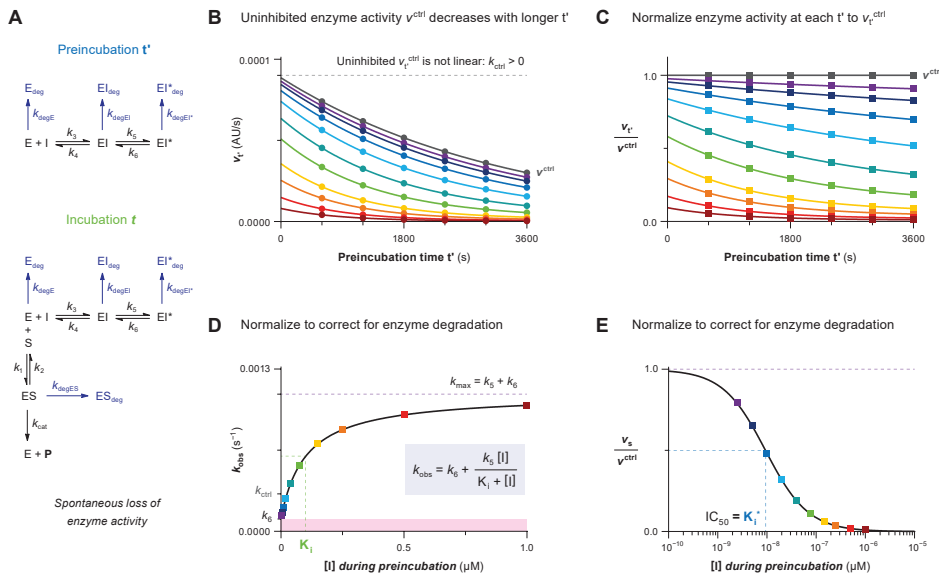


Figure 20 | Data Analysis 3C: Corrections for spontaneous loss of enzyme activity (2-step REV). Simulated with KinDeg for 2-step REV inhibitor B with 1 pM enzyme, 100 nM substrate S1, and $k_{\text{degE}} = k_{\text{degES}} = k_{\text{degEI}} = 0.0003 \text{ s}^{-1}$. (A) Schematic enzyme dynamics during preincubation in absence of substrate and during incubation after substrate addition with spontaneous enzyme degradation. (B) Uninhibited enzyme activity after preincubation v_t^{ctrl} is not linear. Fitting preincubation time-dependent enzyme activity v_t to Equation V (shown in Figure 14D) for each inhibitor concentration gives observed rates of inactivation k_{obs} , as well as the rate of nonlinearity k_{ctrl} for uninhibited activity v_t^{ctrl} . Inhibitor concentration-dependent k_{obs} and steady-state velocity v_s will be driven by spontaneous enzyme degradation if enzyme activity is not normalized. (C) Enzyme activity v_t is normalized to the uninhibited enzyme activity v_t^{ctrl} after each preincubation time before fitting to Equation V (shown in Figure 14D). (D) Inhibitor concentration-dependent k_{obs} has been corrected for enzyme degradation/denaturation by fitting normalized enzyme activity v_t/v_t^{ctrl} and does not require further corrections (even if $k_{\text{ctrl}} > k_6$). (E) Steady-state velocity v_s has been corrected for enzyme degradation/denaturation by fitting normalized enzyme activity v_t/v_t^{ctrl} and does not require further corrections (even if $k_{\text{ctrl}} > k_6$). Final velocity v_s obtained from uncorrected v_t is ‘contaminated’ by the contribution of irreversible inactivation to the time-dependent inhibition, and does not result in accurate estimates of steady-state inhibition constant K_i^* (illustrated in Figure 9D).

good estimates of the kinetic parameters without further correction, even when k_{ctrl} is faster than the covalent dissociation rate k_6 ($k_{\text{ctrl}} > k_6$). We strongly advise that enzyme activity be normalized prior to analysis of reversible covalent inhibition even when k_{ctrl} is not directly obvious from the uninhibited control v_t^{ctrl} .

METHOD IV: Preincubation Time-Dependent Inhibition With Dilution/Competition

Preincubation time-dependent inhibition with dilution and/or competition is a variant of *Method III* reported for kinetic analysis of irreversible covalent inhibitors (Figure 21).⁸³ Enzyme and inhibitor are preincubated in absence of competing substrate to form noncovalent EI complex and covalent EI* adduct, followed by dilution in a 10-100× larger volume ($V_{\text{sub}} \gg V_t$)

and/or addition of a high concentration of competing substrate ($[S] \gg K_M$) (**Figure 21A**). The inhibitor concentration after substrate addition is far below the equilibrium concentration ($[I]_t \ll 0.1K_i^{\text{app}}$), thereby inducing dissociation of inhibitor from the noncovalent enzyme-inhibitor complex EI and quenching the formation of covalent EI* during incubation ($\Delta[\text{EI}^*]_t = 0$). The approach is two-pronged: either dilution (reducing $[I]_t$) or saturating substrate concentration (increasing K_i^{app} and decreasing $k_{\text{chem}}^{\text{app}}$) can be sufficient as long as covalent EI* adduct formation is fully quenched, for example by dissociation of noncovalent EI complex. Preincubation time-dependent product formation velocity v_t reflects the inhibition by covalent EI* adduct formed during preincubation, and is calculated from the linear slope of product formation (**Figure 21B**). Enzyme activity v_t decreases exponentially from 0% covalent adduct without preincubation (Y -intercept = v^{ctrl}) to reach a plateau at 100% covalent adduct upon reaction completion ($t' > 5t_{1/2}$) for irreversible covalent inhibitors (**Figure 21C**). Observed rate of reaction completion k_{obs} (from 0-100% inhibition) is obtained by fitting to bounded exponential decay **Equation VI** (shown in **Figure 21D**). This is a simplified version of **Equation v** (shown in **Figure 14D**) in *Method III* (constraining $v_s = 0$) because we only consider 2-step irreversible inhibition (*Data Analysis 4A*) and 1-step irreversible inhibition (*Data Analysis 4B*). Reversible (2-step) covalent inhibition with a slow rate of covalent dissociation k_6 ($t_{1/2\text{diss}} = \text{LN}(2)/k_6$) can be analyzed with preincubation dilution assays using the initial product formation velocity after rapid/jump dilution^{29, 33} but will not be discussed here because the (slow) dissociation of covalent EI* adduct may complicate algebraic analysis.

Generally, preincubation assays are disfavored because their experimental execution requires more material and measurements than incubation assays with continuous read-out. However, as already mentioned in *Method III*, preincubation methods are favored for inhibitors that have a slow covalent reaction rate and/or a poor noncovalent affinity. Additionally, dilution in excess substrate can resolve issues for enzyme assays that do not generate enough product for a robust signal (slow v^{ctrl}), as the maximum incubation time to calculate v_t is not limited by formation of EI* during incubation ($\Delta[\text{EI}^*]_t = 0$): incubation time can be longer than preincubation time. It is important to mention that there is still a limit to the incubation time: competition and/or dilution cannot fully mitigate the covalent adduct formation reaction, but it can be reduced to a negligible rate during the incubation. Finally, this method allows the assessment of covalent adduct formation potency without contamination by reversible inhibition. This can be beneficial in the analysis of 2-step covalent inhibitors that exhibit tight-binding behavior (customary for kinase inhibitors that have to compete with ATP): very potent noncovalent affinity 'shields' or 'contaminates' the rate of covalent adduct formation in the other protocols but not in this method, as detection is based solely on inhibition by covalent EI* adduct. However, the enzyme concentration during incubation is much lower than during preincubation, and inhibitor has to be present in excess during preincubation (*pseudo-first order conditions*), thus limiting the inhibitor concentration to higher concentrations than with other methods, which might be impractical. Be aware that dilution in (excess) substrate will change the absolute enzyme/inhibitor concentrations from preincubation to incubation, and make sure to calculate the desired enzyme concentration during incubation accordingly. Reaction completion ($v_t < 0.1v^{\text{ctrl}}$) should not be reached before the first (shortest) preincubation time

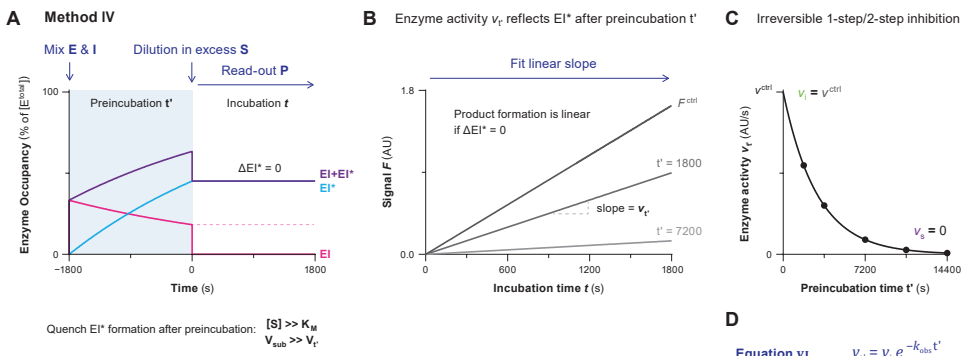


Figure 21 | Method IV: Preincubation time-dependent inhibition with dilution/competition. Simulated with **KinVol** for 100 pM enzyme and 50 nM inhibitor **C** (before dilution) in $V_t = 1$, and 10 μ M substrate **S1** in $V_{sub} = 99$; corresponding with 100-fold dilution in excess substrate ($[S] = 10K_M$). **(A)** Enzyme is preincubated with inhibitor to form noncovalent complex EI and covalent adduct EI^* in absence of competing substrate, followed by dilution in excess substrate. Initial noncovalent EI complex forms rapidly ($[EI]_t/K_i = 0.5$) but fully dissociates upon dilution in a large volume ($V_{sub} \gg V_t$) and/or addition of a high concentration of competing substrate ($[S] > K_M$), as the $E + I \leftrightarrow EI$ equilibrium has shifted towards fully unbound enzyme ($[I]_t/K_i^{app} \ll 0.1$). **(B)** Preincubation time-dependent enzyme activity v_t is obtained from the (linear) slope of product formation velocity. Dilution in excess substrate quenches EI^* formation after substrate addition ($\Delta EI^* = 0$), thus enabling longer incubation times compared to *Method III*. This measurement must be performed separately after each preincubation time. **(C)** Enzyme activity v_t decreases exponentially from 0% covalent adduct (y -intercept = enzyme activity without preincubation v_i) to 100% covalent adduct ($v_s = 0$). Enzyme activity without preincubation v_i equals the uninhibited enzyme activity v^{ctrl} for 1-step as well as 2-step irreversible inhibitors: dilution in excess substrate should induce full dissociation of noncovalently bound inhibitor ($[I]_t \ll 0.1K_i^{app}$), and covalent adduct does not form instantly. **(D)** Bounded exponential decay **Equation VI** to fit preincubation time-dependent enzyme activity v_t after dilution in (excess) competing substrate against preincubation time t' for irreversible 1-step and 2-step inhibition. This is a simplified version of **Equation V** (shown in **Figure 14D**): constraining $v_s = 0$ (inactivation at reaction completion). v_i = enzyme activity without preincubation = uninhibited enzyme activity v^{ctrl} because covalent adduct has not yet been formed and noncovalent complex has been disrupted by dilution in excess substrate. v_t = preincubation time-dependent enzyme activity reflecting covalent EI^* adduct formed. t' = preincubation time of enzyme and inhibitor before substrate addition. k_{obs} = observed rate of time-dependent inhibition from initial v_i to final v_s .

because it will be impossible to detect time-dependent changes in enzyme activity. This can be resolved by increasing the measurement interval (shorter dt') or reducing the inhibitor concentration whenever possible. This method is less suitable for inhibitors with a very fast covalent adduct formation k_{inact} because preincubation is performed in absence of competing substrate (thus allowing the maximum rate of covalent adduct formation possible at this inhibitor concentration).

Data Analysis 4A: 2-Step Irreversible Covalent Inhibition.

Data obtained for 2-step irreversible inhibitors (**Figure 22A**) is processed with *Data Analysis Protocol 4*, followed by *Data Analysis Protocol 4Ai* or *4Aii*. Kinetic analysis of enzyme activity with dilution/competition after preincubation in the presence of a 2-step covalent inhibitor is similar to data analysis of preincubation without dilution/competition (*Data Analysis 3A*), with the exception that longer incubation times are possible to calculate

Data Analysis 4A: 2-step IRREV

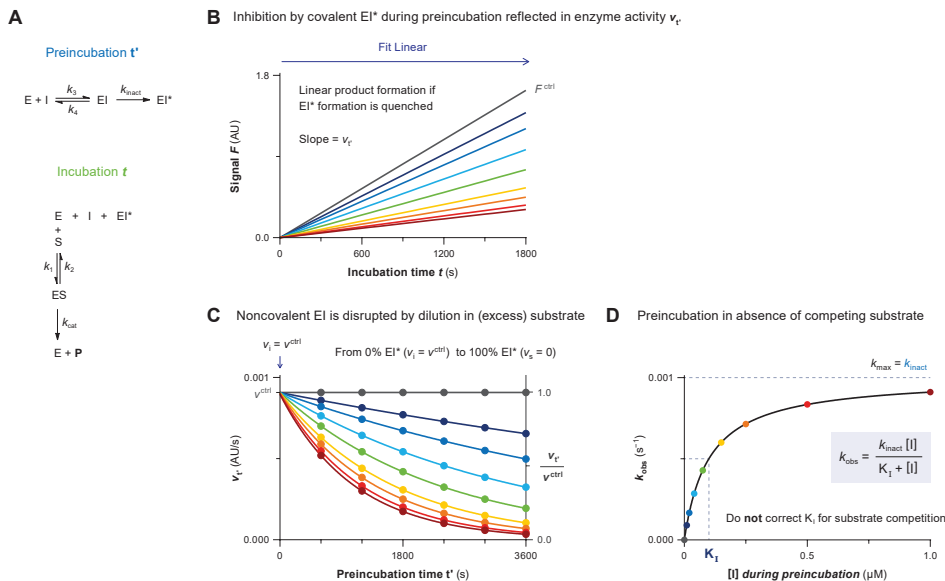


Figure 22 | Data Analysis 4A: Preincubation time-dependent inhibition with dilution/competition for 2-step irreversible covalent inhibition. Simulated with **KinVol** for 2-step IRREV inhibitor **C** with 100 pM enzyme in $V_t = 1$ ($[E^{\text{total}}]_{t'} = 100$, $[E^{\text{total}}]_t = 1$), and 10 μM substrate **S1** ($[S] = 10K_M$) in $V_{\text{sub}} = 99$. **(A)** Schematic enzyme dynamics during preincubation in absence of substrate and during incubation after dilution in excess substrate. **(B)** Time-dependent product formation after preincubation ($t' = 1800$ s) in absence of inhibitor F^{ctrl} or in presence of various inhibitor concentrations. Enzyme activity after preincubation v_t is obtained from the linear slope. **(C)** Preincubation time-dependent enzyme activity v_t is fitted to **Equation VI** (shown in **Figure 21D**) for each inhibitor concentration with global shared value for v_i ($v_i = v^{\text{ctrl}}$) to obtain observed rates of inactivation k_{obs} . Alternatively, v_t can be normalized to a fraction of the uninhibited enzyme activity v^{ctrl} . **(D)** Half-maximum $k_{\text{obs}} = \frac{1}{2}k_{\text{inact}}$ is reached when inhibitor concentration during preincubation equals the inactivation constant K_I . No correction for substrate competition: v_t reflects the remaining unbound/noncovalent enzyme activity after preincubation in absence of competing substrate.

enzyme activity v_t from the slope (**Figure 22B**), and enzyme activity without preincubation v_i should be equal to the uninhibited enzyme activity v^{ctrl} (**Figure 22C**). Contrary to *Method III*, this does not imply that the inhibitors show 1-step behavior: it merely confirms that extensive dilution/substrate competition successfully induced inhibitor dissociation from noncovalent EI complex to unbound enzyme. It is essential to plot the rate of covalent adduct formation k_{obs} against the inhibitor concentration during preincubation (**Figure 22D**) to obtain kinetic parameters: k_{obs} is based on the formation of EI^* during preincubation, and the inhibitor concentration during preincubation is much higher than the inhibitor concentration after dilution in substrate ($[I]_{t'} \gg [I]_t$). Insufficient dilution/competition will partially disrupt noncovalent EI complex, resulting in a time-dependent decrease of enzyme activity due to formation of EI^* after substrate addition, and deviation from $v_i = v^{\text{ctrl}}$, as noncovalent complex EI contributes to inhibition without preincubation. Increasing substrate concentration and/or

Data Analysis 4A: 2-step IRREV

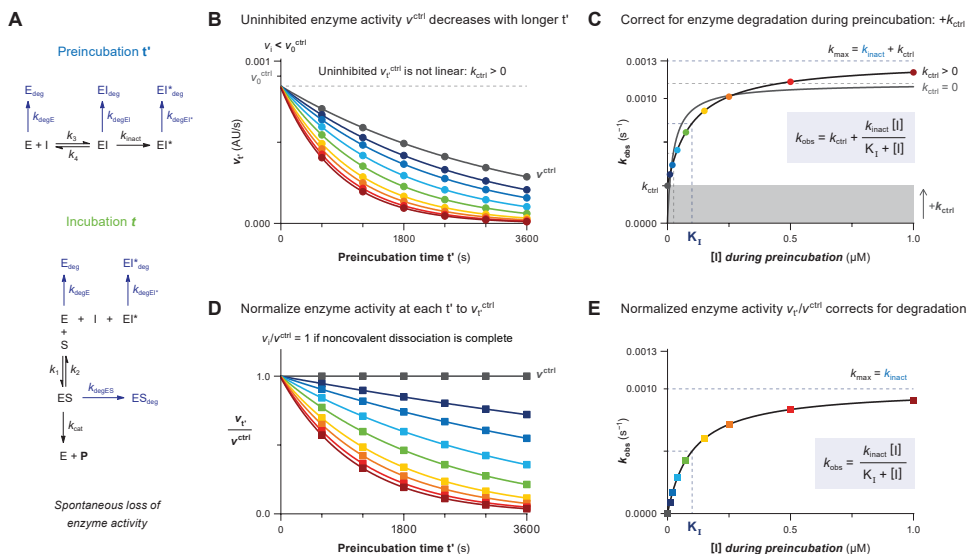


Figure 23 | Data Analysis 4A: Corrections for spontaneous loss of enzyme activity (2-step IRREV). Simulated with KinVolDeg for 2-step IRREV inhibitor C with 100 pM enzyme in $V_t = 1$ ($[E^{\text{total}}]_t = 100$, $[E^{\text{total}}]_t = 1$), and 10 μM substrate S1 ($[S] = 10K_M$) in $V_{\text{sub}} = 99$, and $k_{\text{degr}} = k_{\text{degES}} = k_{\text{degEI}} = 0.0003 \text{ s}^{-1}$. **(A)** Schematic enzyme dynamics during preincubation in absence of substrate and during incubation after dilution in excess substrate with spontaneous enzyme degradation/denaturation. **(B)** Uninhibited enzyme activity after preincubation v_t^{ctrl} decreases with longer preincubation. Enzyme activity v_t is fitted to Equation VI (shown in Figure 21D) for each inhibitor concentration during preincubation with globally shared value for v_i ($v_i = v_0^{\text{ctrl}}$) to obtain observed rates of inactivation k_{obs} , as well as fitting uninhibited activity v_t^{ctrl} to obtain the rate of nonlinearity k_{ctrl} . **(C)** Inhibitor concentration-dependent k_{obs} with spontaneous enzyme degradation increases with k_{ctrl} but the span from k_{min} ($= k_{\text{ctrl}}$) to k_{max} ($= k_{\text{inact}} + k_{\text{ctrl}}$) still equals k_{inact} . Fit with algebraic correction for nonlinearity (black line, $k_{\text{ctrl}} > 0$). Ignoring the nonlinearity (gray line, constrain $k_{\text{ctrl}} = 0$) results in underestimation of K_1 (overestimation of potency) and overestimation of k_{inact} . **(D)** Normalized enzyme activity v_t/v_0^{ctrl} is fitted to Equation VI (shown in Figure 21D) for each inhibitor concentration during preincubation (constrain $v_i/v_0^{\text{ctrl}} = 1$) to obtain corrected observed rates of inactivation k_{obs} . **(E)** Inhibitor concentration-dependent k_{obs} has been corrected for enzyme degradation by fitting normalized enzyme activity v_t/v_0^{ctrl} and does not require further corrections.

dilution in a larger volume might resolve this. Alternatively, enzyme activity with partial disruption of noncovalent EI analyzed with *Data Analysis Protocol 3A* still results in reliable estimates of k_{obs} . Please note that, although detection based only on covalent adduct formation allows analysis of 2-step inhibitors displaying tight-binding behavior (very high noncovalent affinity resulting in full inhibition at all inhibitor concentrations), these inhibitor concentrations are saturating if they comply with the rapid equilibrium approximation ($K_1 \approx K_1$); thus, it would only be possible to determine the lower limit of k_{inact} and the upper limit of K_1 (see Figure 3G).

Correction for enzyme (in)stability during preincubation (Figure 23A) by correcting for the rate of spontaneous degradation k_{ctrl} has been reported for dilution experiments with irreversible covalent inhibitors (Figure 23B-C).⁸⁶ Alternatively, enzyme activity after preincubation v_t can be normalized to the uninhibited enzyme activity after preincubation v_0^{ctrl} (Figure 23D-E).

Data Analysis 4B: 1-Step Irreversible Covalent Inhibition.

Data obtained for 1-step irreversible inhibitors (Figure 24A) is processed with *Data Analysis Protocol 4*, followed by *Data Analysis Protocol 4Bi* or *4Bii*. Kinetic analysis of enzyme activity with dilution/competition after preincubation in presence of a 1-step covalent inhibitor is almost identical to data analysis of preincubation without dilution in excess substrate (*Data Analysis 3B*), with the exception that enzyme activity v_t can now be calculated from the slope after longer incubation times (Figure 24B). It is essential to plot the rate of covalent adduct formation k_{obs} (Figure 24C) against the inhibitor concentration during preincubation (Figure 24D) to obtain kinetic parameters: k_{obs} is based on the formation of EI^* during preincubation, and the inhibitor concentration during preincubation will be much higher than the inhibitor concentration after dilution in substrate ($[\text{I}]_{t'} \gg [\text{I}]_t$). Dilution/competition does not disrupt any noncovalent EI complex, as this is nonexistent for 1-step inhibitors, but the rate of covalent adduct formation k_{obs} should be negligible after dilution in

Data Analysis 4B: 1-step IRREV

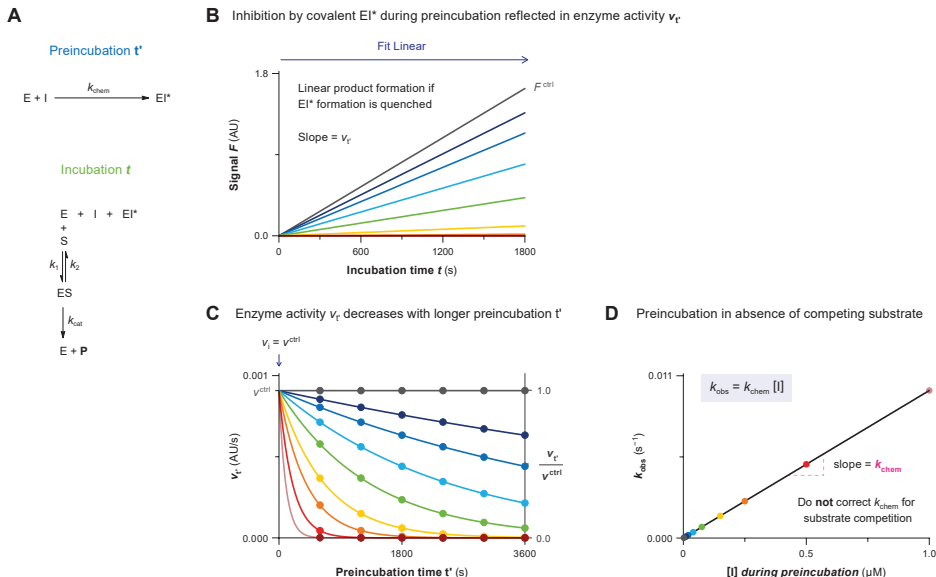


Figure 24 | Data Analysis 4B: Preincubation time-dependent inhibition with dilution/competition for 1-step irreversible covalent inhibition. Simulated with **KinVol** for 1-step IRREV inhibitor **D** with 100 pM enzyme in $V_{t'} = 1$ ($[\text{E}^{\text{total}}]_{t'} = 100$, $[\text{E}^{\text{total}}]_t = 1$), and 10 μM substrate **S1** ($[\text{S}] = 10K_M$) in $V_{\text{sub}} = 99$. **(A)** Schematic enzyme dynamics during preincubation in absence of substrate and during incubation after dilution in excess substrate. **(B)** Time-dependent product formation after preincubation ($t' = 1800$ s) in absence of inhibitor F^{ctrl} or in presence of various inhibitor concentrations. Enzyme activity after preincubation v_t is obtained from the linear slope. **(C)** Preincubation time-dependent enzyme activity v_t is fitted to **Equation VI** (shown in **Figure 21D**) for each inhibitor concentration with global shared value for v_i ($v_i = v^{\text{ctrl}}$) to obtain observed rates of inactivation k_{obs} . Alternatively, v_t can be normalized to a fraction of the uninhibited enzyme activity v^{ctrl} . Inhibitor concentrations where $v_t = 0$ at the earliest time-point are excluded from the fit. **(D)** Inhibitor concentration-dependent k_{obs} increases linearly with inhibitor concentration during preincubation, with k_{chem} as the slope. No correction for substrate competition: v_t reflects the remaining unbound enzyme activity after preincubation in the absence of competing substrate.

excess substrate, to prevent formation of covalent EI^* . Insufficient dilution and/or competition ($\Delta[EI^*]_t > 0$) can result in time-dependent decrease of enzyme activity due to formation of EI^* after substrate addition. Increasing substrate concentration and/or dilution in a larger volume might resolve this if necessary, but simply performing analysis with *Data Analysis Protocol 3B* also results in reliable estimates of k_{obs} . Inhibitor concentrations that reach reaction completion during the shortest preincubation time should be excluded from the fit (highest concentration in **Figure 24C**) as these fits are not reliable.

Correction for enzyme (in)stability (**Figure 25A**) using the rate of spontaneous degradation k_{ctrl} has been reported for dilution experiments with irreversible covalent inhibitors (**Figure 25B-C**).⁸⁶ Alternatively, enzyme activity after preincubation v_t can be normalized to the uninhibited enzyme activity after preincubation v_t^{ctrl} (**Figure 25D-E**).

Data Analysis 4B: 1-step IRREV

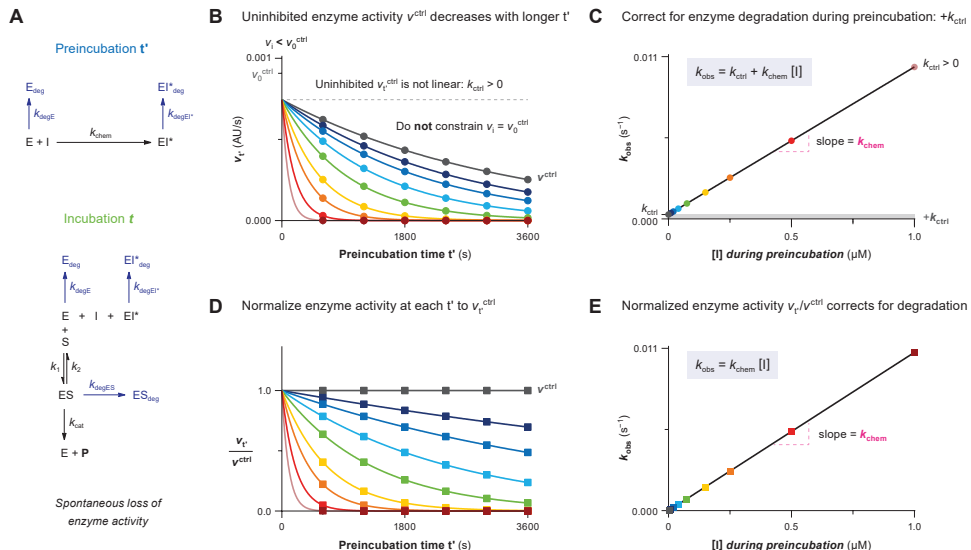


Figure 25 | Data Analysis 4B: Corrections for spontaneous loss of enzyme activity (1-step IRREV). Simulated with *KinVolDeg* for 1-step IRREV inhibitor **D** with 100 pM enzyme in $V_v = 1$ ($[E^{\text{total}}]_t = 100$, $[E^{\text{total}}]_i = 1$), and 10 μ M substrate **S1** ($[S] = 10K_M$) in $V_{\text{sub}} = 99$, and $k_{degE} = k_{degES} = k_{degEI} = 0.0003 \text{ s}^{-1}$. **(A)** Schematic enzyme dynamics during preincubation in absence of substrate and during incubation after dilution in excess substrate with spontaneous enzyme degradation/denaturation. **(B)** Uninhibited enzyme activity after preincubation v_t^{ctrl} decreases with longer preincubation. Enzyme activity v_t is fitted to **Equation VI** (shown in **Figure 21D**) for each inhibitor concentration during preincubation with globally shared value for v_i ($v_i = v_0^{ctrl}$) to obtain observed rates of inactivation k_{obs} , along with fitting uninhibited activity v_0^{ctrl} to obtain the rate of nonlinearity k_{ctrl} . **(C)** Inhibitor concentration-dependent k_{obs} with spontaneous enzyme degradation/denaturation increases by k_{ctrl} . Fit with algebraic correction for nonlinearity (black line, $k_{ctrl} > 0$) or ignoring nonlinearity (gray line, constrain $k_{ctrl} = 0$). Ignoring the nonlinearity (assuming Y-intercept = 0) results in overestimation of k_{chem} (steeper slope). **(D)** Normalized enzyme activity v_t/v_t^{ctrl} is fitted to **Equation VI** (shown in **Figure 21D**) for each inhibitor concentration during preincubation (constrain $v_i/v_0^{ctrl} = 1$) to obtain corrected observed rates of inactivation k_{obs} . **(E)** Inhibitor concentration-dependent k_{obs} has been corrected for enzyme degradation by fitting normalized enzyme activity v_t/v_t^{ctrl} and does not require further corrections.

4. Experimental Protocols

Assay Protocol I. Progress Curve Analysis of Substrate Association Competition

The protocol below provides a generic set of steps to accomplishing this type of measurement.

Materials

- 1× Assay/reaction buffer supplemented with co-factors and reducing agent
- Active enzyme, 4× solution in assay buffer
- Substrate with continuous read-out, 4× solution in assay buffer
- Positive control: vehicle/solvent as DMSO stock, or 2% solution in assay buffer
- Negative control: known inhibitor or alkylating agent as DMSO stock, or 2× solution in assay buffer
- Inhibitor: as DMSO stock, or serial dilution of 2× solution in assay buffer with 2% DMSO
- 384-well low volume microplate with nonbinding surface (e.g. Corning 3820 or 4513) for incubation and read-out
- Optical clear cover/seal (e.g. Perkin Elmer TopSeal-A Plus, #G050185, or Corning 6575 Universal Optical Sealing Tape, or Duck Brand HP260 Packing Tape)
- 1.5 mL (Eppendorf) microtubes to prepare stock solutions
- *Optional:* 96-well microplate to prepare serial dilution of inhibitor concentration
- Microplate reader equipped with appropriate filters to detect product formation (e.g. CLARIOstar microplate reader)
- *Optional:* Automated (acoustic) dispenser (e.g. Labcyte ECHO 550 Liquid Handler acoustic dispenser)

Exemplary assay concentrations

	incubation t		
	[stock]	Volume	[conc] $_t$
Enzyme	4 nM	5 μ L	0.99 nM
Inhibitor	20 nM	10.2 μ L	10.10 nM
Substrate	4 μ M	5 μ L	0.99 μM
<i>Total</i>		20.2 μ L	

Before you start, optimize assay conditions in the uninhibited control to ensure compliance with assumptions and restrictions for progress curve analysis – most importantly linear product formation in the uninhibited control for the duration of the experiment ($k_{ctrl} = 0$) – by activating the enzyme before reaction initiation (e.g. preincubation with reducing agent for proteases, or ATP for kinases and ligases), testing the enzyme activity on the (fluorogenic) substrate in absence of inhibitor, and adjusting the enzyme and substrate concentration ($[S]_0 > 10[E]_0$) to reach maximum 10% substrate conversion at the end of the measurement window ($[P]_t < 0.1[S]_0$). Further optimization typically involves tuning the reader settings for optimal sensitivity, measurement of a calibration curve for product concentration,⁶⁸⁻⁶⁹ and calculation of the Z'-score from the uninhibited and inhibited controls (ideally 8 replicates)⁸⁷ in a separate experiment to validate that enough product is formed for a good signal/noise ratio ($Z' > 0.5$) at the end of the measurement. Consult **Table 6** in *section 5* for common optimization and troubleshooting options. The read-out of product formation must be homogeneous/continuous. Product formation of substrates with a less sensitive read-out (e.g. fluorescence polarization) may generate a relatively low product signal relative to the unprocessed substrate, and substrate depletion is unavoidable to generate a sufficient Z'-score.⁸⁷ Algebraic analysis of 2-step irreversible inhibition with substrate depletion ($[P]_t < 0.1[S]_0$) can be performed with *Data Analysis Protocol 1D* after completion of *steps 2-6 of Assay Protocol I*.

1. Add inhibitor or control to each well with the uninhibited control for full enzyme activity containing the same volume vehicle/solvent instead of inhibitor (we use DMSO in this protocol). Add a constant volume of serially diluted inhibitor in assay buffer supplemented with DMSO (e.g. 10.2 μ L of 2× solution containing 2% DMSO) or add inhibitor and controls by (acoustic) dispensing of the pure DMSO stocks, with DMSO backfill to a constant volume (e.g. 0.2 μ L), followed by addition of assay buffer to each well (e.g. 10 μ L) and gentle shaking (300 rpm) to homogenize the solution.

Typically, measurements are performed in triplicate (or more replicates) with at least 8 inhibitor concentrations. Inhibitor concentrations might need optimization, but a good starting point is $0.1\text{-}10\times IC_{50}$; the highest inhibitor concentration should correspond to maximum 90% initial (noncovalent) inhibition ($v_i > 0.1v^{ctrl}$), as it can be difficult to accurately detect the increase from 90% to 100% inhibition.

2. Add substrate in assay buffer to each well (e.g. 5 μL of 4 \times solution) and homogenize the solutions by gentle shaking (300 rpm).

The order of substrate or inhibitor addition is not important *per se*, as long as enzyme is the last reagent to be added, and DMSO stocks are added prior to buffered (aqueous) solutions. Optionally, gently centrifuge the plate (1 min at 1000 rpm) to ensure that assay components are not stuck at the top of the well.

3. Add active enzyme in assay buffer to each well (e.g. 5 μL of 4 \times solution), with minimal delay between addition to the first and the last well. Optionally, gently centrifuge the plate (1 min at 1000 rpm) if bubbles are formed (especially for buffers containing surfactants), as these will induce assay artifacts, and to ensure assay components are in solution together rather than stuck to the wall at the top of the well.

Manual addition of enzyme solution and physically moving the plate to the plate reader introduces a delay that may slightly affect the accuracy of the measurement, as it can be variable (depending on the total number of wells, distance to the machine and walking pace of the researcher). This should not be significant if the delay is short compared to the total reaction time, but it can affect the outcome in the data analysis when t_0 is actually 1-2 min. One method to monitor the delay between reaction initiation (onset of product formation and inhibition) and the start of product detection in step 6 is evaluation of the Y-intercept values (as discussed in **Table 6, section 5**). Alternatively, enzyme addition with an injector built into the plate reader minimizes the delay between reaction initiation (onset of product formation and inhibition) and starting the measurement.

4. Seal the wells by applying an optical clear cover.

Continuous kinetic measurements are subject to assay artifacts such as drift due to evaporation. In our experience, application of an optical clear cover/seal prior to measurement improves the assay robustness and resolves significant aberrant nonlinearity unrelated to enzyme activity.

5. Measure product formation in microplate reader by detection of the product read-out.

A typical assay measurement window is 60-240 min, with a measurement interval of 1-2 min. The inhibitor-binding reaction does not have to reach completion (100% inhibition for irreversible inhibitors, equilibrium for reversible inhibitors) within this window, but data will be more reliable when completion is reached before the end of the measurement (see also **Figure 5B**).

6. Proceed to Data Analysis Protocols to calculate the appropriate kinetic parameters for each covalent binding mode: *Data Analysis Protocol 1A* for 2-step irreversible inhibitors, *Data Analysis Protocol 1B* for 1-step irreversible inhibitors, *Data Analysis Protocol 1C* for 2-step reversible inhibitors, or *Data Analysis Protocol 1D* for 2-step irreversible inhibitors with substrate depletion.

EXP Conditions	Data Analysis Protocol		
	2-step IRREV	1-step IRREV	2-step REV
$k_{ctrl} = 0$	1A	1B	1C
$k_{degE} > 0$	1A	1B	–
$[P]_t > 0.1[S]_0$	1D	–	–

Data Analysis Protocol 1A for 2-Step IRREV Inhibition

Processing of raw data obtained with *Assay Protocol 1* for 2-step irreversible covalent inhibitors.

1. Plot signal F against incubation time t

Plot signal (in AU) on the Y-axis against incubation time (in s) on the X-axis for each inhibitor concentration and the controls (**Figure 6B**). Product formation in the uninhibited control F^{ctrl} should be linear. Consult **Table 6** (section 5) for

troubleshooting of nonlinearity of the uninhibited control. Optionally, perform background correction to correct for assay artifacts such as bleaching and drift that cause a negative final velocity ($v_s < 0$ AU/s) in the fully inhibited control. This correction can be subtraction of the background in presence of substrate (and inhibitor) but absence of enzyme, or subtraction of the fully inhibited control. Consult the guidelines of your data fitting software for instructions on background corrections (e.g. GraphPad Prism).⁸⁸

2. Fit signal F_t against t to obtain k_{obs}

Fit signal F_t against incubation time t to **Equation II (Figure 6B/E)**. Constrain final velocity $v_s = 0$ for background-corrected product formation, or $v_s =$ value for full inhibition control. A lack of initial noncovalent complex ($v_i = v^{ctrl}$) is indicative of 1-step binding behavior.

$$F_t = v_s t + \frac{v_i - v_s}{k_{obs}} [1 - e^{-k_{obs} t}] + F_0 \quad (\text{II})$$

Nonlinear regression of user-defined explicit equation $Y = (v_s * X) + (((v_i - v_s) / k_{obs}) * (1 - \text{EXP}(-k_{obs} * X))) + Y_0$ with $Y =$ signal F_t (in AU), $X =$ incubation time t (in s), and $v_s =$ final slope v_s (in AU/s, constrained) to find $Y_0 =$ Y-intercept $F_0 =$ background signal at $t = 0$ (in AU), $v_i =$ initial slope v_i (in AU/s) and $k_{obs} =$ observed reaction rate k_{obs} (in s^{-1}).

3. Plot k_{obs} against $[I]$

Plot the mean and standard deviation of k_{obs} (in s^{-1}) on the Y-axis against inhibitor concentration (in M) after reaction initiation by enzyme addition (in the final solution) on the X-axis (**Figure 6C/F**). The plot of k_{obs} against $[I]$ should reach a maximum k_{obs} at saturating inhibitor concentration. Note that a linear curve is indicative of 1-step binding behavior at non-saturating inhibitor concentrations ($[I] \ll 0.1K_i^{app}$; see **Figure 3F**) with $v_i = v^{ctrl}$ (low initial inhibition). Proceed to *step 4 of Data Analysis Protocol 1B* after it has been validated that the linear curve is not resultant from saturating inhibitor concentrations ($[I] \gg 10K_i^{app}$; see **Figure 3G**) as identified by $v_i \ll v^{ctrl}$ (significant initial inhibition), by repeating the measurement with a higher competitive substrate concentration (increase K_i^{app}) and/or lower inhibitor concentration.

4. Fit k_{obs} against $[I]$ to obtain k_{inact} and K_i^{app}

Fit k_{obs} against inhibitor concentration to **Equation VII** to obtain maximum inactivation rate constant k_{inact} and apparent inactivation constant K_i^{app} . Constrain $k_{ctrl} = k_{obs}$ of the uninhibited control (**Figure 6F**). Calculate inactivation constant K_i and irreversible covalent inhibitor potency k_{inact}/K_i with *Sample Calculation 1&2*.

$$k_{obs} = k_{ctrl} + \frac{k_{inact} [I]}{K_i^{app} + [I]} \quad (\text{VII})$$

Nonlinear regression of user-defined explicit equation $Y = Y_0 + ((k_{max} * X) / ((K_i^{app} + X)))$ with $Y =$ observed reaction rate k_{obs} (in s^{-1}), $X =$ inhibitor concentration (in M), and $Y_0 =$ rate of nonlinearity in uninhibited control k_{ctrl} (in s^{-1} , constrained) to find $k_{max} =$ maximum reaction rate k_{inact} (in s^{-1}) and $K_i^{app} =$ Apparent inactivation constant K_i^{app} (in M).

5. EXTRa: Plot and fit v_i against $[I]$ to obtain K_i^{app}

Inhibition constant K_i can be calculated from the initial velocity v_i (obtained in *step 3*), reflecting the rapid (initial) noncovalent enzyme–inhibitor equilibrium. Plot the mean and standard deviation of v_i (in AU/s) on the Y-axis against inhibitor concentration on the X-axis (similar to **Figure 8D**). Fit v_i against $[I]$ to four-parameter nonlinear regression Hill **Equation VIII** to obtain apparent inhibition constant K_i^{app} .³³ Constrain the top to the uninhibited v_i (maximum velocity = v^{ctrl}) and the bottom to the fully inhibited v_i (minimum velocity = v_i^{min}). For (background-)corrected product formation $v_i^{min} = 0$. Calculate inhibition constant K_i with *Sample Calculation 3*.

$$v_i = v_i^{min} + \frac{v^{ctrl} - v_i^{min}}{1 + \left(\frac{[I]}{K_i^{app}} \right)^h} \quad (\text{VIII})$$

Nonlinear regression of four-parameter dose-response equation $Y = \text{Bottom} + (\text{Top} - \text{Bottom}) / (1 + (X / IC50)^{\text{HillSlope}})$ with $Y =$ initial product formation velocity v_i (in AU/s), $X =$ inhibitor concentration (in M), $\text{Bottom} =$ velocity in fully inhibited control v_i^{min} (in AU/s, constrained), and $\text{Top} =$ maximum velocity in uninhibited control v^{ctrl} (in AU/s, constrained) to find $\text{HillSlope} =$ Hill coefficient h (unitless) and $IC50 =$ apparent inhibition constant K_i^{app} (in M).

6. Optional: Validate experimental kinetic parameters with kinetic simulations

Proceed to *Kinetic Simulations 1* to compare the experimental progress curves to the progress curves simulated with scripts **KinGen** and **KinDeg** (using experimental rate constant $k_{inact} = k_s$) to confirm that the calculated kinetic constants are in accordance with the experimental data.

Data Analysis Protocol 1B for 1-Step IRREV Inhibition

Processing of raw data obtained with *Assay Protocol 1* for 1-step irreversible covalent inhibitors and 2-step irreversible inhibitors at non-saturating inhibitor concentrations ($[I] \leq 0.1K_i^{app}$).

1. Plot signal F against incubation time t

Plot signal (in AU) on the Y-axis against incubation time (in s) on the X-axis for each inhibitor concentration and the controls (**Figure 7B**). Product formation in the uninhibited control F_{ctrl} should be linear. Consult **Table 6** (section 5) for troubleshooting of nonlinearity of the uninhibited control. Optionally, perform background correction to correct for assay artifacts such as bleaching and drift that cause a negative final velocity ($v_s < 0$ AU/s) in the fully inhibited control. This correction can be subtraction of the background in the presence of substrate (and inhibitor) but absence of enzyme, or subtraction of the fully inhibited control. Consult the guidelines of your data fitting software for instructions on background corrections (e.g. GraphPad Prism).³⁸

2. Fit F_t against t to obtain k_{obs}

Fit signal F_t against incubation time t to **Equation II (Figure 7B/E)**. Constrain final velocity $v_s = 0$ for background-corrected product formation, or v_s = value for full inhibition control. Initial velocity v_i should be a shared value because noncovalent inhibition does not significantly contribute to the initial inhibition for inhibitors displaying 1-step behavior.

$$F_t = v_s t + \frac{v_i - v_s}{k_{obs}} [1 - e^{-k_{obs} t}] + F_0 \quad (II)$$

Nonlinear regression of user-defined explicit equation $Y=(vs*X)+(((vi-vs)/kobs)*(1-EXP(-kobs*X)))+Y0$ with Y = signal F_t (in AU), X = incubation time t (in s), and vs = final slope v_s (in AU/s) to find $Y0$ = Y-intercept F_0 = background signal at $t = 0$ (in AU), vi = initial slope v_i (in AU/s, shared value), and $kobs$ = observed reaction rate k_{obs} (in s^{-1}).

3. Plot k_{obs} against $[I]$

Plot the mean and standard deviation of k_{obs} (in s^{-1}) on the Y-axis against inhibitor concentration (in M) after reaction initiation by enzyme addition (in the final solution) on the X-axis (**Figure 7C/F**). The plot of k_{obs} against inhibitor concentration $[I]$ is linear for 1-step irreversible inhibitors and for 2-step irreversible inhibitors at non-saturating inhibitor concentrations ($[I] \ll 0.1K_i^{app}$).

4. Fit k_{obs} against $[I]$ to obtain k_{chem}^{app}

Fit k_{obs} against inhibitor concentration to **Equation IX** to obtain apparent inhibitor potency k_{chem}^{app} from the linear slope. Constrain Y-intercept $k_{ctrl} = k_{obs}$ of the uninhibited control (**Figure 7F**). Calculate k_{chem} reflecting inhibitor potency for 1-step irreversible covalent inhibition with *Sample Calculation 4*. Calculate k_{inact}/K_i^{app} and k_{inact}/K_i for 2-step irreversible inhibitors at non-saturating inhibitor concentrations ($[I] \leq 0.1K_i^{app}$) with *Sample Calculation 5 and 6*.

$$k_{obs} = k_{ctrl} + k_{chem}^{app} [I] \quad (IX)$$

Nonlinear regression of straight line $Y=YIntercept+Slope*X$ with Y = observed reaction rate k_{obs} (in s^{-1}), X = inhibitor concentration (in M), and $YIntercept$ = rate of nonlinearity in uninhibited control k_{ctrl} (in s^{-1} , constrained) to find Slope = apparent inactivation rate constant k_{chem}^{app} (in $M^{-1}s^{-1}$).

5. Optional: Validate experimental kinetic parameters with kinetic simulations

Proceed to *Kinetic Simulations 1* to compare the experimental progress curves to the progress curves simulated with scripts **KinGen** and **KinDeg** (using experimental rate constant $k_{chem} = k_3$) to confirm that the calculated kinetic constants are in accordance with the experimental data.

Data Analysis Protocol 1C for 2-Step REV Inhibition

Processing of raw data obtained with *Assay Protocol 1* for 2-step reversible covalent inhibitors.

1. Plot signal F against incubation time t

Plot signal (in AU) on the Y-axis against incubation time (in s) on the X-axis for each inhibitor concentration and the controls (**Figure 8B**). Product formation in the uninhibited control F_{ctrl} should be linear. Consult **Table 6** (section 5) for troubleshooting of nonlinearity of the uninhibited control. Optionally, perform background correction to correct for assay artifacts such as bleaching and drift that cause a negative final velocity ($v_s < 0$ AU/s) in the fully inhibited control. This correction can be subtraction of the background in the presence of substrate (and inhibitor) but absence of

enzyme, or subtraction of the fully inhibited control. Consult the guidelines of your data fitting software for instructions on background corrections (e.g. GraphPad Prism).⁸⁸

2. Fit F_t against t to obtain k_{obs} and v_s

Fit signal F_t against incubation time t to **Equation II (Figure 8B)** to obtain final product formation velocity v_s and the observed reaction rate k_{obs} from initial equilibrium v_i to steady-state equilibrium v_s . Do not constrain initial velocity v_i or final velocity v_s . Also fit the progress curve of the uninhibited control (F^{ctrl}) to validate that product formation is strictly linear ($v_s^{\text{ctrl}} = v_s^{\text{ctrl}}$), because algebraic correction for nonlinearity in the uninhibited control is not possible (illustrated in **Figure 9**). The observed rate k_{obs} reflects the exponential reaction rate from initial noncovalent equilibrium (v_i) to final steady-state equilibrium (v_s).

$$F_t = v_s t + \frac{v_i - v_s}{k_{\text{obs}}} [1 - e^{-k_{\text{obs}} t}] + F_0 \quad (\text{II})$$

Nonlinear regression of user-defined explicit equation $Y = (v_s * X) + (((v_i - v_s) / k_{\text{obs}}) * (1 - \text{EXP}(-k_{\text{obs}} * X))) + Y_0$ with Y = signal F_t (in AU) and X = incubation time t (in s) to find Y_0 = Y-intercept F_0 = background signal at $t = 0$ (in AU), v_i = initial slope v_i (in AU/s), v_s = final slope v_s (in AU/s), and k_{obs} = observed reaction rate k_{obs} (in s^{-1}).

3. Plot and fit v_s against $[I]$ to obtain K_i^{app}

Apparent steady-state inhibition constant K_i^{app} can be calculated from the final velocity v_s (obtained in the previous step) reflecting enzyme activity after reaching the steady-state inhibitor equilibrium (*reaction completion*). Plot the mean and standard deviation of v_s (in AU/s) on the Y-axis against inhibitor concentration (in M) on the X-axis and fit to four-parameter nonlinear regression Hill **Equation X** to obtain apparent steady-state inhibition constant K_i^{app} (**Figure 8D**).³³ Constrain the top to uninhibited velocity v_s^{ctrl} (maximum velocity = v_s^{max}) and the bottom to the fully inhibited v_s (v_s^{min} , minimum velocity). For (background-)corrected product formation, $v_s^{\text{min}} = 0$. Accurate values are only obtained when uninhibited product formation is strictly linear ($k_{\text{ctrl}} = 0$) or when the rate of spontaneous inactivation k_{ctrl} is much smaller than the covalent dissociation k_6 (**Figure 9D**). Validate that v_s is not driven by spontaneous enzyme degradation ($k_{\text{ctrl}} \ll k_6$) by also fitting without constraints for v_s^{max} . Calculate steady-state inhibition constant K_i^* with *Sample Calculation 7*.

$$v_s = v_s^{\text{min}} + \frac{v_s^{\text{ctrl}} - v_s^{\text{min}}}{1 + \left(\frac{[I]}{K_i^{\text{app}}} \right)^h} \quad (\text{X})$$

Nonlinear regression of four-parameter dose-response equation $Y = \text{Bottom} + (\text{Top} - \text{Bottom}) / (1 + (X / IC50)^{\text{HillSlope}})$ with Y = final product formation velocity v_s (in AU/s), X = inhibitor concentration (in M), Bottom = velocity in fully inhibited control v_s^{min} (in AU/s, constrained) and Top = maximum velocity in uninhibited control v_s^{ctrl} (in AU/s, constrained) to find HillSlope = Hill coefficient h (unitless) and $IC50$ = apparent steady-state inhibition constant K_i^{app} (in M).

4. Optional: Plot and fit k_{obs} against $[I]$ to obtain K_i^{app} , k_5 , and k_6

This is an optional data processing step to obtain kinetic parameters by fitting to the observed rate k_{obs} (obtained in *step 2 of Data Analysis 1C*), and is used to validate K_i^{app} values found in the previous step, to check if nonlinearity in the uninhibited control k_{ctrl} affects the fit, and/or to generate experimental k_5 and k_6 values to use in kinetic simulations. Plot the mean and standard deviation of k_{obs} (in s^{-1}) on the Y-axis against inhibitor concentration (in M) on the X-axis (**Figure 8C**). Exclude k_{obs} of uninhibited control (k_{ctrl}) from the fit. Fit k_{obs} against inhibitor concentration to **Equation XI** to obtain rate constants for the covalent association k_5 and covalent dissociation k_6 , as well as apparent noncovalent inhibition constant K_i^{app} reflecting the rapid (initial) noncovalent equilibrium. Use the inhibitor concentration after reaction initiation by enzyme addition (in the final solution). Accurate values are only obtained when uninhibited product formation is strictly linear ($k_{\text{ctrl}} = 0$). Y-intercept approaching k_{ctrl} despite the uninhibited control not being included in the fit is a red flag that should not be ignored, as this is indicative of spontaneous enzyme degradation rather than k_6 dominating k_{obs} at low inhibitor concentrations, for which algebraic corrections are not available (**Figure 9C**). Calculate noncovalent inhibition constant K_i^* with *Sample Calculation 8*. Optionally, perform *step 6 of Data Analysis 1A* to obtain apparent noncovalent inhibition constant K_i^{app} from the initial velocity v_i (obtained in *step 2 of Data Analysis Protocol 1C*).

$$k_{\text{obs}} = k_6 + \frac{k_5 [I]}{K_i^{\text{app}} + [I]} \quad (\text{XI})$$

Nonlinear regression of user-defined explicit equation $Y = Y_0 + ((k_{\text{max}} * X) / ((K_{\text{app}}) + X))$ with Y = observed reaction rate k_{obs} (in s^{-1}) and X = inhibitor concentration (in M) to find Y_0 = covalent dissociation rate constant k_6 (in s^{-1}), k_{max} = covalent association rate constant k_5 (in s^{-1}) and K_{app} = Apparent inhibition constant K_i^{app} (in M).

5. Optional: Validate experimental kinetic parameters with kinetic simulations

Proceed to *Kinetic Simulations 1* to compare the experimental progress curves to the progress curves simulated with scripts **KinGen** and **KinDeg** to confirm that the calculated kinetic constants are in accordance with the experimental data. Experimental estimates of k_5 and k_6 are generated in the previous step of this protocol.

Data Analysis Protocol 1D for 2-Step IRREV Inhibition with Substrate Depletion

Processing of raw data obtained with *Assay Protocol 1* for 2-step irreversible covalent inhibitors with nonlinearity in the uninhibited control resultant from substrate depletion ($[P]_t < 0.1[S]_0$).

Before you start, validate compliance with essential assay reaction conditions such as the Hit-and-Run model. This algebraic correction for substrate depletion has additional requirements for assay conditions,⁸⁴ and is only compatible with 2-step irreversible inhibition (Figure 10). Validate that the product formation reaction complies with the Hit-and-Run model $E + S \rightarrow E + P$ (shown in Figure 10A): substrate concentration must be far below the K_M ($[S]_0 < 0.1K_M$) to calculate the pseudo-first order reaction rate constant for enzymatic product formation $k_{sub} = k_{cat}/K_M$ ($M^{-1}s^{-1}$). Observed nonlinearity in the uninhibited control should be fully attributed to substrate depletion (Figure 10B). Convert the maximum signal F^{ctrl} (in AU) into product concentration (in M) using the product coefficient r_p (in AU/M product) as determined in a separate product calibration experiment.⁶⁸⁻⁶⁹ Validate that the total substrate conversion to product exceeds 10% of the initial substrate concentration ($[P]^{ctrl}_t > 0.1[S]_0$), and that substrate depletion is the only factor that contributes to the observed nonlinearity: uninhibited product formation should be linear when incubation times are shorter ($[P]_t < 0.1[S]_0$) or enzyme concentration is lower. Alternatively, perform kinetic analysis by numeric solving if one or more assumptions are violated.⁸⁰

$$[P]_t = \frac{F_t - F_0}{r_p}$$

Calculate: $Pt = (Ft - F0) / rp$ with Pt = product concentration at the end of the incubation $[P]_t$ (in M), F_t = signal in uninhibited control at the end of the incubation time F_t (in AU), F_0 = substrate background signal F_0 (in AU) and rp = product coefficient r_p (in AU/M product).

1. Plot signal F against incubation time t

Plot signal (in AU) on the Y-axis against incubation time (in s) on the X-axis for each inhibitor concentration (Figure 10C). Label the columns with the inhibitor concentration (in M).

2. Perform background correction

Correct for assay artifacts such as fluorescence bleaching and drift that cause a declining signal in the fully inhibited control. This correction can be subtraction of the time-dependent background in absence of enzyme but in presence of substrate (and inhibitor), or subtraction of the fully inhibited control. Consult the guidelines of your data fitting software for instructions on background corrections (e.g. GraphPad Prism).⁸⁸

3. Globally fit F_t against t to obtain k_{inact} and K_i^{app}

Globally fit the progress curves of time-dependent signal F_t for all inhibitor concentrations to **Equation III** (Figure 10C). Consult the guidelines of your data fitting software for instructions on user-defined (implicit) equations.⁶⁶ Exclude the dataset of the fully inhibited control from the fit. Constrain $[E]_0$ (in M), $[S]_0$ (in M), and $[I] = [I]_0$ (in M) to their theoretical values. Originally, $[I]_0$ was locally optimized,⁸⁰ but we used fixed values of $[I]_0$ in GraphPad Prism. Constrain product coefficient r_p (in AU/M product) to the value determined in a separate product calibration experiment. Constrain k_{inact} , K_i , and k_{sub} to a shared value that must be greater than 0 for all datasets and provide initial values that are in the anticipated range. Note that **Equation III** is in agreement with **equation C.16** in Appendix C of the original publication,⁸⁴ but $[I]_0$ and k_{inact} were unintentionally displaced in **equation 3** in the main text of this publication. Calculate inactivation constant K_i and irreversible covalent inhibitor potency k_{inact}/K_i with *Sample Calculations 1 and 2*.

$$F_t = F_0 + r_p [S]_0 \left\{ 1 - e^{-\beta(1 - e^{-\alpha t})} \right\}$$

$$\alpha = \frac{k_{inact} [I]}{K_i^{app} + [I]} \quad (III)$$

$$\beta = \left(\frac{[E]_0 k_{sub}}{k_{inact}} \right) \left(\frac{K_i^{app}}{[I]} \right)$$

Nonlinear regression of user-defined explicit equation:

```

a=kinact*I0/(I0+KIapp)
b=(E0*ksub/kinact)*(KIapp/I0)
P=S0*(1-exp(-b*(1-exp(-a*X))))
Y=Y0+(rp*P)

```

with Y = time-dependent signal F_t (in AU), X = incubation time t (in s), rp = product coefficient r_p (AU/M product, constrained), $E0$ = maximum unbound enzyme concentration at reaction initiation $[E]_0$ (in M, constrained), $S0$ = maximum unbound substrate concentration at reaction initiation $[S]_0$ (in M, constrained) and $I0$ = maximum unbound inhibitor concentration $[I]$ (in M, column value) to find globally shared values for $ksub$ = product formation rate constant $k_{sub} = k_{cat}/K_M$ ($M^{-1}s^{-1}$, shared), $kinact$ = maximum rate of inactivation k_{inact} (s^{-1} , shared) and $KIapp$ = apparent inactivation constant K_i^{app} (in M, shared).

4. *Optional:* Validate experimental kinetic parameters with kinetic simulations

Proceed to *Kinetic Simulations 1* to compare the experimental progress curves to the progress curves simulated with script **KinSubDpl** (using experimental rate constant $k_{\text{inact}} = k_s$) to confirm that the calculated kinetic constants are in accordance with the experimental data.

Assay Protocol II. Incubation Time-Dependent Potency $IC_{50}(t)$

The below protocol provides a generic set of steps to accomplishing this type of measurement.

Materials

- 1× Assay/reaction buffer supplemented with co-factors and reducing agent
- Active enzyme, 4× solution in assay buffer
- Competitive substrate with continuous or quenched read-out, 4× solution in assay buffer
- Positive control: vehicle/solvent as DMSO stock, or 2% solution in assay buffer
- Negative control: known inhibitor or alkylating agent as DMSO stock, or 2× solution in assay buffer
- Inhibitor: as DMSO stock, or serial dilution of 2× solution in assay buffer with 2% DMSO
- *Optional:* Development/quenching solution
- 384-well low volume microplate with nonbinding surface (e.g. Corning 3820 or 4513) for incubation/read-out
- Optical clear cover/seal (e.g. Perkin Elmer TopSeal-A Plus, #6050185, Corning 6575 Universal Optical Sealing Tape or Duck Brand HP260 Packing Tape) for continuous read-out, or a general microplate cover/lid (e.g. Corning 6569 Microplate Aluminum Sealing Tape) for noncontinuous read-out
- 1.5 mL (Eppendorf) microtubes to prepare stock solutions
- *Optional:* 96-well microplate to prepare serial dilution of inhibitor concentration
- *Optional:* Microtubes to perform incubations (e.g. Eppendorf Protein Lobind Microtubes, #022431018)
- Microplate reader equipped with appropriate filters to detect product formation (e.g. CLARIOstar microplate reader)
- *Optional:* Automated (acoustic) dispenser (e.g. Labcyte ECHO 550 Liquid Handler acoustic dispenser)

Exemplary assay concentrations

	incubation t		
	[stock]	Volume	[conc] _t
Enzyme	4 nM	5 µL	0.99 nM
Inhibitor	20 nM	10.2 µL	10.10 nM
Substrate	4 µM	5 µL	0.99 µM
<i>Total</i>		20.2 µL	

Before you start, optimize assay conditions in the uninhibited control to ensure compliance with assumptions and restrictions as outlined for *Assay Protocol I* (see also **Figure 13**). It is crucial to ensure that uninhibited product formation is linear with incubation time for the duration of the measurement: no enzyme degradation ($k_{\text{deg}} = 0$) or other factors contributing to a nonlinearity in product formation in the uninhibited control ($k_{\text{ctrl}} = 0$) are allowed, as correction for nonlinearity is not possible in *Data Analysis Protocol 2*. This method is compatible with homogeneous (continuous) assays but also with assays that require a development/quenching step to visualize formed product.

1. Add inhibitor or control (e.g. 0.2 µL) and assay buffer (e.g. 10 µL) to each well with the uninhibited control for full enzyme activity containing the same volume of vehicle/solvent instead of inhibitor as outlined in *step 1 of Assay Protocol I*.

Typically, measurements are performed in triplicate (or more replicates) with at least 8 inhibitor concentrations spanning the $IC_{50}(t)$. Inhibitor concentrations might need optimization, but a good starting point is $[I] = 0.1\text{-}5 \times IC_{50}(t)$ at the shortest incubation time t . Alternatively, larger-volume incubations can be performed in (Eppendorf) Protein Lobind microtubes, from which aliquots are transferred to a microplate after the indicated incubation time. Whether incubation in tube or plate is performed is a matter of personal preference, compatibility with lab equipment and automation, and convenience of dispensing small volumes.

2. Add substrate in assay buffer to each well (e.g. 5 μ L of 4 \times solution) and homogenize the solutions by gentle shaking (1 min at 300 rpm).

The order of substrate or inhibitor addition is not important *per se*, as long as DMSO stocks are added prior to buffered (aqueous) solutions and the enzyme is the last reagent to be added, to avoid unintentional preincubation. Inhibitor binding mode must be competitive with substrate. Optionally, gently centrifuge the plate or microtubes (1 min at 1000 rpm) to ensure assay components are not stuck at the top of the well.

3. Add active enzyme in assay buffer to each well (e.g. 5 μ L of 4 \times solution) or tube as outlined in *step 3 of Assay Protocol I*.

The accuracy of the measurement improves if the incubation time is monitored precisely.

4. Seal the wells by applying an (optical clear) cover or lid, or close the caps of microtubes to prevent evaporation of assay components during incubation.

5. *Optional:* Transfer aliquots (e.g. 20 μ L) from the reaction mixture to the microplate after each time point; if incubation is performed in large volumes (in Protein Lobind microtubes or 96-well NBS plate) rather than incubation of replicates in a 384-well microplate.

6. *Quenching:* Add development solution to the reaction mixture in the microplate to quench the product formation reaction for assay formats that require a development/quenching step to visualize formed product.

Incubation time t is the elapsed time between reaction initiation by enzyme addition (*step 3*) and (optional) quenching of the enzyme activity by addition of development/quenching solution (*step 6*).

7. Measure formed product after incubation by detection of the product read-out in microplate reader.

Follow manufacturer advice on waiting time after addition of development solution before read-out. A typical assay measurement window is >2 hours, measuring cumulative product formation every 5-30 min (**Figure 11B**). The best results are obtained when inhibitor concentrations cover at least 50% of the DRC at all incubation times and there is a significant decrease from the earliest to the last $IC_{50}(t)$ value (**Figure 12D**).

8. Proceed to *Data Analysis Protocol 2* to calculate relevant kinetic parameters for 2-step irreversible covalent inhibition.

Data Analysis Protocol

EXP Conditions	2-step IRREV	1-step IRREV	2-step REV
$k_{ctrl} = 0$	2	-	-

Data Analysis Protocol 2 for 2-Step IRREV Inhibition

Processing of raw data obtained with *Assay Protocol I* or *Assay Protocol II* for 2-step irreversible covalent inhibitors.

1. Plot signal F against incubation time t

Plot cumulative signal (in AU) on the Y-axis against incubation time (in s) on the X-axis for each inhibitor concentration and for the controls (**Figure 12B**). Label the columns with the inhibitor concentration (in M). It is not possible to algebraically correct for spontaneous loss of enzyme activity. Validate that the product formation in the uninhibited control F^{ctrl} is linear ($v_i = v_s$) by performing *steps 1-3 of Data Analysis Protocol 1A* with $k_{obs} = k_{ctrl}$. Consult **Table 6** (*section 5*) for troubleshooting of nonlinearity of the uninhibited control.

2. Perform background correction

Correct for assay artifacts such as fluorescence bleaching and drift that cause a declining signal in the fully inhibited control. This correction can be subtraction of the time-dependent background in absence of enzyme but in presence of substrate (and inhibitor), or subtraction of the fully inhibited control. Consult the guidelines of your data fitting software for instructions on background corrections (e.g. GraphPad Prism).⁸⁸

3. Transpose to plot signal F_t against inhibitor concentration $[I]$

For each incubation time, transpose the X and Y values to plot signal F_t (in AU) on the Y-axis against inhibitor concentration (in M) on the X-axis. Also include product formation in the uninhibited control F_t^{ctrl} ($[I] = 0$).

4. Normalize F_t/F_t^{ctrl}

Normalize F_t to lowest value = 0 and highest value = uninhibited product formation F_t^{ctrl} to obtain fractional product formation in presence of inhibitor F_t/F_t^{ctrl} . Consult the guidelines of your data fitting software for instructions on data normalization to the positive and negative controls.⁸⁸

5. Plot and fit F_t/F_t^{ctrl} against $[I]$ to obtain the incubation time-dependent potency $IC_{50}(t)$

Plot the dose-response curve of fractional signal F_t/F_t^{ctrl} against inhibitor concentration (in M), and fit to four-parameter nonlinear regression Hill **Equation XII** to obtain the incubation time-dependent potency $IC_{50}(t)$ (**Figure 12C**).³³ Use the inhibitor concentration during incubation: after reaction initiation by enzyme addition but before the (optional) addition of development solution (*Assay Protocol II, step 3*).

$$\frac{F_t}{F_t^{\text{ctrl}}} = \frac{1}{1 + \left(\frac{IC_{50}(t)}{[I]} \right)^h} \quad (\text{xii})$$

Nonlinear regression of four-parameter dose-response equation $Y = \text{Bottom} + (\text{Top} - \text{Bottom}) / (1 + (IC_{50}/X)^h)$ with Y = fractional product signal F_t/F_t^{ctrl} (unitless), X = inhibitor concentration $[I]$ (in M), Bottom = normalized fully inhibited product signal = 0 (unitless, constrained), and Top = normalized uninhibited product signal $F_t^{\text{ctrl}}/F_0^{\text{ctrl}} = 1$ (unitless, constrained) to find h = Hill coefficient h (unitless) and IC_{50} = incubation time-dependent potency $IC_{50}(t)$ (in M).

6. Plot and fit $IC_{50}(t)$ against t to obtain k_{inact} and K_I

Plot the mean and standard deviation of $IC_{50}(t)$ (in M) on the Y-axis against incubation time t (in s) on the X-axis (**Figure 12D**). The rate of covalent bond formation at saturating inhibitor concentration k_{inact} and inactivation constant K_I are obtained by solving implicit **Equation IV** (shown in **Figure 12E**).⁸¹ Use the substrate concentration during incubation (*Assay Protocol II, step 3*): after reaction initiation by enzyme addition but before (optional) addition of development/quenching solution. It is important that the Michaelis constant K_M be accurate for the reaction conditions (buffer, temperature, substrate), as this value is directly used to correct inactivation constant K_I for substrate competition. Consult the guidelines of your data-fitting software (e.g. GraphPad Prism)⁶⁶ for instructions on solving implicit equations (where Y appears on both sides of the equal sign). Proceed to *Sample Calculation 2* to calculate irreversible covalent inhibitor potency k_{inact}/K_I with propagation of error.

$$IC_{50}(t) = K_I \left(1 + \frac{[S]_0}{K_M} \right) \left(\frac{2 - 2e^{-\eta k_{\text{inact}} t}}{\eta k_{\text{inact}} t} - 1 \right) \quad \text{with} \quad \eta = \frac{IC_{50}(t)}{K_I \left(1 + \frac{[S]_0}{K_M} \right) + IC_{50}(t)} \quad (\text{iv})$$

Nonlinear regression of user-defined implicit equation: $Y = (K_I * (1 + (S/K_M))) * (((2 - (2 * \text{EXP}(-Y / ((K_I * (1 + (S/K_M))) + Y))) * k_{\text{inact}} * X)) / ((Y / ((K_I * (1 + (S/K_M))) + Y)) * k_{\text{inact}} * X) - 1)$, with Y = incubation time-dependent potency $IC_{50}(t)$ (in M), X = incubation time t (in s), S = maximum unbound substrate concentration at reaction initiation $[S]_0$ (in M, constrained), and KM = Michaelis constant K_M (in M, constrained) to find k_{inact} = inactivation rate constant k_{inact} (in s^{-1}) and K_I = inactivation constant K_I (in M).

7. Optional: Validate experimental kinetic parameters with kinetic simulations

Proceed to *Kinetic Simulations 1* to compare the experimental read-out to the product formation simulated with scripts **KinGen** and **KinDeg** (using experimental rate constant $k_{\text{inact}} = k_5$) to confirm that the calculated kinetic constants are in accordance with the experimental data and found $IC_{50}(t)$ values.

Assay Protocol III. Preincubation Time-Dependent Inhibition Without Dilution

The protocol below provides a generic set of steps to accomplishing this type of measurement.

Materials

- 1× Assay/reaction buffer supplemented with co-factors and reducing agent
- Active enzyme, 2× solution in assay buffer
- Substrate with continuous or quenched read-out, 11× solution in assay buffer
- Positive control: vehicle/solvent as DMSO stock, or 2% solution in assay buffer
- Negative control: known inhibitor or alkylating agent as DMSO stock, or 2× solution in assay buffer
- Inhibitor: as DMSO stock, or serial dilution of 2× solution in assay buffer with 2% DMSO
- *Optional:* Development/quenching solution
- 1.5 mL (Eppendorf) microtubes to prepare stock solutions
- 384-well low volume microplate with nonbinding surface (e.g. Corning 3820 or 4513) for preincubation/read-out
- General microplate cover/lid (e.g. Corning 6569 Microplate Aluminum Sealing Tape) if preincubation is conducted in a microplate
- *Optional:* 96-well microplate to prepare serial dilution of inhibitor concentration
- *Optional:* Microtubes to perform preincubations (e.g. Eppendorf Protein Lobind Microtubes, #022431018)
- Microplate reader equipped with appropriate filters to detect product formation (e.g. CLARIOstar microplate reader)
- *Optional:* Automated (acoustic) dispenser (e.g. Labcyte ECHO 550 Liquid Handler acoustic dispenser)

Exemplary assay concentrations

	preincubation t'			incubation t		
	[stock]	Volume	[conc] _{t'}	[stock]	Volume	[conc] _{t}
Enzyme	2 nM	10 μ L	0.99 nM	–	–	0.90 nM
Inhibitor	20 nM	10.2 μ L	10.10 nM	–	–	9.19 nM
Substrate	–	–	–	11 μ M	2 μ L	0.99 μM
<i>Total</i>		20.2 μ L			22.2 μ L	

Before you start, optimize assay conditions in the uninhibited control to ensure compliance with assumptions and restrictions, as outlined in section 2.3 and in Assay Protocol I. Consult Table 6 (section 5) for common optimization and troubleshooting options. Specific adjustments for Method III are that substrate concentration should be relatively low ($[S]_0 \ll K_m$) to minimize disruption of the noncovalent E + I \leftrightarrow EI equilibrium or reduction of reaction rates by competition (illustrated in Figure 14A); adjustment of the enzyme concentration might be required to ensure that maximum 10% of the substrate is processed during the read-out ($[P]_t < 0.1[S]_0$) and product formation is linear in the uninhibited control. Furthermore, incubation time t must be relatively short to minimize additional time-dependent enzyme inhibition after substrate addition. As a rule of thumb, incubation must be much shorter than the shortest preincubation ($t < t'$), unless the product formation read-out is continuous (more details in Data Analysis Protocol 3, step 3). Validate that enough product is formed for a good signal/noise ratio ($Z' > 0.5$) by calculating the Z'-score from the uninhibited and inhibited controls (ideally 8 replicates) in a separate experiment.⁵⁷ This method is compatible with homogeneous (continuous) assays but also with assays that require a development/quenching step to visualize formed product. Note that this protocol was designed for preincubation and read-out in a 384-well microplate.

1. Add inhibitor or control (e.g. 0.2 μ L) and assay buffer (e.g. 10 μ L) to each well with the uninhibited control for full enzyme activity containing the same volume vehicle/solvent instead of inhibitor as outlined in step 1 of Assay Protocol I.

Gently shake to mix DMSO with the aqueous buffer. Typically, measurements are performed in triplicate (or more replicates) with at least 8 inhibitor concentrations for at least 5 preincubation times. Inhibitor concentrations might need optimization, but a rational starting point is to use inhibitor concentrations below $5 \times IC_{50}$ at the shortest preincubation time t' : inhibition is expected to improve in a time-dependent manner and the best results are obtained when full inhibition is not achieved already at the shortest preincubation time. Alternatively, larger-volume preincubations (e.g. >200 μ L) can be performed in (Eppendorf) microtubes from which aliquots (e.g. 20.2 μ L) are transferred to a microplate after the indicated preincubation time. Whether preincubation is performed in a tube or microplate is a matter of personal preference, compatibility with lab equipment and automation, and convenience of dispensing small volumes.

2. Add active enzyme in assay buffer to each well (e.g. 10 μ L of 2 \times solution) or tube to start preincubation of enzyme with inhibitor and homogenize the solution by gently shaking (1 min at 300 rpm). Alternatively, dispensing the enzyme at a high flow rate will also mix the components.

The order of enzyme and inhibitor addition is not important *per se*, as long as DMSO stocks are added prior to buffered (aqueous) solutions. Inhibitor must be present in excess during preincubation ($[I]_0 > 10[E]_0$). Optionally, gently centrifuge the plate or microtubes (1 min at 1000 rpm) to ensure assay components are not stuck at the top of the well.

3. Seal the wells with a cover or lid, and close the caps of microtubes to prevent evaporation of assay components during preincubation.
4. *Optional:* Transfer aliquots (e.g. 20.2 μ L) from the reaction mixture to the microplate after completion of preincubation if performed in larger volumes.

5. Add substrate in assay buffer (e.g. 2 μ L of 11 \times solution) to (at least) three replicates after preincubation time t' .

Typically, preincubation can run anywhere from several minutes to hours depending on the enzyme stability and anticipated inhibitor potency, with superior accuracy if the preincubation time is monitored precisely. Substrate should be added in a negligible volume ($V_{\text{sub}} < 0.1V_t$) to minimize disruption of the noncovalent equilibria by dilution ($V_t = V_{t'}$) (**Figure 14A**). Because at steady-state the equilibrium can be disrupted by dilution in too much competitive substrate, keep the substrate volume V_{sub} and substrate concentration low ($[S]_0 < 0.1K_M$) for successful analysis of 2-step reversible inhibitors (*Data Analysis 3C*). Optionally, homogenize the solutions by gentle shaking (300 rpm) and centrifuge the plate or microtubes (1 min at 1000 rpm) to ensure that assay components are not stuck at the top of the well.

6. *Quenching:* Add development solution to the reaction mixture in the microplate to quench the product formation reaction if read-out of product formation requires a development/quenching step to visualize formed product after incubation time t .

Follow manufacturer advice on waiting time after addition of development solution before read-out. Incubation time t is the elapsed time between onset of product formation by substrate addition (*step 5*) and addition of development/quenching solution (*step 6*). A possible advantage to the use of a quenched assay is the possibility to store the samples after addition of quenching/development solution (*step 6*) and measure product formation (*step 7*) in all samples after completion of the final preincubation rather than performing multiple separate measurements (after each preincubation time).

7. Measure formed product after incubation by detection of the product read-out in microplate reader.

Incubation time (after substrate addition) is relatively short ($t \ll \ln(2)/k_{\text{obs}}$) to minimize additional (time-dependent) inhibition of enzyme activity during incubation (illustrated in **Figure 14B**).

8. Repeat *steps 4-7 of Assay Protocol III* for at least another four preincubation times.

Preincubation time t' is the elapsed time between onset of inhibition by mixing enzyme and inhibitor (*step 2*) and addition of substrate (*step 5*). A typical preincubation assay consists of multiple hours of measuring enzyme activity every 5-30 min, depending on enzyme stability and inhibitor reaction rates. Best results are obtained if the incubation time t used to calculate enzyme activity is kept constant at all preincubation times.

9. Proceed to *Data Analysis Protocol 3* to convert the raw experimental data into preincubation time-dependent enzyme activity.

Data Analysis Protocol 3 for all binding modes

Processing of raw experimental data obtained with *Assay Protocol III*.

1. Plot signal F against incubation time t

Plot signal F (in AU) on the Y-axis against the incubation time (in s) on the X-axis for each inhibitor concentration and for the controls (**Figure 14B**). Do this separately for each preincubation time. Proceed to *step 3* of this protocol for continuous read-out assays that require a longer incubation time to produce enough product for a good signal/noise ratio.

2. Fit F_t against t to obtain v_t

Fit signal F against incubation time t to **Equation XIII (Figure 15B/Figure 17B, left)** to obtain preincubation time-dependent product formation velocity v_t from the linear slope. Consult **Table 6** (section 5) for troubleshooting if product formation is not linear.

$$F_t = F_0 + v_t \cdot t \quad (\text{XIII})$$

Nonlinear regression of straight line $Y=Y\text{Intercept}+Slope*X$ with Y = signal F_t (in AU) and X = incubation time t (in s) to find $Y\text{Intercept}$ = background signal at reaction initiation F_0 (in AU) and Slope = preincubation time-dependent product formation velocity v_t (in AU/s).

3. Alternative for continuous: Fit F_t against t to obtain v_t

This is an alternative method to obtain v_t from the initial velocity for assays with a continuous read-out, using the initial velocity in progress curve analysis (*Method I*). Fit signal F_t against incubation time t to exponential association **Equation XIV (Figure 15B/Figure 17B, right)** to obtain preincubation time-dependent product formation velocity v_t from the initial velocity. This resolves issues with low signal/noise ratios for continuous read-out assays where v_t is not linear (due to additional covalent modification during the incubation) by allowing longer incubation times to produce sufficient signal.

$$F_t = v_s t + \frac{v_t - v_s}{k} [1 - e^{-kt}] + F_0 \quad (\text{XIV})$$

Nonlinear regression of user-defined explicit equation $Y=(vs*X)+(((vi-vs)/kobs)*(1-EXP(-kobs*X)))+Y0$ with Y = signal F_t (in AU) and X = incubation time t (in s) to find $Y0$ = Y -intercept F_0 = background signal at $t = 0$ (in AU), vi = initial slope = preincubation time-dependent product formation velocity v_t (in AU/s), vs = final slope v_s (in AU/s) and $kobs$ = nonlinearity reaction rate k (in s^{-1}).

4. Proceed to Data Analysis Protocols to obtain the appropriate kinetic parameters for each covalent binding mode: *Data Analysis Protocol 3Ai* or *3Aii* for 2-step irreversible inhibitors, *Data Analysis Protocol 3Bi* or *3Bii* for 1-step irreversible inhibitors, and *Data Analysis Protocol 3C* for 2-step reversible inhibitors.

Selection of a data analysis method for inhibitors with an irreversible binding mode depends on the desired visual representation as well as personal preference. Generally, *Data Analysis Protocols 3Ai* and *3Bi* have less data processing/manipulation and are more informative for comparison of various inhibitors on a single enzyme target, as they are compatible with assessment of inhibitor potency simultaneous with visual assessment of time-dependent enzyme stability k_{ctrl} (**Figure 16B** and **Figure 18B**). *Alternative Data Analysis Protocols 3Aii* and *3Bii* involve normalization of the enzyme activity that aids visual assessment of inhibitory potency of a single inhibitor on multiple enzyme targets (that might have a variable stability) (**Figure 16D** and **Figure 18D**).

Data Analysis Protocol

EXP Conditions	2-step IRREV	1-step IRREV	2-step REV
$k_{ctrl} = 0$	3Ai	3B	3C
$k_{degE} > 0$	3Ai or 3Aii	3Bi or 3Bii	3C

Data Analysis Protocol 3Ai for 2-Step IRREV Inhibition

Processing of experimental data obtained with *Assay Protocol III* that has been processed according to *Data Analysis Protocol 3* for 2-step irreversible covalent inhibitors.

1. Plot v_t against preincubation time t' for each inhibitor concentration

Plot the mean and standard deviation of v_t (in AU/s) on the Y-axis against preincubation time t' (in s) on the X-axis for each inhibitor concentration and the uninhibited control (**Figure 15C**). Validate that inhibitor concentrations are not too high: inhibition should be less than 100% at the shortest t' for at least six inhibitor concentrations. Check whether the uninhibited enzyme activity is independent of preincubation time ($v_0^{\text{ctrl}} = v_t^{\text{ctrl}}$, **Figure 15C**): an algebraic correction for enzyme instability ($k_{\text{ctrl}} > 0$, **Figure 16B**) can be performed in *step 4* of this protocol by accounting for nonlinearity in the uninhibited control in the secondary k_{obs} plot (**Figure 16C**). Alternatively, proceed to *Alternative Data Analysis Protocol 3Aii* to correct for enzyme instability ($v_0^{\text{ctrl}} > v_t^{\text{ctrl}}$) by normalization of the enzyme activity v_t/v_t^{ctrl} (**Figure 16D-E**).

2. Fit v_t against preincubation time t' to obtain k_{obs}

Fit the mean and standard deviation of v_t against preincubation time t' (**Figure 15C**/**Figure 16B**) to **Equation V**. Constrain v_s = value in fully inhibited control to obtain the observed reaction rate k_{obs} from initial velocity v_i (Y-intercept) to full inactivation (Plateau = 0). A lack of initial noncovalent complex ($v_i = v_0^{\text{ctrl}}$) is indicative of 1-step binding behavior.

$$v_t = v_s + (v_i - v_s) e^{-k_{\text{obs}} t'} \quad (\text{V})$$

Nonlinear regression of exponential one-phase decay equation $Y=(Y0-\text{Plateau})*\text{EXP}(-k*X)+\text{Plateau}$ with Y = preincubation time-dependent product formation velocity v_t (in AU/s), X = preincubation time t' (in s), and Plateau = final velocity in the fully inhibited control v_s (in AU/s, constrained) to find $Y0$ = Y-intercept = initial velocity v_i (in AU/s) and k = observed reaction rate k_{obs} (in s^{-1}).

3. Plot k_{obs} against $[I]$

Plot the mean and standard deviation of k_{obs} (in s^{-1}) on the Y-axis against inhibitor concentration (in M) during preincubation (*before* addition of substrate) on the X-axis (**Figure 15D**/**Figure 16C**). The plot of k_{obs} against $[I]$ should reach a maximum k_{obs} at saturating inhibitor concentration. Note that a linear curve is indicative of 1-step binding behavior at non-saturating inhibitor concentrations ($[I] \ll 0.1K_i^{\text{app}}$: see **Figure 3F**) with $v_i = v_0^{\text{ctrl}}$ (shared Y-intercept in the previous step). Proceed to *step 4* of *Data Analysis Protocol 3Bi* after it has been validated that the linear curve is not resultant from saturating inhibitor concentrations ($[I] \gg 10K_i^{\text{app}}$: see **Figure 3G**) as identified by $v_i \ll v_0^{\text{ctrl}}$, by repeating the measurement with lower inhibitor concentrations.

4. Fit k_{obs} against $[I]$ to obtain k_{inact} and K_i

Fit k_{obs} against inhibitor concentration during preincubation to **Equation xv** to obtain maximum inactivation rate constant k_{inact} and inactivation constant K_i . Constrain $k_{\text{ctrl}} = k_{\text{obs}}$ of the uninhibited control (**Figure 15C**). Inactivation constant K_i does not have to be corrected for substrate competition because preincubation is conducted in absence of competing substrate. Calculate irreversible covalent inhibitor potency k_{inact}/K_i with propagation of error with *Sample Calculation 2*.

$$k_{\text{obs}} = k_{\text{ctrl}} + \frac{k_{\text{inact}} [I]}{K_i + [I]} \quad (\text{xv})$$

Nonlinear regression of user-defined explicit equation $Y=Y0+((k_{\text{max}}*X)/((K_i)+X))$ with Y = observed reaction rate k_{obs} (in s^{-1}), X = inhibitor concentration during preincubation (in M), and $Y0$ = rate of nonlinearity in uninhibited control k_{ctrl} (in s^{-1} , constrained) to find k_{max} = maximum reaction rate k_{inact} (in s^{-1}) and K_i = Inactivation constant K_i (in M).

5. *Optional:* Validate experimental kinetic parameters with kinetic simulations

Proceed to *Kinetic Simulations 1* to compare the experimental read-out to the product formation simulated with scripts **KinGen** and **KinDeg** (using experimental rate constant $k_{\text{inact}} = k_s$) to confirm that the calculated kinetic constants are in accordance with the experimental data. Also perform simulations with **KinVol** and **KinVolDeg** to confirm that addition of substrate does not significantly affect the noncovalent interactions.

Alternative Data Analysis Protocol 3Aii for 2-Step IRREV Inhibition

Processing of experimental data obtained with *Assay Protocol III* that has been processed according to *Data Analysis Protocol 3* for 2-step irreversible covalent inhibitors.

1. Plot v_t against preincubation time t' for each inhibitor concentration

Plot the mean and standard deviation of v_t (in AU/s) on the Y-axis against preincubation time t' (in s) on the X-axis for each inhibitor concentration and the uninhibited control (**Figure 15C**/**Figure 16B**). Validate that inhibitor concentrations are not too high: inhibition should be less than 100% at the shortest t' for at least six inhibitor concentrations.

2. Normalize v_t to obtain v_t/v^{ctrl}

Normalize v_t of each inhibitor concentration and the controls to lowest value = 0 (or full inhibition control) and highest value = uninhibited product formation v_t^{ctrl} to obtain normalized enzyme activity v_t/v^{ctrl} . Perform this correction separately for each preincubation time.

3. Plot and fit v_t/v^{ctrl} against preincubation time t' to obtain k_{obs}

Plot the mean and standard deviation of v_t/v^{ctrl} on the Y-axis against preincubation time t' (in s) on the X-axis (**Figure 16D**). Fit to exponential decay **Equation XVI** to obtain k_{obs} from initial velocity v_i/v_0^{ctrl} to full inactivation (Plateau = 0). A lack of initial noncovalent complex ($v_i/v_0^{ctrl} = 1$) is indicative of 1-step binding behavior.

$$\left(\frac{v_t}{v_t^{ctrl}} \right) = \left(\frac{v_i}{v_0^{ctrl}} \right) e^{-k_{obs} t'} \quad (\text{xvi})$$

Nonlinear regression of exponential one-phase decay equation $Y=(Y0-Plateau)*EXP(-k*X)+Plateau$ with Y = normalized preincubation time-dependent product formation velocity v_t/v^{ctrl} (unitless), X = preincubation time t' (in s), and Plateau = normalized final velocity $v_t/v_0^{ctrl} = 0$ (unitless, constrained) to find $Y0$ = Y-intercept = normalized initial velocity v_i/v_0^{ctrl} (unitless) and k = observed reaction rate k_{obs} (in s^{-1}).

4. Plot k_{obs} against $[I]$

Plot the mean and standard deviation of k_{obs} (in s^{-1}) on the Y-axis against inhibitor concentration (in M) during preincubation (*before addition of substrate*) on the X-axis (**Figure 16E**). The plot of k_{obs} against $[I]$ should have a Y-intercept = 0 and reach a maximum k_{obs} at saturating inhibitor concentration. Note that a linear curve is indicative of 1-step binding behavior at non-saturating inhibitor concentrations ($[I] \ll 0.1K_1^{app}$: see **Figure 3F**) with $v_i = v_0^{ctrl}$ (shared Y-intercept = 1 in the previous step). Proceed to *step 5 of Data Analysis Protocol 3Bii* after it has been validated that the linear curve is not resultant from saturating inhibitor concentrations ($[I] \gg 10K_1^{app}$: see **Figure 3G**) as identified by $v_i \ll v_0^{ctrl}$ (shared Y-intercept = 0 in the previous step), by repeating the measurement with lower inhibitor concentrations.

5. Fit k_{obs} against $[I]$ to obtain k_{inact} and K_1

Fit k_{obs} against inhibitor concentration during preincubation to **Equation XVII** to obtain maximum inactivation rate constant k_{inact} and inactivation constant K_1 (**Figure 16E**). Do not correct for enzyme instability ($k_{ctrl} > 0$), as this correction has already been performed by normalizing v_t to v_t/v^{ctrl} in *step 2* of this protocol. Inactivation constant K_1 does not have to be corrected for substrate competition because preincubation is conducted in absence of competing substrate. Calculate irreversible covalent inhibitor potency k_{inact}/K_1 with propagation of error with *Sample Calculation 2*.

$$k_{obs} = \frac{k_{inact} [I]}{K_1 + [I]} \quad (\text{xvii})$$

Nonlinear regression of user-defined explicit equation $Y=Y0+((kmax*X)/((K1)+X))$ with Y = observed reaction rate k_{obs} (in s^{-1}), X = inhibitor concentration during preincubation (in M), and $Y0 = 0$ (in s^{-1} , constrained) to find $kmax$ = maximum reaction rate k_{inact} (in s^{-1}) and $K1$ = inactivation constant K_1 (in M).

6. *Optional:* Validate experimental kinetic parameters with kinetic simulations

Proceed to *Kinetic Simulations 1* to compare the experimental read-out to the product formation simulated with scripts **KinGen** and **KinDeg** (using experimental rate constant $k_{inact} = k_s$) to confirm that the calculated kinetic constants are in accordance with the experimental data. Also perform simulations with **KinVol** and **KinVolDeg** to confirm that addition of substrate does not significantly affect the noncovalent interactions.

Data Analysis Protocol 3Bi for 1-step IRREV Inhibition

Processing of experimental data obtained with *Assay Protocol III* that has been processed according to *Data Analysis Protocol 3* for 1-step irreversible covalent inhibitors and 2-step irreversible inhibitors at non-saturating inhibitor concentrations ($[I] \leq 0.1K_I$).

1. Plot $v_{t'}$ against preincubation time t' for each inhibitor concentration

Plot the mean and standard deviation of $v_{t'}$ (in AU/s) on the Y-axis against preincubation time t' (in s) on the X-axis for each inhibitor concentration and the uninhibited control (**Figure 17C**). Validate that inhibitor concentrations are not too high: inhibition should be less than 100% at the shortest t' for at least six inhibitor concentrations. Check whether the uninhibited enzyme activity is independent of preincubation time ($v_0^{\text{ctrl}} = v_{t'}^{\text{ctrl}}$, **Figure 17C**): an algebraic correction for enzyme instability ($k_{\text{ctrl}} > 0$, **Figure 18B**) can be performed in *step 4* of this protocol by accounting for nonlinearity in the uninhibited control in the secondary k_{obs} plot (**Figure 18C**). Alternatively, proceed to *Alternative Data Analysis Protocol 3Bi* to correct for enzyme instability ($v_0^{\text{ctrl}} > v_{t'}^{\text{ctrl}}$) by normalization of the enzyme activity $v_{t'}/v_{t'}^{\text{ctrl}}$ (**Figure 18D-E**).

2. Fit $v_{t'}$ against preincubation time t' to obtain k_{obs}

Fit the mean and standard deviation of $v_{t'}$ against preincubation time t' (**Figure 17C/Figure 18B**) to **Equation V**. Constrain v_s = value in fully inhibited control to obtain the observed reaction rate k_{obs} from initial velocity v_i (Y-intercept) to full inactivation (Plateau = 0). A lack of initial noncovalent complex ($v_i = v_0^{\text{ctrl}}$) is indicative of 1-step binding behavior.

$$v_{t'} = v_s + (v_i - v_s) e^{-k_{\text{obs}} t'} \quad (\text{V})$$

Nonlinear regression of exponential one-phase decay equation $Y=(Y0-\text{Plateau}) * \text{EXP}(-k*X) + \text{Plateau}$ with Y = preincubation time-dependent product formation velocity $v_{t'}$ (in AU/s), X = preincubation time t' (in s), and Plateau = final velocity in the fully inhibited control v_s (in AU/s, constrained) to find $Y0$ = Y-intercept = initial velocity v_i = uninhibited initial velocity v_0^{ctrl} (in AU/s, shared value), and k = observed reaction rate k_{obs} (in s^{-1}).

3. Plot k_{obs} against $[I]$

Plot the mean and standard deviation of k_{obs} (in s^{-1}) on the Y-axis against inhibitor concentration (in M) during preincubation (*before* addition of substrate) on the X-axis (**Figure 17D/Figure 18C**). The plot of k_{obs} against inhibitor concentration $[I]$ is linear for 1-step irreversible inhibitors and for 2-step irreversible inhibitors at non-saturating inhibitor concentrations ($[I] \ll 0.1K_I$).

4. Fit k_{obs} against $[I]$ to obtain k_{chem}

Fit k_{obs} against inhibitor concentration during preincubation to **Equation XVIII** to obtain inhibitor potency k_{chem} from the linear slope. Constrain Y-intercept $k_{\text{ctrl}} = k_{\text{obs}}$ of the uninhibited control (**Figure 18C**). Inhibitor potency k_{chem} does **not** have to be corrected for substrate competition because preincubation is conducted in absence of competing substrate. Calculate k_{inact}/K_I for 2-step irreversible inhibitors at non-saturating inhibitor concentrations ($[I] \leq 0.1K_I$) with *Sample Calculation 9*.

$$k_{\text{obs}} = k_{\text{ctrl}} + k_{\text{chem}} [I] \quad (\text{XVIII})$$

Nonlinear regression of straight line $Y=Y\text{Intercept}+Slope*X$ with Y = observed reaction rate k_{obs} (in s^{-1}), X = inhibitor concentration during preincubation (in M) and $Y\text{Intercept}$ = rate of nonlinearity in uninhibited control k_{ctrl} (in s^{-1} , constrained) to find Slope = inactivation rate constant k_{chem} (in $\text{M}^{-1}\text{s}^{-1}$).

5. Optional: Validate experimental kinetic parameters with kinetic simulations

Proceed to *Kinetic Simulations 1* to compare the experimental read-out to the product formation simulated with scripts **KinGen** and **KinDeg** (using experimental rate constant $k_{\text{chem}} = k_3$) to confirm that the calculated kinetic constants are in accordance with the experimental data. Also perform simulations with **KinVol** and **KinVolDeg** to confirm that addition of substrate does not significantly affect the reaction rates by dilution and/or competition.

Alternative Data Analysis Protocol 3Bii for 1-step IRREV Inhibition

Processing of experimental data obtained with *Assay Protocol III* that has been processed according to *Data Analysis Protocol 3* for 1-step irreversible covalent inhibitors and 2-step irreversible inhibitors at non-saturating inhibitor concentrations ($[I] \leq 0.1K_I$).

1. Plot v_t against preincubation time t' for each inhibitor concentration

Plot the mean and standard deviation of v_t (in AU/s) on the Y-axis against preincubation time t' (in s) on the X-axis for each inhibitor concentration and the uninhibited control (**Figure 17C**/**Figure 18B**). Validate that inhibitor concentrations are not too high: inhibition should be less than 100% at the shortest t' for at least six inhibitor concentrations.

2. Normalize v_t to obtain v_t/v^{ctrl}

Normalize v_t of each inhibitor concentration and the controls to lowest value = 0 (or full inhibition control) and highest value = uninhibited product formation v_t^{ctrl} to obtain normalized enzyme activity v_t/v^{ctrl} . Perform this correction separately for each preincubation time.

3. Plot and fit v_t/v^{ctrl} against preincubation time t' to obtain k_{obs}

Plot the mean and standard deviation of v_t/v^{ctrl} on the Y-axis against preincubation time t' (in s) on the X-axis (**Figure 18D**). Fit to exponential decay **Equation XIX** to obtain k_{obs} from initial velocity v_t/v_0^{ctrl} to full inactivation (Plateau = 0). A lack of initial noncovalent complex ($v_t/v_0^{ctrl} = 1$) is indicative of 1-step binding behavior.

$$\left(\frac{v_t}{v_t^{ctrl}} \right) = e^{-k_{obs} t'} \quad (\text{XIX})$$

Nonlinear regression of exponential one-phase decay equation $Y=(Y0-Plateau)*\text{EXP}(-k*X)+Plateau$ with Y = normalized preincubation time-dependent product formation velocity v_t/v^{ctrl} (unitless), X = preincubation time t' (in s), $Y0$ = Y-intercept = normalized initial velocity $v_t/v_0^{ctrl} = 1$ (unitless, constrained), and $Plateau$ = normalized final velocity $v_t/v^{ctrl} = 0$ (unitless, constrained) to find k = observed reaction rate k_{obs} (in s^{-1}).

4. Plot k_{obs} against $[I]$

Plot the mean and standard deviation of k_{obs} (in s^{-1}) on the Y-axis against inhibitor concentration (in M) during preincubation (*before* addition of substrate) on the X-axis (**Figure 18E**). The plot of k_{obs} against inhibitor concentration $[I]$ is linear for 1-step irreversible inhibitors and for 2-step irreversible inhibitors at non-saturating inhibitor concentrations ($[I] \ll 0.1K_I$).

5. Fit k_{obs} against $[I]$ to obtain k_{chem}

Fit k_{obs} against inhibitor concentration during preincubation to **Equation XX** to obtain inhibitor potency k_{chem} from the linear slope (**Figure 18E**). Do not correct for enzyme instability ($k_{ctrl} > 0$), as this correction has already been performed by normalizing v_t to v_t/v^{ctrl} in step 2 of this protocol. Inhibitor potency k_{chem} does not have to be corrected for substrate competition because preincubation is conducted in absence of competing substrate. Calculate k_{inact}/K_I for 2-step irreversible inhibitors at non-saturating inhibitor concentrations ($[I] \leq 0.1K_I$) with *Sample Calculation 9*. Alternatively, inhibitor potency k_{chem} or k_{inact}/K_I can be directly calculated from a single k_{obs} and $[I]$ with *Sample Calculation 10*.

$$k_{obs} = k_{chem} [I] \quad (\text{XX})$$

Nonlinear regression of straight line $Y=Y\text{Intercept}+\text{Slope}\cdot X$ with Y = observed reaction rate k_{obs} (in s^{-1}), X = inhibitor concentration during preincubation (in M), and $Y\text{Intercept} = 0$ (in s^{-1} , constrained) to find Slope = inactivation rate constant k_{chem} (in $M^{-1}s^{-1}$).

6. Optional: Validate experimental kinetic parameters with kinetic simulations

Proceed to *Kinetic Simulations 1* to compare the experimental read-out to the product formation simulated with scripts **KinGen** and **KinDeg** (using experimental rate constant $k_{chem} = k_3$) to confirm that the calculated kinetic constants are in accordance with the experimental data. Also perform simulations with **KinVol** and **KinVolDeg** to confirm that addition of substrate does not significantly affect the reaction rates by dilution and/or competition.

Data Analysis Protocol 3C for 2-Step REV Inhibition

Processing of experimental data obtained with *Assay Protocol III* that has been processed according to *Data Analysis Protocol 3* for 2-step reversible covalent inhibitors.

1. Plot v_t' against preincubation time t' for each inhibitor concentration

Plot the mean and standard deviation of v_t' (in AU/s) on the Y-axis against preincubation time t' (in s) on the X-axis for each inhibitor concentration and the uninhibited control (**Figure 19C/Figure 20B**). Validate that inhibitor concentrations are not too high: inhibition should be less than 100% at the shortest t' for at least six inhibitor concentrations. Enzyme activity is never truly independent of preincubation time ($v_0^{\text{ctrl}} > v_t^{\text{ctrl}}$) and kinetic analysis of reversible inhibitors is very sensitive to small deviations (as illustrated in **Figure 9**). Therefore, correction for enzyme instability is always performed by normalization of the enzyme activity v_t/v_t^{ctrl} in the next step (illustrated in **Figure 20**).

2. Normalize v_t' to obtain v_t/v_t^{ctrl}

Normalize v_t' of each inhibitor concentration and the controls to lowest value = 0 (or full inhibition control) and highest value = uninhibited product formation v_t^{ctrl} to obtain normalized enzyme activity v_t/v_t^{ctrl} (**Figure 20C**). Perform this correction separately for each preincubation time.

3. Plot and fit v_t/v_t^{ctrl} against preincubation time t' to obtain k_{obs} and v_s/v_s^{ctrl}

Plot the mean and standard deviation of v_t/v_t^{ctrl} on the Y-axis against preincubation time t' (in s) on the X-axis (**Figure 20C**). Fit to exponential decay **Equation XXI** to obtain k_{obs} from initial velocity v_t/v_0^{ctrl} reflecting rapid noncovalent equilibrium (Y-intercept $v_t/v_0^{\text{ctrl}} \leq 1$) to the final velocity v_s/v_s^{ctrl} reflecting steady-state equilibrium (Plateau $v_s/v_s^{\text{ctrl}} \geq 0$).

$$\left(\frac{v_t}{v_t^{\text{ctrl}}} \right) = \left(\frac{v_s}{v_s^{\text{ctrl}}} \right) + \left(\frac{v_i}{v_0^{\text{ctrl}}} - \frac{v_s}{v_s^{\text{ctrl}}} \right) e^{-k_{\text{obs}} t'} \quad (\text{xxi})$$

Nonlinear regression of exponential one-phase decay equation $Y=(Y0-\text{Plateau})*\text{EXP}(-k*X)+\text{Plateau}$ with Y = normalized preincubation time-dependent product formation velocity v_t/v_t^{ctrl} (unitless) and X = preincubation time t' (in s) to find $Y0$ = Y-intercept = normalized initial velocity v_t/v_0^{ctrl} (unitless), Plateau = normalized final velocity v_s/v_s^{ctrl} (unitless), and k = observed reaction rate k_{obs} (in s^{-1}).

4. Plot and fit v_s/v_s^{ctrl} against $[I]$ to obtain K_i^*

Steady-state inhibition constant K_i^* can be calculated from v_s/v_s^{ctrl} (obtained in the previous step) reflecting remaining fractional enzyme activity after reaching the steady-state inhibitor equilibrium (*reaction completion*) (**Figure 20E**). Plot the mean and standard deviation of v_s/v_s^{ctrl} on the Y-axis against inhibitor concentration (in M) during preincubation (*before* addition of substrate) on the X-axis (**Figure 20E**), and fit the dose-response curve to four-parameter nonlinear regression Hill **Equation XXII** to obtain steady-state inhibition constant K_i^* .³³ The maximum product formation velocity at reaction completion corresponds with the uninhibited enzyme activity $v_s^{\text{ctrl}}/v_s = 1$ and minimum velocity $v_s^{\text{min}}/v_s^{\text{ctrl}} = 0$ for (background-)corrected enzyme activity in the full inhibition control. Steady-state equilibrium constant K_i^* does not have to be corrected for substrate competition because preincubation is conducted in absence of competing substrate.

$$\left(\frac{v_s}{v_s^{\text{ctrl}}} \right) = 1 + \frac{1}{1 + \left(\frac{[I]}{K_i^*} \right)^h} \quad (\text{xxii})$$

Nonlinear regression of four-parameter dose-response equation $Y=\text{Bottom}+(\text{Top}-\text{Bottom})/(1+(X/\text{IC50})^{\text{HillSlope}})$ with Y = fractional steady-state product formation velocity v_s/v_s^{ctrl} (unitless), X = inhibitor concentration during preincubation (in M), Bottom = velocity in fully inhibited control $v_s^{\text{min}}/v_s^{\text{ctrl}} = 0$ (unitless, constrained), and Top = uninhibited enzyme activity $v_s/v_s^{\text{ctrl}} = 1$ (unitless, constrained) to find HillSlope = Hill coefficient h (unitless) and IC50 = steady-state inhibition constant K_i^* (in M).

5. *Optional:* Plot and fit k_{obs} against $[I]$ to obtain K_i , k_s , and k_6

This is an optional data processing step to obtain kinetic parameters by fitting to the observed rate k_{obs} (obtained in *step 3 of Data Analysis Protocol 3C*), and can be used to validate K_i^* values found in the previous step or to find values for k_s and k_6 to use in kinetic simulations (next step in this protocol). Plot the mean and standard deviation of k_{obs} (in s^{-1}) on the Y-axis against inhibitor concentration *during preincubation* (in M) on the X-axis (**Figure 20D**). Exclude the uninhibited control ($k_{\text{ctrl}} = 0$ for normalized enzyme activity) from the fit because Y-intercept = k_6 rather than k_{ctrl} . Fit k_{obs} against inhibitor concentration to **Equation XXIII** to obtain rate constants for the covalent association k_s and covalent dissociation k_6 as well as noncovalent inhibition constant K_i reflecting the rapid (initial) noncovalent equilibrium. Noncovalent equilibrium constant K_i does not have to be corrected for substrate competition because preincubation

is conducted in absence of competing substrate. Proceed to *Sample Calculation 8* to calculate steady-state inhibition constant K_i^* from experimental values of K_i , k_5 , and k_6 .

$$k_{\text{obs}} = k_6 + \frac{k_5 [I]}{K_i + [I]} \quad (\text{XXIII})$$

Nonlinear regression of user-defined explicit equation $Y=Y0+((k\text{max}\times X)/((K_i)+X))$ with Y = observed reaction rate k_{obs} (in s^{-1}) and X = inhibitor concentration during preincubation (in M) to find $Y0$ = covalent dissociation rate constant k_6 (in s^{-1}), $k\text{max}$ = covalent association rate constant k_5 (in s^{-1}), and K_i = inhibition constant K_i (in M).

6. Optional: Validate experimental kinetic parameters with kinetic simulations

Proceed to *Kinetic Simulations 1* to compare the experimental read-out to the product formation simulated with scripts **KinGen** and **KinDeg** to confirm that the calculated kinetic constants are in accordance with the experimental data. Also perform simulations with **KinVol** and **KinVolDeg** to confirm that addition of substrate does not significantly affect the noncovalent interactions/equilibria or reaction rates by dilution and/or competition. Experimental estimates of k_5 and k_6 are generated in the previous step of this protocol.

Assay Protocol IV. Preincubation Time-Dependent Inhibition With Dilution/Competition

The protocol below provides a generic set of steps to accomplish this type of measurement.

Materials

- 1x Assay/reaction buffer supplemented with co-factors and reducing agent
- Active enzyme, 200x solution in assay buffer
- Substrate with continuous or quenched read-out, 1x solution in assay buffer
- Positive control: vehicle/solvent as DMSO stock, or 2% solution in assay buffer
- Negative control: known inhibitor or alkylating agent as DMSO stock, or 200x solution in assay buffer with 2% DMSO
- Inhibitor: as DMSO stock, or serial dilution of 200x solution in assay buffer with 2% DMSO
- *Optional:* Development/quenching solution
- 1.5 mL (Eppendorf) microtubes to prepare stock solutions
- 384-well low volume microplate with nonbinding surface (e.g. Corning 3820 or 4513) for preincubation
- Microplate cover/lid (e.g. Corning 6569 Microplate Aluminum Sealing Tape) to seal 384-well plate during preincubation
- 96-well low volume microplate with nonbinding surface (e.g. Corning 3650 or 3820) for quenching and read-out
- *Optional:* 96-well microplate to prepare serial dilution of inhibitor concentration
- *Optional:* Microtubes to perform preincubations (e.g. Eppendorf Protein Lobind Microtubes, #022431018)
- *Optional:* 384-well low volume microplate with nonbinding surface (e.g. Corning 3820 or 4513) for read-out
- Microplate reader equipped with appropriate filters to detect product formation (e.g. CLARIOstar microplate reader)
- *Optional:* Automated (acoustic) dispenser (e.g. Labcyte ECHO 550 Liquid Handler acoustic dispenser)

Exemplary assay concentrations

	incubation t'			incubation t		
	[stock]	Volume	[conc] $_{t'}$	[stock]	Volume	[conc] $_{t}$
Enzyme	200 nM	10 μL	99 nM	–	1 μL	1.0 nM
Inhibitor	2000 nM	10.2 μL	1010 nM	–	1 μL	10 nM
Substrate	–	–	–	10 μM	198 μL	9.9 μM
<i>Total</i>		20.2 μL			200 μL	

Before you start, optimize assay conditions in the uninhibited control to ensure compliance with assumptions and restrictions, as outlined in *Assay Protocol I*. Consult **Table 6** (section 5) for common optimization and troubleshooting options.

Specific adjustments for Method IV

Substrate should be added in a large volume ($V_{\text{sub}} \gg V_t$) and/or at a high concentration ($[S]_0 \gg K_M$) to quench time-dependent enzyme inhibition (as illustrated in [Figure 21](#)). Enzyme concentration after dilution $[E^{\text{total}}]_t$ should be adjusted to correspond to maximum 10% substrate conversion until the end of the incubation in the uninhibited control ($[P]_t < 0.1[S]_0$), and substrate should be present in excess ($[S]_0 > 10[E^{\text{total}}]_t$). Preincubation-dependent enzyme activity should be calculated from initial, linear product formation after substrate addition. Validate that enough product is formed for a good signal:noise ratio ($Z' > 0.5$) by calculating the Z' -score from the uninhibited and inhibited controls (ideally 8 replicates) in a separate experiment.⁸⁷ This method is compatible with homogeneous (continuous) assays but also with assays that require a development/quenching step to visualize formed product. Note that preincubation in very small volumes ($<10 \mu\text{L}$) is not representative/reliable and the volume after 100-fold dilution in substrate will often exceed the maximum well volume of assay plates. Therefore, preincubation is typically performed in a larger volume (tube or plate) from which aliquots are removed at the end of the preincubation. In this protocol, we perform incubations in triplicate (20 μL per replicate) in a 384-well plate, from which 2 μL aliquots are removed and quenched in 198 μL substrate in a 96-well plate that is also used for read-out. Optionally, it is possible to then transfer 20 μL to a 384-well plate for read-out, but multiple transfers of assay solutions will introduce errors. Alternatively, preincubation can be performed in microtubes or a 96-well plate.

1. Add inhibitor or control (e.g. 0.2 μL) and assay buffer (e.g. 10 μL) to each well with the uninhibited control for full enzyme activity containing the same volume vehicle/solvent instead of inhibitor, as outlined in [step 1 of Assay Protocol III](#).

Gently shake to mix DMSO with the aqueous buffer. Typically, measurements are performed in triplicate (or more replicates) with at least 8 inhibitor concentrations for at least 5 preincubation times. Inhibitor concentrations might need optimization, but a rational starting point is to use inhibitor concentrations below $5 \times IC_{50}$ at the shortest preincubation time t' : inhibition is expected to improve in a time-dependent manner, and the best results are obtained when full inhibition is not achieved already at the shortest preincubation time. Whether preincubation is performed in a tube or microplate is a matter of personal preference, compatibility with lab equipment and automation, and convenience of dispensing small volumes.

2. Add active enzyme in assay buffer to each well (e.g. 10 μL of 200 \times solution) or tube to start preincubation of enzyme with inhibitor and homogenize the solution by gently shaking (1 min at 300 rpm). Alternatively, dispensing the enzyme at a high flow rate will also mix the components.

The order of enzyme and inhibitor addition is not important *per se*, as long as DMSO stocks are added prior to buffered (aqueous) solutions. Inhibitor must be present in excess during preincubation ($[I]_0 > 10[E]_0$). Optionally, gently centrifuge the plate or microtubes (1 min at 1000 rpm) to ensure assay components are not stuck at the top of the well.

3. Seal the wells with a cover or lid, and close the caps of microtubes to prevent evaporation of assay components during preincubation.

4. Remove a single aliquot in volume V_t (e.g. 2 μL) from the reaction mixture, and transfer to a 96-well microplate already containing a large volume (volume V_{sub}) of substrate (e.g. 198 μL of 1 \times solution in assay buffer) after preincubation time t' .

Substrate should be added in a large volume ($V_t \ll V_{\text{sub}}$) and/or at a high concentration ($[S] \gg K_M$) to quench time-dependent addition enzyme inhibition during incubation by dilution ($[I]_t \ll [I]_0$) or competition (increasing K_i^{app} or decreasing $k_{\text{chem}}^{\text{app}}$). Dilution to inhibitor concentration far below the equilibrium concentration ($[I]_t \ll K_i^{\text{app}}$) promotes dissociation of noncovalently bound inhibitor after substrate addition (illustrated in [Figure 21A](#)). The accuracy of the measurement improves if the preincubation time is monitored precisely. Optionally, homogenize the solutions by gentle shaking (300 rpm) and centrifuge the plate (1 min at 1000 rpm) to ensure assay components are not stuck at the top of the well.

5. **Quenching:** Add development solution to the reaction mixture in the microplate to quench the product formation reaction if read-out of product formation requires a development/quenching step to visualize formed product after incubation time t .

Follow manufacturer advice on waiting time after addition of development solution before read-out. Incubation time t is the elapsed time between onset of product formation by substrate addition ([step 4](#)) and addition of development/quenching solution ([step 5](#)). A possible advantage to the use of a quenched assay is the ability to store the samples

after addition of quenching/development solution (*step 5*) and measure product formation (*step 6*) in all samples after completion of the final preincubation rather than performing multiple separate measurements (after each preincubation time).

6. *Optional:* Transfer aliquot (e.g. 20 μ L) to a 384-well microplate for read-out.

Typically, the total volume after dilution in substrate solution ($V_t = V_{\text{sub}} + V_t'$) exceeds the maximum well volume of a 384-well microplate. Transfer an appropriate amount of reaction mixture (at least two technical replicates) to a microplate. This step can be skipped if read-out is performed in a 96-well plate.

7. Measure formed product after incubation by detection of the product read-out in reader.

Incubation time t (after substrate addition) is arbitrary as long as product formation is linear in uninhibited as well as inhibited samples (**Figure 21B**).

8. Repeat steps 4-7 of *Assay Protocol IV* for at least another four preincubation times.

Preincubation time t' is the elapsed time between onset of inhibition by mixing enzyme and inhibitor (*step 2*) and addition of substrate (*step 4*). A typical preincubation assay is multiple hours measuring enzyme activity every 5-30 min, depending on enzyme stability and inhibitor reaction rates. Best results are obtained if the incubation time t used to calculate enzyme activity is kept constant at all preincubation times.

9. Proceed to *Data Analysis Protocol 4* to convert the raw experimental data into preincubation time-dependent enzyme activity.

Data Analysis Protocol 4 for 1-step and 2-step IRREV Inhibition

Processing of raw experimental data obtained with *Assay Protocol IV* for irreversible inhibitors.

1. Plot signal F against incubation time t

Plot signal F (in AU) on the Y-axis against the incubation time (in s) on the X-axis for each inhibitor concentration and for the controls (**Figure 22B**, **Figure 24B**). Do this separately for each preincubation time.

2. Fit F_t against t to obtain v_t'

Fit signal F_t against incubation time t to **Equation XIII** (**Figure 22B**, **Figure 24B**) to obtain preincubation time-dependent product formation velocity v_t' from the linear slope. Linear product formation is indicative of effective disruption of additional covalent modification during incubation by dilution in excess substrate (**Figure 21A**). If product formation is not linear: consult **Table 6** (*section 5*) for troubleshooting or change to *Data Analysis Protocol 3*.

$$F_t = F_0 + v_t' t \quad (\text{XIII})$$

Nonlinear regression of straight line $Y=Y\text{Intercept}+Slope*X$ with Y = signal F_t (in AU) and X = incubation time t (in s) to find $Y\text{Intercept}$ = background signal at reaction initiation F_0 (in AU) and Slope = preincubation time-dependent product formation velocity v_t' (in AU/s).

3. Proceed to Data Analysis Protocols to obtain the appropriate kinetic parameters for each covalent binding mode: *Data Analysis Protocol 4Ai* or *4Aii* for 2-step irreversible inhibitors and *Data Analysis Protocol 4Bi* or *4Bii* for 1-step irreversible inhibitors

Selection of a data analysis protocols for inhibitors with an irreversible binding mode depends on the desired visual representation as well as personal preference. Generally, *Data Analysis Protocols 4Ai* and *4Bi* have less data processing/manipulation and are more informative for comparison of various inhibitors on a single enzyme target, as they are compatible with assessment of inhibitor potency simultaneous with visual assessment of time-dependent enzyme stability k_{ctrl} (**Figure 23B-C**, **Figure 25B-C**). *Alternative Data Analysis Protocols 4Aii* and *4Bii* involve normalization of the enzyme activity that aids visual assessment of inhibitory potency of a single inhibitor on multiple enzyme targets (that might have a variable stability) (**Figure 23D-E**, **Figure 25D-E**).

Data Analysis Protocol

EXP Conditions	2-step IRREV	1-step IRREV	2-step REV
$k_{\text{ctrl}} = 0$	4Ai or 4Aii	4Bi or 4Bii	–
$k_{\text{degE}} > 0$	4Ai or 4Aii	4Bi or 4Bii	–

Data Analysis Protocol 4Ai for 2-step IRREV Inhibition

Processing of experimental data obtained with *Assay Protocol IV* that has been processed according to *Data Analysis Protocol 4* for 2-step irreversible inhibitors.

1. Plot v_t against preincubation time t' for each inhibitor concentration

Plot the mean and standard deviation of v_t (in AU/s) on the Y-axis against preincubation time t' (in s) on the X-axis for each inhibitor concentration and the uninhibited control (**Figure 22C**). Validate that inhibitor concentrations are not too high: inhibition should be less than 100% at the shortest t' for at least six inhibitor concentrations. Check whether the uninhibited enzyme activity is independent of preincubation time ($v_0^{\text{ctrl}} = v_t^{\text{ctrl}}$): an algebraic correction for enzyme instability ($k_{\text{ctrl}} > 0$, **Figure 23B**) can be performed in step 4 of this protocol by accounting for nonlinearity in the uninhibited control in the secondary k_{obs} plot (**Figure 23C**). Alternatively, proceed to *Alternative Data Analysis Protocol 4Bii* to correct for enzyme instability ($v_0^{\text{ctrl}} > v_t^{\text{ctrl}}$) by normalization of the enzyme activity v_t/v_t^{ctrl} (**Figure 23D-E**).

2. Fit v_t against preincubation time t' to obtain k_{obs}

Fit the mean and standard deviation of v_t against preincubation time t' (**Figure 22C/Figure 23B**) for each inhibitor concentration to bounded exponential decay **Equation VI** with shared value for initial velocity v_i to obtain the observed reaction rate k_{obs} from initial velocity v_i (Y-intercept) to full inactivation (v_s in fully inhibited control). A lack of initial noncovalent complex ($v_i = v_0^{\text{ctrl}}$) is indicative of effective disruption of noncovalent interactions by dilution in excess substrate. Validate this by fitting without constraints for v_i . Proceed to *Data Analysis Protocol 3Ai* if deviations ($v_i < v_0^{\text{ctrl}}$) are observed.

$$v_t = v_0^{\text{ctrl}} e^{-k_{\text{obs}} t'} \quad (\text{VI})$$

Nonlinear regression of exponential one-phase decay equation $Y=(Y0-Plateau)*EXP(-k*X)+Plateau$ with Y = preincubation time-dependent product formation velocity v_t (in AU/s), X = preincubation time t' (in s) and Plateau = final velocity $v_s = 0$ or v_s^{ctrl} in fully inhibited control (in AU/s, constrained) to find $Y0$ = Y-intercept = initial velocity v_i = uninhibited velocity v_0^{ctrl} (in AU/s, shared value) and k = observed reaction rate k_{obs} (in s^{-1}).

3. Plot k_{obs} against $[I]$

Plot the mean and standard deviation of k_{obs} (in s^{-1}) on the Y-axis against inhibitor concentration (in M) during preincubation (before addition of substrate) on the X-axis (**Figure 22D/Figure 23C**). The plot of k_{obs} against $[I]$ should reach a maximum k_{obs} at saturating inhibitor concentration. Note that a linear curve is indicative of 1-step binding behavior at non-saturating inhibitor concentrations ($[I] <> 0.1K_i^{\text{app}}$; see **Figure 3F**) with $v_i = v_0^{\text{ctrl}}$ (shared Y-intercept in the previous step). Proceed to step 4 of *Data Analysis Protocol 4B* after it has been validated that the linear curve is not resultant from saturating inhibitor concentrations ($[I] >> 10K_i^{\text{app}}$; see **Figure 3G**) as identified by $v_i << v_0^{\text{ctrl}}$, by repeating the measurement with lower inhibitor concentrations.

4. Fit k_{obs} against $[I]$ to obtain k_{inact} and K_i

Fit k_{obs} against inhibitor concentration during preincubation to **Equation xv** to obtain maximum inactivation rate constant k_{inact} and inactivation constant K_i . Constrain $k_{\text{ctrl}} = k_{\text{obs}}$ of the uninhibited control (**Figure 23C**). Inactivation constant K_i does not have to be corrected for substrate competition because preincubation is conducted in absence of competing substrate. Calculate irreversible covalent inhibitor potency k_{inact}/K_i with propagation of error with *Sample Calculation 2*.

$$k_{\text{obs}} = k_{\text{ctrl}} + \frac{k_{\text{inact}} [I]}{K_i + [I]} \quad (\text{xv})$$

Nonlinear regression of user-defined explicit equation $Y=Y0+((kmax*X)/((KI)+X))$ with Y = observed reaction rate k_{obs} (in s^{-1}), X = inhibitor concentration during preincubation (in M), and $Y0$ = rate of nonlinearity in uninhibited control k_{ctrl} (in s^{-1} , constrained) to find k_{max} = maximum reaction rate k_{inact} (in s^{-1}), and KI = Inactivation constant K_i (in M).

5. Optional: Validate experimental kinetic parameters with kinetic simulations

Proceed to *Kinetic Simulations 1* to compare the experimental read-out to the product formation simulated with scripts *KinVol* and *KinVolDeg* (using experimental rate constant $k_{\text{inact}} = k_s$) to confirm that the calculated kinetic constants are in accordance with the experimental data.

Alternative Data Analysis Protocol 4Aii for 2-step IRREV Inhibition

Processing of experimental data obtained with *Assay Protocol IV* that has been processed according to *Data Analysis Protocol 4* for 2-step irreversible inhibitors.

1. Plot v_t against preincubation time t' for each inhibitor concentration

Plot the mean and standard deviation of v_t (in AU/s) on the Y-axis against preincubation time t' (in s) on the X-axis for each inhibitor concentration and the uninhibited control (**Figure 23B**). Validate that inhibitor concentrations are not too high: inhibition should be less than 100% at the shortest t' for at least six inhibitor concentrations.

2. Normalize v_t to obtain v_t/v^{ctrl}

Normalize v_t of each inhibitor concentration and the controls to lowest value = 0 (or full inhibition control) and highest value = uninhibited product formation v_t^{ctrl} to obtain normalized enzyme activity v_t/v^{ctrl} . Perform this correction separately for each preincubation time.

3. Plot and fit v_t/v^{ctrl} against preincubation time t' to obtain k_{obs}

Plot the mean and standard deviation of v_t/v^{ctrl} on the Y-axis against preincubation time t' (in s) on the X-axis (**Figure 23D**). Fit to exponential decay **Equation XIX** to obtain k_{obs} from initial velocity v_i/v_0^{ctrl} to full inactivation (Plateau = 0). A lack of initial noncovalent complex ($v_i = v_0^{ctrl}$) is indicative of effective disruption of noncovalent interactions by dilution in excess substrate. Validate this by fitting without constraints for v_i . Proceed to *Data Analysis Protocol 3Aii* if deviations ($v_i < v_0^{ctrl}$) are observed.

$$\left(\frac{v_t}{v_t^{ctrl}} \right) = e^{-k_{obs}t'} \quad (\text{XIX})$$

Nonlinear regression of exponential one-phase decay equation $Y = (Y0 - \text{Plateau}) * \text{EXP}(-k*X) + \text{Plateau}$ with Y = normalized preincubation time-dependent product formation velocity v_t/v^{ctrl} (unitless), X = preincubation time t' (in s), $Y0$ = Y-intercept = normalized initial velocity $v_i/v_0^{ctrl} = 1$ (unitless, constrained), and Plateau = normalized final velocity $v_s/v_s^{ctrl} = 0$ (unitless, constrained) to find k = observed reaction rate k_{obs} (in s^{-1}).

4. Plot k_{obs} against $[I]$

Plot the mean and standard deviation of k_{obs} (in s^{-1}) on the Y-axis against inhibitor concentration (in M) during preincubation (before addition of substrate) on the X-axis (**Figure 23E**). The plot of k_{obs} against $[I]$ should reach a maximum k_{obs} at saturating inhibitor concentration. Note that a linear curve is indicative of 1-step binding behavior at non-saturating inhibitor concentrations ($[I] << 0.1K_i^{\text{app}}$: see **Figure 3F**) with $v_i = v_0^{ctrl}$ (shared Y-intercept = 1 in the previous step). Proceed to *step 5 of Data Analysis Protocol 4Bii* after it has been validated that the linear curve is not resultant from saturating inhibitor concentrations ($[I] >> 10K_i^{\text{app}}$: see **Figure 3G**) as identified by $v_i << v_0^{ctrl}$ (shared Y-intercept = 0 in the previous step), by repeating the measurement with lower inhibitor concentrations.

5. Fit k_{obs} against $[I]$ to obtain k_{inact} and K_i

Fit k_{obs} against inhibitor concentration during preincubation to **Equation XVII** to obtain maximum inactivation rate constant k_{inact} and inactivation constant K_i (**Figure 23E**). Do not correct for enzyme instability ($k_{ctrl} > 0$), as this correction has already been performed by normalizing v_t . Inactivation constant K_i does not have to be corrected for substrate competition because preincubation is conducted in absence of competing substrate. Calculate irreversible covalent inhibitor potency k_{inact}/K_i with propagation of error with *Sample Calculation 2*.

$$k_{obs} = \frac{k_{inact}[I]}{K_i + [I]} \quad (\text{XVII})$$

Nonlinear regression of user-defined explicit equation $Y = Y0 + ((kmax * X) / ((K_i) + X))$ with Y = observed reaction rate k_{obs} (in s^{-1}), X = inhibitor concentration during preincubation (in M), and $Y0 = 0$ (in s^{-1} , constrained) to find $kmax$ = maximum reaction rate k_{inact} (in s^{-1}) and K_i = Inactivation constant K_i (in M).

6. *Optional:* Validate experimental kinetic parameters with kinetic simulations

Proceed to *Kinetic Simulations 1* to compare the experimental read-out to the product formation simulated with scripts **KinVol** and **KinVolDeg** (using experimental rate constant $k_{inact} = k_s$) to confirm that the calculated kinetic constants are in accordance with the experimental data.

Data Analysis Protocol 4Bi for 1-step IRREV Inhibition

Processing of experimental data obtained with *Assay Protocol IV* that has been processed according to *Data Analysis Protocol 4* for 1-step irreversible covalent inhibitors and 2-step irreversible inhibitors at non-saturating inhibitor concentrations ($[I] \leq 0.1K_I$).

1. Plot $v_{t'}$ against preincubation time t' for each inhibitor concentration

Plot the mean and standard deviation of $v_{t'}$ (in AU/s) on the Y-axis against preincubation time t' (in s) on the X-axis for each inhibitor concentration and the uninhibited control (**Figure 24C**). Validate that inhibitor concentrations are not too high: inhibition should be less than 100% at the shortest t' for at least six inhibitor concentrations. Check whether the uninhibited enzyme activity is independent of preincubation time ($v_0^{\text{ctrl}} = v_{t'}^{\text{ctrl}}$); an algebraic correction for enzyme instability ($k_{\text{ctrl}} > 0$, **Figure 25B**) can be performed in *step 4* of this protocol by accounting for nonlinearity in the uninhibited control in the secondary k_{obs} plot (**Figure 25C**). Alternatively, proceed to *Alternative Data Analysis Protocol 4Bi* to correct for enzyme instability ($v_0^{\text{ctrl}} > v_{t'}^{\text{ctrl}}$) by normalization of the enzyme activity $v_{t'}/v_{t'}^{\text{ctrl}}$ (**Figure 25D-E**).

2. Fit $v_{t'}$ against preincubation time t' to obtain k_{obs}

Fit the mean and standard deviation of $v_{t'}$ against preincubation time t' (**Figure 24C/Figure 25B**) for each inhibitor concentration to bounded exponential decay **Equation VI**. Constrain initial velocity v_i to a shared value to obtain observed reaction rate k_{obs} from initial velocity v_i (Y-intercept) to full inactivation ($v_s = 0$ or value in fully inhibited control).

$$v_{t'} = v_0^{\text{ctrl}} e^{-k_{\text{obs}} t'} \quad (\text{VI})$$

Nonlinear regression of exponential one-phase decay equation $Y=(Y0-\text{Plateau}) * \text{EXP}(-k*X) + \text{Plateau}$ with Y = preincubation time-dependent product formation velocity v_i (in AU/s), X = preincubation time t' (in s), and Plateau = final velocity $v_s = 0$ or v_s^{ctrl} in fully inhibited control (in AU/s, constrained) to find $Y0$ = Y-intercept = initial velocity v_i = uninhibited velocity v_0^{ctrl} (in AU/s, shared value) and k = observed reaction rate k_{obs} (in s^{-1}).

3. Plot k_{obs} against $[I]$

Plot the mean and standard deviation of k_{obs} (in s^{-1}) on the Y-axis against inhibitor concentration (in M) during preincubation (*before* addition of substrate) on the X-axis (**Figure 24D/Figure 25C**). The plot of k_{obs} against inhibitor concentration $[I]$ is linear for 1-step irreversible inhibitors and for 2-step irreversible inhibitors at non-saturating inhibitor concentrations ($[I] \ll 0.1K_I$).

4. Fit k_{obs} against $[I]$ to obtain k_{chem}

Fit k_{obs} against inhibitor concentration during preincubation (in M) to **Equation XVIII** to obtain inhibitor potency k_{chem} from the linear slope. Constrain Y-intercept to $k_{\text{ctrl}} \cdot k_{\text{obs}}$ of the uninhibited control (**Figure 25C**). Inhibitor potency k_{chem} does **not** have to be corrected for substrate competition because preincubation is conducted in absence of competing substrate. Calculate k_{inact}/K_I for 2-step irreversible inhibitors at non-saturating inhibitor concentrations ($[I] \leq 0.1K_I$) with *Sample Calculation 9*.

$$k_{\text{obs}} = k_{\text{ctrl}} + k_{\text{chem}} [I] \quad (\text{XVIII})$$

Nonlinear regression of straight line $Y=Y\text{Intercept}+Slope*X$ with Y = observed reaction rate k_{obs} (in s^{-1}), X = inhibitor concentration during preincubation (in M), and $Y\text{Intercept}$ = rate of nonlinearity in uninhibited control k_{ctrl} (in s^{-1} , constrained) to find Slope = inactivation rate constant k_{chem} (in $\text{M}^{-1}\text{s}^{-1}$).

5. Optional: Validate experimental kinetic parameters with kinetic simulations

Proceed to *Kinetic Simulations 1* to compare the experimental read-out to the product formation simulated with scripts **KinVol** and **KinVolDeg** (using experimental rate constant $k_{\text{chem}} = k_3$), to confirm that the calculated kinetic constants are in accordance with the experimental data.

Alternative Data Analysis Protocol 4Bii for 1-step IRREV Inhibition

Processing of experimental data obtained with *Assay Protocol IV* that has been processed according to *Data Analysis Protocol 4* for 1-step irreversible covalent inhibitors and 2-step irreversible inhibitors at non-saturating inhibitor concentrations ($[I] \leq 0.1K_I$).

1. Plot v_t against preincubation time t' for each inhibitor concentration

Plot the mean and standard deviation of v_t (in AU/s) on the Y-axis against preincubation time t' (in s) on the X-axis for each inhibitor concentration and the uninhibited control (**Figure 25B**). Validate that inhibitor concentrations are not too high: inhibition should be less than 100% at the shortest t' for at least six inhibitor concentrations.

2. Normalize v_t to obtain v_t/v_{ctrl}

Normalize v_t of each inhibitor concentration and the controls to lowest value = 0 (or full inhibition control) and highest value = uninhibited product formation v_t^{ctrl} to obtain normalized enzyme activity v_t/v_{ctrl} . Perform this correction separately for each preincubation time.

3. Plot and fit v_t/v_{ctrl} against preincubation time t' to obtain k_{obs}

Plot the mean and standard deviation of v_t/v_{ctrl} on the Y-axis against preincubation time t' (in s) on the X-axis (**Figure 25D**). Fit to exponential decay **Equation XIX** to obtain k_{obs} from initial velocity v_t/v_0^{ctrl} (shared value) to full inactivation (Plateau = 0).

$$\left(\frac{v_t}{v_t^{ctrl}} \right) = e^{-k_{obs}t'} \quad (\text{XIX})$$

Nonlinear regression of exponential one-phase decay equation $Y = (Y0 - \text{Plateau}) * \text{EXP}(-k*X) + \text{Plateau}$ with Y = normalized preincubation time-dependent product formation velocity v_t/v_{ctrl} (unitless), X = preincubation time t' (in s), Plateau = normalized final velocity $v_t/v_s^{ctrl} = 0$ (unitless, constrained), and Y0 = Y-intercept = normalized initial velocity $v_t/v_0^{ctrl} = 1$ (unitless, constrained) to find k = observed reaction rate k_{obs} (in s^{-1}).

4. Plot k_{obs} against $[I]$

Plot the mean and standard deviation of k_{obs} (in s^{-1}) on the Y-axis against inhibitor concentration (in M) during preincubation (*before* addition of substrate) on the X-axis (**Figure 25E**). The plot of k_{obs} against inhibitor concentration $[I]$ is linear for 1-step irreversible inhibitors and for 2-step irreversible inhibitors at non-saturating inhibitor concentrations ($[I] \ll 0.1K_I$).

5. Fit k_{obs} against $[I]$ to obtain k_{chem}

Fit k_{obs} against inhibitor concentration during preincubation to **Equation XX** to obtain inhibitor potency k_{chem} from the linear slope (**Figure 25E**). Do not correct for enzyme instability ($k_{ctrl} > 0$), as this correction has already been performed by normalizing v_t to v_t/v_{ctrl} in step 2 of this protocol. Inhibitor potency k_{chem} does not have to be corrected for substrate competition because preincubation is conducted in absence of competing substrate. Calculate k_{inact}/K_I for 2-step irreversible inhibitors at non-saturating inhibitor concentrations ($[I] \leq 0.1K_I$) with propagation of error with *Sample Calculation 9*. Alternatively, inhibitor potency k_{chem} or k_{inact}/K_I can be directly calculated from a single k_{obs} and $[I]$ with *Sample Calculation 10*.

$$k_{obs} = k_{chem} [I] \quad (\text{XX})$$

Nonlinear regression of straight line $Y = \text{YIntercept} + \text{Slope} * X$ with Y = observed reaction rate k_{obs} (in s^{-1}), X = inhibitor concentration during preincubation (in M), and YIntercept = 0 (in s^{-1} , constrained) to find Slope = inactivation rate constant k_{chem} (in $M^{-1}s^{-1}$).

6. Optional: Validate experimental kinetic parameters with kinetic simulations

Proceed to *Kinetic Simulations 1* to compare the experimental read-out to the product formation simulated with scripts **KinVol** and **KinVolDeg** (using experimental rate constant $k_{chem} = k_3$), to confirm that the calculated kinetic constants are in accordance with the experimental data.

4.1. Sample Calculations

The values obtained in the data analysis protocols have to be converted into relevant inhibition parameters. These are fairly straightforward linear calculations and can be performed with more basic software like Microsoft EXCEL. For each equation, the values on the right-hand side of the equal sign are known, so it becomes a linear calculation to obtain the parameter on the left-hand side. The calculations are listed in order of appearance in the manuscript. We have outlined the key assumptions and a little background on the used variables for improved readability and direct applicability following the protocols.

Sample Calculation 1. Calculate K_i from K_i^{app}

Apparent inactivation constant K_i^{app} (in M) found in *Data Analysis Protocols 1A* or *1D* for competitive 2-step irreversible inhibitors is corrected for substrate competition to obtain inactivation constant K_i (in M), with propagation of error. Use substrate concentration $[S]$ (in M) after reaction initiation and K_M (in M) as determined for these specific assay conditions (buffer, temperature, enzyme, substrate). Proceed to *Sample Calculation 2* to calculate k_{inact}/K_i .

$$K_i = \frac{K_i^{\text{app}}}{\left(1 + \frac{[S]}{K_M}\right)} \quad \sigma_{K_i} = \sqrt{\left(\frac{1}{1 + \frac{[S]}{K_M}}\right)^2 \sigma_{K_i^{\text{app}}}^2 + \left(-\frac{K_i^{\text{app}} K_M}{(K_M + [S])^2}\right)^2 \sigma_{[S]}^2 + \left(\frac{K_i^{\text{app}} [S]}{([S] + K_M)^2}\right)^2 \sigma_{K_M}^2}$$

Sample Calculation 2. Calculate k_{inact}/K_i from k_{inact} and K_i

Irreversible covalent inhibitor potency k_{inact}/K_i (in $M^{-1}s^{-1}$) is calculated from k_{inact} (in s^{-1}) and K_i (in M) values found in *Data Analysis Protocols 1A, 1D, 2, 3Ai, 3Aii, 4Ai* or *4Aii* and *Sample Calculation 1* for 2-step irreversible inhibitors, with propagation of error.

$$\left(\frac{k_{\text{inact}}}{K_i}\right) = \frac{k_{\text{inact}}}{K_i} \quad \sigma_{\frac{k_{\text{inact}}}{K_i}} = \left(\frac{k_{\text{inact}}}{K_i}\right) \sqrt{\left(\frac{\sigma_{k_{\text{inact}}}}{k_{\text{inact}}}\right)^2 + \left(\frac{\sigma_{K_i}}{K_i}\right)^2}$$

Sample Calculation 3. Calculate K_i from K_i^{app}

Apparent inhibition constant K_i^{app} (in M) found in *Data Analysis Protocols 1A, 1C, 3Ai, 3Aii* or *3C* for competitive 2-step (ir)reversible inhibitors is corrected for substrate competition to obtain inhibition constant K_i (in M) for the initial noncovalent equilibrium.⁸⁹ Use substrate concentration $[S]$ (in M) after reaction initiation and K_M (in M) as determined for these specific assay conditions (buffer, temperature, enzyme, substrate). Inhibition constant K_i approximates inactivation constant K_i for 2-step irreversible inhibitors if covalent bond formation is rate-limiting (*rapid equilibrium assumption*).

$$K_i = \frac{K_i^{\text{app}}}{\left(1 + \frac{[S]}{K_M}\right)} \quad \sigma_{K_i} = \sqrt{\left(\frac{1}{1 + \frac{[S]}{K_M}}\right)^2 \sigma_{K_i^{\text{app}}}^2 + \left(-\frac{K_i^{\text{app}} K_M}{(K_M + [S])^2}\right)^2 \sigma_{[S]}^2 + \left(\frac{K_i^{\text{app}} [S]}{([S] + K_M)^2}\right)^2 \sigma_{K_M}^2}$$

Sample Calculation 4. Calculate k_{chem} from $k_{\text{chem}}^{\text{app}}$

Apparent inhibitor potency $k_{\text{chem}}^{\text{app}}$ (in $M^{-1}s^{-1}$) found in *Data Analysis Protocol 1B* for competitive 1-step irreversible inhibitors is corrected for substrate competition to obtain inhibition potency k_{chem} (in $M^{-1}s^{-1}$) with propagation of error. Use substrate concentration $[S]$ (in M) after reaction initiation and K_M (in M) as determined for these specific assay conditions (buffer, temperature, enzyme, substrate).

$$k_{\text{chem}} = k_{\text{chem}}^{\text{app}} \left(1 + \frac{[S]}{K_M}\right) \quad \sigma_{k_{\text{chem}}} = \sqrt{\left(1 + \frac{[S]}{K_M}\right)^2 \sigma_{k_{\text{chem}}^{\text{app}}}^2 + \left(\frac{k_{\text{chem}}^{\text{app}}}{K_M}\right)^2 \sigma_{[S]}^2 + \left(-\frac{k_{\text{chem}}^{\text{app}} [S]}{K_M^2}\right)^2 \sigma_{K_M}^2}$$

Sample Calculation 5. Calculate k_{inact}/K_I^{app} from k_{chem}^{app}

The linear slope k_{chem}^{app} (in $M^{-1}s^{-1}$) found in *Data Analysis Protocol 1B* for 2-step irreversible inhibitors equals k_{inact}/K_I^{app} when all inhibitor concentrations are non-saturating ($[I] \leq 0.1K_I^{app}$). It is not possible to obtain individual values of k_{inact} and K_I from a linear graph, but it is possible to estimate the upper and lower limits: K_I^{app} is much larger than the highest inhibitor concentration if this concentration is non-saturating ($K_I^{app} \gg [I]_{max}$). An unchanged slope upon constraining the Y-intercept k_{ctrl} (step 5 in *Data Analysis Protocol 1B*) to the experimental value for the uninhibited control validates that all inhibitor concentrations are non-saturating (see **Figure 3F**) rather than saturating (see **Figure 3G**). Proceed to *Sample Calculation 6* to calculate k_{inact}/K_I .

$$k_{chem}^{app} = \left(\frac{k_{inact}}{K_I^{app}} \right)$$

Sample Calculation 6. Calculate k_{inact}/K_I from k_{inact}/K_I^{app}

Apparent inactivation potency k_{inact}/K_I^{app} (in $M^{-1}s^{-1}$) found in *Data Analysis Protocols 1A* or *1D*, or calculated in *Sample Calculation 5* for competitive 2-step irreversible inhibitors is corrected for substrate competition to obtain k_{inact}/K_I (in M) with propagation of error. Use substrate concentration $[S]$ (in M) after reaction initiation and K_M (in M) as determined for these specific assay conditions (buffer, temperature, enzyme, substrate).

$$\frac{k_{inact}}{K_I} = \left(\frac{k_{inact}}{K_I^{app}} \right) \left(1 + \frac{[S]}{K_M} \right) \quad \sigma_{\frac{k_{inact}}{K_I}} = \sqrt{\left(1 + \frac{[S]}{K_M} \right)^2 \sigma_{\frac{k_{inact}}{K_I^{app}}}^2 + \left(\frac{\left(\frac{k_{inact}}{K_I^{app}} \right)^2}{K_M} \right) \sigma_{[S]}^2 + \left(- \frac{\left(\frac{k_{inact}}{K_I^{app}} \right) [S]}{K_M^2} \right)^2 \sigma_{K_M}^2}$$

Sample Calculation 7. Calculate K_i^* from K_i^{app}

Apparent steady-state inhibition constant K_i^{app} (in M) found in *Data Analysis Protocols 1C* or *3C* for competitive 2-step reversible covalent inhibitors is corrected for substrate competition to obtain steady-state inhibition constant K_i^* (in M). Use substrate concentration $[S]$ (in M) after reaction initiation and K_M (in M) as determined for these specific assay conditions (buffer, temperature, enzyme, substrate).

$$K_i^* = \frac{K_i^{app}}{\left(1 + \frac{[S]}{K_M} \right)} \quad \sigma_{K_i^*} = \sqrt{\left(\frac{1}{1 + \frac{[S]}{K_M}} \right)^2 \sigma_{K_i^{app}}^2 + \left(- \frac{K_i^{app} K_M}{(K_M + [S])^2} \right)^2 \sigma_{[S]}^2 + \left(\frac{K_i^{app} [S]}{([S] + K_M)^2} \right)^2 \sigma_{K_M}^2}$$

Sample Calculation 8. Calculate K_i^* from K_i , k_5 , and k_6

Steady-state inhibition constant K_i^* (in M) of 2-step reversible inhibitors can be calculated from experimental values of K_i (in M), k_5 (in s^{-1}), and k_6 (in s^{-1}) found with *Data Analysis Protocols 1C* or *3C*, and *Sample Calculation 3*. Reliable (relatively) small k_6 -values can only be obtained with more sensitive methods such as rapid dilution assays.^{29,33} The uninhibited control must be strictly linear ($k_{ctrl} = 0$) for values found with *Data Analysis Protocol 1C*. This calculation is not the preferred method to obtain K_i^* due to its sensitivity to (experimental) errors in k_6 and contribution of k_{ctrl} : values obtained in *Data Analysis Protocol 1C* or *3C* and *Sample Calculation 7* should generally be considered as more reliable.

$$K_i^* = \frac{K_i}{\left(1 + \frac{k_5}{k_6} \right)} \quad \sigma_{K_i^*} = \sqrt{\left(\frac{1}{1 + \frac{k_5}{k_6}} \right)^2 \sigma_{K_i}^2 + \left(- \frac{K_i k_6}{(k_6 + k_5)^2} \right)^2 \sigma_{k_5}^2 + \left(\frac{K_i k_5}{(k_5 + k_6)^2} \right)^2 \sigma_{k_6}^2}$$

Sample Calculation 9. Calculate k_{inact}/K_I from k_{chem}

The linear slope k_{chem} (in $\text{M}^{-1}\text{s}^{-1}$) found in *Data Analysis Protocols 3Bi*, *3Bii*, *4Bi* or *4Bii* for 2-step irreversible inhibitors equals k_{inact}/K_I when all inhibitor concentrations are non-saturating ($[I] \leq 0.1K_I$). It is not possible to obtain individual values of k_{inact} and K_I from a linear graph, but it is possible to estimate the upper and lower limits: K_I is much larger than the highest inhibitor concentration if this concentration is non-saturating ($K_I \gg [I]_{\text{max}}$). An unchanged slope upon constraining the Y-intercept k_{ctrl} to the experimental value for the uninhibited control in step 4 of *Data Analysis Protocols 3Bi* and *4Bi* validates that all inhibitor concentrations are non-saturating (see **Figure 3F**) rather than saturating (see **Figure 3G**).

$$k_{\text{chem}} = \left(\frac{k_{\text{inact}}}{K_I} \right)$$

Sample Calculation 10. Calculate k_{chem} or k_{inact}/K_I from k_{obs} and $[I]$

Divide the k_{obs} -value (in s^{-1}) obtained in *Alternative Data Analysis Protocols 3Bii* or *4Bii* by its corresponding inhibitor concentration (in M) to calculate irreversible inhibitor potency k_{chem} (in $\text{M}^{-1}\text{s}^{-1}$) or k_{inact}/K_I (in $\text{M}^{-1}\text{s}^{-1}$). This calculation is only accurate for normalized k_{obs} values (unaffected by contribution of k_{ctrl}), in absence of competing substrate, and (only applicable for 2-step irreversible inhibitors) at non-saturating inhibitor concentration.

$$k_{\text{chem}} = \frac{k_{\text{obs}}}{[I]}$$

$$\left(\frac{k_{\text{inact}}}{K_I} \right) = \frac{k_{\text{obs}}}{[I]}$$

4.2. Kinetic simulations

The figures illustrating the protocols in this work are generated using kinetic simulation scripts. These scripts are available online and can be used to validate the obtained kinetic parameters or help in optimizing your assay. On a more educational level, these scripts can show what your assay result could look like when using wildly different parameters to obtain more insight into how these affect your assay. A tutorial on how to perform kinetic simulations can be found on the website of our kinetic simulation scripts. Note: loading this page for the first time can take up to 5 minutes, and involves an automatic redirection (reloading) to the Landing Page.

Materials

- Kinetic Simulation Script (<https://tinyurl.com/kineticsimulations>)
- Software to open csv files (e.g. EXCEL)
- Data fitting software (e.g. GraphPad Prism)
- Experimental values found in *Data Analysis Protocols 1-4*

Kinetic Simulation 1. Validation of Experimental Values

Perform kinetic simulations to validate that calculated kinetic parameters are in accordance with experimental RAW data. Estimate microscopic rate constants from reported (literature) values, or use association rate constants $k_1 = k_3 = 10^6\text{-}10^9 \text{ M}^{-1}\text{s}^{-1}$ (rapid noncovalent association) to calculate the dissociation rate constants from the experimental equilibrium constants: $k_4 = K_I \times k_3$ (**Table S1**) and $k_2 = (K_M \times k_1) - k_{\text{cat}}$ (**Figure S1**). Ideally, also simulate the HTS reaction conditions to validate that the calculated kinetic constants give rise to the experimental inhibition or IC_{50} .³⁵

Kinetic Simulation 2. Rational Design of Validation Assays

Perform kinetic simulations with the calculated kinetic parameters to rationalize assay conditions for subsequent validation assays such as the minimum/maximum (pre)incubation times for reversibility assays or MS detection of the covalent adduct (formulas can be found in **Table 5**).

Table 5 | Calculations to rationalize assay conditions.

Reaction conditions for linearity in uninhibited control	$E + S \leftrightarrow ES \rightarrow E + P$
Maximum enzyme concentration $[E]_0$ for 10% substrate conversion during incubation in the uninhibited control ($[S]_0 \geq 10[E]_0$)	$[E]_0 = \frac{0.1 ([S] + K_M)}{k_{cat} t} = \frac{[S] + K_M}{10 k_{cat} t}$
Maximum incubation time t for 10% substrate conversion in the uninhibited control ($[S]_0 \geq 10[E]_0$)	$t = \frac{[S] + K_M}{10 k_{cat} [E]_0}$
Reaction conditions for covalent occupancy	$E + I \leftrightarrow EI \rightarrow EI^*$
Expected covalent occupancy $[EI^*]_{t'} / [E]_0$ after preincubation t' (in absence of competitor)	$\frac{[EI^*]_{t'}}{[E]_0} = 1 - e^{-k_{obs} t'}$
Minimum preincubation time t' (in absence of competitor) to reach covalent occupancy $[EI^*]_{t'} / [E]_0 \geq 0.6$	$t' = \frac{\ln \left(1 - \frac{[EI^*]_{t'}}{[E]_0} \right)}{k_{obs}} = \frac{\ln (1 - 0.6)}{k_{obs}}$

5. Troubleshooting

Like with any experimental method, our described methods will also require the necessary optimization. Since data analysis depends heavily on the experimental input, it is very important to optimize assay conditions, rather than trying to apply data corrections, to obtain reliable kinetic parameters. As the assay conditions will vary widely, depending on the enzyme used,⁷⁹ we can only give general pointers on the optimization of the assay conditions (**Table 6**). Luckily, many model substrates come with a satisfactory user manual or are described in extensive methods papers.⁶⁸⁻⁶⁹ These resources generally state reagents required for the reaction (e.g. fresh reducing agent, for cysteine-based catalysis) or additives that stabilize the read-out (such as BSA or Tween-20; to prevent aspecific aggregation). The control for full inhibition of (catalytic) cysteines is typically a thiol-alkylating reagent such as iodoacetamide (IAc) or N-methylmaleimide (NEM), or a known inhibitor.

As the assay performance is essential to get reliable fits, we recommend focusing on potential experimental problems before looking into issues with fitting. A great guide for general assay optimization can be found online in the assay guidance manual of the NCATS.⁹⁰ A comprehensive troubleshooting table with potential solutions that deal with various issues causing a troublesome read-out can be found on the next pages (**Table 6**). For the first half of **Table 6**, these solutions are generally related to the assay conditions and can generally be executed in the optimization stage. The latter half of **Table 6** is more geared towards after the data analysis of an initial experiment. The problems and accompanying solutions deal more with the experimental setup: how much inhibitor or substrate one needs to add becomes more apparent after these first data points. Some solutions, like changing inhibitor or substrate concentrations, can be simulated with our set of interactive kinetic simulation scripts. For better understanding and help in optimizing, we recommend simulating these conditions with our scripts to see what would happen when changing the concentrations.

Table 6 | Troubleshooting and Optimization Experimental Assay Conditions.

Problem	Possible cause	Solutions
Difference positive and negative control is not significant (poor Z'-score)	Enzyme is not active (enough)	Increase [E] (not always possible with very potent inhibitors) Increase [S] to increase absolute maximum signal Optimize buffer components Switch to a substrate that is processed faster Activate enzyme with fresh reagents (e.g. DTT, ATP) in single-use aliquots Minimize freeze/thaw cycles
	Signal product is not significant compared to substrate	Change fluorophore/read-out Optimize buffer components
	Negative control or inhibitor does not inhibit	Change to reported (specific) inhibitor Use thiol-alkylating reagent (e.g. NEM, IAc) for cysteines Use no-enzyme as negative control Increase concentration of inhibitor Make fresh dilution/aliquots of inhibitor solution
	DMSO in positive control acts as inhibitor	<u>Validate</u> : compare enzyme activity with/without DMSO Reduce DMSO to max. 1% of final solution
	Machine settings/ sensitivity	Check if $[P]$ is within the sensitivity range of used machine Optimize gain settings for $[P] = 0\text{--}20\% [S]_0$ Check if correct wavelengths/settings are selected
	Pipetting error	Frequently replace pipette tips to avoid contamination of positive control with inhibitor (from negative control) Avoid well-to-well contamination by using an automated dispenser
	Substrate depletion ($[P]_t > 0.1[S]_0$)	Decrease [E] Increase [S] Shorter incubation time
	Spontaneous inactivation of enzyme ($k_{\text{deg}} > 0$)	Optimize buffer conditions for stability Use nonbinding surface plates Shorter incubation time
	Drift/evaporation	Cover/seal plate with optical clear cover Shorter incubation time
	Pre-steady state kinetics (lag phase)	Increase [S] to reach $E + S \leftrightarrow ES$ equilibrium faster Preincubate enzyme with reducing agent/ATP
Nonlinear uninhibited product formation curve F^{ctrl}	Solution is not homogeneous	Introduce mixing step before addition of final component
	Fluorescence bleaching/ quenching	Optimize excitation conditions (e.g. lower no. of flashes) Longer measurement intervals/less measurements
	Inhibition is not time-dependent (or k_{obs} is too slow)	Longer (pre)incubation time ($t > 0.1t\% I$) Increase $[I]$ Reduce [S] to decrease competition Activate enzyme with fresh reagents (e.g. DTT, ATP) Validate with different enzyme batch/construct
	Noncovalent affinity is too potent ($[I] \gg K_i^{\text{app}}$)	Reduce $[I]$ Higher [S] to increase competition (higher K_i^{app}) Use method based on covalency (<i>Method IV</i> or direct detection)
	k_{obs} is too fast for detection/resolvable range (inhibition is not slow-binding)	Shorter minimal (pre)incubation time Higher [S] to increase competition (slower k_{obs}) Reduce $[I]$ (slower k_{obs})
Linear inhibited progress curve F_t	Full initial inhibition for all $[I]$ ($v_i = 0$)	
	k_{obs} is too fast for detection/resolvable range (inhibition is not slow-binding)	

Table 6 continues on the next page

Table 6 | Troubleshooting and Optimization Experimental Assay Conditions. (continued)

Problem	Possible cause	Solutions
F_0 is not constant	Delay between enzyme addition and read-out	Reduce $[E]$ (less substrate conversion during delay) Correcting $t = 0$ for actual time after addition Use injector in plate reader Validate row effect: change lay-out of plate (first well has higher F_0 than last well, but containing same components) and reduce number of samples in one measurement.
F_0 is not constant	Fluorescence interference inhibitor	Validate: check F_0 for inhibitor (no substrate and enzyme), substrate (no enzyme) and substrate and inhibitor (no enzyme) Exclude high $[I]$ Background subtraction (subtract values substrate/inhibitor without enzyme from enzyme/substrate/inhibitor signal)
F_0 is not constant	Pipetting error substrate	Check for bubbles when pipetting Use low-binding tips
k_{obs} values are low compared to uninhibited control k_{ctrl}	Enzyme is unstable (high k_{ctrl})	Optimize assay conditions to improve linearity of uninhibited control (lower k_{ctrl}) Use preincubation protocol (<i>Method III & IV</i>): higher k_{obs} without competition
k_{obs} values are low compared to uninhibited control k_{ctrl}	Enzyme is not reactive (low k_{obs})	Optimize buffer conditions to increase enzyme reactivity Add (fresh) reagents (e.g. DTT, ATP) in single-use aliquots Validate with different enzyme batch/construct Too many freeze/thaw cycles
k_{obs} values are low compared to uninhibited control k_{ctrl}	Low inhibitor concentration ($[I] \ll K_i^{app}$)	Decrease $[S]$ to reduce competition Increase $[I]$ Use preincubation protocol (<i>Method III & IV</i>): higher k_{obs} without competition
k_{obs} values are low compared to uninhibited control k_{ctrl}	Slow reaction k_{obs}	Reduce $[S]$ (less competition) Longer (pre)incubation time ($t > 0.1t\frac{1}{2}$) Use preincubation protocol (<i>Method III & IV</i>): higher k_{obs} without competition Optimize buffer conditions to increase enzyme reactivity
k_{obs} vs. $[I]$ is linear	Inhibitor has 1-step binding mode	Validate: Y-intercept = k_{ctrl} in k_{obs} vs. $[I]$ plot Validate: $v_i = v_0^{ctrl}$ in $[P_i]$ vs. t or v_t vs. t' plots Increase $[I]$ to exclude 2-step $[I] \ll K_i^{app}$ Decrease $[S]$ to exclude 2-step $[I] \ll K_i^{app}$
k_{obs} vs. $[I]$ is linear	2-step IRREV inhibitor is non-saturating ($[I] \ll K_i^{app}$)	Validate: Y-intercept = k_{ctrl} in k_{obs} vs. $[I]$ plot Validate: $v_i = v_0^{ctrl}$ in $[P_i]$ vs. t or v_t vs. t' plots Fit k_{obs} vs. $[I]$ to linear function for combined value k_{inact}/K_i Increase $[I]$ Decrease $[S]$ to reduce competition (lower K_i^{app}) Use preincubation protocol (<i>Method III & IV</i>): no competition
k_{obs} vs. $[I]$ is linear	2-step IRREV inhibitor is saturating ($[I] \gg K_i^{app}$)	Validate: Y-intercept $> k_{ctrl}$ in k_{obs} vs. $[I]$ plot Validate: $v_i < v_0^{ctrl}$ in $[P_i]$ vs. t or v_t vs. t' plots Decrease $[I]$ Increase $[S]$ to increase competition (higher K_i^{app})
k_{obs} decreases with increasing $[I]$	Inhibitor concentration beyond resolvable range: noncovalent affinity is too potent ($[I] \gg K_i^{app}$)	Optimize $[I]$ range ($v_i = 0.1-0.9 \times v^{ctrl}$) Increase $[S]$ (increase competition to increase K_i^{app}) Exclude unlikely values from fit
k_{obs} decreases with increasing $[I]$	Incorrect formula to calculate K_{obs}	Validate if correct equation is used to determine k_{obs} : reversible covalent/irreversible covalent, 1-step/2-step etc.

6. Conclusion

The background of covalent inhibition kinetics and critical parameters for enzyme activity assays can be found in *section 2*. It is recommended to refer to this section before setting up your kinetic inhibition experiments as well as the core references by Copeland to get a general background on enzyme activity assays.³²⁻³³ We would like to reiterate that good experimental performance is essential for obtaining reliable parameters for your covalent inhibitor. Our kinetic simulation scripts can help validate the found values by ‘rerunning’ the experiment without human error or experimental artifacts. Not only will this give insight into the reliability of your assay, but it can also help to improve the assay setup and can show what wildly different values of concentrations would do for the read-out. In fact, figures in this manuscript have been created this way, and can as such be reproduced. Keep in mind that these are simulations, and real-life examples will always deviate due to machine artifacts or pipetting errors. Nevertheless, with a working activity assay and these instructions in hand, adequate analysis of covalent inhibitors should be very feasible.

Acknowledgements

In memory of Prof. Dr. Huib Ovaar, his passion for science will always be an inspiration to us. The authors would like to thank Dr. Anthe Janssen for proof reading. This work was supported by the EU/EFFPIA/OICR/McGill/KTH/Diamond Innovative Medicines Initiative 2 Joint Undertaking (EUbOPEN grant no. 875510).

Data and Materials Availability

All figures in this work can be recreated with the information in **Table 1** and **Table 2**. Interactive versions of the simulation scripts are available free of charge at <https://mybinder.org/v2/gh/sroet/Elma/main?labpath=Landing%20Page.ipynb> (Full URL).

Author Contributions

E.M.: Conceptualization, Formal Analysis, Investigation, Visualization, Writing – Original Draft, Writing – Review & Editing. S.R.: Conceptualization, Resources, Software, Writing – Review & Editing. R.Q.K.: Supervision, Validation, Writing – Original Draft, Writing – Review & Editing. M.P.C.M.: Project Administration, Supervision, Writing – Review & Editing.

7. References

1. Ward, R.A.; Grimster, N.P. The Design of Covalent-Based Inhibitors. *Ann. Rep. Med. Chem.* **2021**, *56*, 2-284.
2. Bauer, R.A. Covalent Inhibitors in Drug Discovery: From Accidental Discoveries To Avoided Liabilities and Designed Therapies. *Drug Discov. Today* **2015**, *20*, 1061-1073. doi: 10.1016/j.drudis.2015.05.005.
3. Singh, J.; Petter, R.C.; Baillie, T.A.; Whitty, A. The Resurgence of Covalent Drugs. *Nat. Rev. Drug Discov.* **2011**, *10*, 307-317. doi: 10.1038/nrd3410.
4. De Cesco, S.; Kurian, J.; Dufresne, C.; Mittermaier, A.K.; Moitessier, N. Covalent Inhibitors Design and Discovery. *Eur. J. Med. Chem.* **2017**, *138*, 96-114. doi: 10.1016/j.ejmech.2017.06.019.
5. Abdeldayem, A.; Raouf, Y.S.; Constantinescu, S.N.; Moriggl, R.; Gunning, P.T. Advances in Covalent Kinase Inhibitors. *Chem. Soc. Rev.* **2020**, *49*, 2617-2687. doi: 10.1039/C9CS00720B.
6. Zhang, T.; Hatcher, J.M.; Teng, M.; Gray, N.S.; Kostic, M. Recent Advances in Selective and Irreversible Covalent Ligand Development and Validation. *Cell Chem. Biol.* **2019**, *26*, 1486-1500. doi: 10.1016/j.chembiol.2019.09.012.
7. Engel, J.; Richters, A.; Getlik, M.; Tomassi, S.; Keul, M.; Termathe, M.; Lategahn, J.; Becker, C.; Mayer-Wrangowski, S.; Grüter, C., et al. Targeting Drug Resistance in EGFR with Covalent Inhibitors: A Structure-Based Design Approach. *J. Med. Chem.* **2015**, *58*, 6844-6863. doi: 10.1021/acs.jmedchem.5b01082.
8. Kathman, S.G.; Statsyuk, A.V. Methodology for Identification of Cysteine-Reactive Covalent Inhibitors. *Methods Mol. Biol.* **2019**, *1967*, 245-262. doi: 10.1007/978-1-4939-9187-7_15.

9. Resnick, E.; Bradley, A.; Gan, J.; Douangamath, A.; Krojer, T.; Sethi, R.; Geurink, P.P.; Aimon, A.; Amitai, G.; Bellini, D., et al. Rapid Covalent-Probe Discovery by Electrophile-Fragment Screening. *J. Am. Chem. Soc.* **2019**, *141*, 8951-8968. doi: 10.1021/jacs.9b02822.

10. Dalton, S.E.; Campos, S. Covalent Small Molecules as Enabling Platforms for Drug Discovery. *ChemBioChem* **2020**, *21*, 1080-1100. doi: 10.1002/cbic.201900674.

11. Ray, S.; Murkin, A.S. New Electrophiles and Strategies for Mechanism-Based and Targeted Covalent Inhibitor Design. *Biochemistry* **2019**, *58*, 5234-5244. doi: 10.1021/acs.biochem.9b00293.

12. Lagoutte, R.; Patouret, R.; Winssinger, N. Covalent Inhibitors: An Opportunity for Rational Target Selectivity. *Curr. Opin. Chem. Biol.* **2017**, *39*, 54-63. doi: 10.1016/j.cbpa.2017.05.008.

13. Bradshaw, J.M.; McFarland, J.M.; Paavilainen, V.O.; Bisconte, A.; Tam, D.; Phan, V.T.; Romanov, S.; Finkle, D.; Shu, J.; Patel, V., et al. Prolonged and Tunable Residence Time using Reversible Covalent Kinase Inhibitors. *Nat. Chem. Biol.* **2015**, *11*, 525-531. doi: 10.1038/nchembio.1817.

14. Gehring, M.; Laufer, S.A. Emerging and Re-Emerging Warheads for Targeted Covalent Inhibitors: Applications in Medicinal Chemistry and Chemical Biology. *J. Med. Chem.* **2019**, *62*, 5673-5724. doi: 10.1021/acs.jmedchem.8b01153.

15. Lee, C.-U.; Grossmann, T.N. Reversible Covalent Inhibition of a Protein Target. *Angew. Chem. Int. Ed.* **2012**, *51*, 8699-8700. doi: 10.1002/anie.201203341.

16. Shindo, N.; Ojida, A. Recent Progress in Covalent Warheads for In Vivo Targeting of Endogenous Proteins. *Bioorg. Med. Chem.* **2021**, *47*, 116386. doi: 10.1016/j.bmc.2021.116386.

17. Barf, T.; Kaptein, A. Irreversible Protein Kinase Inhibitors: Balancing the Benefits and Risks. *J. Med. Chem.* **2012**, *55*, 6243-6262. doi: 10.1021/jm3003203.

18. Kim, H.; Hwang, Y.S.; Kim, M.; Park, S.B. Recent Advances in the Development of Covalent Inhibitors. *RSC Med. Chem.* **2021**, *12*, 1037-1045. doi: 10.1039/D1MD00068C.

19. Gabizon, R.; London, N. A Fast and Clean BTK Inhibitor. *J. Med. Chem.* **2020**, *63*, 5100-5101. doi: 10.1021/acs.jmedchem.0c00597.

20. Serafimova, I.M.; Pufall, M.A.; Krishnan, S.; Duda, K.; Cohen, M.S.; Maglathlin, R.L.; McFarland, J.M.; Miller, R.M.; Frödin, M.; Taunton, J. Reversible Targeting of Noncatalytic Cysteines with Chemically Tuned Electrophiles. *Nat. Chem. Biol.* **2012**, *8*, 471-476. doi: 10.1038/nchembio.925.

21. Owen, D.R.; Allerton, C.M.N.; Anderson, A.S.; Aschenbrenner, L.; Avery, M.; Berritt, S.; Boras, B.; Cardin, R.D.; Carlo, A.; Coffman, K.J., et al. An Oral SARS-CoV-2 M^{pro} Inhibitor Clinical Candidate for the Treatment of COVID-19. *Science* **2021**, *374*, 1586-1593. doi: 10.1126/science.abl4784.

22. Holdgate, G.A.; Meek, T.D.; Grimley, R.L. Mechanistic Enzymology in Drug Discovery: A Fresh Perspective. *Nat. Rev. Drug Discov.* **2017**, *17*, 115. doi: 10.1038/nrd.2017.219.

23. Harris, C.M.; Foley, S.E.; Goedken, E.R.; Michalak, M.; Murdock, S.; Wilson, N.S. Merits and Pitfalls in the Characterization of Covalent Inhibitors of Bruton's Tyrosine Kinase. *SLAS Discov.: Adv. Sci. Drug Discov.* **2018**, *23*, 1040-1050. doi: 10.1177/247555218787445.

24. Johnson, D.S.; Weerapana, E.; Cravatt, B.F. Strategies for Discovering and Derisking Covalent, Irreversible Enzyme Inhibitors. *Future Med. Chem.* **2010**, *2*, 949-964. doi: 10.4155/fmc.10.21.

25. Stresser, D.M.; Mao, J.; Kenny, J.R.; Jones, B.C.; Grime, K. Exploring Concepts of *In Vitro* Time-Dependent CYP Inhibition Assays. *Expert Opin. Drug Metab. Toxicol.* **2014**, *10*, 157-174. doi: 10.1517/17425255.2014.856882.

26. Mons, E.; Kim, R.Q.; van Doodewaerd, B.R.; van Vleelen, P.A.; Mulder, M.P.C.; Ovaa, H. Exploring the Versatility of the Covalent Thiol-Alkyne Reaction with Substituted Propargyl Warheads: A Deciding Role for the Cysteine Protease. *J. Am. Chem. Soc.* **2021**, *143*, 6423-6433. doi: 10.1021/jacs.0c01513.

27. Liclican, A.; Serafini, L.; Xing, W.; Czervieniec, G.; Steiner, B.; Wang, T.; Brendza, K.M.; Lutz, J.D.; Keegan, K.S.; Ray, A.S.; Schultz, B.E.; Sakowicz, R.; Feng, J.Y. Biochemical Characterization of Tirabrutinib and Other Irreversible Inhibitors of Bruton's Tyrosine Kinase Reveals Differences in On- and Off-Target Inhibition. *Biochim. Biophys. Acta, Gen. Subj.* **2020**, *1864*, 129531. doi: 10.1016/j.bbagen.2020.129531.

28. Mons, E.; Jansen, I.D.C.; Loboda, J.; van Doodewaerd, B.R.; Hermans, J.; Verdoes, M.; van Boeckel, C.A.A.; van Veelen, P.A.; Turk, B.; Turk, D.; Ovaa, H. The Alkyne Moiety as a Latent Electrophile in Irreversible Covalent Small Molecule Inhibitors of Cathepsin K. *J. Am. Chem. Soc.* **2019**, *141*, 3507-3514. doi: 10.1021/jacs.8b11027.

29. Copeland, R.A.; Basavapatrur, A.; Moyer, M.; Scott, M.P. Impact of Enzyme Concentration and Residence Time on Apparent Activity Recovery in Jump Dilution Analysis. *Anal. Biochem.* **2011**, *416*, 206-210. doi: 10.1016/j.ab.2011.05.029.

30. Smith, S.; Keul, M.; Engel, J.; Basu, D.; Eppmann, S.; Rauh, D. Characterization of Covalent-Reversible EGFR Inhibitors. *ACS Omega* **2017**, *2*, 1563-1575. doi: 10.1021/acsomega.7b00157.

31. Auld, D.S.; Ingles, J.; Dahlin, J.L. Assay Interference by Aggregation. In *Assay Guidance Manual* [Online], Eli Lilly & Company and the National Center for Advancing Translational Sciences: Bethesda (MD), 2017. <https://www.ncbi.nlm.nih.gov/books/NBK442297/>.

32. Copeland, R.A. *ENZYMES: A Practical Introduction to Structure, Mechanism, and Data Analysis*. Second ed.; John Wiley & Sons, Inc: New York, NY, 2000. doi: 10.1002/0471220639.

33. Copeland, R.A. *Evaluation of Enzyme Inhibitors in Drug Discovery: A Guide for Medicinal Chemists and Pharmacologists*. Second ed.; John Wiley & Sons, Inc.: Hoboken, New Jersey, 2013. doi: 10.1002/9781118540398.

34. Potratz, J.P. Making Enzyme Kinetics Dynamic via Simulation Software. *J. Chem. Educ.* **2018**, *95*, 482-486. doi: 10.1021/acs.jchemed.7b00350.

35. Pollard, T.D.; De La Cruz, E.M. Take Advantage of Time in Your Experiments: A Guide to Simple, Informative Kinetics Assays. *Mol. Biol. Cell* **2013**, *24*, 1103-1110. doi: 10.1091/mbc.e13-01-0030.

36. Walkup, G.K.; You, Z.; Ross, P.L.; Allen, E.K.H.; Daryaee, F.; Hale, M.R.; O'Donnell, J.; Ehmann, D.E.; Schuck, V.J.A.; Buurman, E.T.; Choy, A.L.; Hajec, L.; Murphy-Benhamo, K.; Marone, V.; Patey, S.A.; Grosser, L.A.; Johnstone, M.; Walker, S.G.; Tonge, P.J.; Fisher, S.L. Translating Slow-Binding Inhibition Kinetics into Cellular and *In Vivo* Effects. *Nat. Chem. Biol.* **2015**, *11*, 416-423. doi: 10.1038/nchembio.1796.

37. Strelow, J.M. A Perspective on the Kinetics of Covalent and Irreversible Inhibition. *SLAS Discov.: Adv. Life Sci. R&D* **2017**, *22*, 3-20. doi: 10.1177/1087057116671509.

38. Lu, S.; Zhang, J. Designed Covalent Allosteric Modulators: An Emerging Paradigm in Drug Discovery. *Drug Discov. Today* **2017**, *22*, 447-453. doi: 10.1016/j.drudis.2016.11.013.

39. Tuley, A.; Fast, W. The Taxonomy of Covalent Inhibitors. *Biochemistry* **2018**, *57*, 3326-3337. doi: 10.1021/acs.biochem.8b00315.

40. Yang, J.; Jamei, M.; Yeo, K.R.; Tucker, G.T.; Rostami-Hodjegian, A. Kinetic Values for Mechanism-Based Enzyme Inhibition: Assessing the Bias Introduced by the Conventional Experimental Protocol. *Eur. J. Pharm. Sci.* **2005**, *26*, 334-340. doi: 10.1016/j.ejps.2005.07.005.

41. Copeland, R.A. Chapter 6. Slow Binding Inhibitors. In *Evaluation of Enzyme Inhibitors in Drug Discovery: A Guide for Medicinal Chemists and Pharmacologists*, Second ed.; John Wiley & Sons, Inc: Hoboken, New Jersey, 2013; pp 203-244. doi: 10.1002/9781118540398.ch6.

42. Copeland, R.A. Chapter 9. Irreversible Enzyme Inactivators. In *Evaluation of Enzyme Inhibitors in Drug Discovery: A Guide for Medicinal Chemists and Pharmacologists*, Second ed.; John Wiley & Sons, Inc.: Hoboken, New Jersey, 2013; pp 345-382. doi: 10.1002/9781118540398.
43. Copeland, R.A. The Dynamics of Drug-Target Interactions: Drug-Target Residence Time and Its Impact on Efficacy and Safety. *Expert Opin. Drug Discov.* **2010**, *5*, 305-310. doi: 10.1517/17460441003677725.
44. Copeland, R.A.; Pompliano, D.L.; Meek, T.D. Drug-Target Residence Time and Its Implications for Lead Optimization. *Nat. Rev. Drug Discov.* **2006**, *5*, 730-739. doi: 10.1038/nrd2082.
45. Schwartz, P.A.; Kuzmic, P.; Solowiej, J.; Bergqvist, S.; Bolanos, B.; Almaden, C.; Nagata, A.; Ryan, K.; Feng, J.; Dalvie, D.; Kath, J.C.; Xu, M.; Wani, R.; Murray, B.W. Covalent EGFR Inhibitor Analysis Reveals Importance of Reversible Interactions to Potency and Mechanisms of Drug Resistance. *Proc. Natl. Acad. Sci.* **2014**, *111*, 173. doi: 10.1073/pnas.1313733111.
46. McWhirter, C. Chapter One - Kinetic Mechanisms of Covalent Inhibition. *Annu. Rep. Med. Chem.* **2021**, *56*, 1-31. doi: 10.1016/bs.armc.2020.11.001.
47. Mah, R.; Thomas, J.R.; Shafer, C.M. Drug Discovery Considerations in the Development of Covalent Inhibitors. *Bioorg. Med. Chem. Lett.* **2014**, *24*, 33-39. doi: 10.1016/j.bmcl.2013.10.003.
48. Guan, I.; Williams, K.; Pan, J.; Liu, X. New Cysteine Covalent Modification Strategies Enable Advancement of Proteome-wide Selectivity of Kinase Modulators. *Asian J. Org. Chem.* **2021**, *10*, 949-963. doi: 10.1002/ajoc.202100036.
49. Lonsdale, R.; Burgess, J.; Colclough, N.; Davies, N.L.; Lenz, E.M.; Orton, A.L.; Ward, R.A. Expanding the Armory: Predicting and Tuning Covalent Warhead Reactivity. *J. Chem. Inf. Model.* **2017**, *57*, 3124-3137. doi: 10.1021/acs.jcim.7b00553.
50. Martin, J.S.; MacKenzie, C.J.; Fletcher, D.; Gilbert, I.H. Characterising Covalent Warhead Reactivity. *Bioorg. Med. Chem.* **2019**, *27*, 2066-2074. doi: 10.1016/j.bmc.2019.04.002.
51. Telliez, J.-B.; Dowty, M.E.; Wang, L.; Jussif, J.; Lin, T.; Li, L.; Moy, E.; Balbo, P.; Li, W.; Zhao, Y., et al. Discovery of a JAK3-Selective Inhibitor: Functional Differentiation of JAK3-Selective Inhibition over pan-JAK or JAK1-Selective Inhibition. *ACS Chem. Biol.* **2016**, *11*, 3442-3451. doi: 10.1021/acschembio.6b00677.
52. Zhai, X.; Ward, R.A.; Doig, P.; Argyrou, A. Insight into the Therapeutic Selectivity of the Irreversible EGFR Tyrosine Kinase Inhibitor Osimertinib through Enzyme Kinetic Studies. *Biochemistry* **2020**, *59*, 1428-1441. doi: 10.1021/acs.biochem.0c00104.
53. Meara, J.P.; Rich, D.H. Measurement of Individual Rate Constants of Irreversible Inhibition of a Cysteine Proteinase by an Epoxysuccinyl Inhibitor. *Bioorg. Med. Chem. Lett.* **1995**, *5*, 2277-2282. doi: 10.1016/0960-894X(95)00396-B.
54. Rocha-Pereira, J.; Nascimento, M.S.J.; Ma, Q.; Hilgenfeld, R.; Neyts, J.; Jochmans, D. The Enterovirus Protease Inhibitor Rupintrivir Exerts Cross-Genotypic Anti-Norovirus Activity and Clears Cells from the Norovirus Replicon. *Antimicrob. Agents Chemother.* **2014**, *58*, 4675-4681. doi: 10.1128/AAC.02546-13.
55. Fell, J.B.; Fischer, J.P.; Baer, B.R.; Blake, J.F.; Bouhana, K.; Briere, D.M.; Brown, K.D.; Burgess, L.E.; Burns, A.C.; Burkard, M.R., et al. Identification of the Clinical Development Candidate MRTX849, a Covalent KRAS^{G12C} Inhibitor for the Treatment of Cancer. *J. Med. Chem.* **2020**, *63*, 6679-6693. doi: 10.1021/acs.jmedchem.9b02052.
56. Hansen, R.; Peters, U.; Babbar, A.; Chen, Y.; Feng, J.; James, M.R.; Li, L.-S.; Ren, P.; Liu, Y.; Zarrinkar, P.P. The Reactivity-Driven Biochemical Mechanism of Covalent KRAS^{G12C} Inhibitors. *Nat. Struct. Mol. Biol.* **2018**, *25*, 454-462. doi: 10.1038/s41594-018-0061-5.
57. Lanman, B.A.; Allen, J.R.; Allen, J.G.; Amegadzie, A.K.; Ashton, K.S.; Booker, S.K.; Chen, J.J.; Chen, N.; Frohn, M. J.; Goodman, G., et al. Discovery of a Covalent Inhibitor of KRAS^{G12C} (AMG 510) for the Treatment of Solid Tumors. *J. Med. Chem.* **2020**, *63*, 52-65. doi: 10.1021/acs.jmedchem.9b01180.
58. Johansson, H.; Isabella Tsai, Y.-C.; Fantom, K.; Chung, C.-W.; Küpper, S.; Martino, L.; Thomas, D.A.; Eberl, H.C.; Muelbaier, M.; House, D.; Rittinger, K. Fragment-Based Covalent Ligand Screening Enables Rapid Discovery of Inhibitors for the RBR E3 Ubiquitin Ligase HOIP. *J. Am. Chem. Soc.* **2019**, *141*, 2703-2712. doi: 10.1021/jacs.8b13193.
59. Kathman, S.G.; Xu, Z.; Statsyuk, A.V. A Fragment-Based Method to Discover Irreversible Covalent Inhibitors of Cysteine Proteases. *J. Med. Chem.* **2014**, *57*, 4969-4974. doi: 10.1021/jm500345q.
60. Johnson, K.A. Fitting Enzyme Kinetic Data with KinTek Global Kinetic Explorer. *Meth. Enzymol.* **2009**, *467*, 601-626. doi: 10.1016/S0076-6879(09)67023-3.
61. Kuzmić, P. Chapter 10 - DynaFit—A Software Package for Enzymology. *Meth. Enzymol.* **2009**, *467*, 247-280. doi: 10.1016/S0076-6879(09)67010-5.
62. Mayer, J.; Khairy, K.; Howard, J. Drawing an Elephant with Four Complex Parameters. *Am. J. Phys.* **2010**, *78*, 648-649. doi: 10.1119/1.3254017.
63. Perrin, C.L. Linear or Nonlinear Least-Squares Analysis of Kinetic Data? *J. Chem. Educ.* **2017**, *94*, 669-672. doi: 10.1021/acs.jchemed.6b00629.
64. Rufer, A.C. Drug Discovery for Enzymes. *Drug Discov. Today* **2021**, *26*, 875-886. doi: 10.1016/j.drudis.2021.01.006.
65. Motulsky, H.J.; Christopoulos, A. *Fitting Models to Biological Data Using Linear and Nonlinear Regression: A Practical Guide to Curve Fitting*. Second ed.; GraphPad Software Inc.: San Diego, CA, 2003. www.graphpad.com.
66. Motulsky, H.J. Entering a User-Defined Model Into Prism. In *GraphPad Curve Fitting Guide* [Online], GraphPad Software, LLC: 1995-2021. https://www.graphpad.com/guides/prism/latest/curve-fitting/reg_writing_models.htm.
67. Wu, G.; Yuan, Y.; Hodge, C.N. Determining Appropriate Substrate Conversion for Enzymatic Assays in High-Throughput Screening. *J. Biomol. Screen.* **2003**, *8*, 694-700. doi: 10.1177/1087057103260050.
68. Dharadh, S.; Kim, R.Q.; Uckelmann, M.; Sixma, T.K. Chapter Thirteen - Quantitative analysis of USP activity in vitro. *Meth. Enzymol.* **2019**, *618*, 281-319. doi: 10.1016/bs.mie.2018.12.023.
69. Janssen, A.P.A.; van Hengst, J.M.A.; Béquignon, O.J.M.; Deng, H.; van Westen, G.J.P.; van der Stelt, M. Structure Kinetics Relationships and Molecular Dynamics Show Crucial Role for Heterocycle Leaving Group in Irreversible Diacylglycerol Lipase Inhibitors. *J. Med. Chem.* **2019**, *62*, 7910-7922. doi: 10.1021/acs.jmedchem.9b00686.
70. Miyawaki, O.; Kanazawa, T.; Maruyama, C.; Dozen, M. Static and Dynamic Half-life and Lifetime Molecular Turnover of Enzymes. *J. Biosci. Bioeng.* **2017**, *123*, 28-32. doi: 10.1016/j.jbiosc.2016.07.016.
71. Selwyn, M.J. A Simple Test for Inactivation of an Enzyme During Assay. *Biochim. Biophys. Acta, Enzymol. Biol. Oxid.* **1965**, *105*, 193-195. doi: 10.1016/S0926-6593(65)80190-4.
72. Ferrall-Fairbanks, M.C.; Kieslich, C.A.; Platt, M.O. Reassessing Enzyme Kinetics: Considering Protease-As-Substrate Interactions in Proteolytic Networks. *Proc. Natl. Acad. Sci.* **2020**, *117*, 3307. doi: 10.1073/pnas.1912207117.
73. Johnson, I.D. Introduction to Fluorescence Techniques. In *Molecular Probes Handbook: A Guide to Fluorescent Probes and Labeling Technologies* [Online], 11th ed.; Life Technologies Corporation: 2010. <https://www.thermofisher.com/nl/en/home/references/molecular-probes-the-handbook/introduction-to-fluorescence-techniques.html>.
74. Kuzmić, P. A Steady-State Algebraic Model for the Time Course of Covalent Enzyme Inhibition. *bioRxiv* **2020**. doi: 10.1101/2020.06.10.144220.

75. Copeland, R.A. Chapter 7. Tight Binding Inhibition. In *Evaluation of Enzyme Inhibitors in Drug Discovery: A Guide for Medicinal Chemists and Pharmacologists*, Second ed.; John Wiley & Sons, Inc: Hoboken, New Jersey, 2013; pp 245-285. doi: 10.1002/9781118540398.ch7.

76. Murphy, D.J. Determination of Accurate K_i Values for Tight-Binding Enzyme Inhibitors: An In Silico Study of Experimental Error and Assay Design. *Anal. Biochem.* **2004**, *327*, 61-67. doi: 10.1016/j.ab.2003.12.018.

77. Copeland, R.A. Appendix 1: Kinetics of Biochemical Reactions. In *Evaluation of Enzyme Inhibitors in Drug Discovery: A Guide for Medicinal Chemists and Pharmacologists*, Second ed.; John Wiley & Sons, Inc: Hoboken, New Jersey, 2013; pp 471-482. doi: 10.1002/9781118540398.app1.

78. Acker, M.G.; Auld, D.S. Considerations for the Design and Reporting of Enzyme Assays in High-Throughput Screening Applications. *Perspectives in Science* **2014**, *1*, 56-73. doi: 10.1016/j.pisc.2013.12.001.

79. Biswanger, H. Enzyme Assays. *Perspectives in Science* **2014**, *1*, 41-55. doi: 10.1016/j.pisc.2014.02.005.

80. Kuzmić, P. *Determination of k_{inact} and K_i for Covalent Inhibition Using the Omnia® Assay*; Technical Note TN-2015-02; BioKin Ltd: Watertown MA, [Online], 2015. www.biokin.com/TN/2015/02 (accessed 2021-07-23).

81. Krippendorff, B.-F.; Neuhaus, R.; Lienau, P.; Reichel, A.; Huisenga, W. Mechanism-Based Inhibition: Deriving K_i and k_{inact} Directly from Time-Dependent IC_{50} Values. *J. Biomol. Screen.* **2009**, *14*, 913-923. doi: 10.1177/1087057109336751.

82. Ito, K.; Iwatsubo, T.; Kanamitsu, S.; Ueda, K.; Suzuki, H.; Sugiyama, Y. Prediction of Pharmacokinetic Alterations Caused by Drug-Drug Interactions: Metabolic Interaction in the Liver. *Pharmacol. Rev.* **1998**, *50*, 387-412.

83. Kitz, R.; Wilson, I.B. Esters of Methanesulfonic Acid as Irreversible Inhibitors of Acetylcholinesterase. *J. Biol. Chem.* **1962**, *237*, 3245-3249. doi: 10.1016/S0021-9258(18)50153-8.

84. Kuzmić, P.; Solowiej, J.; Murray, B.W. An Algebraic Model for the Kinetics of Covalent Enzyme Inhibition at Low Substrate Concentrations. *Anal. Biochem.* **2015**, *484*, 82-90. doi: 10.1016/j.ab.2014.11.014.

85. Kuzmić, P.A. Two-point IC_{50} Method for Evaluating the Biochemical Potency of Irreversible Enzyme Inhibitors. *bioRxiv* **2020**. doi: 10.1101/2020.06.25.171207.

86. Obach, R.S.; Walsky, R.L.; Venkatakrishnan, K. Mechanism-Based Inactivation of Human Cytochrome P450 Enzymes and the Prediction of Drug-Drug Interactions. *Drug Metab. Dispos.* **2007**, *35*, 246. doi: 10.1124/dmd.106.012633.

87. Zhang, J.-H.; Chung, T.D.Y.; Oldenburg, K.R. A Simple Statistical Parameter for Use in Evaluation and Validation of High Throughput Screening Assays. *J. Biomol. Screen.* **1999**, *4*, 67-73. doi: 10.1177/108705719900400206.

88. Motulsky, H.J. *GraphPad Curve Fitting Guide*. 1995-2021. <https://www.graphpad.com/guides/prism/latest/curve-fitting/index.htm>.

89. Cheng, Y.-C.; Prusoff, W.H. Relationship Between the Inhibition Constant (K_i) and the Concentration of Inhibitor which Causes 50 Per Cent Inhibition (I_{50}) of an Enzymatic Reaction. *Biochem. Pharmacol.* **1973**, *22*, 3099-3108. doi: 10.1016/0006-2952(73)90196-2.

90. National Center for Advancing Translational Sciences. *Assay Guidance Manual*. Eli Lilly & Company and the National Center for Advancing Translational Sciences: Bethesda (MD), 2004-2021. <https://www.ncbi.nlm.nih.gov/books/NBK53196/>.

8. Supporting Information

8.1. Symbols

E	Unbound enzyme
I	Unbound inhibitor
EI	Noncovalent enzyme–inhibitor complex
EI^*	Covalent enzyme–inhibitor adduct
S	Unbound substrate
ES	Noncovalent enzyme–substrate complex
P	(Detectable) product
k_1	Second order association rate constant for $E + S \leftrightarrow ES$ reaction (in $M^{-1}s^{-1}$)
k_2	First order dissociation rate constant for $E + S \leftrightarrow ES$ equilibrium (in s^{-1})
k_3	Second order association rate constant for $E + I \leftrightarrow EI$ reaction (in $M^{-1}s^{-1}$)
k_4	First order dissociation rate constant for $E + I \leftrightarrow EI$ equilibrium (in s^{-1})
k_5	First order association rate constant for $EI \rightarrow EI^*$ reaction (in s^{-1})
k_6	First order dissociation rate constant for $EI \leftrightarrow EI^*$ equilibrium (in s^{-1})
F_t	Detected signal reflecting product formation in presence of inhibitor after incubation t (in AU)
F_{ctrl}	Detected signal reflecting product formation in the uninhibited control (in AU)
F_0	Background signal at reaction initiation (in AU)
r_p	Product coefficient for detected signal per formed product (in AU/M)
V_i	Initial product formation velocity in presence of inhibitor (in AU/s)
V_s	Steady-state/final product formation velocity in presence of inhibitor (in AU/s)
V_{t^*}	Product formation velocity after preincubation t^* (in AU/s)
V_{ctrl}	Product formation velocity in the uninhibited control (in AU/s)
V_{t^*ctrl}	Product formation velocity in the uninhibited control after preincubation t^* (in AU/s)
V_0	Product formation velocity in the uninhibited control without preincubation: $t^* = 0$ (in AU/s)
t	Incubation time after onset of product formation (in s)
t'	Preincubation time after onset of enzyme inhibition (in s)
$t\frac{1}{2}$	Half-life for reaction progress (in s)
$t\frac{1}{2}_{diss}$	Half-life for dissociation reaction (in s)
τ	Target residence time (in s)
k_{obs}	Observed reaction rate constant (in s^{-1})
k_{max}	Maximum reaction rate constant at saturating inhibitor concentration for 2-step inhibition (in s^{-1})
k_{inact}	Inactivation rate constant for $EI \rightarrow EI^*$ at saturating inhibitor concentration for 2-step IRREV inhibition (in s^{-1})
k_{ctrl}	Reaction rate constant for nonlinearity or loss of enzyme activity in uninhibited control (in s^{-1})
k_{degE}	Enzyme degradation rate constant for $E \rightarrow Edeg$ (in s^{-1})
k_{cat}	Product formation rate constant for $ES \rightarrow E + P$ (in s^{-1}) at saturating substrate concentration
k_{sub}	Reaction rate constant for $E + S \rightarrow E + P$ (in $M^{-1}s^{-1}$) ($= k_{cat}/K_M$ if $[S] \ll 0.1K_M$)
k_{chem}	Reaction rate constant for $E + I \rightarrow EI^*$ of 1-step IRREV inhibitors (in $M^{-1}s^{-1}$)
k_{off}	Overall dissociation rate constant from bound to unbound enzyme $EI + EI^* \rightarrow E + I$ (in s^{-1})
K_i	Inhibition/dissociation constant (in M) for noncovalent $E + I \leftrightarrow EI$ equilibrium of 2-step inhibition
K_i^{app}	Apparent noncovalent inhibition constant (in M): with substrate competition
K_i^*	Steady-state inhibition constant (in M) for $E + I \leftrightarrow EI + EI^*$ equilibrium of 2-step REV inhibition
K_i^{*app}	Apparent steady-state inhibition constant (in M): with substrate competition
K_i	Inactivation constant for $E + I \rightarrow EI^*$ (in M) of 2-step IRREV inhibition
K_i^{app}	Apparent inactivation constant (in M): with substrate competition
K_M	Michaelis-Menten constant for $E + S \rightarrow E + P$ (in M)
k_{inact}/K_i	Inactivation efficiency: reaction rate constant for $E + I \rightarrow EI^*$ of 2-step IRREV inhibitors (in $M^{-1}s^{-1}$)
IC_{50}	Inhibitor concentration resulting in half-maximum inhibition (in M)
$IC_{50}(t)$	Inhibitor concentration resulting in half-maximum inhibition after incubation time t (in M)
$[E]^{total}$	Combined total concentration of all enzyme species ($E^{total} = E + EI + EI^* + ES + E_{deg} + EI_{deg} + EI^*_{deg} + ES_{deg}$)
$[E]_0$	Unbound enzyme concentration at reaction initiation (before binding to inhibitor/substrate)
$[I]_0$	Unbound inhibitor concentration at onset of inhibition (before binding to enzyme)
$[S]_0$	Unbound substrate concentration at onset of product formation (before binding to enzyme)
$[EI]_{eq}$	Noncovalent EI concentration at (steady-state) equilibrium
$[X]_0$	Concentration of component X at reaction initiation (before binding to other reaction components)
$[X]_t$	Concentration of component X at incubation time t
$[X]_{t^*}$	Concentration of component X at preincubation time t^*
V_t	Incubation reaction volume containing enzyme, inhibitor and substrate ($V_t = V_{t^*} + V_{sub}$)
V_{t^*}	Preincubation reaction volume containing enzyme and inhibitor
V_{sub}	Volume containing substrate

8.2. Kinetic Parameters and Microscopic Rate Constants

Table S1 | Kinetic parameters and microscopic rate constants for pseudo-first order reactions.

	1-step REV	2-step REV	2-step IRREV	1-step IRREV
$K_i (M)$	$\frac{k_4}{k_3}$	$\frac{k_4}{k_3}$	$\frac{k_4}{k_3}$	-
$K_i^* (M)$	-	$\frac{k_4}{k_3 + \frac{k_3 k_5}{k_6}}$	-	-
$K_i (M)$	-	-	$\frac{k_4 + k_{inact}}{k_3}$	-
$k_{off} (s^{-1})$	k_4	$\frac{k_4 k_6}{k_4 + k_5 + k_6}$	0	0
$k_{obs} (s^{-1})$	$k_4 + k_3 [I]$	$k_6 + \frac{k_5 [I]}{\left(\frac{k_4}{k_3}\right) + [I]}$	$k_6 + \frac{k_{inact} [I]}{\left(\frac{k_4 + k_{inact}}{k_3}\right) + [I]}$	$k_{chem} [I]$
<i>Inactivation rate constant ($M^{-1}s^{-1}$)</i>	-	-	$\frac{k_{inact}}{K_i} = \frac{k_3 k_{inact}}{k_4 + k_{inact}}$	k_{chem}
$t_{1/2} (s)$	$\frac{\ln(2)}{k_4 + k_3 [I]}$	$\frac{\ln(2)}{k_6 + \frac{k_5 [I]}{\left(\frac{k_4}{k_3}\right) + [I]}}$	$\frac{\left(\frac{k_4 + k_{inact}}{k_3} + [I]\right) \ln(2)}{k_{inact} [I]}$	$\frac{\ln(2)}{k_{chem} [I]}$
$t_{1/2_{diss}} (s)$	$\frac{\ln(2)}{k_4}$	$\frac{(k_3 + k_5 + k_6) \ln(2)}{k_4 k_6}$	0	0
$\tau (s)$	$\frac{1}{k_4}$	$\frac{(k_3 + k_5 + k_6)}{k_4 k_6}$	∞	∞

8.3. Similarities Michael-Menten Enzyme Kinetics and 2-step IRREV Inhibition

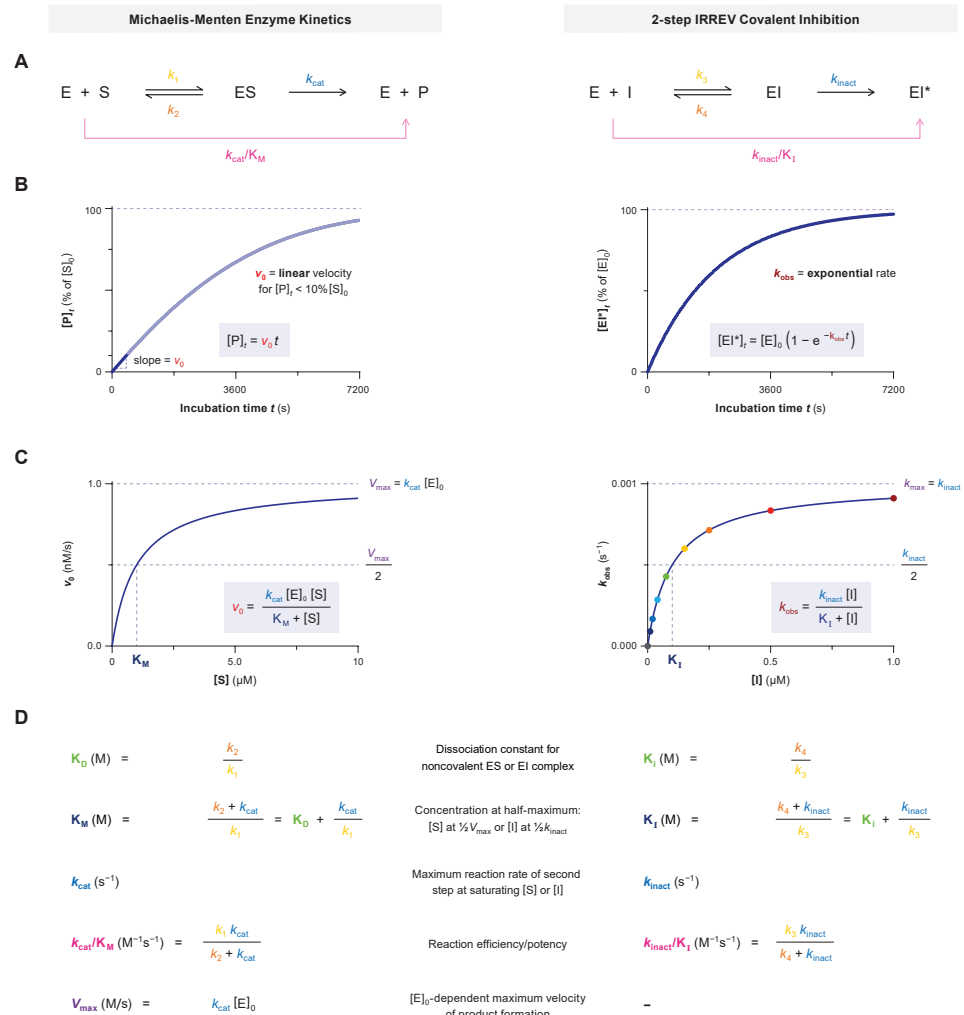


Figure S1 | Similarities and differences between MM enzyme kinetics and 2-step IRREV inhibition. Simulated for substrate **S1** with **KinSubDpl** (left) and 2-step IRREV inhibitor **C** with **KinGen** (right). **(A)** Binding mode. **(B)** Time-dependent product formation at $[S] = K_M$ (left) or $[I] = K_I$ (right). The biggest difference here is that a linear or an exponential model is fitted. **(C)** Secondary plot fits a bounded one-phase exponential equation. The maximum is driven by the rate of the second (irreversible) step and relevant kinetic parameters are derived from the maximum and the concentration at half-maximum. **(D)** Similarities in parameters for kinetic description of substrate hydrolysis for enzymes complying with Michaelis-Menten kinetics, and inactivation potency of 2-step IRREV inhibitors. K_D = dissociation constant for noncovalent $E + S \leftrightarrow ES$ equilibrium (M). k_1 = association rate constant for $E + S \leftrightarrow ES$ equilibrium ($M^{-1}s^{-1}$). k_2 = dissociation rate constant for $E + S \leftrightarrow ES$ equilibrium (s^{-1}). k_{cat} = rate constant for irreversible $ES \rightarrow E + P$ reaction (s^{-1}). K_M = Michaelis constant for substrate hydrolysis (M). K_I = inhibition constant for noncovalent $E + I \leftrightarrow EI$ equilibrium (M). k_3 = association rate constant for $E + I \leftrightarrow EI$ equilibrium ($M^{-1}s^{-1}$). k_4 = dissociation rate constant for $E + I \leftrightarrow EI$ equilibrium (s^{-1}). k_{inact} = k_5 = association rate constant for $EI \rightarrow EI^*$ reaction (s^{-1}). K_I = inactivation constant for 2-step inactivation (M). $V_0 = [S]$ -dependent initial velocity (M/s). V_{max} = maximum initial velocity (M/s). k_{obs} = $[I]$ -dependent observed rate constant for reaction from $[EI^*] = 0\%$ to $[EI^*] = 100\%$ (s^{-1}).

8.4. Linear vs. Nonlinear Regression

Linear regression methods are sometimes used to analyze preincubation-dependent enzyme inhibition (*Method III and IV*) because linear regression does not require dedicated graphical software, and benchmark protocols promoting linear regression originate from a time that computation with nonlinear regression was not readily available.⁸²⁻⁸³ Here, observed reaction rate k_{obs} is calculated from the linear slope of the natural logarithm of the percentage remaining enzyme activity against preincubation time (Figure S2A). The straight line enables relatively simple visual inspection of the fit. For readers that prefer this visual output, we recommend fitting the data by nonlinear regression but plotting the preincubation time-dependent enzyme activity on a semilog scale (Figure S2B).

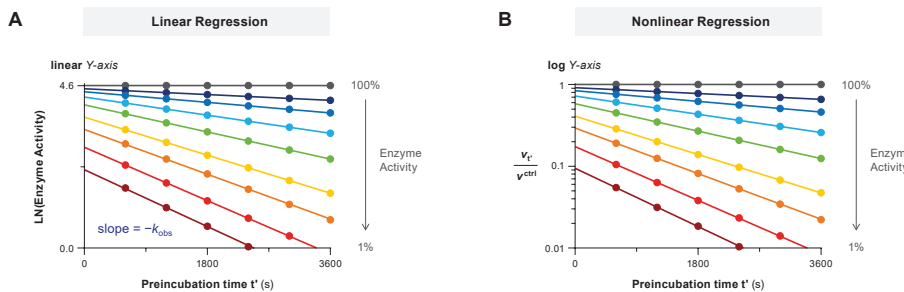


Figure S2 | Comparison of linear and nonlinear regression illustrated with the data of inhibitor C in *Method III* (original data in **Figure 15C**). (A) Linear regression. Reaction rate k_{obs} is obtained from the negative slope of the natural logarithm of percentage enzyme activity against preincubation time t' . $\text{LN}(\text{enzyme activity}) = \text{LN}(100\% \times v_t/v^{\text{ctrl}})$. Negative values for $\text{LN}(\text{enzyme activity})$ corresponding with enzyme activity below 1% are excluded as assay sensitivity is normally insufficient to accurately distinguish 99% from 99.9% inhibition though this error will significantly affect the linear fit of k_{obs} . (B) Nonlinear regression. Plot preincubation time-dependent enzyme activity against preincubation time on a semilog scale for visual inspection of the fit.



Chapter 4

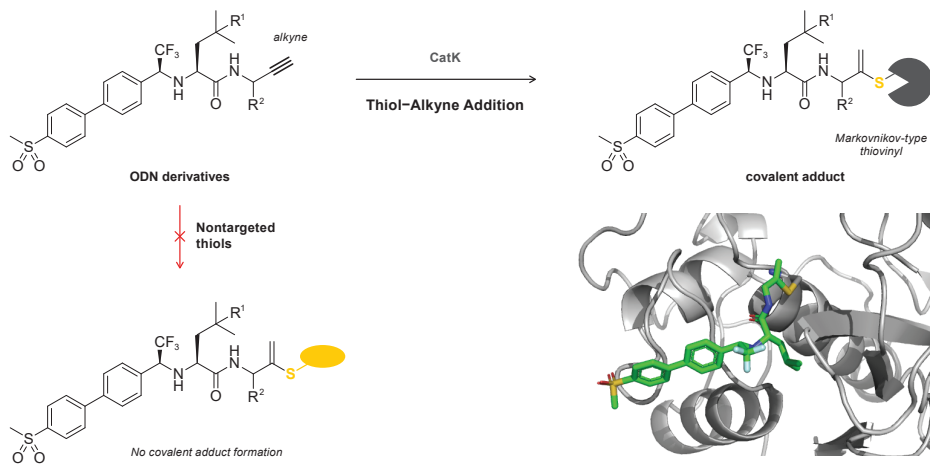


Nonactivated Alkynes in Irreversible Covalent Cathepsin K Inhibitors

Adapted from:

Mons, E.; Jansen, I.D.C.; Loboda, J.; van Doodewaerd, B.R.; Hermans, J.; Verdoes, M.; van Boeckel, C.A.A.; van Veelen, P.A.; Turk, B.; Turk, D.; Ovaa, H. The Alkyne Moiety as a Latent Electrophile in Irreversible Covalent Small Molecule Inhibitors of Cathepsin K. *J. Am. Chem. Soc.* **2019**, *141*, 3507-3514. doi:10.1021/jacs.8b11027

Abstract. Irreversible covalent inhibitors can have a beneficial pharmacokinetic/pharmacodynamics profile but are still often avoided due to the risk of indiscriminate covalent reactivity and the resulting adverse effects. To overcome this potential liability, we introduced an alkyne moiety as a latent electrophile into small molecule inhibitors of cathepsin K (CatK). Alkyne-based inhibitors do not show indiscriminate thiol reactivity but potently inhibit CatK protease activity by formation of an irreversible covalent bond with the catalytic cysteine residue, confirmed by crystal structure analysis. The rate of covalent bond formation (k_{inact}) does not correlate with electrophilicity of the alkyne moiety, indicative of a proximity-driven reactivity. Inhibition of CatK-mediated bone resorption is validated in human osteoclasts. Together, this work illustrates the potential of alkynes as latent electrophiles in small molecule inhibitors, enabling the development of irreversible covalent inhibitors with an improved safety profile.

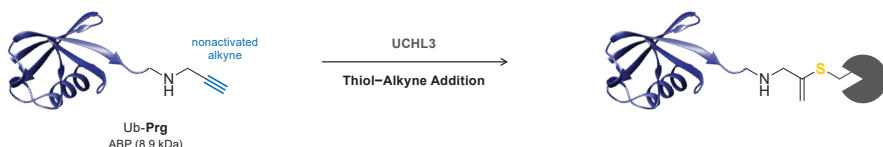


1. Introduction

Irreversible covalent inhibition of a target protein minimizes the required systemic drug exposure as protein activity can only be restored by *de novo* protein synthesis, resulting in a prolonged therapeutic effect long after the compound is cleared from the blood.¹⁻² Strategically placing an electrophilic moiety on the inhibitor will allow it to undergo attack by a nucleophilic amino acid residue upon binding to the target protein, forming a(n) (ir)reversible bond that is much stronger than typical noncovalent interactions. However, the ability to form a covalent bond with the target enzyme has raised concerns about indiscriminate reactivity with off-target proteins,³⁻⁵ even though some of the most prescribed drugs are covalent irreversible binders.⁶⁻⁷ This led to the disfavor of covalent modifiers as drug candidates until the recent successful development of irreversible covalent kinase inhibitors ibrutinib and afatinib, which form an irreversible covalent bond between an acrylamide warhead and a nonconserved cysteine residue on the ATP-binding site^{2, 8-10} but also with nontargeted cellular thiols.¹¹ The ability to form covalent adducts with off-target proteins has been linked to an increased risk of unpredictable idiosyncratic toxicity along with the daily drug dose administered to patients.¹¹⁻¹⁴ This risk can be reduced by incorporating less reactive electrophilic moieties into irreversible covalent inhibitors.

Terminal alkynes are generally considered “inert” toward cellular components – in absence of radical initiators, metal catalysts, and metabolic activators – and are therefore often used in bioorthogonal approaches as chemoselective “Click” handles.¹⁵⁻¹⁶ However, our group has shown a C-terminal propargyl moiety on ubiquitin to react in an activity-based manner with the catalytic cysteine residue in deubiquitinating enzymes (DUBs), forming an irreversible thioether bond *via* an *in situ* thiol–alkyne addition (Figure 1A).¹⁷ Markovnikov hydrothiolation of (terminal) alkynes with aliphatic thiols has been described for metal-catalyzed reactions,¹⁹⁻²² but has not been reported to occur outside the active site of a cysteine

A



B

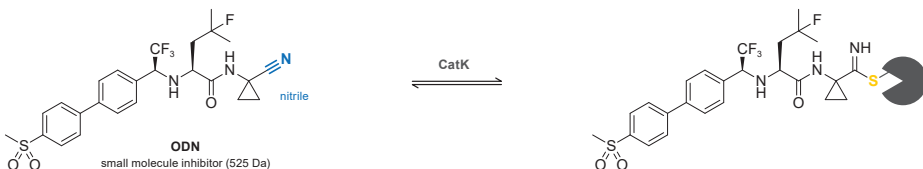


Figure 1 | Terminal alkyne moiety as latent electrophile for thiol–alkyne addition. **(A)** ABPs with ubiquitin recognition element and propargyl (Prg) warhead covalently modify the catalytic Cys in CysDUB proteases, forming a Markovnikov-type thiovinyl adduct. **(B)** The nitrile warhead in the established covalent inhibitor odanacatib (ODN) forms a reversible covalent adduct with catalytic Cys25 of cysteine protease CatK.¹⁸

protease under physiological conditions. The alkyne moiety on ubiquitin did not react with cysteine residues present in nontargeted proteins nor with excess thiol. Work by Sommer *et al.* revealed that the catalytic triad does not have to be intact for covalent bond formation, indicating a proximity-driven reactivity.²³ It is believed that the reactivity of the alkyne resulted from a template effect – recognition of (large) protein fragments driving the formation of the thermodynamically unfavored Markovnikov-type thiovinylic product²⁴ – and here we show that strong enough binding can be achieved with a small molecule recognition part. This study highlights the potential of alkynes as latent electrophiles in irreversible covalent small molecule inhibitors, as demonstrated for cathepsin K (CatK). CatK is a cysteine protease that is highly expressed in osteoclasts and is the most important protease in bone degradation.²⁵ Implicated in diseases such as osteoporosis, its inhibition has been of therapeutic interest for the past decade.²⁶ The most promising small molecule CatK inhibitor to date was odanacatib (ODN),¹⁸ a nonlysosomotropic inhibitor with a nitrile moiety as reversible covalent warhead that binds to catalytic Cys25 (Figure 1B). ODN has a high selectivity for CatK versus other cathepsins and only has to be taken once weekly because of its very long half-life of 66–93 h.²⁷ Clinical development was terminated after phase III clinical trials showed side effects including increased stroke risks and cardiovascular events.^{28–30} It is currently unclear whether this is due to inhibition of nonskeletal degradation properties of CatK or because of off-target inhibition.³¹ Nonetheless, the close proximity of the nitrile moiety relative to Cys25 made it a suitable model to incorporate an alkyne moiety as electrophile.

2. Results and Discussion

Synthesis and design. Derivatives of ODN were obtained by functionalization of precursor **1**, according to reported procedures (Figure 2, Scheme S1).^{32–33} Replacing the nitrile with an alkyne led to compromised solubility in aqueous media for alkyne EM03, which could be overcome by removal of the hydrophobic cyclopropane in nitrile EM02, propargyl EM04, and monomethylated propargyl EM05. The cyclopropane moiety is not essential for CatK inhibition but was introduced in the development of ODN to reduce metabolic liabilities.¹⁸ Alkyne electrophilicity increases if an electron-withdrawing substituent is introduced on the terminal position,^{20, 34} while remaining less electrophilic than acrylamides. Therefore, electron-

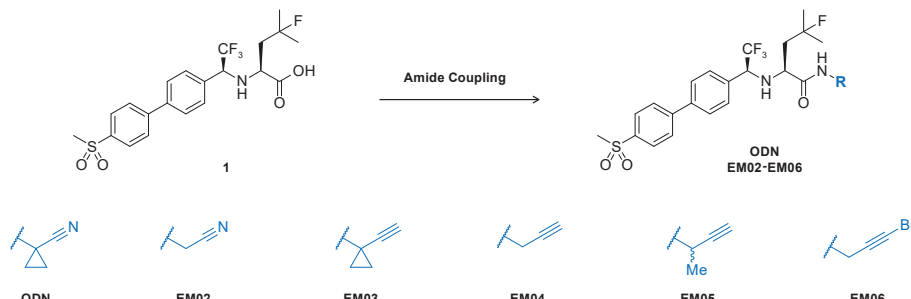


Figure 2 | Design of nitriles **ODN** and **EM02**, nonactivated alkyne analogues **EM03-EM05**, and electron-deficient bromoalkyne analogue **EM06**. Synthesis and yields can be found in **Scheme S1**.

deficient alkyne EM06 was taken along to investigate the effect of electrophilicity on the inhibitor selectivity. Conjugate addition of cysteine has been reported for electron-deficient internal alkynes such as the 2-butynamide warhead – the electrophile in irreversible covalent BTK inhibitor acalabrutinib.^{20, 35-36}

Indiscriminate thiol reactivity. Indiscriminate thiol reactivity was assessed following an established protocol in which nitrile-based inhibitors form an irreversible covalent adduct with cysteine (Figure 3).³⁷ Nitrile-based inhibitors ODN and EM02 show adduct formation that increases upon increasing the pH of the buffer, as do acrylamide-based kinase inhibitors ibrutinib and afatinib, and irreversible pan-cathepsin inhibitor E-64.³⁸ The cysteine adduct was not detected for alkyne-based inhibitors EM03, EM04, and EM05, supporting our hypothesis that the nonactivated alkyne is not reactive toward cysteine residues in nontargeted proteins. As expected,³⁶ adduct formation with electron-deficient alkynes EM06 and acalabrutinib was observed, underlining the importance of alkyne electrophilicity in indiscriminate thiol reactivity. Glutathione (GSH), a tripeptide with a cellular concentration of 0.5-10 mM,³⁹ is a commonly used biological thiol to assess the risk of idiosyncratic toxicity. Covalent adduct was observed upon incubation with 5 mM GSH for acrylamides and electron-deficient alkynes, as reported,^{11, 36} but not for any of the nitriles or nonactivated alkynes. The lack of nitrile adduct detection with nitriles ODN and EM02 is not representative, as these form a reversible covalent adduct with GSH that quickly dissociates under denaturing conditions.

In vitro inhibition. A recurring issue in CatK drug development is the difference in amino acids at the active site for rodentCatK compared to humanCatK, thus reducing the apparent potency of ODN up to 182-fold in mice and rats.⁴⁰ The potency of our inhibitors was assessed

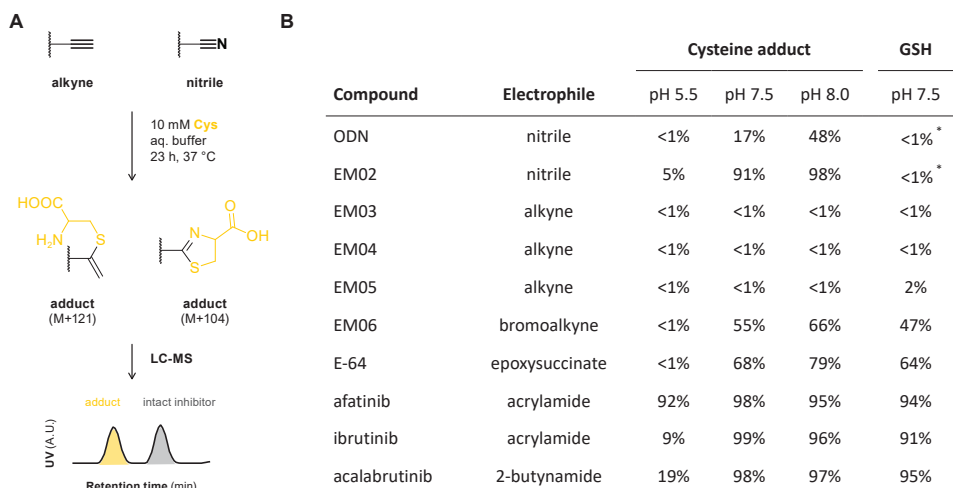


Figure 3 | Indiscriminate thiol reactivity assessed by LC-MS analysis following established protocol.³⁷ (A) Schematic overview. Thiol adducts formed upon incubation with cysteine are quantified from LC-MS UV traces. Nitrile warheads form an irreversible adduct with cysteine. (B) Adduct formation upon 23 h incubation with 10 mM cysteine or 5 mM GSH at 37 °C in aqueous buffer. Details in Table S1. * Reversible adduct.

in an *in vitro* activity assay on recombinant human cathepsins (**Table 1**). As reported, ODN is selective for hCatK with an IC₅₀ below 1 nM. Noncovalent interactions were optimized for ODN, and we anticipated that replacing the polarized nitrile moiety by a nonpolarized alkyne moiety would decrease the noncovalent interaction with active site residues, thereby reducing the noncovalent affinity (K_i). This is indeed reflected in increased IC₅₀ values for all alkyne-based inhibitors. Selectivity for CatK over related human cathepsins CatS, CatV, CatL, and CatB was conserved for alkynes EM04 and EM05, while all selectivity is lost for electron-deficient alkyne EM06. Inhibition of hCatK activity was validated in a gel-based probe labeling experiment with quenched activity-based probe (qABP) BMV109 (**Figure S2**).

Binding mode of alkynes is irreversible and covalent. Reversibility of hCatK inhibition was assessed in a jump dilution assay.⁴¹ Recombinant hCatK was incubated with inhibitor at high concentration to allow full active site occupation and subsequently diluted 300-fold into fluorogenic substrate (Z-FR-AMC) solution (**Figure 4**). For reversible inhibitors, rapid/jump dilution induces inhibitor dissociation from the enzyme when the inhibitor concentrations before and after dilution span the IC₅₀, resulting in an increase of substrate hydrolysis. For inhibitors with an irreversible binding mode, dilution does not induce inhibitor dissociation and does not affect enzyme inhibition. The progress curves show that ODN is a (fast) reversible inhibitor, while inhibition by alkynes EM04, EM05, and EM06 is irreversible. The covalent nature of the cathepsin-inhibitor interaction was elucidated by LC-MS analysis of intact CatK and CatK-inhibitor adducts (**Figure 5**). An increase in the deconvoluted mass corresponding to addition of the inhibitor to hCatK was observed for nitrile ODN and alkynes EM04, EM05, and EM06, confirming the formation of a covalent hCatK-inhibitor adduct. For ODN, unbound CatK was predominantly detected despite the inhibitor concentration far above the K_i. This

Table 1 | IC₅₀ values (nM) against proteolytic activity of recombinant purified cysteine proteases.

	hCatK	hCatL	hCatS	hCatV	hCatB	papain
ODN	0.56 ± 0.0022	(5.8 ± 0.72)×10 ³	24 ± 0.57	600 ± 40	63 ± 2.5	690 ± 58
EM02	0.57 ± 0.0090	>10 ³	18 ± 0.30	910 ± 110	21 ± 0.66	230 ± 12
EM03	(26 ± 2.2)×10 ³	>10 ⁵	>10 ⁵	>10 ⁵	>10 ⁵	>10 ⁵
EM04	290 ± 8.7	>10 ⁵	(11 ± 0.84)×10 ³	(24 ± 1.4)×10 ³	(9.4 ± 0.63)×10 ³	(14 ± 1.8)×10 ³
EM05	350 ± 12	>10 ⁵	(16 ± 1.8)×10 ³	(46 ± 2.3)×10 ³	(40 ± 4.4)×10 ³	(22 ± 3.9)×10 ³
EM06	47 ± 1.8	100 ± 4.6	55 ± 2.9	16 ± 0.88	99 ± 5.9	(6.3 ± 0.73)×10 ³
EM07	351 ± 7.6	N.A.	N.A.	N.A.	N.A.	N.A.
E-64	1.9 ± 0.032	3.4 ± 0.18	N.A.	N.A.	N.A.	2.4 ± 0.82

Preincubation of human cysteine protease and inhibitor for 30 min prior to addition of fluorogenic substrate. Mean ± SD for a single representative experiment (triplicate measurement). N.A. = not available. Dose-response curves are available in **Figure S1**.

is probably due to the reversible covalent binding mode; the denaturing conditions induce reversible inhibitor dissociation, but the off-rate for ODN is slow enough to still detect the adduct.

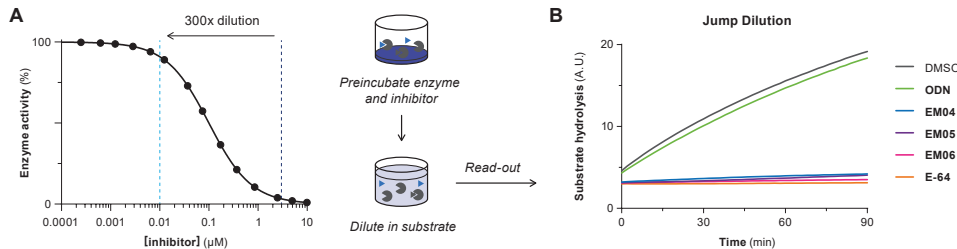


Figure 4 | Jump dilution assay to evaluate reversibility of inhibitor binding. **(A)** Principle of jump dilution. 300-fold dilution results in inhibitor concentrations corresponding to full inhibition (*before dilution*) to full activity (*after dilution*). **(B)** Progress curves for hCatK proteolytic activity after dilution in 4 μ M Z-FR-AMC. Control: E-64 is an irreversible pan-cathepsin inhibitor. Progress curves for control samples (without dilution) are available in **Figure S3**.

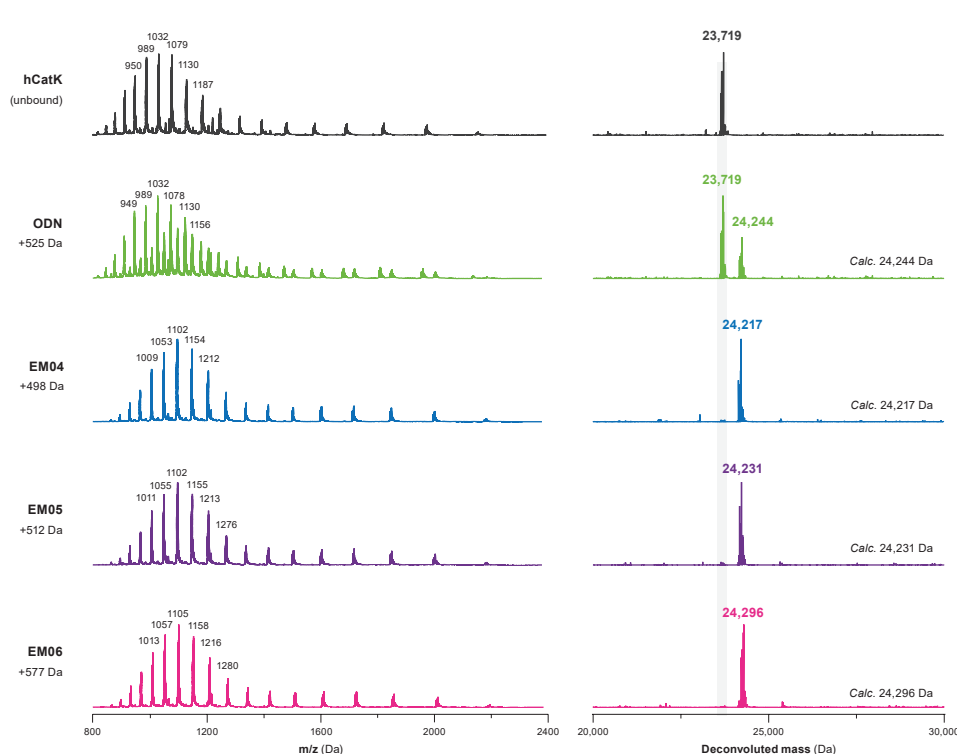


Figure 5 | Intact protein MS analysis. Representative ionization envelope (*left*) and deconvoluted electrospray ionization mass spectrum (*right*) upon incubation of recombinant hCatK for 6 h with excess inhibitor. Covalent adduct is detected by an increase in m/z values and deconvoluted mass (in Da).

Alkynes form a covalent thiovinylic bond with catalytic cysteine residue. Covalent CatK-EM04 adduct was submitted to bottom-up proteomic analysis to identify which amino acid residue is modified. In the tryptic digestion of unreacted CatK, the various length variant peptides containing the NQGQCGSCW-stretch have both Cys22 and Cys25 labeled with a carbamidomethyl group due to the alkylation reaction with iodoacetamide during the sample processing (Table S2). After reaction with alkyne EM04, these peptides disappear, but various peptides containing the NQGQCGSCW-stretch appear labeled with one carbamidomethyl group and one inhibitor. Tandem mass spectrometric analysis by HCD and EThcD analysis of peptide NQGQCGSCWAFSSVGAGLQLKKK indicates EM04 is on the second cysteine residue (Cys25; Table S3). Together, this clearly shows that one of these cysteine residues is labeled, most likely catalytic Cys25.

The formation of a vinyl thioether linkage between catalytic Cys25 on hCatK and the internal carbon of the alkyne moiety was confirmed by solving the crystal structure of CatK-EM07 adduct (Figure 6). Mature CatK was inactivated with MMTS (*S*-methyl methanethiosulfonate) for purification and storage, and reactivated with DTT in the presence of alkyne inhibitors at high concentration (200 μ M) to prevent self-degradation of CatK. Solubility of alkynes EM04 and EM05 was not sufficient, which was contributed to the fluoroleucine moiety. We therefore synthesized alkyne EM07 – a closely related derivative in which the fluorine on the L-leucine building block was replaced by a proton to improve solubility (synthesis shown in Scheme S2). The resulting CatK-EM07 adduct was crystallized using a sitting drop method, and the structure could be solved at 1.7 \AA resolution using maximum-likelihood free-kick (ML FK) electron density map.⁴² The refined structure unambiguously revealed the presence of a bond between the thiol atom of Cys25 and the internal carbon in alkyne EM07, with a C-S distance of 1.8 \AA (Figure 6B).

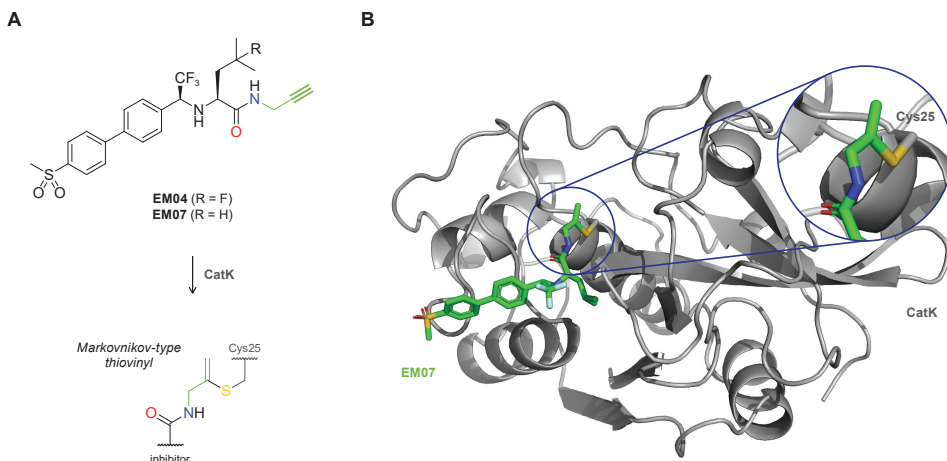


Figure 6 | Crystal structure of covalent CatK-EM07 adduct. **(A)** Structure of EM07 before and after covalent bond formation with CatK. **(B)** X-ray structure of EM07 bound to catalytic Cys25 in CatK. Coordinates and structure factors for the CatK-EM07 adduct have been submitted to the protein data bank (PDB), accession number 6QBS. Data analysis, refinement statistics and details are provided in Figure S4.

Kinetic evaluation. The apparent potency of irreversible covalent inhibitors increases upon longer incubation with the enzyme, since the interaction of inhibitor with enzyme is not at equilibrium.^{1, 43-46} As a result, the potency of these compounds can better be assessed by comparison of the k_{inact}/K_i ratio, which can be derived from the progress curve of substrate hydrolysis when the reaction is initiated by addition of the enzyme.⁴³ Interestingly, the maximum rate of covalent bond formation (k_{inact}) did not correlate with reactivity of the alkyne, as k_{inact} for alkyne EM05 is faster than for electron-deficient alkyne EM06 (Table 2). We hypothesize that halogen bonding by the terminal bromine with the thiol moiety on hCatK positions the alkyne less optimal relative to the cysteine residue thus reducing the rate of proximity-driven C-S bond formation.⁴⁷ The rate of covalent bond formation for ODN (k_5) is faster than for the alkynes (k_{inact}), also when correcting for the reverse reaction (k_6).

Inhibition of bone resorption activity in osteoclasts. Having established the covalent and irreversible inhibition of CatK on purified recombinant enzyme, we decided to test the inhibitory properties in a biologically relevant setting; inhibition of bone resorption by osteoclasts (OCs). OCs are the cells that degrade the bone matrix by secretion of acid and CatK into the resorption lacunae, resulting in the cleavage of collagen type I (Figure S6A). OCs are essential in bone repair, and aberrant activity is observed in numerous diseases including osteoporosis, rheumatoid arthritis, giant cell tumor of the bone, and bone metastases.⁴⁸⁻⁵⁰

Table 2 | *In vitro* kinetic evaluation of hCatK inhibition.

Irreversible covalent



$k_{\text{inact}} (\times 10^{-3} \text{ s}^{-1})$
 $K_i^{\text{app}} (\text{nM})$
 $k_{\text{inact}}/K_i (\times 10^3 \text{ M}^{-1} \text{ s}^{-1})$

EM04	0.19 ± 0.012	211 ± 47	0.95 ± 0.22
EM05	0.79 ± 0.061	3255 ± 602	0.26 ± 0.052
EM06	0.32 ± 0.045	193 ± 83	1.8 ± 0.81
E-64	1.3 ± 0.086	11 ± 1.6	N.A.

Reversible covalent



$k_5 (\times 10^{-3} \text{ s}^{-1})$
 $k_6 (\times 10^{-3} \text{ s}^{-1})$
 $K_i^{\text{app}} (\text{nM})$
 $K_i^* (\text{nM})$

ODN	2.0 ± 0.76	0.66	5.7 ± 4.6

Activity assay using 100 pM recombinant hCatK and 4 μM fluorogenic substrate Z-FR-AMC. Reaction initialization by addition of CatK. Mean \pm SD for a single representative experiment (triplicate measurement). Progress curves and fits are available in Figure S5.

Inhibition of osteoclastic CatK was studied by culturing OCs on cortical bone slices in the presence of inhibitor. Mature OCs were obtained by treatment of CD14⁺ monocytes with M-CSF (macrophage colony stimulating factor) and RANKL (receptor activator of nuclear factor κ B ligand) to stimulate differentiation to mature OCs (Figure 7A).⁵¹ Mature OCs are formed by merging of mononuclear osteoclast precursors to form large multinucleated cells, a process that continued until the end of the culturing period. When the culturing medium was refreshed (every 3 days), inhibitor was freshly added to make sure there always is inhibitor present to inhibit CatK in the newly formed mature OCs. The OCs were cultured on bone slices for sufficient time to clearly observe bone resorption. After culturing for 21 days, the OCs were washed off the bone slices and the resorption pits were stained to visualize bone resorption activity. OCs with normal CatK activity form trenches, resorbing the bone while they move over the surface of the bone. Previously published observations in OCs from CatK^{-/-} mice show that OCs lacking CatK are still able to form shallow pits, but unable to form trenches, with accumulation of collagen I fragments in the lysosomes.⁵²

Staining of bone slices for bone resorption showed formation of deep trenches for samples treated with 3 nM ODN, while 15 nM ODN resulted in the formation of shallow pits (Figure 7B), corresponding to an effective dose of around 15 nM.⁵³ Treatment with EM04 successfully inhibited bone resorption at concentrations from 80 nM, while inhibition with EM05 was nonconclusive; we observed trenches as well as pits at all tested concentrations. Quantification of the total resorption area confirmed these observations, even though it is not possible to distinguish between shallow pits and deep trenches (Figure S6). From this experiment, we concluded that alkynes EM04 and EM05 inhibit bone resorption with a higher potency than expected based on their potency to inhibit recombinant CatK.

Next, we treated the OC lysates with cathepsin qABP BMV109 to assess whether the observed inhibition of bone resorption could be correlated with CatK activity (Figure 7C). CatK activity for OCs treated with DMSO is low, which is expected because mature CatK in its uninhibited form is self-degrading,⁵⁴ and the observed bone resorption is the result of secreted mature CatK activity. Additionally, we expect that intracellular CatK is predominantly catalytic inactive proCatK, which is activated by cleavage of the activation peptide, an autoproteolytic event that requires an environment with a low pH for example lysosomes and the resorption lacunae.⁵⁵ Interestingly, we observe a strong increase of mature CatK activity in all samples treated with ODN, while samples with EM04 or EM05 do not show any CatK activity. The observed increase in mature CatK activity for ODN-treated samples does not reflect the actual intracellular proteolytic activity, but is the result of displacement of reversibly bound ODN by excess of irreversible qABP BMV109. Alkynes EM04 and EM05 form an irreversible covalent bond with CatK, and can thus not be displaced by BMV109. Western blotting for CatK revealed an increase in the intracellular levels of mature CatK for OCs that were treated with high concentration of any inhibitor, which could be the result of inhibition of proteolytic CatK activity, which would normally degrade mature CatK.

Counting OCs that were cultured on plastic revealed an increase in the number of OCs for the highest concentrations of ODN, EM04 and EM05 (Figure S7). This is in agreement with previous reports that observed an increase of OC maturation as a response to CatK activity

loss; the same number of bone marrow cells from $\text{CatK}^{-/-}$ mice led to a greater number of active OCs compared to bone marrow cells from the control mice.⁵² A significant increase in CatK expression upon 100 nM ODN treatment has been reported, without an increase in the number of OCs.⁵⁶ We hypothesize that complete inhibition of CatK activity stimulates the maturation of OCs, and further investigations are advised to identify the feedback mechanism.

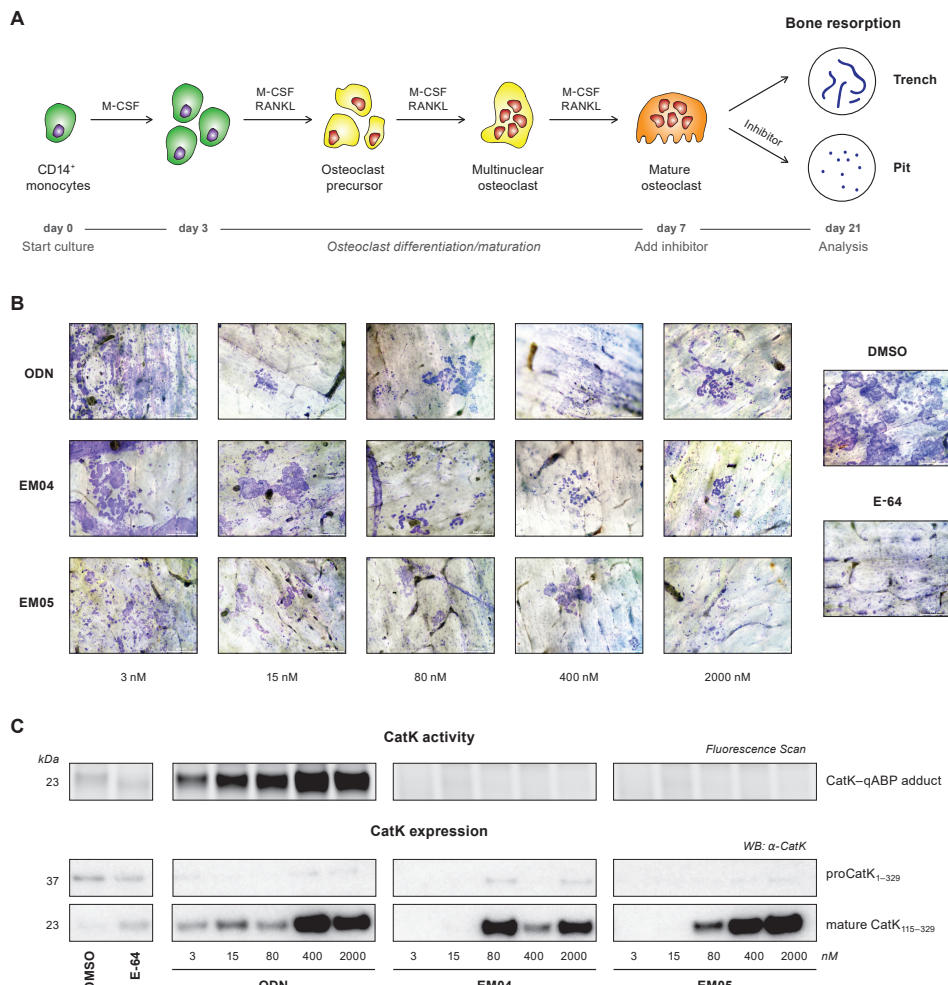


Figure 7 | Inhibition of CatK activity in human osteoclasts (OCs). **(A)** Maturation of OCs from monocytes (top) and schematic overview of cellular assay (bottom). CD14⁺ monocytes on bone slices were treated with M-CSF (day 0) and RANKL (day 3) to stimulate differentiation to mature OCs. Medium containing either inhibitor or DMSO was refreshed on day 7, 10, 13, and 16. On day 21, OCs were washed away and lysed, and bone slices were stained to visualize bone resorption. Normal OCs predominantly form deep trenches (paths), while OCs lacking CatK form small pits (circular dots). **(B)** Bone resorption visualized by staining of resorption pits with Coomassie Brilliant Blue. More staining means more resorption pits and, thus, more bone resorption activity. **(C)** CatK activity and expression in OC lysates. *Top:* fluorescence scan of CatK bound to irreversible qABP BMV109 shows mature, active CatK. *Middle/bottom:* Western blotting against CatK shows total amount of CatK present in OC lysates. Darker bands indicate more CatK activity/expression. Full gel scans can be found in **Figure S8**.

3. Conclusion

To conclude, nonactivated alkynes are not only suitable as latent electrophiles in (large) peptides but also in small molecule inhibitors, as demonstrated here for inhibition of cysteine protease cathepsin K (CatK). Alkyne-based covalent inhibitors do not show indiscriminate thiol reactivity but do form an irreversible covalent bond formation with CatK, as confirmed by MS analysis of intact CatK-inhibitor adducts. X-ray crystallography confirmed the formation of the Markovnikov-type product between the active site cysteine thiol and the internal carbon of the alkyne moiety. Kinetic evaluation shows that the rate of covalent bond formation (k_{inact}) does not correlate with electrophilicity of the alkyne, supporting our hypothesis of proximity-driven reactivity. Optimization of the alkyne position relative to the cysteine residue could result in more potent compounds with faster covalent bond formation while not compromising on indiscriminate thiol reactivity. Treatment of human osteoclasts (OCs) with alkynes EM04 and EM05 showed a potent inhibition of CatK-mediated bone resorption activity, with only a 5-fold difference in effective dose between ODN and EM04. Further investigations into the biological effect of irreversible inhibition of CatK are ongoing.

Finally, we urge everyone using the alkyne moiety as a Click handle to be careful with the assumption that the nonactivated alkyne is truly bioorthogonal; the binding of a small molecule inhibitor can be strong enough to initiate a thiol–alkyne reaction when the alkyne moiety is positioned in close proximity to a cysteine residue. More importantly, based on the proof-of-concept studies described herein, we foresee latent electrophiles such as the alkyne to be of great value in future development of cysteine-targeting covalent inhibitory drugs with a reduced risk of idiosyncratic toxicity.

Acknowledgements

We thank Patrick Celie at The Netherlands Cancer Institute (NKI) protein facility for the expression and purification of proCatK and Stephanie Hoppe from the NKI for the gift of ibrutinib and afatinib. This work was supported by VICI grant 724.013.002 (H.O.) from The Netherlands Organization for Scientific Research (NWO), and by P1-0140 (B.T.) and P1-0048 (D.T.) grants from Slovene Research Agency.

Competing Interests

The authors declare the following competing financial interest: E.M., H.O., and C.A.A.v.B. are inventors on patent WO2019112426A1, which covers the use of the herein described cathepsin K inhibitors.⁵⁷

Author Contributions

E.M.: Conceptualization, Methodology, Investigation (*Chemical Synthesis, Biochemical Assays*), Formal Analysis, Writing – Original Draft, Writing – Review & Editing. I.D.C.J.: Investigation (*Cellular Assays*), Formal Analysis, Writing – Original Draft, Writing – Review & Editing. J.L.: Investigation (*Crystallography*), Formal Analysis, Writing – Review & Editing. B.R.v.D.: Investigation (*Top-Down MS*). J.H.: Investigation (*Chemical Synthesis*). M.V.: Resources, Writing – Review & Editing. C.A.A.v.B.: Conceptualization, Writing – Review & Editing. P.A.v.V.: Investigation (*Bottom-Up MS/MS*), Formal Analysis. B.T.: Resources, Writing

– Review & Editing. D.T.: Supervision, Writing – Review & Editing. H.O.: Conceptualization, Supervision, Funding Acquisition, Writing – Review & Editing.

4. Materials and Methods: *Biochemistry*

General

Assay buffers are freshly supplemented with DTT (Chem-Impex, #00127), stored in single-use aliquots at -20°C (1M aqueous solution). Protease incubations in larger volumes ($>50\text{ }\mu\text{L}$) were performed in Protein Lobind Microtubes (Eppendorf, #022431018) to minimize loss of enzyme and activity. Established irreversible cathepsin inhibitor E-64 (Apollo Sci, #BIMI2157), reversible covalent CatK inhibitor odanacatib (ODN; *in-house* synthesis, see *section 5.2*), thiol-alkylating agent iodoacetamide (IAc; SigmaAldrich, #I6125) were taken along as controls.

4.1. Indiscriminate Thiol Reactivity

Inhibitor (10 mM in DMSO) was diluted 100-fold in aqueous buffer containing 10 mM cysteine or 5 mM GSH, to a final concentration of 100 μM inhibitor. Aqueous buffers were freshly supplemented with cysteine or GSH, and consisted of PBS pH 7.5 (10 mM phosphate buffer pH7.5, 140 mM NaCl, 2.7 mM KCl), PBS pH 8.0, and MES pH5.5 (50 mM MES pH5.5, 25 mM EDTA). Reaction mixtures were incubated at 37°C for 23 h under gentle agitation (300 rpm), after which the reaction was quenched by 2-fold dilution in 0.1% FA in 1% DMSO (aq). The samples were submitted to LC-MS analysis as soon as possible, at most 5 h post quenching. Samples were analyzed on the Waters Alliance 2795 Separation Module system equipped with Waters 2996 Photodiode Array Detector (190-750 nm), Waters Xbridge C18 column (2.1 \times 30 mm, 3.5 μm) and LCT ESI- Orthogonal Acceleration Time of Flight Mass Spectrometer. Samples were run with a 13 min gradient using 2 mobile phases: A = 1% MeCN, 0.1% FA in water and B = 1% water and 0.1% FA in MeCN. Data processing was performed using Waters MassLynx Mass Spectrometry Software 4.1. UV trace area was calculated by defining the start and end of the peaks using the ‘Edit – integrated peaks’ functionality. The intensity of UV signal was determined at a fixed wavelength, corresponding to maximum absorption by the compound and adduct: 265 nm (ODN and analogues), 192 nm (E-64), 260 nm (afatinib/ibrutinib) or 292 nm (acalabrutinib). Adduct formation was quantified from peak integration of the UV trace for the peaks corresponding to the intact compound and thiol adduct, and normalized to 100%. More details can be found in *section 7.2*.

$$\text{Adduct} = 100\% \frac{\text{UV}_{\text{adduct}}}{(\text{UV}_{\text{adduct}} + \text{UV}_{\text{inhibitor}})}$$

4.2. *In vitro* Activity Assays (Fluorogenic Substrate Cleavage)

Human recombinant cathepsin K/L/V/S/B for *in vitro* activity assays were prepared as published previously.⁵⁸⁻⁶⁰ Purified human cathepsins are diluted in freshly prepared reaction buffer (50 mM MES pH5.5, 25 mM EDTA, 2.5 mM DTT), CatK reaction buffers were freshly supplemented with 0.05% Tween20 (v/v). Papain (SigmaAldrich, #P3125) was diluted in freshly prepared reaction buffer consisting of 50 mM Tris pH7.6, 100 mM NaCl, 1 mM DTT, 1 mg/mL CHAPS and 0.5 mg/mL BGG. Controls are E-64 for cathepsins and iodoacetamide for papain. Activity assays were conducted in Corning 3820 Low Volume 384 Well Assay Plate in a final assay volume of 20 μL . Compounds were transferred using an ECHO 550 Liquid Handler (Labcyte Inc) acoustic dispenser. Plates were shaken at 600 rpm for 1 min and centrifuged at 1000 rpm for 1 min prior to incubation. Protease activity was quantified using synthetic fluorogenic peptide substrate: Z-FR-AMC (Bachem, #I-1160), Z-RR-AMC (SigmaAldrich, #C5429), or Z-FVR-AMC. Fluorescence intensity ($\lambda_{\text{ex}} = 350\text{ nm}$, $\lambda_{\text{em}} = 440\text{ nm}$) was measured every 2 min in arbitrary units (A.U.) on a CLARIOstar (BMG Labtech) microplate reader. All measurements were performed in triplicate. Data were plotted and analyzed using GraphPad Prism 8. Graphical data represents the mean \pm standard deviation for a single representative experiment.

Potency (IC_{50})

Inhibitors (200 nL, 100x final concentration in DMSO) were dispensed using an ECHO acoustic dispenser and diluted with reaction buffer (10 μ L). Purified human cathepsin (5 μ L, 4x final concentration, *see below*) was added and the reaction mixture was incubated for 30 min at room temperature. Fluorogenic substrate (5 μ L, 4x final concentration, *see below*) was added and fluorescence was measured every 2 min for 90 min. Dose-response curves were calculated from the initial velocity v_i (slope 0-20 min, steady state kinetics), and fitted to obtain IC_{50} -values using nonlinear least squares curve fitting (GraphPad Prism: [inhibitor] vs. response – variable slope (four parameters)) with fixed values for the top (DMSO control) and bottom (E-64 for cathepsins; IC for papain). More details can be found in *section 7.3*.

Protease	[E] (nM)	Fluorogenic substrate	[S] (μ M)	K_M (μ M)	Ref
hCatK	0.15	Z-FR-AMC	40	48.5	61
hCatL	0.005	Z-FR-AMC	4	2.2	62
hCatS	1	Z-FVR-AMC	8	8	62
hCatV	0.025	Z-FR-AMC	4	4.8	63
hCatB	1	Z-RR-AMC	25	173	64
Papain	3	Z-FR-AMC	10	420	65

Concentrations reported above are final concentrations (after addition of substrate)

Jump Dilution Assay

Recombinant purified CatK (EnzoLifeSci, #BML-SE553-0010) in assay buffer containing 10 mM DTT was activated at 37 °C for 10 min before addition to inhibitor. The plate is mixed (600 rpm, 1 min) and centrifuged (1000 rpm, 1 min). Inhibitors and CatK are preincubated at 37 °C for 40 min, followed by preincubation at 26 °C for 20 min. Then, samples are diluted 300-fold in reaction buffer containing substrate (*jump dilution samples*), or substrate is added without significant dilution (*control samples*). The plates are shaken (600 rpm, 26 °C, 1 min) and centrifuged (1000 rpm, 1 min) prior to read-out. The total volume/well and final concentration of CatK and Z-FR-AMC were kept constant between the controls and jump dilution samples. Inhibitor concentrations were selected to correspond to full inhibition prior to dilution ($3 \times IC_{90}$), and full activity after dilution (IC_{10}), which was validated in the control samples without dilution. Positive and negative controls are DMSO and E-64 (19 nM). More details and results can be found in *section 7.4*.

Jump dilution samples. Inhibitor (100 nL) was transferred to a 384-well plate and DMSO (1 μ L) was added, followed by CatK (8.9 μ L; 120 nM). The reaction mixtures were mixed, centrifuged and preincubated as described above. Then 1 μ L was diluted 100-fold in Z-FR-AMC (4 μ M), of which 30 μ L was diluted 3-fold in Z-FR-AMC (4 μ M): final CatK concentration = 0.35 nM. An aliquot (25 μ L) was transferred to a 384-well plate for read-out.

Control samples. Inhibitor (2.5-250 nL) was transferred to a 384-well plate with DMSO backfill to 250 nL, and DMSO (2.25 μ L) was added, followed by CatK (17.5 μ L; 0.5 nM). The reaction mixtures were mixed, centrifuged and preincubated as described above. Then 5 μ L Z-FR-AMC (20 μ M) was added (final CatK concentration is 0.35 nM) and submitted for read-out.

	ODN	EM04	EM05	EM06
$3 \times IC_{90} = [I] \text{ before 300-fold dilution}$	5.6 nM	33 μ M	50 μ M	5 μ M
$IC_{10} = [I] \text{ after 300-fold dilution}$	0.019 nM	0.11 μ M	0.17 μ M	0.017 μ M

Kinetic Progress Curve Analysis

Inhibitors (200 nL; 100× final concentration in DMSO) were dispensed using an ECHO acoustic dispenser and diluted with reaction buffer (10 μ L). Fluorogenic substrate Z-FR-AMC (5 μ L; 16 μ M, 4× final concentration) was added and the reaction was started by addition of CatK (5 μ L; 400 pM, 4× final concentration). Fluorescence intensity was measured every 2 min for 60 min, and data were analyzed using GraphPad Prism 8 to obtain kinetic parameters. Measurements were performed in triplicate ($n = 3$). Baseline was removed (GraphPad Prism: Remove Baseline and Column Math – Value-Baseline with Baseline = First Row) to give the corrected fluorescence intensity F_t (in RFU). Data analysis was tailored to inhibitor binding mode (as determined in *jump dilution assays*). More details and results can be found in section 7.7.

2-step irreversible covalent inhibitors. Time-dependent fluorescence intensity F_t (in RFU) was plotted against incubation time t (in s) for each inhibitor concentration, and the first 60 min were fitted to the one-phase exponential association equation below to find the initial velocity v_i (in RFU/s) and the observed reaction rate constant k_{obs} (in s^{-1}) for time-dependent formation of fluorescent product AMC. The progress curve of the uninhibited DMSO control was also fitted to find k_{ctrl} .

$$F_t = \frac{v_i}{k_{obs}} (1 - e^{-k_{obs} t})$$

The means and standard errors of k_{obs} (in s^{-1}) were plotted against inhibitor concentration (in M), and fitted to the equation below to obtain maximum inactivation rate constant k_{inact} (in s^{-1}) and apparent inactivation constant K_i^{app} (in M) in presence of 4 μ M Z-FR-AMC. Nonlinearity in uninhibited k_{ctrl} was constrained to the k_{obs} of the uninhibited control.

$$k_{obs} = k_{ctrl} + \frac{k_{inact} [I]}{K_i^{app} + [I]}$$

A correction for substrate competition was performed to obtain inactivation constant K_i (in M) with Gaussian error propagation. The K_M value for hCatK Z-FR-AMC affinity was constrained to the reported $K_M = 48.5 \mu$ M.⁶¹

$$K_i = \frac{K_i^{app}}{\left(1 + \frac{[S]}{K_M}\right)} \quad \sigma_{K_i} = \sqrt{\left(\frac{1}{1 + \frac{[S]}{K_M}}\right)^2 \sigma_{K_i^{app}}^2 + \left(-\frac{K_i^{app} K_M}{(K_M + [S])^2}\right)^2 \sigma_{[S]}^2 + \left(\frac{K_i^{app} [S]}{([S] + K_M)^2}\right)^2 \sigma_{K_M}^2}$$

2-step reversible covalent inhibitors. Time-dependent fluorescence intensity F_t (in RFU) was plotted against incubation time t (in s) for each inhibitor concentration, and the first 60 min were fitted to the one-phase exponential association equation below to find the initial velocity v_i (in RFU/s), steady-state velocity v_s (in RFU/s), and the observed reaction rate constant k_{obs} (in s^{-1}) for time-dependent formation of fluorescent product AMC. The progress curve of the uninhibited DMSO control was also fitted to find k_{ctrl} and v_s^{ctrl} .

$$F_t = v_s t + \frac{v_i - v_s}{k_{obs}} (1 - e^{-k_{obs} t})$$

The means and standard errors of k_{obs} (in s^{-1}) were plotted against inhibitor concentration (in M), and fitted to the equation below to obtain covalent association rate constant k_5 (in s^{-1}), covalent dissociation rate constant k_6 (in s^{-1}), and apparent inhibition constant K_i^{app} (in M). To obtain stable values, the value for k_6 was constrained to k_{ctrl} .

$$k_{obs} = k_6 + \frac{k_5 [I]}{K_i^{app} + [I]}$$

The means and standard errors of steady-state velocity v_s (in RFU/s) were plotted against inhibitor concentration (in M), and fitted to Morrison's quadratic equation with constraints for $[E]_0 = 0.1$ nM, $[S]_0 = 4$ μ M, and $K_M = 48.5$ μ M to obtain steady-state inhibition constant K_i^* (in M).

$$v_s = v_s^{\text{ctrl}} \left[1 - \frac{\left([E]_0 + [I]_0 + K_i^* \left(1 + \frac{[S]}{K_M} \right) \right) - \sqrt{\left([E]_0 + [I]_0 + K_i^* \left(1 + \frac{[S]}{K_M} \right) \right)^2 - 4 [E]_0 [I]_0}}{2 [E]_0} \right]$$

4.3. Activity Assays with qABP (In-gel Fluorescence)

Recombinant purified CatK (50 nM) in assay buffer (50 mM MES pH5.5, 25 mM EDTA, 2.5 mM DTT, 0.05% Tween20) was incubated with inhibitor (100 μ M) for 2 h at 37 °C. Then, quenched fluorescent probe BMV109 (500 nM) was added,⁶⁶ and the reaction mixture was incubated at 37 °C for an additional 2 h. The reaction was quenched by addition of loading buffer (3x SDS-PAGE loading buffer, NuPAGE, Invitrogen) containing β -mercaptoethanol as a reducing agent and boiling the samples for 10 min at 94 °C. Samples were loaded on 12% Bis-Tris gels (Invitrogen) and resolved by SDS-PAGE gel electrophoresis with MES (NuPAGE MES SDS running buffer 20x, Novex by Life Technologies) as running buffer. Labeled enzyme was visualized by in-gel fluorescence using Typhoon FLA 9500 imaging system (GE Healthcare Life Sci) ($\lambda_{\text{ex}} = 635$ nm, $\lambda_{\text{em}} = 665$ nm). Subsequently, gels were stained with InstantBlue™ Ultrafast Protein Stain (Expedeon Protein Solutions) and scanned using an Amersham Imager 600. More details and results can be found in section 7.3.

4.4. MS Analysis of Covalent Adduct

Recombinant purified CatK (~1.5 μ M) in reaction buffer (20 μ L) was incubated with inhibitor (100 μ M) at 37 °C for 6 h to form the covalent adduct prior to MS analysis. Reaction buffer (50 mM MES pH5.5, 25 mM EDTA, 2.5 mM DTT) was not supplemented with Tween20.

Intact protein MS

1 μ L injections of the samples containing covalent adduct were made onto a Waters XEVO-G2 XS QTOF UPLC-MS system with a Waters Acquity CM detector. Chromatographic separation was carried out on a Waters ACQUITY UPLC Protein BEH C4 Column (300 Å, 1.7 μ m, 2.1 \times 50 mm) over a 12 min gradient elution of 2-100% MeCN in water (0.1% FA) at a flow rate of 0.500 mL/min. For the first 4 min the flow was diverted to the waste to avoid contamination of the MS with high concentrations of buffer components. After 4 min, the gradient was started and the elution flow was ionized with an ESI ionization source in positive ion mode. The data was analyzed using Waters MassLynx Mass Spectrometry Software V4.1. The total mass of the adduct was obtained by deconvolution of electrospray ionization mass spectrum envelope (average isotopes) with the MaxEnt1 function.

Bottom-up MS/MS

Samples containing unbound CatK and preformed CatK-EM04 adduct were run on a 4-12% polyacrylamide gradient gel (NuPAGE Bis-Tris Precast Gel, Life Technologies), and stained with Coomassie protein stain. The CatK band was cut out, and the proteins subjected to reduction with DTT, alkylation with iodoacetamide and in-gel trypsin digestion using Proteineer DP digestion robot (Bruker). Tryptic peptides were extracted from the gel slices, lyophilized, dissolved in 95:3:0.1 water/MeCN/FA (v/v/v) and subsequently analyzed by on-line C18 nanoHPLC MS/MS with a system consisting of an Easy nLC 1200 gradient HPLC system (Thermo, Bremen, Germany), and a LUMOS mass spectrometer (Thermo). Digests were injected onto a homemade precolumn

(100 $\mu\text{m} \times 15$ mm; Reprosil-Pur C18-AQ 3 μm , Dr. Maisch, Ammerbuch, Germany) and eluted via a homemade analytical nano-HPLC column (75 $\mu\text{m} \times 15$ cm; Reprosil-Pur C18-AQ 3 μm). The gradient was run from 0% to 50% solvent B (20:80:0.1 water/MeCN/FA (v/v/v)) in 20 min. The nano-HPLC column was drawn to a tip of ~ 5 μm and acted as the electrospray needle of the MS source. The LUMOS mass spectrometer was operated in data-dependent MS/MS (top-10 mode) with collision energy at 32 V and recording of the MS2 spectrum in the orbitrap. In the master scan (MS1) the resolution was 120,000, the scan range 400-1500, at an AGC target of 400,000 @maximum fill time of 50 ms. Dynamic exclusion after $n = 1$ with exclusion duration of 10 s. Charge states 2-5 were included. For MS2 precursors were isolated with the quadrupole with an isolation width of 1.2 Da. HCD collision energy was set to 32 V. First mass was set to 110 Da. The MS2 scan resolution was 30,000 with an AGC target of 50,000 @maximum fill time of 60 ms. EThcD was performed at an AGC value of 50,000, at a max fill time of 240 ms, and performed with an additional activation of 15 V. Fragment ion spectra were recorded at 120,000 resolution. In a post-analysis process, raw data were first converted to peak lists using Proteome Discoverer version 2.2 (Thermo Electron), and then submitted to the Homo sapiens database (71591 entries), using Mascot v2.2.04 (www.matrixscience.com) for protein identification. Mascot searches were with 10 ppm and 0.02 Da deviation for precursor and fragment mass, respectively, and trypsin as enzyme. Up to four missed cleavages were allowed, and methionine oxidation, and carbamidomethyl on cysteine, and the warhead on cysteine and lysine were set as a variable modification. More details and results can be found in section 7.5.

4.5. Protein Crystallography

Expression, purification, and activation of hCatK. *pPIC9* vector (Invitrogen) carrying cDNA of human procathepsin K (Deutsche Ressourcenzentrum für Genomforschung) was introduced into *P. Pastoris* strain GS115 (Invitrogen) by electroporation. The highest expressing transformant was selected by screening according to Invitrogen *Pichia* Expression kit (Invitrogen, #K1710-01). Large scale expression took place in ten 5L Erlenmeyer flasks of 400 mL of BMMY with the addition of 40 μL antifoam 204 (Sigma, #A8311) per flask, feeding interval 1% MeOH per day and 22 °C for 4 days. The supernatant was then collected, concentrated to 300 mL and diluted at 1:1 ratio with 20 mM HEPES pH7.1. Then 25 mL of SP-sepharose FF (GE Healthcare, #17-079-01) was added to the sample and left shaking overnight at 6 °C. Procathepsin K (proCatK) was eluted from the exchanger with elution buffer (10 mM HEPES pH7.1, 400 mM NaCl), concentrated to 0.5 mg/mL and stored at -80 °C. Activation of proCatK was initiated by adding DTT (5 mM final conc.) to purified proCatK and the sample was diluted at 1:1 ratio with the activation buffer (100 mM NaOAc pH4) containing 40 $\mu\text{g}/\text{mL}$ pepsin (Sigma, #P6887) and incubated for 45 min at 37 °C. Pepsin was inactivated by raising pH of the sample to approximately 5.5 with 1M Tris (pH8.5). The sample was then purified on MONO S 5/50 column (GE Healthcare, #17-5168-01) on Äkta Express system (GE Healthcare). Mature hCatK was captured with elution buffer (50 mM NaOAc pH5.5) at approximately 1M NaCl and its proteolytic activity was blocked by incubating with approximately 10-fold molar excess of MMTS (Sigma, #208795) for 20 min at 6 °C. The sample was desalting using HiTrap 5 mL column (GE Healthcare) to the final buffer (50 mM NaOAc pH5.5, 50 mM NaCl) and stored at -80 °C. Active enzyme concentration was determined by titration with E-64 (Sigma, #E3132) based on previously described procedures.^{40, 55, 62}

Adduct formation and crystallization of CatK-EM07 adduct. DTT (final conc. 10 mM) and 160 μL of inhibitor EM07 (10 mM stock in DMSO, final inhibitor conc. 200 μM , final conc. DMSO 2%) were added to 8 mL of hCatK (approx. 20 μM) and incubated at 37 °C for 8 h. To ensure complete inhibition, the sample was spiked with DTT (final 3 mM) after 8 h and left incubating for additional 2 h. The adduct was then centrifuged and supernatant was collected and concentrated with Amicon Ultra devices (cut-off 10 kDa) to 15 mg/mL and stored at -80°C. Crystals suitable for data collection grew from 20% PEG-3350, 0.2M CaCl_2 at 20 °C with sitting drop method. For the optimization, the adduct was diluted to 10 mg/mL and drop sizes of both precipitant and adduct were varied. Best diffracting crystal grew from the drop consisting of 0.5 μL of adduct and 1 μL of precipitant. The crystal was soaked in 35% PEG-3350, 0.2M CaCl_2 for 10 seconds for cryoprotection.

Data collection, structure determination, and refinement for X-ray diffraction. Diffraction data was collected at XRD2 beamline at Elettra synchrotron, Trieste⁶⁷ under cryogenic conditions. Data were first processed with XDS software,⁶⁸ and the unmerged HKL file was used as an input for Pointless, Aimless and Ctruncate (CCP4 suite)⁶⁹⁻⁷¹ to obtain the merged MTZ file. The CatK part of the 2FTD model from the Protein Data Bank⁷² was used for molecular replacement with Molrep (CCP4 suite).⁷³ The refinement was done with MAIN software⁷⁴ with ML FK target function.⁴² Inhibitor EM07 was introduced in the model during refinement and fitted in the difference ML FK map. The geometric restraints for EM07 were generated by PURY.⁷⁵ The established adduct was then further refined. Figures were generated in PyMOL v2.2.0. More details and results can be found in *section 7.6*.

4.6. Human Osteoclast Activity

Isolation of CD14⁺ cells from PBMCs. Osteoclast precursors (CD14⁺ cells) were isolated from human peripheral blood mononuclear cells (PBMCs). Briefly, human buffy coats were obtained from Sanquin Blood Supply (Amsterdam, NL), diluted 1:1 with PBS containing 1% citrate, and spun down (800 G for 30 min, without brake) in Lymphoprep gradient solution (Elitech). The resulting interphase containing peripheral blood mononuclear cells (PBMCs) was collected and washed with 1% citrate in PBS before it was passed through a 40 µm cell strainer (Greiner Bio-One) to ensure the recovery of a pure mononuclear cell population. The cells were counted on a Muse cell counter (Merck), and cell pellet was resuspended in 80 µL buffer (PBS containing 0.5% BSA and 2 mM EDTA) for 10⁷ cells. 20 µL of magnetic MACS CD14 MicroBeads human (Miltenyi Biotec) was added to this cell suspension. According to manufacturer instructions, the cells and CD14 microbeads were mixed and incubated for 15 min at 4 °C. The column was placed in the magnetic field, rinsed and subsequently the cell suspension was applied onto the column. Unlabeled cells pass through. Then the column was removed from the magnet and CD14⁺ cells were flushed out and collected.

Human osteoclast cultures. Osteoclast precursors (CD14⁺ cells) were plated in CellStar 96 well plates (Greiner Bio-One) on plastic and on bovine cortical bone slices (650 µm thick) at a density of 1.3×10⁶ cells/well. Cells were cultured for 21 days in α-MEM (Gibco, Paisley, UK) supplemented with 5% fetal calf serum (HyClone), 1× antibiotic antimycotic solution containing 100 U/mL penicillin, 100 µg/mL streptomycin and 250 ng/mL amphotericin B (Sigma, #A5955), and 25 ng/mL human recombinant M-CSF (R&D systems). After 3 days, the concentration of M-CSF was reduced to 10 ng/mL and combined with 2 ng/mL recombinant RANKL (R&D systems) until the end of the culture period. From day 7 on, various concentrations of CatK inhibitors were added to the cultures. An equal amount of vehicle (DMSO) was added to the control cultures without inhibitors. During culture the cells were maintained at 37 °C and 5% CO₂ and culture media were refreshed every 3-4 days. After 21 days of culture, wells were washed with PBS and either fixed in 4% PBS buffered formaldehyde, stored at 4 °C, and used for tartrate-resistant acid phosphatase (TRAcP) staining, or the cells were lysed with lysis buffer (100 mM phosphate buffer pH6.0, 0.1% Triton-X100). This cell extract/lysate was stored at -20 °C and used for CatK activity assays in osteoclast lysates. The bone slices were stored in MilliQ water at 4 °C for bone resorption visualization. More details and results can be found in *section 7.8*.

Staining of resorption pits on bone slices. Resorption was measured on slices of bovine cortical bone of 650 µm thick and fit into a 96-well plate. CD14⁺ monocytes were cultured on these bone slices for 21 days with M-CSF and RANKL and without or with inhibitors in various concentrations, as described above. After this period, the cells present on the bovine cortical bone slices were removed with 0.25M NH₄OH. The slices were washed in distilled water, incubated in a saturated alum (KAl(SO₄)₂·12H₂O) solution, washed in distilled water, and stained with Coomassie Brilliant Blue. Resorption pits were visualized by light microscopy (Leica DFC320). The resorbed area micrographs were made with 10× magnification. Total resorbed area was quantified using Image Pro Plus (Media Cybernetics) and calculated as a percentage of the total area.

TRAcP staining and cell counting. The cells were stained for TRAcP using the Leukocyte Acid Phosphatase (TRAP) Kit from Sigma (SigmaAldrich, #387A) following manufacturer instructions. Nuclei were visualized with 4'6-diamino-2-phenylindole dihydrochloride (DAPI). Multinucleated TRAcP⁺ cells with three or more nuclei

were considered osteoclasts and were counted on bone in standardized fields and on plastic per well from a combination of light and fluorescence microscopy using a Leica DFC320 FireWire Digital Microscope Camera (Leica Microsystems).

CatK activity in osteoclast lysates (qABP labeling). Osteoclast lysates (stored at -20 °C and thawed before use) were treated with quenched fluorescent probe BMV109 (1 μ M),⁶⁶ and the reaction mixture was incubated at 37 °C for 2 h. As a positive control, 5 nM recombinant active hCatK (Enzo Lifesci, #BML-SE553-0010) was also treated with qABP. The reaction was quenched by addition of loading buffer (3 \times SDS-PAGE loading buffer, NuPAGE, Invitrogen) containing β -mercaptoethanol as a reducing agent and boiling the samples for 10 min at 94 °C. Samples were loaded on 12% Bis-Tris gels (Invitrogen) and resolved by SDS-PAGE gel electrophoresis with MES (NuPAGE MES SDS running buffer 20x, Novex by Life Technologies) as running buffer. Labeled enzyme was visualized by in-gel fluorescence using Typhoon FLA 9500 imaging system (GE Healthcare Life Sci) ($\lambda_{\text{ex}} = 635$ nm, $\lambda_{\text{em}} = 665$ nm). Subsequently, gels were stained with InstantBlue Ultrafast Protein Stain (Expedeon Protein Solutions) and scanned on an Amersham Imager 600.

CatK expression in osteoclast lysates (Western blotting). Proteins in osteoclast lysates (stored at -20 °C and thawed before use) were resolved using gel electrophoresis conditions described above. Recombinant mature hCatK (230 ng) and recombinant proCatK (300 ng) were included as references. Gels were transferred to nitrocellulose membrane using a Trans-Blot Turbo Transfer System (Biorad) and subjected to standard Western Blotting protocols. Antibodies: primary rabbit anti-CatK (1:500; Abcam, #19027), primary mouse anti- β -Actin (1:10,000; SigmaAldrich, #A5441), secondary swine anti-rabbit HRP (1:5,000; Dako, #P0217) and secondary goat anti-mouse 800CW (1:5,000; LiCOR, #926-32210). Blots with fluorescent secondary antibodies were scanned on a LiCOR Odyssey system v3.0. Blots with HRP secondary antibody were incubated with SuperSignal West Dura Extended Duration Substrate (Thermo Sci, #34076) according to manufacturer protocols and scanned on an Amersham Imager 600 (chemiluminescence).

4

5. Materials and Methods: *Chemical Synthesis*

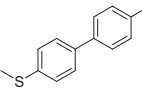
Synthetic schemes can be found in *section 7.1* for precursor carboxylic acid **1**, inhibitor odanacatib (ODN), and odanacatib derivatives EM02-EM06 (**Scheme S1**), for desfluoro precursor **8** and inhibitor EM07 (**Scheme S2**), for building block cyclopropane propargyl **16** for the synthesis of EM03 (**Scheme S3**), and for building block bromoalkyne **19** for the synthesis of EM06 (**Scheme S4**).

General. All commercially available reagents and solvents were used as purchased. Nuclear magnetic resonance (NMR) spectra were recorded on a Bruker Avance 300 (300 MHz for ^1H , 75.00 MHz for ^{13}C) using the residual solvent as internal standard (^1H : δ 7.26 ppm for CDCl_3 and 2.50 ppm for DMSO. ^{13}C : δ 77.16 ppm for CDCl_3 and 39.52 ppm for DMSO). Chemical shifts (δ) are given in ppm and coupling constants (J) are quoted in hertz (Hz). Resonances are described as s (singlet), d (doublet), t (triplet), q (quartet), b (broad) and m (multiplet) or combinations thereof. Compounds were analyzed using 2D NMR techniques HSQC and HMBC, and coupling constants (J) are reported accordingly. ^{13}C NMR (APT) spectra were obtained to assign C–F coupling constants (J) when relevant. Analytical LC-MS analysis was performed on a Waters Alliance 2795 Separation Module system equipped with Waters 2996 Photodiode Array Detector (190-750 nm), Waters Xbridge C18 column (2.1 \times 100 mm, 3.5 μ m) and LCT ESI- Orthogonal Acceleration Time of Flight Mass Spectrometer. Samples were run with a 13 min gradient using 2 mobile phases: A = 1% MeCN, 0.1% FA in water and B = 1% water and 0.1% FA in MeCN. Data processing was performed using Waters MassLynx Mass Spectrometry Software 4.1. Electrospray Ionization (ESI) high-resolution mass spectrometry (HRMS) was carried out using a Waters XEVO-G2 XS QTOF UPLC-MS system with a Waters Acquity CM detector in positive ion mode in combination with a Waters Acquity UPLC system equipped with a ACQUITY UPLC Protein BEH C4 Column (300 \AA , 1.7 μ m, 2.1 \times 50 mm) using water/MeCN mixtures containing 0.1% FA. Thin Layer Chromatography (TLC) was performed using TLC plates from Merck (SiO_2 , Kieselgel 60 F254 neutral, on aluminum with fluorescence indicator) and compounds were visualized by

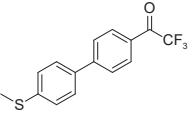
UV detection (254 nm) unless mentioned otherwise. Flash column chromatography (FCC) purifications were performed using Grace Davisil Silica Gel (particle size 40–63 μm , pore diameter 60 \AA) and the indicated eluent. Reversed phase preparative HPLC/MS was carried out on a Waters AutoPurification system equipped with a Waters 2998 photodiode array detector, Waters 3100 mass detector and a Waters 2767 sample manager using preparative Waters X-bridge C18 column (5 μm , 30 mm \times 150 mm or 19 mm \times 150 mm) in combination with water/MeCN mixtures containing 0.1% TFA. Fractions containing the product were automatically collected based on observed mass and UV signals after which they were lyophilized to obtain the pure products. Reported yields are not optimized.

5.1. Synthesis of Precursors **1** and **8**

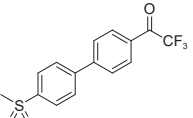
(4'-bromo-[1,1'-biphenyl]-4-yl)(methyl)sulfane **9**

 (4-methylthio)phenylboronic acid (3.81 g, 23 mmol), 1-bromo-4-iodobenzene (5.83 g, 21 mmol) and sodium carbonate (6.55 g, 62 mmol) were dissolved in a 4:1 (v/v) DME/water mixture (180 mL). The mixture was degassed with argon for 5 min, then bis(triphenylphosphine)palladium(II) dichloride (579 mg, 0.82 mmol) was added and the mixture was heated to 100 $^{\circ}\text{C}$. After stirring for 5 hours, the reaction mixture was allowed to cool to room temperature. The reaction was quenched with water and extracted with EtOAc (2X). The combined organic layers were washed with brine (2X), dried over Na_2SO_4 , and concentrated under vacuum to give a reddish solid as residue (18.5 g). The crude material was coated on silica and purified by FCC (5% diisopropyl ether in heptane) to give product **9** as a white solid (4.04 g, 14 mmol, 66%). Spectral data was in agreement with published data.³²

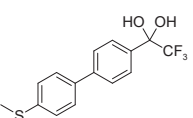
2,2,2-trifluoro-1-(4'-(methylthio)-[1,1'-biphenyl]-4-yl)ethanone **10**

 According to published procedure,³² the reaction of (4'-bromo-[1,1'-biphenyl]-4-yl)(methyl)sulfane **9** (4.04 g, 15 mmol) with ethyl trifluoroacetate (3.44 mL, 29 mmol) and n-BuLi (8.68 mL, 2.5M in hexanes, 22 mmol) afforded product **10** as a light-yellow solid (2.27 g, 7.7 mmol, 53%). Spectral data was in agreement with published data.³²

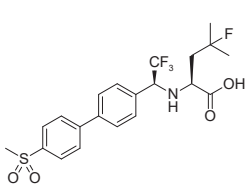
2,2,2-trifluoro-1-(4'-(methylsulfonyl)-[1,1'-biphenyl]-4-yl)ethanone **11**

 According to published procedure,³² the reaction between 2,2,2-trifluoro-1-(4'-(methylthio)-[1,1'-biphenyl]-4-yl)ethanone **10** (2.27 g, 7.7 mmol), tetrabutylammonium hydrogen sulfate (130 mg, 0.38 mmol), sodium tungstate dehydrate (126 mg, 0.38 mmol) and 30% aqueous hydrogen peroxide (2.3 mL, 23 mmol) afforded ketone **11** as a white solid (2.42 g). The material was then dehydrated in a Dean-Stark setup by drying the water/toluene azeotrope over molecular sieves. The toluene solution (250 mL) was refluxed overnight. The solution was then cooled to room temperature and concentrated under vacuum to afford ketone **11** as a white crystalline solid (2.30 g, 7.0 mmol, 91%) which was used in the next step. Spectral data was in agreement with published data.³² ^1H NMR (300 MHz, CDCl_3) δ 8.19 (ddt, J = 8.0, 2.3, 1.1 Hz, 2H), 8.11 – 8.03 (m, 2H), 7.89 – 7.74 (m, 4H), 3.11 (s, 3H). ^{13}C NMR (75 MHz, CDCl_3) δ 180.1 (q, J = 35.4 Hz), 146.0, 144.7, 140.8, 131.0 (q, J = 2.0 Hz), 129.8, 128.5, 128.4, 128.2, 116.7 (q, J = 291 Hz), 44.7.

2,2,2-trifluoro-1-(4'-(methylsulfonyl)-[1,1'-biphenyl]-4-yl)ethane-1,1-diol **12**

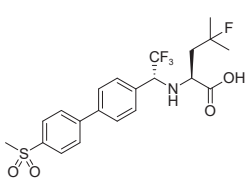
 Analysis of ketone **11** in acetone- d_6 or DMSO- d_6 containing trace amounts of water resulted in the (partial) formation of hydrate **12**, which was confirmed by the shift of the CF_3 signal from 180.1 ppm to 123.5 ppm in ^{13}C NMR (APT). ^1H NMR (300 MHz, DMSO- d_6) δ 8.05 – 7.93 (m, 4H), 7.85 – 7.70 (m, 4H), 7.67 (s, 2H), 3.27 (s, 3H). ^{13}C NMR (75 MHz, DMSO- d_6) δ 144.5, 139.9, 139.0 (d, J = 4.6 Hz), 128.3, 127.7, 127.7, 126.7, 123.5 (q, J = 289 Hz), 92.5 (q, J = 31.2 Hz), 43.6.

(S)-4-fluoro-4-methyl-2-(((S*)-2,2,2-trifluoro-1-(4'-(methylsulfonyl)-[1,1'-biphenyl]-4-yl)ethyl)amino)pentanoic acid (*S,S*)-1*



According to published procedure,⁷⁶ the reaction of ketone **11** (1.23 g, 3.8 mmol) with (*S*)-ethyl 2-amino-4-fluoro-4-methylpentanoate hydrochloride (1.00 g, 4.7 mmol), potassium carbonate (2.07 g, 15 mmol), and subsequent reduction with zinc chloride (1.02 g, 7.5 mmol) and sodium borohydride (567 mg, 15 mmol) afforded a mixture of desired (*S,S*)-1 and (*R,S*)-1, which were separated by preparative RP-HPLC to yield precursor (*S,S*)-1 as a white solid (460 mg, 1.0 mmol, 27%). Spectral data of (*S,S*)-1 was in agreement with published data.¹⁸ LC-MS Rt = 7.32 min, m/z = 462.11 [M+H]⁺. ¹H NMR (300 MHz, CDCl₃) δ 8.08 – 7.96 (m, 2H), 7.83 – 7.73 (m, 2H), 7.68 – 7.59 (m, 2H), 7.51 (d, J = 8.1 Hz, 2H), 4.31 (q, J = 7.1 Hz, 1H), 3.68 (dd, J = 8.1, 4.1 Hz, 1H), 3.10 (s, 3H), 2.19 (ddd, J = 24.8, 15.1, 4.2 Hz, 1H), 1.99 (ddd, J = 17.7, 15.0, 8.1 Hz, 1H), 1.48 (d, J = 21.8 Hz, 3H), 1.46 (d, J = 21.7 Hz, 3H). ¹³C NMR (75 MHz, CDCl₃) δ 175.9, 145.8, 140.6, 139.7, 133.9, 129.4, 128.2, 128.2, 125.3 (q, J = 282 Hz), 95.8 (d, J = 165 Hz), 62.9 (q, J = 29.5 Hz), 56.6, 44.7, 43.6 (d, J = 21.5 Hz), 27.5 (d, J = 24.3 Hz), 26.8 (d, J = 24.4 Hz).

(S)-4-fluoro-4-methyl-2-(((R*)-2,2,2-trifluoro-1-(4'-(methylsulfonyl)-[1,1'-biphenyl]-4-yl)ethyl)amino)pentanoic acid (*R,S*)-1*

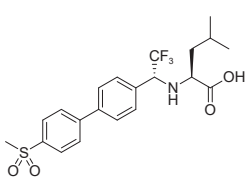


(*R,S*)-1 was obtained as the minor isomer in above described synthesis. LC-MS Rt = 7.04 min, m/z = 462.11 [M+H]⁺. ¹H NMR (300 MHz, CDCl₃) δ 8.08 – 7.99 (m, 2H), 7.82 – 7.73 (m, 2H), 7.67 (d, J = 8.2 Hz, 2H), 7.52 (d, J = 7.9 Hz, 2H), 4.12 (q, J = 7.1 Hz, 1H), 3.47 – 3.37 (m, 1H), 3.11 (s, 3H), 2.15 – 1.91 (m, 2H), 1.39 (d, J = 22.1 Hz, 3H), 1.15 (d, J = 21.6 Hz, 3H). ¹³C NMR (75 MHz, CDCl₃) δ 174.5, 145.6, 140.7, 139.8, 133.0, 129.7, 128.2, 128.1, 124.7 (q, J = 281 Hz), 96.5 (d, J = 164 Hz), 63.5 (q, J = 29.6 Hz), 56.7, 44.8, 43.1 (d, J = 20.2 Hz), 28.3 (d, J = 24.3 Hz), 25.5 (d, J = 24.5 Hz).

*(2S)-4-Methyl-2-[(*1S*)-2,2,2-trifluoro-1-(4'-methanesulfonyl-biphenyl-4-yl)-ethylamino]-pentanoic acid (*S,S*)-8*

According to published procedure,⁷⁶ the reaction of ketone **11** (484 mg, 1.5 mmol) with L-Leucine methyl ester hydrochloride (307 mg, 1.7 mmol), potassium carbonate (749 mg, 5.4 mmol), and subsequent reduction with zinc chloride (371 mg, 2.7 mmol) and sodium borohydride (207 mg, 5.5 mmol) afforded a mixture of (*S,S*)-8 and (*R,S*)-8, which could be separated by preparative RP-HPLC to yield the major isomer (*S,S*)-8 as a white solid (93.9 mg, 0.21 mmol, 14%). Spectral data of (*S,S*)-8 was in agreement with published data.⁷⁷ LC-MS Rt = 7.68 min, m/z = 444.14 [M+H]⁺. ¹H NMR (300 MHz, CDCl₃) δ 8.06 – 7.96 (m, 2H), 7.81 – 7.69 (m, 2H), 7.68 – 7.58 (m, 2H), 7.52 (d, J = 8.1 Hz, 2H), 4.18 (q, J = 7.0 Hz, 1H), 3.58 (dd, J = 8.7, 5.3 Hz, 1H), 3.10 (s, 3H), 1.93 (dp, J = 13.4, 6.5 Hz, 1H), 1.67 – 1.41 (m, 2H), 0.97 (d, J = 6.5 Hz, 3H), 0.95 (d, J = 6.7 Hz, 3H). ¹³C NMR (75 MHz, CDCl₃) δ 180.3, 145.9, 140.1, 139.6, 135.2, 129.2, 128.1, 128.1, 127.9, 126.0 (q, J = 282 Hz), 63.2 (q, J = 29.2 Hz), 58.6, 44.7, 42.7, 24.9, 23.0, 21.8.

*((R)-2,2,2-trifluoro-1-(4'-(methylsulfonyl)-[1,1'-biphenyl]-4-yl)ethyl)-L-leucine (*R,S*)-8*



(*R,S*)-8 was obtained as the minor isomer in above described synthesis. LC-MS Rt = 7.42 min, m/z = 444.14 [M+H]⁺. ¹H NMR (300 MHz, CDCl₃) δ 8.11 – 7.95 (m, 2H), 7.90 – 7.73 (m, 2H), 7.71 – 7.61 (m, 2H), 7.56 (d, J = 8.1 Hz, 2H), 4.31 (q, J = 7.1 Hz, 1H), 3.18 – 3.12 (m, 1H), 3.11 (s, 3H), 1.97 – 1.77 (m, 1H), 1.54 (t, J = 7.1 Hz, 2H), 0.92 (d, J = 6.6 Hz, 3H), 0.76 (d, J = 6.5 Hz, 3H). ¹³C NMR (75 MHz, CDCl₃) δ 178.7, 145.9, 140.5, 139.7, 133.6, 130.0, 128.2, 128.2, 127.9, 124.9 (q, J = 281 Hz), 63.0 (q, J = 29.1 Hz), 56.4, 44.8, 42.9, 24.7, 23.2, 21.7.

5.2. Synthesis of Odanacatib Derivatives

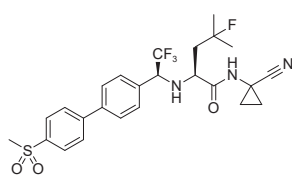
General Procedure A: Amide coupling with HATU/DIPEA in DMAc

Adjustment of reported procedure.⁷⁸ Precursor (S,S)-1 (60 mg, 0.13 mmol) was dissolved in 3 mL DMAc and cooled to 0 °C. Amine (0.16 mmol) and HATU (59 mg, 0.16 mmol) were added. The resulting solution was stirred for 15 min and DIPEA (68 mL, 0.39 mmol) was added. The reaction was stirred for 2.5 h. Water was slowly added dropwise and the slurry was stirred 2.5 h at room temperature. The mixture was filtered and the solid material was washed with a 1:1.2 DMF/water solution, with water, and with 2-propanol. The material was removed from the filter by addition of THF. The filtrate was concentrated and purified by FCC (gradient 0-2% MeOH in DCM). The product was obtained as a white solid.

General Procedure B: Amide coupling with HATU/Et₃N in DMF

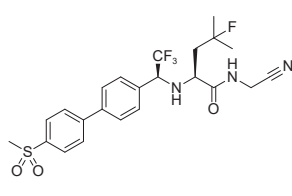
Adjustment of reported procedure.³³ Precursor (S,S)-1 (21.3 mg, 0.046 mmol) was dissolved in 400 μL DMF and cooled to 0 °C. HATU (21.8 mg, 0.057 mmol) and triethylamine (6 μL, 0.043 mmol) were added. To this solution was added to amine (0.067 mmol) and further triethylamine (12 μL, 0.086 mmol) was added to the mixture. After 2 h, ice cooling was removed and the mixture was stirred an additional 2 h. The reaction mixture was concentrated *in vacuo*, redissolved in EtOAc and extracted with saturated NH₄Cl solution (aq) and brine. The organic layer was dried over Na₂SO₄ and filtered. The filtrate was concentrated *in vacuo* and the residue was purified by FCC (gradient 0-2% MeOH in DCM), and if needed, further purified using Reversed phase preparative HPLC/MS and lyophilized to obtain product as a white solid.

(S)-N-(1-cyanocyclopropyl)-4-fluoro-4-methyl-2-((S)-2,2,2-trifluoro-1-(4'-(methylsulfonyl)-[1,1'-biphenyl]-4-yl)ethyl)amino)pentanamide ODN



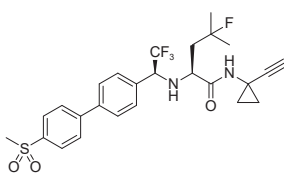
According to *general procedure A*, the reaction between precursor (S,S)-1 (59.8 mg, 0.13 mmol) and 1-amino-cyclopropanecarbonitrile hydrochloride (18.5 mg, 0.16 mmol) afforded product **ODN** as a white solid (40.7 mg, 0.077 mmol, 60%). TLC R_f = 0.18 (1:1 EtOAc/heptane). LC-MS Rt = 7.43 min, m/z = 526.112 [M+H]⁺. ¹H NMR (300 MHz, CDCl₃) δ 8.03 (d, J = 8.4 Hz, 2H), 7.77 (d, J = 8.8 Hz, 2H), 7.65 (d, J = 8.1 Hz, 2H), 7.48 (d, J = 8.1 Hz, 2H), 7.42 (s, 1H), 4.17 (q, J = 7.2 Hz, 1H), 3.59 (dd, J = 8.9, 3.3 Hz, 1H), 3.10 (s, 3H), 2.17 – 1.85 (m, 2H), 1.56 – 1.44 (m, 2H), 1.47 (d, J = 21.7 Hz, 3H), 1.44 (d, J = 22.0 Hz, 3H), 1.11 – 0.85 (m, 2H). ¹³C NMR (75 MHz, CDCl₃) δ 174.4, 145.7, 140.6, 139.9, 134.5, 129.4, 128.2, 128.2, 126.0 (q, J = 279 Hz), 119.6, 96.8 (d, J = 164 Hz), 63.4 (q, J = 29.3 Hz), 59.0, 44.8, 43.6 (d, J = 19.9 Hz), 28.4 (d, J = 24.4 Hz), 25.8 (d, J = 24.7 Hz), 20.2, 16.9, 16.5. HRMS (ESI⁺): calculated for C₂₅H₂₈F₄N₃O₃S [M+H]⁺ 526.1788, found: 526.1816.

(S)-N-(cyanomethyl)-4-fluoro-4-methyl-2-((S)-2,2,2-trifluoro-1-(4'-(methylsulfonyl)-[1,1'-biphenyl]-4-yl)ethyl)amino)pentanamide EM02



According to *general procedure B*, the reaction between precursor (S,S)-1 (21.3 mg, 0.046 mmol) and aminoacetonitrile (6.2 mg, 0.067 mmol) afforded product **EM02** as a white solid (15.3 mg, 0.030 mmol, 66%). TLC R_f = 0.15 (1:1 EtOAc/heptane). LC-MS Rt = 7.30 min, m/z = 500.144 [M+H]⁺. ¹H NMR (300 MHz, CDCl₃) δ 8.01 (d, J = 8.4 Hz, 2H), 7.76 (d, J = 8.4 Hz, 2H), 7.65 (d, J = 8.4 Hz, 2H), 7.50 (d, J = 8.2 Hz, 2H), 7.45 (t, J = 6.7 Hz, 1H), 4.24 (q, J = 7.1 Hz, 1H), 4.21 – 3.96 (m, 2H), 3.66 (dd, J = 8.8, 3.3 Hz, 1H), 3.10 (s, 3H), 2.21 – 1.89 (m, 2H), 1.47 (d, J = 21.7 Hz, 3H), 1.45 (d, J = 22.0 Hz, 3H). ¹³C NMR (75 MHz, CDCl₃) δ 173.8, 145.7, 140.5, 139.7, 134.2, 129.4, 128.2, 125.4 (q, J = 283 Hz), 115.7, 96.8 (d, J = 164 Hz), 63.1 (q, J = 28.7 Hz), 58.5, 44.7, 43.6 (d, J = 19.9 Hz), 28.4 (d, J = 24.2 Hz), 27.3, 25.7 (d, J = 24.7 Hz). HRMS (ESI⁺): calculated for C₂₃H₂₆F₄N₃O₃S [M+H]⁺ 500.1631, found: 500.1638.

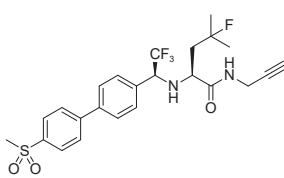
*(S)-N-(1-ethynylcyclopropyl)-4-fluoro-4-methyl-2-((S)-2,2,2-trifluoro-1-(4'-(methylsulfonyl)-[1,1'-biphenyl]-4-yl)ethyl)amino)pentanamide **EM03***



According to *general procedure A*, the reaction between precursor (S,S)-**1** (60.7 mg, 0.13 mmol) and 1-ethynylcyclopropan-1-amine hydrochloride **16** (18.3 mg, 0.16 mmol) afforded product **EM03** as a white solid (46.6 mg, 0.089 mmol, 68%). TLC R_f = 0.24 (1:1 EtOAc/heptane). LC-MS R_t = 7.66 min, m/z = 525.124 [M+H]⁺. ¹H NMR (300 MHz, CDCl₃) δ 8.02 (d, J = 8.5 Hz, 2H), 7.76 (d, J = 8.4 Hz, 2H), 7.62 (d, J = 8.3 Hz, 2H), 7.47 (d, J = 8.1 Hz, 2H), 7.32 (s, 1H), 4.14 (q, J = 7.2 Hz, 1H), 3.58 (dd, J = 9.0, 3.2 Hz, 1H),

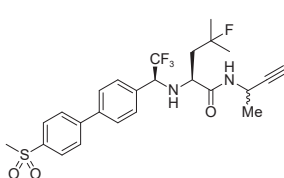
3.10 (s, 3H), 2.94 (s, 1H), 2.10 (s, 1H), 2.19 – 1.84 (m, 2H), 1.46 (d, J = 21.7 Hz, 6H), 1.43 (d, J = 22.0 Hz, 6H), 1.27 – 1.07 (m, 2H), 0.95 – 0.86 (m, 1H), 0.75 – 0.66 (m, 1H). ¹³C NMR (75 MHz, CDCl₃) δ 173.9, 145.8, 140.2, 139.7, 135.0, 129.3, 128.2, 128.0, 125.5 (q, J = 283 Hz), 97.0 (d, J = 163 Hz), 84.7, 67.0, 63.0 (q, J = 28.8 Hz), 59.2, 44.7, 43.6 (d, J = 19.9 Hz), 28.4 (d, J = 24.3 Hz), 25.7 (d, J = 24.7 Hz), 22.5, 17.7, 17.2. HRMS (ESI⁺): calculated for C₂₆H₂₉F₄N₂O₃S [M+H]⁺ 525.1835, found: 525.1824.

*(S)-4-fluoro-4-methyl-N-(prop-2-yn-1-yl)-2-((S)-2,2,2-trifluoro-1-(4'-(methylsulfonyl)-[1,1'-biphenyl]-4-yl)ethyl)amino)pentanamide **EM04***



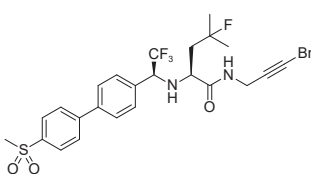
According to *general procedure B*, the reaction between precursor (S,S)-**1** (20.6 mg, 0.045 mmol) and propargylamine (10 μ L, 0.16 mmol) afforded product **EM04** as a white solid (11.3 mg, 0.023 mmol, 51%). TLC R_f = 0.25 (1:1 EtOAc/heptane). LC-MS R_t = 7.50 min, m/z = 499.116 [M+H]⁺. ¹H NMR (300 MHz, CDCl₃) δ 8.02 (d, J = 8.5 Hz, 2H), 7.76 (d, J = 8.6 Hz, 2H), 7.63 (d, J = 8.4 Hz, 2H), 7.51 (d, J = 8.1 Hz, 2H), 7.22 (t, J = 5.5 Hz, 1H), 4.23 (q, J = 7.2 Hz, 1H), 3.94 (qdd, J = 17.6, 5.5, 2.6 Hz, 2H), 3.69 (dd, J = 9.2, 3.1 Hz, 1H), 3.42 (s, 1H), 3.10 (s, 3H), 2.18 (t, J = 2.6 Hz, 1H), 2.14 – 1.89 (m, 2H), 1.48 (d, J = 21.7 Hz, 3H), 1.45 (d, J = 22.0 Hz, 3H). ¹³C NMR (75 MHz, CDCl₃) δ 173.8, 145.9, 140.3, 139.7, 134.6, 129.4, 128.2, 128.0, 125.5 (q, J = 283 Hz), 97.0 (d, J = 164 Hz), 78.9, 71.9, 63.0 (q, J = 28.7 Hz), 58.7, 44.7, 43.7 (d, J = 19.8 Hz), 29.2, 28.6 (d, J = 24.5 Hz), 25.5 (d, J = 24.8 Hz). HRMS (ESI⁺): calculated for C₂₄H₂₇F₄N₂O₃S [M+H]⁺ 499.1679, found: 499.1713.

*(S)-N-((R/S)-but-3-yn-2-yl)-4-fluoro-4-methyl-2-((S)-2,2,2-trifluoro-1-(4'-(methylsulfonyl)-[1,1'-biphenyl]-4-yl)ethyl)amino)pentanamide **EM05***



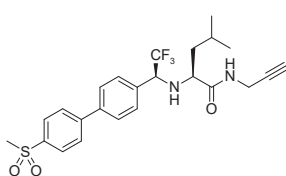
According to *general procedure B*, the reaction between precursor (S,S)-**1** (19.9 mg, 0.043 mmol) and 1-methyl-prop-2-ynylamine hydrochloride (16.5 mg, 0.16 mmol) afforded an inseparable 1:1 mixture of diastereoisomers (S,S,R)-**EM05** and (S,S,S)-**EM05** as a white solid (10.0 mg, 0.020 mmol, 45%). Reported ppm-values are average values. TLC R_f = 0.31 (1:1 EtOAc/heptane). LC-MS R_t = 7.77 min, m/z = 513.130 [M+H]⁺. ¹H NMR (300 MHz, CDCl₃) δ 8.02 (d, J = 8.6 Hz, 2H), 7.76 (d, J = 8.6 Hz, 2H), 7.63 (d, J = 8.3 Hz, 2H), 7.51 (d, J = 8.2 Hz, 2H), 7.21 (d, J = 8.3 Hz, 1H), 4.74 – 4.58 (m, 1H), 4.20 (q, J = 14.5 Hz, 1H), 3.68 (t, J = 7.7 Hz, 1H), 3.60 (s, 1H), 3.10 (s, 3H), 2.20 (d, J = 9.0 Hz, 1H), 2.16 – 1.86 (m, 2H), 1.47 (dd, J = 22.0, 10.0 Hz, 6H), 1.24 (d, J = 6.9 Hz, 3H). ¹³C NMR (75 MHz, CDCl₃) δ 173.0, 145.9, 140.2, 139.7, 134.8, 129.4, 128.1, 125.5 (q, J = 284 Hz), 97.1 (d, J = 163 Hz), 83.4, 70.8, 63.0 (q, J = 28.6 Hz), 59.0, 44.7, 43.7 (d, J = 19.8 Hz), 36.9, 28.6 (d, J = 24.3 Hz), 25.4 (d, J = 24.7 Hz), 22.0. HRMS (ESI⁺): calculated for C₂₅H₂₉F₄N₂O₃S [M+H]⁺ 513.1835, found: 513.1829.

(S)-N-(3-bromoprop-2-yn-1-yl)-4-fluoro-4-methyl-2-(((S*)-2,2,2-trifluoro-1-(4'-(methylsulfonyl)-[1,1'-biphenyl]-4-yl)ethyl)amino)pentanamide **EM06***



According to *general procedure A*, the reaction between precursor *(S,S)-1* (60.8 mg, 0.13 mmol) and 3-bromoprop-2-yn-1-amine hydrochloride **19** (26.6 mg, 0.16 mmol) afforded product **EM06** as a white solid (13.6 mg, 0.024 mmol, 18%). TLC *Rf* = 0.33 (1:1 EtOAc/heptane). LC-MS *Rt* = 7.93 min, *m/z* = 577.036 & 579.038 [M+H]⁺. ¹H NMR (300 MHz, CDCl₃) δ 8.03 (d, *J* = 8.4 Hz, 2H), 7.78 (d, *J* = 8.4 Hz, 2H), 7.65 (d, *J* = 8.2 Hz, 2H), 7.50 (d, *J* = 8.1 Hz, 2H), 7.16 (t, *J* = 5.3 Hz, 1H), 4.21 (q, *J* = 7.2 Hz, 1H), 4.13 – 3.81 (m, 2H), 3.68 (dd, *J* = 9.2, 3.1 Hz, 1H), 3.11 (s, 3H), 2.20 – 1.88 (m, 3H), 1.49 (d, *J* = 21.7 Hz, 6H), 1.45 (d, *J* = 22.0 Hz, 6H). ¹³C NMR (75 MHz, CDCl₃) δ 173.1, 145.9, 140.2, 139.7, 134.8, 129.4, 128.2, 128.1, 128.0, 125.6 (q, *J* = 284 Hz), 97.0 (d, *J* = 163 Hz), 75.5, 62.9 (q, *J* = 28.6 Hz), 58.9, 44.7, 43.8 (d, *J* = 19.9 Hz), 43.2, 30.0, 28.6 (d, *J* = 24.4 Hz), 25.5 (d, *J* = 24.7 Hz). HRMS (ESI⁺): calculated for C₂₄H₂₆BrF₄N₂O₃S [M+H]⁺ 577.0784, found: 577.0809 (minor) & 579.0781 (major).

*(S)-4-methyl-N-(prop-2-yn-1-yl)-2-((*S*)-2,2,2-trifluoro-1-(4'-(methylsulfonyl)-[1,1'-biphenyl]-4-yl)ethyl)amino)pentanamide **EM07***



According to *general procedure B*, the reaction between precursor *(S,S)-8* (26.9 mg, 0.06 mmol) and propargylamine (14 μ L, 0.22 mmol) afforded product **EM07** as a white solid (10.1 mg, 0.02 mmol, 35%). TLC *Rf* = 0.13 (1:2 EtOAc/heptane). LC-MS *Rt* = 8.41 min, *m/z* = 481.01 [M+H]⁺. ¹H NMR (300 MHz, CDCl₃) δ 8.05 – 7.99 (m, 2H), 7.79 – 7.73 (m, 2H), 7.65 – 7.59 (m, 2H), 7.51 (d, *J* = 8.1 Hz, 2H), 6.87 (t, *J* = 5.4 Hz, 1H), 4.20 (q, *J* = 7.2 Hz, 1H), 4.05 – 3.84 (m, 2H), 3.43 (dd, *J* = 8.9, 4.7 Hz, 1H), 3.11 (s, 3H), 2.19 (t, *J* = 2.6 Hz, 1H), 1.81 (tt, *J* = 12.8, 6.4 Hz, 1H), 1.69 – 1.42 (m, 2H), 0.97 (d, *J* = 6.5 Hz, 3H), 0.96 (d, *J* = 6.6 Hz, 3H). ¹³C NMR (75 MHz, CDCl₃) δ 174.4, 145.9, 140.3, 139.7, 134.6, 129.4, 128.2, 128.0, 125.5 (q, *J* = 283 Hz), 79.1, 71.9, 63.4 (q, *J* = 28.7 Hz), 59.8, 44.8, 43.0, 29.2, 25.0, 23.3, 21.9.

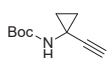
5.3. Synthesis of Alkyne **16**

tert-butyl (1-(methoxy(methyl)carbamoyl)cyclopropyl)carbamate **13**

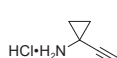
A solution of 1-(Boc-amino)cyclopropanecarboxylic acid (200 mg, 0.99 mmol) in DCM (2.5 mL) under argon was cooled to -15 °C. *N,O*-Dimethylhydroxylamine hydrochloride (100 mg, 1.0 mmol) was added, followed by 4-methylmorpholine (113 mL, 1.0 mmol). After 5 min, 1-(3-methylaminopropyl-3-ethylcarbodiimide hydrochloride (195 mg, 1.0 mmol) was added and the reaction was allowed to reach room temperature and stirred overnight. Water was added and the solution was extracted with DCM (3X). The combined organic phases were washed with brine, dried over Na₂SO₄, and concentrated *in vacuo* to obtain pure Weinreb amide **13** as an off-white solid (1.08 g, 0.99 mmol, quantitative). TLC *Rf* = 0.35 (1:1 EtOAc/heptane). ¹H NMR (300 MHz, CDCl₃) δ 5.22 (s, 1H), 3.74 (s, 3H), 3.18 (s, 3H), 1.44 (q, *J* = 5.2 Hz, 2H), 1.44 (s, 9H), 1.03 (q, *J* = 4.8 Hz, 2H). ¹³C NMR (75 MHz, DMSO-*d*₆) δ 171.9, 155.3, 78.0, 60.6, 34.0, 28.2, 21.2, 14.7.

tert-butyl (1-formylcyclopropyl)carbamate **14**

tert-butyl (1-(methoxy(methyl)carbamoyl)cyclopropyl) carbamate **13** (500 mg, 2.3 mmol) was dissolved in anhydrous Et₂O (50 mL) under argon and cooled to 0 °C. Lithium Aluminum Hydride (3.0 mL, 1M in Et₂O, 3.0 mmol) was added dropwise and the reaction mixture was stirred for 2 h at this temperature. The reaction was quenched by addition of 1N HCl (2.5 mL) and stirred vigorously for a few minutes. The organic layer was extracted with 1N HCl and brine, dried over Na₂SO₄, filtered and concentrated to obtain the product aldehyde **14** as a colorless oil. Use crude in the next step. TLC *Rf* = 0.47 (1:1 EtOAc/heptane).

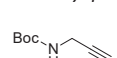
tert-butyl (1-ethynylcyclopropyl)carbamate 15

Dimethyl (1-diazo-2-oxopropyl)phosphonate (443 mL, 2.8 mmol) was dissolved in MeCN (25 mL) and potassium carbonate (767 mg, 5.6 mmol) was added. The suspension was stirred at room temperature for 10 min, then the freshly prepared aldehyde **14** (428 mg, 2.3 mmol) in MeOH (9 mL) was added. Stirring was continued overnight. The solvents were removed *in vacuo* and the residue was dissolved in 1:1 Et₂O/water. The layers were separated and the organic layer was washed with water and brine, and dried over Na₂SO₄. The yellowish oil was purified by FCC (1:2 EtOAc/heptane) to give product **15** as a pale white solid (165 mg, 0.90 mmol, 39%). TLC R_f = 0.66 (1:1 EtOAc/heptane). ¹H NMR (300 MHz, CDCl₃) δ 5.00 (s, 1H), 2.13 (s, 1H), 1.46 (s, 9H), 1.23 – 1.16 (m, 2H), 1.12 – 1.01 (m, 2H). ¹³C NMR (75 MHz, CDCl₃) δ 155.5, 85.8, 80.3, 66.8, 28.5, 23.7, 18.1.

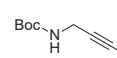
1-ethynylcyclopropan-1-amine hydrochloride 16

To a solution of *tert*-butyl (3-bromoprop-2-yn-1-yl)carbamate **15** (165 mg, 0.91 mmol) in MeOH (4.5 mL) was added 1.25N HCl in MeOH (1.82 mL, 2.3 mmol). The reaction mixture was left to stir overnight, volatiles were removed *in vacuo* and the resulting solid was triturated with Et₂O to obtain alkyne **16** as a white solid (79 mg, 0.67 mmol, 74%). ¹H NMR (300 MHz, DMSO-d₆) δ 8.74 (s, 3H), 3.59 (s, 1H), 1.26 (m, 2H), 1.23 – 1.07 (m, 2H). ¹³C NMR (75 MHz, DMSO-d₆) δ 81.8, 74.4, 23.9, 13.7.

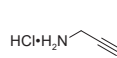
5.4. Synthesis of Alkyne **19**

tert-butyl prop-2-yn-1-ylcarbamate 17

According to published procedure,⁷⁹ the reaction between 3-amino-1-propyne (3.2 mL, 50 mmol) and di-*tert*-butyl dicarbonate (10.9 g, 50 mmol) afforded product **17** (7.8 g, 50 mmol, quantitative) as a yellow solid. TLC R_f = 0.78 (1:1 EtOAc/heptane). ¹H NMR (300 MHz, CDCl₃) δ 4.92 (s, 1H), 3.86 (dd, J = 5.9, 2.5 Hz, 2H), 2.18 (t, J = 2.5 Hz, 1H), 1.40 (s, 9H). ¹³C NMR (75 MHz, CDCl₃) δ 155.4, 80.2, 80.0, 71.2, 30.4, 28.4.

tert-butyl (3-bromoprop-2-yn-1-yl)carbamate 18

Tert-butyl prop-2-yn-1-ylcarbamate **17** (583 mg, 3.8 mmol) was dissolved in 19 mL DMF and silver nitrate (64 mg, 0.38 mmol) was added, followed by the addition of *N*-bromosuccinimide (735 mg, 4.1 mmol, 1.1 eq). The mixture was covered with aluminum foil and stirred at room temperature for 2 h, and was diluted with EtOAc and extracted with water (2X). The combined organic layers were dried over Na₂SO₄, filtered over celite and concentrated to give a yellow solid. The crude material was purified by FCC (3:1:2:1 EtOAc in heptane) to give bromoalkyne **18** (618 mg, 2.64 mmol, 70%) as an off-white solid. TLC R_f = 0.58 (1:2 EtOAc/heptane). ¹H NMR (300 MHz, CDCl₃) δ 4.69 (s, 1H), 3.94 (d, J = 5.5 Hz, 2H), 1.45 (s, 9H). ¹³C NMR (75 MHz, CDCl₃) δ 155.3, 80.2, 76.5, 42.8, 31.5, 28.4.

3-bromoprop-2-yn-1-amine hydrochloride 19

To *tert*-butyl (3-bromoprop-2-yn-1-yl)carbamate **18** (69 mg, 0.29 mmol) was added 4N HCl in dioxane (2 mL, 8 mmol). The reaction mixture was left to stir 1 h, volatiles were removed *in vacuo* and the resulting solid was triturated with Et₂O to obtain product **19** (51.4 mg, 0.32 mmol, quantitative) as a white solid. ¹H NMR (300 MHz, DMSO-d₆) δ 8.58 (s, 3H), 3.75 (s, 2H). ¹³C NMR (75 MHz, DMSO-d₆) δ 73.5, 48.9, 29.2.

6. References

1. Singh, J.; Petter, R.C.; Baillie, T.A.; Whitty, A. The Resurgence of Covalent Drugs. *Nat. Rev. Drug Discov.* **2011**, *10*, 307-317. doi: 10.1038/nrd3410.
2. Bauer, R.A. Covalent Inhibitors in Drug Discovery: From Accidental Discoveries To Avoided Liabilities and Designed Therapies. *Drug Discov. Today* **2015**, *20*, 1061-1073. doi: 10.1016/j.drudis.2015.05.005.
3. Silva, D.G.; Ribeiro, J.F.R.; De Vita, D.; Cianni, L.; Franco, C.H.; Freitas-Junior, L.H.; Moraes, C.B.; Rocha, J.R.; Burtoloso, A.C.B.; Kenny, P.W.; Leitão, A.; Montanari, C.A. A Comparative Study of Warheads for Design of Cysteine Protease Inhibitors. *Bioorg. Med. Chem. Lett.* **2017**, *27*, 5031-5035. doi: 10.1016/j.bmcl.2017.10.002.
4. Lonsdale, R.; Burgess, J.; Colclough, N.; Davies, N.L.; Lenz, E.M.; Orton, A.L.; Ward, R.A. Expanding the Armory: Predicting and Tuning Covalent Warhead Reactivity. *J. Chem. Inf. Model.* **2017**, *57*, 3124-3137. doi: 10.1021/acs.jcim.7b00553.
5. Barf, T.; Kaptein, A. Irreversible Protein Kinase Inhibitors: Balancing the Benefits and Risks. *J. Med. Chem.* **2012**, *55*, 6243-6262. doi: 10.1021/jm3003203.
6. Baillie, T.A. Targeted Covalent Inhibitors for Drug Design. *Angew. Chem. Int. Ed.* **2016**, *55*, 13408-13421. doi: 10.1002/anie.201601091.
7. González-Bello, C. Designing Irreversible Inhibitors—Worth the Effort? *ChemMedChem* **2015**, *11*, 22-30. doi: 10.1002/cmcd.201500469.
8. Solca, F.; Dahl, G.; Zoepfl, A.; Bader, G.; Sanderson, M.; Klein, C.; Kraemer, O.; Himmelsbach, F.; Haaksma, E.; Adolf, G.R. Target Binding Properties and Cellular Activity of Afatinib (BIBW 2992), an Irreversible ErBB Family Blocker. *J. Pharmacol. Exp. Ther.* **2012**, *343*, 342-350. doi: 10.1124/jpet.112.197756.
9. Pan, Z.; Scheerens, H.; Li, S.-J.; Schultz, B.E.; Sprengeler, P.A.; Burrill, L.C.; Mendonca, R.V.; Swerney, M.D.; Scott, K.C.K.; Grothaus, P.G.; Jeffery, D.A.; Spoerke, J.M.; Honigberg, L.A.; Young, P.R.; Dalrymple, S.A.; Palmer, J.T. Discovery of Selective Irreversible Inhibitors for Bruton's Tyrosine Kinase. *ChemMedChem* **2006**, *2*, 58-61. doi: 10.1002/cmcd.200600221.
10. Liu, Q.; Sabnis, Y.; Zhao, Z.; Zhang, T.; Buhrlage, S.J.; Jones, L.H.; Gray, N.S. Developing Irreversible Inhibitors of the Protein Kinase Cysteine. *Chem. Biol.* **2013**, *20*, 146-159. doi: 10.1016/j.chembiol.2012.12.006.
11. Shiba, Y.; Chiba, M. The Role of Extrahepatic Metabolism in the Pharmacokinetics of the Targeted Covalent Inhibitors Afatinib, Ibrutinib, and Neratinib. *Drug Metab. Dispos.* **2015**, *43*, 375.
12. Nakayama, S.; Atsumi, R.; Takakusa, H.; Kobayashi, Y.; Kurihara, A.; Nagai, Y.; Nakai, D.; Okazaki, O. A Zone Classification System for Risk Assessment of Idiosyncratic Drug Toxicity Using Daily Dose and Covalent Binding. *Drug Metab. Dispos.* **2009**, *37*, 1970. doi: 10.1124/dmd.109.027797.
13. Schwöbel, J.A.H.; Koleva, Y.K.; Enoch, S.J.; Bajot, F.; Hewitt, M.; Madden, J.C.; Roberts, D.W.; Schultz, T.W.; Cronin, M.T.D. Measurement and Estimation of Electrophilic Reactivity for Predictive Toxicology. *Chem. Rev.* **2011**, *111*, 2562-2596. doi: 10.1021/cr100098n.
14. Zhao, Z.; Bourne, P.E. Progress with Covalent Small-Molecule Kinase Inhibitors. *Drug Discov. Today* **2018**, *23*, 727-735. doi: 10.1016/j.drudis.2018.01.035.
15. Wright, M.H.; Sieber, S.A. Chemical Proteomics Approaches for Identifying the Cellular Targets of Natural Products. *Nat. Prod. Rep.* **2016**, *33*, 681-708. doi: 10.1039/C6NP00001K.
16. Talele, T.T. Acetylene Group, Friend or Foe in Medicinal Chemistry. *J. Med. Chem.* **2020**, *63*, 5625-5663. doi: 10.1021/acs.jmedchem.9b01617.
17. Ekkebus, R.; van Kasteren, S.I.; Kulathu, Y.; Scholten, A.; Berlin, I.; Geurink, P.P.; de Jong, A.; Goerdalay, S.; Neefjes, J.; Heck, A.J.R.; Komander, D.; Ova, H. On Terminal Alkynes That Can React with Active-Site Cysteine Nucleophiles in Proteases. *J. Am. Chem. Soc.* **2013**, *135*, 2867-2870. doi: 10.1021/ja309802n.
18. Gauthier, J.Y.; Chauret, N.; Cromlish, W.; Desmarais, S.; Duong, L.T.; Falgueyret, J.-P.; Kimmel, D.B.; Lamontagne, S.; Léger, S.; LeRiche, T., et al. The Discovery of Odanacatib (MK-0822), a Selective Inhibitor of Cathepsin K. *Bioorg. Med. Chem. Lett.* **2008**, *18*, 923-928. doi: 10.1016/j.bmcl.2007.12.047.
19. Orlov, N.V. Metal Catalysis in Thiolation and Selenation Reactions of Alkynes Leading to Chalcogen-Substituted Alkenes and Dienes. *ChemistryOpen* **2015**, *4*, 682-697. doi: 10.1002/open.201500137.
20. Castarlenas, R.; Di Giuseppe, A.; Pérez-Torrente, J.J.; Oro, L.A. The Emergence of Transition-Metal-Mediated Hydrothiolation of Unsaturated Carbon–Carbon Bonds: A Mechanistic Outlook. *Angew. Chem. Int. Ed.* **2012**, *52*, 211-222. doi: 10.1002/anie.201205468.
21. Lowe, A.B. Thiol-Yne 'Click'Coupling Chemistry and Recent Applications in Polymer and Materials Synthesis and Modification. *Polymer* **2014**, *55*, 5517-5549. doi: 10.1016/j.polymer.2014.08.015.
22. Jayasree, E.G.; Reshma, S. A Computational Study on the Reaction Mechanism and Energetics of Markovnikov and Anti-Markovnikov Addition in Alkyne Hydrothiolation Reactions. *Comput. Theor. Chem.* **2016**, *1098*, 13-21. doi: 10.1016/j.comptc.2016.10.012.
23. Sommer, S.; Weikart, N.D.; Linne, U.; Mootz, H.D. Covalent Inhibition of SUMO and Ubiquitin-Specific Cysteine Proteases by an In Situ Thiol-Alkyne Addition. *Bioorg. Med. Chem.* **2013**, *21*, 2511-2517. doi: 10.1016/j.bmcl.2013.02.039.
24. Arkona, C.; Rademann, J. Propargyl Amides as Irreversible Inhibitors of Cysteine Proteases—A Lesson on the Biological Reactivity of Alkynes. *Angew. Chem. Int. Ed.* **2013**, *52*, 8210-8212. doi: 10.1002/anie.201303544.
25. Turk, V.; Stoka, V.; Vasiljeva, O.; Renko, M.; Sun, T.; Turk, B.; Turk, D. Cysteine Cathepsins: From Structure, Function and Regulation to New Frontiers. *Biochim. Biophys. Acta, Proteins Proteom.* **2012**, *1824*, 68-88. doi: 10.1016/j.bbapap.2011.10.002.
26. Vizovišek, M.; Fonović, M.; Turk, B. Cysteine Cathepsins in Extracellular Matrix Remodeling: Extracellular Matrix Degradation and Beyond. *Matrik Biol.* **2019**, *75*-76, 141-159. doi: 10.1016/j.mabio.2018.01.024.
27. Stoch, S.A.; Zajic, S.; Stone, J.; Miller, D.L.; Van Dyck, K.; Gutierrez, M.J.; De Decker, M.; Liu, L.; Liu, Q.; Scott, B.B.; Panebianco, D.; Jin, B.; Duong, L.T.; Gottesdiener, K.; Wagner, J.A. Effect of the Cathepsin K Inhibitor Odanacatib on Bone Resorption Biomarkers in Healthy Postmenopausal Women: Two Double-Blind, Randomized, Placebo-Controlled Phase I Studies. *Clin. Pharmacol. Ther.* **2009**, *86*, 175-182. doi: 10.1038/clpt.2009.60.
28. Brömmle, D.; Lécaillé, F. Cathepsin K Inhibitors for Osteoporosis and Potential Off-Target Effects. *Expert Opin. Invest. Drugs* **2009**, *18*, 585-600. doi: 10.1517/13543780902832661.
29. Brömmle, D.; Panwar, P.; Turan, S. Cathepsin K Osteoporosis Trials, Pycnodysostosis and Mouse Deficiency Models: Commonalities and Differences. *Expert Opin. Drug Discov.* **2016**, *11*, 457-472. doi: 10.1517/17460441.2016.1160884.
30. Mullard, A. Merck & Co. Drops Osteoporosis Drug Odanacatib. *Nat. Rev. Drug Discov.* **2016**, *15*, 669-669. doi: 10.1038/nrd.2016.207.
31. Selenit, J.; Kaleta, J.; Li, Z.; Lalmanach, G.; Brömmle, D. Selective Inhibition of the Collagenase Activity of Cathepsin K. *J. Biol. Chem.* **2007**, *282*, 16492-16501. doi: 10.1074/jbc.M700242200.
32. Dolman, S.J.; Gosselin, F.; O'Shea, P.D.; Davies, I.W. Selective Metal-Halogen Exchange of 4,4'-Dibromobiphenyl Mediated by Lithium Tributylmagnesiate. *Tetrahedron* **2006**, *62*, 5092-5098. doi: 10.1016/j.tet.2006.03.039.

33. O’Shea, P.D.; Chen, C.-Y.; Gauvreau, D.; Gosselin, F.; Hughes, G.; Nadeau, C.; Volante, R.P. A Practical Enantioselective Synthesis of Odanacatib, a Potent Cathepsin K Inhibitor, via Triflate Displacement of an α -Trifluoromethylbenzyl Triflate. *J. Org. Chem.* **2009**, *74*, 1605-1610. doi: 10.1021/jo8020314.

34. Liu, G.; Kong, L.; Shen, J.; Zhu, G. A Regio- and Stereoselective Entry to (Z)- β -Halo Alkenyl Sulfides and Their Applications to Access Stereodefined Trisubstituted Alkenes. *Org. Biomol. Chem.* **2014**, *12*, 2310-2321. doi: 10.1039/C4OB00103F.

35. Shiu, H.-Y.; Chan, T.-C.; Ho, C.-M.; Liu, Y.; Wong, M.-K.; Che, C.-M. Electron-Deficient Alkynes as Cleavable Reagents for the Modification of Cysteine-Containing Peptides in Aqueous Medium. *Chem. Eur. J.* **2009**, *15*, 3839-3850. doi: 10.1002/chem.200800669.

36. Barf, T.; Covey, T.; Izumi, R.; van de Kar, B.; Gulrajani, M.; van Lith, B.; van Hoek, M.; de Zwart, E.; Mittag, D.; Demont, D.; Verkaik, S.; Krantz, F.; Pearson, P.G.; Ulrich, R.; Kaptein, A. Acalabrutinib (ACP-196): A Covalent Bruton Tyrosine Kinase Inhibitor with a Differentiated Selectivity and In Vivo Potency Profile. *J. Pharmacol. Exp. Ther.* **2017**, *363*, 240. doi: 10.1124/jpet.117.242909.

37. Oballa, R.M.; Truchon, J.-F.; Bayly, C.I.; Chauret, N.; Day, S.; Crane, S.; Berthelette, C. A Generally Applicable Method for Assessing the Electrophilicity and Reactivity of Diverse Nitrile-Containing Compounds. *Bioorg. Med. Chem. Lett.* **2007**, *17*, 998-1002. doi: 10.1016/j.bmcl.2006.11.044.

38. Siklos, M.; BenAissa, M.; Thatcher, G.R.J. Cysteine Proteases as Therapeutic Targets: Does Selectivity Matter? A Systematic Review of Calpain and Cathepsin Inhibitors. *Acta Pharm. Sin. B* **2015**, *5*, 506-519. doi: 10.1016/j.apsb.2015.08.001.

39. Lushchak, V.I. Glutathione Homeostasis and Functions: Potential Targets for Medical Interventions. *J. Amino Acids* **2012**, *2012*, 736837. doi: 10.1155/2012/736837.

40. Law, S.; Andrault, P.-M.; Aguda, A.H.; Nguyen, N.T.; Kruglyak, N.; Brayer, G.D.; Brömmе, D. Identification of Mouse Cathepsin K Structural Elements that Regulate the Potency of Odanacatib. *Biochem. J.* **2017**, *474*, 851-864. doi: 10.1042/BJCJ20160985.

41. Copeland, R.A.; Basavapathruni, A.; Moyer, M.; Scott, M.P. Impact of Enzyme Concentration and Residence Time on Apparent Activity Recovery in Jump Dilution Analysis. *Anal. Biochem.* **2011**, *416*, 206-210. doi: 10.1016/j.ab.2011.05.029.

42. Pražníkár, J.; Turk, D. Free Kick Instead of Cross-Validation in Maximum-Likelihood Refinement of Macromolecular Crystal Structures. *Acta Crystallogr., Sect. D: Biol. Crystallogr.* **2014**, *70*, 3124-3134. doi: 10.1107/S1399004714021336.

43. Strelow, J.M. A Perspective on the Kinetics of Covalent and Irreversible Inhibition. *SLAS Discov.: Adv. Life Sci. R&D* **2017**, *22*, 3-20. doi: 10.1177/1087057116671509.

44. Holdgate, G.A.; Meek, T.D.; Grimley, R.L. Mechanistic Enzymology in Drug Discovery: A Fresh Perspective. *Nat. Rev. Drug Discov.* **2017**, *17*, 115. doi: 10.1038/nrd.2017.219.

45. Strelow, J.M.; Dewe, W.; Iversen, P.W.; Brooks, H.B.; Radding, J.A.; McGee, J.; Weidner, J. Mechanism of Action Assays for Enzymes. In *Assay Guidance Manual* [Online], Eli Lilly & Company and the National Center for Advancing Translational Sciences: Bethesda (MD), 2012. <https://www.ncbi.nlm.nih.gov/books/NBK92001/> (accessed 2012-10-01).

46. Copeland, R.A. Chapter 9. Irreversible Enzyme Inactivators. In *Evaluation of Enzyme Inhibitors in Drug Discovery: A Guide for Medicinal Chemists and Pharmacologists*, Second ed.; John Wiley & Sons, Inc.: Hoboken, New Jersey, 2013; pp 345-382. doi: 10.1002/978118540398.

47. Cavallo, G.; Metrangolo, P.; Milani, R.; Pilati, T.; Priimagi, A.; Resnati, G.; Terraneo, G. The Halogen Bond. *Chem. Rev.* **2016**, *116*, 2478-2601. doi: 10.1021/acs.chemrev.5b00484.

48. Drake, M.T.; Clarke, B.L.; Oursler, M.J.; Khosla, S. Cathepsin K Inhibitors for Osteoporosis: Biology, Potential Clinical Utility, and Lessons Learned. *Endocr. Rev.* **2017**, *38*, 325-350. doi: 10.1210/er.2015-1114.

49. Lindeman, J.H.N.; Hanemajer, R.; Mulder, A.; Dijkstra, P.D.S.; Szuhai, K.; Bromme, D.; Verheijen, J.H.; Hogendoorn, P.C.W. Cathepsin K Is the Principal Protease in Giant Cell Tumor of Bone. *Am. J. Pathol.* **2004**, *165*, 593-600. doi: 10.1016/S0002-9440(10)63232-8.

50. Edgington-Mitchell, L.E.; Rautela, J.; Duivenvoorden, H.M.; Jayatilleke, K.M.; van der Linden, W.A.; Verdoes, M.; Bogyo, M.; Parker, B.S. Cysteine Cathepsin Activity Suppresses Osteoclastogenesis of Myeloid-Derived Suppressor Cells in Breast Cancer. *Oncotarget* **2015**, *6*, 27008-27022. doi: 10.18633/oncotarget.4714.

51. Nicholson, G.C.; Malakellis, M.; Collier, F.M.; Cameron, P.U.; Holloway, W.R.; Gough, T.J.; Gregorio-King, C.; Kirkland, M.A.; Myers, D.E. Induction of Osteoclasts from CD14-Positive Human Peripheral Blood Mononuclear Cells by Receptor Activator of Nuclear Factor κ B Ligand (RANKL). *Clin. Sci.* **2000**, *99*, 133. doi: 10.1042/cs0990133.

52. Kirvanta, R.; Morko, J.; Alatalo, S. L.; NicAmhlaobh, R.; Risteli, J.; Laitala-Leinonen, T.; Vuorio, E. Impaired Bone Resorption in Cathepsin K-Deficient Mice is Partially Compensated by Enhanced Osteoclastogenesis and Increased Expression of Other Proteases via an Increased RANKL/OPG Ratio. *Bone* **2005**, *36*, 159-172. doi: 10.1016/j.bone.2004.09.020.

53. Pirapaharan, D.C.; Søe, K.; Panwar, P.; Madsen, J.S.; Bergmann, M.L.; Overgaard, M.; Brömmе, D.; Delaisse, J.-M. A Mild Inhibition of Cathepsin K Paradoxically Stimulates the Resorptive Activity of Osteoclasts in Culture. *Calcif. Tissue Int.* **2019**, *104*, 92-101. doi: 10.1007/s00223-018-0472-7.

54. Thompson, S.K.; Halbert, S.M.; Bossard, M.J.; Tomaszek, T.A.; Levy, M.A.; Zhao, B.; Smith, W.W.; Abdel-Meguid, S.S.; Janson, C.A.; D’Alessio, K.J., et al. Design of Potent and Selective Human Cathepsin K Inhibitors That Span the Active Site. *Proc. Natl. Acad. Sci.* **1997**, *94*, 14249. doi: 10.1073/pnas.94.26.14249.

55. McQueney, M.S.; Amegadzie, B.Y.; D’Alessio, K.; Hanning, C.R.; McLaughlin, M.M.; McNulty, D.; Carr, S.A.; Ijames, C.; Kurdyla, J.; Jones, C.S. Autocatalytic Activation of Human Cathepsin K. *J. Biol. Chem.* **1997**, *272*, 13955-13960. doi: 10.1074/jbc.272.21.13955.

56. Leung, P.; Pickarski, M.; Zhuo, Y.; Masarachia, P.J.; Duong, L.T. The Effects of the Cathepsin K Inhibitor Odanacatib on Osteoclastic Bone Resorption and Vesicular Trafficking. *Bone* **2011**, *49*, 623-635. doi: 10.1016/j.bone.2011.06.014.

57. Ovaa, H.; Mons, M.W.E.; van Boeckel, S. Cathepsin Inhibitors. WO2019112426A1, 13 June, 2019.

58. Mihelić, M.; Doberšek, A.; Gunčar, G.; Turk, D. Inhibitory Fragment from the p41 Form of Invariant Chain Can Regulate Activity of Cysteine Cathepsins in Antigen Presentation. *J. Biol. Chem.* **2008**, *283*, 14453-14460. doi: 10.1074/jbc.M801283200.

59. Brömmе, D.; Nallaseth, F.S.; Turk, B. Production and Activation of Recombinant Papain-Like Cysteine Proteases. *Methods* **2004**, *32*, 199-206. doi: 10.1016/S1046-2023(03)00212-3.

60. Rozman, J.; Stojan, J.; Kuhelj, R.; Turk, V.; Turk, B. Autocatalytic Processing of Recombinant Human Procathepsin B Is a Bimolecular Process. *FEBS Lett.* **1999**, *459*, 358-362. doi: 10.1016/S0014-5793(99)01302-2.

61. Choe, Y.; Leonetti, F.; Greenbaum, D.C.; Lecaille, F.; Bogyo, M.; Brömmе, D.; Ellman, J.A.; Craik, C.S. Substrate Profiling of Cysteine Proteases Using a Combinatorial Peptide Library Identifies Functionally Unique Specificities. *J. Biol. Chem.* **2006**, *281*, 12824-12832. doi: 10.1074/jbc.M513331200.

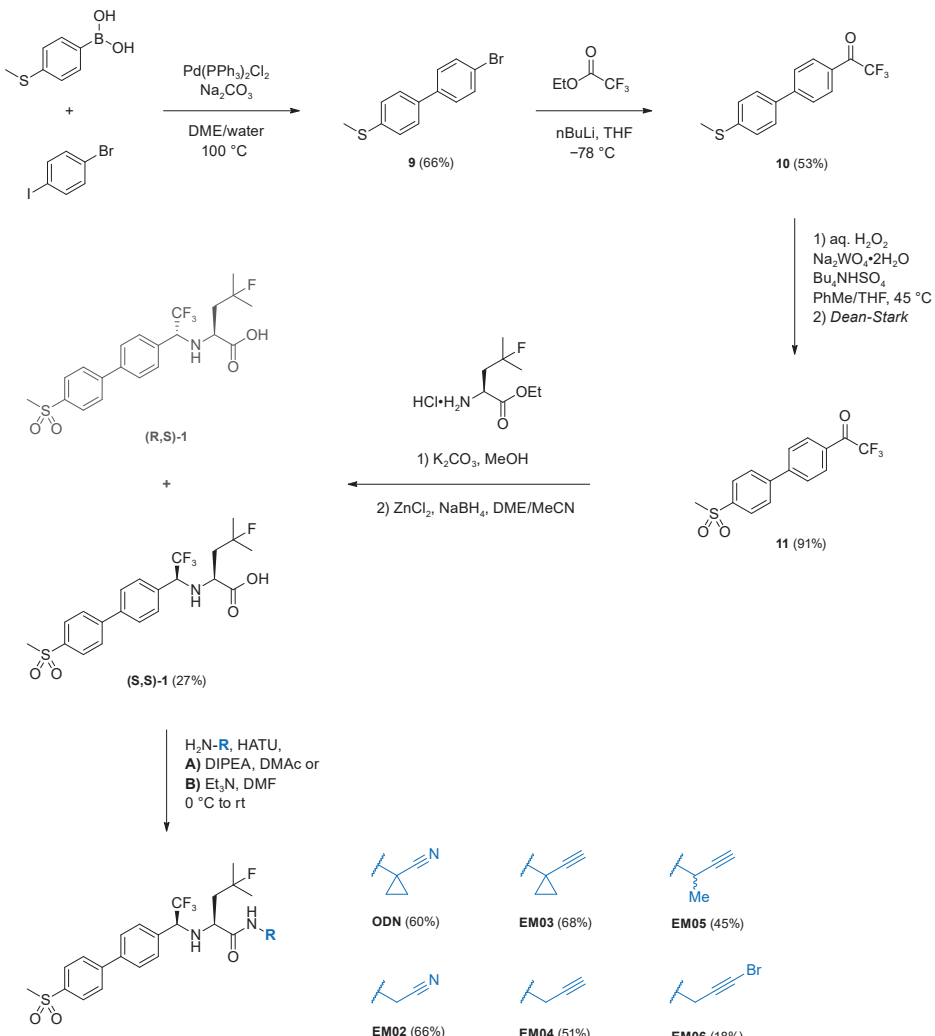
62. Boršek, J.; Vizovišek, M.; Sosnowski, P.; Turk, B.; Turk, D.; Mohar, B.; Novič, M. Development of *N*-(Functionalized benzoyl)-homocycloleucyl-glycinonitrides as Potent Cathepsin K Inhibitors. *J. Med. Chem.* **2015**, *58*, 6928-6937. doi: 10.1021/acs.jmedchem.5b00746.

63. Yasuda, Y.; Li, Z.; Greenbaum, D.; Bogyo, M.; Weber, E.; Brömmе, D. Cathepsin V, a Novel and Potent Elastolytic Activity Expressed in Activated Macrophages. *J. Biol. Chem.* **2004**, *279*, 36761-36770. doi: 10.1074/jbc.M403986200.

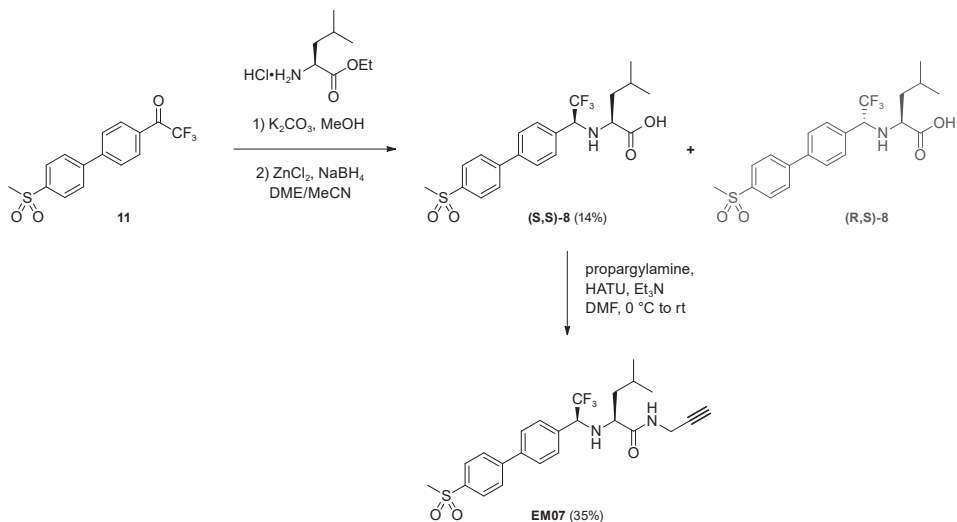
64. Kramer, L.; Renko, M.; Završnik, J.; Turk, D.; Seeger, M.A.; Vasiljeva, O.; Grüter, M.G.; Turk, V.; Turk, B. Non-invasive *In Vivo* Imaging of Tumour-Associated Cathepsin B by a Highly Selective Inhibitory DARPin. *Theranostics* **2017**, *7*, 2806-2821. doi: 10.7150/thno.19081.
65. Menard, R.; Khouri, H.E.; Plouffe, C.; Dupras, R.; Ripoll, D.; Vernet, T.; Tessier, D.C.; Laliberte, F.; Thomas, D.Y.; Storer, A.C. A Protein Engineering Study of the Role of Aspartate 158 in the Catalytic Mechanism of Papain. *Biochemistry* **1990**, *29*, 6706-6713. doi: 10.1021/bi00480a021.
66. Verdoes, M.; Oresic Bender, K.; Segal, E.; van der Linden, W.A.; Syed, S.; Withana, N.P.; Sanman, L.E.; Bogyo, M. Improved Quenched Fluorescent Probe for Imaging of Cysteine Cathepsin Activity. *J. Am. Chem. Soc.* **2013**, *135*, 14726-14730. doi: 10.1021/ja4056068.
67. Lausi, A.; Polentarutti, M.; Onesti, S.; Plaisier, J.R.; Busetto, E.; Bais, G.; Barba, L.; Cassetta, A.; Campi, G.; Lamba, D.; Pifferi, A.; Mande, S.C.; Sarma, D.D.; Sharma, S.M.; Paolucci, G. Status of the Crystallography Beamlines at Elettra. *Eur. Phys. J. Plus* **2015**, *130*, 43. doi: 10.1140/epjp/i2015-15043-3.
68. Kabsch, W. Integration, Scaling, Space-Group Assignment and Post-Refinement. *Acta Crystallogr., Sect. D* **2010**, *66*, 133-144. doi: 10.1107/S0907444909047374.
69. Winn, M.D.; Ballard, C.C.; Cowtan, K.D.; Dodson, E.J.; Emsley, P.; Evans, P.R.; Keegan, R.M.; Krissinel, E.B.; Leslie, A.G.W.; McCoy, A.; McNicholas, S.J.; Murshudov, G.N.; Pannu, N.S.; Potterton, E.A.; Powell, H.R.; Read, R.J.; Vagin, A.; Wilson, K.S. Overview of the CCP4 Suite and Current Developments. *Acta Crystallogr., Sect. D: Biol. Crystallogr.* **2011**, *67*, 235-242. doi: 10.1107/S0907444910045749.
70. Evans, P. Scaling and Assessment of Data Quality. *Acta Crystallogr., Sect. D* **2006**, *62*, 72-82. doi: 10.1107/S0907444905036693.
71. Evans, P.R.; Murshudov, G.N. How Good are My Data and What Is the Resolution? *Acta Crystallogr., Sect. D: Biol. Crystallogr.* **2013**, *69*, 1204-1214. doi: 10.1107/S0907444913000061.
72. Yamashita, D.S.; Marquis, R.W.; Xie, R.; Nidamarty, S.D.; Oh, H.-J.; Jeong, J.U.; Erhard, K.F.; Ward, K.W.; Roethke, T.J.; Smith, B.R., et al. Structure Activity Relationships of 5-, 6-, and 7-Methyl-Substituted Azepan-3-one Cathepsin K Inhibitors. *J. Med. Chem.* **2006**, *49*, 1597-1612. doi: 10.1021/jm050915u.
73. Vagin, A.; Teplyakov, A. MOLREP: an Automated Program for Molecular Replacement. *J. Appl. Crystallogr.* **1997**, *30*, 1022-1025. doi: 10.1107/S0021889897006766.
74. Turk, D. MAIN Software for Density Averaging, Model Building, Structure Refinement and Validation. *Acta Crystallogr., Sect. D: Biol. Crystallogr.* **2013**, *69*, 1342-1357. doi: 10.1107/S0907444913008408.
75. Andrejasic, M.; Praznikar, J.; Turk, D. PURY: a Database of Geometric Restraints of Hetero Compounds for Refinement in Complexes with Macromolecular Structures. *Acta Crystallogr., Sect. D* **2008**, *64*, 1093-1109. doi: 10.1107/S0907444908027388.
76. Gauthier, J.Y.; Black, W.C.; Courchesne, I.; Cromlish, W.; Desmarais, S.; Houle, R.; Lamontagne, S.; Li, C.S.; Massé, F.; McKay, D.J.; Ouellet, M.; Robichaud, J.; Truchon, J.-F.; Truong, V.-L.; Wang, Q.; Percival, M.D. The Identification of Potent, Selective, and Bioavailable Cathepsin S Inhibitors. *Bioorg. Med. Chem. Lett.* **2007**, *17*, 4929-4933. doi: 10.1016/j.bmcl.2007.06.023.
77. Roy, A.; Gosselin, F.; O'Shea, P.D.; Chen, C.Y. Diastereoselective Aryllithium Addition to an α -Trifluoromethyl Imine. Practical Synthesis of a Potent Cathepsin K Inhibitor. *J. Org. Chem.* **2006**, *71*, 4320-4323. doi: 10.1021/jo052430j.
78. O'Shea, P.; Gosselin, F. Amidation Process for the Preparation of Cathepsin K Inhibitors. WO2008119176A1, 9 October, 2008.
79. Ishida, T.; Kobayashi, R.; Yamada, T. Novel Method of Tetramic Acid Synthesis: Silver-Catalyzed Carbon Dioxide Incorporation into Propargylic Amine and Intramolecular Rearrangement. *Org. Lett.* **2014**, *16*, 2430-3. doi: 10.1021/o1500806u.
80. Wang, Z. Weinreb Ketone Synthesis. In *Comprehensive Organic Name Reactions and Reagents*, 2010; pp 2963-2967. doi: 10.1002/9780470638859.conrr661.
81. Dhameja, M.; Pandey, J. Bestmann-Öhring Reagent: A Convenient and Promising Reagent in the Chemical World. *Asian J. Org. Chem.* **2018**, *7*, 1502-1523. doi: 10.1002/ajoc.201800051.
82. Halbes-Letinois, U.; Weibel, J.-M.; Pale, P. The Organic Chemistry of Silver Acetylides. *Chem. Soc. Rev.* **2007**, *36*, 759-769. doi: 10.1039/B602151B.
83. Fernández, A.; Vendrell, M. Smart Fluorescent Probes for Imaging Macrophage Activity. *Chem. Soc. Rev.* **2016**, *45*, 1182-1196. doi: 10.1039/C5CS00567A.
84. Rodan, S.B.; Duong, L.T. Cathepsin K – A New Molecular Target for Osteoporosis. *IBMS BoneKey* **2008**, *5*, 16-24. doi: 10.1138/20080294.
85. Hayman, A.R. Tartrate-Resistant Acid Phosphatase (TRAP) and the Osteoclast/Immune Cell Dichotomy. *Autoimmunity* **2008**, *41*, 218-223. doi: 10.1080/08916930701694676.

7. Supporting Information

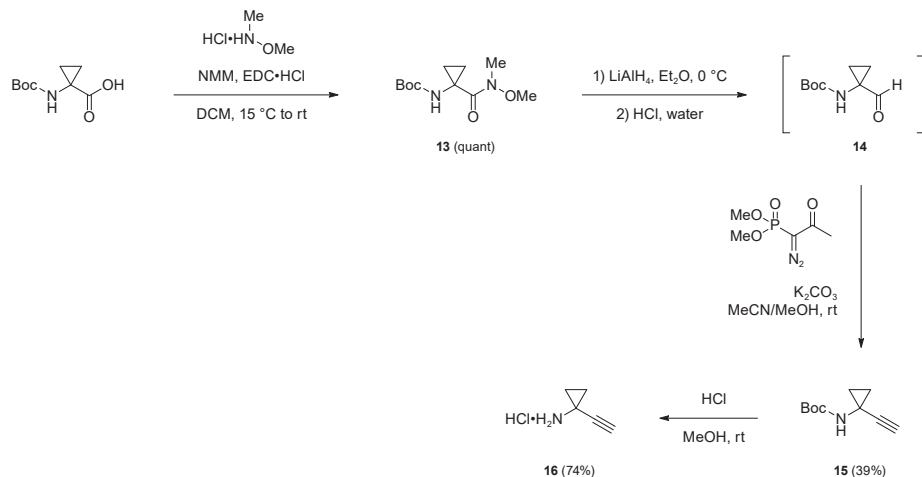
7.1. Chemical Synthesis



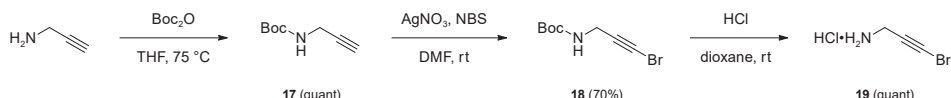
Scheme S1 | Synthesis of ODN and derivatives from affordable building blocks. Synthesis of precursor **1** was started with a Suzuki coupling between commercially available boronic acid and 1-bromo-4-iodobenzene. Obtained product **9** was lithiated in the presence of ethyl trifluoroacetate to give sulfide **10**. Subsequent oxidation resulted in ketone **11**, which is prone to hydrolysis forming hydrate **12**. Ketone **11** was submitted to a diastereoselective reductive amination. The imine intermediate was formed with 4-fluoro-L-leucine, after which it was reduced with $\text{NaBH}_4/\text{ZnCl}_2$. Aqueous acidic work-up and purification by flash chromatography resulted in a mixture of diastereoisomers, which could be separated on preparative RP-HPLC. Diastereoisomers **(S,S)-1** and **(R,S)-1** were assigned based on comparison of ^1H NMR to the published spectra of **(S,S)-1**.³³ Ester hydrolysis of both diastereoisomers was also observed. Precursor **(S,S)-1** was then submitted to HATU-catalyzed amide coupling (*conditions A* or *B*) to give the final compounds.



Scheme S2 | Synthesis of **EM07** for crystallography. Ketone **11** was submitted to a diastereoselective reductive amination. The imine intermediate was formed with L-leucine, after which it was reduced with $NaBH_4/ZnCl_2$. Aqueous acidic work-up resulted in a mixture of diastereoisomers, which could be separated on preparative RP-HPLC with (S,S)-**8** as the major isomer.³³ Peptide coupling with propargylamine finally resulted in **EM07**. Stereocenters were assigned based on the X-ray diffraction data of the CatK-EM07 adduct.



Scheme S3 | Synthesis of building block (cyclopropyl)propargylamine **16**. Treatment of Boc-protected 1-amino-cyclopropanecarboxylic acid with *N,O*-dimethylhydroxylamine in presence of water-soluble coupling reagent EDC formed Weinreb amide **13**,⁸⁰ which was obtained pure after a simple aqueous extraction. A reduction in a Weinreb-Nahm ketone synthesis reaction with lithium aluminum hydride followed by aqueous acid treatment formed aldehyde **14**, and solvents were only partially removed *in vacuo* (400 mbar, room temperature) to minimize loss of the volatile product. Crude aldehyde **14** was directly submitted to a Seydel-Gilbert homologation reaction with Ohira-Bestmann reagent to form Boc-protected alkyne **15**.⁸¹ The Boc-protecting group was removed with HCl to yield the hydrochloride salt of amine **16**.



Scheme S4 | Synthesis of building block bromoalkyne **19**. Installation of a protecting group increases the boiling point (reducing loss of volatile free amine in solvent evaporation steps) and changed the physical appearance from an oil to a solid – greatly improving compound handling – while increasing the molecular weight to above 100 Da facilitates LC-MS detection and NMR analysis. Boc-protected propargylamine **17** was obtained by Boc protection of propargylamine using standard published conditions.⁷⁹ Subsequent direct silver-mediated halogenation was achieved by displacement of the terminal alkyne proton of alkyne **17** with silver nitrate to form a silver acetylidy intermediate, which reacted with *N*-bromosuccinimide (NBS) to form Boc-protected bromoalkyne **18**.⁸² Remnants of unreacted Boc-propargylamine **17** could be removed by flash column chromatography. HCl treatment, removal of solvents *in vacuo* and trituration with Et₂O finally yielded the hydrochloride salt of amine **19**.

7.2. Thiol Reactivity Assay

Table S1 | Retention times and m/z for unbound inhibitors and thiol adducts.

Compound	Unbound		Cys adduct		GSH adduct	
	Rt (min)	m/z ^a	Rt (min)	m/z ^a	Rt (min)	m/z ^a
ODN	7.17	526	6.89 5.94	630 648 ^b	N.D.	833
EM02	7.04	500	6.69 5.82	604 622 ^b	5.68	807
EM03	7.37	525	N.D.	646	N.D.	832
EM04	7.22	499	5.95	620	5.86	806
EM05	7.45 7.20	513 531 ^b	6.08	634	5.84	820
EM06	7.62	577 & 579	6.12	698 & 700	6.04	884 & 886
E-64	3.48	358	2.29	479	2.59 2.80	665 665
afatinib	4.24	486	3.83	607	3.88	793
ibrutinib	6.52	441	5.48	562	5.41 5.21	748 764 ^b
acalabrutinib	4.37 3.98	466 484 ^b	3.65 3.83	587 587	3.93	773

Data related to **Figure 3**. Detection of unbound inhibitor and adducts by LC-MS, with quantification of UV trace.

^aValues in *italics* are expected/calculated values, not detected. ^bHydrolysis of inhibitor/adduct. N.D. = not detected.

7.3. Activity Assays

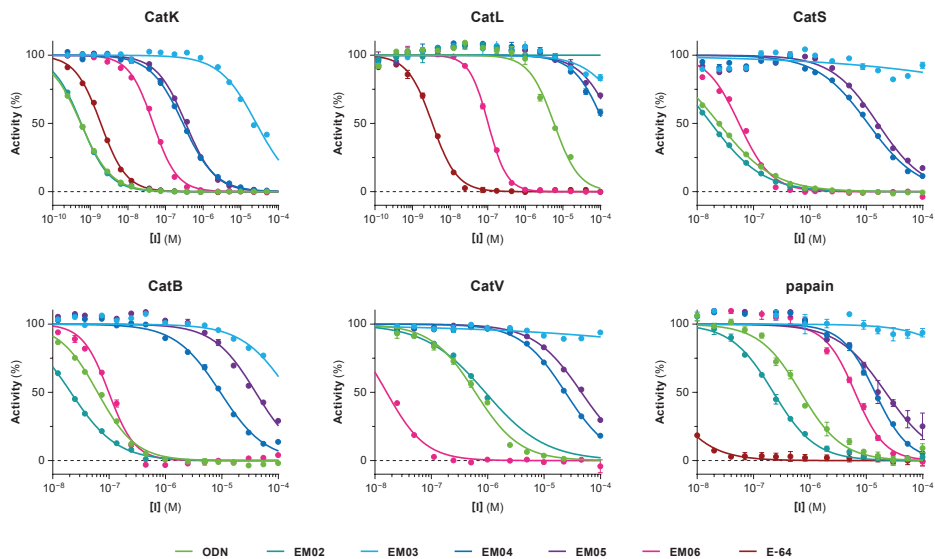


Figure S1 | Dose-Response Curves (DRC) for cysteine protease inhibition. Data accompanying **Table 1**. Graphical data represents the mean \pm standard deviation for a single representative experiment.

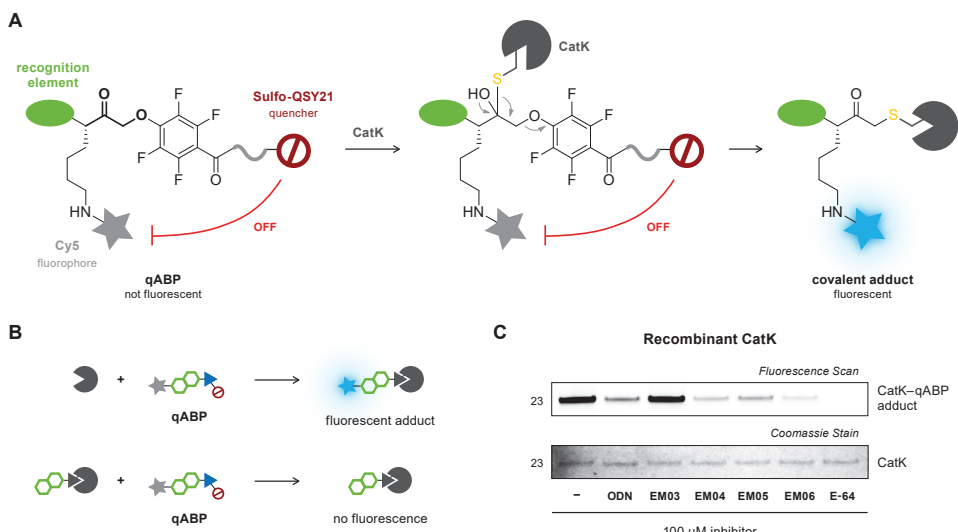


Figure S2 | Evaluation of recombinant hCatK activity with quenched fluorescent ABP (qABP) BMV109. (A) Schematic overview.⁸³ Fluorescent adduct is formed upon covalent thiol addition, with the quencher as leaving group. (B) Recombinant CatK is preincubated with inhibitor (2 h) followed by treatment with qABP BMV109 (500 nM) for 2 h. CatK-inhibitor adduct formation blocks formation of fluorescent CatK-qABP adduct.⁶⁶ (C) Gel electrophoresis results. Top: Fluorescence scan ($\lambda_{ex} = 635$ nm, $\lambda_{em} = 665$ nm) for CatK-qABP adducts. Darker bands = more CatK activity. Bottom: Coomassie protein stain as loading control.

7.4. Jump Dilution Assay

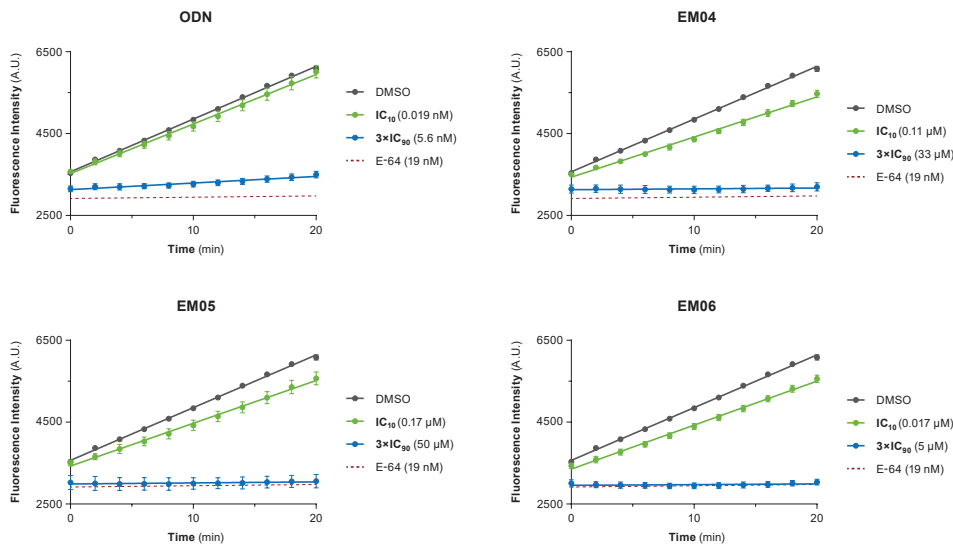


Figure S3 | CatK activity in control samples without dilution (jump dilution assay). Data accompanying **Figure 4**. Recombinant CatK was preincubated with inhibitor followed by addition of substrate Z-FR-AMC (final conc. 4 μ M) to establish inhibitory potency without dilution. Inhibitor concentrations shown are after addition of Z-FR-AMC substrate, and correlate with the inhibitor concentration before and after 300-fold dilution in the jump dilution assay (progress curves shown in **Figure 4B**). E-64 is the full inhibition control (*dashed line*).

7.5. Bottom-up MS Analysis

Sequence mature human CatK (Uniprot; P43235), with underlined proteolytic peptide containing catalytic residue (Cys25) after trypsin digestion;

GYVTPVK**NQG** QCGSCWAFSS V^{GALEGQL}KK KTGKLLNLSP QNLVDCVSEN DGCGGGYMTN AFQYVQKNRG IDSEDAYPYV
GQEESCMYNP TGKA^{AKCRG}Y REIPEGNEKA LKRAVARVGP VSVAIDASLT SFQFYSKGVY YDESCNSDNL NHAVLAVGYG
IQKGNKHWII KNSWGENWGN KG^{YILM}ARNK NNACGIANLA SFPKM

Table S2 | Tryptic peptides identified with Mascot (v2.2.04) after alkylation (using iodoacetamide) and tryptic digestion of recombinant hCatK or covalent hCatK-EM04 adduct.

	Unbound hCatK	hCatK-EM04
Peptide sequence	NQGQCGSCWAFSSVGALEGQLKK C5-carbamidomethyl (57.02 Da) C8-carbamidomethyl (57.02 Da)	NQGQCGSCWAFSSVGALEGQLKKK C5-carbamidomethyl (57.02 Da) C8-EM04 (498.16 Da)
Charge	+3	+4
Monoisotopic m/z	838.1 Da	771.11 Da

Bottom-up MS analysis. For the hCatK-EM04 adduct, double carbamidomethylated peptide NQGQC*GSC*WAFSSVGALEGQLKK₁₈₋₄₀ disappears nearly completely, with appearance of peptide NQGQC*GSC[®]WAFSSVGALEGQLKKK₁₈₋₄₁ with a single carbamidomethyl (*) and a single warhead (®).

Table S3 | Tandem MS analysis. Detected fragment ions of modified tryptic CatK-EM04 peptide.

Sequence	y ⁺	y ²⁺	y _#
N			24
Q			23
G			22
Q			21
C*			20
G			19
S			18
C [®]			17
W	875.0		16
A	782.0		15
F	746.3		14
S	672.9		13
S	629.4		12
V	1170.7	585.9	11
G	1071.7	536.3	10
A	1014.6		9
L	943.6		8
E	830.5		7
G	701.5		6
Q	644.4		5
L			4
K	403.3		3
K	275.2		2
K			1

Tandem MS analysis for NQGQC*GSC[®]WAFSSVGALEGQLKK peptide (m/z = 771.11⁴⁺) related to **Table S2**. Obtained by alkylation and trypsin digestion of covalent CatK-EM04 adduct. * = carbamidomethyl. [®] = EM04.

7.6. Protein Crystallography

A

Data Collection		Refinement	
Unit cell		PDB ID	6QBS
a, b, c	75.351, 75.351, 340.184 Å	Resolution range	47.09 – 1.7 Å
α, β, γ	90.0°, 90.0°, 120.0°	No. reflections in working set	64031
Space group	P61 2 2 (number 178)	No. reflections in test set	64031
Molecules per au	2	R -kick value	21.0
Wavelength	0.97912 Å	RMSD	
Resolution range	47.09 – 1.7 Å	RMSD Bond lengths	0.02 Å
No. of unique reflections	64186	RMSD Bond angles	2.0°
Completeness (last shell)	99.9% (99.3%)	No. of atoms in au	4018
Multiplicity (last shell)	33.1 (24)	Protein atoms	3298
R_{meas} (last shell)	0.177% (0.978%)	Water molecules	654
I/σ	16.3 (2.2)	Cl^-	2
		Ca^{2+}	1
		Mean B value	19.3 Å ²
		Ramachandran plot statistics	
		Favored	412
		Allowed	14
		Outliers	0

4

B

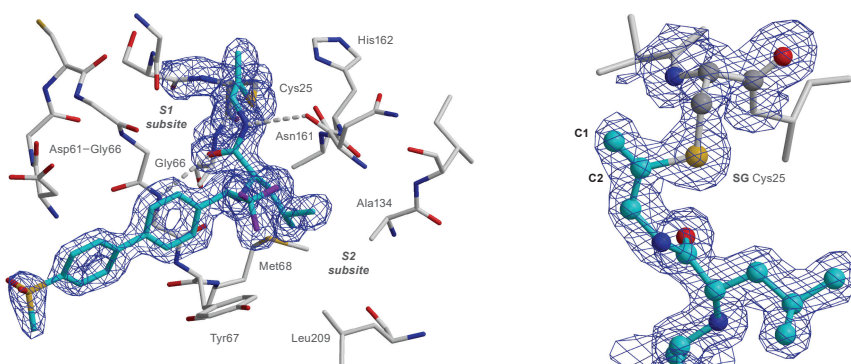


Figure S4 | Protein crystallography of alkyne **EM07** bound covalent to catalytic Cys25 in CatK. Data accompanying Figure 6. (A) Data collection and refinement statistics for covalent CatK–EM07 adduct. (B) Free kick weighted electron density map⁴² around inhibitor **EM07** and Cys25. Blue represents maximum-likelihood free-kick (ML FK) map contoured at 1.3 σ . Relevant CatK residues are shown with stick model. Inhibitor is shown in stick model (left) or ball-and-stick model (right). Nitrogen, oxygen, fluorine, and sulfur atoms are shown in blue, red, violet, and yellow, respectively. Carbon atoms of **EM07** and CatK are shown in cyan and gray, respectively.

7.7. Kinetic Evaluation

Assay conditions were optimized to obtain a robust signal with a linear increase in product formation for 60 minutes, but a strictly linear rate of product formation for the DMSO control could not be obtained ($k_{ctrl} > 0$). Full curves and fits are shown in **Figure S5**.

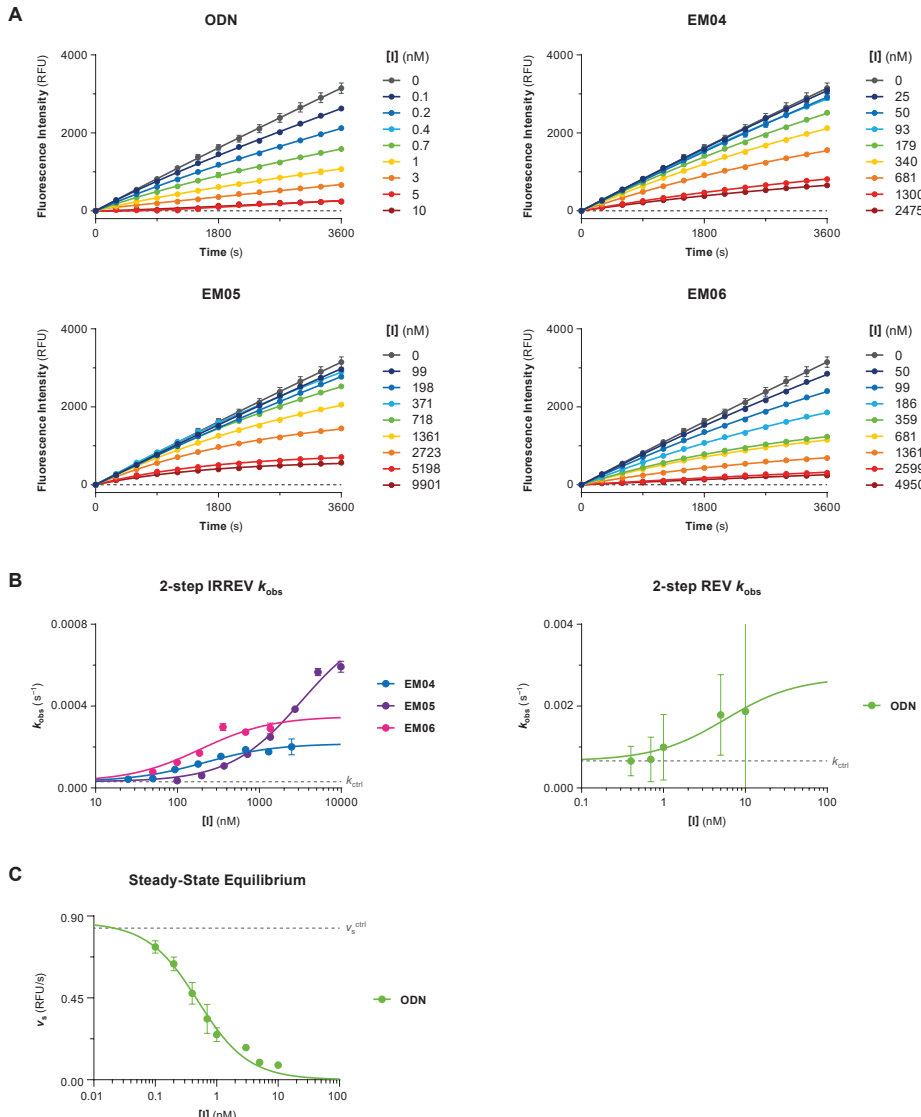


Figure S5 | Kinetic evaluation of covalent inhibitors. Data accompanying **Table 2**. **(A)** Progress curves for baseline-corrected substrate hydrolysis were fitted to one-phase exponential association (constrained $v_s = 0$ for irreversible inhibitors) to find k_{obs} . **(B)** Plots of k_{obs} against inhibitor concentration were fitted to their respective equations – based on inhibitor binding mode – to obtain relevant kinetic parameters. **(C)** Plot of v_s against inhibitor concentration was fitted to Morrison’s quadratic equation to obtain steady-state equilibrium constant K_i^* .

7.8. Human Osteoclast Assays

Bone resorption quantification. The total bone resorption area was quantified because bone resorption by osteoclasts is not homogeneously distributed over bone slices, and it can be hard to select representative areas on the bone (**Figure S6B**). Please note that this only considers the area of resorption, not the depth of the resorption pits: trenches are deeper than pits, so more bone is resorbed in the same area. An overview to compare the total bone resorption on a bone slices, as judged by visual assessment, has also been included (**Figure S6C**). A larger number of resorption areas correlates with more active, resorbing osteoclasts. Trenches are characteristic of fully functional osteoclasts; pits are more commonly seen in osteoclasts with impaired CatK activity. However, trenches and pits can be observed in both cases, possibly because mature osteoclasts are formed between day 3 and day 7 (in absence of inhibitor): osteoclasts that matured before day 7 already started to resorb the bone before inhibitor treatment was started.

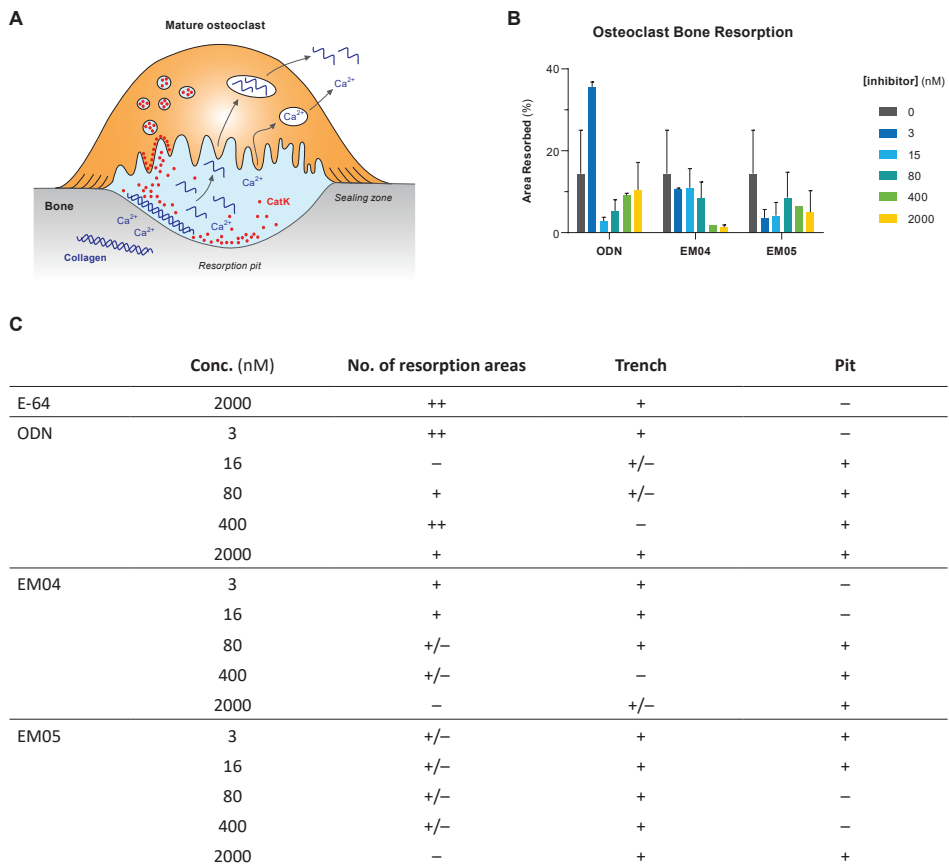


Figure S6 | Bone resorption by human osteoclasts. Data accompanying **Figure 7B**. **(A)** Schematic overview of osteoclast bone resorption. A resorbing osteoclast secretes lysosomal CatK into the acidified resorption lacunae, resulting in degradation of collagen I and bone demineralization. Adapted from Rodan and Duong.⁸⁴ **(B)** Quantification of bone resorption area. Bone resorption quantified as percentage of the total area on each bone slice. This measurement does not distinguish between pits and trenches, so depth of the resorption pit is not taken into account. **(C)** Qualitative assessment of bone resorption profile.

TRAcP staining and cell counting. Mature, resorbing osteoclasts are multinucleated and are TRAcP positive. Tartrate-resistant acid phosphatase (TRAcP) is a commonly used histochemical marker of osteoclasts, and secretion of TRAcP is correlated with resorptive behavior.⁸⁵ TRAcP is upregulated upon selective CatK inhibition (either genetic or pharmaceutical).⁵⁶ The number of mature osteoclasts increased upon treatment with high inhibitor concentrations (**Figure S7**).

qABP labeling. Osteoclast (OC) lysates were incubated with quenched activity-based probe (qABP) BMV109, that forms a fluorescent protease–qABP adduct with active, uninhibited protease (**Figure S8A**, see also **Figure S2**). Fluorescence scan reveals that only small amounts of mature CatK are present in DMSO-treated OCs, possibly because mature CatK is self-degrading. Coomassie protein staining shows that differences in mature CatK are not the result of loading differences. The observed CatK activity in ODN-treated OC lysates is an artifact and does not reflect CatK activity in the lysate: excess of irreversible qABP can outcompete reversible inhibitor ODN from CatK-ODN complexes and adducts.

Western Blotting. Osteoclast lysates were loaded as concentrated as possible (10 μ L/lane) because the CatK concentration in OC lysate is otherwise too low for detection, even when using an HRP secondary antibody to amplify the signal. The different CatK species – full-length proCatK_{1–329}, proCatK_{16–329} without the signal peptide, and mature CatK_{115–329} – can clearly be identified in the mature CatK and proCatK controls (**Figure S8B–C**). An increase in mature CatK is observed for ODN (all concentrations), and high concentrations of EM04 and EM05.

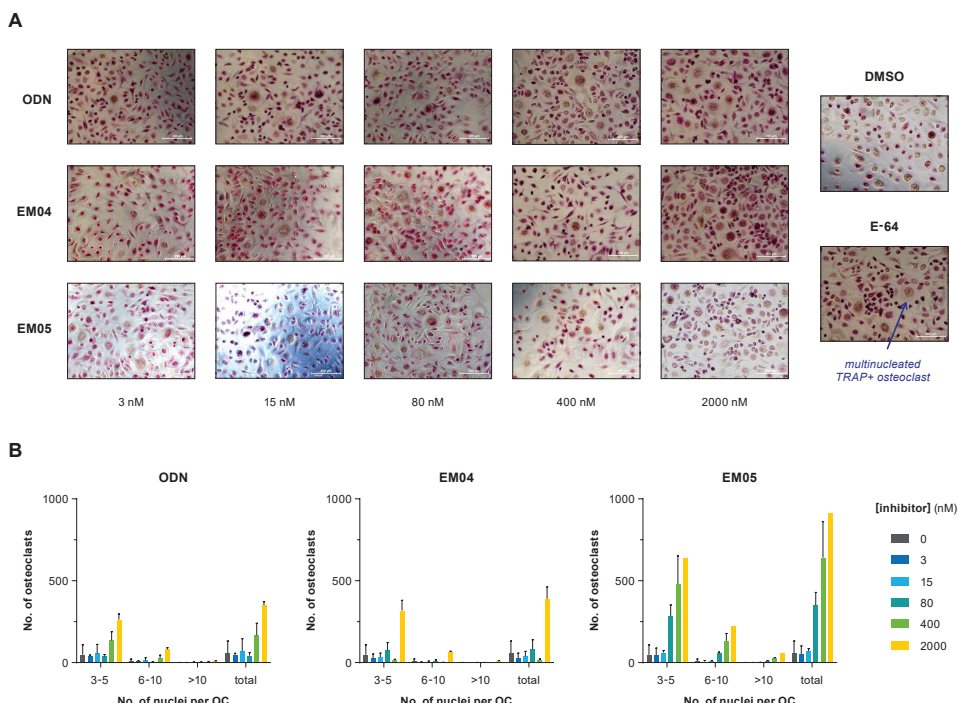


Figure S7 | Counting mature OCs on plastic. **(A)** Representative TRAcP-stained OCs on plastic treated with ODN, EM04 or EM05. **(B)** Osteoclast formation on plastic with different inhibitor concentrations. For all inhibitors, an increase in the number of mature OCs is observed at high inhibitor concentration.

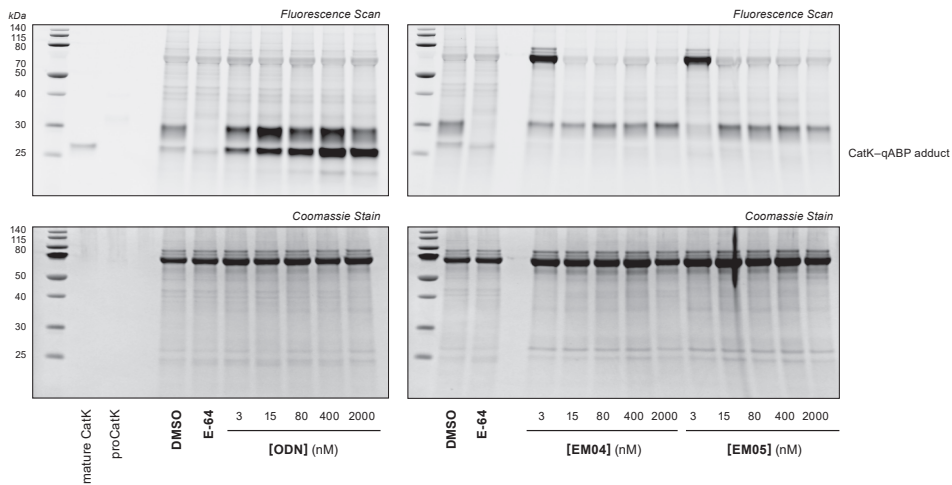
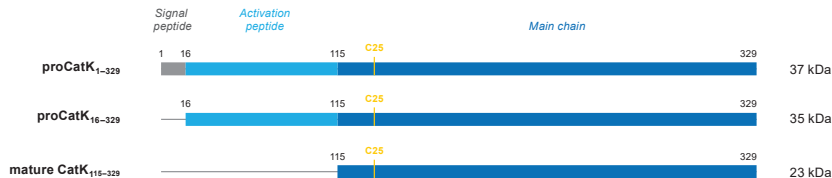
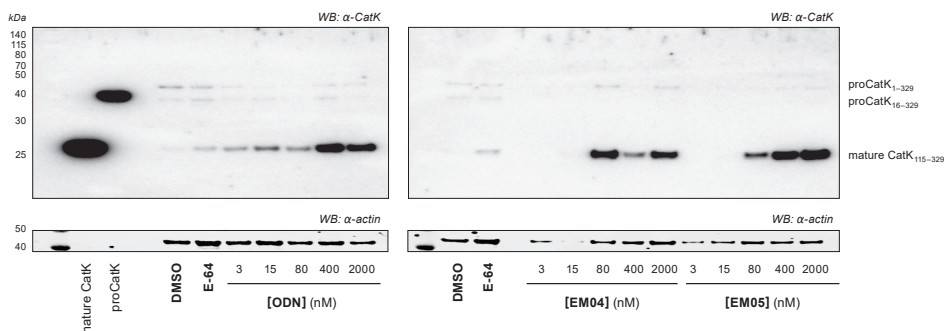
A CatK activity in OCs**B****C** CatK expression in OCs

Figure S8 | CatK activity and expression in osteoclast (OC) lysates. Data accompanying **Figure 7C**. **(A)** Full gel scans for OC lysates treated with qABP BMV109 (1 μ M) for 2 h. Darker bands = more CatK activity. *Top*: Fluorescence scan ($\lambda_{\text{ex}} = 635$ nm, $\lambda_{\text{em}} = 665$ nm) for protease–qABP adducts. *Bottom*: Coomassie protein stain as loading control. **(B)** Schematic overview of various cathepsin K species. Inactive proCatK is activated by acid-mediated autoproteolysis to form mature, active CatK.⁵⁵ **(C)** Full blots for OC lysates. *Top*: anti-CatK (chemiluminescence). *Bottom*: anti-Actin ($\lambda = 785$ nm).



Chapter 5



Covalent EGFR Inhibitors With a Nonactivated Alkyne Warhead

Abstract. Irreversible covalent inhibitors have a crucial role in (receptor) kinase inhibition as they were able to overcome (acquired) resistance to noncovalent inhibitors. Targeted kinase inhibitors (TKIs) covalently target a noncatalytic cysteine thiol at the ATP binding site of the target kinase, that is not present in related kinases. In this work, we investigate if the nonactivated alkyne can be used as a latent electrophile targeting noncatalytic Cys797 in EGFR, as this would reduce the metabolic inactivation and improve the safety profile. To this end, we replaced the acrylamide warhead in approved covalent pan-HER inhibitor **neratinib** (Nerlynx, HKI-272) with a propargylamine (**8RK57**) or 1-amino-3-butyne (**8RK58**). Alkyne-based inhibitors do not exhibit indiscriminate thiol reactivity and potently inhibit EGFR activity, both on recombinant protein as well as in cellular EGFR (auto)phosphorylation assays. Conclusive evidence on a covalent binding mode was not found, and further studies (with alkyne derivatives of other kinase inhibitors) are required to conclude whether the nonactivated alkyne warhead is compatible with kinases such as EGFR, and noncatalytic cysteine thiols in general.



1. Introduction

Many regulatory pathways that keep a cell in check are disrupted in cancer, leading to uncontrollable growth, eventually at the expense of life itself.¹ Traditional cytotoxic chemotherapies cause DNA damage beyond repair thereby inducing cell death, but this is a blunt weapon: all dividing cells will be affected, but cancer cells are affected more because these go through the cell cycle faster (divide more regularly).² Personalized or precision medicine is a more selective approach: the genetic or phenotypic tumor profile is used to identify (mutated) proteins or receptors that are (over)expressed in the tumor cells, and treated with targeted therapies that specifically inhibit the function of these oncogenes.³⁻⁴ Tumor cells overexpressing an oncogenic kinase rely on its constitutive kinase activity for survival and/or proliferation – a phenomenon known as oncogene addition – and are disproportionately sensitive to blockage of this signaling: healthy cells express numerous kinases in lower quantities, so their growth and survival is less affected by inhibition of a single kinase.⁵⁻⁶ This led to the development of orally bioavailable targeted kinase inhibitors (TKIs) that specifically inhibit the activity of important oncogenic (mutant) kinases such as the BCR-Abl fusion protein, the BRAF^{V600E} mutant, and growth factor receptor HER2.⁷⁻¹⁰

Overexpression of epidermal growth factor receptors (ErbB/HER) is associated with malignant phenotypes in several cancer types including breast, non-small cell lung, colorectal and ovarian cancer.¹¹ The HER/ErbB family of RTKs (receptor tyrosine kinases) has four members; EGFR (also known as HER1, ErbB1), HER2 (ErbB2), HER3 (ErbB3) and HER4 (ErbB4) (**Figure 1A**). Growth factor-mediated signal transduction is generally initiated by dimerization of EGFR with another EGFR (homodimerization) or with an ErbB receptor family member (heterodimerization) upon extracellular binding of EGF (epidermal growth factor) or an EGF-like ligand.¹¹ HER2 – the most oncogenic RTK of the ErbB family – is the favored RTK for EGFR heterodimerization as it does not require ligand-induced conformational change prior to dimerization and has little ability to self-regulate: there is no known growth factor/ligand for HER2.¹¹⁻¹³ An inactive RTK monomer consists of a ligand-binding extracellular domain (ECD), a hydrophobic transmembrane domain, an intracellular tyrosine kinase domain (TKD) and a C-terminal tail (**Figure 1B**). Ligand-mediated receptor dimerization induces intracellular conformational changes in the cytoplasmic tyrosine kinase domain which adopts an active kinase conformation.¹⁴ The active TKD then mediates phosphorylation of specific tyrosine residues on the C-terminal tail of the dimerization partner (*trans*-autophosphorylation), initiating phosphorylation of intracellular signaling kinases thus activating oncogenic downstream signaling pathways implicated in proliferation, survival, adhesion, invasiveness, migration and tumor angiogenesis, eventually leading to tumor growth and survival.¹⁴⁻¹⁵

Two classes of approved targeted cancer therapies directly interfere with EGFR and/or HER2 signaling: extracellular monoclonal antibodies (mAb) and intracellular targeted kinase inhibitors (TKI) (**Figure 1B**). Monoclonal antibodies are immunoglobulins that bind to the ECD; cetuximab (Erbitux) prevents receptor dimerization by obstructing ligand binding to EGFR,²⁰⁻²¹ trastuzumab (Herceptin) blocks constituent activation and dimerization of HER2,²² and pertuzumab (Perjeta, 2C4) blocks the dimerization domain of HER2.²³ Antibody therapy is characterized by high target selectivity but is not effective against mutant RTKs that have

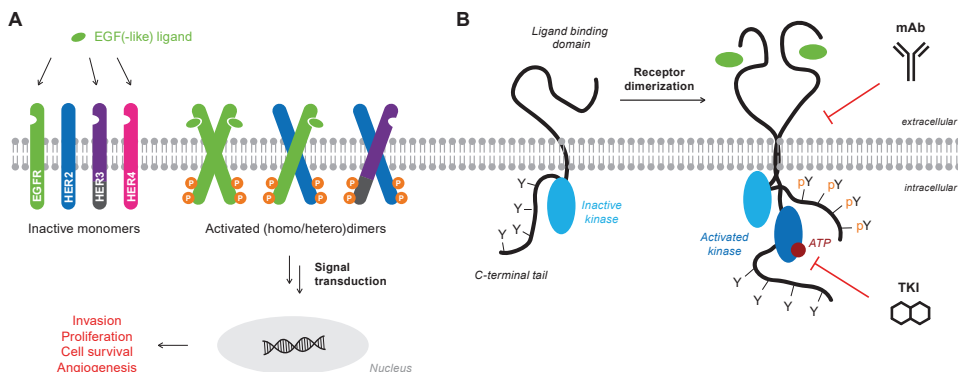


Figure 1 | Activation and inhibition of EGFR/HER2-mediated signal transduction. (A) Extracellular binding of growth factor to inactive ErbB receptor tyrosine kinase (RTK) monomers promotes receptor (homo/hetero) dimerization, which initiates downstream phosphorylation of an oncogenic signaling cascades eventually leading to tumor growth and survival. HER2 and HER3 are exceptions to this general mechanism; there is no known growth factor/ligand for HER2 (depicted as missing a ligand binding domain) and HER3 is believed to have an inactive “pseudokinase” domain that is not activated upon dimerization (displayed as gray area) but is *trans*-phosphorylated by its heterodimerization partner for cell signaling.¹⁶⁻¹⁷ The HER2/HER3 heterodimer is the most active signaling unit upon neuregulin stimulation, making HER3 the optimal dimerization partner for HER2 despite HER3 not having (significant) kinase activity.¹⁸⁻¹⁹ (B) EGFR dimerization induces intracellular conformational changes that activate the kinase domain for *trans*-autophosphorylation of the C-terminal tail. Monoclonal antibodies (mAbs) interfere with the extracellular receptor dimerization/activation while tyrosine kinase inhibitors (TKIs) block ATP binding to the intracellular kinase domain. Adapted from Ferguson.¹⁴

a consecutively active kinase domain or lack most of the extracellular binding domain; an issue observed with HER2⁺ tumors since the ECD of HER2 is redundant for its activity, and is often cleaved by proteases.^{18, 24} TKIs are small molecule inhibitors that bind to the intracellular kinase domain at the ATP-binding site, thereby inhibiting receptor (auto)phosphorylation.²⁵ HER2-targeting TKIs have a number of advantageous characteristics over the HER2-targeting mAb therapies, such as oral bioavailability – instead of intravenous dosing with mAbs – and their ability to cross the blood-brain barrier required to treat brain metastases that commonly occur in patients with HER2⁺ breast cancer.²⁴ HER2-targeting TKIs in combination therapy with cytostatic agent capecitabine were found to effectively treat and prevent formation of brain metastases.²⁶⁻²⁷ Furthermore, HER2-targeting TKIs directly interfere with kinase activity, thereby retaining activity against the highly active p95HER2 mutant – a truncated form of HER2 that lacks most of the ECD rendering it resistant to mAb therapy (e.g. trastuzumab).^{24, 28} To date, noncovalent dual EGFR/HER2 TKI lapatinib (Tykerb, GW572016), noncovalent HER2-selective TKI tucatinib (Tukysa, ONT-380), and covalent pan-HER TKI neratinib (Nerlynx, HKI-272) have been approved for HER2⁺ breast cancer.²⁹⁻³²

Initially, the kinase ATP-binding site was considered a poor drug target: TKIs need to overcome competition with 1-5 mM cellular ATP concentrations that greatly exceed the micromolar ATP affinity,³³ and ATP is a substrate for many other kinases and non-kinase proteins, thereby challenging the development of inhibitors selective for a single kinase.¹¹ Identification of the 4-anilinoquinazoline core significantly improved the potency towards EGFR and led to

the approval of first-generation noncovalent TKIs erlotinib (Tarceva, OSI-774) and gefitinib (Iressa, ZD1839) for treatment of NSCLC (non-small cell lung cancer) (**Figure S1**).¹¹ However, clinical drug resistance to first-generation TKIs inevitably occurred within 1-2 years after starting therapy,³⁴⁻³⁷ because acquired point mutation (T790M) of gatekeeper threonine residue at the ATP-binding site causes steric hindrance while increasing the ATP affinity (**Table S1**, **Table S2**).³⁸⁻³⁹ Second-generation TKI afatinib (Gilotrif, BIBW 2992) overcame this resistance by covalent targeting of the exposed thiol side chain of a nonconserved cysteine residue that is uniquely present located at the ATP-binding site of the ErbB/HER family (Cys797 in EGFR, Cys805 in HER2) while not being present in other closely related kinase families.^{33, 40-41} Third-generation EGFR TKIs with selectivity for EGFR mutants over EGFR^{WT} have been developed to reduce dose-limiting toxicity – e.g. skin rash and gastrointestinal adverse effects occur at clinically relevant doses for NSCLC treatment – which is associated with concurrent inhibition of EGFR^{WT} in healthy tissue.^{25, 39} The mutational burden in HER2-overexpressing breast cancers is lower than in NSCLC, and simultaneous inhibition of EGFR^{WT} (homodimerization) and HER2 (heterodimerization) is an effective strategy.⁴²⁻⁴⁴ Fourth-generation TKIs and combination therapies are currently in (pre)clinical development to overcome the inevitable resistance to covalent TKIs in NSCLC.^{25, 34, 40}

The clinical approval of covalent TKIs targeting (mutant) EGFR/HER2⁴⁵⁻⁴⁸ and the vast number of covalent TKIs in (clinical) development⁴⁹⁻⁵⁰ illustrate the success of a covalent binding mode.^{7, 41, 51} Irreversible covalent inhibition did not only overcome ATP competition (**Table S2**) but also improved therapeutic efficiency with a prolonged effect long after metabolic clearance since kinase activity is not regained until *de novo* protein synthesis (PK-PD decoupling).^{45, 52-53} Safety concerns pertaining the intrinsic ability to form a covalent bond with (nontargeted) thiols no longer automatically eliminate irreversible covalent inhibitors in drug discovery, but low reactivity with nontargeted thiols is desirable nonetheless; adduct formation with biologically relevant thiols reduces the concentration of available unbound inhibitor thereby increasing metabolic clearance and impairing clinical potency.⁴⁸

Targeting EGFR with covalent (nonactivated) alkynes. In our previous work,⁵⁴ we demonstrated that the nonactivated alkyne moiety can be employed to covalently target the catalytic cysteine residue of CatK without showing intrinsic reactivity towards nontargeted thiols. In this work, we investigate whether the scope of the nonactivated alkyne warhead can be expanded to TKIs targeting noncatalytic cysteine residues. As a proof-of-concept, we replaced the warhead in covalent pan-HER TKI neratinib⁵⁵⁻⁵⁶ with a nonactivated alkyne moiety, and evaluated the biochemical potency and binding mode of our analogues.

2. Results and Discussion

Synthesis and design of neratinib analogues. Nonactivated alkyne derivatives were designed with carefully alignment of the reactive alkyne carbon with the reactive acrylamide carbon, by adjusting the linker length (**Figure 2**). The acrylamide warhead of neratinib is introduced in the final synthesis step by reacting 6-amino-quinoline **1** with an acid chloride,⁵⁷⁻⁵⁹ or at an earlier stage in the synthesis using the same amidation methodology.⁵⁶ This synthetic strategy

had to be adjusted to incorporate alkyne warheads connected to the quinoline core through a secondary aniline bond instead of an amide group. Alkyne derivatives 8RK57 and 8RK58 were obtained by treatment of 6-bromoquinoline **2** with propargylamine or 1-amino-3-butyne under Buchwald-Hartwig amination conditions as recommended in the user guide by Surry and Buchwald.⁶⁰ A detailed synthetic scheme is provided in **Scheme S1**.

Indiscriminate thiol reactivity. Promiscuous covalent thiol binding of irreversible covalent cysteine-targeting drugs can be assessed with reduced glutathione (GSH) – a naturally occurring tripeptide that traps reactive electrophiles (thus protecting the cell) and is widely used as a benchmark reagent.⁶¹⁻⁶⁵ Intrinsic chemical reactivity of (clinical) drug candidates can be assessed by LC-MS detection of unbound inhibitor and covalent inhibitor–thiol adduct upon incubation with a large excess of GSH in aqueous buffer (**Figure 3A**).⁶³⁻⁶⁷ Unbound inhibitor and GSH adduct were quantified from the baseline-separated UV absorbance areas after various incubation times following established protocol.⁶⁷ As expected, significant GSH adduct formation was observed with acrylamides afatinib and neratinib but not with noncovalent inhibitor gefitinib nor with alkyne derivatives 8RK57 and 8RK58 (**Figure 3B**).

Covalent EGFR-alkyne adduct is not detected by intact protein MS. Top-down mass spectrometric (MS) analysis of intact protein (adduct) was next performed to evaluate if our alkyne derivatives have a covalent binding mode.⁶⁸ Adduct formation of recombinant purified EGFR kinase domain with covalent inhibitors has been reported,⁶⁹⁻⁷⁰ therefore EGFR (instead of HER2) was selected for MS analysis. Commercially available EGFR kinase domains all had a GST tag (26 kDa), and preliminary MS analysis of unbound recombinant GST-EGFR kinase domain revealed poor ionization and did not form an ionization envelope that could be deconvoluted, possibly related to its large size (>90 kDa) or unfavorable properties of the GST tag (**Figure 4A**).⁷¹⁻⁷² An untagged construct of the EGFR kinase domain (695-1022) has previously been used in intact protein MS studies to detect the covalent EGFR-dacomitinib adduct,⁶⁹ and the His-tagged version of this construct was indeed compatible with top-down MS (**Figure 4B**). His-EGFR was submitted to LC-MS analysis after incubation with DMSO (unbound) or excess inhibitor for 4 hours. An increase in the deconvoluted mass corresponding with addition of covalent inhibitor was detected upon incubation with covalent inhibitor neratinib, but not with noncovalent inhibitor gefitinib or with alkynes 8RK57 and 8RK58 (**Figure 4B**). Extending the incubation time to 24 hours incubation at room temperature also did not result in detection of a covalent adduct with alkynes 8RK57 and 8RK58 (**Table S4**). Increasing the reaction temperature to speed up the reaction was not a viable strategy as this impaired protein stability and had a detrimental effect on the resolution. Altogether, a covalent EGFR-alkyne adduct was not detected by top-down MS analysis.

Alkynes exhibit tight-binding behavior in a LanthaScreen kinase binding assay. Our efforts shifted to evaluation of biochemical EGFR binding, and whether the alkyne derivatives exhibit time-dependent behavior, as this is a hallmark of (irreversible) covalent inhibition.^{52, 75} Considering the dramatic reduction in noncovalent affinity that was observed for alkyne derivatives of ODN,⁵⁴ we decided to evaluate EGFR binding potency in the LanthaScreen Eu kinase binding assay: this homogeneous assay is conducted in absence of competing ATP and has successfully been used to evaluate biochemical binding potency and binding reversibility

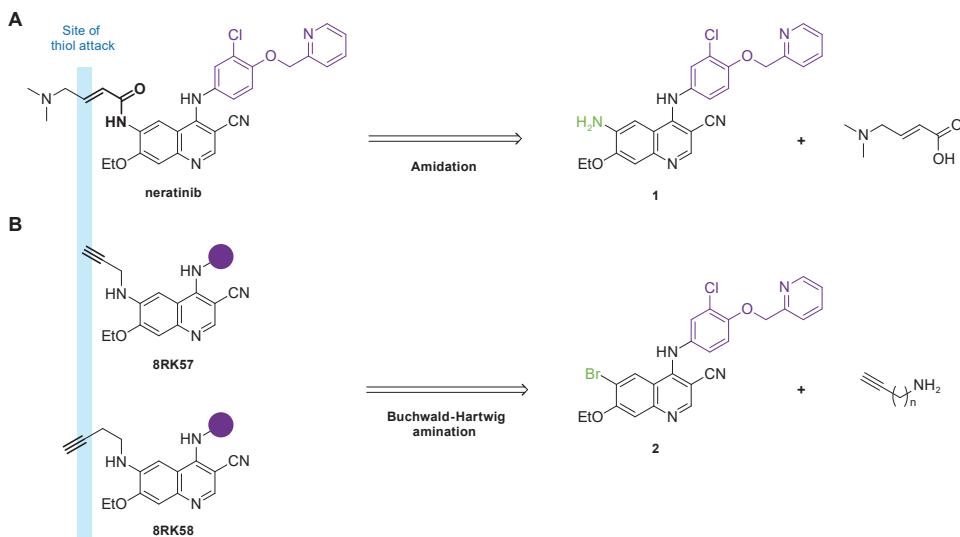


Figure 2 | Synthetic strategy and design of neratinib (derivatives). Alkynes were introduced onto the quinoline core with alignment of the reactive carbon. **(A)** Introduction of acrylamide warhead by late-stage amide coupling. **(B)** Preparation of alkyne derivatives **8RK57** and **8RK58** using Buchwald-Hartwig amination conditions. The 6-bromoquinoline **2** building block was obtained from Mercachem (see also **Scheme S1**).

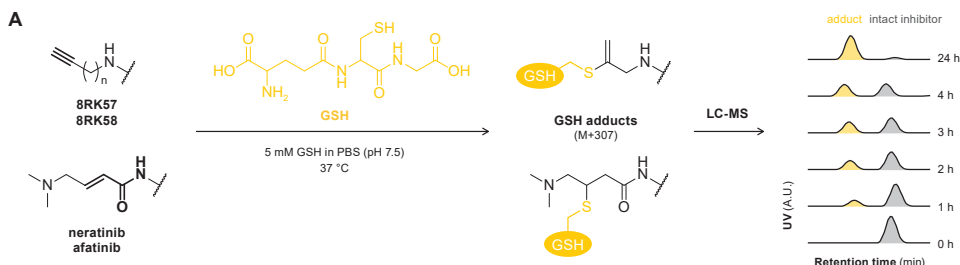


Figure 3 | Intrinsic thiol reactivity assessed by LC-MS analysis following established protocol.^{54, 67} **(A)** Schematic overview. Parent compound and GSH adduct are quantified from the LC-MS UV trace ($\lambda_{\text{abs}} = 350 \text{ nm}$) after incubation with 5 mM GSH. **(B)** Time-dependent GSH adduct formed upon incubation with 5 mM GSH as percentage of total UV area (left) and fitted kinetic parameters (right). Values are mean \pm SD. k_{GSH} = pseudo-first order reaction rate constant reflecting intrinsic GSH reactivity. Retention times, m/z values and integrated UV areas used for quantification are provided in **Table S3**. Details on calculations of GSH occupancy and fits can be found in *section 4.1*.

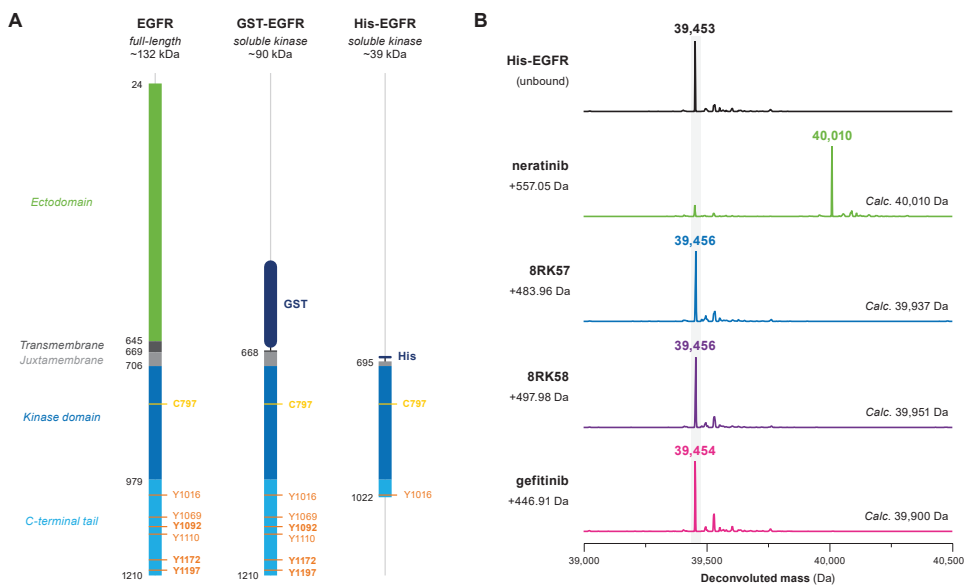


Figure 4 | Direct detection of covalent EGFR–inhibitor adducts by intact protein MS analysis. **(A)** Schematic alignment of full-length EGFR with recombinant kinase domains GST-EGFR and His-EGFR. Adapted from Jura⁷³ and Cho.⁷⁴ EGFR has multiple tyrosine autophosphorylation sites (marked in orange) on its C-terminal tail, which have been omitted in the His-EGFR kinase construct used for intact protein MS analysis. **(B)** Deconvoluted mass of recombinant His-EGFR kinase domain (1 μ M) incubated with inhibitor (100 μ M) for 4 hours at room temperature. Deconvoluted mass with acrylamide neratinib matches the calculated mass of the covalent adduct, but not for noncovalent inhibitor gefitinib or with alkyne derivatives 8RK57 and 8RK58. Full UPLC traces and ionization envelopes provided in **Figure S2**.

of various kinase inhibitors.⁷⁶ EGFR binding potency is detected based on inhibitor-mediated displacement of FRET acceptor tracer 199 (KT199), resulting in a lower FRET signal than in the uninhibited control (**Figure 5A**).⁷⁷⁻⁷⁸ KT199 consists of FRET acceptor AlexaFluor647 (AF647) conjugated to staurosporine – a known pan-kinase inhibitor that binds at the kinase ATP-binding site (**Figure S3A**, **Table S2**). At a tracer concentration of 25 nM (below the tracer K_m of 45 nM, **Figure S3B**) the TR-FRET originating from the biological binding event was optimally balanced with an acceptable background originating from diffusion-enhanced FRET (**Figure 5B**). To evaluate inhibitor potency of tracer displacement, an adjusted kinetic Probe Competition Assay (kPCA) protocol was employed, following tracer binding in presence of inhibitor after reaction initiation by EGFR addition.⁸¹⁻⁸² Neratinib was unable to fully displace the tracer even at concentrations far above its reported potency ($IC_{50} = 1$ nM),⁸³ possibly because inhibitor binding does not fully block tracer binding (**Figure 5C**). To our surprise, maximum tracer displacement by 8RK57 and 8RK58 was achieved at reaction initiation, indicative of potent ($IC_{50} < 20$ nM) binding (**Figure 5C**). This high potency is not indicative of a covalent binding mode: the reported potency of TKIs for the EGFR^{C797S} mutant is in the nM range even though a covalent adduct cannot be formed.⁸⁴ Efforts to resolve this tight-binding behavior were unsuccessful (**Figure S3C**). Instead, we evaluated inhibitory potency in an enzymatic activity assay in presence of competing ATP.

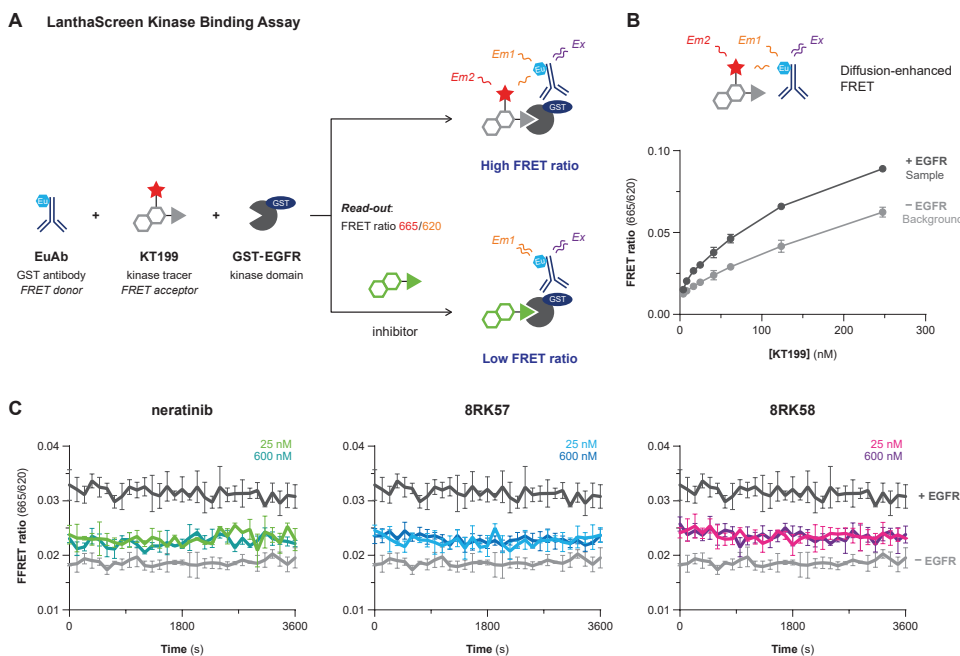


Figure 5 | Biochemical binding potency assessed in a Lanthaseen Eu Kinase Binding Assay. Details on assay optimization are provided in *section 7.5*. **(A)** Assay principle. Upon excitation, Time-Resolved Fluorescence Resonance Energy Transfer (TR-FRET)⁷⁹⁻⁸⁰ is detected if the FRET donor EuAb (lanthanide Europium (Eu) chelated to an anti-GST antibody) and the FRET acceptor tracer KT199 (AlexaFluor647 conjugated to pan-kinase inhibitor staurosporine, shown in **Figure S3A**) simultaneously bind to the recombinant GST-EGFR kinase domain. KT199 and ATP-competitive inhibitors competitively bind at the kinase ATP binding site, resulting in a dose-dependent decrease of the FRET ratio (acceptor emission/donor emission) as inhibitor outcompetes tracer. **(B)** FRET ratio in absence or presence of EGFR (2 nM) shows tracer-dependent background due to diffusion-enhanced TR-FRET. **(C)** Kinetic probe competition assay (kPCA). Displacement of tracer KT199 (25 nM) by inhibitor (25–600 nM), with reaction initiation by EGFR (2 nM) addition. Maximum tracer displacement was already achieved at reaction initiation.

Alkynes do not exhibit time-dependent behavior in a PhosphoSens kinase activity assay. Most commercial assays to evaluate biochemical kinase inhibition are not compatible with continuous kinetic measurements⁸⁵⁻⁸⁶ because they require a blocking/quenching/development step prior to read-out for detection of substrate phosphorylation⁸⁷ or (³²P-labeled) ADP formation/ATP consumption.⁸⁸⁻⁸⁹ Contrastingly, kinase activity assays based on the Sox technology (PhosphoSens® and its predecessor Omnia®) enable continuous detection of phosphorylation of a Sox-containing peptidic substrate^{86, 90-91} in presence of physiological ATP concentrations (1 mM) (**Figure 6A**). This technology is the benchmark method to analyze biochemical potency of covalent clinical candidates,⁹²⁻⁹⁷ and was selected to evaluate inhibitor potency.⁹⁸

An established method based on kinetic measurement of substrate processing under pseudo-first order reaction conditions (see also *Method I* in **Chapter 3**)⁹⁹ was employed, thus requiring an absolutely linear curve in the uninhibited sample.¹⁰⁰ Covering the wells with an

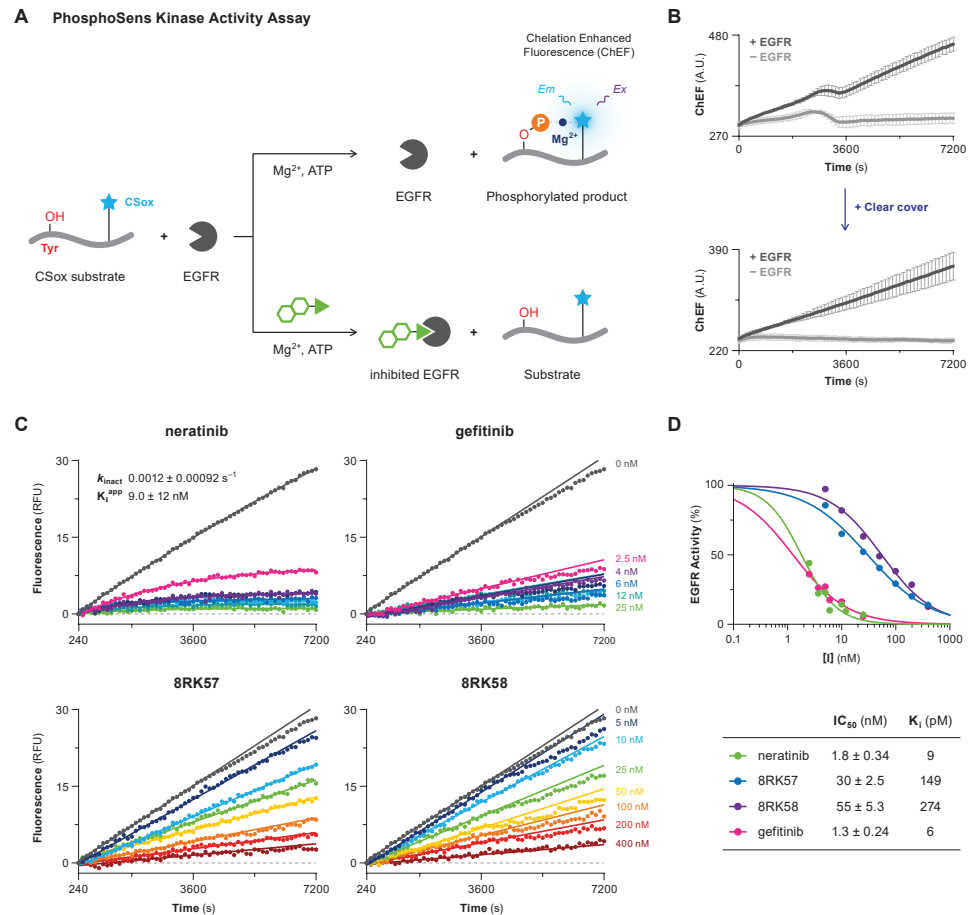


Figure 6 | Biochemical EGFR inhibition assessed with PhosphoSens kinase activity assay, in presence of 1 mM ATP. **(A)** Assay principle of the CSox technology for fluorescent kinase activity assays. Phosphorylation of a nearby tyrosine residue increases the Mg²⁺ affinity of the unnatural fluorogenic CSox amino acid, resulting in detection of Chelation-Enhanced Fluorescence (ChEF). ¹⁰⁸⁻¹⁰⁹ See also **Figure S4A** for details and structure of the CSox substrate. **(B)** Assay optimization with GST-EGFR kinase domain. Aberrant nonlinearity incompatible with progress curve analysis (*top*) was resolved by covering the wells with a clear adhesive cover (*bottom*). **(C)** Progress curves for CSox substrate phosphorylation initiated by GST-EGFR (0.25 nM) addition, with kinetic competitive association of 2.5-25 nM (gefitinib, neratinib) or 5-400 nM (8RK57, 8RK58) inhibitor. The first 4 min were omitted to correct for a lag in EGFR activity (more details in *section 7.6*). **(D)** Dose-response curves for EGFR phosphorylation assay in presence of 1 mM ATP. IC₅₀ values represent mean ± standard deviation. Inhibitory constant K_i calculated based on reported K_{M,ATP} = 5 μM for EGFR^{WT}.¹¹⁰

optical clear cover, per recommendation by the supplier to prevent ‘drift’¹⁰¹ surprisingly also resolved the aberrant nonlinearity observed in the kinetic progress curves of CSox substrate phosphorylation in absence and presence of EGFR kinase domain (**Figure 6B**). This aberrant nonlinearity is not a unique property related to Chelation-Enhanced Fluorescence ($\lambda_{\text{ex}} = 360$ nm, $\lambda_{\text{em}} = 492$ nm): we previously observed a similar effect in kinetic assays with detection of fluorescent AMC ($\lambda_{\text{ex}} = 350$ nm, $\lambda_{\text{em}} = 440$ nm), Rho110-Gly ($\lambda_{\text{ex}} = 487$ nm, $\lambda_{\text{em}} = 535$ nm),

and Rhodol ($\lambda_{\text{ex}} = 490 \text{ nm}$, $\lambda_{\text{em}} = 545 \text{ nm}$) (*unpublished data*). Optimization of assay conditions is further discussed in *section 7.6*. EGFR activity in presence of covalent inhibitor neratinib exhibited a clear time-dependence (**Figure 6C**), with kinetic parameters in agreement with reported values.⁹³ Desired EGFR reactivity – reflected in k_{inact}/K_I – is several magnitudes bigger than the thiol reactivity reflected in k_{GSH} (**Figure 3B**).¹⁰² Time-dependence was not observed for noncovalent inhibitor gefitinib or alkyne derivatives 8RK57 and 8RK58, so their potency for EGFR inhibition is reflected in the equilibrium IC_{50} , which was in the nM range (in presence of 1 mM ATP) (**Figure 6D**).

Irreversible inhibition of cellular EGFR (auto)phosphorylation. Inhibition of cellular EGFR (auto)phosphorylation was evaluated with EGFR activity assays in intact HeLa cells¹⁰³⁻¹⁰⁴ – a cervical cancer cell line expressing EGFR and HER2 (HER2⁺, EGFR⁺)¹⁰⁵⁻¹⁰⁶ without surface expression of HER3.¹⁰⁷ Briefly, HeLa cells starved of nutrients were incubated with 1 μM inhibitor, optionally followed by treatment with EGF to stimulate receptor (auto)phosphorylation, followed by immunoblotting for EGFR and phosphorylated tyrosine (pY). Visual inspection of the blots indicates that all tested inhibitors inhibited EGFR (auto)phosphorylation at this concentration (**Figure 7A**). Inhibitor reversibility was evaluated in a washout experiment: after incubation with inhibitor (and optionally EGF stimulation), culture medium was replaced by inhibitor-free medium and cells were incubated for another hour (**Figure 7B**). This washout removes unbound inhibitor and stimulates dissociation of reversibly bound inhibitors, thus resulting in higher levels of phosphorylated EGFR for reversible inhibitors while inhibition is retained for inhibitors with an irreversible covalent binding mode. In samples that were not stimulated with EGF (**Figure 7C, left**), increased EGFR phosphorylation was indeed observed for reversible inhibitor gefitinib while irreversible inhibitors afatinib and neratinib continued to block receptor (auto)phosphorylation. Surprisingly, EGFR phosphorylation levels with 8RK57 or 8RK58 were not significantly affected by the washout, indicative of an irreversible binding mode. A clear increase in EGFR phosphorylation was observed for all inhibitors in the EGF-stimulated samples after washout (**Figure 7C, right**). This can be attributed to *de novo* expression of active EGFR protein during the 1 hour incubation with EGF following inhibitor depletion: EGF stimulation in cell culture promotes lysosomal degradation of internalized EGFR, resulting in a much shorter metabolic half-life of EGFR in presence of EGF ($t_{1/2} = 1.5 \text{ h}$) than in absence of EGF ($t_{1/2} = 6.5 \text{ h}$).¹¹¹ A preliminary dose-response experiment with EGF-stimulated HeLa cells resulted in a cellular potency of 2 nM for neratinib (**Figure 7D**) – similar to the reported inhibitory potency for (auto)phosphorylation of EGFR ($\text{IC}_{50} = 3 \text{ nM}$) and HER2 ($\text{IC}_{50} = 5 \text{ nM}$) in cellular assays on skin cancer cell line A431 (HER2⁺, EGFR⁺⁺⁺) and breast cancer cell line BT474 (HER2⁺⁺⁺, EGFR⁺).¹¹² Alkyne derivatives 8RK57 and 8RK58 are >20-fold less potent than neratinib, in line with our findings in the kinase activity assay on recombinant GST-EGFR kinase domain (see **Figure 6D**). Interestingly, the IC_{50} of 30 nM for gefitinib is much higher than its potency on recombinant EGFR. This may be attributed to the low HER2 inhibitory potency of gefitinib (see **Table S2**) as EGFR phosphorylation is detected using a general phosphorylated tyrosine (pY) antibody: phosphorylated HER2 (136 kDa) and phosphorylated EGFR (132 kDa) run at a similar height on gel, which ‘contaminates’ the results. To validate this hypothesis, follow-up experiments with an EGFR-selective phosphotyrosine antibody are required.

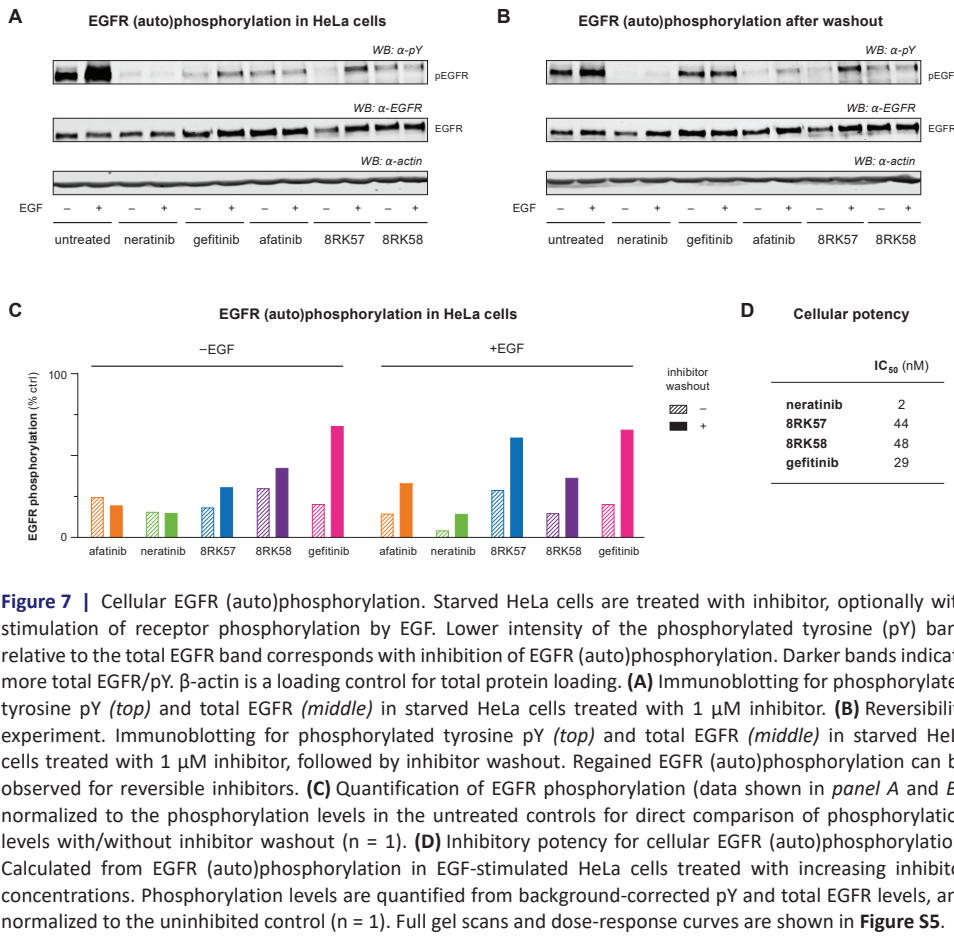


Figure 7 | Cellular EGFR (auto)phosphorylation. Starved HeLa cells are treated with inhibitor, optionally with stimulation of receptor phosphorylation by EGF. Lower intensity of the phosphorylated tyrosine (pY) band relative to the total EGFR band corresponds with inhibition of EGFR (auto)phosphorylation. Darker bands indicate more total EGFR/pY. β -actin is a loading control for total protein loading. **(A)** Immunoblotting for phosphorylated tyrosine pY (top) and total EGFR (middle) in starved HeLa cells treated with 1 μ M inhibitor. **(B)** Reversibility experiment. Immunoblotting for phosphorylated tyrosine pY (top) and total EGFR (middle) in starved HeLa cells treated with 1 μ M inhibitor, followed by inhibitor washout. Regained EGFR (auto)phosphorylation can be observed for reversible inhibitors. **(C)** Quantification of EGFR phosphorylation (data shown in panel A and B), normalized to the phosphorylation levels in the untreated controls for direct comparison of phosphorylation levels with/without inhibitor washout ($n = 1$). **(D)** Inhibitory potency for cellular EGFR (auto)phosphorylation. Calculated from EGFR (auto)phosphorylation in EGF-stimulated HeLa cells treated with increasing inhibitor concentrations. Phosphorylation levels are quantified from background-corrected pY and total EGFR levels, and normalized to the uninhibited control ($n = 1$). Full gel scans and dose-response curves are shown in Figure S5.

3. Conclusion and Outlook

In this work, we replaced the warhead in approved covalent kinase inhibitor neratinib (Nerlynx, HKI-272) with a propargylamine (**8RK57**) or 1-but-3-yne (**8RK58**) warhead to investigate whether nonactivated alkynes can covalently target noncatalytic Cys797 at the EGFR ATP-binding site. Covalent adduct formation with nontargeted thiol GSH was not observed, but intact protein MS analysis with recombinant EGFR indicated that covalent EGFR-alkyne adduct was not formed. Preliminary cellular assays were indicative of an irreversible binding mode but kinase activity assays on recombinant GST-EGFR kinase domain did not support this binding mode: **8RK57** and **8RK58** potently inhibit biochemical EGFR activity but did not exhibit time-dependent behavior. Together, these preliminary results indicate alkyne analogues **8RK57** and **8RK58** do not have a covalent binding mode. This may be attributed to experimental design and practical challenges, incompatibility with the mechanism of the thiol-alkyne reaction, or suboptimal inhibitor design.

We cannot exclude the possibility that 8RK57 and 8RK58 have a covalent binding mode, but that contribution of covalent adduct formation was too slow to have a detectable effect on the inhibitory potency, or that we did not detect the covalent adduct due to practical and experimental factors. The covalent thiol–alkyne reaction with the CatK catalytic cysteine residue was relatively slow,⁵⁴ and the reaction with a noncatalytic cysteine is expected to result in slower reaction rates: the nucleophilicity of EGFR noncatalytic Cys797 thiol ($pK_a \sim 5.5$)¹¹³ is less than catalytic cysteine thiolate ($pK_a \sim 4/4.5$) – though more nucleophilic than general thiols such as the glutathione thiol ($pK_a \sim 8.9$).¹¹⁴⁻¹¹⁵ Preliminary cellular experiments revealed that 8RK57 and 8RK58 effectively inhibit EGFR (auto)phosphorylation in HeLa cells, which was retained in washout experiments – an encouraging indication that 8RK57 and 8RK58 may have an irreversible binding mode. However, it was not possible to validate inhibitor (ir)reversibility in jump dilution assays with recombinant EGFR as we experienced technical/practical issues with diminishing EGFR activity and stability of recombinant EGFR. Recombinant GST-EGFR was unusually sensitive to freeze-thaw cycles and aliquoting, and loss of EGFR activity in single-use aliquots was inevitable: complete loss of enzymatic activity was observed after two freeze-thaw cycles (in the main stock) which could not be resolved by preparation of aliquots (in PCR tubes) as this also inactivated the enzyme. Further investigations into the stability and catalytic activity of recombinant EGFR constructs are desired.

In line with these findings, it is possible that the recombinant His-EGFR construct used for intact protein MS was in an inactive confirmation: all relevant tyrosines except Y1016 have been trimmed from the C-terminal tail. *In vitro* adduct formation with neratinib is expected to be less affected by subtle conformational changes in the recombinant His-EGFR kinase domain – the electrophilic acrylamide has a high intrinsic thiol reactivity (shown in **Figure 3**) – while this could severely impact the rate of *in situ* thiol–alkyne addition, especially compared to reactivity in a cellular context where the EGFR kinase domain is in an active conformation and has an intact C-terminal tail. This may provide an explanation to the lack of covalent EGFR–alkyne adduct detection but more conclusive evidence on the existence of a covalent adduct might be derived from experiments with native (full-length) EGFR – for example in cellular context using bottom-up MS after enrichment for EGFR, or with inhibitor-derived ABPs (these techniques are further discussed in **Chapter 2**).⁶⁸ Alternatively, 8RK57 and 8RK58 may actually not have a covalent binding mode. Based on the current data, we cannot exclude the possibility that the thiol–alkyne reaction is incompatible with noncatalytic cysteines in kinases such as EGFR because stabilization of a carbanion intermediate in the oxyanion hole (*mechanism D* in **Chapter 1**) is an essential step in covalent adduct formation. However, alkyne derivatives of other kinase inhibitors should be studied before concluding that nonactivated alkynes are incompatible as latent electrophiles to target noncatalytic cysteine thiols. The design of 8RK57 and 8RK58 may not have facilitated covalent adduct formation: thiol–alkyne adduct formation is a proximity-driven reaction, and suboptimal orientation or juxtaposition of the reactive carbon in the alkyne warhead hampers adduct formation. In **Chapter 4**,⁵⁴ we showed that a small molecule recognition element was sufficient to form a covalent adduct with alkyne **EM04** when we replaced the ODN nitrile group with an isosteric alkyne. To make alkyne analogues of neratinib, we had to replace an acrylamide moiety with a nonactivated alkyne which may have affected the positioning negatively.

The reactive warhead in neratinib is a 4-(dimethylamino)crotonamide: the acrylamide is modified with a polar, basic tertiary dimethylamine group on the β -carbon. The dimethylamine moiety improves aqueous solubility, and binding models suggest that it is a directing group that facilitates deprotonation of Cys805 to form the reactive thiolate (Figure 8A), thus promoting adduct formation with HER2 while sterically hindering adduct formation with nontargeted thiols.^{45, 83, 112} We did not include this directing group in our inhibitor design because it is not essential for the appropriate juxtaposition of the electrophile relative to the nucleophilic EGFR Cys797 thiolate: covalent TKIs including osimertinib (AZD-9292, Tagrisso) and canertinib (CI-1033, PD183805) covalently modify Cys797 without the need for this directing group. However, the dimethylamine group does contribute to potency: Wissner and Mansour⁵⁵ report that the cellular EGFR/HER2 potency of acrylamide **6** (PD168393) was lower than its dimethylamine derivative **9a**, and a similar trend was observed for 2-butyrynamide **7** (CL-387785, EKI-785)¹¹⁶ and its dimethylamine derivative **10**. Other indications of a beneficial contribution of a directing group are the basic piperidine moiety on the terminal position of approved TKI dacotinib (PF-00299804, Vizimpro): Wood *et al.*¹¹⁷ found that introduction of a basic pyrrolidine moiety onto the alkyne warhead increases the rate of EGFR adduct formation with 6-ethynyl-thienopyrimidines. It is worthwhile to investigate if introduction of a basic (tertiary) amine moiety on the terminal position of the nonactivated alkyne promotes covalent EGFR-alkyne adduct formation (Figure 8B). Neratinib displays a low off-target reactivity with Src kinase despite sharing the 4-phenylamino-3-quinolincarbonitrile core with ATP-competitive Src kinase inhibitors,¹¹⁸ which may be attributed to the 4-(dimethylamino) crotonamide warhead on the quinoline C6 position: introduction of water-solubilizing group on C6 has been reported to mitigate Src kinase inhibition.¹¹⁹ Nonactivated alkyne derivatives **8RK57** and **8RK58** likely exhibit off-target Src kinase reactivity, which may be mitigated by including a basic solubilizing group on the terminal position.

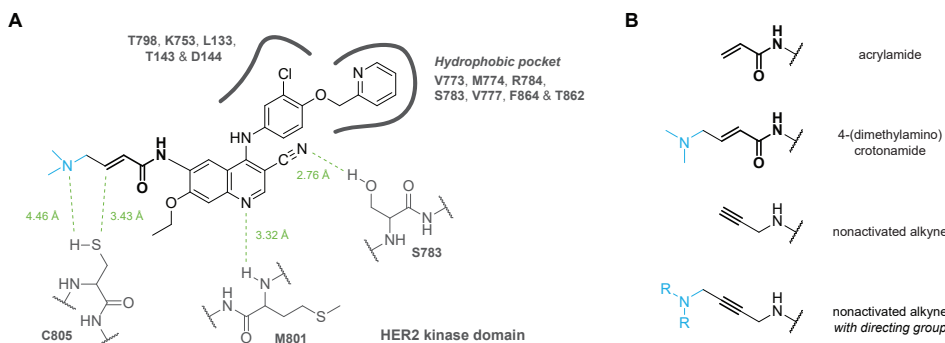


Figure 8 | Role of dimethylamine moiety as directing groups promoting covalent adduct formation. (A) Binding model of neratinib with HER2 before covalent adduct formation. Adapted from Tsou *et al.*⁵⁶ Introduction of the lipophilic 2-pyridinylmethyl motif improved HER2 potency by occupying a hydrophobic pocket. The basic dimethylamine moiety on the acrylamide warhead promotes adduct formation with HER2 Cys805.⁵⁵ (B) Structures of acrylamide warhead, 4-(dimethylamino)crotonamide warhead with a dimethylamine directing group on the terminal position, nonactivated alkyne warhead, and proposed nonactivated alkyne warhead with a basic directing group on the terminal position.

To investigate whether the nonactivated alkyne is compatible with kinases – the most prevalent category of irreversible covalent inhibitors – future efforts should be directed towards nonactivated alkyne derivatives of other scaffolds. Here, the focus should be on acrylamides rather than 4-(dimethylamino)crotonamides – these have a higher chance of success because they do not need a directing group – ideally targeting mutant EGFR as assay tools to study mutant EGFR adduct formation are more widely available compared to HER2. In this context, EGFR^{T790M}-selective inhibitor osimertinib (AZD-9292, Tagrisso) would be an appropriate model: the acrylamide has successfully been replaced to generate allenamide analogues,¹²⁰ indicating a flexibility in warhead architecture. Alternatively, replacing an electron-deficient alkyne with a nonactivated alkyne could be explored, such as the 2-butynamide warhead in 4-anilinopyrido[3,4-d]pyrimidine **29**,¹²¹ or in 4-anilinoquinazoline CL-387785 (EKI-785).¹¹⁶

To conclude, we were unable to demonstrate whether the nonactivated alkyne is a suitable latent electrophile for targeting the noncatalytic Cys797 in EGFR kinase. However, this is no definitive evidence that the nonactivated alkynes are unsuitable in general, and they still have a potential role in irreversible covalent TKI development. Future studies should be directed towards modification of the inhibitor scaffold and optimization of the electrophile position relative to the reactive cysteine thiol.

Acknowledgements

Patrick Celie (NKI protein facility) is thanked for the expression and purification of His-EGFR. Guido Janssen is thanked for his help with 2D NMR analysis of bromoquinoline **2** and Bjorn van Doodewaerd for his support with intact protein MS measurements.

Author Contributions

E.M.: Methodology, Investigation (*Chemical Synthesis, Biochemical Assays*), Writing – Original Draft. R.K.: Investigation (*Chemical Synthesis*). A.S.: Investigation (*Cellular Assays*), Writing – Review & Editing. R.Q.K.: Supervision, Writing – Review & Editing. M.P.C.M.: Supervision, Writing – Review & Editing. H.O.: Conceptualization, Supervision.

4. Materials and Methods: *Biochemistry*

General

Reaction buffers are freshly supplemented with DTT (Chem-Impex, #00127), stored in single-use aliquots at –20 °C (1M in water). Established EGFR TKIs neratinib (Adv. ChemBlocks, #10409) and afatinib are taken along as irreversible covalent inhibitor controls, and gefitinib (SigmaAldrich, #SML1657) as reversible noncovalent inhibitor control. Purified recombinant human EGFR (UniProtID: P00533) kinase domains used in this work can be found below.

Enzyme	Tag	Domain	Source or reference
His-EGFR	His	CD ^{WT} (695-1022)	<i>In-house</i> . This work
GST-EGFR	GST	CD ^{WT} (668-1210)	ThermoFisher, #PV3872
GST-EGFR	GST	CD ^{WT} (668-1210)	SignalChem, #E10-112G

4.1. Intrinsic Thiol Reactivity Assay

A reaction mixture containing inhibitor (100 μ M) and GSH (5 mM) in PBS (10 mM phosphate buffer pH7.45, 140 mM NaCl, 2.7 mM KCl) was incubated at 37 °C under gentle agitation (300 rpm) for the indicated incubation time (0/1/2/3/4/24 h) after which a sample (25 μ L) was removed. The samples were quenched by 2-fold diluted in 0.1% FA (aq) and submitted to LC-MS analysis. Chromatographic separation and MS analysis (10 μ L injection) was carried out on a Waters ACQUITY UPLC H-class System equipped with Waters ACQUITY Quaternary Solvent Manager (QSM), Waters ACQUITY UPLC Photodiode Array (PDA) eλ Detector (λ = 210–800 nm), Waters ACQUITY UPLC BEH C18 Column (300 Å, 1.7 μ m, 2.1 \times 50 mm) and LCT Premier Orthogonal Acceleration Time of Flight Mass Spectrometer (m/z = 100–1600) in ES+ mode. Samples were run with a 1.6 min 2–100% gradient (run time 3 min) using 96% water and 96% MeCN mixed with 2.5% FA in water/MeCN as mobile phases (flow rate = 0.5 mL/min). Data processing was performed using Waters MassLynx Mass Spectrometry Software V4.2. Time-dependent unreacted inhibitor and GSH adduct signal in each sample was quantified from the baseline-separated UV absorbance peak area at a fixed wavelength (λ_{abs} = 350 nm) using the MassLynx Integrated peaks functionality. Data were plotted and analyzed using GraphPad Prism 8.4.2. Graphical data represents mean \pm standard error obtained for a single representative experiment from fitting biological duplicates (n = 2).

The GSH occupancy was calculated by dividing the integrated UV area of GSH adduct over the integrated UV area of GSH adduct and unbound inhibitor, and normalized to 100%.

$$\text{GSH Occupancy} = 100\% \frac{\text{UV}_{\text{adduct}}}{(\text{UV}_{\text{adduct}} + \text{UV}_{\text{inhibitor}})}$$

Time-dependent GSH occupancy (% of total) was plotted against incubation time for each inhibitor and fitted to the exponential one-phase association equation below (GraphPad Prism: One-phase association, with restrained values Y_0 = 0% and plateau = 100%) to obtain rate of adduct formation k_{obs} in presence of 5 mM GSH.

$$(\text{GSH Occupancy})_t = 100\% (1 - e^{-k_{obs} t})$$

Observed rate k_{obs} was then used to calculate the pseudo-first order rate constant k_{GSH} reflecting the intrinsic GSH reactivity. The standard deviation σ of k_{GSH} was calculated with Gaussian error propagation.

$$k_{GSH} = \frac{k_{obs}}{[\text{GSH}]} \quad \text{with} \quad \sigma_{k_{GSH}} = \frac{\sigma_{k_{obs}}}{[\text{GSH}]}$$

4.2. Protein Expression and Purification

Human EGFR (residues 695–1022) was cloned into baculovirus shuttle vector pNK12.13 harboring an N-terminal His-tag and a 3C protease site using LIC cloning.¹²² The construct was sequence-verified before transposition into baculovirus vector (Bacmid) using DH10Bac cells. His-EGFR was expressed using baculovirus expression in *Spodoptera frugiperda* (Sf9) using an adapted Bac-to-Bac system (Invitrogen). Bacmids were isolated from DH10Bac cells using isopropanol precipitation and 10 μ g was transfected into 0.8 \times 10⁶ sedentary Sf9 cells using CellFectin (Invitrogen) in SFM-II medium (Gibco) in a 6-well plate at 28 °C. After 72 h cells were checked for swelling and the medium was harvested (P0) for infection of P1 cultures; 50 mL of 1 \times 10⁶ cells/mL in SFM-II medium. P1 cultures were incubated at 28 °C whilst shaking for 72 h and then harvested by spinning down at 500 G for 5 min. The supernatant was used to infect P2 cultures (like P1, but now 500 mL), whilst the pellet was used to check for expression and purification optimization. P2 cultures were infected with low MOI and harvested after 72 h shaking at 28 °C. Cell pellets were dissolved in buffer A (50 mM Tris pH8.0, 150 mM NaCl, 5 mM β -mercaptoethanol (BME)) and disrupted using sonication before centrifugation at 24,000 G for 40 min at 4 °C. The supernatant was applied to a 1 mL HisTrap column (GE Healthcare) using buffer A and the protein was eluted using a gradient of buffer B (Buffer A supplemented with 500 mM imidazole). Protein-containing fractions

were pooled, concentrated and applied to gel filtration on a Superdex 200 column (GE Healthcare) in a Tris buffer (20 mM Tris pH8.0, 150 mM NaCl, and 5 mM BME). The protein fractions were concentrated to 2.7 mg/mL before being aliquoted and flash-frozen using liquid nitrogen.

4.3. Intact Protein MS

Recombinant His-tagged EGFR kinase domain (1 μ M) and inhibitor (100 μ M) were incubated in reaction buffer (50 mM HEPES pH7.4, 150 mM NaCl and 5 mM DTT) at 21 °C for 4 h in Protein Lobind Tubes (Eppendorf, #022431018) prior to LC-MS analysis. Chromatographic separation and MS analysis (1 μ L injection) was carried out on a Waters ACQUITY UPLC-MS system equipped with a Waters ACQUITY Quaternary Solvent Manager (QSM), Waters ACQUITY FTN AutoSampler, Waters ACQUITY UPLC Protein BEH C4 Column (300 Å, 1.7 μ m, 2.1 \times 50 mm) and XEVO-G2XS QTOF Mass Spectrometer (m/z = 200-2500) in ES+ mode. Samples were run with a 6 min 18-50% gradient (run time 15 min) using 0.1% FA in MeCN and 0.1% FA in water as mobile phases (flow rate 0.6-0.8 mL/min). The first 4 min the flow (2% solvent B) was diverted to the waste to avoid contamination of the MS with high concentrations of buffer components. After 4 min, the elution flow was ionized with an electrospray ionization (ESI) source in positive ion mode. The data was analyzed using Waters MassLynx Mass Spectrometry Software V4.2. The total mass of the covalent EGFR-inhibitor adducts was obtained by deconvolution of electrospray ionization mass spectrum envelope (average isotopes) with the MaxEnt1 function. Sample carry-over was minimized by running wash runs (run time 3 min) with 80% MeOH in water (5 μ L injection, twice) and 60% MeCN in water (5 μ L injection, twice) after each sample.

4.4. LanthaScreen Eu Kinase Binding Assay

Inhibitor binding to recombinant GST-tagged EGFR kinase domain (ThermoFisher, #PV3872) was assessed in a LanthaScreen Eu Kinase Binding Assay with TR-FRET signal between acceptor Kinase Tracer 199 (KT199; ThermoFisher, #PV5830) and donor LanthaScreen Eu-anti-GST Antibody (ThermoFisher, #PV5594) as read-out.⁷⁸ Assay components were diluted in 1 \times Kinase Buffer A (50 mM HEPES pH7.5, 10 mM MgCl₂, 1 mM EGTA, 0.01% Brij-35) freshly prepared from Invitrogen 5 \times Kinase Buffer A (ThermoFisher, #PV3189). LanthaScreen Eu-anti-GST Antibody was thawed, mixed and centrifuged (10,000 rpm, 10 min) prior to pipetting from the top of the solution and dilution into reaction buffer to prevent artefacts caused by solid particles. A stock solution containing GST-EGFR and anti-GST EuAb was preincubated for at least 30 min prior to addition (to reach the slow EGFR-EuAb equilibrium).

Inhibitors (10-100 μ M in DMSO) and KT199 (25 μ M in DMSO) were transferred to PE OptiPlate-384 White Microplates (PerkinElmer, #6007290) or Corning 4513 White Low Volume NBS 384 Well Microplates (Corning, #4513) using an ECHO 550 Liquid Handler (Labcyte Inc.) acoustic dispenser. Time resolved fluorescence (TRF) of the Eu-labeled donor (λ_{ex} = 337 nm, λ_{em} = 620 \pm 10 nm) and AlexaFluor647-labeled acceptor (λ_{em} = 665 \pm 10 nm) was measured in relative fluorescence units (RFU) on a CLARIOstar (BMG Labtech) microplate reader in well multichromatics mode (Excitation filter: EXTR. Dichroic filter: LPTR. 100 flashes/well. 100 μ s delay before integration start. 200 μ s integration time). The ratiometric TR-FRET emission of acceptor over donor (TRF_{665 nm}/TRF_{620 nm}) was calculated from individual donor/acceptor TRF emission intensities with MARS Data Analysis Software (BMG Labtech). All measurements were performed in triplicate unless otherwise noted. Data were plotted and analyzed using GraphPad Prism 8.4.2. Graphical data represents the mean \pm standard deviation for a single representative experiment.

Tracer dissociation constant K_d . 5-300 nL KT199 (25 μ M in DMSO, with DMSO backfill to 300 nL) was dispensed into an PE OptiPlate-384 microplate using an ECHO acoustic dispenser. Then, 30 μ L of preincubated 1 \times EGFR/EuAb solution (final concentration 2 nM EGFR, 0.5 nM EuAb) or 30 μ L of 1 \times EuAb solution (final concentration 0.5 nM) was added. The plate was shaken to mix (600 rpm, 1 min) and centrifuged (1000 rpm, 1 min). Time Resolved Fluorescence (TRF) was measured every 2 min for 60 min. Background in absence of EGFR (diffusion-enhanced FRET and nonspecific binding) was subtracted from the FRET ratio in presence of EGFR. The

corrected FRET ratio (after 20 min incubation, at equilibrium) was plotted against tracer concentration and fitted to the quadratic equation below with fixed values for $[E]_0$ (EGFR concentration at reaction initiation) and $[L]_0$ (tracer concentration at reaction initiation) to determine tracer binding affinity K_D accounting for ligand depletion ($[tracer]_0 < 10[EGFR]_0$).

$$FRET_{sample}^{corr} = B_{max} \frac{([E]_0 + [L]_0 + K_D) - \sqrt{([E]_0 + [L]_0 + K_D)^2 - 4 [E]_0 [L]_0}}{2 [E]_0}$$

Kinetic Probe Competition Assay (kPCA). 0-270 nL inhibitor (DMSO backfill to 270 nL) and 30 nL KT199 (25 μ M in DMSO, final concentration 25 nM) were dispensed into an PE OptiPlate-384 microplate using an ECHO acoustic dispenser. Then, 4 μ L Kinase Buffer A was added to each well, the plate was shaken to mix (300 rpm, 1 min) and centrifuged (1000 rpm, 1 min). Finally, 26 μ L of the preincubated 1.2 \times EGFR/EuAb solution (final concentration 2 nM EGFR, 0.5 nM EuAb) or 26 μ L of 1.2 \times EuAb solution (final concentration 0.5 nM) was added and the plate was centrifuged (1000 rpm, 1 min). Time Resolved Fluorescence (TRF) was measured every 2 min for 60 min.

4.5. PhosphoSens Protein Kinase Activity Assay

Biochemical inhibition of recombinant EGFR kinase domain (ThermoFisher, #PV3872 or SignalChem, #E10-112G) was assessed in a PhosphoSens Protein Kinase Activity Assay (AssayQuant, #CSKS-AQT0734K) with Chelation-Enhanced Fluorescence (ChEF) upon CSox substrate phosphorylation as read-out. Assay components were stored as stock solutions at -20 °C as recommended by supplier.¹⁰¹ Dry powder stock of PhosphoSens CSox substrate (AssayQuant, #CSKS-AQT0734B) was dissolved in 20% NH_4CO_3 (aq) to a concentration of 1 mM and diluted in distilled water. Single-use aliquots of DTT (100 mM in water) and ATP (100 mM in water) were stored at -20 °C. Buffers were freshly supplemented with EGTA, DTT and ATP before use. Single-use aliquots of purified recombinant human GST-EGFR kinase domain were diluted with enzyme buffer (20 mM HEPES pH7.5, 0.01% Brij-35, 5% Glycerol, 1 mg/mL BSA, 0.1 mM EGTA and 1.0 mM DTT) in Protein Lobind Tubes (Eppendorf, #022431018) to minimize loss of enzyme activity due to precipitation/aggregation. Stock solution of 12.5 μ M CSox substrate AQT734 (AssayQuant, #AQT0734B) was prepared in reaction buffer (62.5 mM HEPES pH7.5, 0.01% Brij-35, 12.5 mM MgCl_2 , 0.69 mM EGTA, 1.25 mM DTT and 1.25 mM ATP). The final buffer composition in each well was 54 mM HEPES, 0.012% Brij-35, 1% Glycerol, 0.20 mg/mL BSA, 0.6 mM EGTA, 10 mM MgCl_2 , 1 mM ATP and 1.2 mM DTT.

Kinetic Competitive Association. 0-200 nL inhibitor (100 \times in DMSO, DMSO backfill to 200 nL) was transferred to Corning 3820 Black Low Volume NBS 384 Well Microplates (Corning, #3820) using an ECHO 550 Liquid Handler (Labcyte Inc.) acoustic dispenser, followed by addition of 16 μ L CSox substrate AQT734 (1.25 \times in reaction buffer, 10 μ M final concentration) to each well. The plate was shaken to mix (300 rpm, 1 min) before addition of 4 μ L GST-EGFR (5 \times in enzyme buffer, 0.25 nM final concentration) or 4 μ L enzyme buffer (no kinase control). The plate was centrifuged at 1,000 rpm for 1 min and the wells were sealed with clear tape (Duck® Brand HP260™ Packing Tape) applied with a roller prior to minimize assay artefacts such as drift due to evaporation. Chelation-Enhanced Fluorescence intensity ($\lambda_{ex} = 360 \pm 15$ nm, $\lambda_{em} = 492 \pm 20$ nm) was measured every 2 min for 120 min on a CLARIOstar (BMG Labtech) microplate reader. All measurements were performed in triplicate. Data were plotted and analyzed using GraphPad Prism 8.4.2. Background fluorescence (time-dependent fluorescence intensity for CSox substrate in absence of EGFR) was subtracted from the time-dependent fluorescence intensities in presence of EGFR (and inhibitor) (GraphPad Prism: Remove Baseline and Column Math – Value-Baseline with Baseline = Selected Column). Values in the lag phase (0-4 min) were excluded before baseline removal to correct for compound fluorescence (GraphPad Prism: Remove Baseline and Column Math – Value-Baseline with Baseline = First Row), to give the corrected fluorescence intensity (in RFU). Graphical data represents the mean \pm standard deviation for a single representative experiment.

Data Analysis: Progress Curve Analysis. Corrected ChEF (in RFU) was plotted against incubation time (in s) for each inhibitor concentration, and fitted to the one-phase exponential association equation below to obtain the rate constant k_{obs} (in s^{-1}) for time-dependent formation of fluorescent phosphorylated CSox product. Lag time was constrained to $t_{\text{lag}} = 240$ s and final velocity v_s was constrained to $v_s = 0$ for irreversible inhibitor neratinib. The progress curve of the uninhibited DMSO control was also fitted to find k_{ctrl} .

$$F_t = v_s(t - t_{\text{lag}}) + \frac{v_i - v_s}{k_{\text{obs}}} \left[1 - e^{-k_{\text{obs}}(t - t_{\text{lag}})} \right] + F_0$$

For irreversible inhibitor neratinib, the means and standard errors of k_{obs} (in s^{-1}) were plotted against inhibitor concentration (in M), and fitted to the equation below to obtain maximum inactivation rate constant k_{inact} (in s^{-1}) and apparent inactivation constant K_i^{app} (in M) in presence of 1 mM ATP. Nonlinearity in uninhibited k_{ctrl} was constrained to the k_{obs} of the uninhibited control.

$$k_{\text{obs}} = k_{\text{ctrl}} + \frac{k_{\text{inact}} [\text{I}]}{K_i^{\text{app}} + [\text{I}]}$$

Data Analysis: Equilibrium Potency. Corrected fluorescence intensity (in RFU) was plotted against incubation time (in s) for each inhibitor concentration, and fitted to a straight line to calculate the phosphorylation velocity v (slope in RFU/s) during the first 4-60 min. The mean and standard error were plotted against inhibitor concentration and fitted to the nonlinear least squares curve equation (GraphPad Prism: [Inhibitor] vs. response – Variable slope (four parameters)) with fixed values for the top (v^{max} , uninhibited control) and bottom ($v^{\text{min}} = 0$) to obtain IC_{50} -values reflecting biochemical inhibitory potency in presence of 1 mM ATP.

$$v = v^{\text{min}} + \frac{v^{\text{max}} - v^{\text{min}}}{1 + \left(\frac{\text{IC}_{50}}{[\text{I}]} \right)^h}$$

Biochemical potency K_i of ATP-competitive reversible inhibitors was obtained using the Cheng-Prusoff equation below. The $K_{M,\text{ATP}}$ value for EGFR^{WT} ATP affinity was constrained to the reported $K_{M,\text{ATP}} = 5 \mu\text{M}$.¹¹⁰

$$K_i = \frac{\text{IC}_{50}}{\left(1 + \frac{[\text{ATP}]}{K_{M,\text{ATP}}} \right)^h}$$

4.6. Cellular EGFR Inhibition and Reversibility Assay

HeLa cells were cultured in DMEM (Dulbecco's Modified Eagle's Medium, Gibco) supplemented with 7.5% FCS. Cells were maintained in a humidified atmosphere of 5% CO₂ at 37 °C and regularly tested for the absence of mycoplasma.

Cellular EGFR (auto)phosphorylation

Inhibition. HeLa cells were seeded into 12 well plates (8×10^4 cells/well) and incubated overnight. Medium was changed to serum-free DMEM to starve the cells, and cells were grown for 2 h. DMSO or inhibitor (1 μM) was added to the serum-free medium and incubated for 1 h. For EGF stimulated samples, 25 ng/mL EGF (Gibco, #PHG0313) was added and cells were incubated for 1 h (after incubation with inhibitor). Medium was removed and plates were stored at -80 °C until the next day. EGFR (auto)phosphorylation was visualized by gel electrophoresis and immunoblotting (see below).

Reversibility/washout. Culturing and treatment of HeLa cells as described for the inhibition assay above. Following inhibitor incubation, medium was replaced by fresh, inhibitor-free medium (optionally containing 25 ng/mL EGF) to evaluate reversibility.

Cellular inhibitory potency. Culturing and treatment of HeLa cells as described for the inhibition assay above, with incubation with DMSO or inhibitor (0-2 μ M), followed by stimulation with EGF. EGFR phosphorylation was visualized and quantified as described below (n = 1). Receptor phosphorylation was plotted against inhibitor concentration, and fitted to obtain IC₅₀-values using non-linear least squares curve fitting (GraphPad Prism: [inhibitor] vs. response – variable slop (four parameters)) with fixed values for the top (100%) and bottom (0%).

Gel Electrophoresis and Western Blotting. 50 μ L of 2x SDS sample buffer containing 20 mM DTT (Invitrogen, #N0007) was added to each well and incubated at 37 °C. Proteins from the whole cell lysate (WCL) were denatured by heating at 100 °C for at least 15 min. Samples (25 μ L) were loaded on 8% Tris-glycine SDS-PAGE gels and resolved by gel electrophoresis. Proteins were transferred to a nitrocellulose membrane (Protran BA85, 0.45 μ m, GE Healthcare) at 300 mA for 2.5 h using a Trans-Blot Turbo Transfer System (Biorad). The membranes were blocked in blocking buffer (5% skim milk powder (Oxioid, #LP0031) in PBS (Sigma-Aldrich, #P1379)) for 1 h. Antibodies were prepared in 5% milk in PBST (0.1% Tween20 in PBS). Primary antibodies: rabbit anti-EGFR (1:1,000; Millipore, #04-338), mouse anti-phosphotyrosine clone 4G10 (1:1,000; Millipore, #05-321), and mouse anti- β -actin clone AC-74 (1:10,000; Sigma-Aldrich, #A2228). Secondary antibodies: IRDye 800CW goat anti-mouse (1:5,000; Li-COR, #926-32210) and IRDye 680LT goat anti-rabbit (1:20,000; Li-COR, #926-68021). The membranes were incubated with a primary antibody, washed three times for 10 min in 0.1% PBST, incubated with the secondary antibody for 30 min, and washed three times again in 0.1% PBST. The signal was detected using direct imaging by the Odyssey Classic imager (LI-COR).

Quantification. Intensity of signals corresponding to total EGFR and phosphorylated EGFR in the pY blot were quantified with ImageJ v1.52a,¹²³⁻¹²⁵ and the gel-specific background was subtracted. Relative receptor phosphorylation (pY/EGFR) was calculated for each sample and then normalized to the maximum receptor phosphorylation, corresponding to pY/EGFR in the respective controls: vehicle-treated samples +/- EGF stimulation, +/- washout. Data were plotted and analyzed using GraphPad Prism 8.

5. Materials and Methods: *Chemical Synthesis*

The synthetic strategy for preparation of **8RK57** and **8RK58** can be found in **Scheme S1**. Chemical synthesis of precursor bromoquinoline **2** was performed at Mercachem BV (Nijmegen, NL). Synthesis of alkyne derivatives **8RK57** and **8RK58** was performed at LUMC (Leiden, NL).

General. All commercially available reagents and solvents were used as purchased, including BrettPhos Palladacycle G3 (Strem Chemicals, #46-0322) and BrettPhos (Strem Chemicals, #15-1152). Reported yields are not optimized. Thin Layer Chromatography (TLC) was performed using TLC plates from Merck (SiO₂, Kieselgel 60 F254 neutral, on aluminum with fluorescence indicator) and compounds were visualized by UV detection (254 nm) and KMnO₄ staining. Flash column chromatography (FCC) purification of precursors **2-5** was performed using the indicated eluent. FCC purification of **8RK57** and **8RK58** was performed using Grace Davisil Silica Gel (particle size 40-63 μ m, pore diameter 60 Å) and the indicated eluent. Nuclear magnetic resonance (NMR) spectra were recorded as indicated on a Bruker Avance 300 (300 MHz for ¹H and 75.00 MHz for ¹³C) instrument or a Bruker Avance 600 (600 MHz for ¹H and 151 MHz for ¹³C) instrument equipped with a Bruker CryoPlatform using the residual solvent (DMSO-*d*₆) as internal standard (δ 2.50 ppm for ¹H and δ 39.52 ppm for ¹³C). Chemical shifts (δ) are given in ppm and coupling constants (*J*) are quoted in hertz (Hz). Resonances are described as s (singlet), d (doublet), t (triplet), q (quartet), b (broad) and m (multiplet) or combinations thereof. Assignment of signals is based on 2D NMR techniques COSY, HSQC and HMBC. High-resolution mass spectrometry (HRMS) measurements were carried out on a Waters ACQUITY UPLC-MS system equipped with a Waters ACQUITY

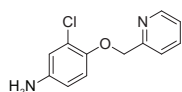
Quaternary Solvent Manager (QSM), Waters ACQUITY FTN AutoSampler, Waters ACQUITY UPLC BEH C18 Column (1.7 μ m, 2.1 \times 50 mm) and XEVO-G2 XS QTOF Mass Spectrometer (m/z = 50-1200) in ES+ mode. Samples were run with a 1.7 min gradient (run time 3 min) using 0.1% FA in MeCN and 0.1% FA in water as mobile phases (flow rate 0.6 mL/min). The elution flow was ionized with an electrospray ionization (ESI) source in positive ion mode. Data processing was performed using Waters MassLynx Mass Spectrometry Software 4.2. Mass spectra were centered to obtain the found mass with the TOF spectrum center function; Process – Center – Half height = 2, Center method = Median. Theoretical mass was calculated with the isotope modelling function; Tools – Isotope model – Charged ion – Charge state = 1.

LC-MS Method I. LC-MS analysis of precursors **3-5** was performed at Mercachem (Nijmegen, NL) on a system equipped with a Diode Array (DAD) Detector (λ = 220-320 nm), Waters XSelect C18 Column (3.5 μ m, 2.1 \times 30 mm), an Electron-Spray Atmospheric Pressure Ionization (ES-API) source and a (MSD) Mass Spectrometer (m/z = 100-800) in ES+ mode. Samples were run with a linear 1.6 min gradient (run time 3 min) of 5-98% solvent A, using A = 95% MeCN + 5% ($(\text{NH}_4)\text{HCO}_3$ (aq) and B = 10 mM ($(\text{NH}_4)\text{HCO}_3$ in water (pH9.0) as mobile phases (flow rate = 1.0 mL/min).

LC-MS Method II. LC-MS analysis of precursor **2** and final compounds **8RK57** and **8RK58** was performed at LUMC (Leiden, NL) on a Waters ACQUITY UPLC H-class System equipped with Waters ACQUITY Quaternary Solvent Manager (QSM), Waters ACQUITY UPLC Photodiode Array (PDA) eλ Detector (λ = 210-800 nm), Waters ACQUITY UPLC BEH C18 Column (130 Å, 1.7 μ m, 2.1 \times 50 mm) and LCT Premier Orthogonal Acceleration Time of Flight Mass Spectrometer (m/z = 100-1600) in ES+ mode. Pure compounds were run with a 7 min 2-100% gradient (run time 10 min) using 96% water and 96% MeCN mixed with 2.5% FA in water/MeCN as mobile phases (flow rate = 0.5 mL/min).

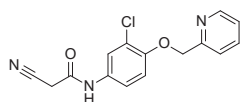
5.1. Synthesis of Precursor 2

3-chloro-4-(2-pyridylmethoxy)aniline **5**

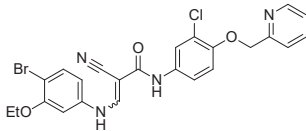


Following published procedure,¹²⁶ 4-amino-2-chlorophenol **6** (5.00 gr, 34.8 mmol, 1.0 eq) was reacted with 2-(chloromethyl)pyridine hydrochloride (6.86 gr, 41.8 mmol, 1.2 eq) in presence of benzaldehyde (3.88 mL, 38.3 mmol, 1.1 eq) and K_2CO_3 (19.25 gr, 139 mmol, 4 eq) in 40 mL DMF, at 50 °C for 24 h. The mixture was concentrated *in vacuo* and carefully dissolved (gas evolution) in 300 mL 2N HCl. The aqueous solution was extracted with EtOAc (3X) and basified by addition of 300 mL 2N NaOH. The resulting suspension was stirred, filtered and thoroughly washed with water. The brownish residue was taken up in EtOAc, washed with water and brine, dried over Na_2SO_4 and concentrated *in vacuo* to give aniline **5** as a light-brown solid (7.46 gr, 29.6 mmol, 85%). The material was used in the next step without further purification. LC-MS (ESI⁺); Rt = 1.88 min, m/z = 235 [M+H]⁺.

N-(3-chloro-4-(2-pyridinemethoxy)phenyl)-2-cyanoacetamide **4**

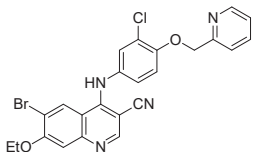


A solution of aniline **5** (2.00 gr, 8.52 mmol, 1 eq) and 2-cyanoacetic acid (761 mg, 8.95 mmol, 1.05 eq) in 30 mL anhydrous THF was heated at reflux, and *N,N'*-diisopropylcarbodiimide (1.39 mL, 8.95 mmol, 1.05 eq) was added dropwise. The resulting mixture was heated at reflux for 1 h. Reaction progress monitored by LC-MS revealed full conversion, and the reaction mixture was cooled to room temperature and concentrated *in vacuo*. The reaction mixture was suspended in 30 mL EtOAc, stirred overnight at room temperature, filtered and dried. LC-MS analysis of the residue revealed contamination with diisopropyl urea, which was removed by coating on Hydromix and purification by FCC (gradient 0-10% MeOH in EtOAc), followed by coating on silica and purification by FCC (gradient 5-10% MeOH in EtOAc) to obtain acetamide **4** as a white solid (1.69 gr, 5.32 mmol, 62.4%). Spectral ¹H NMR data of acetamide **4** is in agreement with published data.⁵⁷ LC-MS (ESI⁺); Rt = 1.92 min, m/z = 302 [M+H]⁺.

(E/Z)-3-(4-bromo-3-ethoxyanilino)-N-[3-chloro-4-(2-pyridinyl-methoxy)phenyl]-2-cyano-2-propenamide 3

Adapted from published procedure,¹²⁷ acetamide **4** (1.00 gr, 3.31 mmol, 1 eq) and 4-bromo-3-ethoxyaniline hydrochloride **7** (837 mg, 3.31 mmol, 1 eq) were suspended in 30 mL iPrOH. Triethyl orthoformate (0.55 mL, 3.31 mmol, 1 eq) was added and the mixture was heated to reflux. Another equivalent of triethyl orthoformate (0.55 mL, 3.31 mmol, 1 eq)

was added 1.5 hours and 3.5 hours after reaction initiation. LC-MS analysis revealed incomplete conversion (60%) therefore additional triethyl orthoformate (1.1 mL, 6.6 mmol, 2 eq) was added and reflux was continued for a further 4 hours, but this did not significantly improve conversion. Additional 4-bromo-3-ethoxyaniline hydrochloride **7** (418 mg, 1.66 mmol, 0.5 eq) and 4 mL iPrOH were added and the mixture was refluxed overnight. Reaction conversion was still incomplete (80%), therefore additional 4-bromo-3-ethoxyaniline hydrochloride **7** (418 mg, 1.66 mmol, 0.5 eq) was added and the mixture was refluxed overnight. The reaction mixture was allowed to cool to room temperature, filtered and dried when consumption of starting material was >90%. The product was obtained by trituration from 20 mL iPrOH. Cyanoacrylamide (E/Z)-**3** was obtained as a cream solid (1.31 gr, 2.14 mmol, 65%) and used in the next step without further purification (78% major isomer, 8.3% minor isomer and 11% starting material). LC-MS (ESI⁺): Rt = 2.41 min, m/z = 527 & 529 [M+H]⁺ (major) + Rt = 2.28 min, m/z = 527 & 529 [M+H]⁺ (minor).

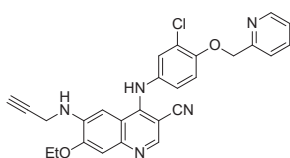
6-bromo-4-((3-chloro-4-(pyridin-2-ylmethoxy)phenyl)amino)-7-ethoxyquinoline-3-carbonitrile 2

Adapted from published procedure,¹²⁷ cyanoacrylamide (E/Z)-**3** (1.31 gr, 2.48 mmol, 1 eq) was suspended in 15 mL anhydrous toluene. Pyridine (0.40 mL, 4.96 mmol, 2 eq) was added and the mixture was heated to reflux. Phosphorus(V) oxychloride (0.46 mL, 4.96 mmol, 2 eq) was added and the mixture refluxed for 1 h. The reaction mixture was concentrated *in vacuo* and resuspended in a mixture of EtOAc/MeOH and 2N NaOH (aq). The aqueous phase was extracted with EtOAc twice, and the combined organic layers were washed with water, brine, dried over Na₂SO₄ and concentrated *in vacuo*. The material was coated on silica and purified by FCC (gradient 80-100% EtOAc in heptane). Fractions containing product were pooled and concentrated to afford 6-bromo-4-anilino-3-quinolinecarbonitrile **2** (0.46 gr, 0.866 mmol, 35%) as an orange-yellow solid. TLC R_f = 0.44 (3:1 EtOAc/heptane). LC-MS (ESI⁺): Rt = 4.62 min, m/z = 509.0 & 511.0 [M+H]⁺. ¹H NMR (600 MHz, DMSO-*d*₆) δ 9.75 (s, 1H), 8.78 (s, 1H), 8.60 (dt, *J* = 4.8, 1.3 Hz, 1H), 8.52 (s, 1H), 7.88 (td, *J* = 7.7, 1.8 Hz, 1H), 7.58 (d, *J* = 7.8 Hz, 1H), 7.47 (d, *J* = 2.2 Hz, 1H), 7.40 (s, 1H), 7.37 (ddd, *J* = 7.6, 4.8, 1.1 Hz, 1H), 7.28 (d, *J* = 8.8 Hz, 1H), 7.26 (dd, *J* = 8.8, 2.2 Hz, 1H), 5.30 (s, 2H), 4.29 (q, *J* = 6.9 Hz, 2H), 1.44 (t, *J* = 6.9 Hz, 3H). ¹³C NMR DEPTQ135 (151 MHz, DMSO-*d*₆) δ 156.91, 156.10, 154.04, 151.86, 150.39, 149.84, 149.16, 137.11, 132.78, 127.18, 127.11, 125.53, 123.10, 121.48, 121.46, 116.88, 114.19, 113.77, 112.43, 109.93, 86.18, 71.18, 65.03, 14.32. HRMS (ESI⁺): calculated 509.0380 & 511.0360 for C₂₄H₁₈N₄O₂BrCl ([M+H]⁺), found: 509.0381 & 511.0364.

5.2. Synthesis of 8RK57 and 8RK58**General Procedure A: Buchwald-Hartwig Amination**

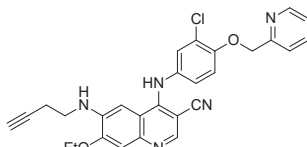
6-bromoquinoline **2** (50 mg, 0.098 mmol, 1 eq), BrettPhos Palladacycle G3 (35.56 mg, 0.039 mmol, 0.4 eq), BrettPhos (21.06 mg, 0.039 mmol, 0.4 eq) and NaOtBu (28.28 mg, 0.29 mmol, 3 eq) were combined in a flame-dried Schlenk flask under argon, to which anhydrous DMF (5 mL) was added. Finally, primary amine (0.98 mmol, 10 eq) was added, and the reaction mixture was stirred overnight at 70 °C. Reaction progress was monitored by TLC and LC-MS (detection of unreacted 6-bromoquinoline **2**). Upon reaction completion the reaction mixture was coated on silica and separated by FCC (gradient 0-100% EtOAc in heptane). Fractions containing desired product were pooled and solvent was removed by rotary evaporation. The product was lyophilized to obtain product as a dry powder.

**4-((3-chloro-4-(pyridin-2-ylmethoxy)phenyl)amino)-7-ethoxy-6-(prop-2-yn-1-ylamino)quinoline-3-carbonitrile
8RK57**



Following general procedure A, Buchwald-Hartwig amination with propargylamine (63 μ L, 0.98 mmol, 10 eq) afforded alkyne **8RK57** as a yellow powder (17 mg, 0.035 mmol, 36%). TLC R_f = 0.49 (4:1 EtOAc/heptane). LC-MS (ESI $^+$); Rt = 3.97 min, m/z = 484.1 [M+H] $^+$. 1 H NMR (300 MHz, DMSO- d_6) δ 9.30 (s, 1H), 8.60 (ddd, J = 4.9, 1.8, 0.9 Hz, 1H), 8.34 (s, 1H), 7.88 (td, J = 7.7, 1.8 Hz, 1H), 7.58 (dt, J = 7.8, 1.1 Hz, 1H), 7.41 (d, J = 2.4 Hz, 1H), 7.37 (ddd, J = 7.6, 4.8, 0.8 Hz, 1H), 7.28 (s, 1H), 7.27 (d, J = 8.7 Hz, 1H), 7.21 (dd, J = 8.8, 2.5 Hz, 1H), 7.20 (s, 1H), 6.05 (t, J = 6.4 Hz, 1H), 5.29 (s, 2H), 4.25 (q, J = 6.9 Hz, 2H), 4.07 (dd, J = 6.4, 2.4 Hz, 2H), 3.04 (t, J = 2.3 Hz, 1H), 1.45 (t, J = 6.9 Hz, 3H). 13 C NMR APT (75 MHz, DMSO- d_6) δ 156.17, 151.36, 151.15, 149.15, 148.88, 148.23, 143.22, 137.71, 137.10, 134.02, 126.26, 124.52, 123.09, 121.54, 121.47, 117.42, 114.35, 114.19, 106.93, 97.88, 86.95, 81.65, 73.01, 71.21, 64.18, 31.83, 14.40. HRMS (ESI $^+$): calculated 484.1540 for $C_{27}H_{22}N_5O_2Cl$ ([M+H] $^+$), found: 484.1537.

**6-(but-3-yn-1-ylamino)-4-((3-chloro-4-(pyridin-2-ylmethoxy)phenyl)amino)-7-ethoxyquinoline-3-carbonitrile
8RK58**



Following general procedure A, Buchwald-Hartwig amination with 1-amino-3-butyne (80 μ L, 0.98 mmol, 10 eq) afforded alkyne **8RK58** as a yellow powder (29 mg, 0.058 mmol, 59%). TLC R_f = 0.33 (3:1 EtOAc/heptane). LC-MS (ESI $^+$); Rt = 4.23 min, m/z = 498.2 [M+H] $^+$. 1 H NMR (300 MHz, DMSO- d_6) δ 9.36 (s, 1H), 8.60 (ddd, J = 4.9, 1.8, 1.0 Hz, 1H), 8.33 (s, 1H), 7.87 (td, J = 7.7, 1.8 Hz, 1H), 7.58 (dt, J = 7.9, 1.1 Hz, 1H), 7.42 (d, J = 2.4 Hz, 1H), 7.37 (ddd, J = 7.6, 4.8, 1.2 Hz, 1H), 7.27 (d, J = 8.9 Hz, 1H), 7.21 (dd, J = 9.0, 2.8 Hz, 1H), 7.20 (s, 1H), 7.19 (s, 1H), 5.71 (t, J = 6.1 Hz, 1H), 5.30 (s, 2H), 4.25 (q, J = 6.9 Hz, 2H), 3.40 (q, J = 7.0 Hz, 2H), 2.90 (t, J = 2.6 Hz, 1H), 2.54 (td, J = 7.3, 2.7 Hz, 2H), 1.45 (t, J = 6.9 Hz, 3H). 13 C NMR APT (75 MHz, DMSO- d_6) δ 156.16, 151.34, 151.11, 149.16, 148.97, 147.81, 142.45, 138.42, 137.10, 133.90, 126.61, 124.89, 123.09, 121.54, 121.48, 117.32, 114.33, 114.30, 106.65, 96.66, 86.78, 82.58, 72.54, 71.22, 64.23, 41.46, 18.01, 14.39. HRMS (ESI $^+$): calculated 498.1697 for $C_{28}H_{24}N_5O_2Cl$ ([M+H] $^+$), found: 498.1695.

6. References

1. Mukherjee, S. *The Emperor of All Maladies: A Biography of Cancer*. Scribner: New York, U.S.A., 2010.
2. Tilsed, C.M.; Fisher, S.A.; Nowak, A.K.; Lake, R.A.; Lesterhuis, W.J. Cancer Chemotherapy: Insights into Cellular and Tumor Microenvironmental Mechanisms of Action. *Front. Oncol.* **2022**, *12*, 960317. doi: 10.3389/fonc.2022.960317.
3. Gambardella, V.; Tarazona, N.; Cejalvo, J.M.; Lombardi, P.; Huerta, M.; Roselló, S.; Fleitas, T.; Roda, D.; Cervantes, A. Personalized Medicine: Recent Progress in Cancer Therapy. *Cancers* **2020**, *12*, 1009. doi: 10.3390/cancers12041009.
4. Schirrmacher, V. From Chemotherapy to Biological Therapy: A Review of Novel Concepts to Reduce the Side Effects of Systemic Cancer Treatment. *Int. J. Oncol.* **2019**, *54*, 407-419. doi: 10.3892/ijo.2018.4661.
5. Carey, L.A. HER2—A Good Addiction. *Nat. Rev. Clin. Oncol.* **2012**, *9*, 196-197. doi: 10.1038/nrclinonc.2012.36.
6. Sharma, S.V.; Settleman, J. Oncogene Addiction: Setting the Stage for Molecularly Targeted Cancer Therapy. *Genes Dev.* **2007**, *21*, 3214-3231. doi: 10.1101/gad.160907.
7. Roskoski, R. Orally Effective FDA-Approved Protein Kinase Targeted Covalent Inhibitors (TCIs). *Pharmacol. Res.* **2021**, *165*, 105422. doi: 10.1016/j.phrs.2021.105422.
8. Zhang, J.; Yang, P.L.; Gray, N.S. Targeting Cancer with Small Molecule Kinase Inhibitors. *Nat. Rev. Cancer* **2009**, *9*, 28-39. doi: 10.1038/nrc2559.
9. Proietti, I.; Skroza, N.; Michelini, S.; Mambrini, A.; Balduzzi, V.; Bernardini, N.; Marchesello, A.; Tolino, E.; Volpe, S.; Maddalena, P.; Di Fraia, M.; Mangino, G.; Romeo, G.; Potenza, C. BRAF Inhibitors: Molecular Targeting and Immunomodulatory Actions. *Cancers* **2020**, *12*, 1823. doi: 10.3390/cancers12071823.
10. Lovly, C.M.; Shaw, A.T. Molecular Pathways: Resistance to Kinase Inhibitors and Implications for Therapeutic Strategies. *Clin. Cancer Res.* **2014**, *20*, 2249-2256. doi: 10.1158/1078-0432.Ccr-13-1610.
11. Roskoski, R. The Erbb/HER Receptor Protein-Tyrosine Kinases and Cancer. *Biochem. Biophys. Res. Commun.* **2004**, *319*, 1-11. doi: 10.1016/j.bbrc.2004.04.150.
12. Pohlmann, P.R.; Mayer, I.A.; Mernaugh, R. Resistance to Trastuzumab in Breast Cancer. *Clin. Cancer Res.* **2009**, *15*, 7479. doi: 10.1158/1078-0432.CCR-09-0636.

13. Arkhipov, A.; Shan, Y.; Kim, E.T.; Dror, R.O.; Shaw, D.E. Her2 Activation Mechanism Reflects Evolutionary Preservation of Asymmetric Ectodomain Dimers in the Human EGFR Family. *eLife* **2013**, *2*, e00708. doi: 10.7554/eLife.00708.
14. Ferguson, K.M. Structure-Based View of Epidermal Growth Factor Receptor Regulation. *Annu. Rev. Biophys.* **2008**, *37*, 353-373. doi: 10.1146/annurev.biophys.37.032807.125829.
15. Díaz-Serrano, A.; Gella, P.; Jiménez, E.; Zugazagoitia, J.; Paz-Ares Rodríguez, L. Targeting EGFR in Lung Cancer: Current Standards and Developments. *Drugs* **2018**, *78*, 893-911. doi: 10.1007/s40265-018-0916-4.
16. Shi, F.; Telesco, S.E.; Liu, Y.; Radhakrishnan, R.; Lemmon, M.A. Erbb3/HER3 Intracellular Domain Is Competent to Bind ATP and Catalyze Autophosphorylation. *Proc. Natl. Acad. Sci.* **2010**, *107*, 7692. doi: 10.1073/pnas.1002753107.
17. van Lengerich, B.; Agnew, C.; Puchner, E.M.; Huang, B.; Jura, N. EGFR and NRG Induce Phosphorylation of HER3/ERBB3 by EGFR Using Distinct Oligomer Mechanisms. *Proc. Natl. Acad. Sci.* **2017**, *114*, E2836-E2845. doi: 10.1073/pnas.1617994114.
18. Arkin, M.; Moasser, M.M. HER2 Directed Small Molecule Antagonists. *Curr. Opin. Investig. Drugs* **2008**, *9*, 1264-1276.
19. Tzahar, E.; Waterman, H.; Chen, X.; Levkowitz, G.; Karunagaran, D.; Lavi, S.; Ratzkin, B.J.; Yarden, Y. A Hierarchical Network of Interreceptor Interactions Determines Signal Transduction by Neu Differentiation Factor/Neuregulin and Epidermal Growth Factor. *Mol. Cell. Biol.* **1996**, *16*, 5276-5287. doi: 10.1128/MCB.16.10.5276.
20. Ciardiello, F.; Tortora, G. EGFR Antagonists in Cancer Treatment. *N. Engl. J. Med.* **2008**, *358*, 1160-1174. doi: 10.1056/NEJMra0707704.
21. Voigt, M.; Braig, F.; Göthel, M.; Schulte, A.; Lamszus, K.; Bokemeyer, C.; Binder, M. Functional Dissection of the Epidermal Growth Factor Receptor Epitopes Targeted by Panitumumab and Cetuximab. *Neoplasia* **2012**, *14*, 1023-1031. doi: 10.1593/neo.121242.
22. Okines, A. F. C.; Cunningham, D. Trastuzumab: A Novel Standard Option for Patients with HER-2-Positive Advanced Gastric or Gastro-Oesophageal Junction Cancer. *Ther. Adv. Gastroenterol.* **2012**, *5*, 301-318. doi: 10.1177/1756283X12450246.
23. Bonello, M.; Sims, A.H.; Langdon, S.P. Human Epidermal Growth Factor Receptor Targeted Inhibitors for the Treatment of Ovarian Cancer. *Cancer Biol. Med.* **2018**, *15*, 375-388. doi: 10.20892/j.issn.2095-3941.2018.0062.
24. Collins, D.M.; Conlon, N.T.; Kannan, S.; Verma, C.S.; Eli, L.D.; Lalani, A.S.; Crown, J. Preclinical Characteristics of the Irreversible Pan-HER Kinase Inhibitor Neratinib Compared with Lapatinib: Implications for the Treatment of HER2-Positive and HER2-Mutated Breast Cancer. *Cancers* **2019**, *11*, 737. doi: 10.3390/cancers11060737.
25. Ayati, A.; Moghimi, S.; Salarinejad, S.; Safavi, M.; Pouramiri, B.; Foroumadi, A. A Review on Progression of Epidermal Growth Factor Receptor (EGFR) Inhibitors as an Efficient Approach in Cancer Targeted Therapy. *Bioorg. Chem.* **2020**, *99*, 103811. doi: 10.1016/j.bioorg.2020.103811.
26. Hurvitz, S.A.; Saura, C.; Oliveira, M.; Trudeau, M.E.; Moy, B.; Delaloge, S.; Gradishar, W.; Kim, S.-B.; Haley, B.; Ryoo, L., et al. Efficacy of Neratinib Plus Capecitabine in the Subgroup of Patients with Central Nervous System Involvement from the NALA Trial. *Oncologist* **2021**, *26*, e1327-e1338. doi: 10.1002/onco.13830.
27. Bachelot, T.; Romieu, G.; Campone, M.; Diéras, V.; Crochet, C.; Dalenc, F.; Jimenez, M.; Le Rhun, E.; Pierga, J.Y.; Gonçalves, A.; Leheurteur, M.; Domont, J.; Gutierrez, M.; Curé, H.; Ferrero, J.M.; Labbe-Dévilliers, C. Lapatinib Plus Capecitabine in Patients with Previously Untreated Brain Metastases from HER2-Positive Metastatic Breast Cancer (LANDSCAPE): a Single-Group Phase 2 Study. *Lancet Oncol.* **2013**, *14*, 64-71. doi: 10.1016/S1470-2045(12)70432-1.
28. Scaltriti, M.; Rojo, F.; Ocaña, A.; Andido, J.; Guzman, M.; Cortes, J.; Di Cosimo, S.; Matias-Guiu, X.; Ramon y Cajal, S.; Arribas, J.; Baselga, J. Expression of p95HER2, a Truncated Form of the HER2 Receptor, and Response to Anti-HER2 Therapies in Breast Cancer. *J. Natl. Cancer Inst.* **2007**, *99*, 628-638. doi: 10.1093/jnci/djk134.
29. Conlon, N.T.; Kooijman, J.J.; van Gerwen, S.J.C.; Mulder, W.R.; Zaman, G.J.R.; Diala, I.; Eli, L.D.; Lalani, A.S.; Crown, J.; Collins, D.M. Comparative Analysis of Drug Response and Gene Profiling of HER2-Targeted Tyrosine Kinase Inhibitors. *Br. J. Cancer* **2021**, *124*, 1249-1259. doi: 10.1038/s41416-020-01257-x.
30. Kulukian, A.; Lee, P.; Taylor, J.; Rosler, R.; de Vries, P.; Watson, D.; Forero-Torres, A.; Peterson, S. Preclinical Activity of HER2-Selective Tyrosine Kinase Inhibitor Tucatinib as a Single Agent or in Combination with Trastuzumab or Docetaxel in Solid Tumor Models. *Mol. Cancer Ther.* **2020**, *19*, 976-987. doi: 10.1158/1535-7163.Mct-19-0873.
31. Singh, H.; Walker, A.J.; Amiri-Kordestani, L.; Cheng, J.; Tang, S.; Balcazar, P.; Barnett-Ringgold, K.; Palmby, T.R.; Cao, X.; Zheng, N., et al. U.S. Food and Drug Administration Approval: Neratinib for the Extended Adjuvant Treatment of Early-Stage HER2-Positive Breast Cancer. *Clin. Cancer Res.* **2018**, *24*, 3486-3491. doi: 10.1158/1078-0432.Ccr-17-3628.
32. U.S. Food and Drug Administration. FDA Approves Neratinib for Metastatic HER2-Positive Breast Cancer. *Approved Drug Products with Therapeutic Equivalence Evaluations (Orange Book) Short Description* [Online], 26 February 2020. <https://www.fda.gov/drugs/resources-information-approved-drugs/fda-approves-neratinib-metastatic-her2-positive-breast-cancer> (accessed 2023-02-26).
33. Berndt, N.; Karim, R.M.; Schönbrunn, E. Advances of Small Molecule Targeting of Kinases. *Curr. Opin. Chem. Biol.* **2017**, *39*, 126-132. doi: 10.1016/j.cbpa.2017.06.015.
34. Lu, X.; Yu, L.; Zhang, Z.; Ren, X.; Small, J.B.; Ding, K. Targeting EGFR^{L858R/T790M} and EGFR^{L858R/T790M/C797S} Resistance Mutations in NSCLC: Current Developments in Medicinal Chemistry. *Med. Res. Rev.* **2018**, *38*, 1550-1581. doi: 10.1002/med.21488.
35. Camidge, D.R.; Pao, W.; Sequist, L.V. Acquired Resistance to TKIs in Solid Tumours: Learning from Lung Cancer. *Nat. Rev. Clin. Oncol.* **2014**, *11*, 473-481. doi: 10.1038/nrclinonc.2014.104.
36. Yun, C.-H.; Boggan, T.J.; Li, Y.; Woo, M.S.; Greulich, H.; Meyerson, M.; Eck, M.J. Structures of Lung Cancer-Derived EGFR Mutants and Inhibitor Complexes: Mechanism of Activation and Insights into Differential Inhibitor Sensitivity. *Cancer Cell* **2007**, *11*, 217-227. doi: 10.1016/j.ccr.2006.12.017.
37. Singh, P.K.; Silakari, O. Chemotherapeutics-Resistance “Arms” Race: An Update on Mechanisms Involved in Resistance Limiting EGFR Inhibitors in Lung Cancer. *Life Sci.* **2017**, *186*, 25-32. doi: 10.1016/j.lfs.2017.08.001.
38. Yun, C.-H.; Mengwasser, K.E.; Toms, A.V.; Woo, M.S.; Greulich, H.; Wong, K.-K.; Meyerson, M.; Eck, M.J. The T790M Mutation in EGFR Kinase Causes Drug Resistance by Increasing the Affinity for ATP. *Proc. Natl. Acad. Sci.* **2008**, *105*, 2070. doi: 10.1073/pnas.0709662105.
39. Zhou, W.; Ercan, D.; Chen, L.; Yun, C.-H.; Li, D.; Capelletti, M.; Cortot, A.B.; Chiriac, L.; Iacob, R.E.; Padera, R.; Engen, J.R.; Wong, K.-K.; Eck, M.J.; Gray, N.S.; Jänne, P.A. Novel Mutant-Selective EGFR Kinase Inhibitors Against EGFR T790M. *Nature* **2009**, *462*, 1070-1074. doi: 10.1038/nature08622.
40. Pisa, R.; Kapoor, T.M. Chemical Strategies to Overcome Resistance Against Targeted Anticancer Therapeutics. *Nat. Chem. Biol.* **2020**, *16*, 817-825. doi: 10.1038/s41589-020-0596-8.
41. Singh, J. The Ascension of Targeted Covalent Inhibitors. *J. Med. Chem.* **2022**, *65*, 5886-5901. doi: 10.1021/acs.jmedchem.1c02134.
42. Paranjpe, R.; Basatneh, D.; Tao, G.; De Angelis, C.; Noormohammed, S.; Ekinci, E.; Abughosh, S.; Ghose, R.; Trivedi, M.V. Neratinib in HER2-Positive Breast Cancer Patients. *Ann. Pharmacother.* **2019**, *53*, 612-620. doi: 10.1177/1060028018824088.

43. Schlam, I.; Swain, S.M. HER2-Positive Breast Cancer and Tyrosine Kinase Inhibitors: The Time Is Now. *npj Breast Cancer* **2021**, *7*, 56. doi: 10.1038/s41523-021-00265-1.

44. Le Du, F.; Diéras, V.; Curigliano, G. The Role of Tyrosine Kinase Inhibitors in the Treatment of HER2+ Metastatic Breast Cancer. *Eur. J. Cancer* **2021**, *154*, 175–189. doi: 10.1016/j.ejca.2021.06.026.

45. Abdeldayem, A.; Raouf, Y.S.; Constantinescu, S.N.; Moriggl, R.; Gunning, P.T. Advances in Covalent Kinase Inhibitors. *Chem. Soc. Rev.* **2020**, *49*, 2617–2687. doi: 10.1039/C9CS00720B.

46. Ghosh, A.K.; Samanta, I.; Mondal, A.; Liu, W.R. Covalent Inhibition in Drug Discovery. *ChemMedChem* **2019**, *14*, 889–906. doi: 10.1002/cmde.201900107.

47. Hossam, M.; Lasheen, D.S.; Abouzid, K.A.M. Covalent EGFR Inhibitors: Binding Mechanisms, Synthetic Approaches, and Clinical Profiles. *Arch. Pharm. Chem. Life Sci.* **2016**, *349*, 573–593. doi: 10.1002/ardp.201600063.

48. Abourehab, M.A.S.; Alqahtani, A.M.; Youssif, B.G.M.; Gouda, A.M. Globally Approved EGFR Inhibitors: Insights into Their Syntheses, Target Kinases, Biological Activities, Receptor Interactions, and Metabolism. *Molecules* **2021**, *26*, 6677. doi: 10.3390/molecules26216677.

49. Singh, M.; Jadhav, H.R. Targeting Non-Small Cell Lung Cancer with Small-Molecule EGFR Tyrosine Kinase Inhibitors. *Drug Discov. Today* **2018**, *23*, 745–753. doi: 10.1016/j.drudis.2017.10.004.

50. Nagasaka, M.; Zhu, V.W.; Lim, S.M.; Greco, M.; Wu, F.; Ou, S.-H.I. Beyond Osimertinib: The Development of Third-Generation EGFR Tyrosine Kinase Inhibitors For Advanced EGFR+ NSCLC. *J. Thorac. Oncol.* **2021**, *16*, 740–763. doi: 10.1016/j.jtho.2020.11.028.

51. Liu, O.; Sabnis, Y.; Zhao, Z.; Zhang, T.; Buhrlage, S.J.; Jones, L.H.; Gray, N.S. Developing Irreversible Inhibitors of the Protein Kinase Cysteineome. *Chem. Biol.* **2013**, *20*, 146–159. doi: 10.1016/j.chembiol.2012.12.006.

52. Singh, J.; Petter, R.C.; Baillie, T.A.; Whitty, A. The Resurgence of Covalent Drugs. *Nat. Rev. Drug Discov.* **2011**, *10*, 307–317. doi: 10.1038/nrd3410.

53. Barf, T.; Kaptein, A. Irreversible Protein Kinase Inhibitors: Balancing the Benefits and Risks. *J. Med. Chem.* **2012**, *55*, 6243–6262. doi: 10.1021/jm3003203.

54. Mons, E.; Jansen, I.D.C.; Loboda, J.; van Doodewaard, B.R.; Hermans, J.; Verdoes, M.; van Boeckel, C.A.A.; van Velen, P.A.; Turk, B.; Turk, D.; Ovaa, H. The Alkyne Moiety as a Latent Electrophile in Irreversible Covalent Small Molecule Inhibitors of Cathepsin K. *J. Am. Chem. Soc.* **2019**, *141*, 3507–3514. doi: 10.1021/jacs.8b11027.

55. Wissner, A.; Mansour, T.S. The Development of HKI-272 and Related Compounds for the Treatment of Cancer. *Arch. Pharm. Pharm. Med. Chem.* **2008**, *341*, 465–477. doi: 10.1002/ardp.200800009.

56. Tsou, H.-R.; Overbeek-Klumper, E.G.; Hallett, W.A.; Reich, M.F.; Floyd, M.B.; Johnson, B.D.; Michalak, R.S.; Nilakantan, R.; Discan, C.; Golas, J.; Rabindran, S.K.; Shen, R.; Shi, X.; Wang, Y.-F.; Upeslaci, J.; Wissner, A. Optimization of 6,7-Disubstituted-4-(arylamino)quinoline-3-carbonitriles as Orally Active, Irreversible Inhibitors of Human Epidermal Growth Factor Receptor-2 Kinase Activity. *J. Med. Chem.* **2005**, *48*, 1107–1131. doi: 10.1021/jm040159c.

57. Papamichalakis, M.; Chew, W. Method of Preparing 3-Cyano-quinolines and Intermediates Made Thereby. US20060270669A1, 30 November, 2006.

58. Wissner, A.; Rabindran Sridhar, K.; Tsou, H.-R. Protein Tyrosine Kinase Enzyme Inhibitors. US20050059678A1, 17 March, 2005.

59. Wissner, A.; Rabindran Sridhar, K.; Tsou, H.-R. Substituted Quinolines as Protein Tyrosine Kinase Enzyme Inhibitors. WO2005034955A1, 21 April, 2005.

60. Surry, D.S.; Buchwald, S.L. Dialkylbiaryl Phosphines in Pd-Catalyzed Amination: A User's Guide. *Chem. Sci.* **2011**, *2*, 27–50. doi: 10.1039/COSC00331J.

61. Keeley, A.; Ábrányi-Balogh, P.; Keserű, G.M. Design and Characterization of a Heterocyclic Electrophilic Fragment Library for the Discovery of Cysteine-Targeted Covalent Inhibitors. *MedChemComm* **2019**, *10*, 263–267. doi: 10.1039/C8MD00327K.

62. Cee, V.J.; Volak, L.P.; Chen, Y.; Bartberger, M.D.; Tegley, C.; Arvedson, T.; McCarter, J.; Tasker, A.S.; Fotsch, C. Systematic Study of the Glutathione (GSH) Reactivity of N-Arylacylamides: 1. Effects of Aryl Substitution. *J. Med. Chem.* **2015**, *58*, 9171–9178. doi: 10.1021/acs.jmedchem.5b01018.

63. Dahal, U.P.; Obach, R.S.; Gilbert, A.M. Benchmarking *In Vitro* Covalent Binding Burden As A Tool To Assess Potential Toxicity Caused by Nonspecific Covalent Binding of Covalent Drugs. *Chem. Res. Toxicol.* **2013**, *26*, 1739–1745. doi: 10.1021/tr400301q.

64. Flanagan, M.E.; Abramite, J.A.; Anderson, D.P.; Aulabaugh, A.; Dahal, U.P.; Gilbert, A.M.; Li, C.; Montgomery, J.; Oppenheimer, S.R.; Ryder, T., et al. Chemical and Computational Methods for the Characterization of Covalent Reactive Groups for the Prospective Design of Irreversible Inhibitors. *J. Med. Chem.* **2014**, *57*, 10072–10079. doi: 10.1021/jm501412a.

65. Ábrányi-Balogh, P.; Petri, L.; Imre, T.; Szijj, P.; Scarpino, A.; Hrast, M.; Mitrović, A.; Fonović, U.P.; Németh, K.; Barreteau, H.; Roper, D.I.; Horváti, K.; Ferenczy, G.G.; Kos, J.; Ilaš, J.; Gobec, S.; Keserű, G.M. A Road Map for Prioritizing Warheads for Cysteine Targeting Covalent Inhibitors. *Eur. J. Med. Chem.* **2018**, *160*, 94–107. doi: 10.1016/j.ejmech.2018.10.010.

66. Lonsdale, R.; Burgess, J.; Colclough, N.; Davies, N.L.; Lenz, E.M.; Orton, A.L.; Ward, R.A. Expanding the Armory: Predicting and Tuning Covalent Warhead Reactivity. *J. Chem. Inf. Model.* **2017**, *57*, 3124–3137. doi: 10.1021/acs.jcim.7b00553.

67. Oballa, R.M.; Truchon, J.-F.; Bayly, C.I.; Chauret, N.; Day, S.; Crane, S.; Berthelette, C. A Generally Applicable Method for Assessing the Electrophilicity and Reactivity of Diverse Nitrile-Containing Compounds. *Bioorg. Med. Chem. Lett.* **2007**, *17*, 998–1002. doi: 10.1016/j.bmcl.2006.11.044.

68. Mons, E.; Kim, R.Q.; Mulder, M.P.C. Technologies for Direct Detection of Covalent Protein–Drug Adducts. *Pharmaceutics* **2023**, *16*, 547. doi: 10.3390/ph16040547.

69. Gajiwala, K.S.; Feng, J.; Ferre, R.; Ryan, K.; Brodsky, O.; Weinrich, S.; Kath, J.C.; Stewart, A. Insights into the Aberrant Activity of Mutant EGFR Kinase Domain and Drug Recognition. *Structure* **2013**, *21*, 209–219. doi: 10.1016/j.str.2012.11.014.

70. Smith, S.; Keul, M.; Engel, J.; Basu, D.; Eppmann, S.; Rauh, D. Characterization of Covalent-Reversible EGFR Inhibitors. *ACS Omega* **2017**, *2*, 1563–1575. doi: 10.1021/acsomega.7b00157.

71. Donnelly, D.P.; Rawlins, C.M.; DeHart, C.J.; Fornelli, L.; Schachner, L.F.; Lin, Z.; Lippens, J.L.; Aluri, K.C.; Sarin, R.; Chen, B., et al. Best Practices and Benchmarks for Intact Protein Analysis for Top-Down Mass Spectrometry. *Nat. Meth.* **2019**, *16*, 587–594. doi: 10.1038/s41592-019-0457-0.

72. Zhang, Y.; Fonslow, B.R.; Shan, B.; Baek, M.-C.; Yates, J.R. Protein Analysis by Shotgun/Bottom-Up Proteomics. *Chem. Rev.* **2013**, *113*, 2343–2394. doi: 10.1021/cr3003533.

73. Jura, N.; Endres, N.F.; Engel, K.; Deindl, S.; Das, R.; Lamers, M.H.; Wemmer, D.E.; Zhang, X.; Kuriyan, J. Mechanism for Activation of the EGFR Receptor Catalytic Domain by the Juxtamembrane Segment. *Cell* **2009**, *137*, 1293–1307. doi: 10.1016/j.cell.2009.04.025.

74. Cho, J.; Kim, S.; Du, J.; Meyerson, M. Autophosphorylation of the Carboxyl-Terminal Domain Is Not Required for Oncogenic Transformation by Lung-Cancer Derived EGFR Mutants. *Int. J. Cancer* **2018**, *143*, 679–685. doi: 10.1002/ijc.31332.

75. Gehringer, M. Covalent Inhibitors: Back On Track? *Future Med. Chem.* **2020**, *12*, 1363–1368. doi: 10.4155/fmc-2020-0118.

76. Harling, J.D.; Deakin, A.M.; Campos, S.; Grimley, R.; Chaudry, L.; Nye, C.; Polyakova, O.; Bessant, C.M.; Barton, N.; Somers, D.; Barrett, J.; Graves, R.H.; Hanns, L.; Kerr, W.J.; Solaro, R. Discovery of Novel Irreversible Inhibitors of Interleukin (IL)-2-inducible Tyrosine Kinase (Itk) by Targeting Cysteine 442 in the ATP Pocket. *J. Biol. Chem.* **2013**, *288*, 28195–28206. doi: 10.1074/jbc.M113.474114.

77. Lebakken, C.S.; Riddle, S.M.; Singh, U.; Frazee, W.J.; Eliason, H.C.; Gao, Y.; Reichling, L.J.; Marks, B.D.; Vogel, K.W. Development and Applications of a Broad-Coverage, TR-FRET-Based Kinase Binding Assay Platform. *J. Biomol. Screen.* **2009**, *14*, 924–935. doi: 10.1177/1087057109339207.

78. Optimization of a *LanthaScreen™* Eu Kinase Binding Assay for EGFR; Manual version 1; Invitrogen: pp 1-17. https://assets.thermofisher.com/TFS-Assets/LSG/manuals/EGFR_LanthaScreen_Binding.pdf (accessed 2021-07-23).

79. HTRF A Guide To Homogeneous Time Resolved Fluorescence; Cisbio Bioassays: 2018. https://www.bio-connectdiagnostics.nl/uploads/pdf/Cisbio-A_Guide_to_HTRF_2693.pdf (accessed 2021-07-23).

80. Crawford, K. Developing a Time-Resolved Fluorescence Resonance Energy Transfer (TR-FRET) Assay; AppNote 3./01; Molecular Devices: 2001. http://mdc.custhelp.com/euf/assets/content/Analyst_App_Note_TR-FRET%20App%20note.pdf (accessed 2021-07-23).

81. Schiele, F.; Ayaz, P.; Fernández-Montalván, A. A Universal Homogeneous Assay for High-Throughput Determination of Binding Kinetics. *Anal. Biochem.* **2015**, *468*, 42–49. doi: 10.1016/j.ab.2014.09.007.

82. Georgi, V.; Schiele, F.; Berger, B.-T.; Steffen, A.; Marin Zapata, P.A.; Briem, H.; Menz, S.; Preusse, C.; Vasta, J.D.; Robers, M.B.; Brands, M.; Knapp, S.; Fernández-Montalván, A. Binding Kinetics Survey of the Drugged Kinome. *J. Am. Chem. Soc.* **2018**, *140*, 15774–15782. doi: 10.1021/jacs.b080048.

83. Davis, M.I.; Hunt, J.P.; Herrgard, S.; Ciceri, P.; Wodicka, L.M.; Pallares, G.; Hocker, M.; Treiber, D.K.; Zarrinkar, P.P. Comprehensive Analysis of Kinase Inhibitor Selectivity. *Nat. Biotechnol.* **2011**, *29*, 1046–1051. doi: 10.1038/nbt.1990.

84. Lategahn, J.; Keul, M.; Klövekorn, P.; Tumbrink, H.L.; Niggenaber, J.; Müller, M.P.; Hodson, L.; Flaßhoff, M.; Hardick, J.; Grabe, T., et al. Inhibition of Osimertinib-Resistant Epidermal Growth Factor Receptor EGFR-T790M/C7975. *Chem. Sci.* **2019**, *10*, 10789–10801. doi: 10.1039/C9SC03445E.

85. Wang, Y.; Ma, H. Protein Kinase Profiling Assays: A Technology Review. *Drug Discov. Today: Technol.* **2015**, *18*, 1–8. doi: 10.1016/j.ddtec.2015.10.007.

86. González-Vera, J.A. Probing the Kinome in Real Time with Fluorescent Peptides. *Chem. Soc. Rev.* **2012**, *41*, 1652–1664. doi: 10.1039/C1CS15198C.

87. Tardieu, J.-L. HTRF® KinEASE™ TK: A New Solution for Tyrosine Kinase Screening. *Nat. Meth.* **2007**, *4*, i–ii. doi: 10.1038/nmeth1082.

88. Zeggouti, H.; Zdanowska, M.; Hsiao, K.; Goueli, S.A. ADP-Glo: A Bioluminescent and Homogeneous ADP Monitoring Assay for Kinases. *Assay Drug Dev. Technol.* **2009**, *7*, 560–572. doi: 10.1089/adt.2009.0222.

89. Wang, Z.; Candelora, C. In Vitro Enzyme Kinetics Analysis of EGFR. *Methods Mol. Biol.* **2017**, *1487*, 23–33. doi: 10.1007/978-1-4939-6424-6_2.

90. Shults, M.D.; Janes, K.A.; Lauffenburger, D.A.; Imperiale, B. A Multiplexed Homogeneous Fluorescence-Based assay for Protein Kinase Activity in Cell Lysates. *Nat. Meth.* **2005**, *2*, 277–284. doi: 10.1038/nmeth747.

91. Luković, E.; González-Vera, J.A.; Imperiale, B. Recognition-Domain Focused Chemosensors: Versatile and Efficient Reporters of Protein Kinase Activity. *J. Am. Chem. Soc.* **2008**, *130*, 12821–12827. doi: 10.1021/ja8046188.

92. Sjin, R.T.T.; Lee, K.; Walter, A.O.; Dubrovskiy, A.; Sheets, M.; St Martin, T.; Labenski, M.T.; Zhu, Z.; Tester, R.; Karp, R., et al. In Vitro and In Vivo Characterization of Irreversible Mutant-Selective EGFR Inhibitors That Are Wild-Type Sparing. *Mol. Cancer Ther.* **2014**, *13*, 1468–1479. doi: 10.1158/1535-7163.MCT-13-0966.

93. Schwartz, P.A.; Kuzmic, P.; Solowjek, J.; Bergqvist, S.; Bolanos, B.; Almaden, C.; Nagata, A.; Ryan, K.; Feng, J.; Dalvie, D.; Kath, J.C.; Xu, M.; Wani, R.; Murray, B.W. Covalent EGFR Inhibitor Analysis Reveals Importance of Reversible Interactions to Potency and Mechanisms of Drug Resistance. *Proc. Natl. Acad. Sci.* **2014**, *111*, 173. doi: 10.1073/pnas.1313733111.

94. Cheng, H.; Nair, S.K.; Murray, B.W.; Almaden, C.; Bailey, S.; Baxi, S.; Behenna, D.; Cho-Schultz, S.; Dalvie, D.; Dinh, D.M., et al. Discovery of 1-[(3R,4R)-3-[(5-Chloro-1H-pyrazol-4-yl)amino]-7H-pyrrolo[2,3-d]pyrimidin-4-yl]oxy)methyl]-4-methoxypyrrrolidin-1-yl]prop-2-en-1-one (PF-06459988), a Potent, WT Sparing, Irreversible Inhibitor of T790M-Containing EGFR Mutants. *J. Med. Chem.* **2016**, *59*, 2005–2024. doi: 10.1021/acs.jmedchem.5b01633.

95. Planken, S.; Behenna, D.C.; Nair, S.K.; Johnson, T.O.; Nagata, A.; Almaden, C.; Bailey, S.; Ballard, T.E.; Bernier, L.; Cheng, H., et al. Discovery of N-[(3R,4R)-4-Fluoro-1-[(6-((3-methoxy-1-methyl-1H-pyrazol-4-yl)amino)-9-methyl-9H-purin-2-yl)pyrrolidine-3-yl]acrylamide (PF-06747775) through Structure-Based Drug Design: A High Affinity Irreversible Inhibitor Targeting Oncogenic EGFR Mutants with Selectivity over Wild-Type EGFR. *J. Med. Chem.* **2017**, *60*, 3002–3019. doi: 10.1021/acs.jmedchem.6b01894.

96. Zhai, X.; Ward, R.A.; Doig, P.; Argyrou, A. Insight into the Therapeutic Selectivity of the Irreversible EGFR Tyrosine Kinase Inhibitor Osimertinib through Enzyme Kinetic Studies. *Biochemistry* **2020**, *59*, 1428–1441. doi: 10.1021/acs.biochem.0c00104.

97. Walter, A.O.; Sjin, R.T.T.; Haringma, H.J.; Ohashi, K.; Sun, J.; Lee, K.; Dubrovskiy, A.; Labenski, M.; Zhu, Z.; Wang, Z., et al. Discovery of a Mutant-Selective Covalent Inhibitor of EGFR that Overcomes T790M-Mediated Resistance in NSCLC. *Cancer Discov.* **2013**, *3*, 1404–1415. doi: 10.1158/2159-8290.CD-13-0314.

98. Laufer, S.; Bajorath, J.; Gehringer, M.; Gray, N.; Frye, S.; Lindsley, C.W. Publication Criteria and Requirements for Studies on Protein Kinase Inhibitors—What Is Expected? *J. Med. Chem.* **2022**, *65*, 6973–6974. doi: 10.1021/acs.jmedchem.2c00623.

99. Mons, E.; Roet, S.; Kim, R.Q.; Mulder, M.P.C. A Comprehensive Guide for Assessing Covalent Inhibition in Enzymatic Assays Illustrated with Kinetic Simulations. *Curr. Protoc.* **2022**, *2*, e419. doi: 10.1002/cp21.419.

100. Hoyt, K.W.; Urul, D.A.; Ogbuo, B.C.; Wittlinger, F.; Laufer, S.A.; Schaefer, E.M.; May, E.W.; Heppner, D.E. Pitfalls and Considerations in Determining the Potency and Mutant Selectivity of Covalent Epidermal Growth Factor Receptor Inhibitors. *ChemRxiv* **2023**. doi: 10.26434/chemrxiv-2023-tkqkq.

101. *PhosphoSens® Protein Kinase Assay Instruction Manual*; #1001.007; AssayQuant Technologies: 2020. <https://www.assayquant.com/resources>.

102. Guan, I.; Williams, K.; Pan, J.; Liu, X. New Cysteine Covalent Modification Strategies Enable Advancement of Proteome-wide Selectivity of Kinase Modulators. *Asian J. Org. Chem.* **2021**, *10*, 949–963. doi: 10.1002/ajoc.202100036.

103. Sapmaz, A.; Berlin, I.; Bos, E.; Wijdeven, R.H.; Janssen, H.; Konietzny, R.; Akkermans, J.J.; Erson-Bensan, A.E.; Koning, R.I.; Kessler, B.M.; Neeffes, J.; Ovaa, H. USP32 Regulates Late Endosomal Transport and Recycling Through Deubiquitylation of Rab7. *Nat. Commun.* **2019**, *10*, 1454. doi: 10.1038/s41467-019-09437-x.

104. Cicek, E.; Cincir, A.; Oyken, M.; Akbulut Caliskan, O.; Dioken, D.N.; Guntekin Ergun, S.; Cetin-Atalay, R.; Sapmaz, A.; Ovaa, H.; Sahin, O.; Erson-Bensan, A.E. EGF-SNX3-EGFR Axis Drives Tumor Progression and Metastasis in Triple-Negative Breast Cancers. *Oncogene* **2022**, *41*, 220–232. doi: 10.1038/s41388-021-02086-9.

105. EGFR. In *The Human Protein Atlas* [Online]. <https://www.proteinatlas.org/ENSG00000146648-EGFR/cell+line>

106. ERBB2. In *The Human Protein Atlas* [Online]. <https://www.proteinatlas.org/ENSG00000141736-ERBB2/cell+line>

107. Chen, B.; Mao, R.; Wang, H.; She, J.-X. Cell Line and Drug-Dependent Effect of ERBB3 on Cancer Cell Proliferation, Chemosensitivity, and Multidrug Actions. *Int. J. High Throughput Screen.* **2010**, *1*, 49–55. doi: 10.2147/IJHTS.S8235.

108. Brescia, P.J.; Banks, P.; Cornell-Kennon, S.; Schaefer, E.; Imperiali, B. *Monitoring of Protein Kinase Activity Using Next Generation CSox-based Substrate Sensors*; AppNote #AN080117_07; BioTek Instruments: 2017. <https://www.biotek.com/resources/application-notes/monitoring-of-protein-kinase-activity-using-next-generation-csox-based-substrate-sensors/> (accessed 2021-07-26).

109. Shultz, M.D.; Imperiali, B. Versatile Fluorescence Probes of Protein Kinase Activity. *J. Am. Chem. Soc.* **2003**, *125*, 14248-14249. doi: 10.1021/ja0380502.

110. Carey, K.D.; Garton, A.J.; Romero, M.S.; Kahler, J.; Thomson, S.; Ross, S.; Park, F.; Haley, J.D.; Gibson, N.; Sliwkowski, M.X. Kinetic Analysis of Epidermal Growth Factor Receptor Somatic Mutant Proteins Shows Increased Sensitivity to the Epidermal Growth Factor Receptor Tyrosine Kinase Inhibitor, Erlotinib. *Cancer Res.* **2006**, *66*, 8163-8171. doi: 10.1158/0008-5472.CAN-06-0453.

111. Baulida, J.; Kraus, M.H.; Alimandi, M.; Fiore, P.P.D.; Carpenter, G. All ErbB Receptors Other Than the Epidermal Growth Factor Receptor Are Endocytosis Impaired. *J. Biol. Chem.* **1996**, *271*, 5251-5257. doi: 10.1074/jbc.271.9.5251.

112. Rabindran, S.K.; Discanfi, C.M.; Rosfjord, E.C.; Baxter, M.; Floyd, M.B.; Golas, J.; Hallett, W.A.; Johnson, B.D.; Nilakantan, R.; Overbeek, E.; Reich, M.F.; Shen, R.; Shi, X.; Tsou, H.-R.; Wang, Y.-F.; Wissner, A. Antitumor Activity of HKI-272, an Orally Active, Irreversible Inhibitor of the HER-2 Tyrosine Kinase. *Cancer Res.* **2004**, *64*, 3958-3965. doi: 10.1158/0008-5472.CAN-03-2868.

113. Awoonor-Williams, E.; Rowley, C.N. How Reactive are Drugable Cysteines in Protein Kinases? *J. Chem. Inf. Model.* **2018**, *58*, 1935-1946. doi: 10.1021/acs.jcim.8b00454.

114. Lalmanach, G.; Saidi, A.; Bigot, P.; Chazeirat, T.; Lecaille, F.; Wartenberg, M. Regulation of the Proteolytic Activity of Cysteine Cathepsins by Oxidants. *Int. J. Mol. Sci.* **2020**, *21*, 1944. doi: 10.3390/ijms21061944.

115. Harris, T.K.; Turner, G.J. Structural Basis of Perturbed pKa Values of Catalytic Groups in Enzyme Active Sites. *IUBMB Life* **2002**, *53*, 85-98. doi: 10.1080/15216540211468.

116. Discanfi, C.M.; Carroll, M.L.; Floyd, M.B.; Hollander, I.J.; Husain, Z.; Johnson, B.D.; Kitchen, D.; May, M.K.; Malo, M.S.; Minnick, A.A.; Nilakantan, R.; Shen, R.; Wang, Y.-F.; Wissner, A.; Greenberger, L.M. Irreversible Inhibition of Epidermal Growth Factor Receptor Tyrosine Kinase with *In Vivo* Activity by *N*-[4-(3-bromophenyl)amino]-6-quinazolinyl]-2-butynamide (CL-387,785). *Biochem. Pharmacol.* **1999**, *57*, 917-925. doi: 10.1016/S0006-2952(98)00356-6.

117. Wood, E.R.; Shewchuk, L.M.; Ellis, B.; Brignola, P.; Brashear, R.L.; Caferro, T.R.; Dickerson, S.H.; Dickson, H.D.; Donaldson, K.H.; Gaul, M., et al. 6-Ethynylthieno[3,2-d]- and 6-Ethynylthieno[2,3-d]pyrimidin-4-anilines as Tunable Covalent Modifiers of ErbB Kinases. *Proc. Natl. Acad. Sci.* **2008**, *105*, 2773. doi: 10.1073/pnas.0708281105.

118. Boschelli, D.H.; Wang, D.Y.; Ye, F.; Yamashita, A.; Zhang, N.; Powell, D.; Weber, J.; Boschelli, F. Inhibition of Src Kinase Activity by 4-anilino-7-thienyl-3-quinolinecarbonitriles. *Bioorg. Med. Chem. Lett.* **2002**, *12*, 2011-2014. doi: 10.1016/S0960-894X(02)00302-5.

119. Boschelli, D.H.; Wang, Y.D.; Ye, F.; Wu, B.; Zhang, N.; Dutia, M.; Powell, D.W.; Wissner, A.; Arndt, K.; Weber, J.M.; Boschelli, F. Synthesis and Src Kinase Inhibitory Activity of a Series of 4-Phenylamino-3-quinolinecarbonitriles. *J. Med. Chem.* **2001**, *44*, 822-833. doi: 10.1021/jm000420z.

120. Chen, D.; Guo, D.; Yan, Z.; Zhao, Y. Allenamide As a Biosisostere of Acrylamide in the Design and Synthesis of Targeted Covalent Inhibitors. *MedChemComm* **2018**, *9*, 244-253. doi: 10.1039/C7MD00571G.

121. Klutcho, S.R.; Zhou, H.; Winters, R.T.; Tran, T.P.; Bridges, A.J.; Althaus, I.W.; Amato, D.M.; Elliott, W.L.; Ellis, P.A.; Meade, M.A., et al. Tyrosine Kinase Inhibitors. 19. 6-Alkynamides of 4-Anilinoquinazolines and 4-Anilinopyrido[3,4-d]pyrimidines as Irreversible Inhibitors of the erbB Family of Tyrosine Kinase Receptors. *J. Med. Chem.* **2006**, *49*, 1475-1485. doi: 10.1021/jm050936o.

122. Luna-Vargas, M.P.A.; Christodoulou, E.; Alfieri, A.; van Dijk, W.J.; Stadnik, M.; Hibbert, R.G.; Sahtoe, D.D.; Clerici, M.; Marco, V.D.; Littler, D.; Celie, P.H.N.; Sixma, T.K.; Perrakis, A. Enabling High-Throughput Ligation-independent Cloning and Protein Expression for the Family of Ubiquitin Specific Proteases. *J. Struct. Biol.* **2011**, *175*, 113-119. doi: 10.1016/j.jsb.2011.03.017.

123. Abramoff, M.; Magalhães, P.; Ram, S.J. Image Processing with ImageJ. *Biophotonics Intern.* **2003**, *11*, 36-42.

124. Rasband, W.S. *ImageJ*. U.S. National Institutes of Health, Bethesda, Maryland, USA: 1997-2018. <https://imagej.nih.gov/ijr>.

125. Schneider, C.A.; Rasband, W.S.; Eliceiri, K.W. NIH Image to ImageJ: 25 Years of Image Analysis. *Nat. Meth.* **2012**, *9*, 671-675. doi: 10.1038/nmeth.2089.

126. Carmi, C.; Galvani, E.; Vacondio, F.; Rivara, S.; Lodola, A.; Russo, S.; Aiello, S.; Bordi, F.; Costantino, G.; Cavazzoni, A.; Alfieri, R.R.; Ardizzone, A.; Petronini, P.G.; Mor, M. Irreversible Inhibition of Epidermal Growth Factor Receptor Activity by 3-Aminopropanamides. *J. Med. Chem.* **2012**, *55*, 2251-2264. doi: 10.1021/jm201507x.

127. Blum, D.M.; Boschelli, D.H.; Feigelson, G.B.; Strong, H.L.; Wiggins Sutherland, K. Process for Preparation of 4-Amino-3-Quinolinecarbonitriles. US20050043537A1, 24 February, 2005.

128. Boschelli, D.H.; Wu, B.; Ye, F.; Wang, Y.; Golas, J.M.; Lucas, J.; Boschelli, F. Synthesis and Src Kinase Inhibitory Activity of a Series of 4-[2,4-Dichloro-5-methoxyphenyl]amino]-7-furyl-3-quinolinecarbonitriles. *J. Med. Chem.* **2006**, *49*, 7868-7876. doi: 10.1021/jm061031t.

129. Fors, B.P.; Watson, D.A.; Biscoe, M.R.; Buchwald, S.L. A Highly Active Catalyst for Pd-Catalyzed Amination Reactions: Cross-Coupling Reactions Using Aryl Mesylates and the Highly Selective Monoarylation of Primary Amines Using Aryl Chlorides. *J. Am. Chem. Soc.* **2008**, *130*, 13552-13554. doi: 10.1021/ja8055358.

130. Kuzmić, P. *Biochemical/Biophysical Kinetics "Made Easy": Software DYNAFIT in Drug Discovery Research*; BioKin Ltd. <http://www.biokin.com/slides/1212-novartis.pdf> (accessed 2021-07-23).

131. *LanthaScreen® TR-FRET ER Beta Competitive Binding Assay*; MAN0010002; Life Technologies: 2014. http://tools.thermofisher.com/content/sfs/manuals/lanthascreen_tr_fret_er_beta_comp_binding_assay_man.pdf (accessed 2021-07-23).

132. Ulusu, N.N. Evolution of Enzyme Kinetic Mechanisms. *J. Mol. Evol.* **2015**, *80*, 251-257. doi: 10.1007/s00239-015-9681-0.

133. Posner, I.; Engel, M.; Levitzki, A. Kinetic Model of the Epidermal Growth Factor (EGF) Receptor Tyrosine Kinase and a Possible Mechanism of Its Activation by EGF. *J. Biol. Chem.* **1992**, *267*, 20638-20647. doi: 10.1016/S0021-9258(19)36734-1.

134. Reytor González, M.L.; Cornell-Kennon, S.; Schaefer, E.; Kuzmić, P. An Algebraic Model to Determine Substrate Kinetic Parameters by Global Nonlinear Fit of Progress Curves. *Anal. Biochem.* **2017**, *518*, 16-24. doi: 10.1016/j.ab.2016.11.001.

135. Kuzmić, P. *Covalent Inhibition Kinetics: Application to EGFR Kinase*; BioKin Ltd: 2014. <http://www.biokin.com/slides/1409-az.pdf> (accessed 2021-07-23).

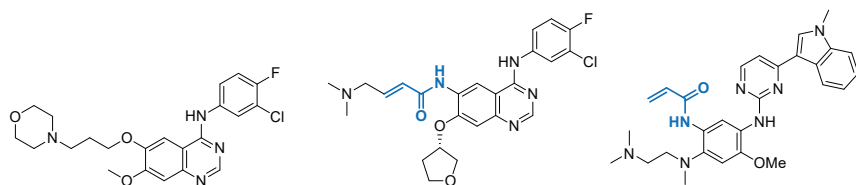
136. Adams, J. A. Kinetic and Catalytic Mechanisms of Protein Kinases. *Chem. Rev.* **2001**, *101*, 2271-2290. doi: 10.1021/cr000230w.

137. Kuzmić, P.; Solowiej, J.; Murray, B.W. An Algebraic Model for the Kinetics of Covalent Enzyme Inhibition at Low Substrate Concentrations. *Anal. Biochem.* **2015**, *484*, 82-90. doi: 10.1016/j.ab.2014.11.014.

138. Beck, J.R.; Peterson, L.B.; Imperiali, B.; Stains, C.I. Quantification of Protein Kinase Enzymatic Activity in Unfractionated Cell Lysates Using CSox-Based Sensors. *Curr. Protoc. Chem. Biol.* **2014**, *6*, 135-156. doi: 10.1002/9780470559277.ch140106.

7. Supporting Information

7.1. Literature Values for EGFR Activity and Inhibition



Biochemical IC ₅₀ (nM)	gefitinib	afatinib	osimertinib
EGFR ^{WT}	0.2	<0.1	1.0
EGFR ^{L858R}	<0.1	<0.1	0.7
EGFR ^{L858R/T790M}	185	0.3	0.3
EGFR ^{L858R/T790M/C797S}	250	25	116

Figure S1 | Chemical structure, name, and *in vitro* biochemical IC₅₀ (nM) against recombinant EGFR (mutant) activity reported by Lategahn *et al.*⁸⁴ Covalent warheads are marked in blue.

Table S1 | Reported ATP affinity of (mutant) EGFR.³⁸

	K _{M,ATP} (μM)	k _{cat} (s ⁻¹)	k _{cat} /K _{M,ATP} (×10 ³ M ⁻¹ s ⁻¹)
EGFR ^{WT}	5.2 ± 0.2	0.026	5
EGFR ^{T790M}	5.9 ± 0.1	0.137	23
EGFR ^{L858R}	148 ± 4	1.484	10
EGFR ^{L858R/T790M}	8.4 ± 0.3	0.456	54

Table S2 | Reported biochemical IC₅₀ values (nM).

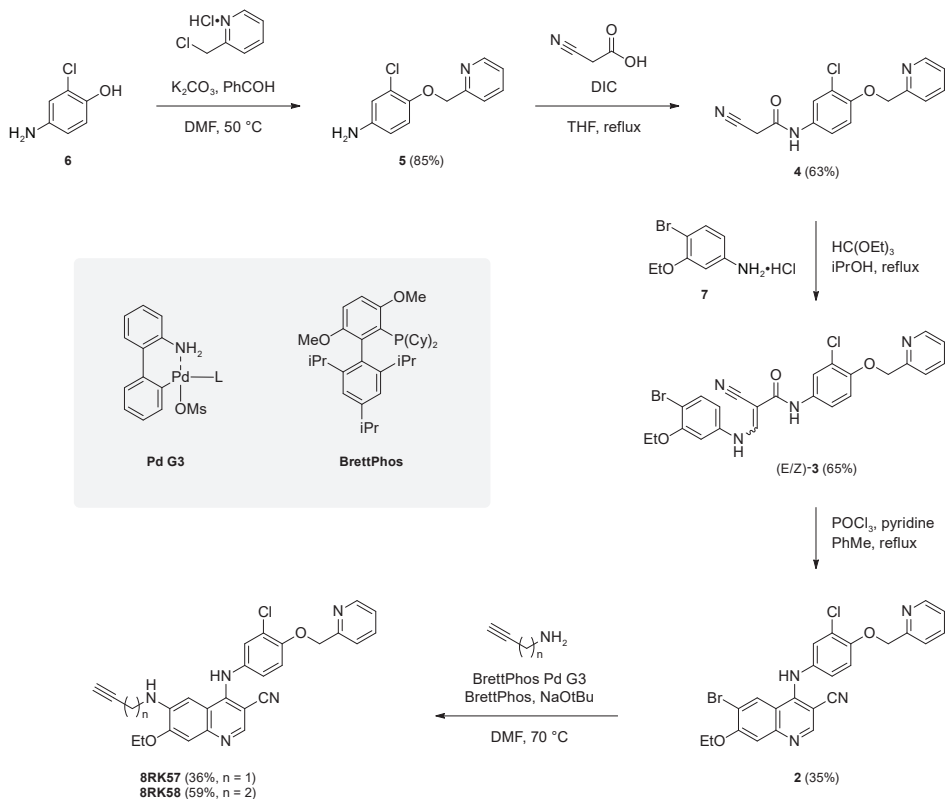
	erlotinib	gefitinib	lapatinib	neratinib	afatinib	vandetanib	staurosporine
EGFR ^{WT}	0.67	1	2.4	1.1 *	0.25 *	9.5	370
EGFR ^{T790M}	140	40	860	1.5 *	0.61 *	100	0.77
EGFR ^{L858R}	0.97	0.94	2.8	0.67 *	0.2 *	8.7	270
EGFR ^{L858R/T790M}	190	140	>104	27 *	1.1 *	230	0.35
HER2	2900	3500	7	6 *	5 *	2600	190
HER3	1100	790	5500	7.7 *	4500 *	160	>104
HER4	230	410	54	2.4 *	6.3 *	480	770
SRC	700	3800	>104	4100 *	2800 *	70	86

Inhibitor potency in ATP site-dependent competition binding assay (KINOMEscan Technology Platform).⁸³ * Values not corrected for irreversible covalent binding mode.

7.2. Chemical Synthesis

Precursor 6-bromoquinoline **2** was prepared at Mercachem (now: Symeres Nijmegen) (**Scheme S1**) by adaptation of reported methodology for large scale preparation of 4-amino-3-quinolinecarbonitriles targeting Src kinase domain¹²⁷⁻¹²⁸ and 3-cyano-quinolines targeting the HER kinase family.⁵⁷

Alkyne derivatives **8RK57** and **8RK58** were obtained in a single step from bromoquinoline **2** by Pd-catalyzed C–N cross-coupling with primary amines under Buchwald–Hartwig amination conditions.⁶⁰ BrettPhos Palladacycle G3 (L = BrettPhos) and BrettPhos are recommended Pd-(pre)catalyst and dialkylbiaryl phosphine ligand for mono N-arylation of primary aliphatic amines.⁶⁰ C–N cross-coupling with a secondary amine is much slower than with a primary amine, thus minimizing formation of undesired biarylation product or homocoupling product.¹²⁹



Scheme S1 | Chemical synthesis of neratinib derivatives. Alkylation of aminophenol **6** to form aniline **5** was followed by DIC-mediated amide coupling with cyanoacetic acid to afford acetamide **4**. Treatment of acetamide **4** with triethyl orthoformate and primary aniline **7** afforded cyanoacrylamide **3** as a mixture of the (E)- and (Z)-isomer. Subsequent phosphorus oxychloride-mediated ring closure resulted in the formation of 6-bromo-4-anilino-3-quinolinecarbonitrile **2**. Treatment of bromoquinoline **2** with excess propargylamine or 1-amino-3-butyne in presence of third generation Pd-precatalyst BrettPhos Palladacycle G3 and dialkylbiaryl phosphine ligand BrettPhos afforded alkyne derivatives **8RK57** and **8RK58**.

7.3. Thiol Reactivity Assay

Table S3 | Thiol Adduct Formation related to **Figure 3**.

Compound	Rt (min)	m/z (Da)	UV area at t (h)						
			0	1	2	3	4		
neratinib	Unbound	1.54	557.2	9859 9047	8138 7542	6567 5669	5576 5444	4599 4058	757 466
	GSH Adduct	1.47	864.3	0 4.7	2246 2159	3380 3187	4105 3968	4397 4118	9019 8373
	GSH occupancy (%)		0.05 ± 0.07	22 ± 0.49	35 ± 1.4	42 ± 0.14	50 ± 1.1	94 ± 1.7	
8RK57	Unbound	1.76	484.1	4237 3738	4103 3883	4197 4655	3992 4638	4165 4192	3987 4528
	GSH Adduct	—	791.2	BLD BLD	BLD BLD	BLD BLD	BLD BLD	BLD BLD	BLD BLD
	GSH occupancy (%)		0	0	0	0	0	0	0
8RK58	Unbound	1.82	498.1	2666 2335	2380 1781	1762 1405	1822 1506	1194 1957	1106 1250
	GSH Adduct	—	805.2	BLD BLD	BLD BLD	BLD BLD	BLD BLD	BLD BLD	BLD BLD
	GSH occupancy (%)		0	0	0	0	0	0	0
gefitinib	Unbound	1.50	447.1	15757 15363	17274 16853	17643 16490	16885 16356	17220 15568	16350 12481
	GSH Adduct	—	754.2	BLD BLD	BLD BLD	BLD BLD	BLD BLD	BLD BLD	BLD BLD
	GSH occupancy (%)		0	0	0	0	0	0	0
afatinib	Unbound	1.51	486.1	7209 7331	4490 4530	2491 2601	1494 1492	897 860	41 38
	GSH Adduct	1.45	793.2	40 49	3400 3642	4945 5274	6020 6175	6421 6617	6965 7137
	GSH occupancy (%)		0.65 ± 0.07	44 ± 1.1	67 ± 0.35	80 ± 0.28	88 ± 0.57	99 ± 0.07	

LC-MS analysis of inhibitor (100 μ M) incubated with 5 mM GSH in PBS pH7.5 at 37 °C. Quantification of unbound inhibitor and GSH adduct (\pm 307 Da) from integration of UV absorbance area ($\lambda_{\text{abs}} = 350$ nm) following established protocol.^{54, 67} BLD = below limit of detection. *italic*: theoretical value for adduct (not observed). Details on calculations of GSH occupancy and kinetic fits can be found in *section 4.1*. Values for GSH occupancy are mean \pm SD.

7.4. Intact Protein MS Analysis

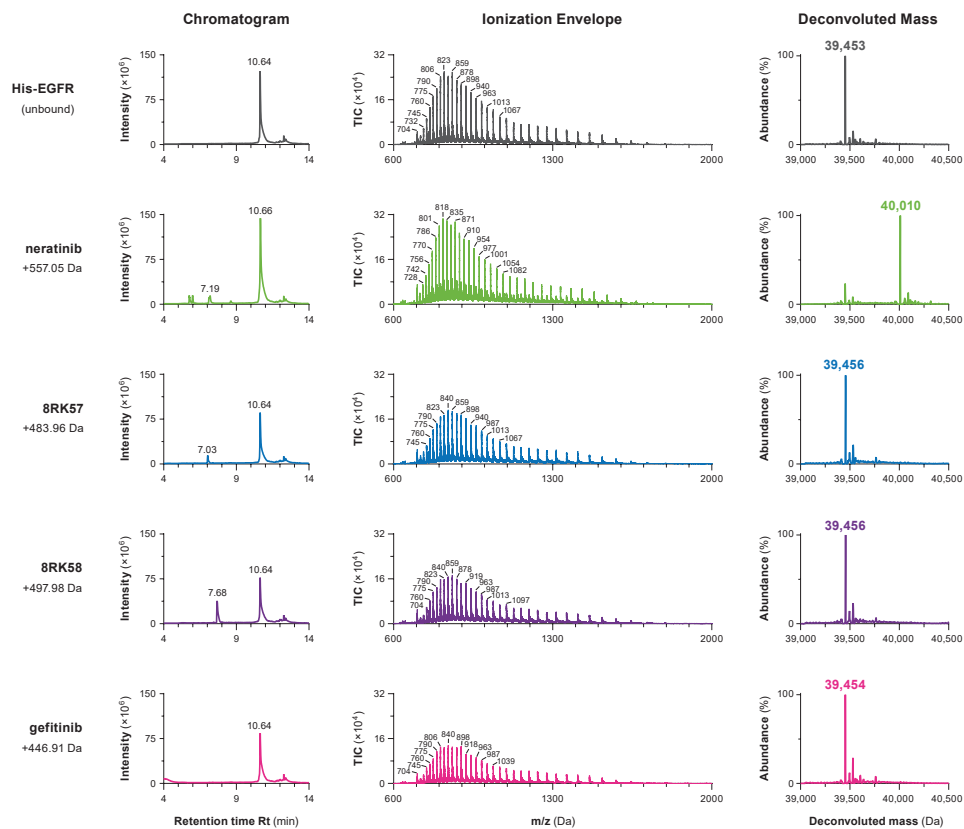


Figure S2 | LC-MS traces for intact protein MS analysis of unbound His-EGFR (1 μ M) incubated with inhibitor (100 μ M) for 4 h at 21 °C. Data accompanying Figure 4. *Left:* UPLC chromatogram. *Middle:* Electrospray ionization mass spectrum. *Right:* Deconvoluted mass (average isotopes).

Table S4 | Screening conditions for covalent adduct formation (intact protein MS analysis).

compound	[compound]	Covalent adduct	
		4 h	24 h
DMSO	—	—	—
neratinib	100 μ M	+ ^a	+ ^b
	10 μ M	N.A.	+
8RK57	100 μ M	—	—
	10 μ M	N.A.	—
8RK58	100 μ M	—	—
	10 μ M	N.A.	—
gefitinib	100 μ M	—	N.A.

Detection of covalent adduct by intact protein MS analysis. His-EGFR (1 μ M) treated with excess compound is incubated at 21 °C for the indicated time. N.A. = not applicable. ^a10:2 adduct/unbound EGFR. ^b10:1:1 adduct/unbound/double adduct (double addition of compound).

7.5. Lanthascreen Kinase Binding Assay

Assay conditions were optimized to maximize the assay window while avoiding inhibitor depletion. An intrinsic issue with kinase binding assays is the minimum required kinase concentration for a detectable signal. We found that 2 nM GST-EGFR was the minimum kinase concentration. At lower kinase concentration, the signal at 620 nm originating from the FRET donor was too high, even in presence of GST-EGFR and FRET acceptor, because a large portion of EuAb is unbound ($K_{D,EuAb} = 0.6$ nM).¹³⁰

FRET acceptor kinase tracer 199 (KT199) was initially used at the recommended concentration of 25 nM.⁷⁸ The optimal tracer concentration depends on the tracer potency, desired competition and assay window. Tracer concentrations above 100 nM are not recommended as these could cause artefacts related to diffusion-enhanced TR-FRET: a signal that is not related to a biological binding event but the result of the FRET donor being in close proximity of the FRET acceptor in solution. Diffusion-enhanced FRET increases with a higher tracer concentration, thereby increasing the background (Figure S3B).¹³¹ Tracer potency and assay window are linked properties: more kinase is engaged in the kinase-tracer complex at a high tracer concentration ($[tracer] \gg K_D$), but if the tracer concentration is too high it induces diffusion-enhanced TR-FRET thus narrowing the assay window (Figure S3C).

Confronted with tight-binding behavior, tracer was increased to the maximum recommended concentration: competitive tracer binding would decrease the apparent inhibitor binding potency. Unfortunately, neratinib was unable to fully displace 100 nM tracer, and the resulting assay window was unsuitable to assess inhibitor binding potency (Figure S3C, left). Incomplete tracer dissociation may be caused by a secondary low-affinity tracer binding site or binding configuration uncompetitive with neratinib binding, thus interfering with tracer displacement at high tracer concentrations.

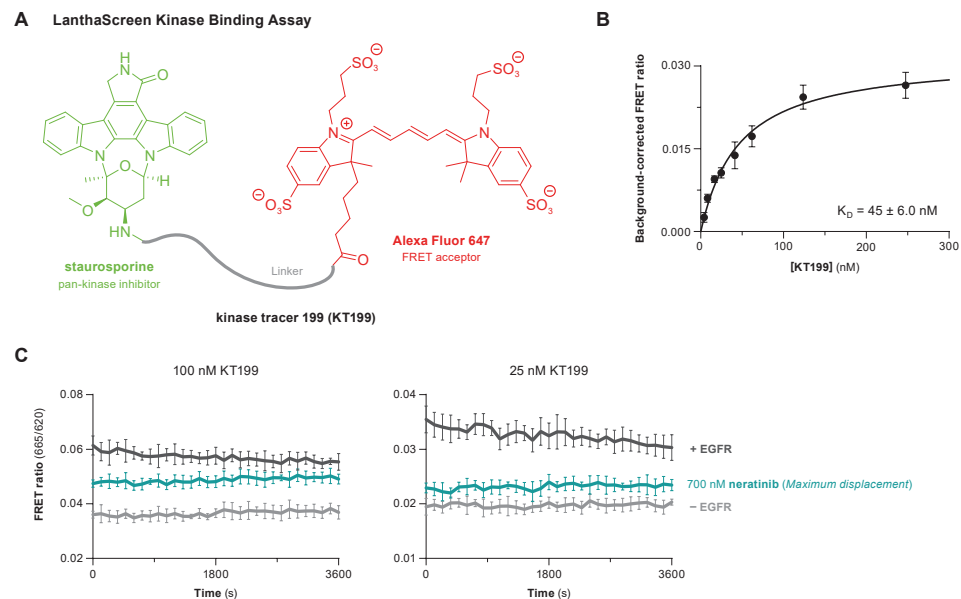


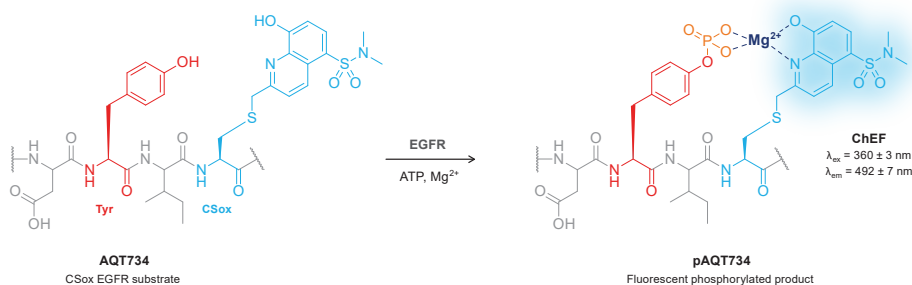
Figure S3 | *In vitro* Lanthascreen kinase binding assay. Data accompanying Figure 5. (A) KT199 is a conjugate of pan-kinase inhibitor stauroporine and FRET acceptor Alexa Fluor 647. (B) Calculation of tracer dissociation constant K_D after baseline correction: subtraction of EuAb + KT199 signal in absence of GST-EGFR. (C) Progress curves for 2 nM GST-EGFR with 100 nM KT199 (left) or 25 nM KT199 (right). Maximum KT199 displacement by 700 nM neratinib is ineffective.

7.6. PhosphoSens Kinase Activity Assay

EGFR-mediated substrate phosphorylation is a bisubstrate reaction which complicates algebraic evaluation of inhibition.¹³²⁻¹³³ Fortunately, the reaction can be simplified to a (truncated) hit-and-run model ($E + S \rightarrow E + P$) because a high ATP concentration (estimated $K_{M,ATP} \ll 1$ mM) and low CSox substrate concentration (estimated $K_{M,CSox} \gg 10$ μ M) are used.^{93, 134-136} Please consult the supporting information accompanying the benchmark manuscript on (ir)reversible EGFR inhibition by Schwartz and co-worker for a detailed description of Sox substrate kinetics.⁹³

Important factors driving EGFR activity observed in PhosphoSens kinase activity assays are the EGFR concentration, the affinity for the Sox-containing substrate (Figure S4A), and the concentrations of chelating reagent Mg^{2+} (10 mM) and ATP (1 mM). Additionally, we found that loss of EGFR activity can be minimized by fresh addition of ATP and DTT from single-use aliquots, addition of EGTA to remove Ca^{2+} interfering with Mg^{2+} chelation to CSox substrate,⁸⁶ and the use of low-bind tubes. Kinase concentration was optimized to ensure maximum 10% substrate conversion during the measurement (Michaelis-Menten kinetics). The reaction with 0.25 nM GST-EGFR resulted in linear product formation without substrate depletion (less than 10% of the substrate was phosphorylated) for the duration of two hours. A delay in EGFR activity was sometimes observed, probably because the kinase domain is not preincubated with competing ATP (Figure S4B). This lag phase, also reported for other Omnia kinase activity assays,¹³⁷⁻¹³⁸ was excluded from (kinetic) fits.

A PhosphoSens Kinase Activity Assay



B

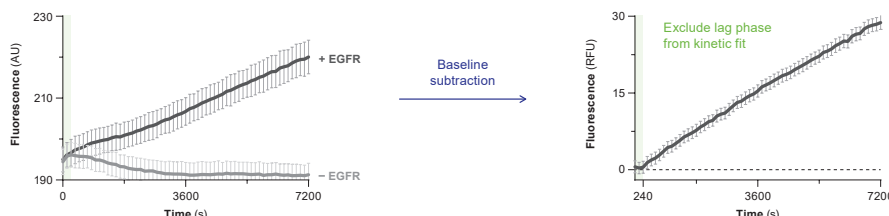


Figure S4 | *In vitro* PhosphoSens kinase activity assay. Data accompanying Figure 6. (A) EGFR substrate AQT734 is a CSox-based fluorescent chemosensor. CSox is an unnatural amino acid consisting of a cysteine residue alkylated with a sulfonamido-oxine (Sox) with a low intrinsic affinity for Mg^{2+} .⁹¹ Phosphorylation of a nearby tyrosine increases the affinity for Mg^{2+} resulting in a 4-fold increase of chelation enhanced fluorescence (ChEF).^{101, 108} (B) EGFR activity exhibits a lag phase of ~4 min. This lag phase is excluded from fits after baseline correction (subtraction of signal in CSox substrate in absence of EGFR).

7.7. Inhibition of Cellular EGFR (Auto)phosphorylation

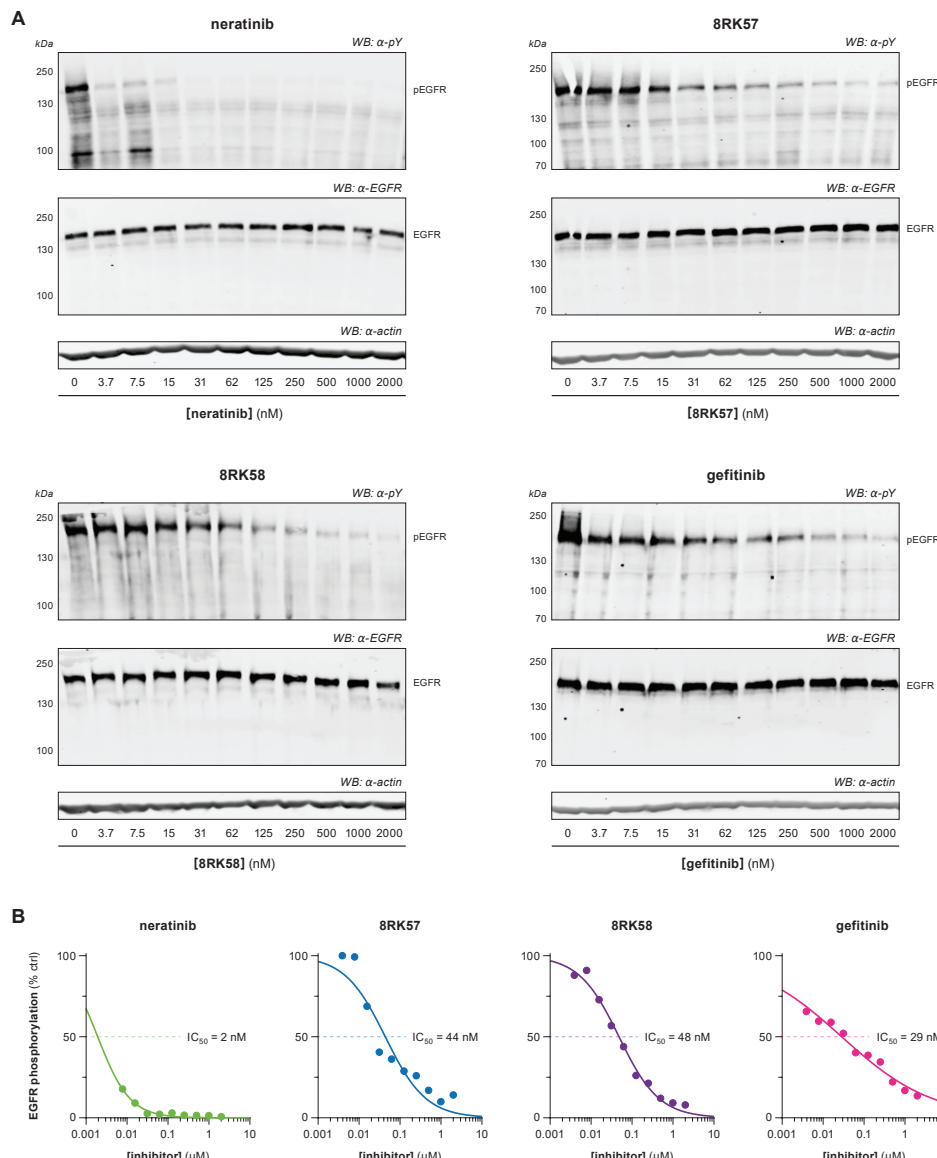


Figure S5 | Cellular EGFR (auto)phosphorylation in intact HeLa cells. Data accompanying **Figure 7D**. HeLa cells are incubated with various inhibitor concentrations for 1 h. EGFR (auto)phosphorylation is visualized and quantified from the Western blots. **(A)** Full gel scans. For each inhibitor, phosphorylated tyrosine residues pY (top), total EGFR (middle), and β -actin (bottom) are visualized by immunoblotting. Darker bands indicate higher intensity of phosphorylated tyrosine/total EGFR/ β -actin. β -actin is a loading control for total protein loading. **(B)** Dose-response curves. Intensity of phosphorylated tyrosine corresponding to pEGFR is divided by intensity of total EGFR, and normalized to the vehicle-treated control. Relative receptor phosphorylation against inhibitor concentration is fitted to the 4-parameter Hill equation to obtain the IC_{50} for inhibition of cellular EGFR (auto)phosphorylation ($n = 1$).



Chapter 6



The Versatility of Substituted Propargyl Warheads in Ub-ABPs

Adapted from:

Mons, E.; Kim, R.Q.; van Doedewaerd, B.R.; van Veelen, P.A.; Mulder, M.P.C.; Ovaa, H. Exploring the Versatility of the Covalent Thiol–Alkyne Reaction with Substituted Propargyl Warheads: A Deciding Role for the Cysteine Protease. *J. Am. Chem. Soc.* **2021**, *143*, 6423–6433. doi:10.1021/jacs.0c10513.

Abstract. Terminal nonactivated alkynes are nowadays considered the golden standard for cysteine-reactive warheads in activity-based probes (ABPs) targeting cysteine deubiquitinating enzymes (CysDUBs). In this work, we study the versatility of the thiol–alkyne addition reaction in more depth. Contrary to previous findings with UCHL3, we now show that covalent adduct formation can progress with substituents on the terminal or internal alkyne position. Strikingly, acceptance of alkyne substituents is strictly CysDUB-specific as this is not conserved among members of the same subfamily. Covalent adduct formation with the catalytic cysteine residue was validated by gel analysis and mass spectrometry of intact ABP-treated USP16CD^{WT} and catalytically inactive mutant USP16CD^{C205A}. Bottom-up mass spectrometric analysis of the covalent adduct with a deuterated propargyl ABP provides mechanistic understanding of *in situ* thiol–alkyne reaction, identifying the alkyne rather than an allenic intermediate as the reactive species. Furthermore, kinetic analysis revealed that introduction of (bulky/electron-donating) methyl substituents on the propargyl moiety decreases the rate of covalent adduct formation, thus providing a rational explanation for the commonly lower level of observed covalent adduct compared to unmodified alkynes. Altogether, our work extends the scope of possible propargyl derivatives in cysteine targeting ABPs from unmodified terminal alkynes to internal and substituted alkynes, which we anticipate will have great value in the development of ABPs with improved selectivity profiles.



1. Introduction

Ubiquitination is a post-translational modification (PTM) which regulates many cellular processes.¹⁻³ Aberrant ubiquitination has been observed in numerous diseases, rendering the enzymes involved as attractive targets for drug design.⁴⁻⁸ Ubiquitination involves ligation of Ubiquitin (Ub), a small 76-amino acid protein, onto the target protein by the E1-E2-E3 ligase machinery. Deubiquitinating enzymes (DUBs) reverse this process by cleavage of the native isopeptide bond between the Ub C-terminus and the target protein Lys (lysine) residue, or between the distal and proximal Ub in poly-Ub chains.⁸⁻⁹ Cysteine DUBs are classified by their catalytic domain, which contains a catalytic cysteine residue essential for their proteolytic function. There are currently six known classes of human cysteine DUBs; USP, OTU, UCH, MJD, MINDY, and ZUFSP.^{1, 10} Their proteolytic activity can be monitored with activity-based probes (ABPs), which covalently trap active enzymes by formation of a covalent bond between an electrophilic warhead on the ABP and the nucleophilic cysteine residue in the targeted enzyme.¹¹⁻¹³ Cysteine DUB ABPs have been utilized to monitor DUB activity during infection, in disease and/or upon inhibitor treatment,¹⁴⁻¹⁷ to identify new DUB (classes) and catalytic cysteine residues in newly discovered DUBs,¹⁸⁻²¹ and to visualize Ub binding in crystal structures of covalent adducts.²²⁻²³

Terminal nonactivated alkynes were believed to be unreactive towards (nontargeted) thiols under physiological conditions, and are therefore widely applied as bioorthogonal handles.²⁴⁻²⁶ However, in 2013 two independent groups²⁷⁻²⁸ discovered that propargylamide on the C-terminus of ubiquitin(-like modifiers; Ubl) can act as a latent electrophile, forming an irreversible covalent adduct with the catalytic cysteine thiol of cysteine proteases that normally cleave the native Ub(l)-Lys isopeptide bond (**Figure S1A**). The propargyl (**Prg**) moiety has since been utilized in various covalent Ub(l)-based ABPs, and is considered the golden standard for DUB ABPs because of its high stability, ease of synthesis and lack of intrinsic reactivity with nontargeted thiols.^{17-18, 29} Formation of a Markovnikov-type thiovinyl bond between active site cysteine thiol and internal (quaternary) alkyne carbon has been confirmed with numerous crystal structures of Ub(l)-**Prg** ABPs bound to human and viral cysteine proteases (summarized in **Table S1**). Recently we showed that the thiol-alkyne reaction can be extended to small molecule inhibitors; a small recognition element is sufficient to initiate covalent thiovinyl bond formation between the cathepsin K catalytic cysteine thiol and the inhibitor alkyne moiety.³⁰

The covalent thiol-alkyne addition forming a Markovnikov-type thiovinyl adduct is a newly discovered reaction for which several reaction mechanisms have been proposed (**Scheme 1**). A radical-mediated thiol-yne mechanism was quickly excluded because covalent adduct formation was not prevented by absence of light and/or addition of radical scavengers, and would have resulted in the *anti*-Markovnikov-type thiovinyl bond adduct with terminal C1 carbon (**Scheme 1A**).³¹⁻³² Ekkebus *et al.*²⁷ and Sommer *et al.*²⁸ both propose a proximity-driven *in situ* thiol(ate)-alkyne addition that involves direct nucleophilic attack of the catalytic cysteine thiol(ate) to the alkyne internal C2 carbon (**Scheme 1B**). However, it was not possible to exclude the possibility that nucleophilic addition actually occurs with a more reactive allenic isomer, present at the enzyme active site in equilibrium with the unreactive terminal alkyne (**Scheme 1C**).³³⁻³⁴ Alternatively, Arkona *et al.*³⁵ propose an enzyme-templated

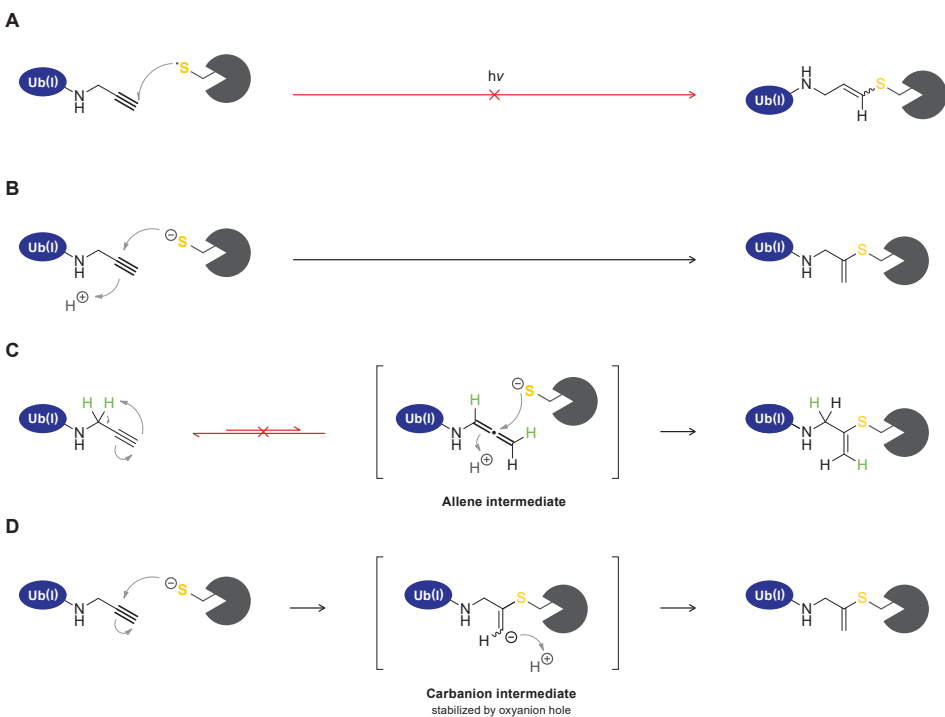
stepwise reaction with stabilization of a secondary carbanion intermediate in the oxyanion hole to overcome the thermodynamically unfavored bond formation (**Scheme 1D**). This stepwise reaction mechanism would be similar to cysteine/serine protease-mediated proteolysis of native amide bonds that involves stabilization of the anion intermediate in the oxyanion hole, *via* interactions with polar residues such as glutamine or by H-bonds with backbone amides.³⁶⁻³⁷

To date, the scope of the thiol–alkyne addition with nonactivated alkynes has been limited to unsubstituted terminal propargylamide; Ekkebus *et al.* report that substituting the hydrogens on either the terminal C1 carbon (CH) or the internal C3 carbon (CH₂) of the propargyl moiety in Ub-Prg mitigates covalent bond formation with UCHL3 (**Figure 1**).²⁷ The lack of reactivity was contributed to mechanistic components, like an important role for the terminal alkyne proton, or formation of a reactive allene intermediate at the active site. Alternatively, we now hypothesize that the lack of reactivity with substituted propargyl derivatives is resultant from specific steric interactions at the UCHL3 active site, and as such not representative for the prospective reactivity with other cysteine DUBs. Variation in the warhead has been reported to affect the adduct formation pattern in cell lysate while keeping the ubiquitin recognition element unchanged,¹⁹ although we would like to note that in those cases the nature of the warhead was changed rather than introduction of (bulky) substituents to the same electrophile.

In this work we show that restrictions on propargyl substitution are DUB-dependent rather than a general property of the *in situ* thiol–alkyne reaction. We selected a panel of substituted alkynes that are incorporated in DUB ABPs, and explore their reactivity both in lysate and on an extensive set of recombinant cysteine DUBs. Formation of a covalent adduct with substituted alkynes is subsequently validated with USP16. Furthermore, we investigate the consequences of substituents on the rate of covalent adduct formation, since introduction of electron-donating substituents on internal and terminal alkyne carbons reduces alkyne electrophilicity. Together, these results illustrate the possibilities and flexibility of the *in situ* thiol–alkyne addition, thereby improving our understanding of its underlying reaction mechanism and expanding the scope of this reaction to substituted and internal alkynes.

2. Results and Discussion

Design and synthesis of ABPs with substituted alkyne warheads. Cysteine DUB activity can be probed by replacing the Ub C-terminal carboxylate (G76) with an electrophile positioned in alignment with the native isopeptide bond (**Figure S1A**), thus covalently trapping the catalytic cysteine residue.³⁸⁻⁴⁰ The binding affinity of the truncated C-terminal Ub peptide at the active site is low, therefore full-length Ub is used as recognition element in cysteine DUB targeting ABPs.⁴¹⁻⁴² In order to elucidate the scope of alkyne substituents in the thiol–alkyne reaction, we prepared a panel of substituted alkynes which were coupled to the C-terminus of fully synthetic Rho-Ub₁₋₇₅ thus generating new ABPs targeting cysteine DUBs (**Figure 2**, **Figure S1B**). Substituents were introduced on the terminal C1 carbon (2 & 3), internal C3 carbon (mono-substitution; 4 & 7, or double substitution; 5 & 8), as well as alterations on the Ub backbone (amide) (9 & 10).



Scheme 1 | Proposed reaction mechanisms for nucleophilic thiol–alkyne addition forming covalent thiovinyl bond between cysteine protease and alkyne. **(A)** Radical-mediated thiol–yne reaction. Excluded because this would form an anti-Markovnikov-type product with alkyne C1 carbon atom.³¹⁻³² **(B)** Proximity-driven *in situ* thiol(ate)–alkyne addition.²⁷⁻²⁸ Direct nucleophilic attack on internal C2 alkyne by cysteine thiol is supported by mutagenesis experiments with SENP1; only catalytic Cys603 was essential to form covalent adduct with SUMO2-Prg.²⁸ **(C)** Spontaneous or enzyme-initiated isomerization (tautomerization) of the terminal alkyne moiety to a thiol-reactive allenic intermediate prior to nucleophilic addition.²⁷ Excluded in this work by MS analysis. **(D)** Enzyme-templated thiol–alkyne addition *via* a secondary carbanion intermediate that is stabilized in the protease oxyanion hole, proposed by Arkona *et al.*³⁵ Contradicted by mutagenesis with SENP1; Q597A mutation of important glutamine residue in oxyanion hole did not mitigate covalent adduct formation with SUMO2-Prg,²⁸ but this does not exclude the role of stabilizing H-bonds with backbone amides.

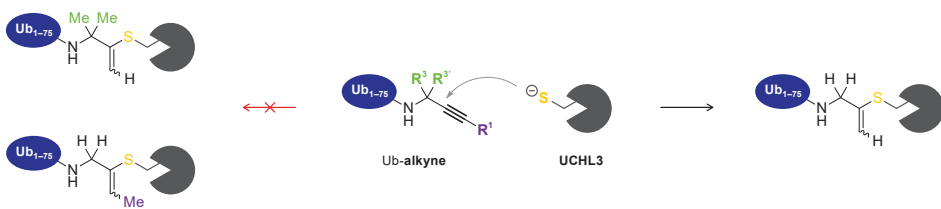


Figure 1 | Covalent adduct formation between catalytic cysteine thiol of recombinant cysteine protease UCHL3 and the alkyne quaternary C2 carbon of Ub-Prg is mitigated when hydrogens are substituted on the propargyl terminal (C1) or internal (C3) carbon.²⁷

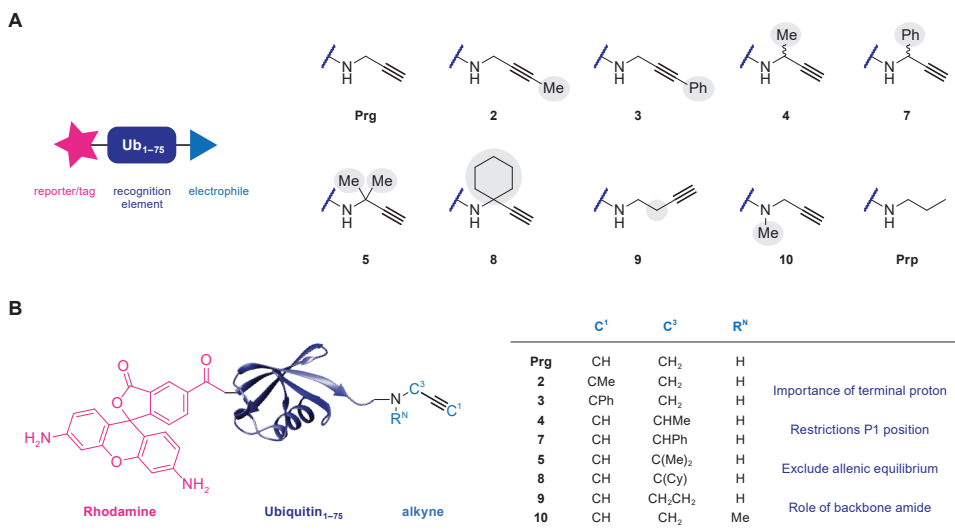


Figure 2 | Panel of substituted alkynes incorporated in activity-based probes (ABPs) targeting cysteine DUBs. **(A)** Synthetic Ubiquitin lacking the C-terminal glycine residue (Ub_{1-75} or $Ub\Delta G$) was modified with fluorescent Rhodamine (Rho) moiety on the N-terminus as reporter tag, and with propargylamide (Prg) or propargylamide derivatives **2-10** as cysteine thiol-reactive electrophiles on the C-terminus. General synthetic scheme can be found in **Figure S1B**. **(B)** Substituents were introduced on the terminal C1 carbon, internal C3 carbon, and on the Ub backbone amide. Propylamide (Prp) is a noncovalent control.

In detail, terminal methylated alkyne **2** and terminal phenylated alkyne **3** were designed to investigate the importance of the terminal proton on C1. The mono-methylated alkyne **4** and mono-phenylated alkyne **7** (increased bulkiness) with a single substituent on the C3 carbon were included to gain further insight in restrictions at the Ub C-terminus (P1 site in substrate nomenclature). The double substituted quaternary C3 derivatives *geminal*-3,3-dimethylated alkyne **5** and cyclohexylated alkyne **8** were included to examine the option of a reactive allene intermediate rather than a reactive alkyne (as presented in **Scheme 1C**). Adduct formation with these quaternary C3 alkynes would exclude the formation of a reactive allene isomer prior to nucleophilic thiol addition, as it is not possible to deprotonate a quaternary C3 carbon. Furthermore, we included butargyl **9** and *N*-methylated alkyne **10** to examine the role of the Ub backbone (amide). The longer linker between the amide and the reactive carbon in butargyl **9** excludes conjugating effects by the Ub amide (but is also not optimally aligned with the native isopeptide bond, **Figure S1A**), whereas the role of the amide proton itself can be examined by replacing it with a methyl group in *N*-methylated propargyl derivative **10**. Finally, propylamide (Prp) was included as a control, as this compound lacks a reactive warhead and should be incapable of forming covalent adducts.

Activity of Rho-Ub-ABPs with substituted alkyne warheads. To explore the reactivity of our panel of substituted alkyne ABPs we explored DUB adduct formation both in lysates and against recombinant DUBs. Whole HEK293 lysate was incubated with the panel of Rho-Ub-ABPs in order to identify DUBs that form covalent adducts with substituted

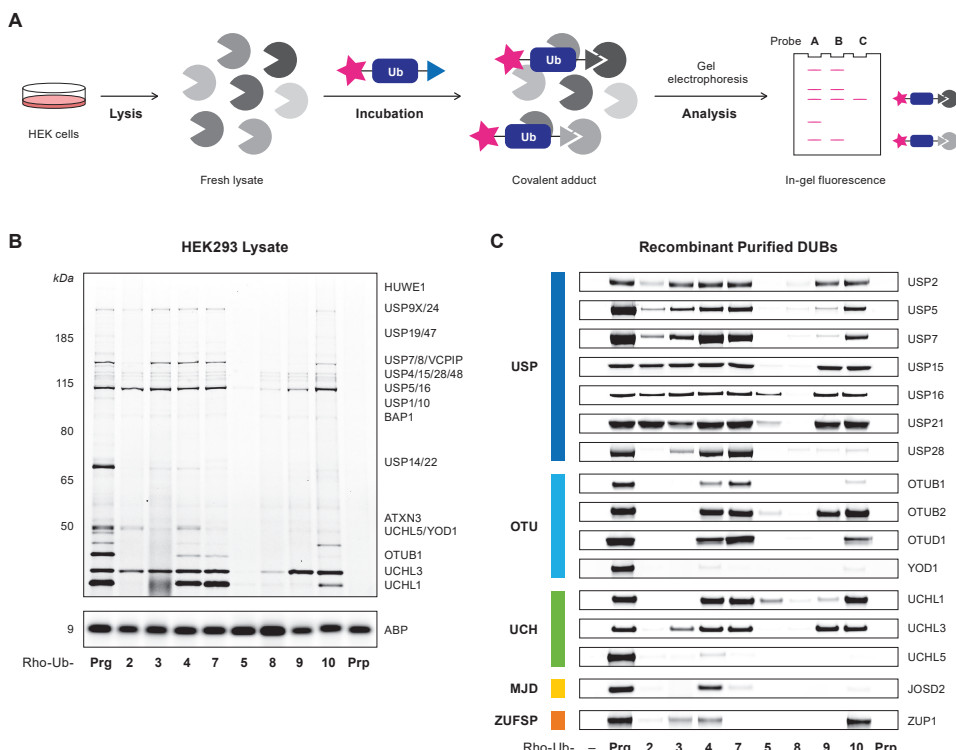


Figure 3 | Incubation of whole lysate and purified recombinant cysteine DUBs (CysDUBs) with Rho-Ub-alkyne ABPs. **(A)** Methodology. Incubation of whole lysate with Rho-Ub-ABPs to identify covalent DUB-ABP adducts. **(B)** Fluorescence scan of HEK293 lysate incubated with 10 μ M Rho-Ub-ABP reveals that acceptance of alkyne substituents is CysDUB-specific. Assignment of labeled CysDUBs based on proteomic analysis by Altun *et al.*¹⁴ Darker bands correlate with more covalent protein-ABP adduct, but the maximum intensity depends on total protein expression. Fluorescence scans of HEK293 and EL4 lysates incubated with 1 or 10 μ M Rho-Ub-ABP are available in **Figure S2**. **(C)** Fluorescence scan of recombinant purified CysDUBs incubated with 10 μ M Rho-Ub-ABP. Fluorescence intensity was adjusted to the signal of adduct with Rho-Ub-Prg. CysDUB conversion to covalent adduct is visualized by Coomassie protein stain (shown in **Figure S3**).

alkynes **2-10** (**Figure 3A**).⁴³ In-gel fluorescence shows the typical labeling pattern for Rho-Ub-Prg, and reveals that substituents on alkynes **2-10** do not fully mitigate covalent adduct formation (**Figure 3B**) as labeling, although to a lesser extent, can still be observed. A similar pattern was observed upon incubation of EL4 lysate (**Figure S2A**). Next, we validated the labeling observed in whole lysates by incubation of purified recombinant cysteine DUBs with Rho-Ub-ABPs (**Figure 3C**). Strikingly, substituted alkynes **2** and **5**, which were previously reported unreactive towards UCHL3,²⁷ showed reactivity towards other cysteine DUBs. A closer look into our data reveals that Rho-Ub-ABPs with terminally modified alkyne **2** or **3** generally do not form covalent adduct with our set of recombinant OTU, UCH, MJD and ZUFSP DUBs, but labeling is observed for several USP DUBs. Moreover, labeling patterns in lysate and

recombinant DUBs show that mono-substituted alkynes **4** (Ala mimic) and **7** are generally accepted, highlighting that variants at the Ub-ABP P1 position are acceptable. There are some controversies in the field on this matter as DUBs are believed to be sensitive to modifications at P1; available crystal structures show Gly76 occupies a restricted tunnel.⁴⁴ The most-described example here is mutant Ub^{G76A}, which renders poly-Ub chains resistant to DUB cleavage while still posing as a substrate for E1 ligases.⁴⁵⁻⁴⁶ However, Wilkinson *et al.*⁴⁷ report that poly-Ub chains with Ub^{G76A} at the distal position, although processed slower than Ub^{WT} chains, are not resistant to USP5-mediated proteolysis. This is in agreement with our findings that Ala mimic **4** forms a covalent adduct with recombinant USP5 (**Figure 3C**). Furthermore, even double substituted alkynes **5** and **8** are accepted by some DUBs. Adduct formation of Rho-Ub-**5** with recombinant purified USP16 was evident (**Figure 3C**) but labeling of endogenous USP16 in HEK lysate was hard to observe (**Figure 3B**). However, adduct formation of Rho-Ub-**5** with USP16 in lysate could be detected when the fluorescence exposure was increased (**Figure S2C**), as well as by incubation of HeLa lysate overexpressing FLAG-HA-USP16 (**Figure S2D**). In addition, lysate treatment reveals that UCHL3 is one of the few DUBs that has enough flexibility at its active site to accommodate the longer linker of butargyl **9**. Even close family members, UCHL1 and UCHL5, do not accommodate the longer linker length, confirming the deciding role of the cysteine protease in adduct formation. Methylation of amide nitrogen in alkyne **10** is accepted by the majority of DUBs included in our panel. As expected, covalent adducts with Rho-Ub-**Prp** were not observed, since this compound lacks an electrophilic warhead.

Based on these results we can conclude that substituents on the alkyne warhead do not generally block covalent adduct formation. Mitigation of covalent adduct formation with the cysteine thiol by introduction of substituents is DUB-specific and could be the result of electronic or steric effects, or a combination thereof. Two alkyne ABPs were selected for validation of the covalent bond formation; terminal modified alkyne **2** to gain insight into the role of the terminal proton (or steric hindrance), and *gem*-dimethylated alkyne **5** as isomerization to a more reactive allene intermediate prior to nucleophilic thiol addition (**Scheme 1C**) is not possible for this substituted alkyne.

ABPs form covalent adducts with catalytic cysteine residue in recombinant USP16. USP16 (Ubp-M) was selected for validation of covalent adduct formation as it forms a covalent adduct with both Rho-Ub-**2** and Rho-Ub-**5** (**Figure 3C**, **Figure S2**). We selected catalytic USP domain rather than full length USP16 for validation because of its higher stability and compatibility with top-down mass spectrometry (MS). Firstly, covalent adduct formation with Rho-Ub-**Prg**, Rho-Ub-**2** and Rho-Ub-**5** was validated by incubation of recombinant USP16CD^{WT}, and resolved by SDS-PAGE under denaturing conditions (**Figure 4A, left**). As expected, a higher running band corresponding to the fluorescent covalent enzyme-ABP adduct (+ 8.9 kDa) was revealed by in-gel fluorescence scanning and protein staining. Preincubation of USP16CD^{WT} with thiol-alkylating reagent *N*-ethylmaleimide (NEM) prior to incubation with ABPs abolishes adduct formation (**Figure 4A, middle**), indicative of adduct formation with a cysteine thiol. Catalytically inactive mutant USP16CD^{C205A} was generated to validate modification of catalytic Cys205 rather than one of the thirteen noncatalytic cysteine residues present in USP16CD,⁴⁸⁻⁴⁹ as covalent adduct formation of ABP Ub-**VS** (vinyl sulfone) with

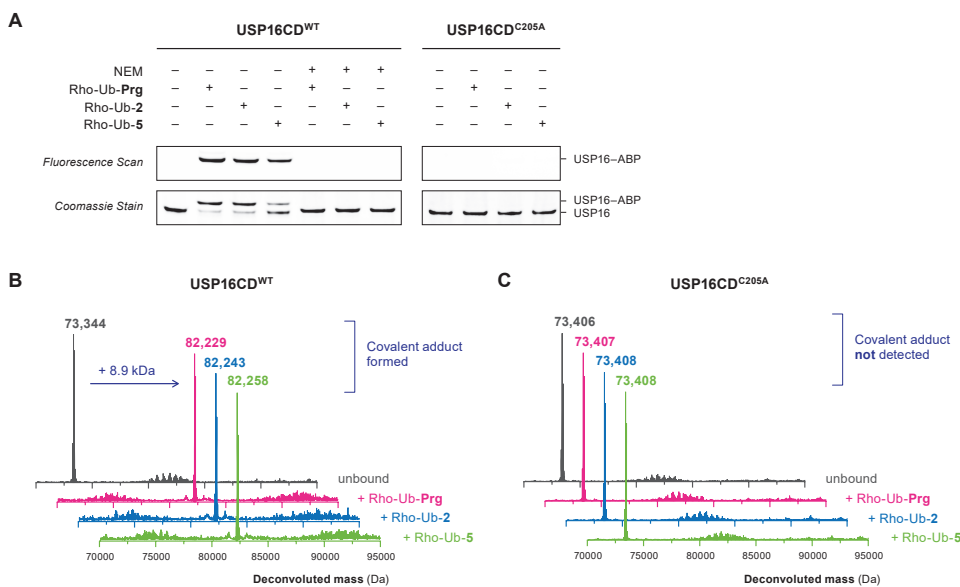


Figure 4 | Validation of covalent adduct between Rho-Ub-alkyne ABPs and catalytic Cys205 in recombinant purified USP16CD (catalytic domain). **(A)** In-gel fluorescence (*top*) and Coomassie stain (*bottom*) of purified recombinant USP16CD^{WT} and mutant USP16CD^{C205A} incubated with ABP (Rho-Ub-Prg, Rho-Ub-2 or Rho-Ub-5). Adduct is formed with USP16CD^{WT} but preincubation with thiol-alkylating reagent *N*-ethylmaleimide (NEM) prior to incubation with ABPs blocks adduct formation, indicating cysteine thiol is required for adduct formation. Adduct is not observed with USP16CD^{C205A}, identifying catalytic Cys205 as the modified cysteine residue. **(B)** Deconvoluted mass from intact protein MS confirms covalent adduct (+8.9 kDa) of USP16CD^{WT} with Rho-Ub-Prg, Rho-Ub-2, and Rho-Ub-5. **(C)** Covalent adduct is not observed in deconvoluted mass from intact protein MS for catalytically inactive mutant USP16CD^{C205A} with Rho-Ub-Prg, Rho-Ub-2 or Rho-Ub-5.

less nucleophilic noncatalytic cysteine residues has been reported for UCHL1 and OTUB1.¹⁸ Covalent adduct formation was not observed upon incubation of USP16CD^{C205A} mutant (**Figure 4A, right**). Top-down MS analysis of intact protein (adducts)⁵⁰⁻⁵¹ confirms covalent CysDUB-ABP adduct formation with USP16CD^{WT} (**Figure 4B**), but covalent adducts are not observed with inactive mutant USP16CD^{C205A} (**Figure 4C**). Together, these findings confirm that USP16 is covalently modified by the Rho-Ub-alkyne ABPs on catalytic Cys205.

Bottom-up mass spectrometric analysis identifies alkyne not allene as the reactive group. Covalent adduct formation of *gem*-dimethylated alkyne **5** with USP16 does not only illustrate the important role of the cysteine DUB in the *in situ* thiol-alkyne addition; the retained ability to form a covalent adduct also has mechanistic implications. Adduct formation with Rho-Ub-**5** cannot occur through isomerization to an allene intermediate prior to nucleophilic addition (**Scheme 1C**); deprotonation of the quaternary C3 carbon atom to form the allene is not possible. To confirm our hypothesis we synthesized Rho-Ub-[D₂]-Prg with deuterated propargylamine [D₂]-Prg as warhead (**Figure 5A**). The covalent adduct of a recombinant DUB with Rho-Ub-[D₂]-Prg will contain two deuterium atoms if the alkyne is indeed the reactive species (**Scheme 1B/D**) while isomerization to an allene intermediate (**Scheme 1C**)

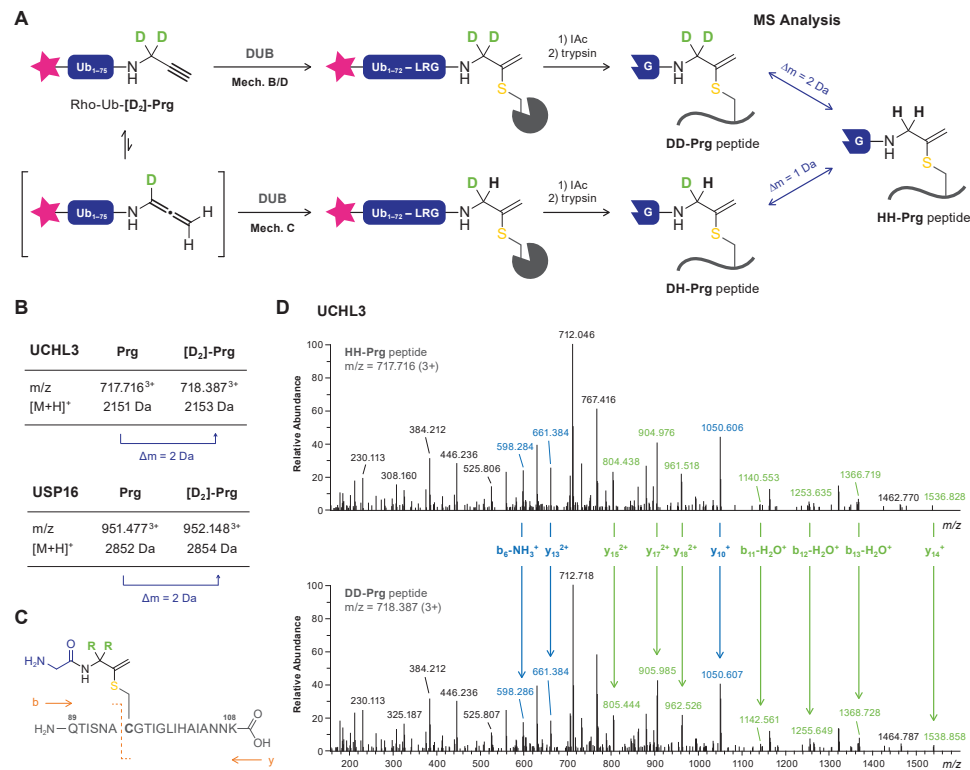
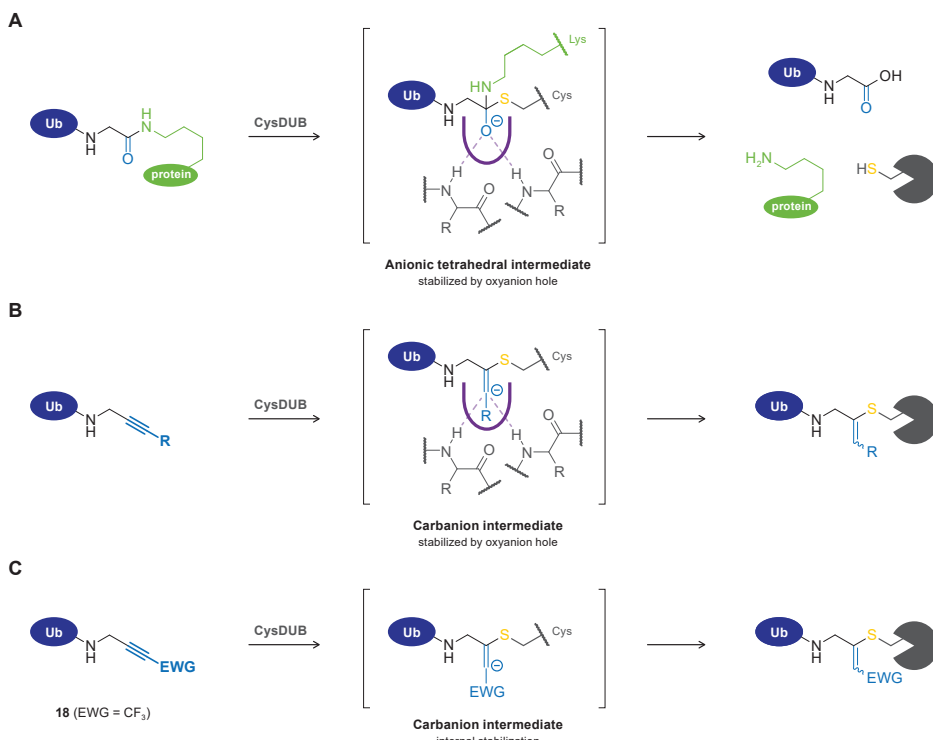


Figure 5 | Bottom-up mass spectrometric analysis of covalent adduct with Rho-Ub-[D₂]-Prg excludes allenic intermediate in mechanism of *in situ* thiol-alkyne addition. Details on chemical synthesis of deuterated propargylamine [D₂]-Prg can be found in **Scheme S1**. (A) Schematic overview of methodology. Incubation of recombinant DUB with Rho-Ub-[D₂]-Prg and Rho-Ub-Prg is followed by alkylation and trypsin digestion to generate modified peptides for mass spectrometric analysis. Isomerization to an allenic intermediate (*Mechanism C* in **Scheme 1C**) will result in replacement of one deuterium atom in the covalent adduct, whilst both deuterium atoms remain for *mechanisms B* and *D* (**Scheme 1B/D**). (B) Modified peptides detected for adducts of Rho-Ub-[D₂]-Prg and Rho-Ub-Prg with UCHL3^{WT} (QTISNACGTIGLIHAIANNK) or USP16CD^{WT} (GLSNLGNTCFFNAVM^(ox)QNLSQLTPVLR) have a mass difference of 2 Da, corresponding with *mechanism B/D*. Details on detected tryptic peptides are provided in **Table S4** and **Table S5**. (C) Tandem MS fragmentation of trypsin-digested UCHL3 peptide QTISNAC*GTIGLIHAIANNK (residues 89-108). (D) Full MS₂ spectrum for UCHL3 peptide QTISNAC*GTIGLIHAIANNK modified with Gly-HH-Prg (**top**) or Gly-DD-Prg (**bottom**). Relevant fragment ions are assigned in green (contains cysteine residue) or blue (does not contain cysteine residue), confirming modification on the cysteine residue with 2 Da mass difference. The m/z values of expected and detected fragment ions are provided in **Table S6**.

would result in replacement of one deuterium atom by a hydrogen atom. Covalent adducts of Rho-Ub-[D₂]-Prg and Rho-Ub-Prg with UCHL3 (unreactive towards Rho-Ub-5) and USP16 (reactive towards Rho-Ub-5) were submitted to alkylation and trypsin digestion to generate peptides for bottom-up mass spectrometric analysis. Peptides of different lengths containing the QTISNACGTIGLIHAIANNK stretch were detected for UCHL3 adducts modified with Prg or [D₂]-Prg, with a mass difference of 2 Da between deuterated and protonated adducts (**Figure 5B**, **Table S4**). For both USP16 adducts, tryptic peptide GLSNLGNTCFFNAVM^(ox)QNLSQLTPVLR

(with oxidized methionine) was detected with a mass difference of 2 Da between deuterated and protonated adducts (**Figure 5B**, **Table S5**). Peptides corresponding with isomerization were not detected for the $[D_2]$ -Prg adducts. Furthermore, tandem mass spectrometric analysis of both modified UCHL3 peptides confirms that the 2 Da mass difference can be attributed to a modification on the catalytic cysteine residue (**Figure 5C-D**, **Table S6**).

Together, this clearly shows that the *in situ* thiol–alkyne addition to unsubstituted alkynes does not involve isomerization to an allene intermediate thereby excluding *mechanism C* (**Scheme 1C**). It is more challenging to conclude whether nucleophilic addition to the alkyne moiety is exclusively proximity-driven (**Scheme 1B**) or goes through enzyme-templated stabilization of a carbanion intermediate in the oxyanion hole (**Scheme 1D**). To our knowledge, all cysteine residues targeted by nonactivated alkynes are located at the active site of cysteine proteases (or ligases), which could stabilize a carbanion intermediate in an oxyanion hole (**Scheme 2**). We cannot exclude nor confirm this mechanism based on our current data, but we



Scheme 2 | Stabilization of anionic intermediates for (enzymatic) reactions with cysteine DUBs. **(A)** CysDUB-mediated isopeptide bond proteolysis. Stabilization of anionic tetrahedral intermediate in the oxyanion hole. Release of ubiquitin, (ubiquitinated) substrate, and CysDUB. **(B)** Proposed enzyme-templated thiol–alkyne addition with stabilization of unfavored carbanion intermediate in the oxyanion hole. Terminal alkynes such as Prg would form a secondary carbanion, but internal alkynes such as terminally methylated alkyne **2** would form a tertiary carbanion intermediate that is internally destabilized if R is an electron-donating group (EDG). **(C)** Non-enzymatic internal stabilization of a carbanion intermediate by inductive effect of electron-withdrawing group. Details on chemical synthesis of trifluoromethylated alkyne **18** are provided in **Scheme S2**.⁵²

would like to note that the inductive effect of the electron-donating methyl-group in alkyne **2** contributes negatively to the internal stabilization of the negative charge, thus reducing the stability of the tertiary carbanion compared to the already unfavored secondary carbanion intermediate that is formed with terminal alkynes (**Scheme 2B**). It is possible that enzyme oxyanion hole sufficiently stabilizes the tertiary carbanion to progress with covalent bond formation, but the proximity-driven reaction seems more likely for internal alkyne **2**.

Kinetic analysis of covalent adduct formation with USP16. Next, we examined whether introduction of bulky and/or electron-donating substituents on the alkyne terminal C1 or internal C3 carbon atom reduces the rate of covalent adduct formation. Incubation of USP16CD^{WT} with 10 μ M Rho-Ub-ABP does indeed show time-dependent increase of the higher running covalent adduct and a decrease of the lower running noncovalent/unbound USP16 for Rho-Ub-**2** and Rho-Ub-**5** (**Figure 6A**). Adduct formation does not progress beyond the first timepoint for Rho-Ub-**Prg**, indicating that reaction completion was reached before the first sample was quenched (within 15 min). This finding is in agreement with exceptionally fast adduct formation reported for Ub(I)-**Prg** ABPs (reaction completion within minutes).²⁷⁻²⁸ Covalent adduct formation of USP16 with Rho-Ub-ABPs is slower with substituted alkynes **2** and **5** than with **Prg**, requiring a longer incubation time to reach maximum covalent occupancy.

We performed a kinetic evaluation of covalent adduct formation to calculate the minimum incubation time to reach reaction completion at a specific ABP concentration (**Figure 6B**). Covalent adduct formation between ABP and cysteine protease is a two-step process; noncovalent enzyme-ABP complex is formed rapidly, followed by covalent adduct formation as the rate-determining step.⁵³⁻⁵⁵ Time-dependent covalent occupancy of irreversible covalent ligands can be directly detected (in absence of competing substrate/ligand) by separation of covalent adduct from noncovalent complex and unbound enzyme on LC-MS or gel, and subsequent quantification of signals.⁵⁸⁻⁶² Here we incubated USP16CD^{WT} with excess Rho-Ub-ABPs, and quantified incubation time-dependent covalent occupancy by gel analysis (**Figure 6C**). Estimates for the rate of covalent adduct formation k_{obs} , reaction half-life $t^{1/2}$ and incubation time to reach reaction completion were obtained assuming maximum covalent occupancy is shared among all ABPs. Adduct formation with all ABPs is concentration-dependent; reaction completion is reached faster at the high ABP concentration. However, covalent adduct formation with Rho-Ub-**Prg** is unusually fast; maximum covalent occupancy is reached within a few minutes at both concentrations, and the reaction rates might be even faster than what we reported here. The half-life and extrapolated incubation time to reach maximum covalent adduct formation provide valuable insights into the reduced reactivity of Rho-Ub-**5** in previous incubation experiments (**Figure 3**, **Figure S2**); reaction completion is reached after more than four hours, which well exceeds the common incubation time for ABPs with lysate or recombinant protein. Incomplete adduct formation is observed as a band with (significantly) lower intensity than the band with Rho-Ub-**Prg** that does reach maximum intensity. Overall, introduction of substituents on propargylamide decreases the rate of covalent adduct formation with USP16CD^{WT} by >30-fold for methylation of the terminal C1 carbon (Rho-Ub-**2**), and >100-fold for *gem*-dimethylation of the internal C3 carbon (Rho-Ub-**5**). This dramatic reduction in

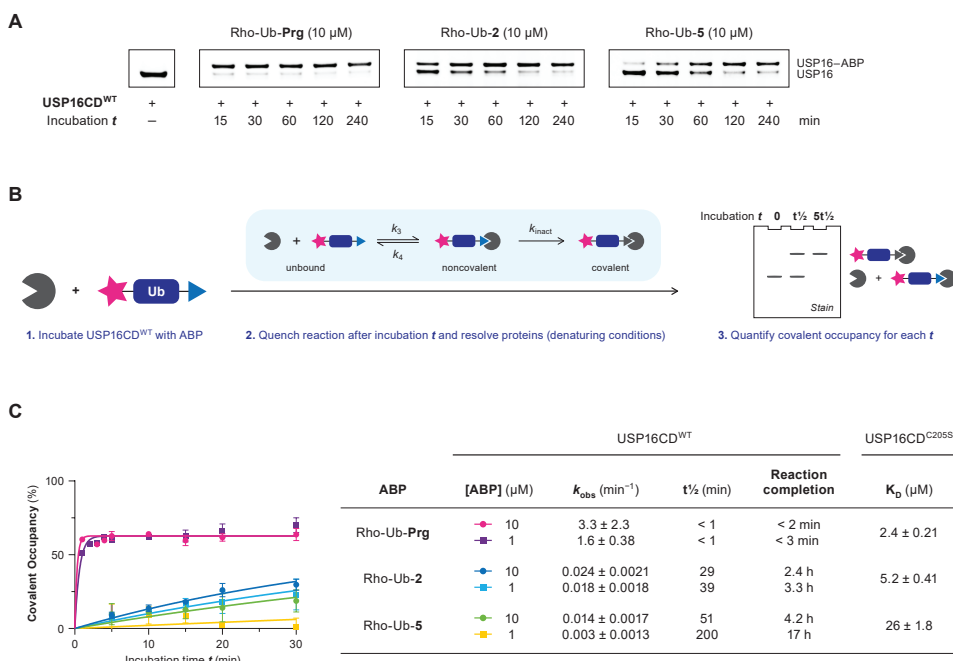


Figure 6 | Kinetic analysis of covalent adduct formation with Rho-Ub-alkyne ABPs. **(A)** Incubation time-dependent covalent adduct formation of Rho-Ub-alkyne ABPs with USP16CD^{WT} visualized by Coomassie stain after gel electrophoresis (denaturing conditions). Intensity of covalent USP16-ABP adduct band increases upon longer incubation time for substituted alkyne ABPs Rho-Ub-2 and Rho-Ub-5, but reaction completion is already reached before the first timepoint for Rho-Ub-Prg. **(B)** General method to obtain kinetic parameters for covalent ligands from incubation time-dependent covalent occupancy. **(C)** Kinetic analysis of covalent adduct formation between USP16CD and Rho-Ub-ABP. USP16CD^{WT} was incubated with excess ABP, and samples were quenched after various incubation times. Covalent occupancy was quantified from gel analysis (triplicate measurement) to obtain the rate of covalent adduct formation k_{obs} , reaction half-life $t\frac{1}{2}$ and reaction completion (details in section 7.7). The maximum occupancy is less than 100%, which can be attributed to commonly observed inactive subpopulations in (recombinant) enzyme.⁵⁶⁻⁵⁷ Adduct formation with Rho-Ub-Prg was completed within 5 minutes, therefore the measurement was repeated with shorter intervals. Reliable estimates for the kinetic parameters could not be obtained because reaction completion was still reached too quickly. K_D -values for noncovalent binding were obtained in a binding assay based on fluorescence polarization (FP) of Rho-Ub-ABPs with excess USP16CD^{C205S} mutant (details in Figure S4, section 7.8).

reaction rate explains the low reactivity of substituted alkynes upon incubation of lysate or recombinant protein as adduct formation is not completed within the standard incubation time of 30–60 min. Rho-Ub-ABPs with slower covalent adduct formation than Rho-Ub-Prg could be desirable as they are more suited to study (ir)reversible inhibitor potency in kinetic competition assays.^{12, 63-64}

Next, a binding assay based on fluorescence polarization (FP) of the Rho-Ub-ABPs with excess catalytic inactive USP16^{C205S} mutant was performed to determine K_D -values independent of electronic factors as covalent adduct formation with USP16^{C205S} does not occur (Figure 6C). Introduction of methyl substituents clearly reduced the noncovalent affinity (reflected in

higher K_D), indicative of disfavored steric interactions. However, electronic effects cannot be disregarded as the rate of adduct formation (k_{obs}) with Rho-Ub-**2** is more than 30-fold slower than with Rho-Ub-**Prg** where the noncovalent affinity (K_D) is less than 3-fold lower. This shows that disfavored steric interactions as well as electronic effects contribute to the reduced rate of covalent adduct formation with methylated alkynes.

Contribution of steric and electronic effects on DUB reactivity towards substituted alkynes. Substituents introduced on the alkyne C1 and C3 position (**Figure 2**) were designed to have a minimal electronic effect, but kinetic evaluation of covalent adduct formation (k_{obs}) and noncovalent affinity (reflected in the K_D) with USP16 revealed that the role of steric and electronic effects cannot be separated completely (**Figure 6C**). To further study the individual contribution of steric and electronic components we included electron-deficient alkyne **18**, with an electron-withdrawing $-CF_3$ group on the terminal alkyne carbon (**Scheme 2C**, **Figure 7A**). Introduction of an electron-withdrawing group (EWG) on the terminal position of an alkyne significantly increases the thiol reactivity as the inductive effect contributes positively to the stabilization of a negative charge, thereby enabling non-enzymatic internal stabilization of a carbanion intermediate (**Scheme 2C**). The increased electrophilicity was indeed reflected in the observation of significant adduct formation with nontargeted thiol glutathione (GSH) (**Figure 7B-C**). Incubation of HEK293T lysate (**Figure 7D**) showed that most DUBs form a covalent adduct with Rho-Ub-**18**, indicating an electronic rather than steric component driving the lack of reactivity with alkyne **2**. Faint covalent adduct formation with Rho-Ub-**18** was observed upon incubation of USP16CD^{C205A} mutant, indicating a preference for the catalytic cysteine residue over other (nontargeted) cysteine residues (**Figure 7E-F**). Altogether, we can conclude that (disfavored) steric as well as electronic properties of the substituent affect DUB reactivity with substituted alkynes.

Implications on the scope of the *in situ* thiol-alkyne addition. Introduction of bulky and/or electron-donating substituents can reduce the rate of covalent bond formation but it is DUB-dependent whether modifications are allowed. We foresee this might be used for the development of ABPs with improved selectivity for a specific DUB. Here, introduction of electron-donating and electron-withdrawing substituents on the C1 and C3 position would tune alkyne reactivity (electronic effect) while simultaneously modulating selectivity (steric effect). Another possibility would be to introduce primed site recognition peptide fragments on the terminal alkyne position to improve selectivity and/or affinity.^{10, 65-66}

The reaction mechanism has extensive consequences for the scope of the *in situ* alkyne–thiol addition. Enzyme-templated stabilization of a carbanion intermediate (*Mechanism D*, **Scheme 1D**) would restrict the applicability in drug design to targeting catalytic cysteine residues with nonactivated alkynes, but it also mitigates the risk of covalent adduct formation with nontargeted thiols. A covalent adduct is not formed with noncatalytic cysteine residues because the carbanion intermediate cannot be stabilized as there is no oxyanion hole present in their vicinity, resulting in a mechanism-based selectivity for the targeted thiol. To date, only electron-deficient (activated) alkynes such as propiolamides, propiolonitriles and alkynylated heteroarenes have been reported to form covalent adducts with noncatalytic cysteine residues (in kinase targets).^{25, 34, 62, 67-69} The inductive effect of (conjugated)

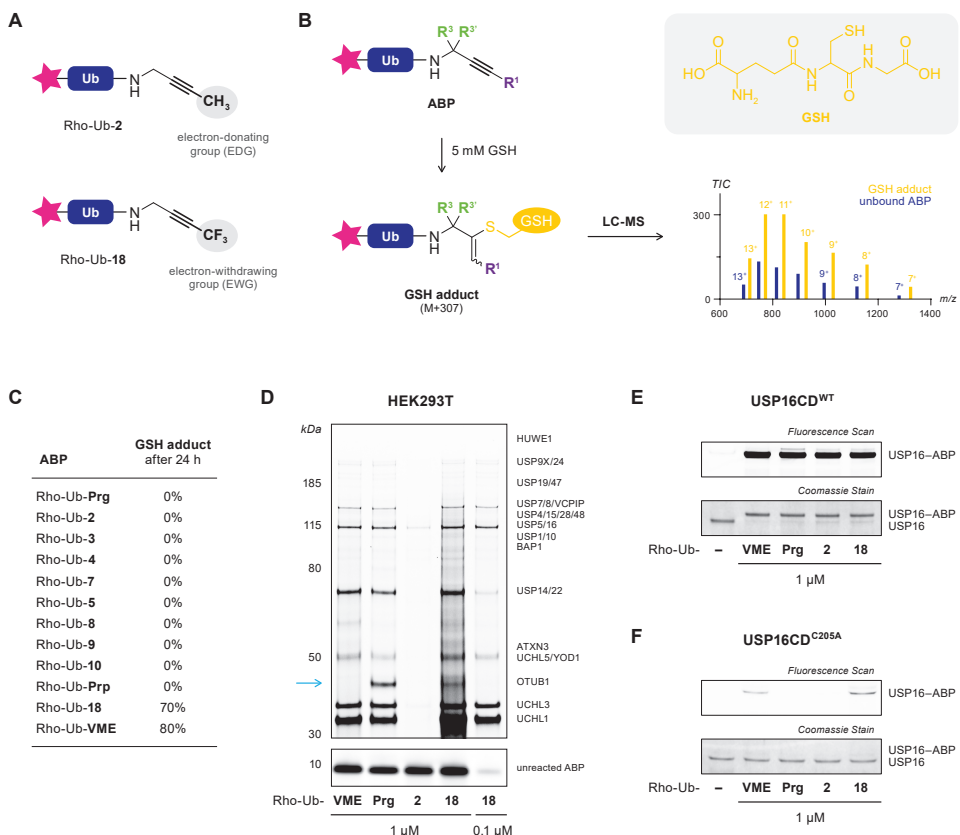


Figure 7 | Selectivity and reactivity of electron-deficient alkyne **18** as warhead in Rho-Ub-ABPs. **(A)** Mildly electron-donating methyl group on terminal C1 position of alkyne **2** and strongly electron-withdrawing trifluoromethyl group on terminal C1 position of alkyne **18**. Synthetic scheme for trifluoromethylation of terminal alkynes to obtain alkyne **18** is provided in **Scheme S2**.⁵² Our design is based on the assumption that the terminal trifluoromethyl ($-CF_3$) in alkyne **18** is sterically similar to the terminal methyl ($-CH_3$) in alkyne **2**, while having the opposite electronic property. **(B)** Schematic overview of methodology for indiscriminate thiol reactivity. Rho-Ub-ABPs are incubated with 5 mM glutathione (GSH) in phosphate-buffered saline (PBS) for 24 h, after which the reaction mixture was submitted to LC-MS analysis. GSH adduct and unreacted ABP are quantified from the total ion count (TIC). **(C)** GSH adduct formed upon incubation with 5 mM GSH for 24 h as percentage of total. Charge states used for quantification are provided in **Table S7**. Adduct formation with GSH does not necessarily equal complete loss of selectivity, as is illustrated by established CysDUB-selective ABP Ub-VME.³⁹ **(D)** Fluorescence scan of HEK293T lysate incubated with Rho-Ub-ABPs reveals the importance of both steric and electronic effects of alkyne substituents. Most but not all CysDUBs that are unreactive with Rho-Ub-**2** do form covalent adducts with Rho-Ub-**18**, indicating an electronic rather than steric component driving the lack of reactivity with Rho-Ub-**2**. The blue arrow marks a CysDUB adduct – previously identified as OTUB1¹⁴ – that is reactive towards Rho-Ub-Prg but unreactive towards the more electrophilic Rho-Ub-VME and Rho-Ub-**18**. This suggests that lack of reactivity for this specific CysDUB could be driven by the available space at the active site to accommodate bulky substituents at the C1 position (disfavored steric interactions) rather than electronic effects. **(E)** In-gel fluorescence (*top*) and Coomassie protein stain (*bottom*) for adduct formation with recombinant USP16CD^{WT} upon incubation with Rho-Ub-ABPs for 1 h. **(F)** In-gel fluorescence (*top*) and Coomassie protein stain (*bottom*) for adduct formation with recombinant USP16CD^{C205A} upon incubation with Rho-Ub-ABPs for 1 h. Faint labeling can be observed for Rho-Ub-VME and Rho-Ub-**18** in the fluorescence scan, indicating that these ABPs are reactive towards noncatalytic cysteines, but CysDUB selectivity is retained: adduct formation with the catalytic cysteine residue is much faster than reaction with nontargeted thiols.

electron-withdrawing groups sufficiently stabilizes the carbanion intermediate to progress with covalent bond formation, with targeted as well as (undesired) nontargeted thiols (**Scheme 2C**). Unfortunately, electron-deficient alkyne **18** is not suited to study whether the *in situ* thiol addition to nonactivated alkynes involves enzymatic stabilization of a carbanion in the oxyanion hole (**Scheme 1D**, **Scheme 2B**) because thiol addition can progress through an alternative, non-enzymatic mechanism (**Scheme 2C**). We believe further research to elucidate the mechanism of thiol addition to nonactivated (internal) alkynes should be directed towards computational studies with enzymes for which structural data is available, or by successfully targeting noncatalytic cysteines with nonactivated alkynes.

3. Conclusion

To conclude, this work shows that the *in situ* thiol–alkyne reaction is more flexible and versatile than previously assumed. A panel of substituted propargylamide derivatives was incorporated into Rho-Ub-ABPs as the electrophilic warhead, and treatment of lysate or recombinant cysteine DUBs showed that covalent adducts can also be formed with internal alkynes and terminal alkynes with (double) substituents on the internal C3 carbon. Covalent adduct formation of terminally methylated alkyne **2** and *gem*-dimethylated alkyne **5** with catalytic Cys205 of USP16 was validated by gel analysis and mass spectrometry of intact covalent adducts. Adduct formation was mitigated by preincubation with thiol-alkylating reagent NEM or by C205A mutation, thus confirming catalytic Cys205 as the targeted amino acid residue. Mechanistically, acceptance of *gem*-dimethylated alkyne **5** together with mass spectrometric analysis of covalent adducts with deuterated ABP Rho-Ub-[D₂]-Prg validates the alkyne moiety rather than an allenic isomer as the reactive species in the *in situ* thiol–alkyne addition. Kinetic analysis revealed reaction completion was reached within a few minutes for Rho-Ub-Prg, while electron-donating/bulky methyl substituents on alkynes **2** and **5** significantly reduced the rate of covalent adduct formation resultant from a combination of (disfavored) steric interactions and electronic effects, reaching maximum covalent occupancy after (several) hours. Whether nucleophilic addition of the catalytic cysteine thiol to the alkyne moiety is solely proximity-driven or involves enzymatic stabilization of a carbanion intermediate could not be concluded definitively.

Altogether, we extended the scope of the *in situ* thiol–alkyne reaction from unmodified terminal alkynes to substituted (internal) alkynes, provided mechanistic insight, and discovered that acceptance of alkyne substituents is CysDUB-dependent. We anticipate substituted nonactivated alkynes not to be restricted to bioorthogonal handles but also to be of great value as electrophiles in future development of cysteine-targeting covalent inhibitors and activity-based probes with improved selectivity profiles.

Acknowledgements

In memory of prof. dr. Huib Ova. His passion for science will always be an inspiration to us. We thank Henk Hilkmann, Dris el Atmioui and Cami Talavera Ormeño for the chemical synthesis of Ubiquitin, and Dris el Atmioui for his support with ABP synthesis. Paul Brundel and Robin van Veen are thanked for their help with the chemical synthesis of building blocks. Angeliki

Moutsiopoulos, Patrick Celie, Ruud Wijdeven, Aysegul Sapmaz, Gabrielle van Tilburg, and Remco Merkx are thanked for expression and purification of recombinant DUBs. Recombinant YOD1 was kindly provided by Tycho Mevissen and David Komander, and recombinant ZUFSP was a gift from Kay Hofmann. Sabina van der Zanden, Yves Leestemaker, Merve Öyken and Lorina Gjonaj are thanked for culturing HEK293, EL4, HEK293T and HeLa cells respectively. We thank Annemarie Otte for mass spectrometric measurements. This work was supported by a VICI grant (no.724.013.002) from The Netherlands Organization for Scientific Research (NWO) to H.O.

Competing Interests

The authors declare the following competing financial interest: H.O. was founder and shareholder of the company UbiQ that markets reagents in the Ub field.

Author Contributions

E.M.: Conceptualization, Investigation (*Chemical Synthesis, Biochemical Assays*), Formal Analysis, Writing – Original Draft, Writing – Review & Editing. R.Q.K.: Investigation (*Protein Expression*), Supervision, Writing – Review & Editing. B.R.v.D.: Investigation (*Top-Down MS*). P.A.v.V.: Investigation (*Bottom-Up MS/MS*), Formal Analysis. M.P.C.M.: Supervision, Writing – Review & Editing. H.O.: Conceptualization, Supervision, Funding acquisition.

4. Materials and Methods: *Biochemistry*

General

Synthesis of Rho-Ub-ABPs is described in *section 5.1*. Incubations are performed in Protein Lobind Tubes (Eppendorf, #022431018) to reduce (time-dependent) loss of enzyme due to precipitation/aggregation. Recombinant purified DUBs used in this work: USP2 (Ubiquigent, #64-0014-050), USP5 (Ubiquigent, #64-0002-050), USP7 (*in-house*, see *section 4.1*), USP15 (*in-house*, see *section 4.1*), USP16FL (*in-house*, see *section 4.1*), USP16CD^{WT} (*in-house*, see *section 4.1*), USP16CD^{C205A} (*in-house*, see *section 4.1*), USP16CD^{C205S} (*in-house*, see *section 4.1*), USP21 (Ubiquigent, #64-0037-050), USP28 (*in-house*, see *section 4.1*), OTUB1 (*in-house*, [Wang, 2009]⁷⁰), OTUB2 (*in-house*, [Nanao, 2004]⁷¹), OTUD1 (*in-house*, [Mevissen, 2013]⁷²), YOD1 (Gift from David Komander, [Mevissen, 2013]⁷²), UCHL1 (*in-house*, [Larsen, 1996]⁷³), UCHL3 (*in-house*, [Larsen, 1996]⁷³), UCHL5 (Novus biochemicals, #NBP1-72315), JOSD2 (Ubiquigent, #64-0032-050), and ZUP1 (Gift from Kay Hofmann, [Hermanns, 2018]⁷⁴).

4.1. Recombinant Protein Expression and Purification

Protein expression constructs. Expression constructs for USP7FL, USP15(D1D2) and OTUB1FL were kind gifts from Titia K. Sixma, Ingrid Dreveny and Frank Sicheri, respectively. Full-length USP16 (UniProtID: Q9Y5T5; isoform 3, Q141H, EY480DN) and USP16CD (residues 196-823; canonical numbering) were cloned into *in-house* baculovirus expression vector pCPF2.13 harboring an N-terminal His-tag and 3C protease site, using IVA cloning.⁷⁵ Point mutations C205A and C205S were introduced using overlapping primer mutagenesis.⁷⁶ USP28FL was cloned into pFastNKL-his3C-LIC using ligase-independent cloning.⁷⁷ OTUD1(CD+UIM) (residues 290-481) was cloned into pGEX-4T-1 with BamHI and HindIII. All expression constructs were sequence-verified.

Expression of USP16 (variants) and USP28FL

USP28FL and all USP16 constructs were expressed using baculovirus expression in *Spodoptera frugiperda* (Sf9) using an adapted Bac-to-Bac system (Invitrogen). Bacmids were generated using EmBacY cells (Geneva Biotech)

or DH10Bac (USP28) and isolated using isopropanol precipitation. 10 µg was transfected into 0.8×10^6 sedentary SF9 cells using CellFectin (Invitrogen) in SFM-II medium (Gibco) in a 6-well plate at 28 °C. After 72 h cells were checked for fluorescence and the medium was harvested (P0) for infection of P1 cultures; 50 mL of 1×10^6 cells/mL in Insect-Express medium (Lonza). P1 cultures were incubated at 28 °C whilst shaking for 72 h and then harvested by spinning down at 500 G for 5 min. The supernatant was used to infect P2 cultures (like P1, but now 500 mL), whilst the pellet was used to check for expression and purification optimization. P2 cultures were infected with low MOI and harvested after 72 h shaking at 28 °C.

Purification of USP16 (variants). Insect cells from P2 expressing USP16 variants were resuspended in lysis buffer (50 mM HEPES pH7.4, 500 mM NaCl, 20 mM imidazole and 5% glycerol), sonicated and centrifuged at 21,000 G at 4 °C to isolate the soluble fraction. The supernatant was applied to charged Ni-NTA beads, which were washed twice extensively with lysis buffer with 20 mM and 50 mM imidazole respectively. The protein was eluted using elution buffer (50 mM HEPES pH7.4, 100 mM NaCl, 200 mM imidazole, 1 mM DTT) and subsequently applied to a HiTrap MonoQ column (GE Healthcare). Protein was eluted using a salt gradient (20 mM HEPES pH7.4, 1 mM DTT, 50 to 1000 mM NaCl) and protein-containing fractions were pooled, concentrated and aliquoted before being flash frozen.

Purification of USP28FL. P2 expression cells were lysed using sonication in lysis buffer (20 mM Tris pH8.0, 500 mM NaCl, 5 mM BME, 10 mM imidazole and protease inhibitor cocktail). The lysates were centrifuged at 20,000 rpm for 30 min at 4 °C. The supernatants were incubated with washed Talon metal affinity resin (Clontech Inc., Palo Alto, CA) for 20 min at 4 °C and the beads were then washed with lysis buffer. Protein was eluted with lysis buffer supplemented 250 mM imidazole. Proteins were dialyzed to remove imidazole and purified over a Superdex200 gel filtration column. USP28(FL) was concentrated, aliquoted and flash-frozen for storage at -80 °C. Purified protein was confirmed via immunoblotting using anti-USP28 antibody (GeneTex, #EPR42492).

Expression and purification of USP7FL

USP7FL was expressed in BL21 (DE3) Rosetta2 bacteria using overnight induction with 0.2 mM IPTG in Terrific Broth medium at 18 °C. Cells were spun down and resuspended in GST buffer (50 mM HEPES pH7.5, 250 mM NaCl, 1 mM EDTA, 1 mM DTT) before being lysed using sonication. After high-speed centrifugation at 21,000 G at 4 °C, the supernatant was applied to Glutathione Sepharose 4B beads (GE Healthcare), which were washed extensively using GST buffer before eluting the protein using GST buffer supplemented with 15 mM GSH. The eluted protein was dialyzed overnight against PorosXQ buffer (20 mM HEPES pH7.5, 50 mM NaCl, 1 mM DTT) after the addition of 3C protease to remove the GST tag. To remove breakdown products and cleaved GST, the sample was purified on a PorosXQ column, eluting the protein using a gradient of buffer B (20 mM HEPES pH7.5, 1M NaCl, 1 mM DTT). Appropriate fractions were concentrated and applied to a Superdex200 gel filtration column (GE Healthcare) using GF buffer (20 mM HEPES pH7.5, 100 mM NaCl, 1 mM DTT). The peak fractions were pooled, concentrated to ~1 mg/mL and flash frozen using LN₂.⁶⁵

Expression and purification of USP15(D1D2)

USP15(D1D2) was expressed in BL21 (DE3) Rosetta2 cells, grown in 2xYT medium. Cells were induced overnight at 25 °C using 0.5 mM IPTG and harvested the next day in His-buffer (50 mM Tris pH7.5, 300 mM NaCl, 20 mM imidazole, 1% glycerol). Cells were lysed using sonication and the insoluble fraction was removed by centrifugation at 21,000 G at 4 °C for 30 min. Supernatant was applied to Ni-charged NTA beads and beads were washed extensively with His-buffer. USP15(D1D2) was eluted with the same buffer supplemented with 200 mM imidazole before being concentrated and applied to a Superdex200 gel filtration column in SEC buffer (20 mM Tris pH7.5, 150 mM NaCl, 1% glycerol). Appropriate fractions were concentrated to ~20 mg/mL, aliquoted and frozen in liquid nitrogen.⁷⁸

4.2. Lysate Preparation

Cell culturing. HEK293 cells (ATCC, Manassas, VA), HeLa cells and HEK293T cells were cultured in Dulbecco's Modified Eagle's medium (DMEM) supplemented with 8-10% FCS/FBS. EL4 cells were cultured in Gibco

RPMI 1640 medium (Life technologies) supplemented with 10% FCS. Cells were maintained in a humidified atmosphere of 5% CO₂ at 37 °C and regularly tested for the absence of mycoplasma. Transfection of HeLa cells with FLAG-HA-USP16 (Addgene, #22595) as reported previously.⁷⁹

Harvesting and cell lysis. Cells were harvested by washing with PBS, trypsinization to dissociate adherent cells from surface, and centrifuged. Fresh cell pellets were resuspended in two pellet volumes of cold lysis buffer, sonicated (5 cycles, high, 30 sec on, 30 sec off) on a Bioruptor Pico (Diagenode), and solute was separated from insoluble fraction by centrifuge (10 min, 13,200 rpm, 4 °C). Supernatant was transferred to clean tube and protein concentration was determined on Nanodrop One spectrophotometer (Isogen Life Science). Subsequently, volume was adjusted by addition of lysis buffer to a protein concentration of 2 mg/mL. Harvesting and cell lysis of HeLa cells as reported previously.⁷⁹

4.3. Gel-Based Activity-Based Probe (ABP) Reactivity

General. Purified Rho-Ub-ABPs are stored at -20 °C as powder or as 500 μM stock solutions in DMSO. The concentration of stock solutions is calculated from the molecular mass and the added amount of dry powder. The concentration of unbound Rho-Ub-ABP stock solutions is within 2-fold range, as validated in gel electrophoresis of unbound Rho-Ub-ABP (10 μM) by quantification of fluorescence intensity and protein intensity with ImageJ.⁸⁰⁻⁸² Rho-Ub-ABPs are added to whole lysate or recombinant DUBs as 2-5x solutions, prepared by careful addition of DMSO stock to reaction buffer. Incubations with Rho-Ub-ABPs are conducted under gentle agitation (300 rpm) with strict restriction of light. Final CysDUB or ABP concentrations listed correspond to the concentration during incubation (before sample buffer addition). Prior to reaction initiation, lysis buffer (50 mM Tris-HCl pH7.4, 5 mM MgCl₂, 250 mM sucrose, 2 mM DTT), HEPES reaction buffer (50 mM HEPES pH7.4, 150 mM NaCl, 5 mM DTT, 0.005% Tween20) or Tris reaction buffer (50 mM Tris pH7.5, 100 mM NaCl, 5 mM DTT) are prepared with fresh addition of DTT and surfactants. Single-use 1M aliquots of DTT (1,4-dithio-DL-threitol; Chem-Impex, #00127) are stored at -20 °C.

General Method I. ABP Labeling Quenching and SDS-PAGE Gel Electrophoresis

After indicated incubation time, the reaction was quenched by addition of 3x reducing sample buffer (150 μL 4x LDS-PAGE loading buffer (NuPAGE, Invitrogen) supplemented with 35 μL water and 15 μL β-mercaptoethanol (BME; Sigma-Aldrich, #M6250)) and boiling the samples for 10 min at 94 °C to abolish noncovalent interactions (denaturing conditions). Multiple timepoints; samples were stored on ice until the experiment was completed. Samples were loaded on precast Bis-Tris gels (Invitrogen) and resolved by SDS-PAGE gel electrophoresis with MES (NuPAGE MES SDS running buffer 20x, Novex by Life Technologies) or MOPS (NuPAGE MOPS SDS running buffer 20x, Novex by Life Technologies) as running buffer. Reference protein standard/ladder; PageRuler™ Plus Prestained Protein Ladder (Thermo Fisher Sci., #26619), PageRuler™ Prestained Protein Ladder (Thermo Fisher Sci., #26616) or SeeBlue™ Plus2 Pre-stained Protein Standard (Invitrogen, LC5925). Covalent enzyme-ABP adducts were visualized by in-gel fluorescence using Typhoon FLA 9500 imaging system (GE Healthcare Life Sciences) with blue LD laser and BPB1 emission filter ($\lambda_{ex} = 473$ nm, $\lambda_{em} = 530 \pm 10$ nm), and protein marker was visualized with red LD laser and LPR emission filter ($\lambda_{ex} = 635$ nm, $\lambda_{em} = 665$ nm). Subsequently, covalent DUB-ABP adduct and unbound DUB were visualized by InstantBlue™ Ultrafast Protein Stain (Expedeon Protein Solutions, #ISB1L), and scanning stained gels using an Amersham Imager 600 (Trans-illumination).

Incubation of whole lysate

EL4/HEK293/HEK293T. 20 μL lysate (final conc. 2 mg/mL) was incubated with 5 μL Rho-Ub-ABP (final conc. 1-10 μM) for 1 h at 37 °C. Reaction was quenched as described in *General Method I*, and samples (10-15 μL) were loaded on 4-12% Bis-Tris gels (Invitrogen) and resolved by SDS-PAGE gel electrophoresis with MES as running buffer. Unreacted ABPs (loading control) were visualized by loading sample (3 μL) on 10% Bis-Tris gels (Invitrogen) and resolved by SDS-PAGE gel electrophoresis with MES as running buffer.

HeLa. 19 μ L Lysate (WT or overexpressing FLAG-HA-USP16) was incubated with 1 μ L Rho-Ub-ABP for 1 h at 37 °C. Reaction was quenched as described in *General Method I*, and samples (10 μ L) were loaded on 4-12% Bis-Tris gels (Invitrogen) and resolved by SDS-PAGE gel electrophoresis with MOPS as running buffer. Gels were transferred to nitrocellulose membrane using a Trans-Blot Turbo Transfer System (Biorad) and subjected to standard Western Blotting protocols. Antibodies: mouse anti-HA (1:1,000; Covance, #MMS-101R) and goat anti-mouse HRP (1:5,000; Dako, #P0447). Blots with HRP secondary antibody were incubated with SuperSignal™ West Dura Extended Duration Substrate (Thermo Sci., #34076) according to manufacturer protocols and scanned on an Amersham Imager 600.

Incubation of recombinant DUBs

Recombinant purified cysteine DUB (final conc. 1 μ M) was incubated with Rho-Ub-ABP (final conc. 10 μ M) for 1 h at 37 °C. Reaction was quenched as described in *General Method I*. Bis-Tris gels and running buffer were adjusted to optimize separation of unbound enzyme and covalent CysDUB–ABP adduct.

Incubation of recombinant USP16CD^{WT} (+/- NEM) and USP16CD^{C205A}

Recombinant purified USP16CD^{WT} or USP16CD^{C205A} mutant (final conc. 0.1 μ M) was incubated with Rho-Ub-ABP (final conc. 10 μ M) for 1 h at 37 °C. Preincubation of USP16CD^{WT} with 10 mM *N*-ethylmaleimide (NEM; SigmaAldrich, #E3876) for 30 min at 37 °C was performed prior to incubation with ABPs to alkylate/block cysteine thiols. The reaction was quenched and resolved as described in *General Method I*. Fluorescence scans for resolved gels with USP16CD^{WT} and USP16CD^{C205A} were obtained with the same settings/sensitivity (PMT = 500), and images were processed simultaneously to ensure observed (lack of) fluorescent covalent adduct is independent of settings.

Time-dependent covalent USP16–ABP adduct formation

Rho-Ub-Prg, Rho-Ub-2, and Rho-Ub-5 solutions were prepared from single-use aliquots of 500 μ M stock solutions in DMSO. USP16CD^{WT} (final conc. 0.25 μ M) was incubated with Rho-Ub-ABP (final conc. 10 μ M) at 37 °C. Samples were removed after indicated incubation time (0.5-4 h), and adduct formation was quenched and resolved as described in *General Method I*.

4.4. MS Analysis

Intact protein MS

Recombinant USP16CD^{WT} or USP16CD^{C205A} (1 μ M) in HEPES reaction buffer (20 μ L) was incubated with Rho-Ub-Prg, Rho-Ub-2 or Rho-Ub-5 (10 μ M) or buffer at 21 °C for at least 2 h prior to analysis. Chromatographic separation and MS analysis was carried out on a Waters ACQUITY UPLC-MS system equipped with a Waters ACQUITY Quaternary Solvent Manager (QSM), Waters ACQUITY FTN AutoSampler, Waters ACQUITY UPLC Protein BEH C4 Column (300 Å, 1.7 μ m, 2.1×50 mm) and XEVO-G2 XS QTOF Mass Spectrometer (m/z = 200-2500) in ES+ mode. Samples were run with a 7 min gradient (run time 15 min) using 0.1% FA in MeCN and 0.1% FA in water as mobile phases (flow rate 0.6-0.8 mL/min). The first 4 min the flow was diverted to the waste to avoid contamination of the MS with high concentrations of buffer components. After 4 min, the elution flow was ionized with an electrospray ionization (ESI) source in positive ion mode. The data was analyzed using Waters MassLynx Mass Spectrometry Software V4.2. The total mass of the covalent USP16–ABP adducts was obtained by deconvolution of electrospray ionization mass spectrum envelope (m/z = 600-1600 Da) with the MaxEnt1 (average isotopes) function.

HRMS of unbound ABPs

Stock solutions of Rho-Ub-Prg and Rho-Ub-[D₂]-Prg in DMSO (500 μ M) were diluted 500-fold in 2% MeCN in water (0.1% FA). MS analysis was carried out on a Waters ACQUITY UPLC-MS system in Resolution Mode, equipped with a Waters ACQUITY Quaternary Solvent Manager (QSM), Waters ACQUITY FTN AutoSampler, Waters ACQUITY UPLC Protein BEH C4 Column (300 Å, 1.7 μ m, 2.1×50 mm) and XEVO-G2 XS QTOF Mass Spectrometer (m/z = 500-2000). Samples were run with a 1.6 min 2-100% gradient (run time 3 min) using

0.1% FA in MeCN and 0.1% FA in water as mobile phases (flow rate 0.6 mL/min). The elution flow was ionized with an electrospray ionization (ESI) source in positive ion mode. Data processing was performed using Waters MassLynx Mass Spectrometry Software 4.2. Theoretical mass was calculated with the isotope modelling function; Tools – Isotope model – Create charge state series. More details in *section 7.5*.

Bottom-up MS analysis

Recombinant purified USP16CD^{WT} (2.4 μ M) or UCHL3FL^{WT} (7 μ M) in HEPES reaction buffer was incubated with Rho-Ub-Prg or Rho-Ub-[D₂]-Prg (final conc. 10 μ M) for 1 h at 37 °C. Reaction was quenched as described in *General Method I*. Samples (21 μ L, corresponding to 2.5 μ g protein/lane) were run on a 10% Bis-Tris gel, and stained with InstantBlue™ Ultrafast Protein Stain. The CysDUB–ABP adduct band was cut out, and the proteins subjected to reduction with DTT, alkylation with iodoacetamide and in-gel trypsin digestion using Proteineer DP digestion robot (Bruker). Tryptic peptides were extracted from the gel slices, lyophilized, dissolved in 95:3:0.1 water/MeCN/FA (v/v/v) and subsequently analyzed by on-line C18 nanoHPLC MS/MS with a system consisting of an Easy nLC 1200 gradient HPLC system (Thermo, Bremen, Germany), and a LUMOS mass spectrometer (Thermo). Digests were injected onto a homemade precolumn (100 μ m \times 15 mm; Reprosil-Pur C18-AQ 3 μ m, Dr. Maisch, Ammerbuch, Germany) and eluted via a homemade analytical nano-HPLC column (15 cm \times 75 μ m; Reprosil-Pur C18-AQ 3 μ m). The gradient was run from 0% to 50% solvent B (20:80:0.1 water/MeCN/FA (v/v/v)) in 20 min. The nano-HPLC column was drawn to a tip of \sim 5 μ m and acted as the electrospray needle of the MS source. The LUMOS mass spectrometer was operated in data-dependent MS/MS (top-10 mode) with collision energy at 32 V and recording of the MS2 spectrum in the orbitrap. In the master scan (MS1) the resolution was 120,000, the scan range 400–1500, at an AGC target of 400,000 @maximum fill time of 50 ms. Dynamic exclusion after $n = 1$ with exclusion duration of 10 s. Charge states 2–5 were included. For MS2 precursors were isolated with the quadrupole with an isolation width of 1.2 Da. HCD collision energy was set to 32 V. The MS2 scan resolution was 30,000 with an AGC target of 50,000 @maximum fill time of 60 ms. In a post-analysis process, raw data were first converted to peak lists using Proteome Discoverer version 2.4 (Thermo Electron), and then submitted to the Homo sapiens database (71591 entries), using Mascot v. 2.2.07 (www.matrixscience.com) for protein identification. Mascot searches were with 10 ppm and 0.02 Da deviation for precursor and fragment mass, respectively, and trypsin as enzyme. Up to two missed cleavages were allowed. Methionine oxidation, carbamidomethyl on cysteine, and the Gly-Prg modification (also in mono and dideuterated form) on cysteine were set as a variable modification. More details in *section 7.6*.

4.5. Kinetic Evaluation of Covalent USP16 Occupancy

Rho-Ub-Prg, Rho-Ub-**2**, and Rho-Ub-**5** solutions were prepared from single-use aliquots of 500 μ M stock solutions in DMSO. USP16CD^{WT} (final conc. 0.1 μ M) was incubated with Rho-Ub-Prg, Rho-Ub-**2** or Rho-Ub-**5** (final conc. 1–10 μ M) at 21 °C in a total volume of 98 μ L. Samples (18 μ L) were removed after indicated incubation time (5–30 min), and adduct formation was quenched as described in *General Method I*. Samples (24 μ L/lane) were loaded on 10% Bis-Tris gels (Invitrogen) and resolved by SDS-PAGE gel electrophoresis with MES as running buffer. Measurements were performed in triplicate ($n = 3$). Details on equations and pseudo-first order reaction conditions are provided in *section 7.7*.

Intensity of signals corresponding to unbound USP16 and covalent USP16–ABP adduct were quantified with ImageJ v1.52a,^{80–82} and the gel-specific background was subtracted. Incubation time-dependent covalent occupancy (Covalent occupancy)_{*t*} (in %) was calculated from background-subtracted intensity of bands corresponding to unbound USP16 and covalent adduct after each incubation time *t*.

$$(\text{Covalent Occupancy})_t = 100\% \frac{(\text{adduct})_t}{(\text{adduct})_t + (\text{unbound})_t}$$

Triplicate values of time-dependent covalent occupancy ($\text{Covalent occupancy}_t$ (in %) were plotted against incubation time t (in min) and fitted to one-phase exponential association (GraphPad Prism 8.1.1, Exponential – One-phase association) with constrained value of $Y_0 = 0$ (covalent occupancy at reaction initiation) and a globally shared value (for all ABPs) for Plateau (maximum covalent occupancy) to obtain the rate of covalent bond formation k_{obs} (in min^{-1}).

$$(\text{Covalent Occupancy})_t = Y_0 + (\text{Plateau} - Y_0) \left(1 - e^{-k_{\text{obs}} t}\right) = \text{Max} \left(1 - e^{-k_{\text{obs}} t}\right)$$

Reaction half-life $t_{1/2}$ (in min) – corresponding to the incubation time to reach 50% of maximum covalent occupancy – was calculated from the pseudo-first order rate of covalent bond formation k_{obs} (in min^{-1}) for each ABP concentration.

$$t_{1/2} = \frac{\ln(2)}{k_{\text{obs}}}$$

Reaction completion (in min) – the incubation time to reach a covalent occupancy corresponding to 97% of the maximum covalent occupancy – is reached after five half-lives ($5t_{1/2}$).

4.6. Fluorescence Polarization (FP) Binding Assay

Binding assays of Rho-Ub-ABPs with catalytically inactive USP16^{C205S} mutant were performed in triplicate using HEPES reaction buffer (50 mM HEPES pH7.4, 150 mM NaCl, 2 mM DTT) supplemented with 0.005% Tween20. Rho-Ub-ABPs (20 nL of 5 μM dilution in 1% DMSO, final conc. 5 nM) were dispensed using an ECHO 550 Liquid Handler (Labcyte Inc.) acoustic dispenser, followed by manual addition of serially diluted purified recombinant USP16CD^{C205S} (20 μL , final conc. 0-64 μM). Fluorescence polarization (FP) of the Rhodamine fluorophore was measured every 3 min for 120 min on a PHERAstar plate reader (BMG LABTECH GmbH, Germany) with 485-520-520 FP module ($\lambda_{\text{ex}} = 485$ nm with detection of polarization at $\lambda_{\text{em}} = 520$ nm). Change in fluorescence polarization (in mP) upon USP16 interaction was calculated using MARS data analysis software (BMG LABTECH GmbH, Germany). The concentration-dependent fluorescence polarization FP (in mP) after sufficient incubation to reach noncovalent equilibrium (60 min) was plotted against USP16CD^{C205S} concentration (in M) for each Rho-Ub-ABP and fitted using nonlinear regression (GraphPad Prism 8.4.2, Binding – Saturation, One site – Total) with globally shared values for nonspecific binding NS (in mP/M), background signal in absence of enzyme (in mP), and maximum specific binding B_{max} (in mP) to obtain the noncovalent dissociation constant K_D (in M) for each Rho-Ub-ABP. More details in section 7.8.

$$FP = \frac{B_{\text{max}} [E]}{K_D + [E]} + \text{NS} \times [E] + \text{background}$$

4.7. Thiol Reactivity Assay

Stock solutions of Rho-Ub-ABPs in DMSO (500 μM) were diluted in PBS (10 mM phosphate buffer pH7.45, 140 mM NaCl, 2.7 mM KCl, Gibco PBS tablets) freshly supplemented with GSH (Chem-Impex, #00159) to a final concentration of 5 μM Rho-Ub-ABP and 5 mM GSH. Immediately a 30 μL sample was removed, quenched by 2-fold dilution in 0.1% FA in water and submitted to LC-MS analysis. The remaining material was incubated at 37 °C under gentle agitation (600 rpm) for 24 h, after which the reaction was quenched by 2-fold dilution in 0.1% FA in water, and submitted to LC-MS analysis. LC-MS analysis was performed on a Waters ACQUITY UPLC H-class System equipped with Waters ACQUITY Quaternary Solvent Manager (QSM), Waters ACQUITY UPLC Photodiode Array (PDA) eλ Detector ($\lambda = 210\text{-}800$ nm), Waters ACQUITY UPLC Protein BEH C4 Column (300 Å, 1.7 μm , 2.1×50 mm) and LCT Premier Orthogonal Acceleration Time of Flight Mass Spectrometer ($m/z = 100\text{-}1600$) in ES+ mode. Samples were run with a 7 min 2-100% gradient (run time 10 min) using 96% water and 96% MeCN mixed with 2.5% FA in water/MeCN as mobile phases (flow rate = 0.5 mL/min). Data processing was performed using Waters MassLynx Mass Spectrometry Software V4.2. Adduct formation was

quantified from the total ion count (TIC) detected for GSH-ABP adduct, remaining unreacted ABP or hydrolysis product; the intensity of the naturally most abundant isotope peak in seven charge states ($z = 7-13$) of the ionization envelope was combined to calculate the ratio of GSH adduct over total ABP content for each sample. More details in *section 7.9*.

$$\text{GSH Adduct} = 100\% \frac{\text{TIC}_{\text{adduct}}}{\left(\text{TIC}_{\text{adduct}} + \text{TIC}_{\text{inhibitor}} \right)}$$

5. Materials and Methods: *Chemical Synthesis*

5.1. Synthesis of Rho-Ub-ABPs

Reagents and solvents were purchased from various suppliers and are used as received. Linear solid phase synthesis of Ub was performed according to established method reported by our group.⁸³ Data processing of LC-MS analysis was performed using Waters MassLynx Mass Spectrometry Software V4.2. Deconvoluted mass was obtained from the electrospray ionization mass spectrum envelope (average isotopes) with the MaxEnt1 function. The calculated mass of Ub (derivatives) is obtained with ChemDraw Professional 16.0.1.1 (PerkinElmer Informatics, Inc.) by calculating the molecular weight of the complete structure. Rho-M20-Prg was obtained by reported *in-house* synthesis.⁷⁹

General Method II. Trial Cleavage and LC-MS Analysis of Crude Mixtures

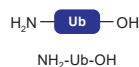
Trial Cleavage. An aliquot is incubated with Trial Cleavage Mix (92.5:2.5:2.5:2.5 TFA/water/iPr₃SiH/DODt) for 30 min at 38 °C under gentle agitation. Resin-bound samples are then transferred to a filter tip and filtered prior to continuation. The reaction mixture or filtrate is treated with cold 1:1 Et₂O/pentane (v/v) to precipitate the product, centrifuged and the soluble material is removed by suction. The precipitate is washed twice with cold Et₂O, and remaining Et₂O is removed by submitting to a gentle air flow. The solid material is dissolved in DMSO, and reaction progress is analyzed by LC-MS.

LC-MS Analysis. LC-MS analysis of crude reaction mixtures and purification fractions was performed on a Waters Alliance 2795 Separation Module system equipped with Waters 2996 Photodiode Array Detector ($\lambda = 190-750$ nm), Waters Xbridge C18 column (130 Å, 3.5 µm, 2.1×30 mm) and LCT Premier Orthogonal Acceleration Time of Flight Mass Spectrometer ($m/z = 300-2000$). Samples were run with a 3 min 5-95% gradient (run time 6 min) using two mobile phases; 1% MeCN + 0.1% FA in water and 1% water + 0.1% FA in MeCN (flow rate = 0.8 mL/min).

Step I. SPPS

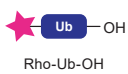
UbiquitinΔG on trityl-resin was prepared by linear solid phase peptide synthesis on a Syro II Automated Peptide Synthesizer (MultiSynTech GmbH, Germany) as described previously.⁸³ Met1 (methionine) was replaced by its close isostere Nle (norleucine) to prevent oxidation, which typically does not affect recognition by DUBs but can reduce cleavage efficiency of linear diUb chains.⁸⁴⁻⁸⁵ Briefly, Glycine-loaded trityl resin (Rapp Polymere, Germany, #RA1213) was incubated twice for 25 min with Fmoc-protected amino acids (4 eq; Novabiochem), DIPEA (8 eq; Biosolve, #041533), and PyBOP (4 eq; SigmaAldrich, #851009) in NMP (Biosolve, #13563202), followed by Fmoc removal by incubating three times for 2 min with 20% piperidine/NMP (v/v). This procedure was repeated for each amino acid coupling cycle, with a total of 68 cycles. Coupling sequence has previously been optimized for incorporation of Fmoc-protected dipeptides.⁸³

Reaction monitoring. An aliquot of protected NH₂-Ub₁₋₇₅-OH on resin was submitted to trial cleavage conditions, and the crude material was submitted to LC-MS analysis as described in *General Method II*. LC-MS Rt = 1.85 min, M = 8490 Da (Calc. 8489.78 Da).



Step II. Rhodamine coupling

Rhodamine coupling to the N-terminus was performed as described previously.⁸⁶ Briefly, *N,N'*-Boc₂-5-carboxy-Rhodamine **11** (4 eq; *in-house synthesis*),⁸⁶ PyBOP (4 eq; SigmaAldrich, #851009), and DIPEA (8 eq; Biosolve, #041533) were dissolved in NMP, and the preactivated mixture was added to NH₂-Ub₁₋₇₅(PG)-resin (1 eq), and incubated overnight. The resin was washed with NMP and DCM, after which trial cleavage was performed on a small aliquot to evaluate reaction progress. The resin-bound material was either resubmitted to reach reaction completion or used in the next step.



Reaction monitoring. An aliquot of protected Rho-Ub₁₋₇₅-OH on resin is submitted to trial cleavage conditions, and the crude material was submitted to LC-MS analysis as described in *General Method II*. LC-MS Rt = 2.37 min, M = 8845 Da (Calc. 8846.12 Da).

Step III. Cleavage from resin

Resin cleavage was performed as described previously: treatment with 1,1,1,3,3,3-hexafluoroisopropylalcohol (HFIP; Chem-Impex, #00080) in DCM cleaves bond between glycine and the trityl resin, while protecting groups on the amino acid side chains remain intact.⁸³ Briefly, (Boc)₂Rho-Ub₁₋₇₅(PG)-resin was washed with DCM to remove all NMP, and then twice incubated for 30 min at room temperature with 20% HFIP/DCM (v/v). The combined filtrate was collected, and the solvent was removed by rotary evaporation. Residual HFIP was removed by co-evaporation 2-3 times with 1,2-dichloroethane (DCE; Acros Organics, #406820025) – to prevent formation of HFIP ester in next steps – and dried to use in the next step.

Step IV. Amine coupling

Amine coupling was performed as described previously.⁸³ Amines were obtained from commercial sources or by chemical synthesis. Briefly, (Boc)₂Rho-Ub₁₋₇₅(PG)-OH was dissolved in DCM (Biosolve, #13790502) or DMF (Biosolve, #4190501), and incubated overnight with amine (4 eq), DIPEA (8 eq) and PyBOP (4 eq). DCM was removed by rotary evaporation or N₂ (g) shower. DMF was removed by dilution of the reaction mixture in 1:1 MeCN/water and subsequently lyophilized. Trial cleavage was performed to evaluate reaction progress by LC-MS. The residue was either resubmitted to coupling conditions until reaction completion was reached or submitted to global deprotection conditions.

Step V. Global deprotection and purification

Global deprotection was performed as described previously.⁷⁹ Briefly, (Boc)₂Rho-Ub₁₋₇₅(PG)-warhead was incubated for 2.5-3 hours with freshly prepared Cleavemix (90:5:2.5:2.5 TFA/water/iPr₃SiH/PhOH) under gentle agitation at room temperature to remove protecting groups from all amino acid sidechains. Then, cold 3:1 Et₂O/pentane (v/v) was added to precipitate the product. The reaction mixture was spun down in the centrifuge (2000 rpm, 5 min, 4 °C), supernatant was removed, and the pellet was washed twice with cold Et₂O. The remaining solvent was removed by a N₂ shower. The solid crude material was dissolved in DMSO and carefully diluted 10-fold in (warm) water (containing 0.05% TFA if required), filtered and submitted to preparative RP-HPLC purification (methods below, determined by synthesis scale).

prepRP-HPLC method A. RP-HPLC purifications (max. 0.5 mL/run) were performed on a Waters AutoPurification HPLC/MS System equipped with a 2767 Sample Manager, 2545 Binary Gradient Module, two 515 HPLC pumps, SFO Fluid Organizer, 2998 Photodiode Array Detector (λ = 210-650 nm), 3100 Mass Detector (m/z = 100-1500), and a Waters Xbridge BEH C18 OBD Prep. Column (130 Å, 5 µm, 19×150 mm). Column was pre-equilibrated depending on the gradient (prerun time 8 min), and samples (0.45 mL/run) were run with a 15 min 10-40% (A1) or 18-48% (A2) gradient (run time 21 min) using water and MeCN as mobile phases (flow rate = 30 mL/min), with additional at column dilution (ACD) of 1.5% TFA in MeCN (flow rate = 1 mL/min). Fraction collection was triggered by mass detection; after column separation, 0.02% of the sample was diverted and sent to the mass detector. Fractions containing the correct mass were collected, pooled and lyophilized to obtain product as a pink powder.

prepRP-HPLC method B. RP-HPLC purifications (max. 5 mL/run) were performed on a Shimadzu LC-20AT HPLC system equipped with an SPD-20A UV/Vis detector, RF-20A Fluorescence Detector ($\lambda_{\text{ex}} = 507 \text{ nm}$, $\lambda_{\text{em}} = 529 \text{ nm}$), FRC-10A fraction collector and a Waters XBridge C18 Prep. Column (130 Å, 5 µm, 10×150 mm). Samples were run with a 15 min 10-70% gradient (run time 22.1 min) using 0.05% TFA in water (v/v) and 0.05% TFA in MeCN (v/v) as mobile phases (flow rate = 6.5 mL/min). Sample collection was triggered by UV/Vis intensity. Pure fractions (checked by LC-MS) were pooled and lyophilized to obtain products as a pink powder.

prepRP-HPLC method C. RP-HPLC purifications (max. 20 mL/run) were performed on a Waters HPLC equipped with a Waters 2489 UV/Vis detector, Waters fraction collector III and a Waters XBridge BEH C18 OBD Prep. Column (130 Å, 5 µm, 30×150 mm). Samples were run with a 13 min 5-20% gradient (run time 25 min) using water, MeCN and 1% TFA in water (v/v) as mobile phases (flow rate = 37.5 mL/min). Fraction collection was triggered by UV intensity ($\lambda = 210 \text{ nm}$). Pure fractions (checked by LC-MS) were pooled and lyophilized to obtain products as a pink powder.

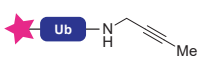
LC-MS evaluation of purified ABPs

Stock solutions of pure ABP (500 µM in DMSO) were diluted 100-fold in 0.1% FA in water, and 10 µL was injected for LC-MS analysis. LC-MS analysis of pure ABPs was performed on a Waters ACQUITY UPLC H-class System equipped with Waters ACQUITY Quaternary Solvent Manager (QSM), Waters ACQUITY UPLC Photodiode Array (PDA) eλ Detector ($\lambda = 210\text{-}800 \text{ nm}$), Waters ACQUITY UPLC Protein BEH C4 Column (300 Å, 1.7 µm, 2.1×50 mm) and LCT Premier Orthogonal Acceleration Time of Flight Mass Spectrometer ($m/z = 100\text{-}1600$) in ES+ mode. Samples were run with a 7 min 2-100% gradient (run time 10 min) using 96% water and 96% MeCN mixed with 2.5% FA in water/MeCN as mobile phases (flow rate = 0.5 mL/min).



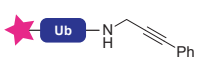
Rho-Ub-Prg

(Boc)₂Rho-Ub₁₋₇₅(PG)-OH (10 µmol) was incubated with propargylamine (SigmaAldrich, #P50900) in DCM, and purified by *prepRP-HPLC method C* to yield Rho-Ub₁₋₇₅-Prg as a solid pink powder. LC-MS Rt = 3.42 min, M = 8883 Da (Calc. 8883.18 Da).



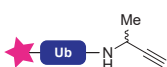
Rho-Ub-2

(Boc)₂Rho-Ub₁₋₇₅(PG)-OH (2 µmol) was incubated with 1-amino-2-butyne hydrochloride (*in-house synthesis*)⁸⁷ in DCM, and purified by *prepRP-HPLC method B* to yield Rho-Ub₁₋₇₅-2 as a solid pink powder. LC-MS Rt = 3.46 min, M = 8897 Da (Calc. 8897.21 Da).



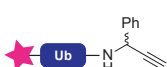
Rho-Ub-3

(Boc)₂Rho-Ub₁₋₇₅(PG)-OH (2 µmol) was incubated with 3-phenylprop-2-yn-1-amine hydrochloride (Enamine, #EN300-26681) in DCM, and purified by *prepRP-HPLC method B* to yield a 7:10 mixture of Rho-Ub₁₋₇₅-3 and hydrolyzed Rho-Ub₁₋₇₅-3b as a solid pink powder. Rho-Ub-3 is prone to hydrolysis or possibly (acid-catalyzed) hydration resulting in hydrolyzed Rho-Ub-3b (M+18) and could thus only be obtained as a mixture. LC-MS Rt = 3.51 min, M = 8959 & 8977 Da (Calc. 8959.28 Da).



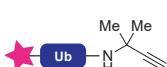
Rho-Ub-4

(Boc)₂Rho-Ub₁₋₇₅(PG)-OH (2 µmol) was incubated with 1-methyl-prop-2-ynylamine hydrochloride (Chem-Impex, #18527) in DMF, and purified by *prepRP-HPLC method A2* to yield Rho-Ub₁₋₇₅-4 as a solid pink powder. LC-MS Rt = 3.44 min, M = 8897 Da (Calc. 8897.21 Da).



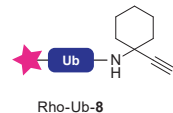
Rho-Ub-7

(Boc)₂Rho-Ub₁₋₇₅(PG)-OH (2 µmol) was incubated with 1-phenylprop-2-yn-1-amine hydrochloride (Enamine, #EN300-190354) in DMF, and purified by *prepRP-HPLC method A2* to yield Rho-Ub₁₋₇₅-7 as a solid pink powder. LC-MS Rt = 3.49 min, M = 8959 Da (Calc. 8959.28 Da).

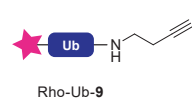


Rho-Ub-5

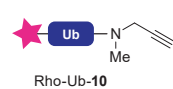
(Boc)₂Rho-Ub₁₋₇₅(PG)-OH (10 µmol) was incubated with 2-methyl-3-butyn-2-amine (SigmaAldrich, #687189) in DCM, and purified by *prepRP-HPLC method C* to yield Rho-Ub₁₋₇₅-5 as a solid pink powder. LC-MS Rt = 3.44 min, M = 8912 Da (Calc. 8911.24 Da).



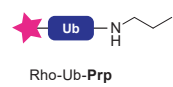
(Boc)₂Rho-Ub₁₋₇₅(PG)-OH (2 μ mol) was incubated with 1-ethynylcyclohexylamine (SigmaAldrich, #177024) in DMF, and purified by *prepRP-HPLC method A2* to yield Rho-Ub₁₋₇₅-**8** as a solid pink powder. LC-MS Rt = 3.49 min, M = 8951 Da (Calc. 8951.30 Da).



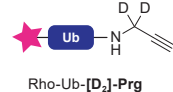
(Boc)₂Rho-Ub₁₋₇₅(PG)-OH (2 μ mol) was incubated with 1-amino-3-butyne (SigmaAldrich, #715190) in DMF, and purified by *prepRP-HPLC method A1* to yield Rho-Ub₁₋₇₅-**9** as a solid pink powder. LC-MS Rt = 3.42 min, M = 8897 Da (Calc. 8897.21 Da).



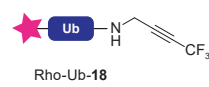
(Boc)₂Rho-Ub₁₋₇₅(PG)-OH (2 μ mol) was incubated with *N*-methylpropargylamine (SigmaAldrich, #150223) in DMF, and purified by *prepRP-HPLC method A2* to yield Rho-Ub₁₋₇₅-**10** as a solid pink powder. LC-MS Rt = 3.44 min, M = 8897 Da (Calc. 8897.21 Da).



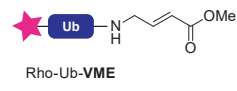
(Boc)₂Rho-Ub₁₋₇₅(PG)-OH (2 μ mol) was incubated with propylamine (Fluka Analytical, #82100) in DMF, and purified by *prepRP-HPLC method A1* to yield Rho-Ub₁₋₇₅-**Prp** as a solid pink powder. LC-MS Rt = 3.44 min, M = 8887 Da (Calc. 8887.22 Da).



(Boc)₂Rho-Ub₁₋₇₅(PG)-OH (2 μ mol) was incubated with prop-2-yn-1,1-*d*₂-1-amine hydrochloride (*in-house synthesis*, see *section 5.2.1*) in DCM, and purified by *prepRP-HPLC method B* to yield Rho-Ub₁₋₇₅-[D₂]-**Prg** as a solid pink powder. LC-MS Rt = 3.39 min, M = 8885 Da (Calc. 8885.20 Da).



(Boc)₂Rho-Ub₁₋₇₅(PG)-OH (2 μ mol) was incubated with 4,4,4-trifluorobut-2-yn-1-amine hydrochloride (*in-house synthesis*, see *section 5.2.2*) in DCM, and purified by *prepRP-HPLC method B* to yield Rho-Ub₁₋₇₅-**18** as a solid pink powder. LC-MS Rt = 3.46 min, M = 8951 Da (Calc. 8951.18 Da).



(Boc)₂Rho-Ub₁₋₇₅(PG)-OH (4 μ mol) was incubated with methyl (*E*)-4-aminobut-2-enoate hydrochloride (*in-house synthesis*)⁴⁸ in DCM, and purified by *prepRP-HPLC method C* to yield Rho-Ub₁₋₇₅-**VME** as a solid pink powder. LC-MS Rt = 3.40 min, M = 8942 Da (Calc. 8943.24 Da).

5.2. Synthesis of Building Blocks

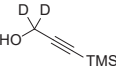
Synthetic schemes can be found in *section 7.2* for deuterated propargylamine **[D₂]-Prg** (**Scheme S1**), trifluoromethylated alkyne **18** (**Scheme S2**), 2-butynylamine **2** (**Scheme S3**), and vinyl methyl ester warhead **VME** (**Scheme S4**).

General. All commercially available reagents and solvents were used as purchased. Reported yields are not optimized. Nuclear magnetic resonance (NMR) spectra were recorded on a Bruker Avance 300 (300 MHz for ¹H, 75.00 MHz for ¹³C) using the residual solvent as internal standard (¹H: 7.26 ppm for CDCl₃, 2.50 ppm for DMSO-*d*₆, and 3.31 ppm for MeOD. ¹³C: 77.16 ppm for CDCl₃, 39.52 ppm for DMSO-*d*₆, and 49.00 ppm for MeOD). Chemical shifts (δ) are given in ppm and coupling constants (J) are quoted in hertz (Hz). Resonances are described as s (singlet), d (doublet), t (triplet), q (quartet), p (quintet), b (broad) and m (multiplet) or combinations thereof. The quaternary CD₂ carbon in ¹³C NMR of deuterated compounds is detected/reported as quintet (p) due to J_{CD} -coupling with ²D ($n = 2$, splitting pattern 2n+1). Carbons in vicinity of trifluoromethyl group in ¹³C NMR are detected/reported as quartet due to J_{CF} -coupling with ¹⁹F ($n = 3$, splitting pattern n+1, up to $^4J_{CF}$). Thin Layer Chromatography (TLC) was performed using TLC plates from Merck (SiO₂, Kieselgel 60 F254 neutral, on aluminum with fluorescence indicator) and compounds were visualized by KMnO₄ or ninhydrin staining. Flash

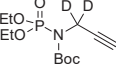
Column Chromatography (FCC) purifications were performed using Grace Davisil Silica Gel (particle size 40-63 μ m, pore diameter 60 \AA) and the indicated eluent.

5.2.1. Synthesis of Amine [D_2]-Prg

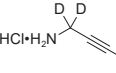
3-(trimethylsilyl)prop-2-yn-1,1- d_2 -1-ol 12

 A 1 M solution of lithium aluminum deuteride in Et_2O (2.2 mL, 2.2 mmol) was cooled to -78°C and diluted with anhydrous Et_2O (8 mL). After stirring for 1 hour, a solution of ethyl 3-(trimethylsilyl)propiolate (1.0 gr, 5.9 mmol) in anhydrous Et_2O (2 mL) was added in portions. The mixture was allowed to stir at room temperature for 18 hours after which the reaction was quenched by addition of 1N HCl solution (aq, 10 mL) and the layers were separated. The aqueous layer was extracted with Et_2O and the combined organic layers were dried over Na_2SO_4 , filtered and carefully concentrated on a rotary evaporator (850 mbar, 42 $^\circ\text{C}$) to avoid loss of the product. Intermediate **12** was obtained as a pale yellow oil (832 mg, quantitative) with some remnant Et_2O , and used crude in the next step. Spectral data was in agreement with structure and reported data.⁸⁸ TLC R_f = 0.67 (1:1 EtOAc/heptane). ^1H NMR (300 MHz, CDCl_3) δ 0.17 (s, 9H). ^{13}C NMR (75 MHz, CDCl_3) δ 104.0, 90.8, 51.3 (p, J = 22.6 Hz), -0.1.

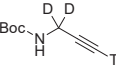
tert-butyl (diethoxyphosphoryl)(3-(trimethylsilyl)prop-2-yn-1-yl-1,1- d_2)carbamate 13

 Adjustment of reported procedure for conversion of alcohols into amines under Mitsunobu conditions.⁸⁹ Crude deuterated 3-(trimethylsilyl)propargyl alcohol **12** (5.87 mmol), triphenylphosphine (1.77 gr, 6.74 mmol) and diethyl *N*-(tert-butoxycarbonyl) phosphoramidate (1.49 gr, 5.87 mmol, 1 eq) were dissolved in anhydrous THF (30 mL). The reaction mixture was flushed with argon and subsequently cooled to 0 $^\circ\text{C}$. Diisopropyl azodicarboxylate (1.33 mL, 6.74 mmol) was added dropwise to the reaction over 10 min. Cooling was removed and the reaction mixture was stirred at room temperature for 18 hours. The solvent was removed *in vacuo* and the crude reaction mixture containing intermediate **13** was directly submitted to the next step.

3-(trimethylsilyl)prop-2-yn-1,1- d_2 -1-amine hydrochloride 14

 Adjustment of reported procedure.²⁷ Crude *tert*-butyl (diethoxyphosphoryl)(3-(trimethylsilyl)prop-2-yn-1-yl-1,1- d_2)carbamate **13** was dissolved in anhydrous toluene (40 mL) in a two-neck flask equipped with an inlet for gaseous hydrogen chloride and an outlet toward a strong alkaline solution to neutralize the acidic gas. HCl (g) was generated continuously (*in situ*) by slow dropwise addition of 37% HCl (aq) onto powdered CaCl_2 in a separate sealed flask, and bubbled through the reaction mixture for 2 hours. The reaction mixture was sealed and left to stir overnight. The reaction mixture was filtered, triturated with Et_2O (3X) and dried *in vacuo* to give product **14**. Additional product was obtained by removal of solvent from the filtrate *in vacuo*, followed by trituration with Et_2O and toluene. Intermediate **14** was obtained as a white solid (426 mg, 2.57 mmol, 44% over 3 steps). TLC R_f = 0.21 (5% MeOH/DCM). ^1H NMR (300 MHz, $\text{DMSO}-d_6$) δ 8.45 (s, 3H), 0.17 (s, 9H). ^{13}C NMR (75 MHz, $\text{DMSO}-d_6$) δ 99.0, 91.2, 28.5 (p, J = 22.3 Hz), -0.4.

tert-butyl (3-(trimethylsilyl)prop-2-yn-1-yl-1,1- d_2)carbamate 15

 To 3-(trimethylsilyl)prop-2-yn-1,1- d_2 -1-amine hydrochloride **14** (42.9 mg, 0.26 mmol) were added DCM (0.8 mL) and triethylamine (72 μL , 0.52 mmol, 2 eq). The suspension was stirred at room temperature for 10 min prior to addition of di-*tert*-butyl dicarbonate (56.5 mg, 0.26 mmol, 1 eq), and additional triethylamine (72 μL , 0.52 mmol, 2 eq) in DCM (2 mL). The clear solution was stirred for 60 min (until full conversion of the starting material was detected by TLC) and concentrated by rotary evaporation to give a white solid. The material was treated with ethyl acetate, water and 1N KHSO_4 (aq). The organic layer was extracted with saturated NaHCO_3 solution (aq), dried over Na_2SO_4 , filtered and concentrated to give a colorless oil (63.4 mg) containing a 2:1 mixture of intermediate **15** with unreacted Boc anhydride. The material was used in the next step without further purification. TLC R_f = 0.87 (5% MeOH/DCM), R_f = 0.72 (1:1 EtOAc/heptane). ^1H NMR (300 MHz, CDCl_3) δ 4.64 (s, 1H), 1.45 (s, 9H), 0.15 (s, 9H).

tert-butyl (prop-2-yn-1-yl-1,1-d₂)carbamate 16

Crude tert-butyl (3-(trimethylsilyl)prop-2-yn-1-yl-1,1-d₂)carbamate **15** (63.4 mg, max. 0.26 mmol) was dissolved in methanol (3 mL), to which potassium carbonate (184 mg, 1.3 mmol, 5 eq) was added. The suspension was stirred at room temperature for 30 min, when full conversion was detected by TLC analysis. The reaction mixture was diluted with EtOAc and water, and layers were separated. The organic layer was extracted with water and brine, dried over Na₂SO₄, filtered and carefully concentrated in vacuo to give intermediate **16** as a colorless oil (26.4 mg, 0.17 mmol, 65% over 2 steps). **Note:** Exposure of intermediate **16** to high vacuum for a few minutes can result in significant loss of material. TLC R_f = 0.74 (5% MeOH/DCM), R_f = 0.64 (1:1 EtOAc/heptane). ¹H NMR (300 MHz, CDCl₃) δ 4.73 (s, 1H), 2.20 (s, 1H), 1.44 (s, 9H).

prop-2-yn-1,1-d₂-1-amine hydrochloride [D₂]-Prg

To a mixture of 3-(trimethylsilyl)prop-2-yn-1,1-d₂-1-amine hydrochloride **14** (20 mg, 0.12 mmol), di-*tert*-butyl dicarbonate (29 mg, 0.13 mmol) and potassium carbonate (83 mg, 0.60 mmol) were added MeOH (0.5 mL) and water (0.5 mL). The reaction mixture was stirred at room temperature for 18 hours, and volatiles (methanol) were removed by rotary evaporation upon reaction completion (as detected by TLC). Analytical details for deuterated Boc-propargylamine **16** described above). The reaction mixture was resuspended in ethyl acetate and extracted with water. The organic layer was dried over Na₂SO₄, filtered and carefully concentrated by rotary evaporation. Crude Boc-protected propargylamine **16** was dissolved in methanol (1.5 mL) to which was added 4N hydrogen chloride in dioxane (1 mL, 4 mmol), and the reaction mixture was left to stir 18 hours. Then the solvent was removed in vacuo, and the precipitate was triturated with Et₂O to obtain hydrochloride salt of deuterated propargylamine [D₂]-Prg as a white solid (10 mg, 0.064 mmol, 53%). TLC R_f = 0.02 (5% MeOH/DCM). ¹H NMR (300 MHz, DMSO-d₆) δ 8.37 (s, 3H), 3.58 (s, 1H). ¹³C NMR (75 MHz, DMSO-d₆) δ 77.8, 76.9, 27.7 (p, J = 22.4 Hz).

5.2.2. Synthesis of Amine 18**tert-butyl (4,4,4-trifluorobut-2-yn-1-yl)carbamate 17**

Adjustment of reported procedure for copper(I)-catalyzed trifluoromethylation of terminal alkynes.⁵² A flask was charged with copper(I) iodide (1.43 gr, 7.5 mmol), potassium carbonate (2.07 gr, 15 mmol), tetramethylethylene diamine (1.12 mL, 7.5 mmol) in DMF (23 mL). The dark blue reaction mixture was stirred vigorously under an atmosphere of air at room temperature for 15 min. trimethyl(trifluoromethyl)silane (1.5 mL, 10 mmol) was added and the resulting dark green reaction mixture was stirred for 5 min under air atmosphere prior to cooling to 0 °C. A solution of *N*-*tert*-butoxycarbonyl-1-amino-3-propyne (776 mg, 5 mmol) and trimethyl(trifluoromethyl)silane (1.5 mL, 10 mmol) in DMF (23 mL), already cooled to 0 °C, was added dropwise in 10 min. The reaction mixture was stirred at 0 °C for 30 min under air atmosphere after which the cooling was removed and the dark blue reaction mixture was left to stir at room temperature for 18 hours. The dark green solution was diluted with water and extracted with Et₂O (2X). The combined organic layers were extracted with water (2X) and brine, dried over MgSO₄ and filtered. The solution was diluted with DCM and transferred to a pad of Hyflo which was washed with Et₂O. The mixture was concentrated to give a crude 2:1 mixture of desired product **17** and undesired dimer **19**, which could be separated by FCC (1:4 EtOAc/heptane) to give intermediate **17** as a yellow oil (260.3 mg, 1.2 mmol, 23%). TLC R_f = 0.76 (1:1 EtOAc/heptane). ¹H NMR (300 MHz, CDCl₃) δ 4.80 (s, 1H), 4.06 (s, 2H), 1.46 (s, 9H). ¹³C NMR (75 MHz, CDCl₃) δ 155.1, 114.0 (q, J = 257 Hz), 84.3 (q, J = 6.3 Hz), 80.9, 70.4 (q, J = 52.6 Hz), 30.1, 28.4.

4,4,4-trifluorobut-2-yn-1-amine hydrochloride 18

To *tert*-butyl (4,4,4-trifluorobut-2-yn-1-yl)carbamate **17** (120 mg, 0.54 mmol) was added $\text{HCl} \cdot \text{H}_2\text{O}$ (1.2 mL, 20 mmol) and 4N HCl in dioxane (2 mL, 8 mmol) and the reaction mixture was stirred for 90 min at room temperature. After 5 min a precipitate started to form. Volatiles were removed by rotary evaporation and the material was triturated with Et_2O to give amine **18** as a white solid (78.1 mg, 0.49 mmol, 91%). TLC R_f = 0.00 (1:1 EtOAc/heptane). ^1H NMR (300 MHz, $\text{DMSO}-d_6$) δ 8.85 (s, 3H), 4.05 (q, J = 3.4 Hz, 2H). ^{13}C NMR (75 MHz, $\text{DMSO}-d_6$) δ 113.4 (q, J = 257 Hz), 84.2 (q, J = 7.3 Hz), 70.9 (q, J = 52.3 Hz), 27.7. Note: product decomposition was observed within a few hours at high concentration in $\text{DMSO}-d_6$, therefore NMR measurements of the electrophilic hydrochloride salt is preferably conducted in deuterated methanol. ^1H NMR (300 MHz, MeOD) δ 4.08 (q, J = 3.2 Hz, 2H). ^{13}C NMR (75 MHz, MeOD) δ 115.1 (q, J = 257 Hz), 81.9 (q, J = 6.3 Hz), 73.8 (q, J = 53.5 Hz), 29.4.

di-*tert*-butyl hexa-2,4-dyne-1,6-diyldicarbamate 19

 Dimer **19** is formed as undesired Glaser-Hay product in the copper(I)-catalyzed synthesis of trifluoromethylated alkyne **17** in presence of TMEDA. Dimer **19** was isolated as a colorless oil after separation by FCC (1:4 EtOAc/heptane). TLC R_f = 0.62 (1:1 EtOAc/heptane). ^1H NMR (300 MHz, CDCl_3) δ 4.69 (s, 2H), 3.99 (d, J = 5.4 Hz, 4H), 1.44 (s, 18H). ^{13}C NMR (75 MHz, CDCl_3) δ 155.2, 80.4, 74.9, 67.5, 31.2, 28.5.

6. References

- Clague, M.J.; Urbé, S.; Komander, D. Breaking the Chains: Deubiquitylating Enzyme Specificity Begets Function. *Nat. Rev. Mol. Cell Biol.* **2019**, *20*, 338-352. doi: 10.1038/s41580-019-0099-1.
- Ebner, P.; Versteeg, G.A.; Ikeda, F. Ubiquitin Enzymes in the Regulation of Immune Responses. *Crit. Rev. Biochem. Mol. Biol.* **2017**, *52*, 425-460. doi: 10.1080/10409238.2017.1325829.
- Deng, L.; Meng, T.; Chen, L.; Wei, W.; Wang, P. The Role of Ubiquitination in Tumorigenesis and Targeted Drug Discovery. *Sig. Transduct. Target. Ther.* **2020**, *5*, 11. doi: 10.1038/s41392-020-0107-0.
- Popovic, D.; Vucic, D.; Dikic, I. Ubiquitination in Disease Pathogenesis and Treatment. *Nat. Med.* **2014**, *20*, 1242-1253. doi: 10.1038/nm.3739.
- Huang, X.; Dixit, V.M. Drugging the Undruggables: Exploring the Ubiquitin System for Drug Development. *Cell Res.* **2016**, *26*, 484-498. doi: 10.1038/cr.2016.31.
- Veggiani, G.; Gerpe, M.C.R.; Sidhu, S.S.; Zhang, W. Emerging Drug Development Technologies Targeting Ubiquitination for Cancer Therapeutics. *Pharmacol. Ther.* **2019**, *199*, 139-154. doi: 10.1016/j.pharmthera.2019.03.003.
- Wertz, I.E.; Wang, X. From Discovery to Bedside: Targeting the Ubiquitin System. *Cell Chem. Biol.* **2019**, *26*, 156-177. doi: 10.1016/j.chembiol.2018.10.022.
- Kemp, M. Chapter Three - Recent Advances in the Discovery of Deubiquitinating Enzyme Inhibitors. *Prog. Med. Chem.* **2016**, *55*, 149-192. doi: 10.1016/bs.pmch.2015.10.002.
- Zhao, B.; Tsai, Y.C.; Jin, B.; Wang, B.; Wang, Y.; Zhou, H.; Carpenter, T.; Weissman, A.M.; Yin, J. Protein Engineering in the Ubiquitin System: Tools for Discovery and Beyond. *Pharmacol. Rev.* **2020**, *72*, 380. doi: 10.1124/pr.118.015651.
- Taylor, N.C.; McGouran, J.F. Strategies to Target Specific Components of the Ubiquitin Conjugation/Deconjugation Machinery. *Front. Chem.* **2020**, *7*, 914. doi: 10.3389/fchem.2019.00914.
- Hewings, D.S.; Flygare, J.A.; Bogyo, M.; Wertz, I.E. Activity-Based Probes for the Ubiquitin Conjugation–Deconjugation Machinery: New Chemistries, New Tools, and New Insights. *FEBS J.* **2017**, *284*, 1555-1576. doi: 10.1111/febs.14039.
- Deng, H.; Lei, Q.; Wu, Y.; He, Y.; Li, W. Activity-Based Protein Profiling: Recent Advances in Medicinal Chemistry. *Eur. J. Med. Chem.* **2020**, *191*, 112151. doi: 10.1016/j.ejmchem.2020.112151.
- Chakrabarty, S.; Kahler, J.P.; van de Plasche, M.A.T.; Vanhoutte, R.; Verhelst, S.H. Recent Advances in Activity-Based Protein Profiling of Proteases. *Curr. Top. Microbiol. Immunol.* **2019**, *420*, 253-281. doi: 10.1007/82_2018_138.
- Altun, M.; Kramer, H.B.; Willems, L.I.; McDermott, J.L.; Leach, C.A.; Goldenberg, S.J.; Kumar, K.G.S.; Konietzny, R.; Fischer, R.; Kogan, E.; Mackeen, M.M.; McGouran, J.; Khoronenkova, S.V.; Parsons, J.L.; Dianov, G.L.; Nicholson, B.; Kessler, B.M. Activity-Based Chemical Proteomics Accelerates Inhibitor Development for Deubiquitylating Enzymes. *Chem. Biol.* **2011**, *18*, 1401-1412. doi: 10.1016/j.chembiol.2011.08.018.
- Love, K.R.; Pandya, R.K.; Spooner, E.; Ploegh, H.L. Ubiquitin C-Terminal Electrophiles Are Activity-Based Probes for Identification and Mechanistic Study of Ubiquitin Conjugating Machinery. *ACS Chem. Biol.* **2009**, *4*, 275-287. doi: 10.1021/cb9000348.
- Resnick, E.; Bradley, A.; Gan, J.; Douangamath, A.; Krojer, T.; Sethi, R.; Geurink, P.P.; Aimon, A.; Amitai, G.; Bellini, D., et al. Rapid Covalent-Probe Discovery by Electrophile-Fragment Screening. *J. Am. Chem. Soc.* **2019**, *141*, 8951-8968. doi: 10.1021/jacs.9b02822.
- Pinto-Fernández, A.; Davis, S.; Schofield, A.B.; Scott, H.C.; Zhang, P.; Salah, E.; Mathea, S.; Charles, P.D.; Damianou, A.; Bond, G.; Fischer, R.; Kessler, B.M. Comprehensive Landscape of Active Deubiquitinating Enzymes Profiled by Advanced Chemoproteomics. *Front. Chem.* **2019**, *7*, 592. doi: 10.3389/fchem.2019.00592.
- Hewings, D.S.; Heideker, J.; Ma, T.P.; AhYoung, A.P.; El Oualid, F.; Amore, A.; Costakes, G.T.; Kirchhofer, D.; Brasher, B.; Pillow, T.; Popovych, N.; Maurer, T.; Schwerdtfeger, C.; Forrest, W.F.; Yu, K.; Flygare, J.; Bogyo, M.; Wertz, I.E. Reactive-Site-Centric Chemoproteomics Identifies a Distinct Class of Deubiquitinase Enzymes. *Nat. Commun.* **2018**, *9*, 1162. doi: 10.1038/s41467-018-03511-6.

19. Borodovsky, A.; Ovaa, H.; Kolli, N.; Gan-Erdene, T.; Wilkinson, K.D.; Ploegh, H.L.; Kessler, B.M. Chemistry-Based Functional Proteomics Reveals Novel Members of the Deubiquitinating Enzyme Family. *Chem. Biol.* **2002**, *9*, 1149–1159. doi: 10.1016/S1074-5521(02)00248-X.
20. Rehman, S.A.A.; Kristariyanto, Y.A.; Choi, S.-Y.; Nkosi, P.J.; Weidlich, S.; Labib, K.; Hofmann, K.; Kulathu, Y. MINDY-1 Is a Member of an Evolutionarily Conserved and Structurally Distinct New Family of Deubiquitinating Enzymes. *Mol. Cell* **2016**, *63*, 146–155. doi: 10.1016/j.molcel.2016.05.009.
21. Hermanns, T.; Wołwode, I.; Guerreiro, R.F.M.; Vogt, R.; Lammers, M.; Hofmann, K. An Evolutionary Approach to Systematic Discovery of Novel Deubiquitinases, Applied to *Legionella*. *Life Sci. Alliance* **2020**, *3*, e202000838. doi: 10.26508/lsa.202000838.
22. Schubert, A.F.; Nguyen, J.V.; Franklin, T.G.; Geurink, P.P.; Roberts, C.G.; Sanderson, D.J.; Miller, L.N.; Ovaa, H.; Hofmann, K.; Pruneda, J.N.; Komander, D. Identification and Characterization of Diverse OTU Deubiquitinases in Bacteria. *EMBO J.* **2020**, *39*, e105127. doi: 10.1525/embj.2020105127.
23. Hausman, J.M.; Kenny, S.; Iyer, S.; Babar, A.; Qiu, J.; Fu, J.; Luo, Z.-Q.; Das, C. The Two Deubiquitinating Enzymes from *Chlamydia trachomatis* Have Distinct Ubiquitin Recognition Properties. *Biochemistry* **2020**, *59*, 1604–1617. doi: 10.1021/acs.biochem.9b01107.
24. Parker, C.G.; Pratt, M.R. Click Chemistry in Proteomic Investigations. *Cell* **2020**, *180*, 605–632. doi: 10.1016/j.cell.2020.01.025.
25. Talele, T.T. Acetylene Group, Friend or Foe in Medicinal Chemistry. *J. Med. Chem.* **2020**, *63*, 5625–5663. doi: 10.1021/acs.jmedchem.9b01617.
26. Wright, M.H.; Sieber, S.A. Chemical Proteomics Approaches for Identifying the Cellular Targets of Natural Products. *Nat. Prod. Rep.* **2016**, *33*, 681–708. doi: 10.1039/C6NP00001K.
27. Ekkbus, R.; van Kasteren, S.I.; Kulathu, Y.; Scholten, A.; Berlin, I.; Geurink, P.P.; de Jong, A.; Goerdalay, S.; Neefjes, J.; Heck, A.J.R.; Komander, D.; Ovaa, H. On Terminal Alkynes That Can React with Active-Site Cysteine Nucleophiles in Proteases. *J. Am. Chem. Soc.* **2013**, *135*, 2867–2870. doi: 10.1021/ja309802z.
28. Sommer, S.; Weikart, N.D.; Linne, U.; Mootz, H.D. Covalent Inhibition of SUMO and Ubiquitin-Specific Cysteine Proteases by an In Situ Thiol-Alkyne Addition. *Bioorg. Med. Chem.* **2013**, *21*, 2511–2517. doi: 10.1016/j.bmc.2013.02.039.
29. Jia, Y.; Claessens, L.A.; Vertegaal, A.C.O.; Ovaa, H. Chemical Tools and Biochemical Assays for SUMO Specific Proteases (SENPs). *ACS Chem. Biol.* **2019**, *14*, 2389–2395. doi: 10.1021/acschembio.9b00402.
30. Mons, E.; Jansen, I.D.C.; Loboda, J.; van Doodewaard, B.R.; Hermans, J.; Verdoes, M.; van Boeckel, C.A.A.; van Veelen, P.A.; Turk, B.; Turk, D.; Ovaa, H. The Alkyne Moiety as a Latent Electrophile in Irreversible Covalent Small Molecule Inhibitors of Cathepsin K. *J. Am. Chem. Soc.* **2019**, *141*, 3507–3514. doi: 10.1021/jacs.8b11024.
31. Fairbanks, B.D.; Sims, E.A.; Anseth, K.S.; Bowman, C.N. Reaction Rates and Mechanisms for Radical, Photoinitiated Addition of Thiols to Alkynes, and Implications for Thiol-Yne Photopolymerizations and Click Reactions. *Macromolecules* **2010**, *43*, 4113–4119. doi: 10.1021/ma1002968.
32. Jayasree, E.G.; Reshma, S. A Computational Study on the Reaction Mechanism and Energetics of Markovnikov and Anti-Markovnikov Addition in Alkyne Hydrothiolation Reactions. *Comput. Theor. Chem.* **2016**, *1098*, 13–21. doi: 10.1016/j.comptc.2016.10.012.
33. Hashmi, A.S.K. Synthesis of Allenes by Isomerization Reactions. *Mod. Allene Chem.* **2004**, *2*, 50. doi: 10.1002/9783527619573.ch1.
34. Gehring, M.; Laufer, S.A. Emerging and Re-Emerging Warheads for Targeted Covalent Inhibitors: Applications in Medicinal Chemistry and Chemical Biology. *J. Med. Chem.* **2019**, *62*, 5673–5724. doi: 10.1021/acs.jmedchem.8b01153.
35. Arkona, C.; Rademann, J. Propargyl Amides as Irreversible Inhibitors of Cysteine Proteases—A Lesson on the Biological Reactivity of Alkynes. *Angew. Chem. Int. Ed.* **2013**, *52*, 8210–8212. doi: 10.1002/anie.201303544.
36. Ménard, R.; Storer, A.C. Oxyanion Hole Interactions in Serine and Cysteine Proteases. *Biol. Chem.* **1992**, *373*, 393–400. doi: 10.1515/bchm3.1992.373.2.393.
37. Shokhen, M.; Traube, T.; Vijayakumar, S.; Hirsch, M.; Uritsky, N.; Albeck, A. Differentiating Serine and Cysteine Protease Mechanisms by New Covalent QSAR Descriptors. *ChemBioChem* **2011**, *12*, 1023–1026. doi: 10.1002/cbic.201000459.
38. Heal, W.P.; Dang, T.H.T.; Tate, E.W. Activity-Based Probes: Discovering New Biology and New Drug Targets. *Chem. Soc. Rev.* **2011**, *40*, 246–257. doi: 10.1039/C0CS00004C.
39. de Jong, A.; Merkx, R.; Berlin, I.; Rodenko, B.; Wijdeven, R.H.M.; El Atmioui, D.; Yaçın, Z.; Robson, C.N.; Neefjes, J.J.; Ovaa, H. Ubiquitin-Based Probes Prepared by Total Synthesis To Profile the Activity of Deubiquitinating Enzymes. *ChemBioChem* **2012**, *13*, 2251–2258. doi: 10.1002/cbic.201200497.
40. Sui, Y.; Wang, Y.; Du, Y.-X.; Liang, L.-J.; Zheng, Q.; Li, Y.-M.; Liu, L. Development and Application of Ubiquitin-Based Chemical Probes. *Chem. Sci.* **2020**, *11*, 12633–12646. doi: 10.1039/DOSC03295F.
41. Hameed, D.S.; Sapmaz, A.; Ovaa, H. How Chemical Synthesis of Ubiquitin Conjugates Helps To Understand Ubiquitin Signal Transduction. *Bioconjug. Chem.* **2017**, *28*, 805–815. doi: 10.1021/acs.bioconjchem.6b00140.
42. Rut, W.; Zmudzinski, M.; Snipas, S.J.; Bekes, M.; Huang, T.T.; Drag, M. Engineered Unnatural Ubiquitin for Optimal Detection of Deubiquitinating Enzymes. *Chem. Sci.* **2020**, *11*, 6058–6069. doi: 10.1039/DOSC01347A.
43. Leestemaker, Y.; de Jong, A.; Ovaa, H. Profiling the Activity of Deubiquitinating Enzymes Using Chemically Synthesized Ubiquitin-Based Probes. *Methods Mol. Biol.* **2017**, *1491*, 113–130. doi: 10.1007/978-1-4939-6439-0_9.
44. Drag, M.; Mikolajczyk, J.; Bekes, M.; Reyes-Turco, F.E.; Ellman, J.A.; Wilkinson, K.D.; Salvesen, G.S. Positional-Scanning Fluorogenic Substrate Libraries Reveal Unexpected Specificity Determinants of DUBs (Deubiquitinating Enzymes). *Biochem. J.* **2008**, *415*, 367–375. doi: 10.1042/BJ20080779.
45. Hodgins, R.R.; Ellison, K.S.; Ellison, M.J. Expression of a Ubiquitin Derivative that Conjugates to Protein Irreversibly Produces Phenotypes Consistent with a Ubiquitin Deficiency. *J. Biol. Chem.* **1992**, *267*, 8807–8812. doi: 10.1016/S0021-9258(19)50351-9.
46. Pickart, C.M.; Kasperek, E.M.; Beal, R.; Kim, A. Substrate Properties of Site-Specific Mutant Ubiquitin Protein (G76A) Reveal Unexpected Mechanistic Features of Ubiquitin-Activating Enzyme (E1). *J. Biol. Chem.* **1994**, *269*, 7115–7123. doi: 10.1016/S0021-9258(17)37255-1.
47. Wilkinson, K.D.; Tashayev, V.L.; O’Connor, L.B.; Larsen, C.N.; Kasperek, E.; Pickart, C.M. Metabolism of the Polyubiquitin Degradation Signal: Structure, Mechanism, and Role of Isopeptidase T. *Biochemistry* **1995**, *34*, 14535–14546. doi: 10.1021/bi00044a032.
48. Kathman, S.G.; Span, I.; Smith, A.T.; Xu, Z.; Zhan, J.; Rosenzweig, A.C.; Statsyuk, A.V. A Small Molecule That Switches a Ubiquitin Ligase From a Processive to a Distributive Enzymatic Mechanism. *J. Am. Chem. Soc.* **2015**, *137*, 12442–12445. doi: 10.1021/jacs.5b06839.
49. Li, Y.-J.; Du, L.; Wang, J.; Vega, R.; Lee, T.D.; Miao, Y.; Aldana-Masangkay, G.; Samuels, E.R.; Li, B.; Ouyang, S.X.; Colayco, S.A.; Bobkova, E.V.; Divljanova, D.B.; Sergienko, E.; Chung, T.D.Y.; Fakih, M.; Chen, Y. Allosteric Inhibition of Ubiquitin-like Modifications by a Class of Inhibitor of SUMO-Activating Enzyme. *Cell. Chem. Biol.* **2019**, *26*, 278–288.e6. doi: 10.1016/j.chembiol.2018.10.026.
50. Tailor, A.; Waddington, J.C.; Meng, X.; Park, B.K. Mass Spectrometric and Functional Aspects of Drug–Protein Conjugation. *Chem. Res. Toxicol.* **2016**, *29*, 1912–1935. doi: 10.1021/acs.chemrestox.6b00147.
51. Backus, K.M. Applications of Reactive Cysteine Profiling. *Curr. Top. Microbiol. Immunol.* **2019**, *420*, 375–417. doi: 10.1007/82_2018_120.

52. Tresse, C.; Guissart, C.; Schweizer, S.; Bouhoute, Y.; Chany, A.-C.; Goddard, M.-L.; Blanchard, N.; Evano, G. Practical Methods for the Synthesis of Trifluoromethylated Alkynes: Oxidative Trifluoromethylation of Copper Acetylides and Alkynes. *Adv. Synth. Catal.* **2014**, *356*, 2051-2060. doi: 10.1002/adsc.201400057.

53. Copeland, R.A. Chapter 9. Irreversible Enzyme Inactivators. In *Evaluation of Enzyme Inhibitors in Drug Discovery: A Guide for Medicinal Chemists and Pharmacologists*, Second ed.; John Wiley & Sons, Inc.: Hoboken, New Jersey, 2013; pp 345-382. doi: 10.1002/9781118540398.

54. Tuley, A.; Fast, W. The Taxonomy of Covalent Inhibitors. *Biochemistry* **2018**, *57*, 3326-3337. doi: 10.1021/acs.biochem.8b00315.

55. Singh, J.; Petter, R.C.; Baillie, T.A.; Whitty, A. The Resurgence of Covalent Drugs. *Nat. Rev. Drug Discov.* **2011**, *10*, 307-317. doi: 10.1038/nrd3410.

56. Bovet, C.; Zenobi, R. Determination of Active Enzyme Concentration using Activity-Based Probes and Direct Mass Spectrometric Readout. *Anal. Biochem.* **2008**, *373*, 380-382. doi: 10.1016/j.ab.2007.11.003.

57. Brocklehurst, K.; Resmini, M.; Topham, C.M. Kinetic and Titration Methods for Determination of Active Site Contents of Enzyme and Catalytic Antibody Preparations. *Methods* **2001**, *24*, 153-167. doi: 10.1006/meth.2001.1176.

58. Johansson, H.; Isabella Tsai, Y.-C.; Fantom, K.; Chung, C.-W.; Küpper, S.; Martino, L.; Thomas, D.A.; Eberl, H.C.; Muelbaier, M.; House, D.; Rittner, K. Fragment-Based Covalent Ligand Screening Enables Rapid Discovery of Inhibitors for the RBR E3 Ubiquitin Ligase HOIP. *J. Am. Chem. Soc.* **2019**, *141*, 2703-2712. doi: 10.1021/jacs.8b13193.

59. Wan, X.; Yang, T.; Cuesta, A.; Pang, X.; Baliaus, T.E.; Irwin, J.J.; Shoichet, B.K.; Taunton, J. Discovery of Lysine-Targeted eIF4E Inhibitors through Covalent Docking. *J. Am. Chem. Soc.* **2020**, *142*, 4960-4964. doi: 10.1021/jacs.9b10377.

60. Klüter, S.; Simard, J.R.; Rode, H.B.; Grüter, C.; Pawar, V.; Raaijmakers, H.C.A.; Barf, T.A.; Rabiller, M.; van Otterlo, W.A.L.; Rauh, D. Characterization of Irreversible Kinase Inhibitors by Directly Detecting Covalent Bond Formation: A Tool for Dissecting Kinase Drug Resistance. *ChemBioChem* **2010**, *11*, 2557-2566. doi: 10.1002/cbic.201000352.

61. Hansen, R.; Firdaus, S.J.; Li, S.; Janes, M.R.; Zhang, J.; Liu, Y.; Zarrinkar, P.P. An Internally Controlled Quantitative Target Occupancy Assay for Covalent Inhibitors. *Sci. Rep.* **2018**, *8*, 14312. doi: 10.1038/s41598-018-32683-w.

62. Watterson, S.H.; Liu, Q.; Beaudoin Bertrand, M.; Batt, D.G.; Li, L.; Pattoli, M.A.; Skala, S.; Cheng, L.; Obermeier, M.T.; Moore, R., et al. Discovery of Branerutinib (BMS-986195): A Strategy for Identifying a Highly Potent and Selective Covalent Inhibitor Providing Rapid In Vivo Inactivation of Bruton's Tyrosine Kinase (BTK). *J. Med. Chem.* **2019**, *62*, 3228-3250. doi: 10.1021/acs.jmedchem.9b00167.

63. Miyahisa, I.; Sameshima, T.; Hixon, M.S. Rapid Determination of the Specificity Constant of Irreversible Inhibitors (k_{inact}/K_i) by Means of an Endpoint Competition Assay. *Angew. Chem. Int. Ed.* **2015**, *54*, 14099-14102. doi: 10.1002/anie.201505800.

64. Sameshima, T.; Tanaka, Y.; Miyahisa, I. Universal and Quantitative Method To Evaluate Inhibitor Potency for Cysteine Proteins Using a Nonspecific Activity-Based Protein Profiling Probe. *Biochemistry* **2017**, *56*, 2921-2927. doi: 10.1021/acs.biochem.7b00190.

65. Kim, R.Q.; Geurink, P.; Mulder, M.P.C.; Fish, A.; Ekkebus, R.; El Oualid, F.; van Dijk, W.J.; van Dalen, D.; Ovaa, H.; van Ingen, H.; Sixma, T.K. Kinetic Analysis of Multistep USP7 Mechanism Shows Critical Role for Target Protein in Activity. *Nat. Commun.* **2019**, *10*, 231. doi: 10.1038/s41467-018-08231-5.

66. Hocek, M.; Fojta, M. Cross-Coupling Reactions of Nucleoside Triphosphates Followed by Polymerase Incorporation. Construction and Applications of Base-functionalized Nucleic Acids. *Org. Biomol. Chem.* **2008**, *6*, 2233-2241. doi: 10.1039/B803664K.

67. Wood, E.R.; Shewchuk, L.M.; Ellis, B.; Brignola, P.; Brashears, R.L.; Caferro, T.R.; Dickerson, S.H.; Dickson, H.D.; Donaldson, K.H.; Gaul, M., et al. 6-Ethynylthieno[3,2-d]- and 6-Ethynylthieno[2,3-d]pyrimidin-4-anilines as Tunable Covalent Modifiers of ErBB Kinases. *Proc. Natl. Acad. Sci.* **2008**, *105*, 2773. doi: 10.1073/pnas.07078281105.

68. McAulay, K.; Hoyt, E.A.; Thomas, M.; Schimpl, M.; Bodnarchuk, M.S.; Lewis, H.J.; Barratt, D.; Bhavas, D.; Robinson, D.M.; Deery, M.J.; Ogg, D.J.; Bernardes, G.J.L.; Ward, R.A.; Waring, M.J.; Kettle, J.G. Alkynyl Benzoxazines and Dihydroquinazolines as Cysteine Targeting Covalent Warheads and Their Application in Identification of Selective Irreversible Kinase Inhibitors. *J. Am. Chem. Soc.* **2020**, *142*, 10358-10372. doi: 10.1021/jacs.9b13391.

69. Barf, T.; Covey, T.; Izumi, R.; van de Kar, B.; Gulrajani, M.; van Lith, B.; van Hoek, M.; de Zwart, E.; Mittag, D.; Demont, D.; Verkaik, S.; Krantz, F.; Pearson, P.G.; Ulrich, R.; Kaptein, A. Acalabrutinib (ACP-196): A Covalent Bruton Tyrosine Kinase Inhibitor with a Differentiated Selectivity and In Vivo Potency Profile. *J. Pharmacol. Exp. Ther.* **2017**, *363*, 240. doi: 10.1124/jpet.117.242909.

70. Wang, T.; Yin, L.; Cooper, E.M.; Lai, M.-Y.; Dickey, S.; Pickart, C.M.; Fushman, D.; Wilkinson, K.D.; Cohen, R.E.; Wolberger, C. Evidence for Bidentate Substrate Binding as the Basis for the K48 Linkage Specificity of Utubain 1. *J. Mol. Biol.* **2009**, *386*, 1011-1023. doi: 10.1016/j.jmb.2008.12.085.

71. Nanao, M.H.; Tcherniuk, S.O.; Chroboczek, J.; Dideberg, O.; Dessen, A.; Balakirev, M.Y. Crystal Structure of Human Utubain 2. *EMBO Rep.* **2004**, *5*, 783-788. doi: 10.1038/sj.emboj.7400201.

72. Mevissen, T.E.T.; Bernenthal, M.K.; Geurink, P.P.; Elliott, P.R.; Akutsu, M.; Arnaudo, N.; Ekkebus, R.; Kulathu, Y.; Wauer, T.; El Oualid, F.; Freund, S.M.V.; Ovaa, H.; Komander, D. OTU Deubiquitinases Reveal Mechanisms of Linkage Specificity and Enable Ubiquitin Chain Restriction Analysis. *Cell* **2013**, *154*, 169-184. doi: 10.1016/j.cell.2013.05.046.

73. Larsen, C.N.; Price, J.S.; Wilkinson, K.D. Substrate Binding and Catalysis by Ubiquitin C-Terminal Hydrolases: Identification of Two Active Site Residues. *Biochemistry* **1996**, *35*, 6735-6744. doi: 10.1021/bi960099f.

74. Hermanns, T.; Pichlo, C.; Woiwode, I.; Klopffleisch, K.; Witting, K.F.; Ovaa, H.; Baumann, U.; Hofmann, K. A Family of Unconventional Deubiquitinases with Modular Chain Specificity Determinants. *Nat. Commun.* **2018**, *9*, 799. doi: 10.1038/s41467-018-03148-5.

75. Garcia-Nafría, J.; Watson, J.F.; Greger, I.H. IVA Cloning: A Single-Tube Universal Cloning System Exploiting Bacterial In Vivo Assembly. *Sci. Rep.* **2016**, *6*, 27459. doi: 10.1038/srep27459.

76. Liu, H.; Naismith, J.H. An Efficient One-Step Site-Directed Deletion, Insertion, Single and Multiple-Site Plasmid Mutagenesis Protocol. *BMC Biotechnol.* **2008**, *8*, 91. doi: 10.1186/1472-6750-8-91.

77. Luna-Vargas, M.P.A.; Christodoulou, E.; Alfieri, A.; van Dijk, W.J.; Stadnik, M.; Hibbert, R.G.; Sahtoe, D.D.; Clerici, M.; Marco, V.D.; Littler, D.; Celic, P.H.N.; Sixma, T.K.; Perrakis, A. Enabling High-Throughput Ligation-independent Cloning and Protein Expression for the Family of Ubiquitin Specific Proteases. *J. Struct. Biol.* **2011**, *175*, 113-119. doi: 10.1016/j.jsb.2011.03.017.

78. Ward, S.J.; Gratton, H.E.; Indrayudha, P.; Michavila, C.; Mukhopadhyay, R.; Maurer, S.K.; Caulton, S.G.; Emsley, J.; Drevney, I. The Structure of the Deubiquitinase USP15 Reveals a Misaligned Catalytic Triad and an Open Ubiquitin-Binding Channel. *J. Biol. Chem.* **2018**, *293*, 17362-17374. doi: 10.1074/jbc.ra118.003857.

79. Gjonaj, L.; Sapmaz, A.; Flierman, D.; Janssen, G.M.C.; van Veelen, P.A.; Ovaa, H. Development of a DUB-Selective Fluorogenic Substrate. *Chem. Sci.* **2019**, *10*, 10290-10296. doi: 10.1039/C9SC02226K.

80. Abramoff, M.; Magalhães, P.; Ram, S.J. Image Processing with ImageJ. *Biophotonics Intern.* **2003**, *11*, 36-42.

81. Rasband, W.S. ImageJ, U. S. National Institutes of Health, Bethesda, Maryland, USA: 1997-2018. <https://imagej.nih.gov/ij/>.

82. Schneider, C.A.; Rasband, W.S.; Eliceiri, K.W. NIH Image to ImageJ: 25 Years of Image Analysis. *Nat. Meth.* **2012**, *9*, 671-675. doi: 10.1038/nmeth.2089.

83. El Oualid, F.; Merkx, R.; Ekkebus, R.; Hameed, D.S.; Smit, J.J.; de Jong, A.; Hilkmann, H.; Sixma, T.K.; Ovaa, H. Chemical Synthesis of Ubiquitin, Ubiquitin-Based Probes, and Diubiquitin. *Angew. Chem. Int. Ed.* **2010**, *49*, 10149-10153. doi: 10.1002/anie.201005995.

84. Moroder, L. Isosteric Replacement of Sulfur with Other Chalcogens in Peptides and Proteins. *J. Pept. Sci.* **2005**, *11*, 187-214. doi: 10.1002/psc.654.

85. Xin, B.-T.; van Tol, B.D.M.; Ovaa, H.; Geurink, P.P. Native Chemical Ligation at Methionine Bioisostere Norleucine Allows for N-Terminal Chemical Protein Ligation. *Org. Biomol. Chem.* **2018**, *16*, 6306-6315. doi: 10.1039/C8OB01627E.

86. Geurink, P.P.; van Tol, B.D.M.; van Dalen, D.; Brundel, P.J.G.; Mevissen, T.E.T.; Pruneda, J.N.; Elliott, P.R.; van Tilburg, G.B.A.; Komander, D.; Ovaa, H. Development of Diubiquitin-Based FRET Probes To Quantify Ubiquitin Linkage Specificity of Deubiquitinating Enzymes. *ChemBioChem* **2016**, *17*, 816-820. doi: 10.1002/cbic.201600017.

87. Nishizawa, R.; Nishiyama, T.; Hisaichi, K.; Hirai, K.; Habashita, H.; Takaoka, Y.; Tada, H.; Sagawa, K.; Shibayama, S.; Maeda, K.; Mitsuya, H.; Nakai, H.; Fukushima, D.; Toda, M. Discovery of Orally Available Spirodiketopiperazine-Based CCR5 Antagonists. *Bioorg. Med. Chem.* **2010**, *18*, 5208-5223. doi: 10.1016/j.bmc.2010.05.057.

88. Rosca, D.-A.; Radkowski, K.; Wolf, L.M.; Wagh, M.; Goddard, R.; Thiel, W.; Fürstner, A. Ruthenium-Catalyzed Alkyne *trans*-Hydrometalation: Mechanistic Insights and Preparative Implications. *J. Am. Chem. Soc.* **2017**, *139*, 2443-2455. doi: 10.1021/jacs.6b12517.

89. Klepacz, A.; Zwierzak, A. New Protocol for Converting Alcohols into Amines. *Synth. Commun.* **2001**, *31*, 1683-1689. doi: 10.1081/SCC-100103987.

90. Rennie, M.L.; Arkinson, C.; Chaugule, V.K.; Toth, R.; Walden, H. Structural Basis of FANCD2 Deubiquitination by USP1-UAF1. *Nat. Struct. Mol. Biol.* **2021**, *28*, 356-364. doi: 10.1038/s41594-021-00576-8.

91. Dharadh, S.; Clerici, M.; van Dijk, W.J.; Fish, A.; Sixma, T.K. A Conserved Two-step Binding for the UAF1 Regulator to the USP12 Deubiquitinating Enzyme. *J. Struct. Biol.* **2016**, *196*, 437-447. doi: 10.1016/j.jsb.2016.09.011.

92. Gersch, M.; Wagstaff, J.L.; Toms, A.V.; Graves, B.; Freund, S.M.V.; Komander, D. Distinct USP25 and USP28 Oligomerization States Regulate Deubiquitinating Activity. *Mol. Cell* **2019**, *74*, 436-451.e7. doi: 10.1016/j.molcel.2019.02.030.

93. Sauer, F.; Klemm, T.; Kollampally, R.B.; Tessmer, I.; Nair, R.K.; Popov, N.; Kisker, C. Differential Oligomerization of the Deubiquitinases USP25 and USP28 Regulates Their Activities. *Mol. Cell* **2019**, *74*, 421-435.e10. doi: 10.1016/j.molcel.2019.02.029.

94. Gersch, M.; Gladkova, C.; Schubert, A.F.; Michel, M.A.; Maslen, S.; Komander, D. Mechanism and Regulation of the Lys6-Selective Deubiquitinase USP30. *Nat. Struct. Mol. Biol.* **2017**, *24*, 920-930. doi: 10.1038/nsmb.3475.

95. Xu, G.; Su, H.; Lu, L.; Liu, X.; Zhao, L.; Tang, B.; Ming, Z. Structural Insights into the Catalytic Mechanism and Ubiquitin Recognition of USP34. *J. Mol. Biol.* **2022**, *434*, 167634. doi: 10.1016/j.jmb.2022.167634.

96. O'Dea, R.; Kazi, N.; Hoffmann-Benito, A.; Zhao, Z.; Recknagel, S.; Wendrich, K.; Janning, P.; Gersch, M. Molecular Basis for Ubiquitin/Fub Cross-Reactivity in USP16 and USP36. *Nat. Chem. Biol.* **2023**. doi: 10.1038/s41589-023-01388-1.

97. Sahtoo, D.D.; van Dijk, W.J.; El Oualid, F.; Ekkebus, R.; Ovaa, H.; Sixma, T.K. Mechanism of UCH-L5 Activation and Inhibition by DEUBAD Domains in RPN13 and INO80G. *Mol. Cell* **2015**, *57*, 887-900. doi: 10.1016/j.molcel.2014.12.039.

98. Mevissen, T.E.T.; Kulathu, Y.; Mulder, M.P.C.; Geurink, P.P.; Maslen, S.L.; Gersch, M.; Elliott, P.R.; Burke, J.E.; van Tol, B.D.M.; Akutsu, M.; El Oualid, F.; Kawasaki, M.; Freund, S.M.V.; Ovaa, H.; Komander, D. Molecular Basis of Lys11-Polyubiquitin Specificity in the Deubiquitinase Cezanne. *Nature* **2016**, *538*, 402-405. doi: 10.1038/nature19836.

99. Kwasna, D.; Rehman, S.A.A.; Natarajan, J.; Matthews, S.; Madden, R.; De Cesare, V.; Weidlich, S.; Virdee, S.; Ahel, I.; Gibbs-Seymour, I.; Kulathu, Y. Discovery and Characterization of ZUFSP/ZUP1, a Distinct Deubiquitinase Class Important for Genome Stability. *Mol. Cell* **2018**, *70*, 150-164.e6. doi: 10.1016/j.molcel.2018.02.023.

100. Li, Y.; De Bolos, A.; Amador, V.; Reverter, D. Structural Basis for the SUMO2 Isoform Specificity of SENP7. *J. Mol. Biol.* **2022**, *434*, 167875. doi: 10.1016/j.jmb.2022.167875.

101. Nair, R.M.; Seenivasan, A.; Liu, B.; Chen, D.; Lowe, E.D.; Lorenz, S. Reconstitution and Structural Analysis of a HECT Ligase-Ubiquitin Complex via an Activity-Based Probe. *ACS Chem. Biol.* **2021**, *16*, 1615-1621. doi: 10.1021/acschembio.1c00433.

102. Hermanns, T.; Pichlo, C.; Baumann, U.; Hofmann, K. A Structural Basis for the Diverse Linkage Specificities Within the ZUFSP Deubiquitinase Family. *Nat. Commun.* **2022**, *13*, 401. doi: 10.1038/s41467-022-28049-6.

103. Dzimianski, J.V.; Mace, S.L.; Williams, I.L.; Freitas, B.T.; Pegan, S.D. Flipping the Substrate Preference of Hazara Virus Ovarian Tumour Domain Protease Through Structure-Based Mutagenesis. *Acta Crystallogr., Sect. D* **2020**, *76*, 1114-1123. doi: 10.1107/S2059798320012875.

104. Deaton, M.K.; Dzimianski, J.V.; Daczkowski, C.M.; Whitney, G.K.; Mank, N.J.; Parham, M.M.; Bergeron, E.; Pegan, S.D. Biochemical and Structural Insights into the Preference of Nairoviral DelSGylases for Interferon-Stimulated Gene Product 15 Originating from Certain Species. *J. Virol.* **2016**, *90*, 8314. doi: 10.1128/JVI.00975-16.

105. Dzimianski, J.V.; Scholte, F.E.M.; Williams, I.L.; Langley, C.; Freitas, B.T.; Spengler, J.R.; Bergeron, É.; Pegan, S.D. Determining the Molecular Drivers of Species-Specific Interferon-Stimulated Gene Product 15 Interactions with Nairovirus Ovarian Tumor Domain Proteases. *PLoS ONE* **2019**, *14*, e0226415. doi: 10.1371/journal.pone.0226415.

106. Békés, M.; van der Heden van Noort, G.J.; Ekkebus, R.; Ovaa, H.; Huang, T.T.; Lima, C.D. Recognition of Lys48-Linked Di-Ubiquitin and Deubiquitinating Activities of the SARS Coronavirus Papain-like Protease. *Mol. Cell* **2016**, *62*, 572-585. doi: 10.1016/j.molcel.2016.04.016.

107. Daczkowski, C.M.; Dzimianski, J.V.; Clasman, J.R.; Goodwin, O.; Mesecar, A.D.; Pegan, S.D. Structural Insights into the Interaction of Coronavirus Papain-Like Proteases and Interferon-Stimulated Gene Product 15 from Different Species. *J. Mol. Biol.* **2017**, *429*, 1661-1683. doi: 10.1016/j.jmb.2017.04.011.

108. Klemm, T.; Ebert, G.; Calleja, D.J.; Allison, C.C.; Richardson, L.W.; Bernardini, J.P.; Lu, B.G.C.; Kuchel, N.W.; Grohmann, C.; Shibata, Y., et al. Mechanism and Inhibition of the Papain-like Protease, PLpro, of SARS-CoV-2. *EMBO J.* **2020**, *39*, e106275. doi: 10.15252/embj.2020106275.

109. Daczkowski, C.M.; Goodwin, O.Y.; Dzimianski, J.V.; Farhat, J.J.; Pegan, S.D. Structurally Guided Removal of DelSGylase Biochemical Activity from Papain-Like Protease Originating from Middle East Respiratory Syndrome Coronavirus. *J. Virol.* **2017**, *91*, e01067-17. doi: 10.1128/JVI.01067-17.

110. Clasman, J.R.; Everett, R.K.; Srinivasan, K.; Mesecar, A.D. Decoupling DelSGylating and Deubiquitinating Activities of the MERS Virus Papain-Like Protease. *Antiviral Res.* **2020**, *174*, 104661. doi: 10.1016/j.antiviral.2019.104661.

111. Durie, I.A.; Dzimianski, J.V.; Daczkowski, C.M.; McGuire, J.; Faaberg, K.; Pegan, S.D. Structural Insights into the Interaction of Papain-Like Protease 2 from the Alphacoronavirus Porcine Epidemic Diarrhea Virus and Ubiquitin. *Acta Crystallogr., Sect. D* **2021**, *77*, 943-953. doi: 10.1107/S205979832100509X.

112. Swatek, K.N.; Aumayr, M.; Pruneda, J.N.; Visser, L.J.; Berryman, S.; Kueck, A.F.; Geurink, P.P.; Ovaa, H.; van Kuppeveld, F.J.M.; Tuthill, T.J.; Skern, T.; Komander, D. Irreversible Inactivation of ISG15 by a Viral Leader Protease Enables Alternative Infection Detection Strategies. *Proc. Natl. Acad. Sci.* **2018**, *115*, 2371. doi: 10.1073/pnas.1710617115.

113. Ramirez, Y.A.; Adler, T.B.; Altmann, E.; Klemm, T.; Tiesmeyer, C.; Sauer, F.; Kathman, S.G.; Statsyuk, A.V.; Sottriffer, C.; Kisker, C. Structural Basis of Substrate Recognition and Covalent Inhibition of Cdu1 from *Chlamydia trachomatis*. *ChemMedChem* **2018**, *13*, 2014-2023. doi: 10.1002/cmdc.201800364.
114. Pruneda, J.N.; Bastidas, R.J.; Bertsoulaki, E.; Swatek, K.N.; Santhanam, B.; Clague, M.J.; Valdivia, R.H.; Urbé, S.; Komander, D. A *Chlamydia* Effector Combining Deubiquitination and Acetylation Activities Induces Golgi Fragmentation. *Nat. Microbiol.* **2018**, *3*, 1377-1384. doi: 10.1038/s41564-018-0271-y.
115. Liu, S.; Luo, J.; Zhen, X.; Qiu, J.; Ouyang, S.; Luo, Z.-Q. Interplay Between Bacterial Deubiquitinase and Ubiquitin E3 Ligase Regulates Ubiquitin Dynamics on Legionella Phagosomes. *eLife* **2020**, *9*, e58114. doi: 10.7554/eLife.58114.
116. Luo, J.; Ruan, X.; Huang, Z.; Li, Z.; Ye, L.; Wu, Y.; Zhen, X.; Ouyang, S. Structural Basis for the Dual Catalytic Activity of the *Legionella pneumophila* Ovarian Tumor (OTU) Domain Deubiquitinase LotA. *J. Biol. Chem.* **2022**, *298*, 102414. doi: 10.1016/j.jbc.2022.102414.
117. Erven, I.; Abraham, E.; Hermanns, T.; Baumann, U.; Hofmann, K. A Widely Distributed Family of Eukaryotic and Bacterial Deubiquitinases Related to Herpesviral Large Tegument Proteins. *Nat. Commun.* **2022**, *13*, 7643. doi: 10.1038/s41467-022-35244-y.
118. Pruneda, J.N.; Durkin, C.H.; Geurink, P.P.; Ovaa, H.; Santhanam, B.; Holden, D.W.; Komander, D. The Molecular Basis for Ubiquitin and Ubiquitin-like Specificities in Bacterial Effector Proteases. *Mol. Cell* **2016**, *63*, 261-276. doi: 10.1016/j.molcel.2016.06.015.
119. Franklin, T.G.; Brzovic, P.S.; Pruneda, J.N. Bacterial Mimicry of Eukaryotic HECT Ubiquitin Ligation. *bioRxiv* **2023**. doi: 10.1101/2023.06.05.543783.
120. Bogyo, M.; Shin, S.; McMaster, J.S.; Ploegh, H.L. Substrate Binding and Sequence Preference of the Proteasome Revealed by Active-Site-Directed Affinity Probes. *Chem. Biol.* **1998**, *5*, 307-320. doi: 10.1016/S1074-5521(98)90169-7.
121. Thompson, S.K.; Heathcock, C.H. Effect of Cation, Temperature, and Solvent on the Stereoselectivity of the Horner-Emmons Reaction of Trimethyl Phosphonoacetate with Aldehydes. *J. Org. Chem.* **1990**, *55*, 3386-3388. doi: 10.1021/jo00297a076.
122. Mons, E.; Roet, S.; Kim, R.Q.; Mulder, M.P.C. A Comprehensive Guide for Assessing Covalent Inhibition in Enzymatic Assays Illustrated with Kinetic Simulations. *Curr. Protoc.* **2022**, *2*, e419. doi: 10.1002/cp21.419.
123. Copeland, R.A. Chapter 2. Chemical Bonds and Reactions in Biochemistry. In *ENZYMES: A Practical Introduction to Structure, Mechanism, and Data Analysis*, Second ed.; John Wiley & Sons, Inc.: New York, NY, 2000; pp 11-41. doi: 10.1002/0471220639.ch2.
124. Copeland, R.A. Chapter 4. Protein-Ligand Binding Equilibria. In *ENZYMES: A Practical Introduction to Structure, Mechanism, and Data Analysis*, Second ed.; John Wiley & Sons, Inc.: New York, NY, 2000; pp 76-108. doi: 10.1002/0471220639.ch4.
125. Hameed, D.S.; Sapmaz, A.; Burggraaff, L.; Amore, A.; Slingerland, C.J.; van Westen, G.J.P.; Ovaa, H. Development of Ubiquitin-Based Probe for Metalloprotease Deubiquitinases. *Angew. Chem. Int. Ed.* **2019**, *58*, 14477-14482. doi: 10.1002/anie.201906790.
126. Morrow, M.E.; Morgan, M.T.; Clerici, M.; Growkova, K.; Yan, M.; Komander, D.; Sikma, T.K.; Simicic, M.; Wolberger, C. Active Site Alanine Mutations Convert Deubiquitinases into High-Affinity Ubiquitin-Binding Proteins. *EMBO Rep.* **2018**, *19*, e45680. doi: 10.15252/embr.201745680.
127. Moerke, N.J. Fluorescence Polarization (FP) Assays for Monitoring Peptide-Protein or Nucleic Acid-Protein Binding. *Curr. Protoc. Chem. Biol.* **2009**, *1*, 1-15. doi: 10.1002/9780470559277.ch090102.
128. Lonsdale, R.; Burgess, J.; Colclough, N.; Davies, N.L.; Lenz, E.M.; Orton, A.L.; Ward, R.A. Expanding the Armory: Predicting and Tuning Covalent Warhead Reactivity. *J. Chem. Inf. Model.* **2017**, *57*, 3124-3137. doi: 10.1021/acs.jcim.7b00553.
129. Crowe, S.O.; Rana, A.S.J.B.; Deol, K.K.; Ge, Y.; Strieter, E.R. Ubiquitin Chain Enrichment Middle-Down Mass Spectrometry Enables Characterization of Branched Ubiquitin Chains in *Cellulo. Anal. Chem.* **2017**, *89*, 4428-4434. doi: 10.1021/acs.analchem.6b03675.
130. Xu, P.; Peng, J. Characterization of Polyubiquitin Chain Structure by Middle-Down Mass Spectrometry. *Anal. Chem.* **2008**, *80*, 3438-3444. doi: 10.1021/ac800016w.

7. Supporting Information

7.1. Crystal Structures

Table S1 | Crystal structures of Ub(I)-Prg ABPs covalently bound to a catalytic cysteine thiol.

Species	Protein	ABP	PDB	Reference
Human	USP1 + UAF1 (truncated)	Ub-Prg	7AY2	[Rennie, 2021] ⁹⁰
	USP12 + UAF1	Ub-Prg	5L8W	[Dharadhar, 2016] ⁹¹
	USP28	Ub-Prg	6HEK	
	USP28 (insertion deleted)	Ub-Prg	6HEI	[Gersch, 2019] ⁹²
	USP28CD ^{E593D}	Ub-Prg	6H4H	[Sauer, 2019] ⁹³
	USP30	Ub-Prg	50HK	
		Ub-Prg	50HN	[Gersch, 2017] ⁹⁴
	USP34CD	Ub-Prg	7W3U	[Xu, 2022] ⁹⁵
	USP36	Fubi-Prg	8BS3	
		Ub-Prg	8BS9	[O'Dea, 2023] ⁹⁶
Insect	UCHL5 + INO80G	Ub-Prg	4UF6	
	UCHL5 + RPN13 DEUBAD	Ub-Prg	4UEL	[Sahtoe, 2015] ⁹⁷
	A20 OTU	Ub-Prg	5LRX	[Mevissen, 2016] ⁹⁸
	MINDY-1	Ub-Prg	5JQS	[Rehman, 2016] ²⁰
	ZUP1 (232-578)	Ub-Prg	6EI1	[Hermanns, 2018] ⁷⁴
	ZUP1	Ub-Prg	6FGE	[Kwasna, 2018] ⁹⁹
	SENP7	SUMO2-Prg	7R2E	[Li, 2022] ¹⁰⁰
	HUWE1 (HECT domain) ^a	Ub-Prg	6XZ1	[Nair, 2021] ¹⁰¹
Mouse	mUSP18	mISG15-Prg	5CHV	[Basters, 2017] ¹⁸
Virus	<i>Tribolium castaneum</i> TcZUP	Ub-Prg	7OJE	[Hermanns, 2022] ¹⁰²
	CCHFV OTU	Ub-Prg	3ZNH	[Ekkebus, 2013] ²⁷
	HAZV OTU	Ub-Prg	7JMS	[Dzimianski, 2020] ¹⁰³
	ERVV OTU	mISG15(CTD)-Prg	5JZE	[Deaton, 2016] ¹⁰⁴
	KUPEV OTU	sheepISG15(CTD)-Prg	6OAR	
	GANV OTU	sheepISG15(CTD)-Prg	6OAT	[Dzimianski, 2019] ¹⁰⁵
	SARS CoV PL ^{pro}	K48 diUb-Prg	5E6J	[Békés, 2016] ¹⁰⁶
	SARS CoV PL ^{pro}	hISG15(CTD)-Prg	5TL6	
		mISG15(CTD)-Prg	5TL7	[Daczkowski, 2017] ¹⁰⁷
	SARS CoV-2 PL ^{pro}	Ub-Prg	6XAA	
		ISG15(CTD)-Prg	6XA9	[Klemm, 2020] ¹⁰⁸
Virus	MERS CoV PL ^{pro}	hISG15(CTD)-Prg	5W8U	
		hISG15(CTD)-Prg	5W8T	[Daczkowski, 2017] ¹⁰⁹
	MERS CoV PL ^{pro}	ISG15-Prg	6BI8	[Clasman, 2020] ¹¹⁰
	PEDV PL ^{pro} 2	Ub-Prg	7MC9	[Durie, 2021] ¹¹¹
	FMDV LB ^{pro}	ISG15-Prg	6FFA	[Swatek, 2018] ¹¹²

Table S1 continues on the next page

Table S1 | Crystal structures of Ub(I)-Prg ABPs covalently bound to a catalytic cysteine thiol. (continued)

Species	Protein	ABP	PDB	Reference
Bacteria	<i>C. trachomatis</i> ChlaDUB1	Ub-Prg	6FDK	[Ramirez, 2018] ¹¹³
	<i>C. trachomatis</i> ChlaDUB1	Ub-Prg	6GZS	[Pruneda, 2018] ¹¹⁴
	<i>C. trachomatis</i> ChlaDUB2 (93-339)	Ub-Prg	6OAM	[Hausman, 2020] ²³
	<i>L. pneumophila</i> Lem27 (1-417)	Ub-Prg	7BU0	[Liu, 2020] ¹¹⁵
	<i>L. pneumophila</i> Lotta (1-542)	Ub-Prg	7W54	[Luo, 2022] ¹¹⁶
	<i>W. chondrophila</i> Wc-VTD1	Ub-Prg	8ADB	[Erven, 2022] ¹¹⁷
	<i>X. campestris</i> XopD	Ub-Prg tSUMO-Prg	5JP3 5JP1	[Pruneda, 2016] ¹¹⁸
	<i>Verrucomicrobia</i> VsHECT (639-847) ^a	Ub-Prg	8ST7	[Franklin, 2023] ¹¹⁹
	<i>S. enterica</i> SopA (603-782) ^a	Ub-Prg	8ST8	[Franklin, 2023] ¹¹⁹
	<i>E. coli</i> NleL (606-782) ^a	Ub-Prg	8ST9	[Franklin, 2023] ¹¹⁹

Structures in PDB (Protein Data Bank) containing ligand AYE (prop-2-en-1-amine) updated until August 2023.

^a E3 ligase. Prg = propargylamide (warhead). Ub = ubiquitin. ISG15 = interferon-stimulated gene 15 protein. SUMO2 = small ubiquitin-like modifier isoform 2. h = human. m = mouse. t = tomato. CTD = C-terminal domain. PL^{pro} = papain-like protease. LB^{pro} = leader protease. CCHFV = Crimean Congo Hemorrhagic fever virus. HAZV = Hazara virus. ERVV = Erve virus. KUPEV = Kupe virus. GANV = Ganjam virus. SARS CoV = Severe acute respiratory syndrome coronavirus. MERS CoV = Middle East respiratory syndrome coronavirus. PEDV = porcine epidemic diarrhea virus. FMDV = Foot-and-mouth disease virus.

7.2. Chemical Synthesis

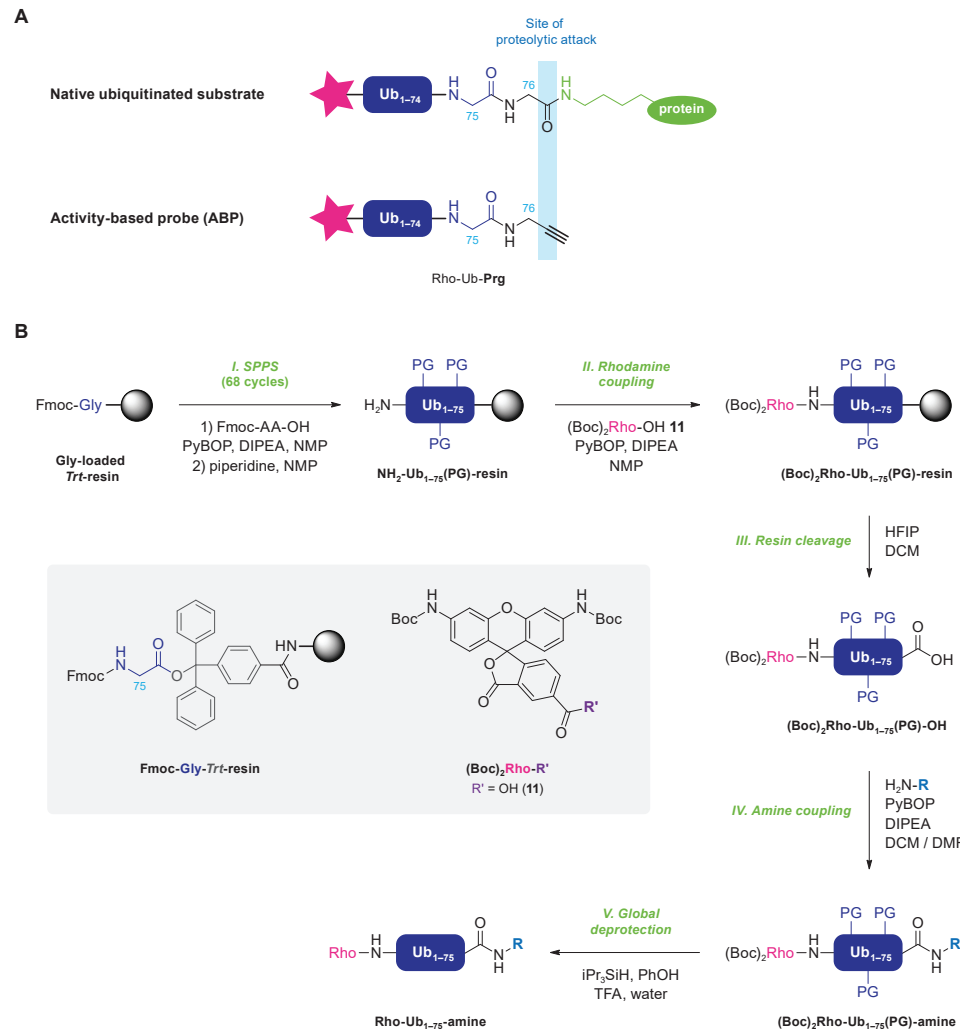
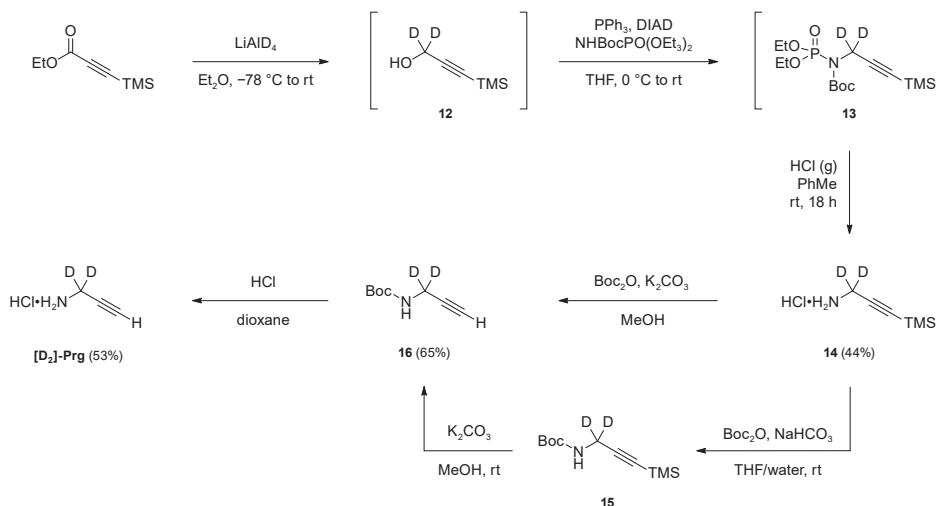


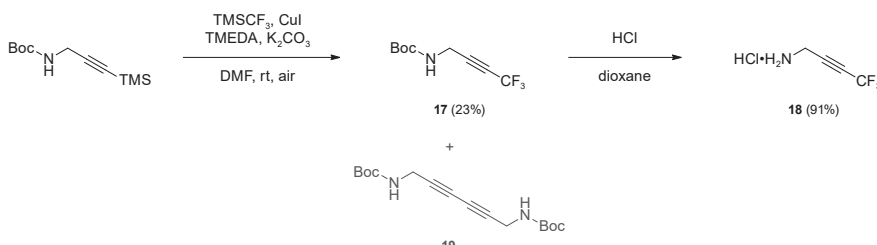
Figure S1 | Design and chemical synthesis of Rho-Ub-ABPs. **(A)** Alignment of warhead with native isopeptide bond. *Top*: nucleophilic attack of catalytic Cys on isopeptide carbonyl between C-terminal Gly76 in Ub and Lys residue in substrate or distal Ub. *Bottom*: nucleophilic attack of catalytic Cys on reactive carbon C2 in alkyne warhead. **(B)** Synthetic scheme for cysteine DUB ABPs with N-terminal 5-carboxy-Rhodamine110 as fluorescent reporter and C-terminal alkyne derivatives as warheads. **Step I.** Linear chemical synthesis of protected Ubiquitin Δ G (Ub₁₋₇₅) on Trt resin *via* solid phase synthesis (SPPS) as described before.⁸³ **Step II.** Coupling of (Boc)₂Rho-OH 11 to the N-terminus. **Step III.** Cleavage from resin while retaining side chain protecting groups. **Step IV.** Coupling of propargylamine (Prg) or derivatives (2-10) to C-terminus. **Step V.** TFA-mediated global deprotection to remove all protecting groups, followed by purification by RP-HPLC to obtain pure Rho-Ub₁₋₇₅-ABPs. PG = acid-labile protecting group. Rho = 5-carboxy-Rhodamine110. DIPEA = N,N-diisopropylethylamine. NMP = N-methyl-2-pyrrolidone. HFIP = hexafluoroisopropanol. DCM = dichloromethane. DMF = dimethylformamide. TFA = trifluoroacetic acid.

Sequence Rho-Ub₁₋₇₅-ABP:

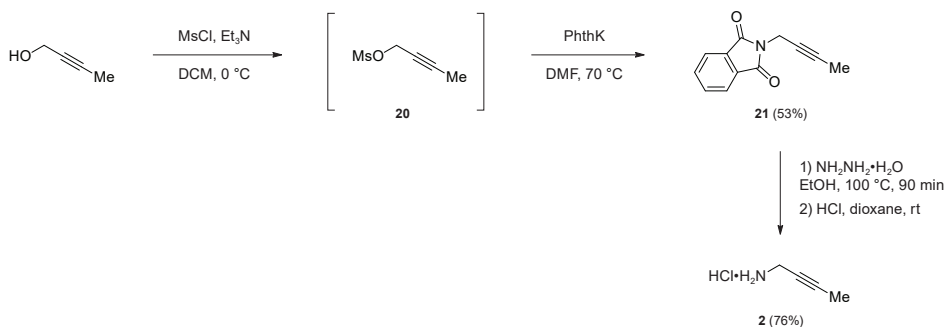
Rho-(Nle)QIFVKTLTGKITLEVEPSDTIENVKAKIQDKEGIPPDQQQLIFAGKQLEDGRTLSYNIQKESTLHLVRLRG-amine



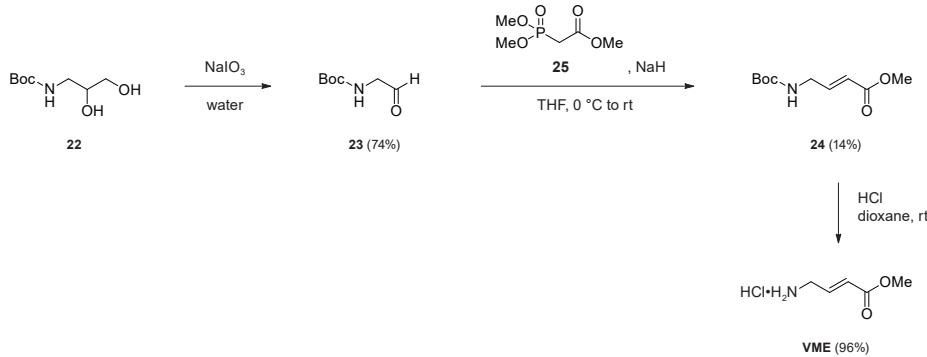
Scheme S1 | Chemical synthesis of deuterated propargylamine **[D₂]-Prg**. **[D₂]-propargyl alcohol** **12** was formed by reduction of ethyl propiolate with lithium aluminum deuteride, and subsequently converted into protected amine **13** under Mitsunobu conditions.⁸⁹ Acid-mediated deprotection generated hydrochloride **[D₂]-propargylamine** **14** bearing an acid-stable terminal TMS protecting group. Base-mediated TMS removal had to be performed after, or simultaneous with, Boc protection as the free amine **[D₂]-propargylamine** is very volatile and cannot be separated from reagents and solvents without loss of the product. The resulting Boc-**[D₂]-Prg** **16** is soluble in organic solvents and can be isolated by simple extraction. Stepwise Boc protection and TMS deprotection was performed to generate intermediates Boc-1-TMS-**[D₂]-Prg** **15** and Boc-**[D₂]-Prg** **16** as reference compounds for reaction progress detection by TLC. Finally, hydrochloride salt of deuterated propargylamine **[D₂]-Prg** could be obtained after acid-mediated Boc deprotection.



Scheme S2 | Chemical synthesis of electron-deficient propargylamine derivative **18**. Direct trifluoromethylation of Boc-propargylamine with Ruppert-Prakash reagent (TMSCF₃)⁵² gave desired trifluoromethylated acetylene **17**, which could be separated by FCC from homocoupling product **19** (an undesired side product generated via a copper-catalyzed Glaser-Hay dimerization). Hydrochloride salt of amine **18** was obtained by treatment of Boc-protected alkyne **17** with hydrochloric acid.



Scheme S3 | Chemical synthesis of methylated propargylamine derivative **2** following reported procedure.⁸⁷ The 2-butynylalcohol starting material was treated with methanesulfonyl chloride to form *O*-mesylated 2-butynyl **20**, which has a mesylate leaving group that is compatible with the subsequent Gabriel amine synthesis. Treatment with potassium phthalimide gave phthalimide **21**, and the amine was deprotected with hydrazine hydrate to form 2-butynylamine **2**. The crude reaction mixture was treated with HCl to form the corresponding hydrochloride salt that could be isolated by trituration with diethyl ether.



Scheme S4 | Chemical synthesis of vinyl methyl ester building block **VME** following reported procedure.⁴⁸ Aldehyde **23** was obtained from Boc-protected isoserinol **22** by oxidative cleavage of the vicinal diol in a Malaprade oxidation with sodium periodate. Horner-Wadsworth-Emmons (HWE) reaction of Boc-glycinal **23** with phosphonate **25** resulted in a mixture of desired (E)-olefin **24** and the undesired (Z)-olefin, which were separable by flash column chromatography. Of note is that the stereoselectivity for (E)-olefin **24** is expected to be lower than for HWE reactions forming olefins derived from other amino acids, which can be attributed to the lack of sidechain substituents on glycine:¹²⁰ bulky α -substituents on the aldehyde are known to sterically hinder formation of (Z)-olefins.¹²¹ Finally, the hydrochloride salt of methyl (E)-4-aminobut-2-enoate (**VME**) was obtained by treatment of Boc-protected amine **24** with hydrochloric acid.

7.3. Gel Electrophoresis

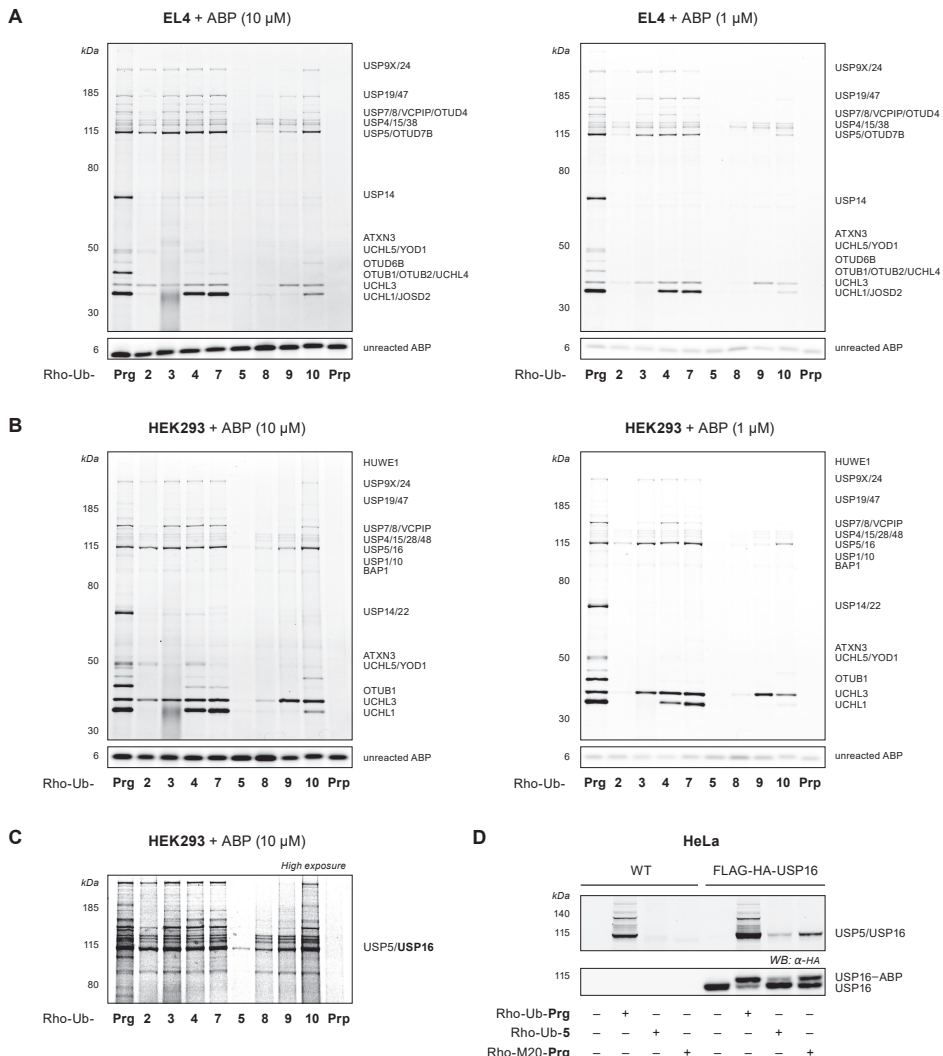


Figure S2 | Lysate incubation with 1-10 μ M Rho-Ub-ABPs. (A) In-gel fluorescence scan of EL4 lysate incubated with 10 μ M (left) or 1 μ M (right) Rho-Ub-ABP. Assignment of labeled DUBs based on proteomic analysis with biotin-Ub-Prg by Ekkebus *et al.*²⁷ Cell lysates of the mouse lymphoma cell line (EL4) are commonly used as benchmark cell line for DUB activity,¹⁹ but do not express (detectable levels of) endogenous USP16.²⁷ (B) In-gel fluorescence scan of HEK293 lysate incubated with 10 μ M (left, also shown in Figure 3B) or 1 μ M Rho-Ub-ABP (right). Assignment of labeled DUBs based on proteomic analysis by Altun *et al.*¹⁴ (C) Alternative image processing (increased exposure, contrast and adjusted levels) of the fluorescence scan shown in panel B (left) to visualize adduct formation between 10 μ M Rho-Ub-5 and endogenous USP16 in HEK293 lysate. Endogenous USP16 levels in HEK293 lysate are low (see panel D), and adduct formation with Rho-Ub-5 is relatively slow (see Figure 6C). (D) Incubation of HeLa cell lysate expressing endogenous levels of USP16 (left) or expressing HA-FLAG-USP16 (right) with Rho-Ub-Prg (1 μ M), Rho-Ub-5 (10 μ M) or USP16-selective ABP Rho-M20-Prg (0.5 μ M).⁷⁹ Adduct formation of Rho-Ub-5 with overexpressed HA-FLAG-USP16 is visualized by in-gel fluorescence (top) and western blotting with HA (bottom).

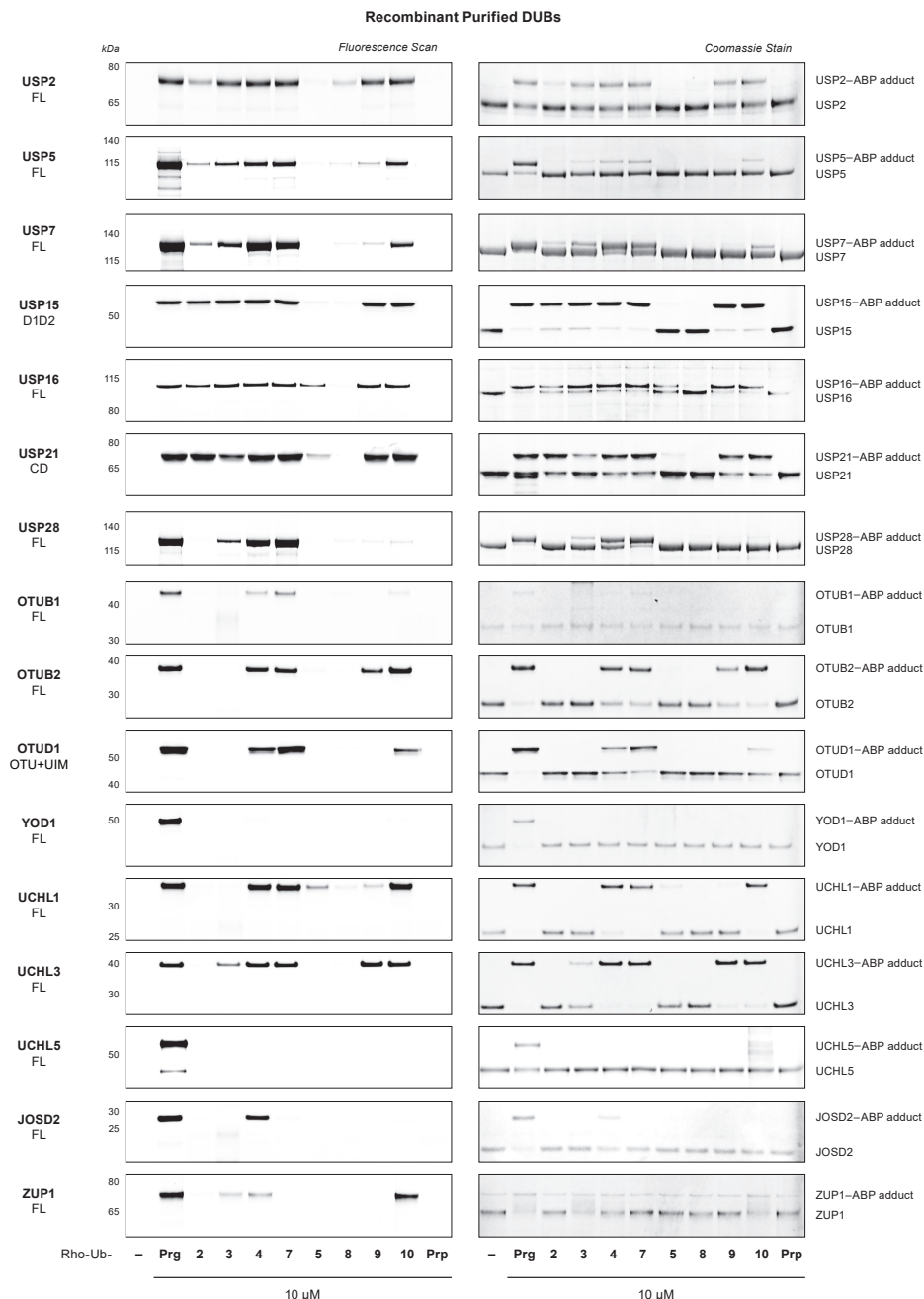


Figure S3 | Gel analysis of covalent DUB-ABP adduct formation between recombinant purified cysteine DUBs (1 μ M) and Rho-Ub-ABPs (10 μ M) related to **Figure 3C**. Unbound DUB and covalent DUB-ABP adduct (+8.9 kDa) are resolved by SDS-PAGE electrophoresis. **Left:** in-gel fluorescence ($\lambda_{ex} = 473$ nm, $\lambda_{em} = 530 \pm 10$ nm). **Right:** Coomassie protein stain.

7.4. Intact Protein MS

Table S2 | Calculated and deconvoluted mass of intact USP16CD^{WT} and USP16CD^{C205A} (adducts)

Enzyme	ABP	Deconvoluted mass (Da)		
		Calc. ^a	Found	Covalent adduct
-	Rho-Ub-Prg	8,883.12	8,884	N.A.
	Rho-Ub-2	8,897.21	8,898	N.A.
	Rho-Ub-5	8,911.24	8,912	N.A.
USP16CD ^{WT}	-	N.A.	73,344 & 73,426	N.A.
	Rho-Ub-Prg	82,228 & 82,310	82,229 & 82,309	+
	Rho-Ub-2	82,243 & 82,324	82,242 & 82,324	+
	Rho-Ub-5	82,258 & 82,339	82,256 & 82,338	+
USP16CD ^{C205A}	-	N.A.	73,406 & 73,488	N.A.
	Rho-Ub-Prg	82,290 & 82,372	73,407 & 73,489	-
	Rho-Ub-2	82,304 & 82,386	73,408 & 73,490	-
		82,318 & 82,400	73,408 & 73,489	-

Data related to **Figure 4B-C**. ^a Mass of USP16-ABP adduct calculated based on deconvoluted mass of unbound ABP and unbound USP16.

7.5. HRMS

Table S3 | Calculated and detected m/z of naturally most abundant peak for each charge state.

Rho-Ub-	m/z (Da)	z					
		13	12	11	10	9	8
Prg	Calc. ^a	684.2974	741.2384	808.5319	889.2842	987.9816	1111.3534
	Found	684.3000	741.2388	808.5306	889.2878	987.9859	1111.3591
[D ₂]-Prg	Calc. ^b	684.4522	741.4059	808.7148	889.4855	988.2053	1111.6050
	Found	684.4553	741.4115	808.7168	889.4891	988.2110	1111.6116

^a Isotope model C₄₀₁H₆₄₃N₁₀₇O₁₂₀. ^b Isotope model C₄₀₁H₆₄₁D₂N₁₀₇O₁₂₀ with D = 2.0141017779 u.

7.6. Bottom-Up MS/MS Analysis

Sequence **UCHL3^{WT}** (Uniprot; P15374) with underlined proteolytic peptide containing catalytic residue (Cys95) after trypsin digestion:

MEGQRWLFLE ANPEVTNQFL KQLGLHPNWQ FVDVYGMDFE LLSMVPRPVC AVLLLFFITE KYEVFRTEEE EKIKSQQGQDV TSSVYFMQK ISNACGTIGL IHAIAANNKDK MHFESGSTLK KFLEESVMS PEERARYLEN YDAIRVTHET SAHEGQTEAP SIDEKVDLHF IALVHVVGHL YELDGRKPFP INHGETSDET LLEDAIEVCK KFMERDPDEL RFNAIALSAA

Table S4 | Tryptic peptides identified with Mascot (v1.36) after alkylation and tryptic digestion of covalent adducts of Rho-Ub-ABPs with recombinant UCHL3. Bottom-up MS analysis related to Figure 5.

UCHL3 ^{WT}		
	Rho-Ub-Prg	Rho-Ub-[D ₂]-Prg
Peptide sequence	QTISNACGTIGL <u>IHAIAANNK</u> C7-Gly-HH-Prg (112.06366 Da)	QTISNACGTIGL <u>IHAIAANNK</u> C7-Gly-DD-Prg (114.07622 Da)
Charge	+3	+3
Monoisotopic m/z	717.71631 Da (+0.16 mmu/+0.22 ppm)	718.38696 Da (-0.04 mmu/-0.05 ppm)
MH⁺	2151.13437 Da	2153.14634 Da
Rt	32.4201 min	32.5055 min

Peptides with DH-Prg (113.06994 Da) modification were not found for the adduct with Rho-Ub-[D₂]-Prg.

Sequence **USP16CD^{WT}** (Uniprot; Q9Y5T5) with underlined proteolytic peptide containing catalytic residue (Cys205) after trypsin digestion:

MAHHHHHHSA ALEVLFQGPK GLSNLGNNTCF FNAMVNQLSQ TPVLRELLKE VKMSGTIVKI EPPDLALTEP LEINLEPPGP LTLAMSQFLN EMQETKKGVV TPKEILFSQVC KKAVRFKGYQ QQDSQELLRY LLDGMRAEEH QRVSKGILKA FGNSTEKLDE ELKNKVKDYE KKKSMPSFVD RIFGGELTSW IMCDQCRTVS LVHESFLDLS LPVLDQSGK KSVNDKNLKK TVEDEDQDSE EEKNDNSYIK ERSIDIPSGTS KHLQKKAKKQ AKKQAKNQRR QQKIQGKVHL LNDICTIDHP EDSDNEAEMS LQGEVNIKSN HISQEGVMHK EYCVNQKDLN GQAKMIESVT DNQKSTEEVD MRNINMDNDL EVLTSSPTRN LNGAYLTEGS NGEVDISNGF KNLNLNAAALH PDEINIEILN DSHTPGTKVY EVVNEDPETA FCTLANREVFT NTDECQIHC LYQFTRNEKL RDANKLLCEV CTRQCNGPK ANIKGERKHV YTNAKKQMLI SLAPPVLTW LKRFQQAGFN LRKVKNHKIF PEILDLAPFC TLKCKNVAEE NTRVLYSLYG VVEHSGTMRS GHYTAYAKAR TANSHLSNLV LHGDIPQDFE MESKGQWFHI SDTHVQAVPT TKVLNSQAYL LFYERIL

Table S5 | Tryptic peptides identified with Mascot (v1.36) after alkylation and tryptic digestion of covalent adducts of Rho-Ub-ABPs with recombinant USP16. Bottom-up MS analysis related to Figure 5.

USP16CD ^{WT}		
	Rho-Ub-Prg	Rho-Ub-[D ₂]-Prg
Peptide sequence	GLSNLGNNTCF FNAMVNQLSQ TPVLRELLKE M15-Oxidation (15.99492 Da) C9-Gly-HH-Prg (112.06366 Da)	GLSNLGNNTCF FNAMVNQLSQ TPVLRELLKE M15-Oxidation (15.99492 Da) C9-Gly-DD-Prg (114.07622 Da)
Charge	+3	+3
Monoisotopic m/z	951.47675 Da (-0.84 mmu/-0.88 ppm)	952.14832 Da (-0.12 mmu/-0.12 ppm)
MH⁺	2852.41568 Da	2854.43039 Da
Rt	41.8239 min	41.9013 min

Peptides with DH-Prg (113.06994 Da) modification were not found for the adduct with Rho-Ub-[D₂]-Prg.

Table S6 | Tandem MS analysis: Expected and detected fragment ions of modified tryptic UCHL3 peptide QTISNACGTIGLIHAANNK.

b _#	b-H ₂ O ⁺		b-NH ₃ ⁺		Sequence	y ⁺	y ²⁺	DD-Prg	HH-Prg	y ⁺	DD-Prg	y ²⁺	DD-Prg
	HH-Prg	DD-Prg	HH-Prg	DD-Prg									
1	212.10297	212.10297	112.03930	Q						1012.04130	1013.04757	19	20
2	325.18703	326.17105	213.08698	T						961.51746	962.52374	18	
3	412.21906	413.20308		I						1924.04019			
4	526.26199	527.24600		S						1810.95613	904.97543	17	
5	597.29910	597.29910	598.28312	N						1721.91155	861.45941	16	
6	812.37195	814.38450	813.35596	A						1723.92410	862.46569	15	
7	859.39341	871.40597	870.37743	C*						1607.86862	804.43795	15	
8	970.44109	972.45364	971.42511	815.36852						1538.84406	805.44423	15	
9	1083.55252	1085.53771	1084.50917	872.38998						768.91939	769.92567	14	
10	1140.54662	1142.55917	1141.53063	G						1321.75866	661.38297	13	
11	1253.63068	1255.64324	1254.61470	T						1264.73720	632.87224	12	
12	1366.71475	1368.72730	1367.69876	1086.52172						1163.68952	582.34840	11	
13	1503.77366	1505.78621	1504.75767	G						1050.60545	525.80637	10	
14	1574.81077	1576.82332	1575.79479	L						993.58399	497.29563	9	
15	1687.89484	1689.90739	1688.87885	1369.71131						880.4993	497.29563	497.29563	8
16	1758.93195	1760.94450	1759.91597	I						767.41586	767.41586	7	
17	1872.97488	1874.98743	1873.95889	A						630.35695	384.21157	6	
18	1987.01780	1989.03036	1988.00182	1875.97145						559.331984	315.68211	5	
19				1990.01437						446.23577	280.16356		
20				N						375.19866	223.62152	4	
				K						261.15573	188.10297	3	
										131.08150	131.08150	2	
										147.11280	74.06004	1	

Tandem MS analysis for QTISNAC^{*}GIGLIHAANNK peptide modified with Gly-HH-Prg (m/z = 717.716³⁺ Da) or Gly-DD-Prg (m/z = 718.387³⁺ Da) related to **Figure 5D** and **Table S4**. Obtained by alkylation and trypsin digestion of covalent UCHL3–Rho-Ub-[D₂]-Prg adduct (HH-Prg) and UCHL3–Rho-Ub-[D₂]-Prg adduct (DD-Prg). **Bold** = detected fragment ions. *Italic* = expected fragment ion (not detected).

7.7. Kinetic Analysis of Covalent USP16 Occupancy

Kinetic evaluation of incubation time-dependent covalent occupancy was performed by quantification of unbound USP16 and covalent USP16-ABP adduct on gel for recombinant USP16CD^{WT} incubated with Rho-Ub-**Prg**, Rho-Ub-**2**, and Rho-Ub-**5** (Figure 6B). Each assay condition was conducted three individual times (biological triplicate, $n = 3$), thus there are three values for covalent occupancy for each ABP concentration/incubation time. Samples were exposed to denaturing conditions to promote disintegration of noncovalent USP16-ABP complexes into unbound USP16 and unbound ABP, while covalent adducts remain intact. To improve the standard deviation for Rho-Ub-**Prg**, 1-5 minute measurements were performed ($n = 1$) but these still showed reaction completion within the first minute. Lowering incubation temperature to 21 °C also resulted in maximum adduct formation with Rho-Ub-**Prg** before the first timepoint. In our experiments, we ensured that ABP is present in large excess at reaction initiation ($t = 0$): $[ABP]_0 \geq 10[USP16]_0$. We selected ABP rather than USP16 to be present in excess because unbound USP16 and covalent adduct can be quantified in the same gel, while quantification of unbound ABP and covalent adduct in a single gel is challenging: either unbound ABP signals overlap with the loading front, or the covalent adduct has run off the gel.

Kinetic analysis is performed under pseudo-first order reaction conditions ($[ABP]_0 \geq 10[USP16]_0$) to enable algebraic analysis: the unbound ABP concentration should not decrease significantly upon USP16 binding. It is essential not to violate this assumption to obtain reliable estimates for the rate of covalent adduct formation k_{obs} . Under pseudo-first order conditions, covalent adduct formation can be fitted to a one-phase exponential increase, with covalent occupancy increasing by 50% every half-life. 97% covalent adduct formation is reached after five half-lives, which generally is considered ‘close enough’ to reaction completion: detection of changes beyond this point will be affected by error margins.

Irreversible ligand binding kinetics. Covalent adduct formation between enzyme and ABP is a two-step ligand binding reaction. We normally assume that the noncovalent equilibrium is reached almost instantly (*rapid equilibrium approximation*)¹²² and that this reaction is much faster than covalent adduct formation.⁵³ The reaction will slow down as the reaction progresses, because the concentration of both ABP and enzyme decreases when neither enzyme nor ABP is present in large excess (*second order reaction conditions*).¹²² Second order reaction conditions complicate algebraic analysis, and Morrisons quadratic equation – used to correct for the shift in equilibrium caused by inhibitor depletion – is limited to reversible ligands. Therefore, reaction kinetics of irreversible ligand binding are studied under pseudo-first order reaction conditions: ¹²³⁻¹²⁴ one of the reactants is present in excess ($[A]_0 \geq 10[B]_0$), so we can assume that the concentration of unbound reactant A (present in excess) will not change significantly upon protein binding ($[A]_t = [A]_0$).

7.8. Fluorescence Polarization (FP) Binding Assay

FP Binding assays of catalytic inactive DUBs with fluorophore-labeled ubiquitin as ligand are commonly performed to determine the noncovalent affinity.^{65, 125} FP binding assays of reporter/ligand Rho-Ub-ABPs (9 kDa) with catalytically inactive USP16CD^{C205S} mutant (73 kDa) were performed to determine K_D -values that are independent of electronic factors as covalent adduct formation with USP16CD^{C205S} does not occur. Catalytic inactive mutant USP16CD^{C205S} rather than USP16CD^{C205A} was used because active site alanine mutations in cysteine DUBs increase the affinity for ubiquitin.¹²⁶ The concentration of Rho-Ub-ABP (5 nM) was kept constant and excess USP16 (>50 nM) was varied, as is common for FP binding assays to maximize the assay window.^{65, 127} The assay was performed under pseudo-first order reaction conditions ($[E]_0 \gg [ABP]_0$): no significant change in unbound enzyme concentration ($[E] = [E]_0$), and equilibrium has been reached. Fluorescence polarization was measured every 3 minutes for 120 minutes (Figure S4A), and values after sufficient incubation (60 minutes) were plotted against USP16 concentration (Figure S4B). High protein concentrations are prone to exhibit nonspecific binding due to hydrophobic interactions and crowding effects, which was observable as the inability to reach a plateau despite supplementing the buffer with 0.005% Tween20 or additional 0.1 mg/mL bovine serum albumin (BSA; Chemcruz, #sc-2323A).¹²⁷ All USP16 concentrations were fitted with a shared value for nonspecific binding (NS > 0, Figure S4B, left) or only USP16 concentrations below 20 μ M, without taking nonspecific binding into account (NS = 0, Figure S4B, right). These restraints affect the absolute K_D -values, but regardless of the settings we observe the same trend; K_D for Prg < 2 < 5.

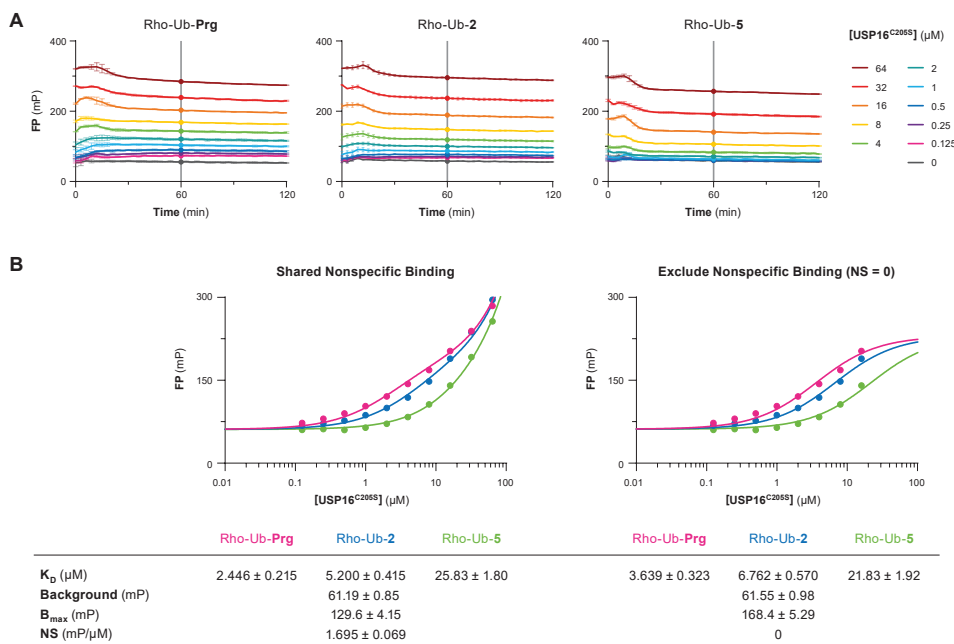


Figure S4 | Fluorescence polarization (FP) binding assay related to Figure 6C. **(A)** Progress curve for fluorescence polarization signal over time for Rho-Ub-ABPs (5 nM) with USP16CD^{C205S} (0–64 μ M). Noncovalent equilibrium between ABP and enzyme is reached after ~30 min. **(B)** Direct binding curve. Fluorescence polarization after incubation for 60 min as a function of USP16CD^{C205S} concentration. Fitted with shared values for NS, B_{max} and background to obtain K_D -value for each Rho-Ub-ABP. *Left:* All USP16 concentrations were fitted with a shared value for nonspecific binding. *Right:* [USP16] < 20 μ M was fitted with nonspecific binding NS = 0. Graphical data represents the mean \pm standard deviation for a single representative experiment.

7.9. Thiol Reactivity Assay

Adduct formation with biological thiols such as cysteine and glutathione (GSH) is an established method to assess intrinsic chemical reactivity of electrophilic warheads towards thiols.¹²⁸ The mass difference of unbound ABP and GSH adduct was clearly detected, but it was not possible to separate the unbound ABP from the GSH adduct for quantification of the LC-MS UV trace. Instead, quantification was performed based on the intensity of the naturally most abundant peak for the most common charge states (z = 7-13) in the ionization envelope of ubiquitin (Table S7), as is more often used for quantification in top- and middle-down mass spectrometry of ubiquitin.¹²⁹⁻¹³⁰

Table S7 | Charge states used for quantification of unbound ABP and GSH adduct in thiol reactivity assay.

ABP	State	M (Da)	m/z (Da)						
			z = 13	z = 12	z = 11	z = 10	z = 9	z = 8	z = 7
Rho-Ub-Prg	unbound	8883	684.2	741.2	808.5	889.2	987.9	1111.3	1270.0
	GSH adduct	9190	707.9	766.8	836.5	920.0	1022.1	1149.8	1313.9
Rho-Ub-2	unbound	8897	685.4	742.3	809.7	890.6	989.4	1113.0	1271.9
	GSH adduct	9204	709.0	768.0	837.7	921.4	1023.7	1151.5	1315.9
Rho-Ub-3	unbound	8959	690.1	747.5	815.4	896.8	996.3	1120.9	1280.7
	GSH adduct	9266	713.8	773.2	843.4	927.6	1030.6	1159.3	1324.7
Rho-Ub-4	hydrolysis	8977	691.5	749.0	817.0	898.7	998.4	1123.1	1283.3
	unbound	8897	685.3	742.4	809.7	890.6	989.5	1113.0	1271.9
Rho-Ub-7	GSH adduct	9204	709.0	768.0	837.7	921.4	1023.7	1151.5	1315.9
	unbound	8959	690.1	747.5	815.3	896.8	996.4	1120.8	1280.7
Rho-Ub-5	GSH adduct	9266	713.8	773.2	843.4	927.6	1030.6	1159.3	1324.7
	unbound	8912	686.4	743.5	811.0	892.0	991.0	1114.9	1273.9
Rho-Ub-8	GSH adduct	9219	710.2	769.3	839.1	922.9	1025.3	1153.4	1318.0
	unbound	8951	689.4	746.8	814.6	896.0	995.5	1119.7	1279.7
Rho-Ub-9	GSH adduct	9258	713.2	772.5	842.6	926.8	1029.7	1158.3	1323.6
	unbound	8897	685.3	742.3	809.6	890.5	989.5	1113.1	1271.9
Rho-Ub-10	GSH adduct	9204	709.0	768.0	837.7	921.4	1023.7	1151.5	1315.9
	unbound	8897	685.3	742.3	809.7	890.5	989.4	1113.0	1271.9
Rho-Ub-Prp	GSH adduct	9194	708.2	767.2	836.8	920.4	1022.6	1150.3	1314.4
	unbound	8887	684.5	741.4	808.8	889.6	988.3	1111.8	1270.4
Rho-Ub-18	GSH adduct	9258	713.1	772.5	842.5	926.8	1029.5	1158.2	1323.4
	unbound	8951	689.5	746.9	814.6	896.0	995.5	1119.8	1279.7
Rho-Ub-VME	GSH adduct	9250	712.5	771.8	841.8	926.0	1028.7	1157.2	1322.4
	unbound	8943	688.8	746.2	813.9	895.2	994.5	1118.7	1278.5

Data related to Figure 7C. Detection of Rho-Ub-ABPs, GSH-ABP adducts (+307 Da), and other ABP derivatives by LC-MS in ES+ mode; $m/z = (M + zH^+)/z$. Values in *italics* are expected/calculated values, not detected.



Chapter 7



Happily Ever After:
A Summary and Discussion

1. Summary

Once upon a time... irreversible covalent inhibitors were discovered by accident and actively avoided in drug development. In **Chapter 1**, a historic perspective on the development of irreversible covalent inhibitors illustrated how compounds with potential covalent binding modes were excluded from industrial drug development programs despite the prevalence of safe blockbuster drugs that were later found to have an irreversible covalent binding mode. The past two decades marked a resurgence of irreversible covalent drugs for protein targets that require prolonged inhibition for therapeutic effect, and led to the development of targeted covalent inhibitors (TCIs) that have a strategically placed electrophilic moiety. TCIs were instrumental in overcoming acquired resistance to noncovalent inhibitors (e.g. third-generation inhibitor **osimertinib** (Tagrisso, AZD9291) targeting EGFR mutants over wild-type), and some TCIs are first-in-class drugs tackling previously ‘undruggable’ oncogenes (e.g. **sotorasib** (Lumakras, AMG 510) and **adagrasib** (Krazati, MRTX849) targeting KRAS^{G12C}).¹⁻² Novel thiol-reactive warheads that balance chemical reactivity with superior target selectivity have an important role to further improve the safety profiles. Acetylenes are a privileged structural motif in drug discovery, and terminal alkynes have been extensively used as bioorthogonal Click handles in chemical biology tools – owing to their selective reactivity with azides in the copper-catalyzed azide–alkyne cycloaddition (CuAAC) while displaying a low propensity of spontaneous engagement in covalent adducts with cellular components. Aside from the CuAAC reaction forming a triazole and the radical-mediated thiol–yne coupling (TYC) forming an *anti*-Markovnikov-type thiovinylic covalent adduct formation with acetylenes requires promotion by metabolic activation, isomerization to a reactive allenic intermediate, metal catalysis, or chemical modification of the acetylene to generate a reactive electron-deficient alkyne. In 2013, the Ovaa³ and Mootz⁴ groups independently discovered that Ub(l)-**Prg** – intended as building blocks for protease-resistant nonhydrolyzable substrates – can form a covalent Markovnikov-type thiovinylic adduct with catalytic cysteine residues of Ub(l) proteases. This serendipitous discovery challenged the paradigm that nonactivated alkynes are ‘inert’ towards cellular components under physiological conditions but covalent adducts were only detected if the propargylated peptide had a relatively large recognition element (>1.8 kDa) and substituents on the propargylamide mitigated adduct formation with UCHL3. In this dissertation, we explored the scope and versatility of the newly-discovered *in situ* thiol–alkyne reaction: from nonactivated alkyne warheads in irreversible covalent small molecule drugs to substituted propargyl analogues in chemical tools.

Part 1: Theoretical Framework for the Evaluation of Covalent Inhibitors

There are many indirect methods to deduce a covalent binding mode from (time-dependent) disappearance of intact drug and/or unbound protein, but experimental detection of the covalent protein–drug adduct ultimately provides conclusive evidence on the covalent binding mode. In **Chapter 2**, we reviewed experimental technologies that can strictly distinguish a noncovalent protein–drug complex from a covalent protein–drug adduct, illustrated by examples from (recent) covalent drug development.² The experimental validation of covalent adduct formation is based on a detectable change that only occurs upon adduct formation:

an increased mass in the adduct (MS), continuous electron-density between protein and drug (protein crystallography), a change in intrinsic spectroscopic properties, chemical shift perturbation in covalently-bound inhibitor (NMR), fluorescence detection of proteins modified with inhibitor-derived ABPs (gel-based/homogeneous ABPP), or enrichment of ABP-modified proteins (chemoproteomic ABPP). Each technology has pros and cons: from compatibility with a reversible covalent binding mode or quantification of covalent occupancy, to mandatory chemical synthesis of labeled drug or incompatibility with complex mixtures. Aside from compatibility, another important factor is the informativeness of the technique: ranging from simple biophysical detection of the covalent adduct to detailed information on the modified amino acid residue, bond layout, and binding mode reversibility. Various MS techniques, protein crystallography, gel-based ABPP, and chemoproteomic ABPP platforms have been used to detect covalent protein–alkyne adducts in *Chapter 4-6*.

In *Chapter 3*, we expanded on the notion that evaluation of covalent binders uses different kinetic parameters to rank inhibitor potency (e.g. k_{inact}/K_I for irreversible covalent inhibitors), focusing on the connection between experimental assay conditions and algebraic models to obtain those kinetic parameters.⁵ Most covalent inhibitors have a two-step binding mode – exerting their inhibitory effect through initial protein association forming a noncovalent complex, followed by covalent adduct formation that may or may not be reversible. Enzymatic assays to evaluate covalent inhibition capitalize on the time-dependence of covalent inhibition: a covalent adduct is not formed instantly (on a kinetic assay timescale) and inhibition improves with longer (pre)incubation times. The kinetic time-dependent enzyme activity can be fitted to algebraic models to extract relevant kinetic parameters. However, embedded in these algebraic equations are assumptions on experimental assay conditions – often implied but rarely explicitly mentioned – and is not always clear what the consequences are if those assumptions are violated. To understand kinetics and the impact of assay conditions, we composed kinetic simulation scripts that translate the mathematical equations into data read-out under relevant experimental assay conditions, which led to the identification of the general assumptions on experimental assay conditions. These simulations were then used to compose a comprehensive guide for evaluation of covalent inhibitors in enzymatic assays: four stepwise experimental protocols with accompanying data analysis protocols tailored to the covalent inhibitor binding mode.⁵ A remaining challenge in the covalent drug development is the direct comparison of potency for reversible and irreversible inhibitors, as there is no shared/universal constant among these compound classes that facilitates hit prioritization. This may have complicated preclinical development, but other properties – such as metabolic stability, selectivity, ADME properties, hapten formation – are still deciding factors in the selection of suitable clinical candidates.

Part 2: Nonactivated Alkynes in Small Molecule Inhibitors

In *Chapter 4*, we showed that a small recognition element (<600 Da) is compatible with the *in situ* thiol–alkyne reaction. Alkyne analogues of **odanacatib** (ODN, MK-0822) – a reversible covalent inhibitor of the main cysteine protease in bone resorption cathepsin K (CatK) – were obtained by replacing the nitrile warhead with an isoelectric alkyne moiety (**Figure 1**).⁶

mice/patients treated with ODN (discussed in more detail in *section 2.1*). Together, this work functions as a proof-of-concept that demonstrates how the nonactivated alkyne optimally balances on-target reactivity with excellent target selectivity, and can act as a latent electrophile in irreversible covalent small molecule inhibitors targeting a catalytic cysteine residue.

Having established that nonactivated alkynes can covalently target the catalytic cysteine residue of CatK, we investigated the possibility to target noncatalytic cysteines in **Chapter 5**. To this end, the acrylamide warhead in approved covalent kinase inhibitor **neratinib** (Nerlynx, HKI-272) targeting noncatalytic Cys797 at the ATP-binding site of EGFR was replaced by propargylamine in 8RK57 or 1-amino-3-butyne in 8RK58 (**Figure 1**). A covalent adduct was not detected with GSH but also not with recombinant EGFR kinase domain. Preliminary cellular assays were indicative of an irreversible mode of action but kinase activity assays on recombinant EGFR kinase domain did not support this binding mode. It is unlikely that alkyne analogues 8RK57 and 8RK58 have a covalent binding mode, which may be attributed to inhibitor design (incorrect orientation of the alkyne relative to the cysteine thiol mitigating covalent adduct formation) or incompatibility of the thiol-alkyne reaction with noncatalytic cysteines (discussed in more detail in *section 2.4*). Altogether, covalent EGFR-alkyne adduct was not detected, but this does not definitively proof that the alkyne is incompatible with noncatalytic cysteine thiols. Alkyne derivatives of other kinase inhibitors may be required to further investigate the potential of the nonactivated alkyne warhead.

Part 3: Substituted Alkynes as Warheads in Ub-ABPs Targeting CysDUBs

Ekkebus *et al.*³ found that Ub-ABPs with methylated internal alkyne Ub-2 and *gem*-dimethylated propargylamide Ub-5 did not form a covalent adduct with the recombinant purified CysDUB UCHL3, which led to the assumption that adduct formation is restricted to unsubstituted propargylamide. In **Chapter 6**, we prepared a panel of propargylamine derivatives and incorporated them into fluorescent Rho-Ub-ABPs to investigate the role of various substituents.⁷ Propargylamide analogues with substituents on the terminal or internal alkyne position were indeed unreactive toward recombinant UCHL3 but proceeded to form covalent adducts with other CysDUBs in whole cell lysates and recombinant protease. The acceptable position and bulkiness of substituents on the propargylamide was specific for the protease: selectivity was not conserved among members of the same CysDUB family. UCHL3 – the recombinant CysDUB that was selected for initial discovery – had a more restricted selectivity profile while USP16 is among the most flexible CysDUBs. Introduction of (bulky and/or electron-donating) methyl groups onto the propargylamide warhead reduces the rate of adduct formation with USP16 through steric as well as electronic effects. Mechanistically, adduct formation with Rho-Ub-5 cannot proceed *via* an allenic intermediate (*mechanism C* in **Figure 5C**) – deprotonation of a *gem*-dimethylated propargylamide to form a reactive allenimide is not possible – but this may have been a USP16-specific exception to the general mechanism. The deuterated covalent adduct of recombinant USP16 and UCHL3 with deuterated propargylamide in Rho-Ub-[D₂]-Prg confirmed that an alkyne rather than an allenic intermediate is the reactive species in the *in situ* thiol-alkyne reaction. Electron-deficient propargylamide ABP Rho-Ub-18 bearing a trifluoromethyl group on the terminal position showed reactivity with noncatalytic cysteines

and was therefore not suited to study the mechanism of the thiol–alkyne reaction: adduct formation with electron-deficient alkynes can progress through an alternative, nonenzymatic mechanism with internal stabilization of a carbanion. Together, this work showed that the scope of the thiol–alkyne reaction is broader than initially assumed, and revealed an important role for the cysteine protease in the compatibility with bulky and/or electron-donating substituents on the propargylamide warhead.

2. Nonactivated Alkynes in Drug Development and Chemical Tools

Since its discovery one decade ago, the covalent thiol–alkyne reaction has gained a lot of traction. In the next sections, we will discuss the future prospects of irreversible CatK inhibition (*section 2.1*), the implementation of nonactivated alkynes in covalent small molecule inhibitors (*section 2.2*), the role of (substituted) propargyl warheads in Ub(I)-ABPs (*section 2.3*), and give an overview of the possible mechanisms of the thiol–alkyne reaction (*section 2.4*).

2.1. Covalent Alkynes in Irreversible CatK Inhibitor Development

Odanacatib (ODN) was the fourth CatK inhibitor that failed in clinical phase II or III, after more than twelve years in clinical development, and pharmaceutical companies seem to have abandoned CatK inhibitors as osteoporosis treatment agents considering the long list of failed attempts.⁸⁻¹¹ Osteoporosis a systemic skeletal condition that affects the elderly population: half of the (postmenopausal) women are likely to experience at least one osteoporotic fracture in their lifetime.¹² The disease is characterized by an unbalance in bone formation and degradation, resulting in fragile and brittle bones that are susceptible to fractures induced by mild stress such as falling or coughing.¹³ Among the treatment options are bisphosphonates: anti-resorptive agents that have a direct apoptotic effect on osteoclasts but can also inhibit activity and proliferation of bone-forming osteoblasts. These agents suppress bone formation along with inhibition of bone degradation, and treatment benefits typically plateau after only three years.¹⁰ ODN was supposed to be Merck's next big blockbuster drug for long-term osteoporosis treatment because of its once-weekly oral administration without concurrent bone formation suppression. Unfortunately, ODN development was discontinued in 2016 due to an increased risk of stroke, atrial fibrillation, cerebrovascular events and overall death.^{9, 14} These adverse effects were unexpected as they are not common in pycnodysostosis¹⁵ – a rare autosomal recessive lysosomal storage disorder associated with production of inactive CatK due to a *CTSK* gene mutation – and preclinical *in vitro* studies mostly indicate that CatK inhibition has a cardioprotective effect.^{8, 16-17} Although it is known that the effect of *CTSK* mutations or knock-down differs from (long-term) CatK inhibition,¹⁸ it is surprising to observe the opposite effect.

2.1.1. Adverse Effects/Rebound Effect

The exact underlying mechanism to the adverse effects is unknown at this moment, but it is possible that these are on-target adverse effects related to CatK functions that are not related to bone resorption.^{16, 19} CatK inhibition causes structural ECM remodeling, and it has been

postulated that this increases the risk of atrial arrhythmia.¹⁴ Ischemic stroke is typically caused by blockage of an artery supplying blood to the brain. This blockage can be a blood clot consisting of an intact plaque or a ruptured plaque.²⁰ Plaque stability decreases upon overexpression of CatK,²¹ or may be the result of the rebound effect resulting in high levels of active mature CatK. A rebound effect has been reported *in vitro* but also in patients: bone resorption activity and osteoclast numbers are elevated during and after ODN treatment.^{8, 22-23} In line with these observations, we observed an elevated level of mature CatK in human osteoclasts upon treatment with CatK inhibitors (**Chapter 4**).⁶ We also found that irreversible qABP BMV109 was able to outcompete ODN, resulting in regained CatK activity that exceeded the activity in vehicle-treated samples. Furthermore, treatment discontinuation studies (*unpublished data*) revealed increased bone resorption activity after discontinuation of ODN treatment (**Figure 2**). This rebound effect was not observed in samples treated with our irreversible CatK inhibitor EM04: catalytic activity of irreversibly inhibited mature CatK cannot be regained. Therefore, we believe that the adverse effects of ODN may be related to the rebound effect that is specific for reversible CatK inhibition, which can be avoided by irreversible CatK inhibitors.

To establish whether the adverse effects are resultant from a rebound effect associated with reversible CatK inhibition, further research is needed. This would include elucidation of the feedback mechanisms that drive osteoclast maturation and CatK expression, identification of proteases involved in mature CatK degradation, and evaluation how (ir)reversible inhibition affects CatK activity and expression levels in non-skeletal tissue. Finally, (expensive) long-term clinical trials are needed to validate whether irreversible CatK inhibition does indeed reduce rebound and possible on-target adverse effects.

2.1.2. CatK Inhibitors for Treatment of Metastatic Bone Disease

Aberrant bone resorption is not only associated with osteoporosis but also with other (skeletal) conditions including Paget's disease of bone,²⁴ periodontal disease,²⁵ rheumatoid arthritis,²⁶ osteoarthritis,²⁷ periprosthetic osteolysis,²⁸ osteolytic bone disease,²⁹ metastatic bone disease,³⁰ and giant cell tumor of the bone.³¹ In metastatic bone disease with an osteolytic phenotype, tumors originating from other tissues metastasize to the bone where they enhance differentiation and activation of osteoclasts, ultimately leading to degradation of the bone matrix.³²⁻³³ Treatment options are overlapping with treatment options for osteoporosis:³⁴ osteoclast inhibitors suppress bone resorption, thereby reducing bone pain, decreasing the incidence of skeletal-related events, and preventing the formation of new osteolytic lesions.³⁵⁻³⁶ The bisphosphonate antiresorptive agents target the osteoclasts recruited by the metastasized tumor, but do not inhibit CatK secreted by the tumor itself: giant cell tumors of the bone and (invasive subpopulations of) tumors that metastasized to the bone have been reported to (over)express hCatK.^{15, 31, 37-40} Selective CatK inhibition has been reported to reduce cancer cell invasiveness, thereby possibly preventing the formation of (bone) metastases.^{15, 37-38} The benefit:risk ratio for CatK inhibition is more likely to be positive for these patient populations as they are expected to have a shorter treatment period (and life expectancy) relative to long-term treatment of osteoporosis patients. Younger patients may also be less prone to some adverse effects – post-menopausal and osteoporotic women have an increased stroke risk⁴¹⁻⁴² and have more unstable plaques.⁴³

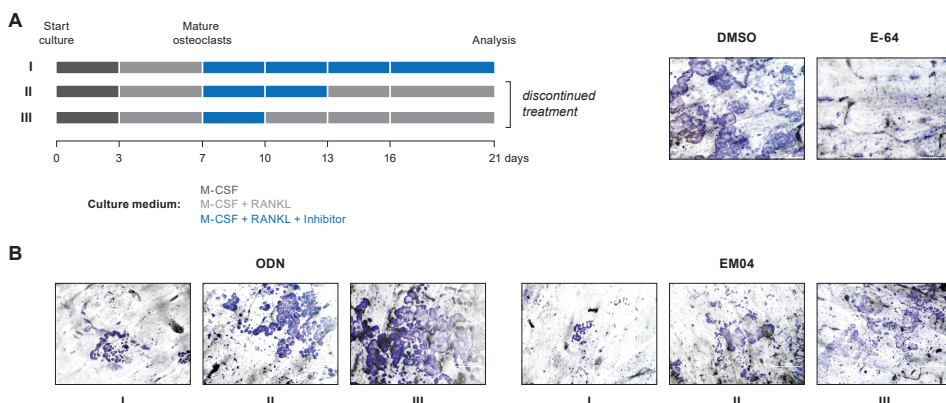


Figure 2 | Preliminary data on CatK activity in human osteoclasts (OCs), upon discontinuation of inhibitor treatment. **(A)** Discontinuation (washout) experiment. Adjustment of the protocol used in **Chapter 4**. Culture medium containing either inhibitor or DMSO was refreshed on day 7, 10, 13, and 16. In *conditions II* and *III*, inhibitor treatment was discontinued by washout and refreshing with medium that does not contain inhibitor. On day 21, OCs were washed away and lysed, and bone slices were stained with Coomassie Brilliant Blue to visualize bone resorption. **(B)** Bone resorption in cultures treated with 2 μ M ODN or EM04. Normal (trench-forming) bone resorption activity is regained after approximately 7 days (*II*). Discontinuation of ODN results in elevated levels of bone resorption relative to the DMSO control (*III*).

Preclinical studies indicate that selective CatK inhibitors prevent establishment and progression of bone metastases of various solid cancers,⁴⁴⁻⁴⁷ and a phase II clinical study of ODN in breast cancer patients with established bone metastases confirmed target engagement.⁴⁸ Unfortunately, we were unable to investigate the *in vivo* efficacy of EM04, because murine CatK (mCatK) – despite sharing 88% homology with human (hCatK) – contains mutations at the enzyme active site that hinder formation of a covalent adduct with active site-directed inhibitors such as ODN.⁴⁹ Established murine disease models to study bone metastases can use human tumor material, but the native osteoclasts still express mCatK, rendering them unsuited as model system.⁵⁰ Rabbits (94% homology) and monkeys (identical to hCatK) are more suitable to study the effects of irreversible covalent CatK inhibition.⁸ However, a transgenic mouse model with a humanized CTSK expressing hCatK or mCatK^{Y61D} – that can be covalently modified by active site-directing inhibitors – would be desirable as they could be employed in established murine models of skeletal disease. To our knowledge, humanized murine models with CatK chimeras have not yet been developed.

2.2. Nonactivated Alkynes in Recent Covalent Drug Development

In **Chapter 4**, our irreversible covalent alkyne derivatives of CatK inhibitor **odanacatib** (ODN, MK-0822) demonstrated that the nonactivated propargyl warhead can act as a latent electrophile in covalent small molecule inhibitors (<600 Da) targeting a catalytic cysteine.⁶ We also found that covalent CatK-alkyne adduct formation is relatively slow, which was an

unexpected finding considering that CysDUB–Ub–**Prg** adduct formation is quantitative within minutes (**Chapter 6**).⁷ The covalent binding mode would have been overlooked without direct detection of the covalent adduct (**Chapter 2**)² and kinetic evaluation (**Chapter 3**)⁵, underlining the crucial importance of dedicated methods tailored to (ir)reversible inhibition. Our proof-of-concept with CatK demonstrated that a small recognition element can be sufficient for covalent thiovinyll adduct formation, and nonactivated terminal alkynes have since gained popularity as irreversible covalent warheads. Our approach of replacing a nitrile warhead for an isoelectric alkyne warhead has since been employed to other cysteine protease targets (**Figure 1**, **Figure 3**).

Behring *et al.*⁵¹ report an extensive panel of dipeptide-derived alkynes and nitriles specifically targeting cathepsin B, S, K or L (**Figure 3**). The covalent binding mode was deduced from irreversibility in a 5-fold dilution assay and kinetic behavior instead of biophysical detection of the covalent protein–inhibitor adduct. Interestingly, reversible binding potency of a dipeptide nitrile did not necessarily translate to a potent alkyne derivative, underlining that alkyne-based covalent drugs would benefit from optimization of noncovalent interactions. These potentially covalent cathepsin dipeptide alkynes are fascinating when we consider that, in the original work by Ekkebus *et al.*³ covalency was not observed with alkyne derivatives of CatS inhibitor Leupeptin (a tripeptide-aldehyde) or Casp1 inhibitor Ac-YVAD-CHO (a tetrapeptide-aldehyde). It is possible that Leupeptin-**Prg** – replacing the reversible covalent aldehyde warhead with a propargyl derivative – may actually have had a covalent binding mode: Leupeptin-**Prg** was assumed to have a noncovalent binding mode because of its dramatic loss of potency in enzymatic activity assays, similar to what we observed for alkyne derivative EM04, which is in agreement with slow covalent thiovinyll bond formation. Tetrapeptide Ac-YVAD-**Prg** (488 Da) was also assumed to be a noncovalent inhibitor of cysteine protease caspase-1 (Casp1) due to its low inhibitory potency in enzymatic assays – detecting the combined noncovalent and covalent inhibition after a short preincubation – while covalent adduct of Casp1 with Cy5-IL-1 β ₁₀₂₋₁₁₆-**Prg** peptide (having a recognition element of 1.8 kDa, excluding the Cy5 fluorophore) was successfully detected by in-gel fluorescence – strictly detecting covalent adducts. Together, this led to the incorrect assumption that the covalent thiol–alkyne reaction requires a relatively large recognition element, as we demonstrated with our covalent alkyne-based small molecule CatK inhibitors.⁶

Brewitz *et al.*⁵² prepared various terminal/internal alkyne derivatives of COVID-19 drug **nirmatrelvir** (Paxlovid, PF-07321332) and several other inhibitors of SARS-CoV-2 main protease (M^{PRO}), and made a side-by-side comparison of the IC_{50} of parent nitriles and their alkyne derivatives (**Figure 3**). Nirmatrelvir alkyne derivative **13** was initially found to be less potent than the parent nitrile, but alkyne derivatives generally retain their activity against the S144A mutant M^{PRO} better than the nitriles. Ser144 is part of the oxyanion hole thus helping to stabilize a tetrahedral anionic intermediate, and Ser144 variations reduce nirmatrelvir potency, which may enable development of nirmatrelvir resistance. Protein crystallography provided mechanistic rational to this observation: the thioimidate nitrogen in the covalent M^{PRO} –nirmatrelvir adduct is positioned in the oxyanion hole (PDB: 7TE0) whereas the terminal olefin carbon in the covalent M^{PRO} –alkyne adduct is pointing away from these residues

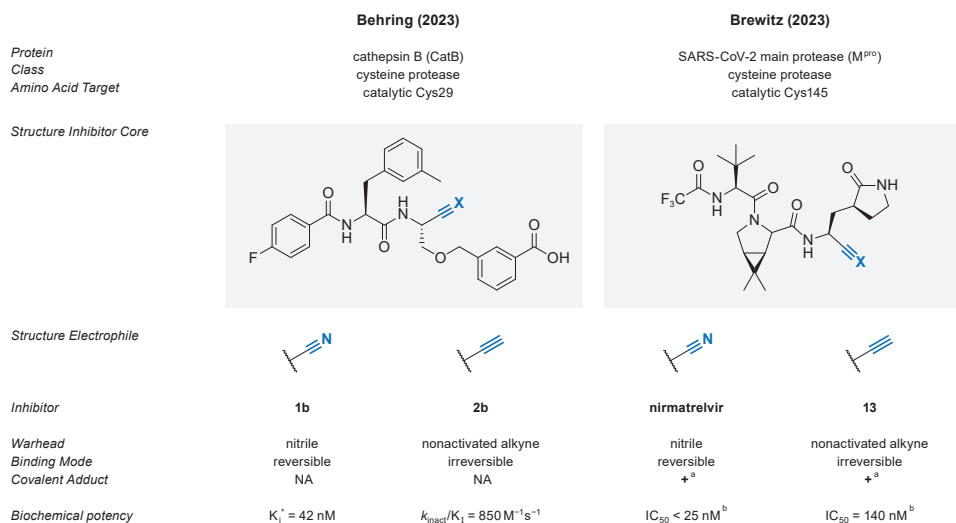


Figure 3 | Nonactivated alkynes as covalent warheads targeting the catalytic cysteine residue in small molecule inhibitors. Irreversible alkyne analogues were obtained by replacing the nitrile warhead by an isoelectric (substituted) propargyl warhead. Behring *et al.*⁵¹ developed cathepsin B (CatB) inhibitors with a dipeptide recognition element. Brewitz *et al.*⁵² replaced the nitrile warhead of SARS-CoV-2 M^{pro} inhibitor nirmatrelvir (Paxlovid, PF-07321332) with an alkyne warhead. ^a Detection of covalent protein–inhibitor adduct by intact protein MS and protein crystallography. ^b Biochemical IC_{50} after preincubation of 50 nM enzyme with inhibitor for 15 min.

(PDB: 8B2T). This observation suggests that an anionic thioimide intermediate is stabilized in the oxyanion hole, whereas covalent thiol–alkyne addition does not involve a carbanion intermediate or is quickly protonated.

Ngo *et al.* synthesized the same nirmatrelvir derivative with a nonactivated alkyne (**4d**), and a two-step ABP derivative **Alk-4d**.⁵³ Furthermore, they then used a two-step ABP **Alk-4i** bearing an electron-deficient trifluoromethylated alkyne as warhead and terminal alkyne as a Click handle to study the residence time of nirmatrelvir, as this modification increased the reactivity (and reaction rate), stating the faster reactivity with this ‘latent’ electrophile is beneficial for SARS-CoV-2 inhibition. In agreement with our findings in *Chapter 6*,⁷ they do observe non-specific proteome labeling with **Alk-4i**, so it is debatable if the trifluoromethylated alkyne actually is a latent electrophile.

Together with the work in this dissertation, the recent incorporation of alkynes into other protease inhibitors underscore the role nonactivated alkynes may have as latent electrophiles in small molecule covalent drug development. Nonactivated alkynes are now not only incorporated by late-stage replacement of a covalent nitrile, but have also been included in a panel of established covalent warheads for the rational design of novel SARS-CoV-2 M^{pro} inhibitors^{54–55} and covalent TKIs targeting Cys552 in FGFR4.⁵⁶ It is unlikely that covalent alkynes

will be identified in covalent fragment screening – covalent fragments (<200 Da) are unlikely to position the alkyne in sufficient proximity to a reactive cysteine thiol to initiate covalent adduct formation – nor do we expect that these findings will affect the use of acetylenes as bioorthogonal handles, but we imagine a promising role for the alkyne warhead in rational/structure-based covalent drug design.

2.3. The Propargylamide Warhead in Ub(l)-ABPs

Since its discovery in 2013, the propargyl (**Prg** or **PA**) warhead has been incorporated into numerous other Ubl-based ABPs including **Rho-UFM1-Prg**,⁵⁷ **ISG15-Prg**,⁵⁸ and **LC3-Prg**,⁵⁹ into ubiquitin variant (UbV) ABPs with specificity for **USP7**,⁶⁰ **USP16**,⁶¹ or **UCHL3**,⁶² and into nonhydrolyzable diUb-**Prg** ABPs with a propargylamide warhead on the proximal C-terminus that bind to the protease S1-S2 sites.⁶³ Nowadays, the covalent **Prg** warhead is considered the golden standard for cysteine-reactive Ub(l)-ABPs: the high stability in physiological conditions and absence of intrinsic reactivity with nontargeted thiols and noncatalytic cysteines is superior to any other (acid-stable) warhead.⁶⁴⁻⁶⁵ Furthermore, Ub(l)-**Prg** ABPs are readily obtained by SPPS in high purity and, contrary to Ub-VME, the **Prg** warhead can be installed using cheap and commercially available propargylamine. The superior selectivity for catalytic cysteines is an important feature of Ub(l)-**Prg**: labeling of noncatalytic cysteines in HEK293T lysate has not been found with HA-Ub-**Prg** but was identified for HA-Ub-VME and HA-Ub-**VS**.⁶⁴ These findings were supported in **Chapter 6**, where minor adduct formation was detected for **Rho-Ub-VME** and **Rho-Ub-18** with catalytically inactive **USP16^{C205A}** mutant but not for **Rho-Ub-Prg**. Another compelling reason to use Ub-**Prg** ABPs in chemoproteomic profiling is the improved reactivity that some CysDUB classes have toward **Prg** compared to **VME** or **Br2**, which enabled comprehensive coverage of the DUBome with HA-Ub-**Prg**.⁶⁵ Ub(l)-**Prg** ABPs were also instrumental in crystallographic studies to solve the Ub(l)-bound structures of cysteine proteases as well as the HECT domain of various E3 ligases.⁶⁶⁻⁶⁷

In **Chapter 6**, we incorporated substituted propargylamine derivatives into Ub-ABPs and discovered that compatibility with electron-donating/bulky substituents is driven by the individual CysDUBs. These substituted propargylamide warheads can be used in the design of CysDUB-selective Ub-ABPs, and our panel of propargylamine derivatives can also conveniently be incorporated into other Ubl-ABPs (e.g. **SUMO2-Prg**, **ISG15-Prg**) to investigate the selectivity (and inhibition) of the corresponding Ubl proteases. We also showed how Rho-Ub-ABPs can be used in quantitative FP binding assays and quantitative gel analysis to evaluate ABP potency in a noncompetitive manner. There is a clear need for quantitative assays to evaluate inhibitor potency, and we have identified several ligand binding competition assay methodologies where Ub-ABPs can act as (ir)reversible ligands. These methodologies are compatible with gel-based or MS-based detection of the enzyme-ABP adduct (**Chapter 2**). For application in high-throughput and/or homogeneous assays – without removal of unbound ABP – Ub-based qABPs or turn-on ABPs would be more suitable.⁶⁸ For example, we predict that ABPs such as Ub-**Prg** can be used to evaluate irreversible cysteine-targeting inhibitors in a preincubation assay using the same concept as *Method IV* in **Chapter 3**. This ligand binding competition assay is theoretically compatible with CysDUBs, and this concept might also be applicable to more

Endpoint competition assays with irreversible covalent probe (ABP)

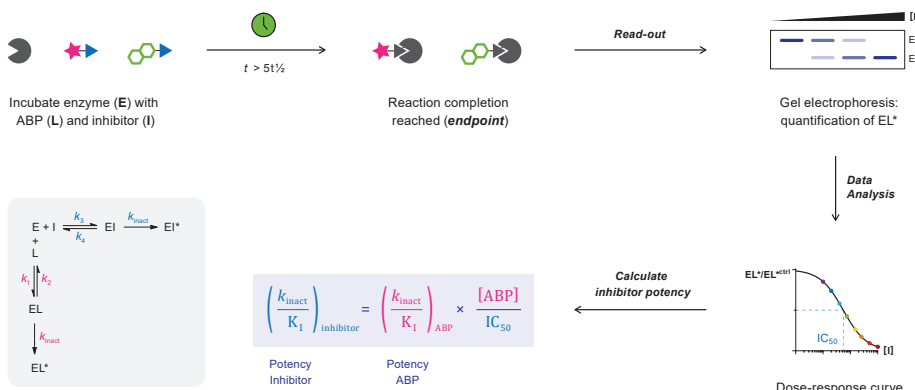


Figure 4 | Endpoint competition assay with irreversible covalent ABPs by Miyahisa *et al.*⁶⁹ Enzyme (E) is incubated with inhibitor (I) and irreversible ABP (L) until reaction completion/endpoint ($t > 5t\frac{1}{2}$): full covalent occupancy of enzyme by inhibitor (EI^*) or ABP (EL^*). Quantification of covalent enzyme–ABP adduct (EL^*) at different inhibitor concentrations enables calculation of an IC_{50} . The inhibitor k_{inact}/K_I is then calculated using the IC_{50} , ABP concentration and ABP k_{inact}/K_I , thus only requiring in-depth kinetic evaluation of the ABP. Read-out before reaction completion is reached ($t < 5t\frac{1}{2}$) results in overestimation of inhibitor k_{inact}/K_I because enzyme–ABP adduct formation is not yet complete.

challenging targets such as E2/E3 ligases, as long as the enzyme has a catalytic cysteine residue. We also foresee that Ub-ABPs may also be used in an endpoint competition assay methodology developed at Takeda (Figure 4).⁶⁹ Using a well-characterized irreversible covalent ABP, irreversible covalent inhibitor potency (k_{inact}/K_I) can be determined from the dose-response of covalent ABP occupancy, without needing to perform detailed kinetic measurements for each inhibitor. This method has the best accuracy when the potency of ABP and inhibitor is within a few orders of magnitude: the inhibitor will not be able to form a covalent enzyme–inhibitor adduct if the ABP is too potent (and fully occupies the enzyme in the enzyme–ABP adduct). The relatively slow adduct formation of Ub-Prg with the catalytic cysteine of E2/E3 ligases may be compatible with this method, though we expect Ub-Prg to be too potent to use with CysDUBs. We foresee a role for our Ub-ABPs with a substituted propargylamide warhead that have a slower reaction rate (e.g. Ub-2).

2.4. Mechanism of Thiol–Alkyne Addition

One of the central unanswered questions in 2013 was by which mechanism the thiol–alkyne addition proceeds (Figure 5). In Chapter 6, we detected the covalent adduct of USP16 with gem-dimethylated propargyl analogue Rho-Ub-5, which could not have occurred *via* an allenic intermediate. Subsequent bottom-up MS detection of adducts with deuterated ABP Ub-[D₂]-Prg provided conclusive evidence that the thiol–alkyne reaction does not involve an allenic intermediate, thereby excluding mechanism C (Figure 5C).⁷

Radical-mediated *mechanism A1* had already been excluded because thiol–yne coupling (TYC) generates the incorrect *anti*-Markovnikov-type adduct (**Figure 5A**). There is no conclusive evidence to exclude radical-initiated *mechanism A2*, but Markovnikov hydrothiolation of ynamides typically occurs *via* an allenic intermediate,⁷⁰⁻⁷¹ which was excluded in **Chapter 6**. The reactions with Ub-**Prg** in our work were performed in strict absence of light – thiyl radicals degrading pharmaceutical products are primarily formed upon exposure to light⁷²⁻⁷³ – but it should be noted that cysteinyl radicals have a role in redox regulation of enzyme activity, also in absence of light, as is utilized by specific enzyme classes (e.g. radical S-adenosylmethionine (SAM) enzymes, glycyl radical enzymes, and ribonucleotide reductases).⁷⁴ A more compelling argument is the observed lack of spontaneous CysDUB reactivity with Ub probes bearing an allyl warhead reported by Taylor *et al.*⁷⁵ The radical-initiated thiol–ene reaction to form a covalent CysDUB–ABP adduct had to be promoted by a radical initiator combined with UV irradiation: a higher intrinsic reactivity with the allyl warhead can be expected if spontaneous thiyl radical formation at the CysDUB cysteine was a common occurrence.

The remaining mechanisms for the thiol–alkyne addition are direct nucleophilic attack with concerted protonation (*mechanism B* in **Figure 5B**) or a stepwise mechanism with stabilization of the carbanion intermediate in the protease oxyanion hole (*mechanism D* in **Figure 5D**). Adduct formation has been detected with cysteine proteases (e.g. CysDUBs, cathepsins, M^{PRO}), which have a nucleophilic cysteine residue essential for proteolytic function that is part of a catalytic triad/dyad, and an oxyanion hole to stabilize an anionic (tetrahedral) intermediate,⁷⁶ which may indicate a role for the oxyanion hole in the thiol–alkyne addition (*mechanism D*). However, this is contradicted by the adduct formation with SENP1^{Q597A} mutant.⁴ An alternative explanation is that catalytic cysteines are simply more nucleophilic – and are typically deprotonated by neighboring basic residues generating the reactive thiolate anion – thus driving the observed reactivity. Unfortunately, CysDUB adduct formation with Rho-Ub-**18** bearing electron-deficient alkyne **18** (terminal CF₃) in **Chapter 6** does not provide evidence on the mechanism of the thiol–alkyne reaction: electron-deficient alkynes have the ability to internally stabilize an anionic intermediate, and may have a different reaction mechanism than nonactivated alkynes. This is confirmed by the higher intrinsic thiol reactivity with nontargeted thiols such as GSH.

The reaction mechanism impacts the possible application to other protein classes: if the selectivity for cysteine proteases over nontargeted thiols is due to stabilization of a carbanion intermediate in an oxyanion hole, then this would restrict adduct formation to (catalytic) cysteines in enzymes bearing an oxyanion hole. By itself, such selectivity is favored but it will restrict applications to catalytic protease cysteines as it will not be compatible with noncatalytic cysteine residues in other protein classes. Covalent adducts with alkyne derivatives 8RK57 and 8RK58 – based on approved covalent dual EGFR/HER2 inhibitor **neratinib** (Nerlynx, HKI-272) – were not observed in **Chapter 5**, suggestive of a role for the oxyanion hole. However, our alkyne derivatives not having a covalent binding mode does not rule out *mechanism B* as this might have been an inhibitor-specific issue: identification of a single covalent kinase inhibitor with an nonactivated alkyne warhead would still provide conclusive evidence that the thiol–alkyne adduct formation does not involve stabilization in an oxyanion hole. Importantly,

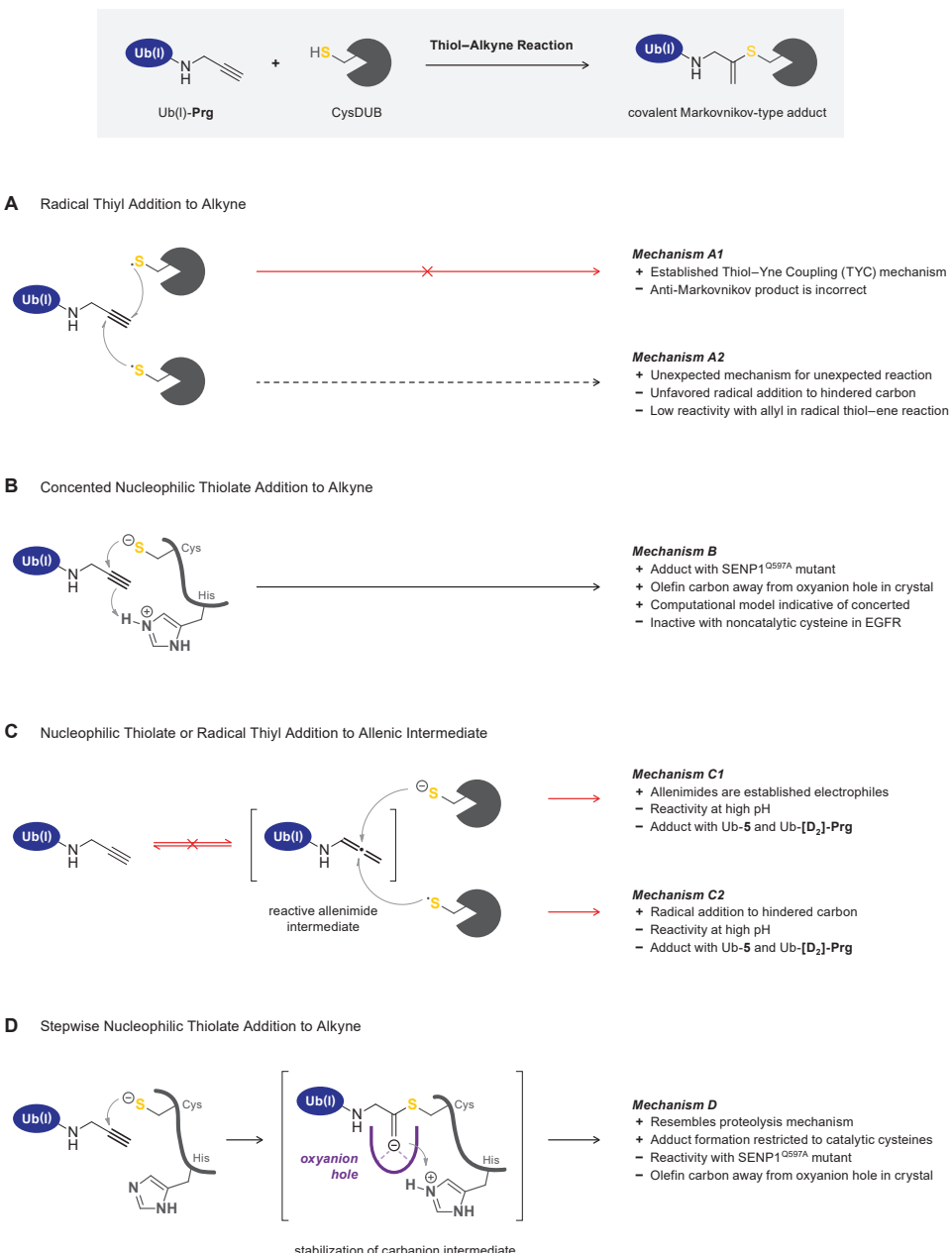


Figure 5 | Reaction mechanisms for Markovnikov-type thiovinylic adduct formation between a catalytic cysteine thiol(ate) and an alkyne warhead, and reasons supporting (+) or contradicting (−) this mechanism. **(A)** Direct addition of thiyl radical to the terminal alkyne is unlikely. **(B)** Proximity-driven *in situ* thiol-alkyne addition with concerted nucleophilic attack and protonation is a possible mechanism. **(C)** Tautomerization of the terminal alkyne moiety to a thiol-reactive allenimide intermediate at the enzyme active site prior to nucleophilic (*top*) or radical (*bottom*) addition has been excluded. **(D)** Stepwise enzyme-templated thiol(ate)-alkyne addition via stabilization of a secondary carbanion intermediate in the enzyme oxyanion hole is a possible mechanism.

a concerted reaction (*mechanism B*) does not necessarily mean that the *in situ* thiol–alkyne addition is compatible with noncatalytic cysteines: a histidine or another basic moiety in the vicinity of the cysteine may be required for concerted protonation, although adduct formation of SUMO2-Prg with SENP1^{H533A} suggests otherwise (*Chapter 1*).⁴

In *section 2.2* we already noticed that the terminal olefin carbon in crystal structures of covalently bound alkynes was pointing away from residues in the oxyanion hole,⁵² which is suggestive of concerted *mechanism B* (**Figure 5B**). MD-based analysis by Endres *et al.*⁷⁷ of the EM07–CatK structure suggests that the alkyne is positioned outside of the binding pocket. The likeliness of a concerted versus stepwise reaction mechanism has further been investigated by computational modelling. Dos Santos and co-workers employed (QM/MM) molecular dynamics reaction simulations to characterize the covalent reaction of CatK with nitrile ODN and alkyne derivatives EM04, EM05 and EM06 at an atomic level.⁷⁸ The crystal structure of the covalent CatK–EM07 adduct (PDB: 6QBS) was used as a starting point to build the computational models of the inhibitors in an enzymatic environment. Free-energy profiles of reaction with nitriles and alkynes showed that nucleophilic thiolate attack by catalytic Cys25 occurs in a concerted manner with proton transfer by the catalytic His162, supporting the *in situ* thiol–alkyne addition of *mechanism B*. The existence of an anionic intermediate could not be excluded for activated bromoalkyne EM06 but was deemed unlikely for ODN, EM04, and EM05. By comparison, (QM/MM) molecular dynamics reaction simulations of covalent adduct formation between ibrutinib and BTK Cys481 suggest a stepwise mechanism, initiated by direct proton transfer from Cys481 to the acrylamide warhead.⁷⁹ However, as with most computational models,^{80–81} potentially stabilizing interactions with Gln19 and other residues in the CatK oxyanion hole were disregarded.⁸² It is therefore not possible to definitively exclude *mechanism D* based on these computational results.

Altogether, the currently available data strongly indicates that nucleophilic attack on the alkyne, in a concerted or stepwise manner, is the most likely mechanism for the *in situ* thiol–alkyne reaction. Regardless of the mechanism, future efforts to unlock the full potential of the nonactivated alkyne as a latent electrophile in covalent drug development should focus on the development of nonactivated alkyne-based kinase inhibitors.

“And they lived happily ever after”

3. References

1. De Vita, E. 10 Years into the Resurgence of Covalent Drugs. *Future Med. Chem.* **2021**, *13*, 193-210. doi: 10.4155/fmc-2020-0236.
2. Mons, E.; Kim, R.Q.; Mulder, M.P.C. Technologies for Direct Detection of Covalent Protein–Drug Adducts. *Pharmaceutics* **2023**, *16*, 547. doi: 10.3390/ph16040547.
3. Ekkебus, R.; van Kasteren, S.I.; Kulathu, Y.; Scholten, A.; Berlin, I.; Geurink, P.P.; de Jong, A.; Goerdhayal, S.; Neefjes, J.; Heck, A.J.R.; Komander, D.; Ovaa, H. On Terminal Alkynes That Can React with Active-Site Cysteine Nucleophiles in Proteases. *J. Am. Chem. Soc.* **2013**, *135*, 2867-2870. doi: 10.1021/ja309802n.
4. Sommer, S.; Weikart, N.D.; Linne, U.; Mootz, H.D. Covalent Inhibition of SUMO and Ubiquitin-Specific Cysteine Proteases by an In Situ Thiol-Alkyne Addition. *Bioorg. Med. Chem.* **2013**, *21*, 2511-2517. doi: 10.1016/j.bmc.2013.02.039.
5. Mons, E.; Roet, S.; Kim, R.Q.; Mulder, M.P.C. A Comprehensive Guide for Assessing Covalent Inhibition in Enzymatic Assays Illustrated with Kinetic Simulations. *Curr. Protoc.* **2022**, *2*, e419. doi: 10.1002/cp21.419.
6. Mons, E.; Jansen, I.D.C.; Loboda, J.; van Doodewaerd, B.R.; Hermans, J.; Verdoes, M.; van Boeckel, C.A.A.; van Veelen, P.A.; Turk, B.; Turk, D.; Ovaa, H. The Alkyne Moiety as a Latent Electrophile in Irreversible Covalent Small Molecule Inhibitors of Cathepsin K. *J. Am. Chem. Soc.* **2019**, *141*, 3507-3514. doi: 10.1021/jacs.8b11027.
7. Mons, E.; Kim, R.Q.; van Doodewaerd, B.R.; van Veelen, P.A.; Mulder, M.P.C.; Ovaa, H. Exploring the Versatility of the Covalent Thiol–Alkyne Reaction with Substituted Propargyl Warheads: A Deciding Role for the Cysteine Protease. *J. Am. Chem. Soc.* **2021**, *143*, 6423-6433. doi: 10.1021/jacs.0c10513.
8. Drake, M.T.; Clarke, B.L.; Oursler, M.J.; Khosla, S. Cathepsin K Inhibitors for Osteoporosis: Biology, Potential Clinical Utility, and Lessons Learned. *Endocr. Rev.* **2017**, *38*, 325-350. doi: 10.1210/er.2015-1114.
9. Millard, A. Merck & Co. Drops Osteoporosis Drug Odanacatib. *Nat. Rev. Drug Discov.* **2016**, *15*, 669-669. doi: 10.1038/nrd.2016.207.
10. Garber, K. Two Pioneering Osteoporosis Drugs Finally Approach Approval. *Nat. Rev. Drug Discov.* **2016**, *15*, 445-446. doi: 10.1038/nrd.2016.132.
11. Lowe, D. Cathepsin K: A Promising Target Fades Out. *In the Pipeline* [Online]. 2016, 30 September. <https://www.science.org/content/blog-post/cathepsin-k-promising-target-fades-out>.
12. Johnell, O.; Kanis, J. Epidemiology of Osteoporotic Fractures. *Osteoporos. Int.* **2005**, *16*, S3-S7. doi: 10.1007/s00198-004-1702-6.
13. U.S. Department of Health and Human Services. *Bone Health and Osteoporosis: A Report of the Surgeon General*. U.S. Department of Health and Human Services, Office of the Surgeon General: Rockville (MD), 2004. <https://www.ncbi.nlm.nih.gov/books/NBK45513/>.
14. McClung, M.R.; O'Donoghue, M.L.; Papapoulos, S.E.; Bone, H.; Langdahl, B.; Saag, K.G.; Reid, I.R.; Kiel, D.P.; Cavallari, I.; Bonaca, M.P., et al. Odanacatib for the Treatment of Postmenopausal Osteoporosis: Results of the LOFT Multicentre, Randomised, Double-Blind, Placebo-Controlled Trial and LOFT Extension Study. *Lancet Diabetes Endocrinol.* **2019**, *7*, 899-911. doi: 10.1016/S2213-8587(19)30346-8.
15. Verbovsek, U.; Van Noorden, C.J.F.; Lah, T.T. Complexity of Cancer Protease Biology: Cathepsin K Expression and Function in Cancer Progression. *Semin. Cancer Biol.* **2015**, *35*, 71-84. doi: 10.1016/j.semcancer.2015.08.010.
16. Dai, R.; Wu, Z.; Chu, H.Y.; Lu, J.; Lyu, A.; Liu, J.; Zhang, G. Cathepsin K: The Action In and Beyond Bone. *Front. Cell Dev. Biol.* **2020**, *8*, 433. doi: 10.3389/fcell.2020.00433.
17. Guo, R.; Hua, Y.; Rogers, O.; Brown, T.E.; Ren, J.; Nair, S. Cathepsin K Knockout Protects Against Cardiac Dysfunction in Diabetic Mice. *Sci. Rep.* **2017**, *7*, 8703. doi: 10.1038/s41598-017-09037-z.
18. Brömmé, D.; Panwar, P.; Turan, S. Cathepsin K Osteoporosis Trials, Pycnodystostosis and Mouse Deficiency Models: Commonalities and Differences. *Expert Opin. Drug Discov.* **2016**, *11*, 457-472. doi: 10.1517/17460441.2016.1160884.
19. Mijanović, O.; Jakovleva, A.; Branković, A.; Zdravkova, K.; Pualic, M.; Belozerskaya, T.A.; Nikitkina, A.I.; Parodi, A.; Zamyatnina, A.A. Cathepsin K in Pathological Conditions and New Therapeutic and Diagnostic Perspectives. *Int. J. Mol. Sci.* **2022**, *23*, 13762. doi: 10.3390/ijms232213762.
20. Rothwell, P.M. Atherothrombosis and Ischaemic Stroke. *Br. Med. J.* **2007**, *334*, 379. doi: 10.1136/bmj.38964.489051.80.
21. Samokhin, A.O.; Wong, A.; Saftig, P.; Brömmé, D. Role of Cathepsin K in Structural Changes in Brachiocephalic Artery During Progression of Atherosclerosis in apoE-Deficient Mice. *Atherosclerosis* **2008**, *200*, 58-68. doi: 10.1016/j.atherosclerosis.2007.12.047.
22. Leung, P.; Pickarski, M.; Zhuo, Y.; Masarachia, P.J.; Duong, L.T. The Effects of the Cathepsin K Inhibitor Odanacatib on Osteoclastic Bone Resorption and Vesicular Trafficking. *Bone* **2011**, *49*, 623-635. doi: 10.1016/j.bone.2011.06.014.
23. Recker, R.; Dempster, D.; Langdahl, B.; Giezek, H.; Clark, S.; Ellis, G.; de Villiers, T.; Valter, I.; Zerbini, C.A.F.; Cohn, D.; Santora, A.; Duong, L.T. Effects of Odanacatib on Bone Structure and Quality in Postmenopausal Women With Osteoporosis: 5-Year Data From the Phase 3 Long-Term Odanacatib Fracture Trial (LOFT) and Its Extension. *J. Bone Miner. Res.* **2020**, *35*, 1289-1299. doi: 10.1002/jbm.3994.
24. Reddy, S.V. Etiology of Paget's Disease and Osteoclast Abnormalities. *J. Cell. Biochem.* **2004**, *93*, 688-696. doi: 10.1002/jcb.20256.
25. AlQranei, M.S.; Chellaiah, M.A. Osteoclastogenesis in Periodontal Diseases: Possible Mediators and Mechanisms. *J. Oral Biosci.* **2020**, *62*, 123-130. doi: 10.1016/j.job.2020.02.002.
26. Behl, T.; Chadha, S.; Sehgal, A.; Singh, S.; Sharma, N.; Kaur, R.; Bhatia, S.; Al-Harrasi, A.; Chigurupati, S.; Alhowail, A.; Bungau, S. Exploring the Role of Cathepsin in Rheumatoid Arthritis. *Saudi J. Biol. Sci.* **2022**, *29*, 402-410. doi: 10.1016/j.sjbs.2021.09.014.
27. Zhu, X.; Chan, Y.T.; Yung, P.S.H.; Tuan, R.S.; Jiang, Y. Subchondral Bone Remodeling: A Therapeutic Target for Osteoarthritis. *Front. Cell Dev. Biol.* **2021**, *8*, 607764. doi: 10.3389/fcell.2020.607764.
28. Shahryar, N.; Bassam, M. Periprosthetic Osteolysis: Genetics, Mechanisms and Potential Therapeutic Interventions. *Can. J. Surg.* **2012**, *55*, 408. doi: 10.1503/cjs.003711.
29. Hecht, M.; von Metzler, I.; Sack, K.; Kaiser, M.; Sezer, O. Interactions of Myeloma Cells with Osteoclasts Promote Tumour Expansion and Bone Degradation Through Activation of a Complex Signalling Network and Upregulation of Cathepsin K, Matrix Metalloproteinases (MMPs) and Urokinase Plasminogen Activator (uPA). *Exp. Cell Res.* **2008**, *314*, 1082-1093. doi: 10.1016/j.yexcr.2007.10.021.
30. Wang, M.; Xia, F.; Wei, Y.; Wei, X. Molecular Mechanisms and Clinical Management of Cancer Bone Metastasis. *Bone Res.* **2020**, *8*, 30. doi: 10.1038/s41413-020-00105-1.
31. Lindeman, J.H.N.; Hanemaaijer, R.; Mulder, A.; Dijkstra, P.D.S.; Szuhal, K.; Bromme, D.; Verheijen, J.H.; Hogendoorn, P.C.W. Cathepsin K Is the Principal Protease in Giant Cell Tumor of Bone. *Am. J. Pathol.* **2004**, *165*, 593-600. doi: 10.1016/S0002-9440(10)63323-8.
32. Sousa, S.; Clézardin, P. Bone-Targeted Therapies in Cancer-Induced Bone Disease. *Calcif. Tissue Int.* **2018**, *102*, 227-250. doi: 10.1007/s00223-017-0353-5.
33. D'Oronzo, S.; Coleman, R.; Brown, J.; Silvestris, F. Metastatic Bone Disease: Pathogenesis and Therapeutic Options: Up-Date on Bone Metastasis Management. *J. Bone Oncol.* **2019**, *15*, 100205. doi: 10.1016/j.jbo.2018.10.004.

34. Skjødt, M.K.; Frost, M.; Abrahamsen, B. Side Effects of Drugs for Osteoporosis and Metastatic Bone Disease. *Br. J. Clin. Pharmacol.* **2019**, *85*, 1063–1071. doi: 10.1111/bcp.13759.

35. Gralow, J.; Tripathy, D. Managing Metastatic Bone Pain: The Role of Bisphosphonates. *J. Pain Symptom Manage.* **2007**, *33*, 462–472. doi: 10.1016/j.jpainsymman.2007.01.001.

36. Ramaswamy, B.; Shapiro, C.L. Bisphosphonates in the Prevention and Treatment of Bone Metastases. *Oncology (Williston Park N.Y.)* **2003**, *17*, 1261–1270. <https://www.cancernetwork.com/view/bisphosphonates-prevention-and-treatment-bone-metastases>

37. Littlewood-Evans, A.J.; Bilbe, G.; Bowler, W.B.; Farley, D.; Włodarski, B.; Kokubo, T.; Inaoka, T.; Sloane, J.; Evans, D.B.; Gallagher, J.A. The Osteoclast-Associated Protease Cathepsin K Is Expressed in Human Breast Carcinoma. *Cancer Res.* **1997**, *57*, 5386–5390.

38. Andrade, S.S.; Gouveia, I.E.; Silva, M.C.C.; Castro, E.D.; de Paula, C.A.A.; Okamoto, D.; Oliveira, L.; Peres, G.B.; Ottaiano, T.; Facina, G.; Nazário, A.C.P.; Campos, A.H.J.F.M.; Paredes-Gamero, E.J.; Juliano, M.; da Silva, I.D.C.G.; Oliva, M.L.V.; Girão, M.J.B.C. Cathepsin K Induces Platelet Dysfunction and Affects Cell Signaling in Breast Cancer - Molecularly Distinct Behavior of Cathepsin K in Breast Cancer. *BMC Cancer* **2016**, *16*, 173. doi: 10.1186/s12885-016-2203-7.

39. Brubaker, K.D.; Vessella, R.L.; True, L.D.; Thomas, R.; Corey, E. Cathepsin K mRNA and Protein Expression in Prostate Cancer Progression. *J. Bone Miner. Res.* **2003**, *18*, 222–230. doi: 10.1359/jbmr.2003.18.2.222.

40. Verbovšek, U.; Motaln, H.; Rotter, A.; Atai, N.A.; Gruden, K.; Van Noorden, C.J.F.; Lah, T.T. Expression Analysis of All Protease Genes Reveals Cathepsin K to Be Overexpressed in Glioblastoma. *PLoS ONE* **2014**, *9*, e111819. doi: 10.1371/journal.pone.0111819.

41. Lisabeth, L.; Bushnell, C. Stroke Risk in Women: The Role of Menopause and Hormone Therapy. *Lancet Neurol.* **2012**, *11*, 82–91. doi: 10.1016/S1474-4422(11)70269-1.

42. Jørgensen, L.; Engstad, T.; Jacobsen, B.K. Bone Mineral Density in Acute Stroke Patients. *Stroke* **2001**, *32*, 47–51. doi: 10.1161/01.STR.32.1.47.

43. Burke, A.P.; Farb, A.; Malcom, G.; Virmani, R. Effect of Menopause on Plaque Morphologic Characteristics in Coronary Atherosclerosis. *Am. Heart J.* **2001**, *141*, 558–562. doi: 10.1067/mhj.2001.109946.

44. Liang, W.; Wang, F.; Chen, Q.; Dai, J.; Escara-Wilke, J.; Keller, E.T.; Zimmermann, J.; Hong, N.; Lu, Y.; Zhang, J. Targeting Cathepsin K Diminishes Prostate Cancer Establishment and Growth in Murine Bone. *J. Cancer Res. Clin. Oncol.* **2019**, *145*, 1999–2012. doi: 10.1007/s00432-019-02950-y.

45. Le Gall, C.; Bonnelye, E.; Clézardin, P. Cathepsin K Inhibitors as Treatment of Bone Metastasis. *Curr. Opin. Support. Palliat. Care* **2008**, *2*, 218–222. doi: 10.1097/SPC.0b013e32830baea9.

46. Le Gall, C.; Bellahcène, A.; Bonnelye, E.; Gasser, J.A.; Castronovo, V.; Green, J.; Zimmermann, J.; Clézardin, P. A Cathepsin K Inhibitor Reduces Breast Cancer-Induced Osteolysis and Skeletal Tumor Burden. *Cancer Res.* **2007**, *67*, 9894–9902. doi: 10.1158/0008-5472.Can-06-3940.

47. Duong, L.T.; Wesolowski, G.A.; Leung, P.; Oballa, R.; Pickarski, M. Efficacy of a Cathepsin K Inhibitor in a Preclinical Model for Prevention and Treatment of Breast Cancer Bone Metastasis. *Mol. Cancer Ther.* **2014**, *13*, 2898–2909. doi: 10.1158/1535-7163.Mct-14-0253.

48. Jensen, A.B.; Wynne, C.; Ramirez, G.; He, W.; Song, Y.; Berd, Y.; Wang, H.; Mehta, A.; Lombardi, A. The Cathepsin K Inhibitor Odanacatib Suppresses Bone Resorption in Women With Breast Cancer and Established Bone Metastases: Results of a 4-Week, Double-Blind, Randomized, Controlled Trial. *Clin. Breast Cancer* **2010**, *10*, 452–458. doi: 10.3816/CBC.2010.n.059.

49. Law, S.; Andrault, P.-M.; Aguda, A.H.; Nguyen, N.T.; Kruglyak, N.; Brayer, G.D.; Brömmel, D. Identification of Mouse Cathepsin K Structural Elements that Regulate the Potency of Odanacatib. *Biochem. J.* **2017**, *474*, 851–864. doi: 10.1042/BCJ20160985.

50. Fantozzi, A.; Christofori, G. Mouse Models of Breast Cancer Metastasis. *Breast Cancer Res.* **2006**, *8*, 212. doi: 10.1186/bcr1530.

51. Behring, L.; Ruiz-Gómez, G.; Trapp, C.; Morales, M.; Wodtke, R.; Köckerling, M.; Kopka, K.; Pisabarro, M.T.; Pietzsch, J.; Löser, R. Dipeptide-Derived Alkynes as Potent and Selective Irreversible Inhibitors of Cysteine Cathepsins. *J. Med. Chem.* **2023**, *66*, 3818–3851. doi: 10.1021/acs.jmedchem.2c01360.

52. Brewitz, L.; Dumjahn, L.; Zhao, Y.; Owen, C.D.; Laidlaw, S.M.; Malla, T.R.; Nguyen, D.; Lukacik, P.; Salah, E.; Crawshaw, A.D.; Warren, A.J.; Trincao, J.; Strain-Damerell, C.; Carroll, M.W.; Walsh, M.A.; Schofield, C.J. Alkyne Derivatives of SARS-CoV-2 Main Protease Inhibitors Including Nirmatrelvir Inhibit by Reacting Covalently with the Nucleophilic Cysteine. *J. Med. Chem.* **2023**, *66*, 2663–2680. doi: 10.1021/acs.jmedchem.2c01627.

53. Ngo, C.; Fried, W.; Aliyari, S.; Feng, J.; Qin, C.; Zhang, S.; Yang, H.; Shanaa, J.; Feng, P.; Cheng, G.; Chen, X.S.; Zhang, C. Alkyne as a Latent Warhead to Covalently Target SARS-CoV-2 Main Protease. *J. Med. Chem.* **2023**, *66*, 12237–12248. doi: 10.1021/acs.jmedchem.3c00810.

54. Di Sarno, V.; Lauro, G.; Musella, S.; Ciaglia, T.; Vestuto, V.; Sala, M.; Scala, M.C.; Smaldone, G.; Di Matteo, F.; Novi, S.; Tecce, M.F.; Moltedo, O.; Bifulco, G.; Campiglia, P.; Gomez-Monterrey, I.M.; Snoeck, R.; Andrei, G.; Ostacolo, C.; Bertamino, A. Identification of a Dual Acting SARS-CoV-2 Proteases Inhibitor Through In Silico Design and Step-By-Step Biological Characterization. *Eur. J. Med. Chem.* **2021**, *226*, 113863. doi: 10.1016/j.ejmech.2021.113863.

55. Tan, B.; Sacco, M.; Tan, H.; Li, K.; Joyce, R.; Zhang, X.; Chen, Y.; Wang, J. Exploring Diverse Reactive Warheads for the Design of SARS-CoV-2 Main Protease Inhibitors. *Eur. J. Med. Chem.* **2023**, *259*, 115667. doi: 10.1016/j.ejmech.2023.115667.

56. Deng, W.; Chen, X.; Jiang, K.; Song, X.; Huang, M.; Tu, Z.-C.; Zhang, Z.; Lin, X.; Ortega, R.; Patterson, A.V.; Small, J.B.; Ding, K.; Chen, S.; Chen, Y.; Lu, X. Investigation of Covalent Warheads in the Design of 2-Aminopyrimidine-based FGFR4 Inhibitors. *ACS Med. Chem. Lett.* **2021**, *12*, 647–652. doi: 10.1021/acsmedchemlett.1c00052.

57. Witting, K.F.; van der Heden van Noort, G.J.; Kofoed, C.; Talavera Ormeño, C.; el Atmioui, D.; Mulder, M.P.C.; Ovaa, H. Generation of the UFM1 Toolkit for Profiling UFM1-Specific Proteases and Ligases. *Angew. Chem. Int. Ed.* **2018**, *57*, 14164–14168. doi: 10.1002/anie.201809232.

58. Basters, A.; Geurink, P.P.; Röcker, A.; Witting, K.F.; Tadayon, R.; Hess, S.; Semrau, M.S.; Storici, P.; Ovaa, H.; Knobeloch, K.-P.; Fritz, G. Structural Basis of the Specificity of USP18 toward ISG15. *Nat. Struct. Mol. Biol.* **2017**, *24*, 270–278. doi: 10.1038/nsmb.3371.

59. Huppelschoten, Y.; Buchardt, J.; Nielsen, T.E.; Sapmaz, A.; van der Heden van Noort, G.J. Total Chemical Synthesis of LC3A and LC3B Activity-Based Probes. *Biomedicines* **2023**, *11*, 884. doi: 10.3390/biomedicines11030884.

60. Gjonaj, L.; Sapmaz, A.; González-Prieto, R.; Vertegaal, A.C.O.; Flierman, D.; Ovaa, H. USP7: Combining Tools towards Selectivity. *Chem. Commun.* **2019**, *55*, 5075–5078. doi: 10.1039/C9CC00969H.

61. Gjonaj, L.; Sapmaz, A.; Flierman, D.; Janssen, G.M.C.; van Veelen, P.A.; Ovaa, H. Development of a DUB-Selective Fluorogenic Substrate. *Chem. Sci.* **2019**, *10*, 10290–10296. doi: 10.1039/C9SC02226K.

62. Hewitt, C.S.; Das, C.; Flaherty, D.P. Rational Development and Characterization of a Ubiquitin Variant with Selectivity for Ubiquitin C-Terminal Hydrolase L3. *Biomolecules* **2022**, *12*, 62. doi: 10.3390/biom12010062.

63. Flierman, D.; van der Heden van Noort, G.J.; Ekkebus, R.; Geurink, P.P.; Mevissen, T.E.T.; Hospenthal, M.K.; Komander, D.; Ovaa, H. Non-hydrolyzable Diubiquitin Probes Reveal Linkage-Specific Reactivity of Deubiquitylating Enzymes Mediated by S2 Pockets. *Cell Chem. Biol.* **2016**, *23*, 472–482. doi: 10.1016/j.chembiol.2016.03.009.

64. Hewings, D.S.; Heideker, J.; Ma, T.P.; AhYoung, A.P.; El Oualid, F.; Amore, A.; Costakes, G.T.; Kirchhofer, D.; Brasher, B.; Pillow, T.; Popovych, N.; Maurer, T.; Schwerdtfeger, C.; Forrest, W.F.; Yu, K.; Flygare, J.; Bogyo, M.; Wertz, I.E. Reactive-Site-Centric Chemoproteomics Identifies a Distinct Class of Deubiquitinase Enzymes. *Nat. Commun.* **2018**, *9*, 1162. doi: 10.1038/s41467-018-03511-6.

65. Pinto-Fernández, A.; Davis, S.; Schofield, A.B.; Scott, H.C.; Zhang, P.; Salah, E.; Mathea, S.; Charles, P.D.; Damianou, A.; Bond, G.; Fischer, R.; Kessler, B.M. Comprehensive Landscape of Active Deubiquitinating Enzymes Profiled by Advanced Chemoproteomics. *Front. Chem.* **2019**, *7*, 592. doi: 10.3389/fchem.2019.00592.

66. Nair, R.M.; Seenivasan, A.; Liu, B.; Chen, D.; Lowe, E.D.; Lorenz, S. Reconstitution and Structural Analysis of a HECT Ligase-Ubiquitin Complex via an Activity-Based Probe. *ACS Chem. Biol.* **2021**, *16*, 1615–1621. doi: 10.1021/acschembio.1c00433.

67. Franklin, T.G.; Brzovic, P.S.; Pruneda, J.N. Bacterial Mimicry of Eukaryotic HECT Ubiquitin Ligation. *bioRxiv* **2023**. doi: 10.1101/2023.06.05.543783.

68. Geurink, P.P.; van Tol, B.D.M.; van Dalen, D.; Brundel, P.J.G.; Mevissen, T.E.T.; Pruneda, J.N.; Elliott, P.R.; van Tilburg, G.B.A.; Komander, D.; Ovaa, H. Development of Diubiquitin-Based FRET Probes To Quantify Ubiquitin Linkage Specificity of Deubiquitinating Enzymes. *ChemBioChem* **2016**, *17*, 816–820. doi: 10.1002/cbic.201600017.

69. Miyahisa, I.; Sameshima, T.; Hixon, M.S. Rapid Determination of the Specificity Constant of Irreversible Inhibitors (k_{inact}/K_i) by Means of an Endpoint Competition Assay. *Angew. Chem. Int. Ed.* **2015**, *54*, 14099–14102. doi: 10.1002/anie.201505800.

70. Takeuchi, Y.; Fujiwara, T.; Shimone, Y.; Miyatake, H.; Satoh, T.; Kirk, K.L.; Hori, H. Possible Involvement of Radical Intermediates in the Inhibition of Cysteine Proteases by Allenyl Esters and Amides. *Bioorg. Med. Chem. Lett.* **2008**, *18*, 6202–6205. doi: 10.1016/j.bmcl.2008.10.007.

71. Castarlenas, R.; Di Giuseppe, A.; Pérez-Torrente, J.J.; Oro, L.A. The Emergence of Transition-Metal-Mediated Hydrothiolation of Unsaturated Carbon–Carbon Bonds: A Mechanistic Outlook. *Angew. Chem. Int. Ed.* **2012**, *52*, 211–222. doi: 10.1002/anie.201205468.

72. Dénès, F.; Pichowicz, M.; Povie, G.; Renaud, P. Thiyil Radicals in Organic Synthesis. *Chem. Rev.* **2014**, *114*, 2587–2693. doi: 10.1021/cr400441m.

73. Schöneich, C. Thiyil Radical Reactions in the Chemical Degradation of Pharmaceutical Proteins. *Molecules* **2019**, *24*, 4357. doi: 10.3390/molecules24234357.

74. McLean, J.T.; Benny, A.; Nolan, M.D.; Swinand, G.; Scanlan, E.M. Cysteinyl Radicals in Chemical Synthesis and in Nature. *Chem. Soc. Rev.* **2021**, *50*, 10857–10894. doi: 10.1039/D1CS00254F.

75. Taylor, N.C.; Hessman, G.; Kramer, H.B.; McGouran, J.F. Probing Enzymatic Activity – A Radical Approach. *Chem. Sci.* **2020**, *11*, 2967–2972. doi: 10.1039/C9SC05258E.

76. Hanpude, P.; Bhattacharya, S.; Dey, A.K.; Maiti, T.K. Deubiquitinating Enzymes in Cellular Signaling and Disease Regulation. *IUBMB Life* **2015**, *67*, 544–555. doi: 10.1002/iub.1402.

77. Endres, E.; Chen, N.Y.; Sotriffer, C. MD-Based Assessment of Covalent Inhibitors in Noncovalent Association Complexes: Learning from Cathepsin K as a Test Case. *J. Chem. Inf. Model.* **2023**, *63*, 3186–3197. doi: 10.1021/acs.jcim.3c00061.

78. Dos Santos, A.M.; Oliveira, A.R.S.; da Costa, C.H.S.; Kenny, P.W.; Montanari, C.A.; Varela, J.J.G. Júnior; Lameira, J. Assessment of Reversibility for Covalent Cysteine Protease Inhibitors Using Quantum Mechanics/Molecular Mechanics Free Energy Surfaces. *J. Chem. Inf. Model.* **2022**, *62*, 4083–4094. doi: 10.1021/acs.jcim.2c00466.

79. Voice, A.T.; Tresadern, G.; Twidle, R.M.; van Vlijmen, H.; Mulholland, A.J. Mechanism of Covalent Binding of Ibrutinib to Bruton's Tyrosine Kinase Revealed by QM/MM Calculations. *Chem. Sci.* **2021**, *12*, 5511–5516. doi: 10.1039/D0SC06122K.

80. Quesne, M.G.; Ward, R.A.; De Visser, S.P. Cysteine Protease Inhibition by Nitrile-Based Inhibitors: a Computational Study. *Front. Chem.* **2013**, *1*, 39. doi: 10.3389/fchem.2013.00039.

81. Bonatto, V.; Lameiro, R.F.; Rocho, F.R.; Lameira, J.; Leitão, A.; Montanari, C.A. Nitriles: An Attractive Approach to the Development of Covalent Inhibitors. *RSC Med. Chem.* **2023**, *14*, 201–217. doi: 10.1039/D2MD00204C.

82. Ma, S.; Devi-Kesavan, L.S.; Gao, J. Molecular Dynamics Simulations of the Catalytic Pathway of a Cysteine Protease: A Combined QM/MM Study of Human Cathepsin K. *J. Am. Chem. Soc.* **2007**, *129*, 13633–13645. doi: 10.1021/ja074222+.



Epilogue



Nederlandse Samenvatting
Curriculum Vitae
List of Publications
Acknowledgements

Alkynen in Covalente Enzym Remmers: Val in het Kinetische Konijnenhol

Er was eens... een tijd waarin remmers met een mogelijke covalent bindingsmechanisme actief werden uitgesloten van industriële geneesmiddelenontwikkelingsprogramma's, ondanks dat er genoeg veilige en veelgebruikte medicijnen zijn waarvan pas later bleek dat ze onomkeerbaar en covalent binden aan het te remmen eiwit. In **Hoofdstuk 1** laten we zien hoe dit sentiment in de afgelopen twee decennia langzaam is omgeslagen, omdat het met covalente remmers mogelijk is om resistentie tegen bestaande medicijnen te overwinnen en voorheen onaantastbare oncogenen te remmen. Dat heeft geleid tot de toegenomen ontwikkeling van gericht covalente remmers (TCI's): medicijnen die een strategisch geplaatst elektrofiel bevatten dat een covalente binding kan vormen met een nucleofiel aminozuur (zoals cysteïne of serine) in het doeleiwit. Een belangrijke factor in het verbeteren van de veiligheid van TCI's is de identificatie van nieuwe chemische groepen die reactief zijn met een cysteïne in het doeleiwit, maar niet te reactief zijn met andere thiolen in de cel. Een verrassende kandidaat hiervoor is het niet-geactiveerde alkyn, of acetyleen, aangezien algemeen geaccepteerd wordt dat niet-geactiveerde alkynen 'inert' zijn ten opzichte van cellulaire componenten onder fysiologische omstandigheden. In 2013 ontdekte de onderzoeksgruppe van Ovaa en Mootz per toeval, en onafhankelijk van elkaar, dat **Ub(I)-Prg** – bedoeld als bouwsteen voor protease-bestendige niet-hydrolyseerbare substraten – een covalent Markovnikov-type thiovinyll adduct kan vormen met het katalytische cysteïne van **Ub(I)-proteases**. Covalente adducten werden echter alleen gedetecteerd wanneer het gepropargyleerde peptide een relatief groot herkenningselement had ($>1,8$ kDa), en introductie van substituenten op het propargylamide hinderden de vorming van adducten met **UCHL3**. In dit proefschrift verkennen we de restricties en veelzijdigheid van de nieuwe *in situ* thiol-alkynadditie: van niet-geactiveerde alkynen als reactieve groep in irreversibele covalente geneesmiddelen tot gesubstitueerde propargyl-analoga in chemische biologie reagentia.

Er zijn veel manieren om indirect van de (tijdsafhankelijke) afname van intact drug en/of eiwit af te leiden dat ze mogelijk een covalente interactie ondergaan, maar uiteindelijk levert alleen de experimentele detectie van het covalente eiwit-medicijn adduct sluitend bewijs op van een covalent bindingsmechanisme. In **Hoofdstuk 2** worden technologieën besproken die een strikt onderscheid kunnen maken tussen een covalent adduct en een niet-covalent complex. De experimentele validatie van een covalent adduct is gebaseerd op een detecteerbare verandering die alleen plaatsvindt bij een covalente binding zoals een toename van de massa (MS), onafgebroken elektronendichtheid tussen het eiwit en het medicijn (eiwitkristallografie), een verandering in intrinsieke spectroscopische eigenschappen, verschuiving van de chemische verschuiving δ (NMR), detectie van eiwitten gemodificeerd met een fluorescente ABP die afgeleid is van het geneesmiddel (gel-eleketroforese-gebaseerde/homogene ABPP), of de verrijking van eiwitten die covalent gemodificeerd zijn met een geneesmiddel-afgeleide ABP (chemische proteomics ABPP).

In **Hoofdstuk 3** zijn we vervolgens dieper ingegaan op het principe dat er andere kinetische parameters gebruikt worden om de sterkte van covalente remmers te vergelijken, waarbij we ons met name gericht hebben op het verband tussen experimentele meetcondities en de algebraïsche modellen die gebruikt worden om die kinetische parameters te bepalen. Een covalent adduct vormt niet instantaan (op een kinetische tijdschaal), dus met het verstrijken van langere (pre)incubatietijden zal de remmende werking toenemen en deze tijdsafhankelijke enzym activiteit kan in algebraïsche modellen ingepast worden om zo de relevante kinetische parameters te achterhalen. In deze algebraïsche formules zijn echter aannames – die zelden explicet vermeld worden – ingebet ten opzichte van de experimentele meetcondities. Met behulp van kinetische simulatiescripts was het mogelijk om de wiskundige formules te vertalen naar gesimuleerde meetresultaten op basis van vooraf ingestelde testcondities, en zo te valideren wat de consequenties zijn als er niet voldaan wordt aan de algebraïsche aannames. Deze simulaties zijn vervolgens gebruikt om een uitgebreide, complete gids samen te stellen voor de evaluatie van covalente remmers in enzymatische metingen: vier stapsgewijze experimentele protocollen met bijbehorende data analyse protocollen afgestemd op de covalente bindingsmodi.

In **Hoofdstuk 4** laten we zien dat een klein herkenningselement (<600 Da) voldoende is voor de *in situ* thiol-alkynreactie. Alkyn-analogen van odanacatib (ODN) – een reversibel covalente remmer van cathepsine K,

het belangrijkste cysteïneprotease bij botresorptie – werden verkregen door het reactieve nitril te vervangen door een iso-elektrische alkyn. Propargylderivaat EM04 heeft een >500 keer hogere IC₅₀ voor CatK remming vergeleken met ODN, maar verdere biochemische evaluatie liet zien dat de niet-geactiveerde alkyn-analogen een irreversibele covalente binding vormen met hCatK (zonder de ongewenste covalente binding van nucleofielen in bijvoorbeeld GSH of cysteïne). Eiwitkristallografie van het covalente adduct met EM07, een derivaat waarbij een fluor is vervangen door een waterstof atoom, bevestigde de vorming van een covalente Markovnikov-type thiovinylibinding tussen het EM07-alkyn en het katalytische Cys25 van hCatK. De vorming van het covalente CatK-alkyn adduct is verrassend langzaam, wat het ongenschijnlijke verlies aan potentie in de initiële activiteitmetingen zou kunnen verklaren. In menselijke osteoclastculturen was EM04 slechts vijf keer minder potent dan ODN in het remmen van botresorptie activiteit, en was er in beide osteoclast culturen een toename te zien van het niveau van volwassen, actief CatK ten opzichte van de onbehandelde osteoclasten. De observatie dat een onomkeerbare qABP in staat was om ODN te verdringen, waardoor er juist meer actief CatK te zien is dan in de onbehandelde controles, verklaart mogelijk waarom er vaak een hogere botresorptie gezien wordt na afloop van een behandeling met ODN (in patiënten en muizen).

In **Hoofdstuk 5** is onderzocht of de niet-geactiveerde alkynen ook toegepast kunnen worden om niet-katalytische cysteïnes te binden. Het reactieve acrylamide in covalente kinaseremmer neratinib, dat een covalente binding vormt met het niet-katalytische Cys797 in de ATP-bindingslocatie van EGFR, werd vervangen door een niet-geactiveerd alkyn in 8RK57 en 8RK58. Helaas resulteerde dit niet in detectie van een covalent adduct met recombinant EGFR-kinasedomein, ondanks dat inhibitie van cellulaire EGFR (auto)fosforylering erop wees dat er sprake zou zijn van een onomkeerbaar bindingsmechanisme. Het is onwaarschijnlijk dat alkyn-analogen 8RK57 en 8RK58 een covalent bindingsmechanisme hebben, wat te wijten kan zijn aan onjuiste oriëntatie van het alkyn ten opzicht van het cysteïne-thiol, maar het is ook mogelijk dat de thiol–alkynreactie in het algemeen niet toepasbaar is op niet-katalytische cysteïnes. Om dit verder te onderzoeken zullen alkynderivaten van andere kinase remmers getest moeten worden.

Op basis van eerdere bevindingen werd verondersteld dat adductvorming alleen mogelijk is met ongesubstitueerd propargylamide, aangezien covalent adduct van de gezuiverde recombinante CysDUB UCHL3 met ubiquitine-ABPs niet werd gedetecteerd als er sprake was van een eindstandig gemethyleerd propargylamine (**Ub-2**) of een gedimethyleerd propargylamine (**Ub-5**). Om de rol van verschillende substituenten te onderzoeken, is in **Hoofdstuk 6** een uitbreid panel van propargylderivaten ingebouwd in fluorescente Rho-Ub-ABPs. Propargylamide-analogenen met substituenten op de terminale danwel interne alkynpositie waren inderdaad niet reactief met UCHL3, maar waren wel in staat om covalente adducten te vormen met andere CysDUB's. USP16 is een van de meest flexibele CysDUB's, en was in staat om een adduct te vormen met zowel Rho-Ub-**2** als Rho-Ub-**5**, maar ook hier zorgden de (grote en/of elektronen-donnerende) methylgroepen voor een verminderde snelheid van adductvorming door zowel sterische als elektronische effecten. De aanvaardbare positie en omvang van substituenten op het propargylamide waren specifiek voor het protease: leden van dezelfde CysDUB-familie lieten niet perse dezelfde selectiviteit zien, wat benadrukt dat er een belangrijke rol is voor het protease in de acceptatie van omvangrijke en/of elektronen-stuwende substituenten op het propargylamide. Reactiviteit met gedimethyleerde propargylamide in Rho-Ub-5 en aanwezigheid van beide deuteriums in adducten met gedeutereerde propargylamide in Rho-Ub-[D₂]-Prg tonen aan dat het reactiemechanisme niet via een reactief alleen intermediair verloopt (*mechanisme C*).

Tot slot zijn in **Hoofdstuk 7** de belangrijkste bevindingen uit dit proefschrift samengevat, met als voornaamste conclusie dat de toepasbaarheid van niet-geactiveerde alkynen breder is dan eerder werd aangenomen: niet alleen is het bruikbaar als elektrofiel in relatief kleine covalente remmers (<600 kDa), maar afhankelijk van het protease is het ook mogelijk om omvangrijke substituenten op het propargylamide te plaatsen. Sindsdien is het onderzoek voortgezet door andere onderzoeksgroepen: er zijn meerdere covalente cysteïneproteaseremmers met een niet-geactiveerd alkyn gepubliceerd, en het reactiemechanisme is verder geëvalueerd met behulp van berekeningen aan geavanceerde modellen. Samenvattend kunnen we stellen dat het niet-geactiveerde alkyn een optimale balans heeft van reactiviteit met het gewenste cysteïneprotease en selectiviteit ten opzichte van andere eiwitten.

Author Biography

Elma Mons was born on the 7th of December 1989 in Almere, the Netherlands. In 2008, she completed her pre-university VWO Gymnasium education (tracks: Nature&Technology and Nature&Health) at the Baken Park Lyceum (Almere, the Netherlands). From a young age she was exposed to – and interested in – the exact sciences and she decided to study Chemistry at the University of Amsterdam (Amsterdam, the Netherlands). In 2011, she obtained her Bachelors' degree *cum honore*: completing the honours program that allowed her to attend extracurricular courses, which she used for (neuro)pharmacology courses that were part of the biomedical curriculum to learn about drug–target interactions, and how systemic drugs know where to find their target. Next, she obtained her Masters' degree in Chemistry (track: Molecular Design, Synthesis, and Catalysis) at the University of Amsterdam (Amsterdam, the Netherlands) in 2014. The curriculum was tailored towards hands-on lab experience with two 6-month research internships. Her first internship was in the *Synthetic Organic Chemistry* group of Henk Hiemstra at the University of Amsterdam (Amsterdam, the Netherlands), where she worked on methodology for the enantioselective and organocatalytic synthesis of tetrahydroisoquinolines. She then applied for – and was awarded – multiple student travel fellowships to financially support her second internship in the *Organic Synthesis and Chemical Biology* group of Karl Gademann at the University of Basel (Basel, Switzerland). Here, she worked on the semisynthetic introduction of a bioorthogonal alkyne handle onto the natural product withanolide A for mode of action studies using chemical proteomics.

Upon returning to the Netherlands in 2014, Elma started her PhD research in the *Chemical Biology* group of Huib Ovaat the Netherlands Cancer Institute (Amsterdam, the Netherlands). In this multidisciplinary environment at the interface of chemistry and (medical) biology, chemical tools were used to study biological processes – particularly post-translational protein modification with ubiquitin. In 2016, the Ovaat and Neefjes groups moved to the Leiden University Medical Center (Leiden, the Netherlands) where she continued her PhD research on the recently discovered covalent thiol–alkyne reaction; exploring the versatility of nonactivated alkynes as (latent) electrophiles in covalent CatK inhibitors as well as activity-based probes (ABPs) targeting the catalytic cysteine of deubiquitinating enzymes. Presented with the challenge of evaluating compounds with a covalent binding mode, she focused on the (kinetic) evaluation of (ir)reversible covalent interactions and rational optimization of experimental assay conditions. The primary findings of her research are described in this dissertation.

As of October 2021, Elma is working as a postdoctoral researcher at Leiden University (Leiden, the Netherlands) in the *Biological Chemistry* group of Nathaniel Martin, where she is the lead scientist on the preclinical development of a promising antibiotic candidate for treatment of serious infections with (drug-resistant) Gram-positive pathogens.

List of Publications

Journal Articles

1. Mons, E.; Kim, R.Q.; Mulder, M.P.C. Technologies for Direct Detection of Covalent Protein–Drug Adducts. *Pharmaceuticals* **2023**, *16*, 547. doi:10.3390/ph16040547.
2. Mons, E.; Roet, S.; Kim, R.Q.; Mulder, M.P.C. A Comprehensive Guide for Assessing Covalent Inhibition in Enzymatic Assays Illustrated with Kinetic Simulations. *Curr. Protoc.* **2022**, *2*, e419. doi:10.1002/cpz1.419.
3. Mons, E.; Kim, R.Q.; van Doodewaerd, B.R.; van Veelen, P.A.; Mulder, M.P.C.; Ovaa, H. Exploring the Versatility of the Covalent Thiol–Alkyne Reaction with Substituted Propargyl Warheads: A Deciding Role for the Cysteine Protease. *J. Am. Chem. Soc.* **2021**, *143*, 6423–6433. doi:10.1021/jacs.0c10513.
4. Mons, E.; Jansen, I.D.C.; Loboda, J.; van Doodewaerd, B.R.; Hermans, J.; Verdoes, M.; van Boeckel, C.A.A.; van Veelen, P.A.; Turk, B.; Turk, D.; Ovaa, H. The Alkyne Moiety as a Latent Electrophile in Irreversible Covalent Small Molecule Inhibitors of Cathepsin K. *J. Am. Chem. Soc.* **2019**, *141*, 3507–3514. doi:10.1021/jacs.8b11027.
5. Crane, E.A.; Heydenreuter, W.; Beck, K.R.; Strajhar, P.; Vomacka, J.; Smiesko, M.; Mons, E.; Barth, L.; Neuburger, M.; Vedani, A.; Odermatt, A.; Sieber, S.A.; Gademann, K. Profiling Withanolide A for Therapeutic Targets in Neurodegenerative Diseases. *Bioorg. Med. Chem.* **2019**, *27*, 2508–2520. doi:10.1016/j.bmc.2019.03.022.
6. Mons, E.; Wanner, M.J.; Ingemann, S.; van Maarseveen, J.H.; Hiemstra, H. Organocatalytic Enantioselective Pictet–Spengler Reactions for the Syntheses of 1-Substituted 1,2,3,4-Tetrahydroisoquinolines. *J. Org. Chem.* **2014**, *79*, 7380–7390. doi:10.1021/jo501099h.

Patents

7. Ovaa, H.; Mons, M. W. E.; van Boeckel, S. Cathepsin Inhibitors. WO2019112426A1, 13 June, 2019.

Acknowledgements

The quest for a PhD cannot be completed without the support of a *fellowship*.

I owe my gratitude to my doctoral supervisor Huib Ovaa, who gave me the scientific freedom to investigate the thiol–alkyne reaction as I saw fit (even if that meant disappearing into a kinetic rabbit hole). Unfortunately, real life did not have a ‘happily ever after’ but I am sure he would have been proud to see the completion of this fairytale. I am also grateful for Sjaak Neefjes and the *Ovaa trinity* (Monique Mulder, Gerbrand van der Heden van Noort, and Paul Geurink), for stepping up after Huib passed away and keeping his legacy alive.

This dissertation would have had a closer resemblance to an encyclopedia than to a storybook, printed in multiple volumes and never truly reaching completion, if it were not for the guidance of my fairy *PhD support team* Monique Mulder and Robbert Kim. Their guidance stimulated me to focus on completing projects, and stop working on abandoned projects, which helped me defeat the seemingly unconquerable mountain of unfinished projects.

I would like to thank Olaf van Tellingen (NKI) and Hermen Overkleeft (LEI) for their support as members of the *OOA doctoral committee*, and Mario van der Stelt (LEI) for supervising the OTUD1 inhibitor project. Although the majority of their work did not make it into this dissertation, my bachelor students Robin van Veen (HSL) and Jill Hermans (HSL) helped with the chemical synthesis of various building blocks and inhibitors.

Special thanks to the past and current members of the Ovaa and Neefjes research groups for the productive and friendly environment: it was normal to help each other, while also having fun in- and outside of the lab, and I consider many of you to be friends rather than former co-workers. I would like to specifically acknowledge the support of Bjorn van Doodewaerd (LUMC) in the detection of covalent adducts by top-down MS, and the work of the protein facilities for expression and purification of (custom) enzymes: Patrick Celie (NKI), Angeliki Moutsopoulou (LUMC), and Robbert Kim (LUMC). It is impossible to overestimate the importance of the peptide facility that provided a steady supply of ubiquitin ABP precursors: Henk Hilkmann (NKI), Dris el Atmioui (NKI/LUMC), Cami Talavera (LUMC), Paul Hekking (LUMC), and Duco van Dalen (NKI). After struggling to survive our first months at the LUMC, our knight(ess) in shining armor Pauline Hoftijzer arrived and she rescued us from many stressful bureaucratic situations. Finally, we could always count on Lennert Janssen and Raymond Kooij for magically keeping the lab stocked and organized (and for handling the fall-out when the cleaning gnomes forgot about their duties after certain theme parties).

My journey into the kinetic rabbit hole of irreversible covalent inhibition would have ended prematurely without Sander Roet (NTNU): his kinetic simulation scripts – along with the long nightly discussions to explain the algebraic models in theoretical articles – were a turning point in my understanding of enzyme kinetics, and together we were able to mix the two ‘flavors’ of covalent inhibitor kinetics literature.* Finally, I would like to thank my friends and (extended) family. Many of you may not have contributed to, or even understand, the science in this dissertation but your moral support was crucial in the past decade.

* Literature pertaining covalent inhibitor kinetics came in two distinct flavors that were hardly ever mixed: the first flavor was a practical experimental protocol for medicinal scientists with a general equation or two for data analysis but devoid of details on assay condition restrictions or kinetic mechanisms. The second flavor was hardcore (enzyme) kinetics for theoretical scientists, with complex mathematical derivations of new (algebraic) models from which it is not always evident how this translates to experimental assay conditions. What was missing was a mix of these flavors: stepwise experimental protocols with the accompanying data analysis protocols, with emphasis on the connection between assay conditions and the algebraic model, and pointers on visual inspection of the (raw) data to identify violations of assumptions embedded in the algebraic models. Experimental data is often ‘contaminated’ by artefacts, and it consumes too much of precious assay reagents, but we were able to establish this link using kinetic simulation data.

All we have to decide is what to do
with the time that is given to us



J.R.R. Tolkien – The Fellowship of The Ring

